ALMA MATER STUDIORUM - UNIVERSITÀ DI BOLOGNA

SCUOLA DI IN INGEGNERIA E ARCHITETTURA

DICAM - DIPARTIMENTO DI INGEGNERIA CIVILE, AMBIENTALE E DEI MATERIALI

CORSO DI LAUREA MAGISTRALE IN INGEGNERIA CIVILE

TESI DI LAUREA

in

TECNINA DELLE COSTRUZIONI LM

SHEAR BEHAVIOUR OF REINFORCED CONCRETE SLAB UNDER CONCENTRATED LOAD: AN INVESTIGATION THROUGH NON-LINEAR AND SEQUENTIALLY LINEAR ANALYSIS

CANDIDATO
Luca Pieraccini

RELATORE
Chiar.mo Prof. Ing. Claudio Mazzotti

CORRELATORI
Prof. Dott. Ing. Joost Walraven
Dott. Ing. Max Hendriks
Ing. Arthur Slobbe

Anno Accademico 2012/13
Sessione II

Alla mia famiglia

ABSTRACT

La problematica della sicurezza di ponti e viadotti esistenti nei Paesi Bassi ha portato il Ministero dei Lavori Pubblici a finanziare una specifica campagna di studi mirata allo valutazione della risposta degli elementi che compongono queste infrastrutture. Pertanto, lo scopo della presente attività è quello di analizzare, mediante modellazione con Elementi Finiti ed il continuo confronto con risultati sperimentali, la risposta in esercizio di lastre in calcestruzzo armato sollecitate da carichi concentrati.
Tali elementi sono caratterizzati da un comportamento ed una crisi per taglio, la cui modellazione è, da un punto di vista computazionale, una sfida piuttosto ardua, a causa del comportamento fragile combinato ad effetti tridimensionali.

La modellazione numerica delle modalità di crisi è studiata attraverso la *Sequentially Linear Analysis* (SLA), metodo di soluzione agli Elementi Finiti alternativo ai classici approcci incrementali e iterativi. Il confronto tra le due differenti tecniche numeriche rappresenta uno dei primi sviluppi e raffronti in ambito tridimensionale ed è inoltre eseguito adottando come riferimento una delle numerose prove di laboratorio su lastre in calcestruzzo armato.
Il vantaggio della SLA è quello di evitare i ben noti problemi di convergenza tipici delle analisi non lineari, specificando direttamente l'incremento di danno sul singolo corpo della mesh attraverso la riduzione di rigidezze e resistenze nel particolare elemento finito, anziché imporre un incremento di carico o di spostamento sull'intera struttura.

Per la prima volta particolare attenzione è stata prestata ad alcuni aspetti specifici degli elementi lastra, quali modellazione delle condizioni di vincolo reali e sensitività della soluzione rispetto alla finezza della mesh.
Questa approfondita analisi di sensitività nei confronti dei più importanti parametri ha infatti evidenziato la forte incidenza dell'energia di frattura, della densità della mesh e del modello scelto sulla soluzione in termini di diagramma forza-spostamento, distribuzione dei quadri fessurativi e meccanismi di crisi per taglio.
Pur mostrando grande versatilità e potenziale, si è mostrato come il codice SLA necessiti di ulteriori sviluppi in merito alla modellazione di differenti condizioni di carico simultanee (costanti e proporzionali) e del comportamento softening di materiali fragili (come il calcestruzzo) in ambito tridimensionale, al fine di ampliare i propri orizzonti a questi nuovi contesti di studio.

Parole chiave: Sequentially Linear Analysis, shear behaviour, reinforced concrete slabs, 3D modeling.

ABSTRACT

The assessment of safety in existing bridges and viaducts led the Ministry of Public Works of the Netherlands to finance a specific campaing aimed at the study of the response of the elements of these infrastructures. Therefore, this activity is focused on the investigation of the behaviour of reinforced concrete slabs under concentrated loads, adopting finite element modeling and comparison with experimental results.
These elements are characterized by shear behaviour and crisi, whose modeling is, from a computational point of view, a hard challeng, due to the brittle behavior combined with three-dimensional effects.

The numerical modeling of the failure is studied through *Sequentially Linear Analysis* (SLA), an alternative Finite Element method, with respect to traditional incremental and iterative approaches. The comparison between the two different numerical techniques represents one of the first works and comparisons in a three-dimensional environment. It's carried out adopting one of the experimental test executed on reinforced concrete slabs as well.
The advantage of the SLA is to avoid the well known problems of convergence of typical non-linear analysis, by directly specifying a damage increment, in terms of reduction of stiffness and resistance in particular finite element, instead of load or displacement increasing on the whole structure
.
For the first time, particular attention has been paid to specific aspects of the slabs, like an accurate constraints modeling and sensitivity of the solution with respect to the mesh density. This detailed analysis with respect to the main parameters proofed a strong influence of the tensile fracture energy, mesh density and chosen model on the solution in terms of force-displacement diagram, distribution of the crack patterns and shear failure mode.
The SLA showed a great potential, but it requires a further developments for what regards two aspects of modeling: load conditions (constant and proportional loads) and softening behaviour of brittle materials (like concrete) in the three-dimensional field, in order to widen its horizons in these new contexts of study.

Key-words: Sequentially Linear Analysis, shear behaviour, reinforced concrete slabs, 3D modeling.

Contents:

1. INTRODUCTION

The present Master Thesis has been developed from September 2012 until March 2013, in the Technische Universiteit of Delft, working under the supervision of Dr.Ir.M.A.N Hendriks and Ir. A.Slobbe of the Computational Mechanics group.
The work is mainly focused on the development of the Finite Element software TNO Diana®, in particular on the implementation and improving of the *Sequentially Linear Analysis* in three-dimension. On the other hand, it makes part of a wide research activity carried out by the TU Delft, collaborating with the Dutch Ministry of Public Works, regarding the project "Assessing of the bearing capacity of existing bridges in the Netherlands".
This Master Thesis regards the numerical investigation about the "Shear Capacity and Behaviour of Reinforced Concrete Slabs subjected to a Concentrated Load Close to the Support", executed using *Diana*, *Nonlinear Finite Element* (NLFE) and *Sequentially Linear* (SL) Analysis.

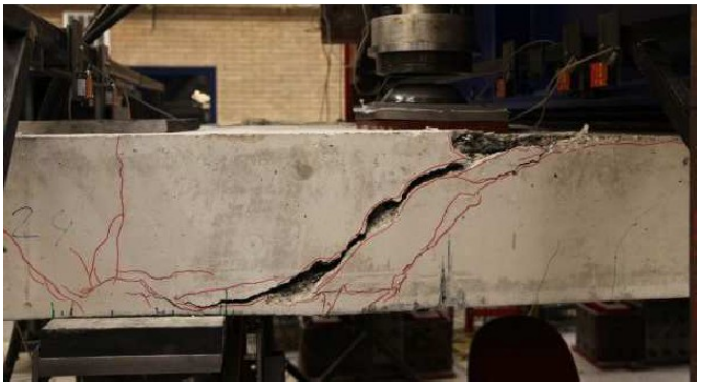

Shear crack in a reinforced concrete slab under concentrated load

The whole work has been carried out in different parts, that correspond to the sections of the current report.
The first part consists in a review of the theoretical background of the Sequentially Linear Analysis for solid elements. A description of the models used in the implementation of this method is reported, in order to represent the constitutive relationships of the materials, their response during and after the cracking process and their Poisson and shear behaviour. This review is fundamental to understand the procedure of the definition of the so called *saw-tooth curve*, essential element for the SLA.
The second part contains a general overview about shear behavior of real structures in reinforced concrete and reports the two possible main alternative responses and crisis mechanisms: One-Way (or Wide Beam) action and Two- Way (or Punching) action. In this section results of experimental tests are reported, in order to better explain the expected development of cracking pattern, estimate the shear bearing capacity and the failure mechanism of concrete slabs. Every consideration will be related to the indications that the main Building Codes provide for design and verification of reinforced concrete slabs.

The third and the forth part contain an extensive description of procedures and results of the experimental survey on the reinforced concrete slab S25T1, executed in StevinLab-II (TU Delft) and the relative study through numerical solutor adopting the *Nonlinear* and *Sequentially Linear Analysis*. Then, analytical and experimental results will be compared, in order to verify the reliability of both Finite Element Method in predicting the real response of the real specimen. Exactly through this comparison is possible to evaluate the reliability of the classical Non-Linear Newton-Raphson and to check the sensitivity of the SLA method.
Furthermore, an investigation above all the aspects of the methods will be presented: difficulty in pre-processing, accuracy of the solutions and computational cost, i.e. the time needed to get to satisfactory conclusions of the analyses.
Particularly, it will focus attention regard to the variation of all the most important parameters used in the Finite Element model.

The last part contains the main considerations regarding to the problems encountered during the entire work, the advantages and the limits of SLA in respect with the other more developed FE methods and an evaluation of the present potentialities of the SLA for structural problems.

1.1 General context of study

The last century has witnessed a quick development of the industrial and commercial activities in the Netherlands and the problem of mobility of people, goods and resources weighs on the infrastructures all over the country.
Bridges assure the continuity of highways, roads, railways and other important infrastructures, so they result strategic components of the transport network of the Netherlands.

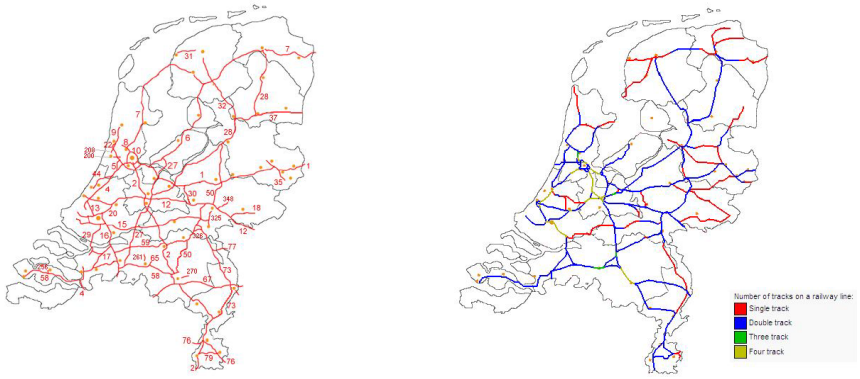

(a) *(b)*

Distribution of highways (a) and railways (b) all over the territory of the Netherlands

A great part of the Dutch bridges is characterized by structures made, designed and realized with reinforced concrete many decades ago. Either for an underestimation in the prevision of the increase of the traffic loads, either for unavoidable decay of the structural and material quality, an assessment of the present condition of the bridge structures seems to be necessary.
To have an immediate idea of the importance of this problem, the following table contains an estimation of the number of the Dutch bridges that causes concern about their actual bearing capacity and the next figures represent three of the most strategic bridges of the Netherlands, subjected to the same safety problem:

Structures	Number
Bridges in Highway	1515
Bridges in main roads	930
Other bridges	711
Tunnels	544
Acqueducts	8
Ecoducts	7
All toghether	**3715**

Number and categories of Dutch bridges
whose actual bearing capacity should be precisely evaluated

The Zeeland Bridge (Zeelandbrug) is the longest bridge in the Netherlands. With a structure made mainly of reinforced concrete and a total length of 5022 m, it connects the islands of Schouwen-Duiveland and Noord-Beveland in the province of Zeeland. The Zeeland Bridge was built between 1963 and 1965.

The Waalbrug is an arch bridge, with a full length of 604 m, over the Waal River in Nijmegen, Netherlands. The bridge was opened in 1936 and in the last years it is affected by large traffic jams during the rush hours. Because of its crucial aspect in regional traffic it has been difficult to renovate the bridge.

The John S. Thompson-Brug is a bridge over the Maas River, in the province of North Brabant in the Netherlands. The bridge was built in 1929 as part of the main road between 's-Hertogenbosch and Nijmegen. It still carries that road, now signed provincial route N324.

The national program of "Assessing the bearing capacity of existing bridges in the Netherlands" [1] has been promoted mainly on the basis of this concern about the safety of the Dutch bridges by the Dutch Ministry of Public Works, involving several private and public organizations, like the Technische Universiteit of Delft.
This study classifies the existing concrete bridges in the Netherlands in six different categories, whose prototypes are:

1. Bridges composed by reinforced solid slabs with $\frac{d}{l} < \frac{1}{10}$ built before 1950 and with $\frac{d}{l} < \frac{1}{15}$ built before 1975;
2. Bridges composed by box girders;
3. Bridges made of precast pre-stressed I-beams with thin webs;
4. Bridges made of T-beams with very thin webs;
5. Crossing bridges;
6. Tunnel roofs.

Stresses on the structures and the residual bearing capacities have to be evaluated as main parameters to determine the level of safety about the various typologies of existing bridge.
Analysis regarding the development of traffic intensity and the increase of the traffic load and the axial load on the bridge structure are a crucial point in order to estimate the entity of stress on the bridges. They are focused on the increase of the traffic, that in the last decades changed first in quality, and secondly in quantity.
On the other side, the research is focalized on the evaluation of the bearing capacity of the existing bridges, through surveys on the following aspects:

- Behavior of higher concrete strength after decades of hydration;
- Evaluation of the sustainability of the loading shear effect on a structural element;
- Estimation of the more favorable shear effect (wide beam shear or punching behavior by virtue of redistribution or dome effect);
- Assessment of the reliability of the prediction of the behavior of structural elements by FEM calculation;
- Utility of proofs loading on real structures.

The present activity is interested in the first class of existing bridges, therefore structures composed by reinforced concrete slabs with $\frac{d}{l} < \frac{1}{10}$ built before 1950 and with $\frac{d}{l} < \frac{1}{15}$ built before 1975) and in the third and fourth aspects of the survey.
In fact this Master Thesis aims to get a global sight on the capacity of Finite Elements Methods (fourth point), in predicting the most important features of the shear capacity and behavior in reinforced concrete slabs (third point), through a comparison with observation made by laboratory tests on similar elements.
An experimental campaigns performed in StevinLab-II regards the behavior of reinforced concrete slabs without shear reinforcements under concentrated loads.
The layout and the dimensions of the reinforced concrete slabs are representative of the most common elements used in a bridge structure; instead the applied concentrated load is limited on an

area of $200x200\ mm$ and $300x300\ mm$. Punching shear with these loads is usually treated in manner similar to punching by a column. It has to be noted that punching shear test performed with a concentrated load simulating a vehicle wheel with pneumatic pressure showed a strong difference. Indeed, it appears that the punching shear with a wheel with pneumatic pressure is less critical: the curvatures tend to be distributed over the surface of applied load rather than concentrated near the edge of the column [2].
Finally, the position of the loading area is varied on various specimens, to model all the possible loading conditions that a slab can bear.

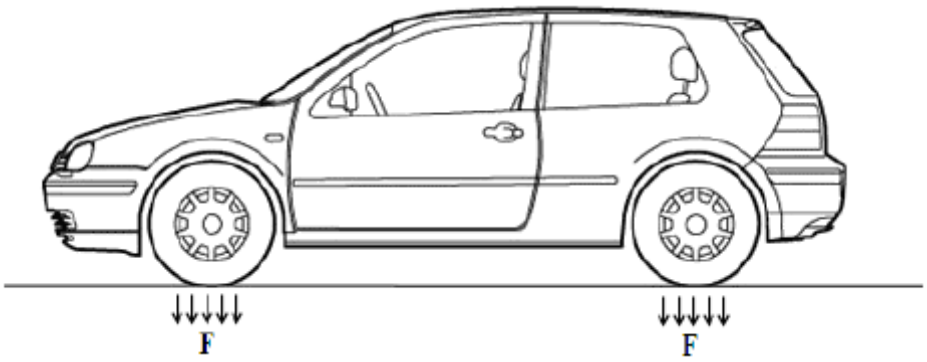

Approximated scheme of the concentrated axial forces applied by a motor vehicle on the road surface

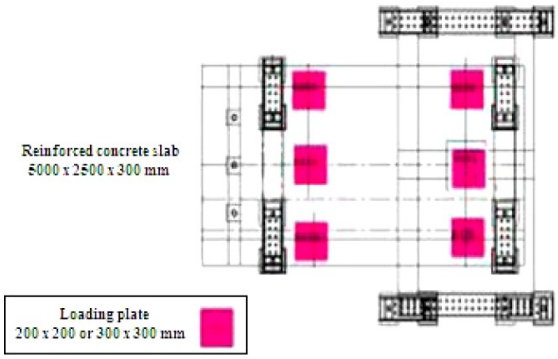

Layout of the loading laboratory tests on reinforced concrete slabs subjected to concentrated loads (the violet squares represent the possible alternative positions of the loading plate)

Under concentrated loads, the response of the reinforced concrete element is characterized by the prevailing features of the shear behavior.
After collecting the experimental data in terms of load-displacement diagrams, distribution of cracking pattern on the surfaces, occurred failure mechanism, the FEM modeling of the slab will be executed.
Then, the results of the computational analyses will be also used as an evaluation of the reliability of the classical Nonlinear approach and of the new Sequentially Linear method implemented in the software *Diana*.

1.2 Purposes and objectives

The present work follows a series of numerical analysis focused on the prediction of the behaviour of bi-dimensional reinforced concrete slabs without shear reinforcement (specimens), in terms of structural response and failure mode: *load-displacement diagram* and *cracking behaviour*.
The present work aims to:

- investigate a new experimental test carried on a reinforced concrete slab;
- study the mesh sensitivity on the solution;
- provide two different models;
- adopt and compare two numerical methods: *Non-Linear* and *Sequentially Linear Analysis*;
- evaluate the sensitivity of the model respect with the *Tensile Fracture Energy* and other parameters.

For the present activity, specimen $S25T1$ is chosen among a large amount of experimental tests carried on in the StevinLab-II. It does not present line load.
The mesh sensitivity will be studied by increasing the amount of elements on the thickness of the model; while the work on the two different models will be carried on in order to study the effects and the consequences on the solution due to a structural compromise in terms of modeling the slab constraints: "continuous support line" with Dywidag bars and full clamped side. Finally, the sensitivity of the models on the main unknown parameters will be studied.

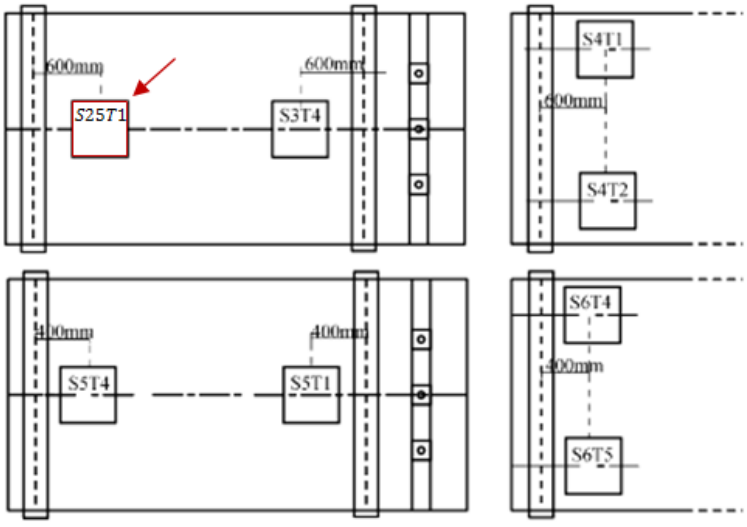

Experimental tests performed in StevinLab-II and selected case of study (red arrow)

2. SEQUENTUALLY LINEAR ANALYSIS FOR SOLID ELEMENTS

2.1 Review of Finite Element Method

Computational methods, like Finite Element Methods, have become useful and indispensable tools for studies, design and verifications of structures in the field of Civil and Structural Engineering. Currently the most commonly method for Finite Elements is certainly the Nonlinear Analysis (NLFEA).

Techniques for nonlinear analysis have been enhanced significantly via improved solution procedures, extended finite element techniques and increased robustness of constitutive models [3].

When analyzing three-dimensional problems with nonlinear finite element analysis (NLFEA) often problems like bifurcation, multiple equilibrium paths and divergence of the solution occur. In particular, cases subjected to tension softening, cracking (like the fracture for brittle material or concrete) and crushing tend to cause these problems.

Indeed, the load-displacement diagram of reinforced concrete structure, such as beams, plates, shells and spatial structures often shows a number of local peaks and snap-backs or valleys associated with the brittle cracking and subsequent stress-redistribution. By adopting softening models, negative tangent stiffness is used and numerical instability, singularity and divergence of the incremental-iterative procedure could occur.

In order to overcome these problems the promising alternative Sequentially Linear Analysis (SLA) method has been developed for three-dimensional cases [4] [5].

In fact, the NLFEA are based on incremental-iterative procedures, i.e. the behavior of one element is evaluated *step-by-step* through subsequent increments of the loads applied on the element and, for each loading step several iterations can be executed, until the satisfaction of certain convergence criteria, fixed in order to reduce the difference between the obtained and the expected results.

In presence of negative stiffness, the nature of the procedure itself produces the just mentioned numerical problems.

To try to solve such problems, users have to resort to arc-length or indirect control schemes: for practicing engineers this is often impracticable, especially when the bifurcations are multiple, the peaks irregular or the snap-backs sharp.

It has been demonstrated that Sequentially Linear Analysis is an alternative to Non-Linear Finite Element Analysis of structures when these kinds of problems arise, like two-dimensional fracture problems [6].

Here, incremental-iterative procedure is replaced by a series of linear analyses used to model the nonlinear behavior of the structure. By directly specifying a damage increment in each linear analysis, e.g. decreasing Young's modulus and tensile strength at the integration point of elements, extensive iterations within the load or displacement increment can be avoided.

To demonstrate its attractiveness, Sequential Linear Analyses are performed, first on tested shear critical reinforced beam without shear reinforcement inside a 2D environment, and then on three-dimensional reinforced concrete slabs without shear reinforcement. These structures are generally

known to behave extremely brittle e therefore difficult to analyze with standard finite element analysis.
At the moment, although the SLA approach has proven its robustness and promising potential already for two-dimensional cases, it has not yet been developed for three-dimensional problems. This innovative study is therefore focused on the extension and implementation of new features of the Sequentially Linear Analysis method to 3D as an alternative to address difficulty of nonlinear fracture behavior. Here, it has to be focused attention on the derivation of orthotropic stress-strain relation for 3D and the discretization of the constitutive relation by saw-tooth.

2.2 Saw-tooth laws for concrete in tension: overall event-by event procedure

The locally brittle snap-type response of many reinforced concrete structures inspired the idea to capture brittle events directly rather than trying to iterate around them in a Newton-Raphson scheme. So, a critical event is traced by directly capturing fracture damage at micro-scale, while modeling the structural response at macro-scale. Subsequently a secant restart is made from the origin for tracing the next critical event. By capturing these fracture "event" directly through damage increments, there is no need to iterate around them like in the classic Newton-Raphson solution procedure.
Hence, the procedure is *sequential* rather than *incremental*.
Moreover, this new method can be interpreted as setting the tolerance at local constitutive level, rather than setting the convergence at global level for nonlinear analysis.
Another interesting feature of the SLA is that it circumvents bifurcation problems [5]. Indeed, the Newton-Raphson method allows multiple integration points to crack simultaneously within the load increment, while in the SLA approach only one integration is allowed to crack at time, i.e., movement from elastic to softening branch.
So, the sequence of critical "events" govern the load-displacement response. To this aim, the softening diagram is replaced by a saw-tooth curve and linear analyses are carried out sequentially.

In fact the Sequentially Linear approach approximates the constitutive stress–strain relationship using a series of saw-teeth which maintain a positive tangent stiffness, as one can see in the following figures. Linear analyses are repeated, each with a reduced positive stiffness, until the global analysis is complete [4]. Thus, the negative tangent stiffness which is characteristic of concrete and masonry softening curves, and can be detrimental to convergence, is evaded entirely.
A further advantage is that the structure can be discretized using standard elastic continuum elements.
Specifically, the modeling procedure is implemented as follows:

- apply a reference proportional load F;
- calculate the principal stresses, σ_1 , through a linear-elastic static analysis;
- determine the critical integration point. This is the point for which the stress level divided by its current strength $f^+{}_{ti}$ is the largest in the whole structure;
- determine the critical load multiplier $\lambda_{crit} = \frac{f^+{}_{ti}}{\sigma_1}$, belonging to the critical integration point, i.e. the current strength divide by the stress level;

- scale the reference load proportionally using the critical load multiplier $\lambda_{crit} \cdot F$ and determine the stress-strain state again;
- increase the damage in the critical integration point by reducing the stiffness and strength according to the saw-tooth tensile based constitutive relation;
- repeat this cycle of step continuously by updating the material properties of a single integration point after each cycle, until the damage has spread sufficiently into the structure;
- the nonlinear response is extracted by linking consecutively the result of each cycle.

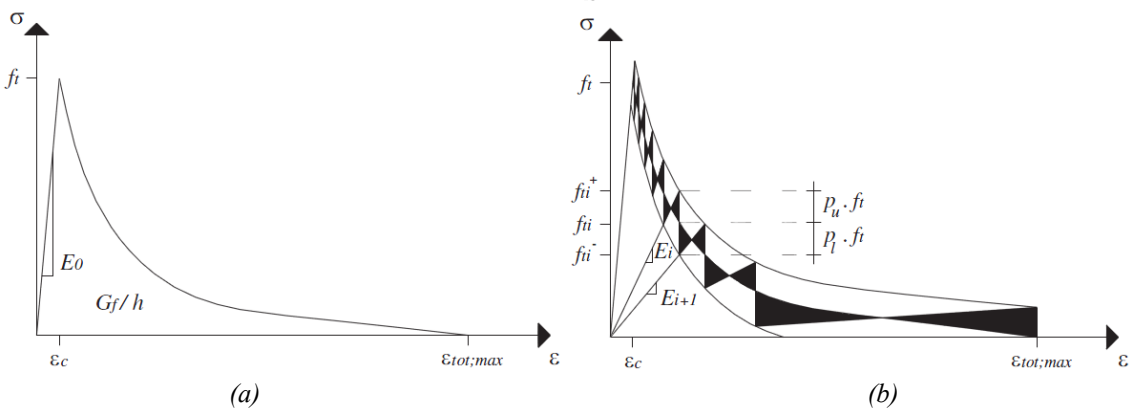

The stress-strain curve for nonlinear -softening (a) and the consistent saw-tooth diagram (b)

The tensile softening stress-strain curve *(a)* is defined by Young's modulus E, the tensile strength f_t, the shape of the diagram, and the area under the diagram. The area under the diagram represents the tensile fracture energy G_f divided by the numerical crack bandwidth h, i.e. the anticipated width of the zone where cracking occurs it is a discretization parameter associated with the size, orientation and integration scheme of the finite element.

Thanks to new developments, the consistent saw-tooth diagram can be optimized also for generic nonlinear tension softening curve. The formulation applies to any shape of any stress-strain constitutive laws, so it permit to model all material components of a structure in a consistent way [7].

Indeed, this generalized method can be applied not only to a nonlinear tension softening curve, but also to others, e.g. hardening curves for concrete in compression and/or steel plasticity curves in tension and in compression.

As shown in the upper image, a strength range $p_u \cdot f_t \div p_l \cdot f_t$ is defined, as a percentage of the maximum tensile strength. A band or "strip" is introduced into the softening diagram, delimited by two curves parallel and equidistant to the original diagram. The number of required teeth (N) and the values of the Young's modulus (E_i) and the tensile strength (f_{ti}) at the current stage i in the saw-tooth diagram are automatically obtained as values depending on this strength range: p is an input variable chosen by the user which modulates the fineness of the saw-tooth approximation.

This is interpreted as a pre-set "ripple curve": the upper curve of the band contains the tensile strength ${f_t}^+$ of each saw-tooth and the lower curve contains the corresponding ${f_t}^-$. These ${f_t}^-$ values are only used to determine the secant lines or reduced stiffness $E_i, E_{i+1}, \dots, E_n$, where the subscript n indicates a pre-set number of saw-teeth. The ${f_t}^+$ values can be found by the determination of the point of intersection between the secant lines and the upper curve of the band.

So, once the strength percentages p_u and p_l are known, the values f_t^+, f_t^- and the reduced stiffness can be calculated successively for each saw-tooth.
For the generation of a proper saw-tooth approximation three condition have to be satisfied: (1) the area underneath the saw-tooth curve $\left(G_f/h\right)_{swt}$ and (2) the ultimate strain of the saw-tooth curve $\left(\epsilon_{tot,max}\right)_{swt}$ should be identical to the corresponding area G_f/h and ultimate strain $\epsilon_{tot,max}$ of the adopted stress-strain base curve respectively. The dissipated energy is conserved, as over- and under-estimation of the area underneath the graph are canceled out by consecutive teeth. This is displayed in figure *(b)*, where the pairs of black triangles, above and below the softening curve, are of equal area.

Furthermore, f_t^- of the last saw-tooth should be equal to zero (3) in order to avoid a contribution of "negative" areas to the calculation of $\left(G_f/h\right)_{swt}$. Combining these three conditions in one objective function leads to:

$$f(p_u, p_l) = \left(\frac{\left(G_f/h\right)_{swt}}{G_f/h} - 1\right)^2 + \left(\frac{\left(\epsilon_{tot,max}\right)_{swt}}{\epsilon_{tot,max}} - 1\right)^2 + \left(\frac{f_{t,n}^-}{f_t}\right)^2 = 0$$

in which $\left(G_f/h\right)_{swt}$ and $\left(\epsilon_{tot,max}\right)_{swt}$ are function of p_u and p_l.
Actually, the saw-tooth curve generation can be considered as a two-dimensional minimization problem. To solve the problem an iterative procedure is adopted in which the steering parameters p_u and p_l are the unknown. They need not to be equal and user defined. The algorithm used for this function minimization is the Downhill Simplex method.
It has to be noted that with the "ripple" saw-tooth approximation a certain overshoot of f_t occured, as can be seen in the previous picture. This arises from the requirement that the dissipated energy has to be kept invariant to the fracture energy G_f/h. With this "ripple" approach and the fact that the area underneath the saw-tooth curve and the ultimate strain $\varepsilon_{tot,max}$ are adjusted to the crack bandwidth h, mesh-size regularization is achieved.
Now, one can be better contextualized how the "ripple" approach can be interpreted as setting the tolerance at local constitutive level for SLA, rather than setting the convergence tolerance at global level for NLFEA, just using the strength percentages p_u and p_l [6].

2.3 Crack model

2.3.1 Total Strain smeared crack

Extending SLA to three-dimensional cases requires to model the fracturing behavior of quasi-brittle materials like reinforced concrete, a large number of different approaches were developed: crack models can be subdivided into continuum, discontinuum (discrete) and mixed models. The continuum based models can be further subdivided into decomposed and total strain based smeared crack models, plasticity based crack models and other continuum approaches [8].

SLA is currently based upon a continuum fracture model, namely the *total strain smeared crack concept* [9] and the three-dimensional extension of this model is based on the theory proposed by Selby & Vecchio [10].
In a smeared crack model a crack is not represented by just a single crack, but it occurs over the element area. In this way, the topology of the original finite element is conserved. Especially in analyses of adequately reinforced structures, the smeared crack concept makes sense, because the resulting cracks are well distributed and they can occur everywhere in the manufactures.
Moreover, the total strain model, as used in SLA, describes stress as a function of the total strain:

$$\varepsilon_{tot} = \varepsilon_{el} + \varepsilon_{cr}$$

it is composed by a first part of elastic strain, relatively to the portion of material that has still an elastic behavior, and a second part of crack strain.
After cracking the stress-strain relationships are evaluated in a coordinate system which is fixed upon the crack direction, resulting very appealing to the physical nature of the problem.

The *stress-total strain* relation of the material can be described in two different coordinate system: fixed (or global) and rotating (or local) system. The first crack that has origin in the finite element individuates the reference system *nts* and these directions are constant in all the process of deformation of the element. The current SLA-program adopts a *fixed crack model* (with orthogonal secondary cracking) that preserves a fixed orientation of the crack during the entire process: after a crack formation the transformation matrix N is kept constant.

During the deformation, the strain vector ε_{xyz} in the element coordinate system *xyz* is updated with the strain increment $\Delta\varepsilon_{xyz}$ according to:

$$^{t+\Delta t}_{i+1}\varepsilon_{xyz} = {}^{t}\varepsilon_{xyz} + {}^{t+\Delta t}_{i+1}\Delta\varepsilon_{xyz}$$

which is transformed to the strain vector in the crack directions with the strain transformation matrix $\boldsymbol{T}$,

$$^{t+\Delta t}_{i+1}\varepsilon_{nst} = \boldsymbol{T_\varepsilon}\, ^{t+\Delta t}_{i+1}\Delta\varepsilon_{xyz}$$

In a fixed model the strain transformation matrix N is fixed upon the cracking, so it will be kept constant.
The strain transformation matrix is determined by calculating the eigenvectors of the strain tensor, e.g. with the Jacobi method [11].

In case of non-proportional loading, like self-weight and pre-stress load, the same procedure can be applied, but the identification of the critical multiplier λ_{crit} becomes more complex. The subject is still under development.
The aforementioned SLA-procedure that uses a scaled loading procedure allows only one integration point to change its status from elastic to softening at a time. Contrary to regular nonlinear finite element analysis this new approach circumvents bifurcation problems, as is shown

in [6]. In NLFEA, the use of load increments implies that multiple integration points may crack simultaneously, through which the local stiffnesses at the these points switches from positive to negative, following softening constitutive laws for quasi-brittle materials. As a consequence of multiple softening points, the system of equation can have more than one solution and so alternative equilibrium states of bifurcations of the equilibrium path. At a bifurcation point a loss of uniqueness of the incremental-iterative solution procedure occurs, and although this incremental-iterative procedure can converge to one of possible equilibrium states, it will not automatically pick up the most critical or the lowest equilibrium path. SLA avoids this problem and via the sequence of events always a unique solution is achieved.

The strain tensor results:

$$\boldsymbol{E} = \begin{bmatrix} \varepsilon_{xx} & \varepsilon_{xy} & \varepsilon_{xz} \\ \varepsilon_{yx} & \varepsilon_{yy} & \varepsilon_{yz} \\ \varepsilon_{zx} & \varepsilon_{zy} & \varepsilon_{zz} \end{bmatrix}$$

The eigenvectors are stored in the rotation matrix **R** which reads:

$$\boldsymbol{R} = [\boldsymbol{n}\ \boldsymbol{s}\ \boldsymbol{t}] = \begin{bmatrix} c_{xn} & c_{xs} & c_{xt} \\ c_{yn} & c_{ys} & c_{yt} \\ c_{zn} & c_{zs} & c_{zt} \end{bmatrix}$$

with $c_{ij} = cos\emptyset_{ij}$ the cosine between the *i* axis and the *j* axis.
The strain transformation matrix $\boldsymbol{T_\varepsilon}$ is then calculated by substituting the appropriate values:

$$\boldsymbol{T_\varepsilon} = \begin{bmatrix} c_{xn}^2 & c_{yn}^2 & c_{zn}^2 c_{xn} c_{yn} & c_{yn} c_{zn} & c_{zn} c_{xn} \\ c_{xs}^2 & c_{ys}^2 & c_{zs}^2\, c_{xs} c_{ys} & c_{ys} c_{zs} & c_{zs} c_{xs} \\ c_{xt}^2 & c_{yt}^2 & c_{zt}^2\, c_{xt} c_{yt} & c_{yt} c_{zt} & c_{zt} c_{xt} \\ 2c_{xn}c_{xs} & 2c_{ys}c_{yn} & c_{xn}c_{ys} + c_{xs}c_{yn} & c_{zn}c_{xs} + c_{xn}c_{zs} & c_{yn}c_{zs} + c_{yn}c_{zn} \quad c_{zn}c_{xn} + c_{xn}c_{zs} \\ 2c_{xs}c_{xt} & 2c_{yn}c_{yt} & c_{xs}c_{yt} + c_{ys}c_{xt} & c_{yn}c_{zt} + c_{zs}c_{yt} & c_{ys}c_{zt} + c_{zs}c_{yt} \quad c_{zs}c_{yt} + c_{zt}c_{xs} \\ 2c_{xn}c_{xt} & 2c_{yt}c_{ys} & c_{xt}c_{yn} + c_{yt}c_{xn} & c_{yt}c_{zn} + c_{zt}c_{yn} & c_{yt}c_{zn} + c_{yn}c_{zt} \quad c_{zt}c_{xn} + c_{xt}c_{zn} \end{bmatrix}$$

in a general three-dimensional stress situation. Different stress situations need an appropriate sub-matrix. Then the constitutive model is formulated in the crack coordinate system as will be explained in the next section.

2.3.2 Constitutive stress-strain relation

The constitutive relationship used in the Sequentially Linear Analysis, is linear-elastic for every step of the analysis, i.e. before and after every event of damage in any generic integration point in the mesh.
Therefore the constitutive model of the generalized *Hooke's laws* is used.
In case of a generic material, anisotropic and asymmetric, the compact expression of the Hooke's law in compliance form is:

$$\boldsymbol{\varepsilon} = \boldsymbol{C\sigma} \qquad \text{or} \qquad \varepsilon_{ij} = C_{ijhk}\sigma_{hk}$$

where $i, j, h, k = 1, 2, \ldots, 6$ for 3-dimensional elements.
In this expression the number of independent variables is 81, which can be reduced by assigning some properties to the material, like homogeneity and isotropy.
In the case study it is assumed that the material acts *isotropic* before any damage will occur, i.e. in the uncracked stage, and *orthotropic* after the first crack is occurred. In fact, on the basis of the Sequentially Linear Analysis concepts, as soon as a crack forms the generic *i*-direction, the elastic properties of the material change only in this direction, independently from the other directions. Successively crack can occur in the other two orthogonal directions, leading at the end to an orthotropic behavior of the material.
On the basis of the theory of the mechanics of continuum, the Hooke's laws, in compliance form, for an isotropic material are:

$$\begin{bmatrix} \varepsilon_{xx} \\ \varepsilon_{yy} \\ \varepsilon_{zz} \\ \varepsilon_{xy} \\ \varepsilon_{yz} \\ \varepsilon_{xz} \end{bmatrix} = \begin{bmatrix} 1 & -v & -v & & & \\ -v & 1 & -v & & 0 & \\ -v & -v & 1 & & & \\ & & & 2(1+v) & 0 & 0 \\ & 0 & & 0 & 2(1+v) & 0 \\ & & & 0 & 0 & 2(1+v) \end{bmatrix} \begin{bmatrix} \sigma_{xx} \\ \sigma_{yy} \\ \sigma_{zz} \\ \sigma_{xy} \\ \sigma_{yz} \\ \sigma_{xz} \end{bmatrix}$$

Where E is the Young's modulus, v is the Poisson's ratio and the tangential stiffness modulus is dependent from the two and can be calculated as:

$$G = \frac{E}{2(1+v)}$$

For rotational equilibrium is possible to determine the relations between stresses with same ij indices:

$$\sigma_{xy} = \sigma_{yx}, \sigma_{xz} = \sigma_{zx}, \sigma_{zy} = \sigma_{yz}$$

It is noted that for isotropic material the independent variables are only the Young's modulus and the Poisson's ratio (E and v).
The constitutive relationship for an orthotropic behavior of the material are determined starting from the general relationship and assigning further properties. It is remembered that, by definition, a 3-dimenisional orthotropic material has 3 orthogonal planes of symmetry, where material properties are independent of direction within each plane. This model well performs the correspondent behaviour of the reinforced concrete when cracking occurs.
The constitutive stress-strain relationship, in compliance form, for an orthotropic material is:

$$\begin{bmatrix}\varepsilon_{xx}\\ \varepsilon_{yy}\\ \varepsilon_{zz}\\ \varepsilon_{xy}\\ \varepsilon_{yz}\\ \varepsilon_{xz}\end{bmatrix} = \begin{bmatrix} \frac{1}{E_x} & \frac{-v_{xy}}{E_y} & \frac{-v_{xz}}{E_z} & & & \\ \frac{-v_{yx}}{E_x} & \frac{1}{E_y} & \frac{-v_{yz}}{E_z} & & 0 & \\ \frac{-v_{zx}}{E_x} & \frac{-v_{zy}}{E_y} & \frac{1}{E_z} & & & \\ & & & \frac{1}{G_{xy}} & 0 & 0 \\ & 0 & & 0 & \frac{1}{G_{yz}} & 0 \\ & & & 0 & 0 & \frac{1}{G_{xz}} \end{bmatrix} \begin{bmatrix}\sigma_{xx}\\ \sigma_{yy}\\ \sigma_{zz}\\ \sigma_{xy}\\ \sigma_{yz}\\ \sigma_{xz}\end{bmatrix}$$

where, due to the aforementioned equilibrium considerations, the stress-strain tensor is symmetric, therefore:

$$\frac{v_{xy}}{E_y} = \frac{v_{yx}}{E_x}, \frac{v_{yz}}{E_z} = \frac{v_{zy}}{E_y}, \frac{v_{zx}}{E_x} = \frac{v_{xz}}{E_z}$$

For an orthotropic material, the constitutive relationship is completely defined by 9 independent variables, i.e. 3 Young's modules E_i, 3 Poisson's ratios v_{ij} and 3 shear modules G_{ij}.
While the Young's modules and the shear modules are representative of normal and transversal stiffness, the Poisson's ratios relative to the generic *i*- , *j*- and *k*-directions represent a different effect of the stresses on the material.
The normal stress σ_{ii}, on the plane normal to the *i*-direction, acting in the same *i*-direction, produces an axial strain on its own direction and also 2 other axial strains in the 2 orthogonal directions (*j* and *k*):

$$\varepsilon_{ii} = \frac{\sigma_{ii}}{E_i}, \varepsilon_{jj} = -v_{ji}\frac{\sigma_{ii}}{E_i}, \varepsilon_{kk} = -v_{ki}\frac{\sigma_{ii}}{E_i}$$

It is noted that a tensile (positive) stress σ_{ii} produces an extension (positive strain) only on the same direction, while in the other two orthogonal direction contractions (negative strains) occur. This phenomena is called "Poisson's effect".
These considerations are valid also for stresses applied in *j* and *k*.
In order to obtain a formulation of the constitutive model that can be used in the implementation of a Finite Element Method, the constitutive relationships are inverted, passing from the *Compatibility form* to the *Stiffness form*, more handy for the purpose of the study.
In compact notation results:

Congruency form *Stiffness form*

$$\boldsymbol{\varepsilon = C\sigma} \quad \rightarrow \quad \boldsymbol{\sigma = C^{-1}\varepsilon = D\varepsilon}$$

where $\boldsymbol{D = C^{-1}}$ is the stiffness matrix and, for an orthotropic material, is expressed as:

$$F\begin{bmatrix} (v_{yz}^2\frac{E_y}{E_z}-1)E_x & -(v_{xy}+v_{yz}v_{zx}\frac{E_y}{E_x})E_x & -(v_{xy}v_{yz}+v_{xz}\frac{E_y}{E_x})E_x & & & \\ -(v_{zx}v_{yz}+v_{xy}\frac{E_x}{E_y})E_y & (v_{zx}^2\frac{E_z}{E_y}-1)E_y & -(v_{yz}+v_{xy}v_{zx}\frac{E_z}{E_y})E_y & & 0 & \\ -(v_{zx}+v_{yz}v_{xy}\frac{E_x}{E_z})E_z & -(v_{zx}v_{xy}+v_{yz}\frac{E_y}{E_z})E_z & (v_{xy}^2\frac{E_x}{E_y}-1)E_z & & & \\ & & & \frac{G_{xy}}{F} & 0 & 0 \\ & 0 & & 0 & \frac{G_{yz}}{F} & 0 \\ & & & 0 & 0 & \frac{G_{xz}}{F} \end{bmatrix}$$

in which F is defined as:

$$F=\frac{E_xE_yE_z}{-E_xE_yE_z+v_{xy}^2E_x^2E_z+v_{zx}^2E_z^2E_y+v_{yz}^2E_y^2E_x+2v_{xy}v_{yz}v_{zx}E_xE_yE_z}$$

During the deformation process, as soon as the tension in the most stressed integration point (called *critical point*) reaches the tensile strength of the material, a crack starts to propagate perpendicular to the most stressed direction (that is the principal direction 1, whose stress in σ_1): a damage increment is assigned in this direction on the critical point.
After the formation of the first crack, the crack direction is fixed and the isotropic formulation is not valid anymore. At this point, the evaluation of the behaviour of the cracked element is carried out in the new global reference system defined by the crack direction.
In fact the first crack individuates the direction *n* of the crack plane, that is perpendicular the direction of the first principal stress, i.e. the greatest tensile stress in the element, σ_1. By consequences, through the evaluation of the other two principal stresses σ_2 and σ_3, for which is valid the relation $\sigma_1 \leq \sigma_2 \leq \sigma_3$, and of their mutually orthogonal directions, a right handed coordinate system is defined. It is noted that the second and the third crack in the element have as pre-fixed directions the second and the third principal directions.
The *nst* axes now represent the global reference system in which SLA method can be applied.

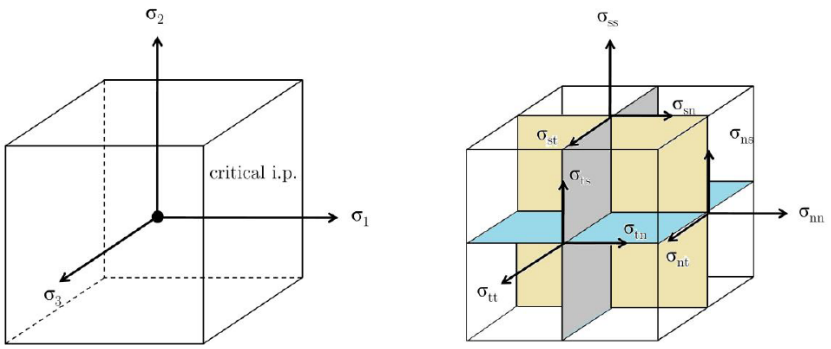

(a) The principal stress directions in the critical integration point before cracking
(b) The three planes of orthotropy, fixed after the beginning of cracking, and the relative 3-dimensional strains in nst-coordinate system

The expression of the constitutive model in stiffness form for an orthotropic material in the global *nst* system, is formally identical to the one in the local *xyz* system:

$$\begin{bmatrix}\sigma_{nn}\\ \sigma_{ss}\\ \sigma_{tt}\\ \sigma_{ns}\\ \sigma_{st}\\ \sigma_{tn}\end{bmatrix} = \begin{bmatrix} (v_{st}^2\frac{E_s}{E_t}-1)E_n & -(v_{ns}+v_{st}v_{tn}\frac{E_s}{E_n})E_n & -(v_{st}v_{tn}+v_{sn}\frac{E_s}{E_n})E_n & & & \\ -(v_{nt}v_{st}+v_{ns}\frac{E_n}{E_s})E_s & (v_{zx}^2\frac{E_z}{E_y}-1)E_y & -(v_{yz}+v_{xy}v_{zx}\frac{E_z}{E_y})E_y & & 0 & \\ -(v_{zx}+v_{yz}v_{xy}\frac{E_x}{E_z})E_z & -(v_{zx}v_{xy}+v_{yz}\frac{E_y}{E_z})E_z & (v_{xy}^2\frac{E_x}{E_y}-1)E_z & & & \\ & & & \frac{G_{ns}}{F} & 0 & 0 \\ & 0 & & 0 & \frac{G_{st}}{F} & 0 \\ & & & 0 & 0 & \frac{G_{tn}}{F} \end{bmatrix} \begin{bmatrix}\varepsilon_{nn}\\ \varepsilon_{ss}\\ \varepsilon_{tt}\\ \varepsilon_{ns}\\ \varepsilon_{st}\\ \varepsilon_{tn}\end{bmatrix}$$

in which F is defined as:

$$F = \frac{E_nE_sE_t}{-E_nE_sE_t + v_{ns}^2E_n^2E_t + v_{tn}^2E_t^2E_n + v_{st}^2E_s^2E_n + 2v_{ns}v_{st}v_{tn}E_nE_sE_t}$$

It is very important to note that, although the formal expression of the stiffness matrix is totally analogous to the precedent *xyz* formulation, now the values of the mechanical parameters E, v and G, have been reduced to simulate the cracking behavior, according to the SLA theory and to the *saw-tooth curve*.

Nevertheless, all the stress and strains have to be evaluated in the local reference system *xyz*. In order to d this, the already mentioned standard strain transformation matrix $\boldsymbol{T_\varepsilon}$ can be used.

It is remembered the relation between strains in *xyz* and *nst* system:

$$\boldsymbol{\varepsilon_{nst} = T_\varepsilon \varepsilon_{xyz}}$$

and the analogous relation between stresses:

$$\boldsymbol{\sigma_{snt} = T_\sigma \sigma_{xyz}}$$

where $\boldsymbol{T_\sigma}$ is the standard stress transformation matrix.

Through the substitution of these two relations in the *nst* constitutive model:

$$\boldsymbol{\sigma_{snt} = D\varepsilon_{nst}}$$

the relation results:

$$\boldsymbol{T_\sigma \sigma_{xyz} = DT_\varepsilon \varepsilon_{xyz} \rightarrow \sigma_{xyz} = T_\sigma^{-1} DT_\varepsilon \varepsilon_{xyz}}$$

Using the property of the transformation matrix, for which the inverse of the stress transformation matrix is equal to the transpose of the strain transformation matrix [12], the definitive expression is determined as:

$$\boldsymbol{\sigma_{xyz} = T_{\varepsilon}^{T} D T_{\varepsilon} \varepsilon_{xyz}}$$

in which all the quantities are already known.
This equation is the constitutive stress-strain relation that accounts for material orthotropy and has been used for implementation in finite element program *DIANA*.
The behaviour in compression in case of a fixed concept is also evaluated in the fixed coordinate system determined, in the same way just described, by the crack directions.

2.3.3 Poisson and shear behavior

In the assignment of the damage increments, the Young's modules and the tensile strength are reduced in *n*, *s* and *t* directions, according to the predefined saw-tooth curve. However, they are not the only quantities in the constitutive relationships that have to be reduced to model the crack behavior of the element in the most accurate way. In fact also the Poisson's ratios and the shear modules are interested by decrements during the cracking process.
After the first crack set, only the Young's modulus normal to the crack plane, E_n, and the relative tensile strength, $f_{t;n}$, are reduced, following the predefined saw-tooth curve. The changing of the Poisson behaviour starts as soon as the second and the third sets of cracks begins to propagate in the orthogonal planes respectively normal to *s* and *t* directions. In fact the reduction of the Young's modules E_n, E_s and E_t, caused by the three sets of cracks, implies the decreasing of all the Poisson's ratios as well.
Due to the orthotropic relations between the various E and v, the Poisson's ratios are assumed to be reduced at an equal rate as the corresponding Young's modules [13]:

$$v_{sn} = v_{tn} = v_0 \frac{E_n}{E_0}, v_{ns} = v_{ts} = v_0 \frac{E_s}{E_0}, v_{nt} = v_{st} = v_0 \frac{E_t}{E_0}$$

in which v_0 and E_0 are the initial elastic properties of the material or, more generally, the properties of the material in the previous step of the analysis, before the application of the last damage increment.
It is remembered that v_{ij} is the Poisson's ratio due to a contraction in direction *i* when an extension is applied in direction *j*. Thus, when a crack is completely opened in the *n*-direction ($E_n = 0$), increasing the crack strain in *n*-direction does not cause a Poisson's effect in *s*-direction and vice versa [5].
Analogously, the three shear modules G_{ns}, G_{st} and G_{tn} are affected as well by the damage increment. The modeling of the shear behavior is only necessary in the fixed crack concept where the shear stiffness is usually reduced after cracking. The correct estimation of this reduction is usually very important, since shear forces can have a strong influence on the total bear capacity on

the whole structures. In fact in many structures, important redistribution effects might take place and large shear stresses can occur.
In most of the cases, the opening of the crack means a reduction of the shear stiffness and capacity of the element, that can be taken into account by two different models: *Constant Shear Retention* and *Variable Shear Retention*.
In the constant shear retention model the three shear modules after the relative damage increment are reduced at a constant rate β:

$$G_{ns} = G_{st} = G_{tn} = \beta G_0$$

where the shear retention factor is $0 \leq \beta \leq 1$ and G_0 is the initial shear modulus of the uncracked material, or, more generally, the modulus of the material in the previous step of the analysis, before the application of the last damage increment.
In this model, care should be taken in the choice of the factor β, regarding the dimensions of the shear planes and all the shear bearing mechanism that occurs in the structure.
For this reason a Variable shear retention model seems to be more accurate in providing a representation of the real shear bearing mechanism. In fact in this model the reduction of the shear modulus is calculated directly in relation with the opening width of the cracks. In this way, completely opened cracks cannot transfer shear forces anymore. Note that this is not the case when constant shear retention is considered, where the structure always possesses some residual capacity.
The variable shear retention is assumed to reduce the shear modules at a rate equal to the minimum of the corresponding Young's modules:

$$G_{ns} = \frac{\min(E_n, E_s)}{2(1 + v_0 \frac{\min(E_n, E_s)}{E_0})}, G_{st} = \frac{\min(E_s, E_t)}{2(1 + v_0 \frac{\min(E_s, E_t)}{E_0})}, G_{nt} = \frac{\min(E_n, E_t)}{2(1 + v_0 \frac{\min(E_n, E_t)}{E_0})}$$

Consequently, the amount of variables in the constitutive stress-strain relation is now reduced to only 3, namely the three Young's modules: E_n, E_s and E_t.

3. SHEAR IN REINFORCED CONCRETE SLABS

The failure modes of reinforced concrete slabs can categorized as: flexural, punching shear and wide beam failure. The first one interests mainly slabs supported by beams or walls; they present a dominant bending behavior and the shear stresses are not generally critical when the loads are distributed on surface or lines. Tangential actions result well distributed along the slab and the shear component will not govern the design. The structures can freely undergo plastic strains without a limitation of their capacity.
However, in the proximity with the local introduction of concentrated supports or action the maximum shear force per unit of length of slab increases, up to become critical and it should be considered in order to prevent shear failure.
Concentrated loads transfer to the slabs through: (1) column in flat plate, (2) from column to footings, (3) from piles to pile caps and (4) from concentrated action such the wheel contact pressure. In this case shear action are often more critical than bending stresses: the slab thickness may be mainly designed in order to avoid shear failure [4].

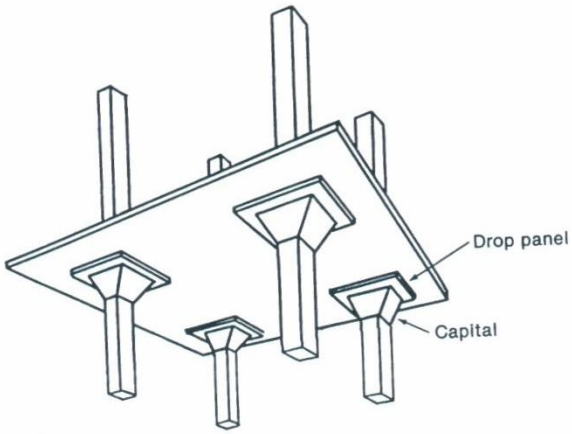

Sample of connection between slab and column capitals

The mechanism of shear failure of the slab in the vicinity of concentrated loads results rather complex (especially without shear reinforcement or stirrups) and less predictable, because unlike flexural failures, shear failures in reinforced concrete structures are brittle and sudden. When they occur, they typically do so with little or no warning [14].
A shear or punching failure may occur either before or after the yielding of flexural reinforcement and hybrid situations between the main mode are commonly found in practical cases [2].
In this kind of structures a proper transverse reinforcement cannot be placed, as The absence of shear reinforcements as the position of the point load due to the vehicle wheels cannot be localized. The solution of placing stirrups along all the structures cannot be considered due to the significant increment of the construction and practical difficulties [15].

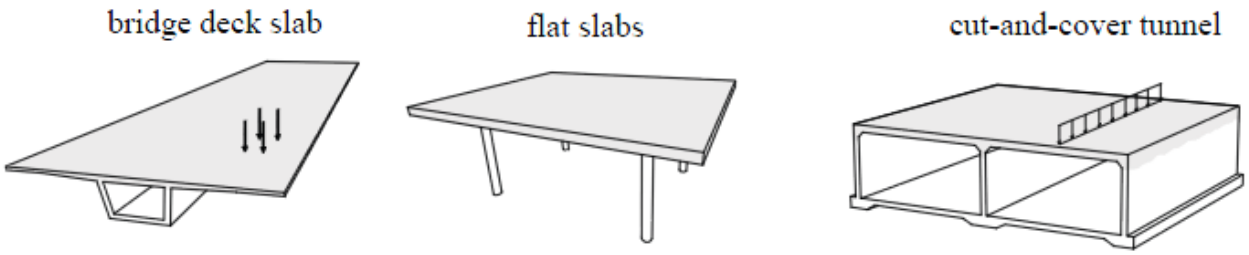

Slabs without shear reinforcement

For slabs without stirrups, shear failure is the most plausible and inclined crack forms before or after flexural cracks are initiated nearby. The subsequent and progressive opening of the cracks changes significantly the force transfer and the condition of static equilibrium [5].
The shear failure can combine two phenomena, either one-way (wide beam action) or two-way (punching shear).

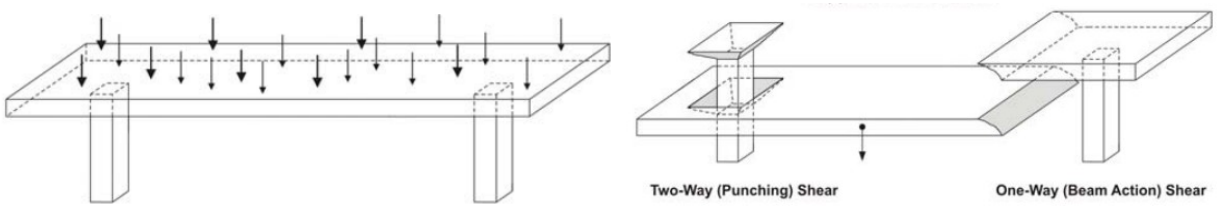

(a) *(b)*

Reinforced concrete slab supported on columns (a) and Shear failure models in slabs (b)

One-way and two-way shear can be better understood by considering the flow of shear forces. Zones in which the principal shear lines run parallel to each other are subjected to potential wide beam failure: this is mostly associated with line loads and linear supports. Instead, zones in which principal shear lines are not running in parallel, as for instance around the point of introduction of a concentrated load, are interested by two-way failure [2].

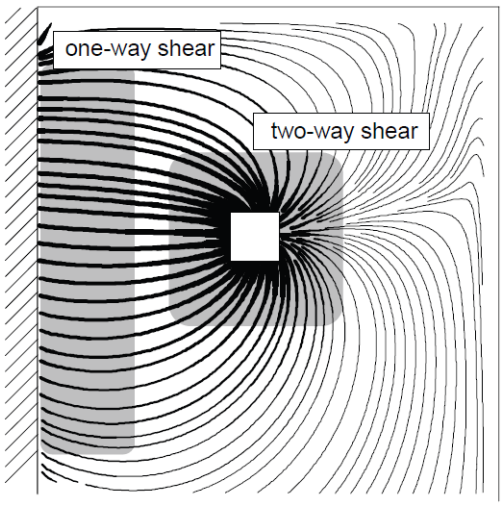

Shear flow in a slab: zones of one-way and two-way shear

3.1 One-way shear (or wide beam action)

One-way shear failures are generally associated with distributed or line loads and linear supports such as walls and beams. So the line load applied is carried by shear forces from the application area to the support along lines running perpendicular to the supported edge [2].

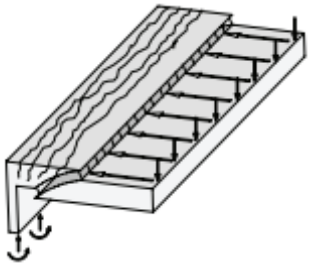

Schematic representation of one-way shear failure

In this kind of action the slab fails for shear crack who extends along a section in a plane across the entire width of the slab. The critical shear crack is often located on a distance d from the concentrated load or constrain reaction. The value d is defined as effective depth, i.e. the distance between the axis of longitudinal reinforcement and the most external compressed fibers [16].
The critical section often follows a 45 degree inclined direction, but the critical section is taken vertical through the critical diagonal shear crack. Then, the slab should be treated as a wide beam and the shear strength equation of the Codes have to be considered.
A slab without shear reinforcement should be checked against one-way shear failure who is generally brittle and can occur without any indication of an impending collapse.
One-way shear failure models are used to predict the shear failure load of reinforced concrete slabs and beams without shear reinforcement. The actual formulations take a great amount of contributions based on the theory of plasticity, fracture mechanics, empirical considerations and numerical simulations (see CEB Bulletin as example).
To better understand the one-way shear failure mechanism inside a reinforced concrete structure, it useful to refer to one of the test performed on beam without stirrups. The actual literature presents a very large amount of data regarding this topic.
The following sample refers to a simple support beam without stirrups, under two concentrated load symmetrically placed with respect to the midspan, so called *four points bending test* (see [17] for more details).
The beam is reinforced with longitudinal bars only on the bottom face, on the tension side.

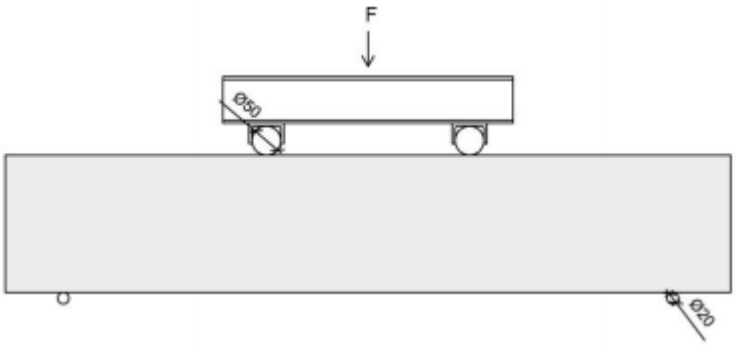

Typical experimental setup for shear tests on beam without stirrups

During the loading process of the reinforced concrete beam three stage can be distinguished: the un-cracked, the cracked and the failure stage.
Initially the beam carries only its own dead weight. Both concrete and steel of rebars are cinematically compatible and the entire concrete section bear the actual low tension field. The materials behavior can be easily schematized with a linear model.
Increasing the load, both the tensile tension on the top fibers and the compression tension on the bottom surface rise. Until the first discrete cracking is not reached, the reinforced concrete can be studied through the an elastic-linear analysis with a butterfly distribution of the normal tension and a parabolic diagram for the tangential stress. The whole concrete section is effective.
When the tensile stress reaches the ultimate tensile edge of the concrete a flexural cracks develops from the bottom side of the midspan forward the compressive tension field of this section. The neutral axis shifts upward and the rebars start to work effectively to resist to the entire tensile stresses in order to provide balance. Locally, concrete and steel are no more cinematically compatible. The discrete nature of this phenomenon affects only the nearby of the crack; both the upper compressed concrete and steel present a linear-elastic behavior. The same happens in the other sections of the beam.
The cracking pattern and its development is defined by the spacing and maximum width of cracks. They depend of many factors, such as level of stress in the rebars, distribution of the longitudinal reinforcement in the section, concrete cover and grade of steel used [4].
Due to the reduction of the moment of inertia of the cracked section, the deflection of the beam is clearly increased.
In the transition from the un-cracked- to the cracked-stage the way of load transmission in the beam will change. This change of internal force flow depends on the configuration of the reinforcement. In casa of beam without stirrups, like in the present sample, the simple strut and tie representation is an unsafe approach.
Further increasing of the load produces formation of new cracks, extending toward the support. However, it's more important to investigate only the wide central cracks than considered the large amount of other small cracks.
The beam is still working mainly with a flexural behaviour.
For a higher load, shear stresses increase as well due to the combination of bending moment and shear force. Diagonal cracks at approximately 45 degree from horizontal sudden arise in the direction of the principal tensile stress. After the formation over a large distance of the beam, the compression zone crushes and the cracks continue at the bottom side as a large horizontal crack along the longitudinal reinforcement bars to the end of the beam [6].

Shear crack in reinforced concrete beam at failure

In the failure stage no internal equilibrium in the beam can be obtained anymore: it leads to the complete loss of bearing capacity of the structure, and the beam collapse suddenly. Beam that fail

due to a shear failure mechanism are called *shear critical beam*. Different shear failure mechanisms are possible, depending on several parameters [6].

3.2 Two-way shear (or punching behavior)

A mechanical explanation of the phenomenon of punching shear in slab without shear reinforcement is related to the opening of critical shear crack and it is generally associated with the introduction of concentrated loads or punctual supports such as columns.
The failure occurs as the column penetrates across the concrete slab, creating a roughly truncated cone, defining a "critical perimeter" in the extrados of the element, i.e. the surface placed in the opposite side with respect to the load [15].
It is to be noted that the once-held concept of the column (or applied load) being pushed through the slab is incorrect.

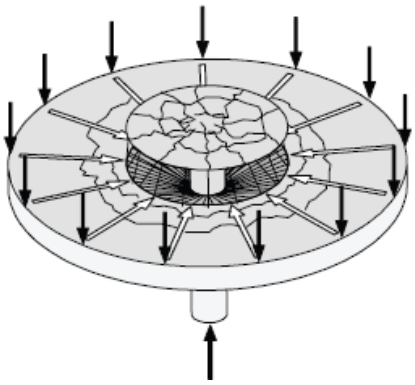

Schematic representation of symmetrical punching shear failure and associated force flow

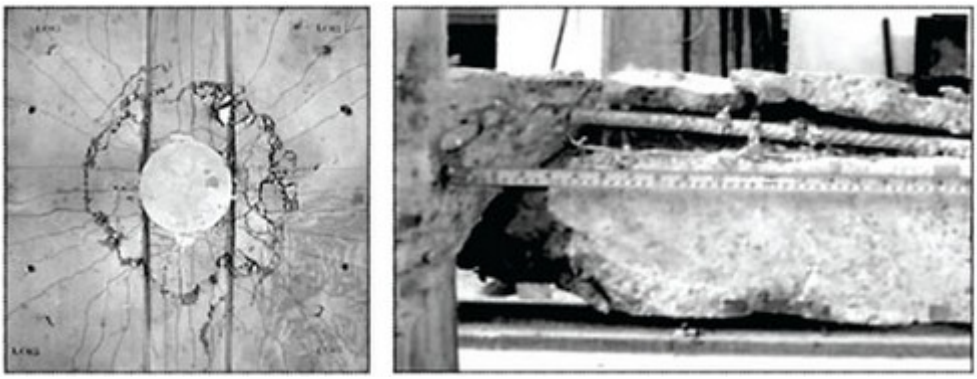

Punching shear failure

This failure mode has a nature similar to that of one-way shear in terms of brittle failure, i.e. it occurs without signs that the collapse of the slab is impending. Punching shear failures have in fact always been a major concern in the design of reinforced concrete flat slabs supported by columns.
The complexity of the problem brings to adopt empiric approaches or formulas based on the shear theory for beam, simply extended to a failure surface.
Punching shear has been the object of an intense experimental effort since the 1950s. One of the first mechanical models was proposed by *Kinnunen* and *Nylander* in the 1960, varying amongst other parameters the amount of flexural reinforcement in the slab.

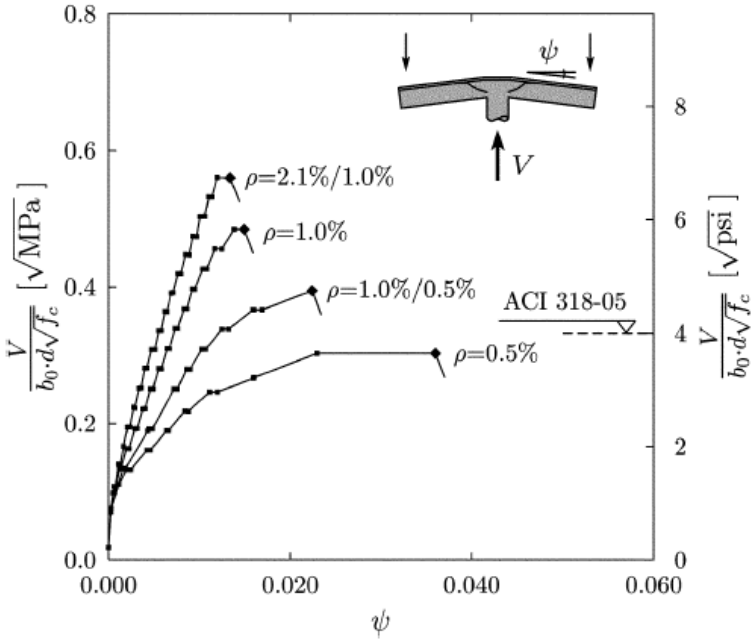

Plots of load-rotation curves for tests by Kinnunen and Nylander

It proposed a model based on the fracture mechanism, on the basis of 61 tests on circular flat slab elements connected on circular [18]. It brings to a rational theory based on the assumption that the punching shear strength is reached for a given critical rotation ψ. This rotation was calculated by simplifying the kinematics of the slab and assuming a bilinear moment-curvature relationship.
The following observations can be made from the load-rotation relationship on the tests:

- for low reinforcement ratio (test with $\rho_l = 0.5\%$) the behavior is ductile, with yielding of the entire flexural reinforcement, as illustrated by the horizontal asymptote of the load-rotation curve. In this case, the strength of the slab is limited by its flexural capacity and punching occurs only after large plastic deformations. The punching failure at the end of the plastic plateau remains brittle and leads to a sudden drop in strength;
- for intermediate reinforcement ratios (tests with $\rho_l = 1.0\%/0.5\%$ and 1.0%), some yielding of the reinforcement is observed in the immediate vicinity of the column, but punching occurs before yielding of the entire slab reinforcement. In this case, the strength of the slab is lower than its flexural capacity;
- For large reinforcement ratios (test with $\rho_l = 2.1\%/1.0\%$), punching occurs before any yielding of the reinforcement takes place, in a very brittle manner. In this case, the strength of the slab is significantly lower than its flexural capacity;
- Increasing the reinforcement ratio increases the punching capacity, but strongly decreases the deformation capacity of the slab;
- The ACI design equation is also plotted in the figure. It predicts a constant strength independent from the reinforcement ratio [17].

As shown by the previous figure, the punching strength decreases with increasing the rotation of the slab. This has been explained by *Muttoni* and *Schwartz* [20]. The shear strength is reduced by the presence of a critical shear crack that propagates through the slab into the inclined compression strut carrying the shear force to the column.

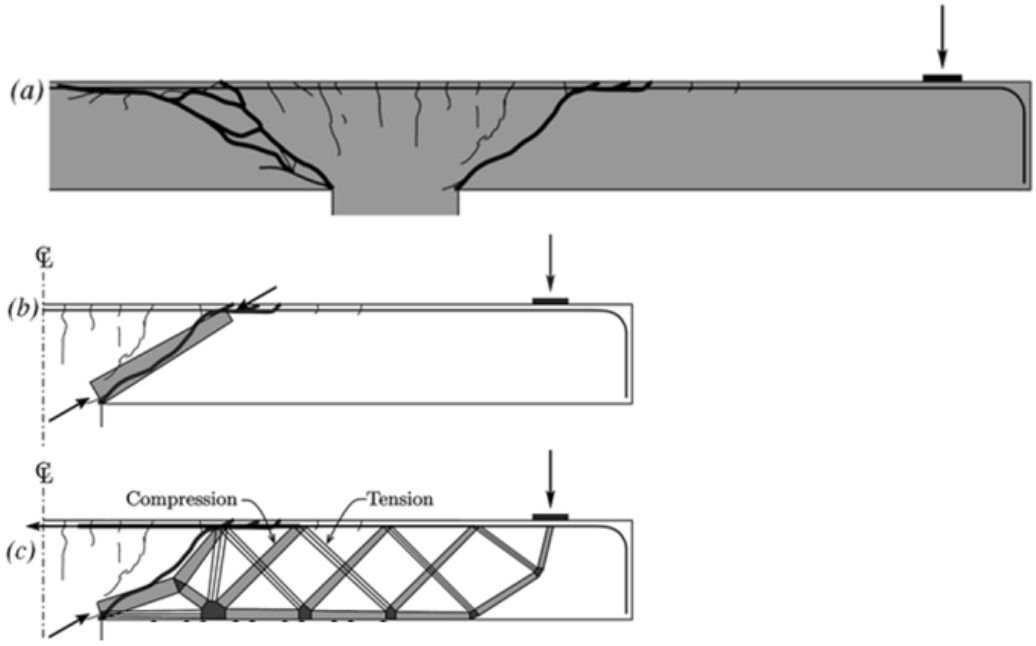

(a) cracking pattern of slab after failure; (b) theoretical strut developing across the critical shear crack; (c) elbow- shaped strut

According to *Muttoni* and *Schwartz* [20], the width of the critical crack can be assumed to be proportional to the product ψd, leading to a semi-empirical failure criterion.
The amount of shear that can be transferred across the critical shear crack depends on the *roughness* of the crack, which in its turn is a function of the maximum aggregate size.
According to *Walraven* [21] and *Vecchio* and *Collins* [22], the roughness of the critical crack and its capacity to carry the shear forces can be accounted by the maximum aggregate size and a reference size equal to 16 mm [17].
The new criterion was so compared to the results of 99 punching test from the literature, resumed in the next table, taking into account the effects of the slab thickness and aggregate size:

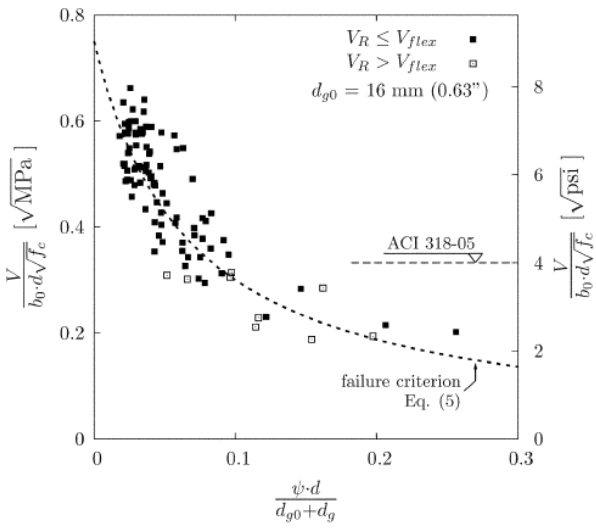

(a)

Reference (year)	d, mm (in.)	No.	Failure criterion V_{test}/V_{th} Average	COV
Tests with same bending reinforcement ratio along orthogonal directions				
Elstner and Hognestad[18] (1956)	115 (4.52)	22	0.98	0.14
Kinnunen and Nylander[8] (1960)	122 (4.80)	12	1.05	0.11
Moe[19] (1961)	114 (4.48)	9	1.13	0.16
Schäfers[20] (1984)	113 to 170 (4.45 to 6.69)	4	1.03	0.20
Tolf[21] (1988)	98 to 200 (3.86 to 7.87)	8	1.06	0.15
Hassanzadeh[22] (1996)	200 (7.87)	3	0.99	0.17
Hallgren[10] (1996)	199 (7.83)	7	0.98	0.25
Ramdane[23] (1996)	98 (3.86)	12	1.10	0.16
Guandalini and Muttoni[13] (2004)	96 to 464 (3.78 to 18.2)	10	1.11	0.22
Σ		87	1.05	0.16
Tests with different bending reinforcement ratio along orthogonal directions				
Nylander and Sundquist[24] (1972)	95 to 202 (3.74 to 7.95)	11	1.04	0.09
Kinnunen et al.[25] (1980)	673 (26.5)	1	0.85	—
Σ		12	1.03	0.10

Note: COV = coefficient of variation.

(b)

Failure criterion: punching shear strength as function of width of critical shear crack compared with 99 experimental results and ACI 318-056 design equation (a), refer to details of test series in table (b).

In 2005 *Guandalini* gave an overview of some of the most important contributions on this subject.
An understanding of the mechanics of punching shear can be gained from the systematic observation of cracking and of the evolution of deformations in punching shear tests. A major limitation of such observations is that the inner cracks across the slab are invisible. On the contrary, tests on slab strips under one-way shear allow observing the formation of cracks and the development of web deformations up to the shear failure.

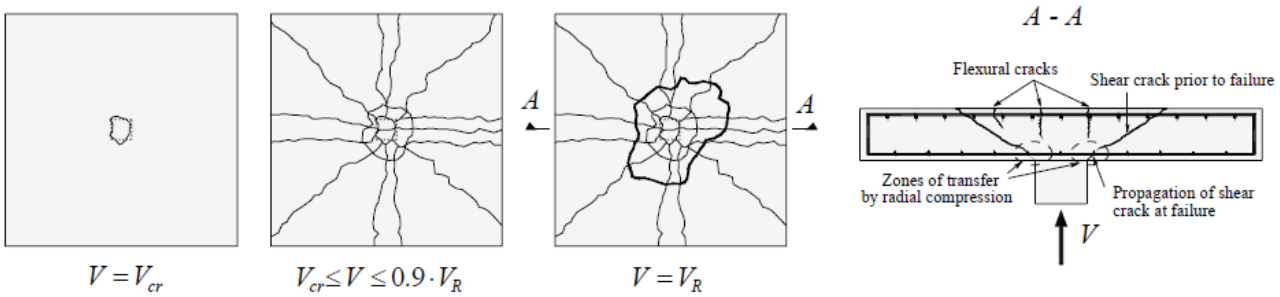

Evolution of crack pattern at the top surface (adapted from Guandalini 2005)

When the slab is supported on four sides and the ratio of the long side to the short side is less than 2, the slab will deflect in double curvature in both directions. In two-way action the slab fails in a local area around the concentrated load. The critical section extends around the concentrated load or column. A punching shear failure occurs along a truncated cone or pyramid caused by the critical diagonal tension crack around the concentrated load or column. In this case conventional theory for beam shear does not apply.

3.3 Shear behaviour of slabs without shear reinforcement:

After this introduction to one- and two-way shear failure for concrete slabs, it has to be noted that these two phenomena occur differently and in mutual combination the most of the times during the failure of the loaded structures. Indeed, the behavior of bridge deck slabs under concentrated loads is more complex. Several load-carrying mechanisms can develop and coexist, depending on the loading and the geometry of the structure. Two-way shear can become prevalent over one-way shear, but with a flow of inner forces quite different from that of symmetric punching shear analyzed and explained since now.
Depending on the loading conditions and the geometry of the structure, yielding of flexural reinforcement can occur before shear or punching shear failure [2]. An interesting sample is found in the literature: the following experimental work is related to the shear strength of bridge decks under concentrated loads.
Miller et al. (1994) performed a destructive test on a 38-year-old decommissioned concrete slab bridge under two concentrated loads (see figures below). The skew bridge had a total length of $31.6\ m$. The abutments and pier line were skewed at 30° to the roadway. The slab was loaded with two $1.525 \times 0.690\ m$ loading blocks simulating the front tandem axle load of a $HS20-44$ truck (the front tandem has a $144\ kN$ axle load). The bridge failed in shear at $Q = 3200\ kN$, which corresponds to the action of $22 \times HS20-44$ trucks. The theoretical flexural failure load was not reached. Yield was reached only just before failure.

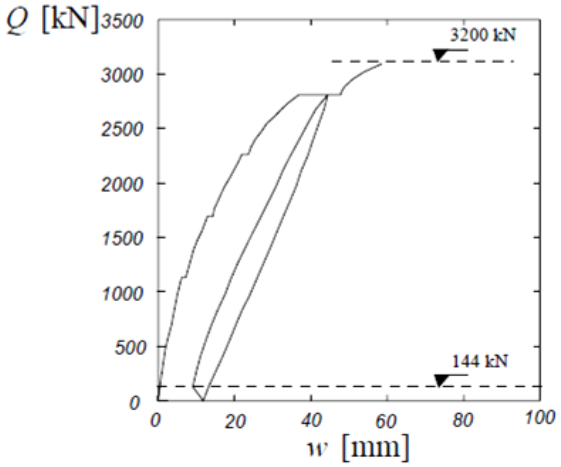

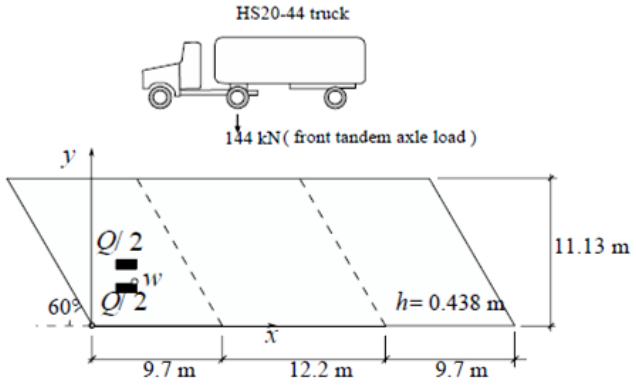

(a) *(b)*

Load-deflection diagram (a); dimensions, loading patterns and HS20-44 truck

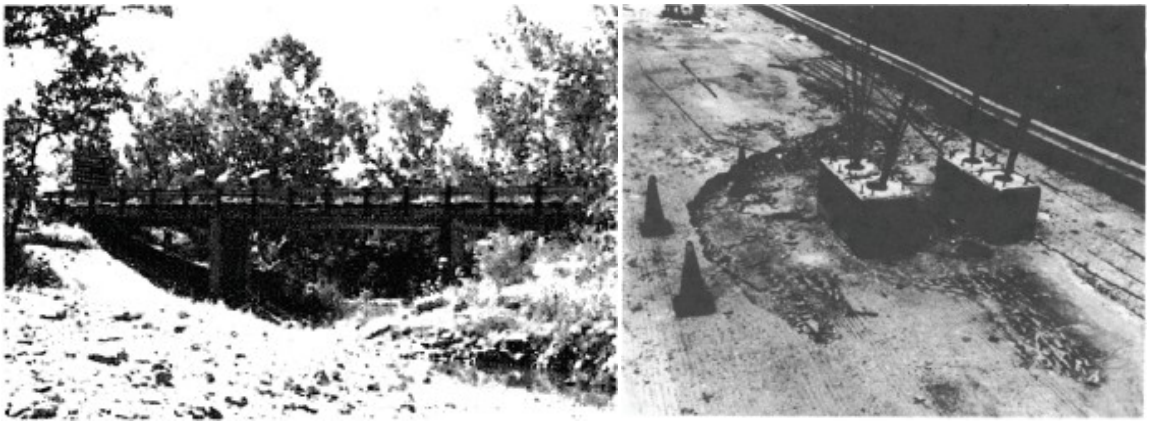

(c) *(d)*

View of bridge slab (c); focus on the failure pattern (d)

3.4 Normative indications for critical section in one- and two-way shear failure

The theoretical punching shear strength for reinforced concrete slab can be predicted adopting different codes.

The ACI 318-05 [23] proposes an expression for square or circular columns of moderate dimensions relative to the thickness of the slab:

$$V_R = \frac{1}{3} b_0 d \sqrt{f'_c} \ (SI\ units: MPa, mm)$$

where d is the average flexural depth of the slab, b_0 is the perimeter of the critical section located to $d/2$ from the face of the column, and f'_c is the specified concrete compressive strength.

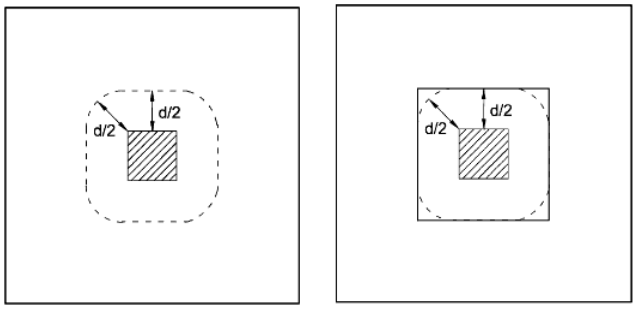

Critical perimeter according to ACI 318-2010

The current version of the EuroCode2 [24] also includes a formulation for estimating the punching shear strength of slabs:

$$V_R = 0.18 b_0 d \xi \left(100 \rho_l f'_c\right)^{\frac{1}{3}} \ (SI\ units: MPa, mm)$$

where b_0 is the control perimeter located to $2d$ from the face of the column, ρ_l accounts for the bending reinforcement ratio (with a maximum value of 0.02) and ξ is a factor accounting for size effect defined by the following expression:

$$\xi = 1 + \sqrt{\frac{200\ mm}{d}} \leq 2.0$$

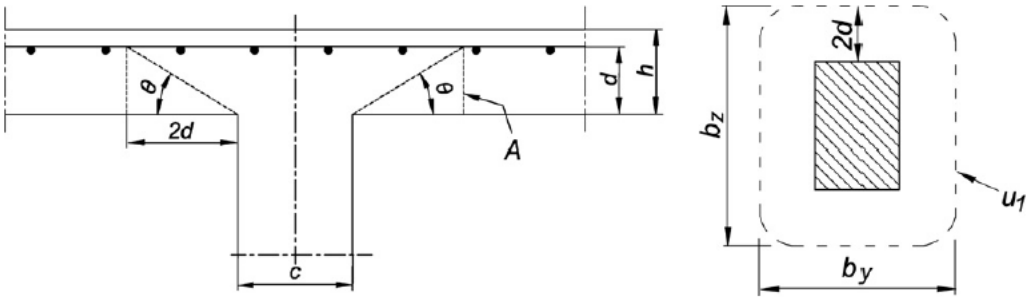

Critical perimeter according to Eurocode 2

The CEB model [25] describes the punching shear resistance as:

$$V_{Rd,c} = k_\psi \frac{\sqrt{f_c}}{\gamma_c} b_0 d \ (SI\ units)$$

where b_0 is the critical perimeter located to $d/2$ from the loaded area, while k_ψ depends on the rotation of the slab around the support region:

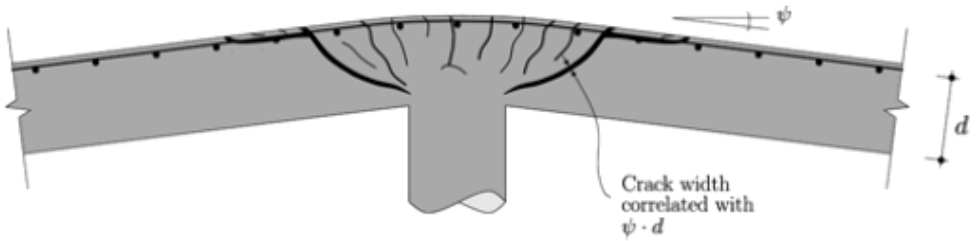

Correlation between opening of critical shear crack, thickness of slab, and rotation ψ

$$k_\psi = \frac{1}{1.5 + 0.6 \cdot \psi \cdot d \cdot k_{dg}} \leq 0.60$$

$$\psi = 1.5 \frac{r_s}{d} \cdot \frac{f_y}{E_s}$$

r_s indicates the position where the radial bending moment is zero, with respect to the column axis, and can be assumed, in agreement with the code equal to $0.22L$ (L side of the slab), d the effective depth, f_y and E_s the yielding stress and Young modulus of the steel and:

$$k_{dg} = \frac{48}{16 + d_g} > 1.15$$

where d_g is the maximum aggregate size.

3.5 Shear strength in elements without shear reinforcement for one- and two-way failure

Nowadays, the research community has not reached consensus on the exact mechanisms of shear transfer in reinforced concrete, since it is related to many parameters. This has slowed the replacement of empirically-based methods with rational methods based on modern theories of the shear behaviour of reinforced concrete. Indeed, flexural design provisions are based on the rational assumption that plane sections remain plane, and this assumption has proven to be accurate over a wide range of reinforced concrete flexural elements. However, the search continues for equally accurate shear design provisions, based on equally rational assumptions, but it is critical for the shear design methods for reinforced concrete be accurate, rational and theoretically sound.
Up to now, most of the experiments are related on heavily reinforced slender beams ($a/d \geq 2.5$) under concentrated load.

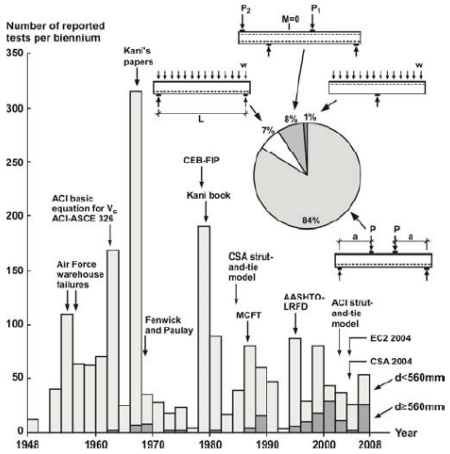

Sixty years of Shear Research on members without shear reinforcement

For this reason, this section aims to understand the behaviour of large, lightly reinforced concrete beams and one-way slabs subjected to shear. Empirically-based shear design methods are largely used, particularly those in the widely-used American Concrete Institute design code for concrete structures (ACI-318). However, they do not accurately predict the behaviour of these important structural elements, and may produce unsafe designs in certain situations [14].

3.5.1 One-way shear strength

As already explained, the behavior of a reinforced slab who fails with a one-way mechanism is comparable with the behavior of a beam and all the considerations made can be used.
The typical brittle failure mode of shear beam evidences four mechanism of shear transfer are [26]:

- shear in the uncracked zone of the beam V_c;
- interface shear transfer due to aggregate interlock of surface roughness of the crack V_i;
- residual tensile stresses across the crack V_r;
- dowel action of the longitudinal reinforcement bar V_d.

as shown in the following figure:

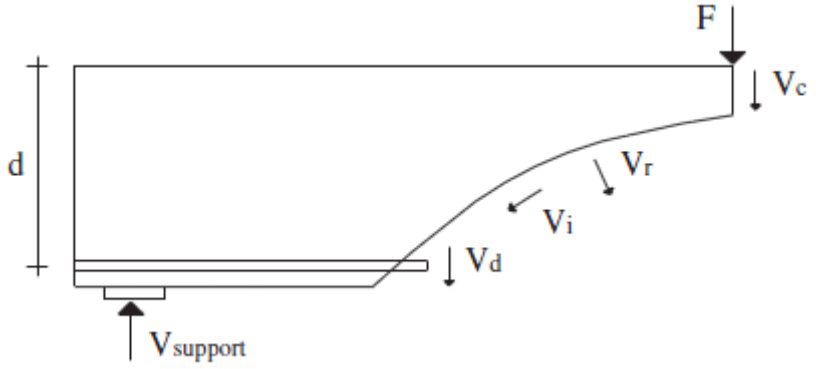

Schematic representation of shear transfer mechanisms

These four factors are the sum of the so called *beam action*. In addition to beam action, *arch action* also contributes to the shear strength.
Despite the complex nature of the shear transfer, those basic mechanism are generally accepted, though different levels of relative importance are imposed by different researches.

Moreover, the shear behavior depends on many parameters: (a) maximum aggregate size, (b) tensile strength of the concrete, (c) shear span-to-depth ratio, (d) reinforcement ratio, (e) size effect, (f) axial forces and (f) effective width [14].
The ACI Code [23] provides a formula for the evaluation of the one-way strength. Here, the shear strength V_c (called $V_{Rc,d}$ inside the Model Code) is equal to the resistance of a beam without stirrups and it's taken equal to the load at which inclined cracking occurs:

$$V_c = \left(0.16\sqrt{f'_c} + 17\frac{\rho_m V_u d}{M_u}\right) b_w d \leq 0.29\sqrt{f'_c} b_w d \ (Si\ units: N, mm)$$

where f'_c is the concrete compressive strength, ρ_m is the longitudinal reinforcement ratio, b_w is the web width (or effective width), M_u is the factored moment at section and $\frac{V_u d}{M_u}$ expresses the shear span to depth ratio $\frac{a}{d}$.
A simplified version is also allowed by the ACI Code:

$$V_c = \frac{\sqrt{f'_c}}{6} b_w d \ (SI\ units: N, mm)$$

3.5.2 Important parameters

The most important parameters responsible for the shear resistance are described.

Coarse aggregate size

A particular aspect of the shear behaviour of reinforced concrete that is deserving of additional attention is the effect of the maximum aggregate size on the shear response of reinforced concrete sections. This is particularly true for reinforced concrete beams and slabs constructed without stirrups, since aggregate interlock is generally believed to be a dominant mechanism of shear transfer in these element types. Indeed, increasing the size of the coarse aggregate produces rougher cracks that are likely better able to transfer shear stresses. Likewise, reducing the maximum aggregate size decreases the shear strength of a concrete section. In concrete elements constructed with high-strength concrete, poor quality aggregate or light-weight aggregate, the aggregate interlock capacity may be greatly reduced because coarse aggregate particles will tend to fracture at cracks, resulting in smooth crack surfaces with a greatly reduced aggregate interlock capacity [14].

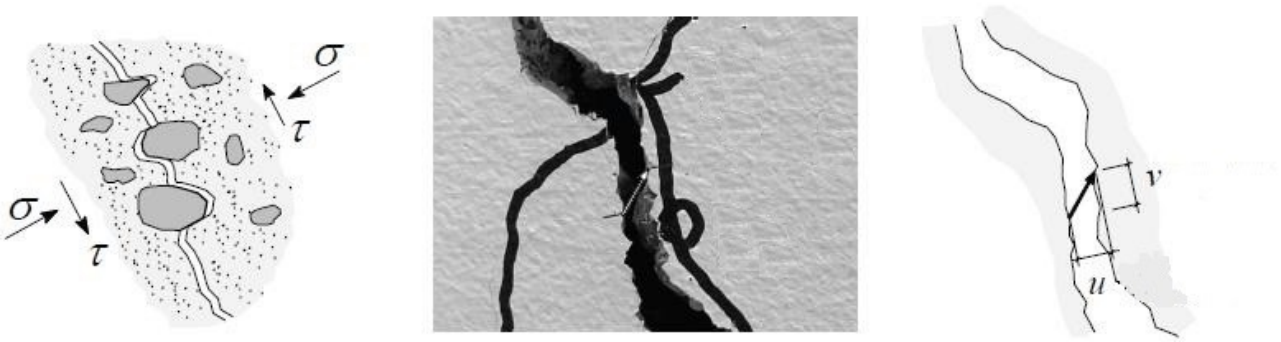

(a) (b) (c)

Shear transfer across crack due to the aggregate interlock (a); experimental evidence of crack kinematics at the concrete surface (b); crack width u and slip v at the concrete surface (c)

Tensile strength of the concrete

As said before, the concrete strength influences the roughness of the crack surface. In addition to this, another feature of the concrete could influence the shear capacity of beam without stirrups: the tensile strength of the concrete f_{ct}, which is in turn related to the compressive capacity f_{cc}. Indeed, the inclined cracking load is a function of the tensile strength of the concrete. The stress state in the web of the beam involves the biaxial principal tension and the compression stresses. The flexural cracking that precedes the inclined cracking disrupts the elastic-stress field to such an extent that inclined cracking occurs at a principal tensile stress roughly half of f_{ct} for the un-cracked section.

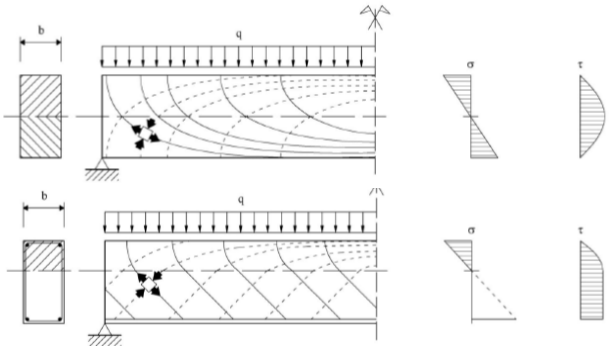

Trend of tensile and compressive isostatics
for un-cracked beam (up) and cracked beam

Longitudinal reinforcement ratio

The shear capacity of reinforced concrete slabs increases if the longitudinal reinforcement ratio ρ_w increases, according to [27].

A small longitudinal reinforcement ratio ρ_w involves higher reinforcement strain, accordingly flexural cracks extend higher into the beam, producing open wider cracks. An increase in crack width cause a reduction of the aggregate interlock action, so regarding to the maximum values of the component of shear transferred across the inclined cracks. On the other hand, the higher amount of longitudinal reinforcement influences the depth of the compressive zone and the axial force strains, but it increases the dowel action.

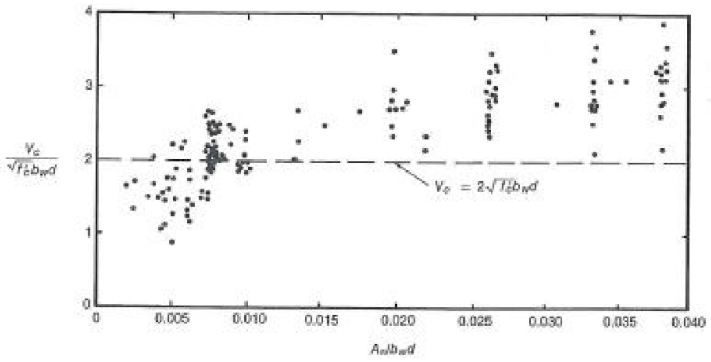

Effect of reinforcement ρ_w ratio on shear capacity of beams constructed with normal-weight concrete and without stirrups

Shear span-to-depth ratio

Shear span-to-depth ratio describes the relation between the span a and the effective depth d, in which the former is the distance between the load and the support. If the shear span decreases, the shear strength capacity will increase: in other words, increasing the span-to-depth ratio the shear capacity of the member will decrease.
Based on the results related to the investigations made by *Leonhardt* and *Walther* (1962) as well as *Kani* (1966) [28], four regimes governing shear failures are discovered:

- $a/d < 1.0$, the capacity of the member is obtained by the yielding strength of the longitudinal reinforcement;
- $1.0 < a/d < 2.5 \div 3.0$, the arch action governs the mechanism;
- $2.5 \div 3.0 < a/d < 8.0 \div 13.0$, the strength depends on the localization of the strains in a shear crack (aggregate interlock);
- $a/d > 8.0 \div 13.0$, the strength is related to the flexural capacity, or better to the yielding strength of the longitudinal reinforcement.

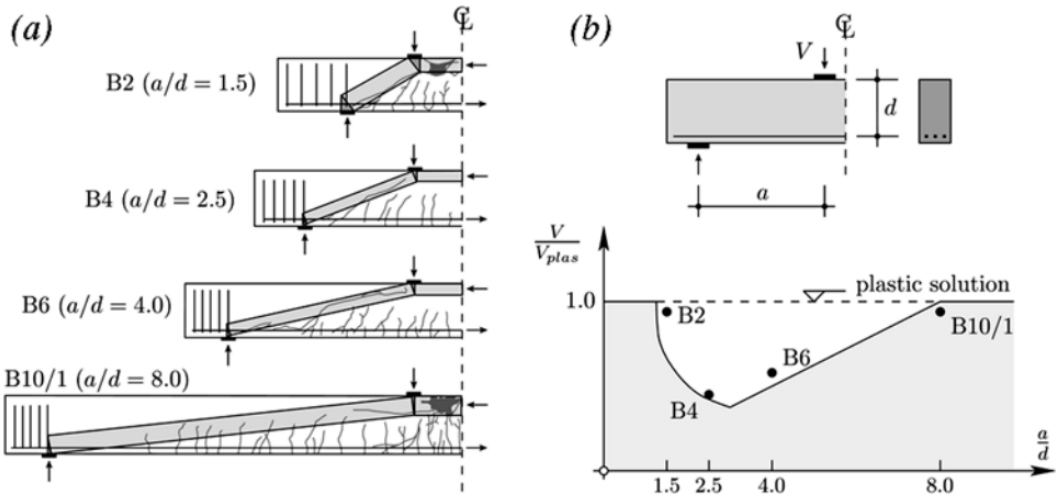

Influence of a/d on shear strength: Tests B2, B4, B6 and B10 by Leonhardt and Walther (a), cracking pattern and theoretical strut position and (b) Kani's valley.

So, the shear span-to-depth ratio a/d affects the inclined cracking shears and capacity of shear span with $a/d < 2.5 \div 3.0$, as shown in the previous figure. Such shear spans are "deep" shear spans. A rate of shear is transferred on the support section through inclined compression (strut element). Indeed, in regions of members within about a member depth d from a discontinuity, load is transferred primarily by "arch action". Indeed, in discussing one-way shear in reinforced concrete, a distinction must be made between behaviour in B-regions (Bernoulli-regions) and D-region (Discontinuity-regions). In regions of members away from discontinuities, load is transferred by beam action, in which the assumption that plane-sections-remain-plane is accurate.
As strut-and-tie action is geometrically incompatible with beam action and since un-cracked concrete obeys the plane sections rule, beam action precedes strut-and-tie action, and it must break down before strut action can control shear strengths.
Hence for longer shear spans the arch action has no more effect due to the stress spreading to the support and the a/d ratio has a little influence on the inclined cracking shear and can be neglected.

Size effect

The size effect in shear is a phenomenon exhibited by slender reinforced concrete members constructed without shear reinforcement in which the failure shear stress decreases as the effective depth increases. However, the severity of the size effect is neither universally known nor understood: the so called "size-effect" was subject of a large experimental campaign carried out by *Leonhardt and Walther* (1962), *Kani* (1967) and *Shioya et. al.* (1989).
An increase in the overall depth of beams results in a decrease on the shear at failure for a given f'_c, ρ_w and a/d. The width of an inclined crack depends on the product of the strain in the reinforcement crossing the crack and the spacing of the cracks. With increasing beam depth, the crack spacing and the crack widths tend to increase: so, larger crack widths occur in larger member, with the consequent reduction of the aggregate interlock [14].
In beams with at least the minimum required web reinforcements, the web reinforcements holds the crack faces together so that the shear transfer across the cracks by aggregate interlock is kept. As a result, the reduction in shear strength due to the size is not observed in beams with web reinforcements.

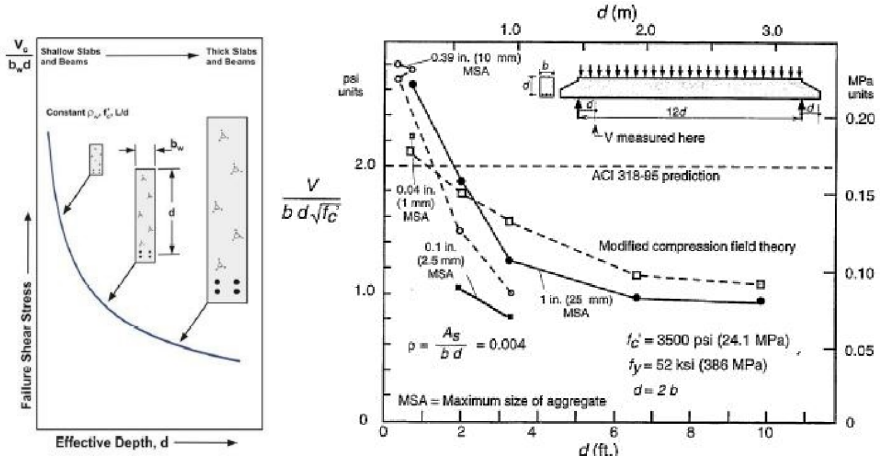

Size-effect idealization (left-hand) and effect of beam depth d on failure shear for beams of various sizes(right-hand) from experimental tests

Using fracture mechanics it has been explained the size effect on the basis of energy released on cracking [29].
The amount of energy released increases with an increase in size, particularly in depth. Although a portion of the size effect results from energy release, the authors believe crack-width explanation of size effect fits the test data trends more closely.

Axial forces

Pre-stressed member or subjected to axial compression will be able to resist higher loads before cracking of the concrete occurs. Axial tensile forces tend to decrease the inclined cracking load, while axial compressive forces tend to increase it. As the axial compressive force is increased, the onset of flexural cracking is delayed, and the flexural cracks do not penetrate as far into the beam. Instead, axial tension forces directly increase the tensile stress overall the beam section, hence the strain becomes higher in the longitudinal reinforcement. This causes an increase in the inclined crack width, which, in turn, results in a decrease the aforementioned aggregate interlock. Accordingly the shear failure load decreases. The opposite occurs for axial compressive forces.

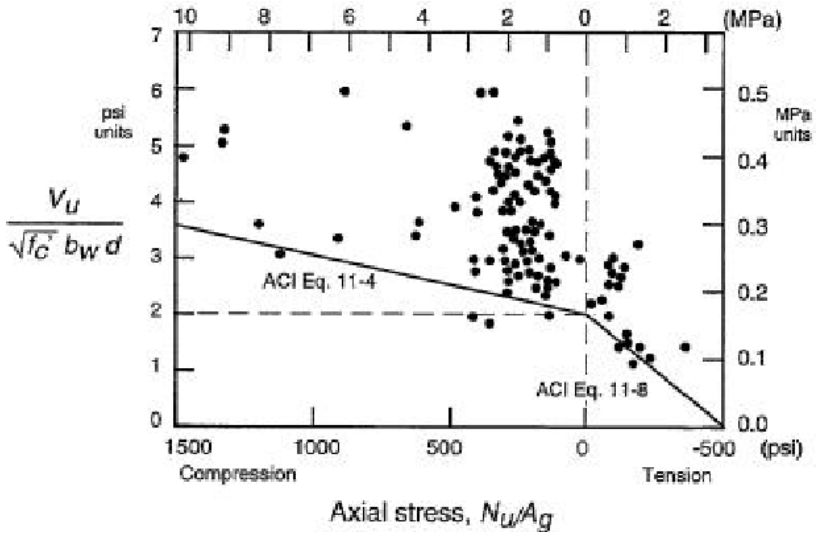

Effect of axial loads on inclined cracking shear

Effective width

The effective width depends on few parameters as: size of the loading plate, size of the supporting plates, slab width and shear span [30]. An other main parameter is the spreading angle of the load: when the concentrated loads are close to the support, the width will reduce to the effective width. It has influences on determining the shear capacity of deep beam and slabs. Although *Furuuchi* developed a formula to calculate the effective width most national and international standards have currently no rules for this parameter [29].

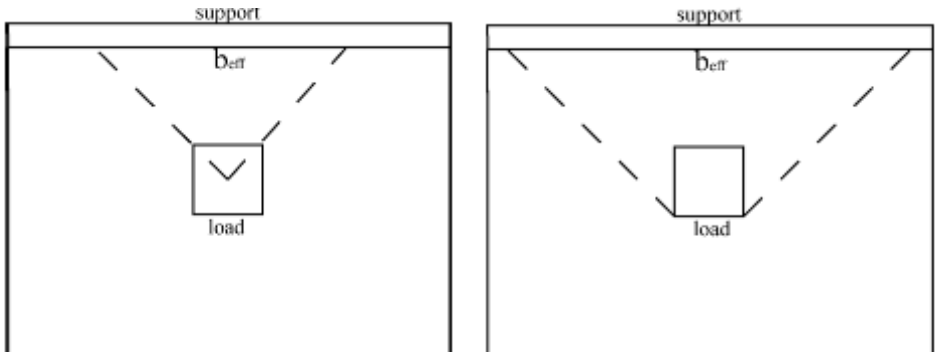

Effective width: 45° load spreading (left-hand) and 45° load spreading – French practice (right-hand)

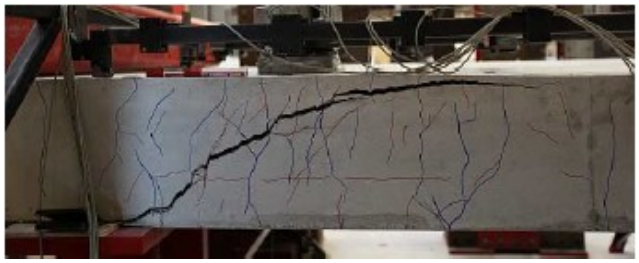

(a)

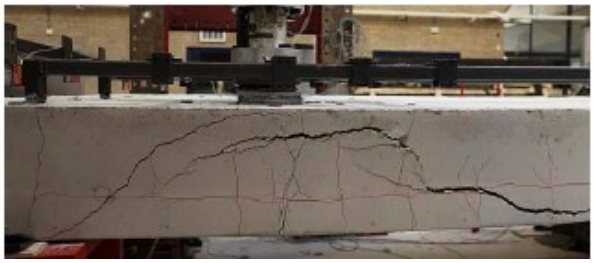

(b)

(a) Beam shear (or one-way) failure and (b) Punching shear (or two-way) failure

4. DESCRIPTION OF EXPERIMENTAL TEST S25T1

4.1 Material properties

4.1.1 Concrete

The cast was executed on 03-08-2011 [30]. The mix was composed of blast furnace B cement, fly ash and gravel aggregates with a particle size between 4 mm and 16 mm, as specified in the following table and in the relative particle size curve.

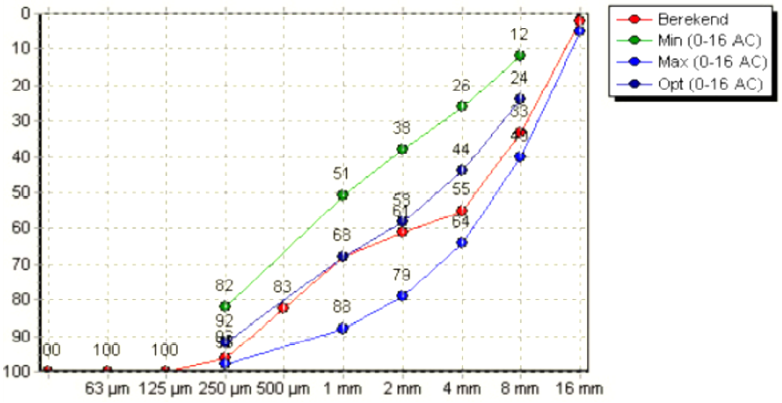

Zeven volgens NEN 2560	Betonzand 0-4	Grind 4-16	Mengsel
Toeleveringscode	11759	11742	
16 mm	0,0%	3,8%	2,1%
8 mm	0,0%	61,1%	33,3%
4 mm	8,6%	94,4%	55,3%
2 mm	15,7%	99,0%	61,1%
1 mm	30,3%	99,5%	68,0%
500 µm	61,6%	100,0%	82,5%
250 µm	91,8%	100,0%	96,2%
125 µm	99,6%	100,0%	99,8%
63 µm	100,0%	100,0%	100,0%
Rest	100,0%	100,0%	100,0%
Fijnheidmodulus:	3,10	6,60	5,01
Vocht	4,0%	2,0%	
Absorptie	0,0%	0,0%	
Verhouding toeslag	100,00%	100,00%	
Fractie	45,53%	54,47%	
Slib			
Humus			

Grondstoffen	producent	Te doseren massa	Droge massa	Volume fijn	T.o.v. cement
CEM III/B 42,5 N LH/HS/NA Neuss	Dyckerhoff	320kg	320kg	108,5L	
Betonzand 0-4	Kuypers B.V. Zand en Grind	847kg	814kg	25,8L	
Grind 4-16	Grensmaas	993kg	974kg	1,9L	
Vliegas	Baumineral	30kg	30kg	13,6L	
VTR VZ 10	Sika Nederland BV	0,700kg	0,700kg	0,0L	0,22% m/m
SPL VC 1550	Sika Nederland BV	0,630kg	0,630kg	0,0L	0,20% m/m
Slibwater	Jonker Bouwmaterialenhandel BV	108kg	108kg	7,7L	
Koud Water	Harex Nederland B.V.	24kg	76kg	0,0L	
Lucht		15L	15L	0,0L	
Totaal		**2324kg**		**157,5L**	

Sieve analysis and mix composition of cast 16, used in S25T1

The air content and the slump of the mix were not measured. The concrete was delivered by a truck mixer and 7.8 m^3 of concrete was used for casting the slab, in 5 layers. During casting poker vibrators were used to compact the concrete of the slabs, while cubes were vibrated on the vibration table at 140Hz during 15 seconds.
For standard tests 36 cubes were cast; a concrete block was cast along with the slabs and stored in the same conditions as the slabs for drilling cores.
After casting the slabs and cubes were covered with plastic sheets. The cubes were demoulded after one day and the slabs after 3 months.
All cubes were stored in the fog room (99% RH and 20°C) and tested at an age of 7, 28, 170 and 184 days. The slabs were stored in the laboratory (65% RH and 15-20°C). S25 was tested at 170, 184, 191 and 194 days.
The results of the standard tests on the cubes are given in the following table, in which f_{cc} is the concrete compressive strength of the cube and f_{cspl} the concrete tensile splitting strength of the cube.

cube	age (days)	f_{cc} (MPa)	f_{cspl} (MPa)
1	7	25,07	
2	7	24,74	
3	7	26,74	
4	7		2,37
5	7		2,52
6	7		2,48
7	28	41,78	
8	28	41,72	
9	28	42,29	
10	28		3,61
11	28		3,73
12	28		3,50
13	170	59,27	
14	170	59,82	
15	170	60,20	
16	170		4,50
17	170		4,72
18	170		4,64
19	184	57,51	
20	184	56,25	
21	184	58,37	
22	184		4,56
23	184		4.16
24	184		4,22

Results of compressive and tensile tests on the concrete for cast 16

The development of the *concrete compression strength* and of the *concrete splitting tensile strength* are given in the following figure.

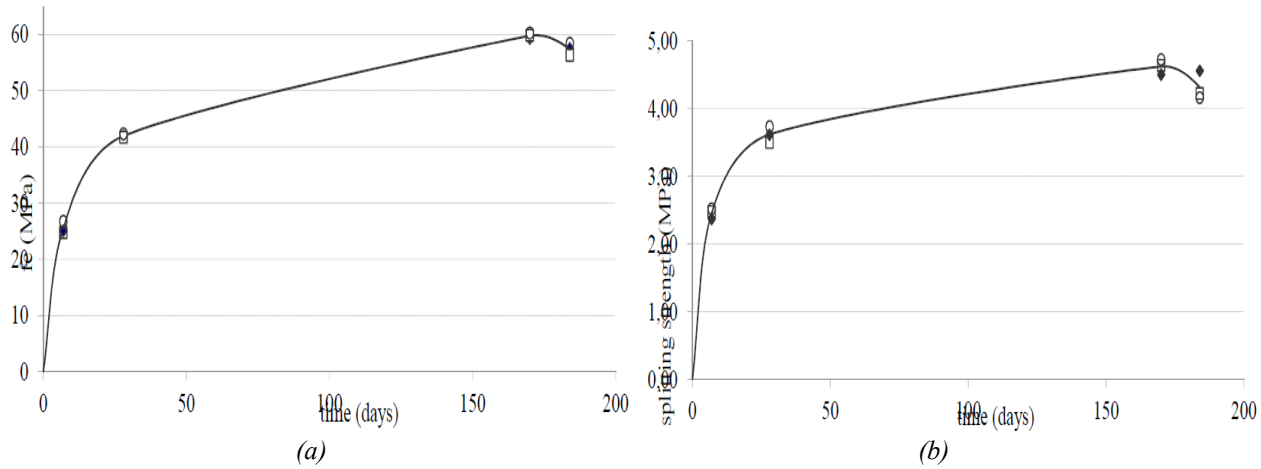

(a) *(b)*

Time development of compressive strength (a) and tensile strength (b) on cast 16, used fot S25T1

A focus about the adopted data is reported in the following table:

Cube	Age (days)	f_{cc} [MPa]
13	170	59,27
14	170	59,82
15	170	60,20
Specimen	**Age (days)**	f_{cspl} [MPa]
16	170	4,50
17	170	4,72
18	170	4,62

Specimens compressive and splitting values

The adopted values refers to the data observed after 170 days, or rather the S25T1 experimental test time after the concrete cast. In accordance with the following values are used in the model:

- **Compressive strength of concrete**: $f_{cc,170days} = 59{,}76\ MPa$;
- **Tensile strength of concrete:** $f_{cspl,170\ days} = 4{,}62\ MPa$.

CEB-FIP Model Codes values for concrete:

To obtain elastic and ultimate strain for concrete, elastic modulus for concrete has to be estimated. In accordance with the CEB-FIB Model Code 2010 relationship the *Young's modulus* is estimated from the mean compressive strength:

$$E_{ci} = E_{c0} \cdot \alpha_E \left(\frac{f_{cm}}{10}\right)^{1/3} [MPa]$$

where:

- E_{ci} is the modulus of elasticity in [MPa] at concrete age of 28 days;
- $E_{c0} = 21.5 \cdot 10^3\ MPa$;
- α_E is assumed to 1.0 for quarzite aggregate;
- f_{cm} is the compressive strength of concrete at 28 days.

Taking the average compressive strength value, f_{cm} is known:

$$f_{cm} = 59{,}76\ MPa$$

$$E_c = 21.5 * 10^3 \left(\frac{59{,}76}{10}\right)^{\frac{1}{3}} MPa = 39016\ MPa$$

Now, the values of the elastic and ultimate strain can be estimated as well. In this specific case the characteristic tensile strains are:

$$\varepsilon_{el} = \frac{f_t}{E_{ci}} = \frac{4{,}62}{39016} = 1{,}184 \cdot 10^{-4}$$

$$\varepsilon_{cu} = 0{,}0025 + 0{,}002\left(1 - \frac{f_{ck}}{100}\right) = 0{,}0025 + 0{,}002\left(1 - \frac{51{,}76}{100}\right) = 3{,}46 \cdot 10^{-3}$$

Where the f_{ck} is obtained inverting the CEB-FIP relationship:

$$f_{cm} = f_{ck} + 8\ MPa\ \rightarrow\ f_{ck} = f_{cm} - 8\ MPa = (59{,}76 - 8)\ MPa = 51{,}76\ MPa$$

Fracture energy of concrete:

The fracture energy of concrete G_f $[N/m]$, defined as the energy required to propagate a tensile crack of unit area. The used concrete belongs to the category of high-strength concretes, thus the equation :

$$G_f = 73 \cdot {f_{cm}}^{0{,}18}$$

provided by the recent CEB-FIP Model Code 2010 can lead to not completely reliable results. However, using this relation, the estimated *tensile fracture energy* is:

$$G_f = 0{,}150\ \frac{Nmm}{mm^2}$$

Approximately, the 2010 Model Code version gives a $+50\%$ than the older one (1990 version). Moreover, the CEB-FIP Model Code 2010 doesn't link G_f value to the maximum aggregate size and it gives an higher magnitude for this significant parameter.

4.1.2 Interface layer

Felt interface

On the supports a layer of felt with 5 mm of total thickness was interposed between the slab and a bottom steel bearings of steel 100 mm x 15 mm x 2500 mm, that is in contact with the wider steel strips with a width of 300 mm.

Detail of the interface layer interposed between the slab and the support

To evaluate the stiffness of 5 mm of *N100 Navima felt*, several tests have been performed, with different cycles of loading. The results of these tests are shown in the following stress-strain diagram. They refer to the third part (Test III) of the test and refer to the 25-26-27 specimens.
An important annotation has to be done regarding the felt behaviour: first it was assumed that the load from the self-weight of the slab was too small to influence the felt properties. The results from Test I were used in several FEM models for the S4 series but the behaviour of the structure in the FEM analysis was not satisfactory. Especially in the beginning of the loading, the FEM analysis showed a very soft response. Therefore, Test II was carried out and a large difference in the initial stiffness of the felt was found (see [31] for more information).
Also Test III was the same as Test II. The stress-strain diagram of this specimen was almost identical to the results from Test II. Therefore no more specimens were tested and Test II was considered as sufficient for the determination of the actual felt properties.

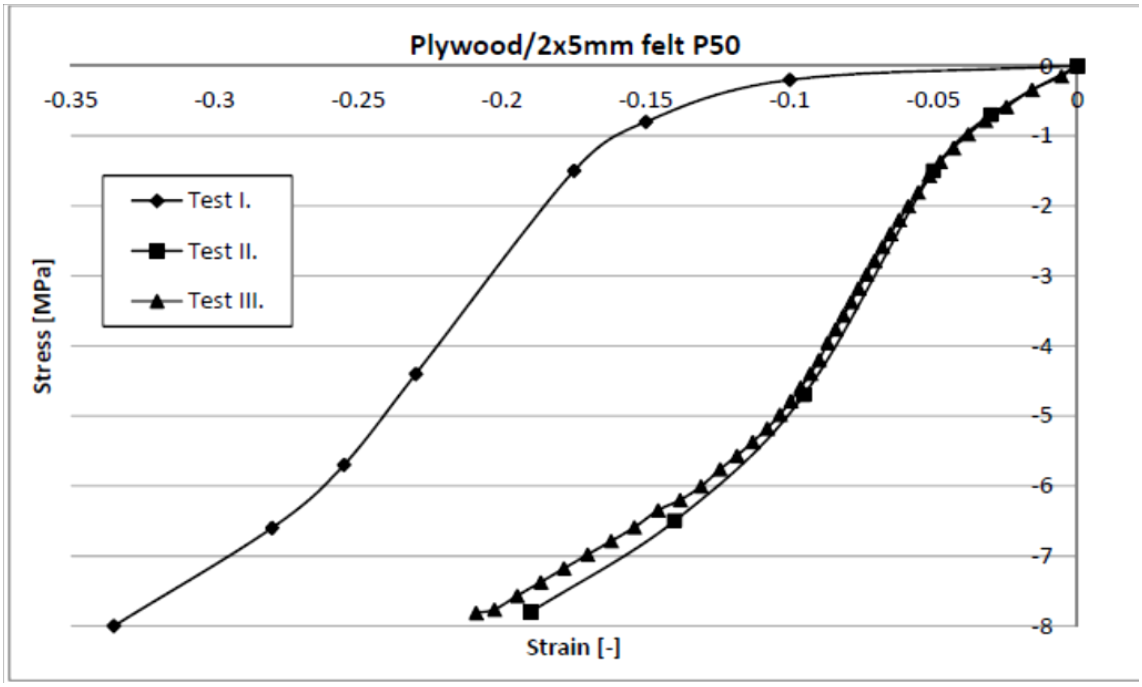

Test I-II-III stress-strain diagram for felt specimens

The following graphs show the result from three felt specimens under load control.
The felt specimens are loaded (1st cycle) and then unloaded; after they are loaded with additional cycles (2nd cycle): as visible, a stiffer and stable response occurs. So, the felt strips are all loaded and reloaded, in order to deal the material.

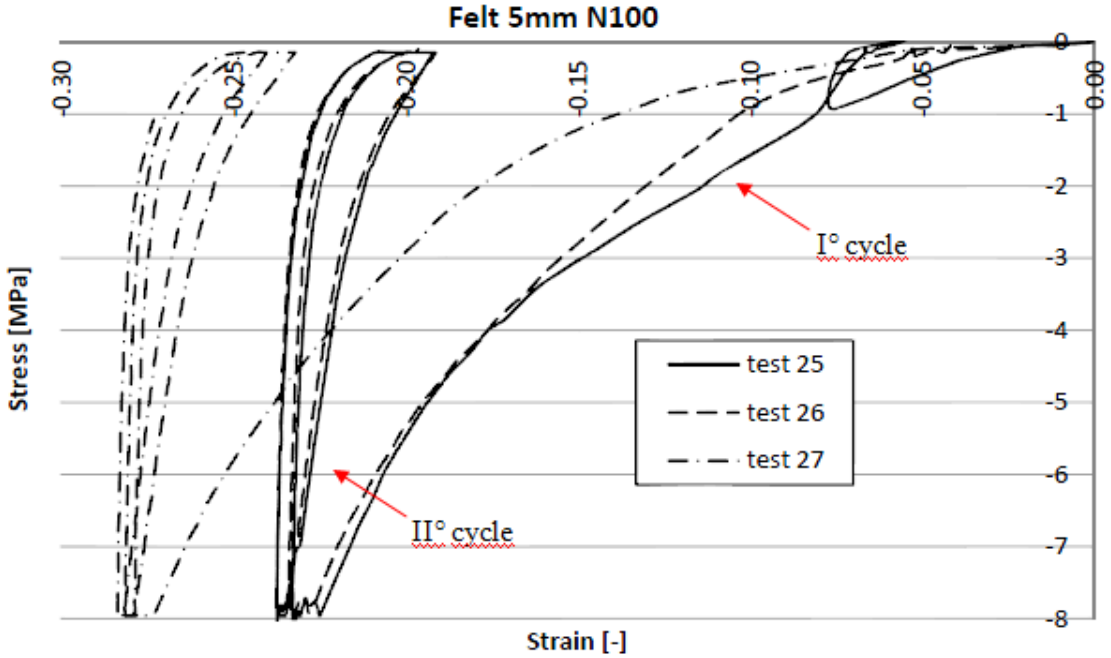

Stress-strain laboratory response for felt specimens

So, for the numerical modeling the second trait is adopted, since the felt is reloaded. A series of main points is defined and the global behavior is taken up.

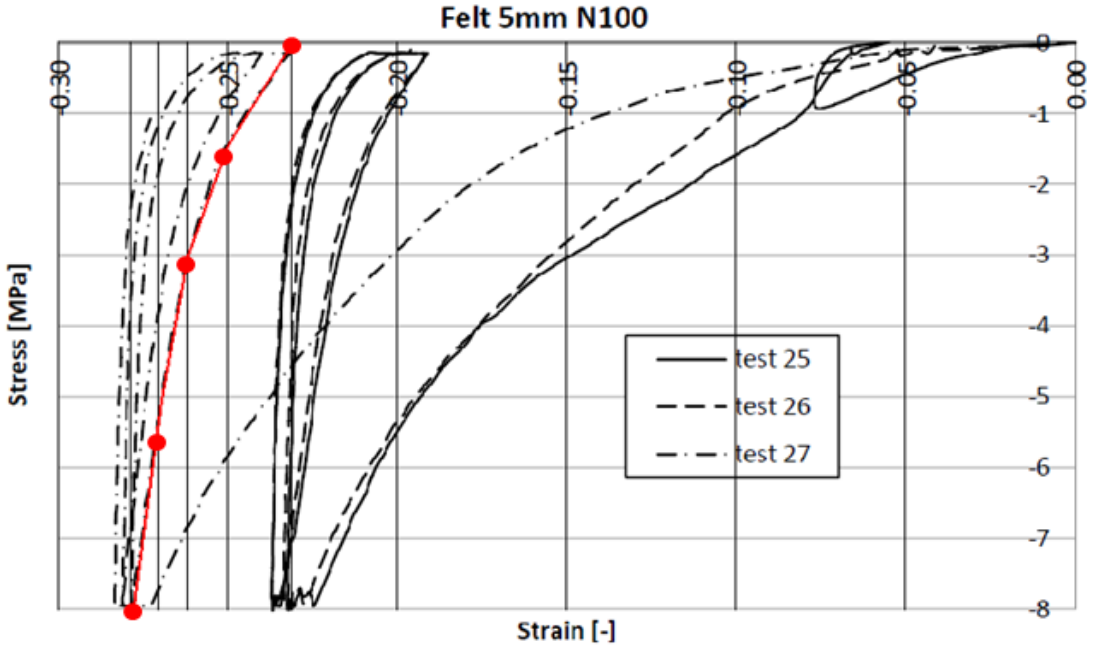

Main points and linear traits interpolation on stress-strain diagram

The present table shows the obtained values for normal stress σ and strain ε:

ε [-]	σ [Mpa]
-10	-0.00001
0	0.00
0.0187	1.43
0.0306	3.00
0.0394	5.00
0.0473	8.00

Main points values

In order to insert the felt behaviour inside the *iDiana* environment is necessary to describe a $\sigma - \Delta u$ diagram for the felt, where Δu is the relative displacement between the two faces of the interface (for this consult [34]):

syntax

```
'MATERI'
SIGDIS    tn1_r un1_r [tn2_r un2_r ...] tnn_r unn_r
TAUDIS    tt1_r ut1_r [tt2_r ut2_r ...] ttn_r utn_r
```

SIGDIS specifies a diagram for the normal direction: values *tn1* ... *tnn* are ($n \leq 100$) the normal tractions t_n, *un1* ... *unn* are the corresponding normal relative displacements Δu_n.

TAUDIS specifies a diagram for the tangential direction: values *tt1* ... *ttn* are ($n \leq 100$) the tangential tractions t_t, *ut1* ... *utn* are the corresponding tangential relative displacements Δu_t.

Both diagrams must start in the compressive (negative) region and end in the tension (positive) region. The specified relative displacements must be in increasing order. For numerical reasons it is recommended to use a continuous slope at (0,0) in both diagrams which corresponds with the elastic stiffness as specified with DSTIF.

Non-linear iDiana interface properties

Taking into account the high stiffness of the steel $HEM300$ beams, we can simplify the Δu definition just doing a negligible approximation:

$$\Delta u = u_{up} - u_{down} = u_p$$

So, u_p is defined as the displacement imposed by the slab reactions.
Thus, taking into account the small thickness of the felt interface we can obtain the corrisponding u_p from a given ε.
Every ε is known thanks to the experimental test on many specimens and the $\sigma(\varepsilon)$ function is given too.
It reads so:

$$\varepsilon_{felt} \cong \frac{u_p}{t}$$

So, we can get:

$$u_p = \varepsilon_{felt} \cdot t$$

It's easy to get the required $\sigma(u_p)$ function for the *iDiana* envirnoment.
The tensile inertia is molded by a flat trait; instead the higher compressive behavior is extrapolated:

δ [mm]	σ [Mpa]
-50.000	-0.00001
0.000	0.00000
0.094	1.43000
0.153	3.00000
0.197	5.00000
0.237	8.00000
3.000	210.73

Main points for the numerical model

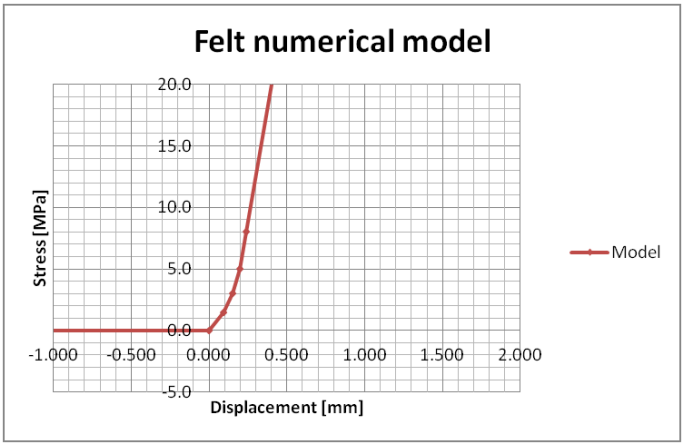

Numerical model for felt ($\sigma(\delta)$; δ)

iDiana requires a linear definition both for the normal and tangential behaviour for the felt interface. It's defined by DSTIF strings; for numerical reasons the elastic value has to match with the first trait stiffness.

The ratio stress/strain is the average Young's modulus for the first range and it can be obtained by the following relationship:

$$E_f = \frac{\Delta\sigma}{\Delta\varepsilon} \cong \frac{1{,}43}{0{,}0187}\ MPa = 76{,}50\ MPa$$

The finite variations $\Delta\sigma$ and $\Delta\varepsilon$ can be read in the upper *stress-strain* table.
Since the layer of interface is $5\ mm$ thick, one can calculate the *linear normal stiffness* of the interface layer:

$$K_n = \frac{E_f}{t} = \frac{76{,}50\ MPa}{5\ mm} = 15{,}20\ \frac{N}{mm^3}$$

As *linear tangential stiffness* a lower value is taken:

$$K_t = \frac{K_n}{100} \cong 0{,}20\ \frac{N}{mm^3}$$

In this case the felt interface is molded as the *Winkler spring soil*, with a nonlinear normal behaviour and a tangential linear behaviour.

4.1.3 Teflon interface

On the loading surface, a Teflon layer is interposed between concrete and steel plate. The material properties were no investigated, so the mechanical properties for the teflon interface are taken from *DuPont's Teflon* tables.

Table 1
Typical Properties of DuPont™ *Tefzel*® Fluoropolymers

Property	ASTM Method	Units	*Tefzel*® Grade 210	200	280
Mechanical					
Melt Flow Rate	D3159	g/10 min	23	7	4
Ultimate Tensile Strength, 23°C (73°F)*	D638	MPa (psi)	40 (5,800)	46 (6,500)	47 (6,700)
Ultimate Elongation, 23°C (73°F)*	D638	%	150–300	150–300	150–300
Compressive Strength, 23°C (73°F)**	D695	MPa (psi)	17 (2,500)	17 (2,500)	17 (2,500)
Flexural Modulus	D790	MPa (psi)	1,200 (170,000)	1,200 (170,000)	1,200 (170,000)
Impact Strength, 23°C (73°F)	D256	J/m (ft-lb/in)	no break no break	no break no break	no break no break
Hardness, Durometer, Shore D	D2240		63	67	72
Coefficient of Friction, Metal/Film	D1894		0.23	0.23	0.23
Deformation Under Load, 23°C (73°F), 1000 psi, 24 hr	D621	%	0.2	0.3	0.2
Linear Coefficient of Expansion	E831				
0–100°C		mm/mm·°C x 10^{-5}	12.6	13.1	13.3
100–150°C			17.6	18.5	20.9
150–200°C			22.3	25.2	25.7
32–212°F		(in/in·°F x 10^{-5})	(7.0)	(7.3)	(7.4)
212–302°F			(9.8)	(10.3)	(11.6)
302–392°F			(12.4)	(14.0)	(14.3)
Specific Gravity	D792		1.72	1.71	1.70
Water Adsorption, 24 hr	D570	%	0.007	0.007	0.005

DuPont Teflon mechanical properties

To fix the stress range the compressive strength is checked up on:

$$\sigma_c = \frac{F}{A} = \frac{1460\ kN}{300 \cdot 300\ mm^2} \cong 16.20\ MPa\ <\ \sigma_{c,ult} = 17\ MPa$$

So, the stiffness values take reference from the following graph:

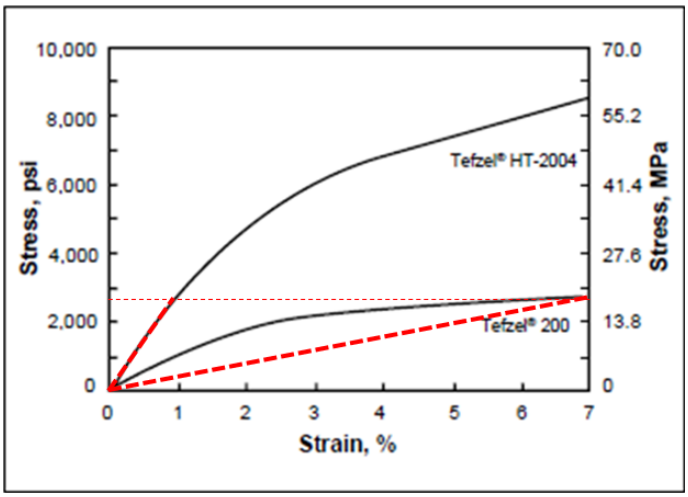

DuPont Teflon mechanical properties: compressive modulus at room temperature

Due to the ultimate compressive stress, the *Young's modulus* range is between 240 MPa and 1700 MPa.
A linear behavior is assumed.
As seen before, adopting an interface with a 2 mm thickness, the *linear normal stiffness* varies from 120 N/mm^3 and 850 N/mm^3. Instead, the *tangential linear stiffness* is kept even to 0.20 N/mm^3.

4.1.4 Steel

In this experiment steel has been used for different elements that are reinforcement bars, loading plate, HEM supports, contrasting beam and pre-stressing bars.

Reinforcement bars

The two topologies of ribbed reinforcements (Ø10 and Ø20) have been subjected to several traction tests [31].
For each diameter has got three tested specimens.
In the two following diagrams the *stress-strain* response of the bars are reported and one can observe by the multiline simplification that their behavior is elastic in the first part, with a 200000 MPa stiffness, while the plastic part is characterized by different hardening behavior.
Every stress-strain model results from the average traction test data.

Average	Φ10 ribbed bars σ-ε model	
Stress [MPa]	Strain [-]	
0	0	
460	0.0024	$\varepsilon_{pl,diagr}$ [-]
471	0.0025	0.00012
481	0.0026	0.00024
490	0.0028	0.00043
500	0.0030	0.00067
510	0.0033	0.00095
521	0.0037	0.00136
531	0.0042	0.00187
540	0.0049	0.00252
550	0.0057	0.00336
560	0.0068	0.00445
570	0.0083	0.00589
580	0.01029	0.007920
590	0.01309	0.010720
600	0.01695	0.014573
610	0.02243	0.020053
620	0.03136	0.028987
627	0.05113	0.048760

Average $\sigma - \varepsilon$ data for Ø10 specimens

Average	Φ20 ribbed bars σ-ε model	
Stress [MPa]	Strain [-]	
0	0	
540	0.0032	$\varepsilon_{pl,diagr}$ [-]
541	0.0149	0.01168
550	0.0175	0.01424
560	0.0212	0.01798
570	0.0240	0.02078
580	0.0272	0.02396
590	0.0306	0.02736
600	0.0346	0.03136
610	0.0392	0.03600
620	0.0446	0.04140
630	0.0512	0.04796
640	0.0602	0.05692
650	0.0739	0.07062
658	0.1269	0.12368

Average $\sigma - \varepsilon$ data for Ø20 specimens

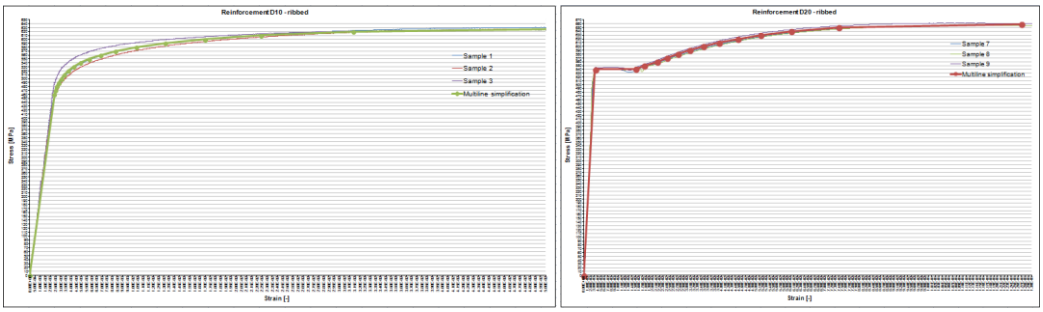

Stress-strain relation for ϕ10 (left-hand) and ϕ20 (right-hand) ribbed bar

For Ø10 reinforcements the mechanical properties that can be calculated are:

- **Young's modulus:** $E_{s,D10} = 200000\ MPa$;
- **Poison's Ratio:** $\upsilon_s = 0{,}30$;
- **Tensile Yielding stress:** $\sigma_{y,D10} = 460\ MPa$;
- **Tensile ultimate stress:** $\sigma_{u,D10} = 625\ MPa$.

Instead, for Ø20 reinforcements the mechanical properties they are:

- **Young's modulus:** $E_{s,D10} = 200000\ MPa$;
- **Poison's Ratio:** $\upsilon_s = 0{,}30$;
- **Tensile Yielding stress:** $\sigma_{y,D20} = 575\ MPa$;
- **Tensile ultimate stress:** $\sigma_{u,D20} = 660\ MPa$.

Pre-stressing bars

For the pre-stressing trusses Ø36 Dywidag bars are used. *Dywidag Prestressing Steel Threadbar* is a high tensile alloy steel bar which features a coarse right-hand thread over its full length.
No tests are made and properties refer to the product declaration, which are reported in table below (for more information see [33]).

Nominal Diameter	Steel Grade	Ultimate Strength *fpu*	0.1% (a) Proof Strength	70% (b) Ultimate Strength	50% Ultimate Strength	Cross Sectional Area	Diameter Over Threads	Thread Pitch	Bar Weight
mm	N/mm²	kN	kN	kN	kN	mm²	mm	mm	kg/m
15	900/1100	195	159	136	98	177	17	10	1.44
20	900/1100	345	283	241	173	314	23	10	2.56
26.5	950/1050	579	523	405	290	551	30	13	4.48
32	950/1050	844	764	591	422	804	36	16	6.53
36	950/1050	1069	967	748	535	1018	40	18	8.27
40	950/1050	1320	1194	924	660	1257	45	20	10.21
47	950/1050	1822	1648	1275	911	1735	52	21	14.10
57	835/1035	2671	2155	1870	1335	2581	64	21	20.95
65	835/1035	3447	2771	2413	1724	3318	71	23	27.10
75	835/1035	4572	3645	3200	2286	4418	82	24	35.90

Technical Data for Prestressing Steel Threadbar

So, the main features are:

- **Young's modulus:** $E_{s,D} = 205000\ N/mm2 \pm 5\%$;
- **Tensile Yielding stress:** $\sigma_y = 950\ MPa$;
- **Tensile Ultimate stress:** $\sigma_u = 1050\ MPa$;
- **Tensile Yielding strain:** $\boldsymbol{\varepsilon_y} = 0.1\%$;
- **Tensile Ultimate strain:** $\boldsymbol{\varepsilon_u} = 10\%$;
- **Cross area:** $A = 1018\ mm^2$.

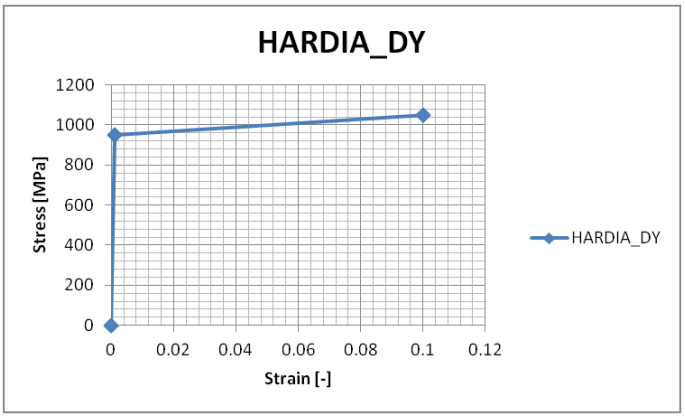

Stress-strain relation for ϕ36 Dywidag bars

Loading plate and HEM beams

For what regards to the loading plate and the supports, no tests on these steel have been performed, but the mechanical properties has been provided by the producer. Since the response of these elements will not be object of the present study, is sufficient to consider only the stiffness of the steel, that is $200000\ MPa$ for the loading plate and $210000\ MPa$ for the HEM supports and the value of the *Poison's ratio* that is 0.3.

Contrasting system

The contrasting system (or "nut beam") is a steel box profile reinforced by metallic ribs, so it's material properties are the same: $200000\ MPa$ as *Young's modulus* and 0.3 for the *Poison's ratio*.

4.2 Experimental test on the slab

4.2.1 Specimen

The slab S25T1 presents a rectangular shape with dimensions of 5000 mm length, 2500 mm wide and thickness of 300 mm.

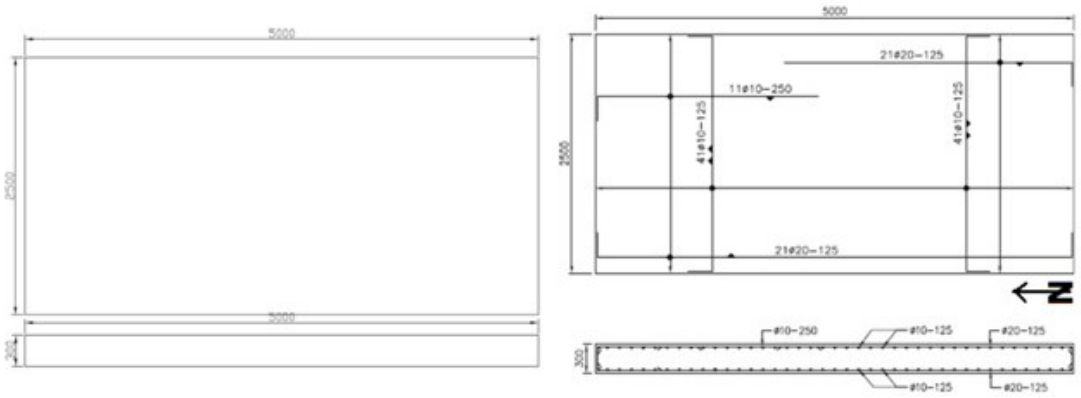

(a) *(b)*

Layout of the tested slab (a) and reinforcement bars (b)

The layout of reinforcements is presented in the previous figure and is composed by 5 groups of bars:

1) longitudinal principal on the top face $\emptyset 20$ – 125 mm (a total of 21 bars), with length of 3000 mm measuring from the east frontal face;
2) longitudinal principal on the bottom face $\emptyset 20$ – 125 mm (a total of 21 bars), on the entire length of the slab;
3) longitudinal secondary on the top face $\emptyset 10$ – 250 mm (a total of 11 bars), with a length of 2200 mm measuring from the west frontal face;
4) transversal on the top face $\emptyset 10$ – 125 mm (a total of 41 bars), on the entire length of the slab;
5) transversal on the bottom face $\emptyset 10$ – 125 mm (a total of 41 bars), on the entire length of the slab.

It has to be observed that the values of the length can be slightly different, to ensure that the external cover of concrete on reinforcement is 25 mm in all the points of the slab.
To use more general and synthetic values the mechanical percentages of reinforcements are calculated:

- **Mechanical percentage of longitudinal reinforcements:** $\rho_l = 0.996\%$;
- **Mechanical percentage of transversal reinforcements:** $\rho_t = 0.258\%$.

4.2.2 Loading and measuring schemes

The scheme of loading and the layout of the constraints are presented in the following figures.

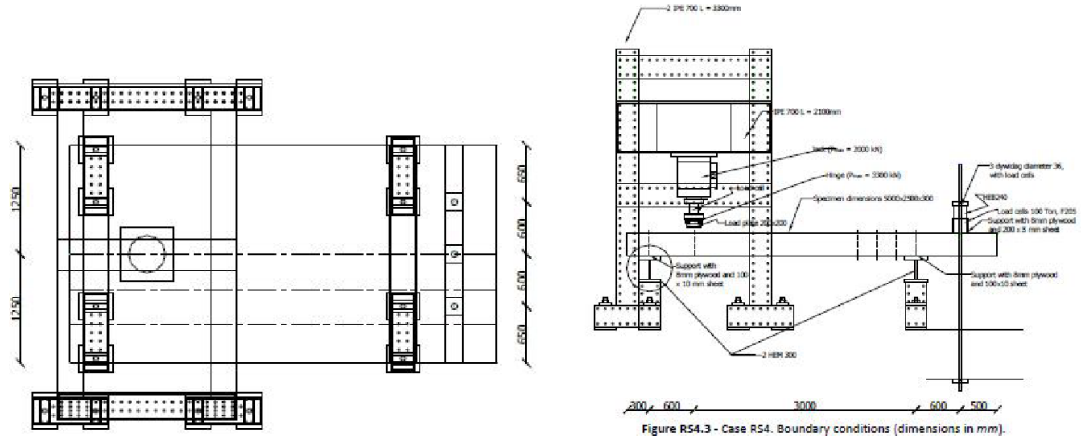

Figure RS4.3 - Case RS4. Boundary conditions (dimensions in *mm*).

Loading device and layout of the experimental test

Continuous supports are placed along short edges of the slab: the North edge is simply supported, while the South edge is clamped by pre-stressed bars in order to avoid rotations.
Steel profiles realize the continuous boundary condition. Continuous felt layers avoid concentration of stresses at supports and minimize the in-plain restraints.
3 Ø 36 Dywidag bars, having a total length of 3.00 m and a used length of 2.58 m, prevent rotation, a pretension equal to $\pm 15\ kN/bar$ has been applied before test.
The load is applied in correspondence at midspan of transversal axis; the load is symmetric with respect to the longitudinal axis. A detail of support and loading conditions is reported in the following figure.

Detail of loading device

The load is applied by a hydraulic jack, by a square-shaped loading plate of 300 mm x 300 mm was used, in contact with the tested slab through a Teflon layer and by controlling the deformation at a constant rate. The load is kept constant while marking the cracks. The loading sequence is illustrated in the following figure.

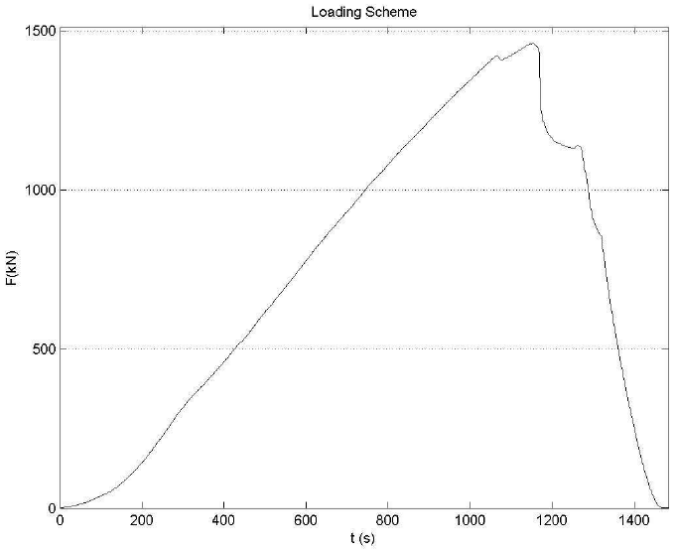

Time-Applied Force diagram relative to slab S25T1

4.2.3 The observations made during the test

Date: 20-01-2012
Load position concentrated load: $a = 600mm$, $b_r = 1250mm$, at simple support.
In this experiment, only a concentrated load was applied (no line load) to check the support conditions.
The position of the load cells is mirrored as compared to all previous experiments. Failure occurred at $1461\ kN$. After failure, the maximum measured crack widths were as follows:

- on the bottom face: $0.1\ mm$ for a north-south crack in the middle from the support towards the span, passing the center of the load; $0.25\ mm$ for a crack in the east west direction close to the support; $3\ mm$ for punching damage at the west side of the bottom face and $0.2\ mm$ for a north south crack at the west side at $48\ cm$ from the free edge;
- on the front face: $0.05\ mm$ for a through crack in the middle; $0.05\ mm$ for cracks towards the east side, not fully through and starting from the bottom;
- on the side faces, no cracks were visible, not even flexural cracks.

Cracking pattern at the bottom face for S25T1 slab

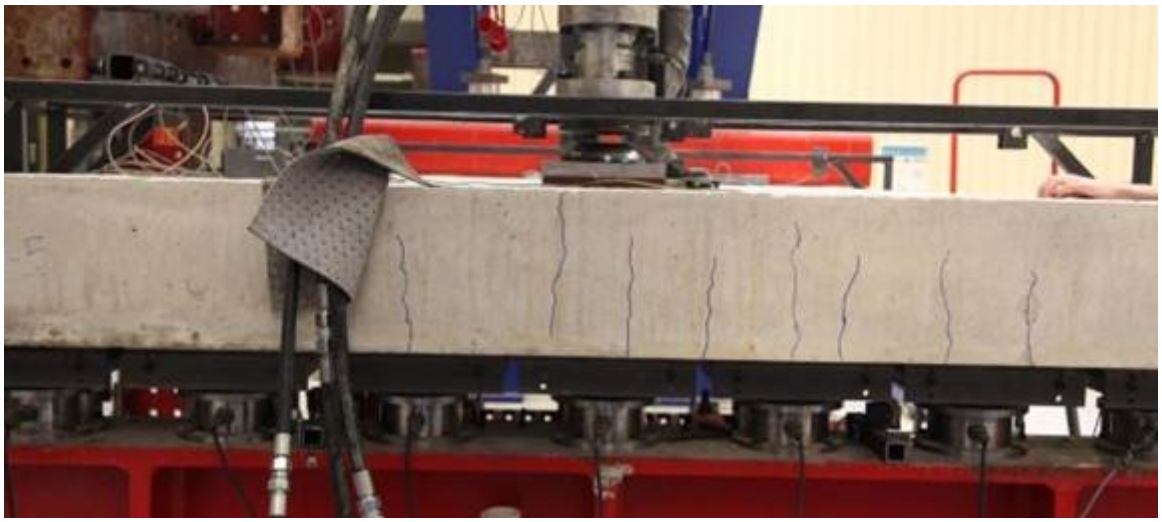

Cracking pattern at front face for S25T1 slab

One of the most important and meaningful results of the experimental test is the *Load-Displacement diagram*. To build it a series of laser measurements are used, in particular the diagram above shows an average displacement among the four lasers located in the X and Y directions, 37 mm from the edge of the loading plate, in order to avoid the affection of local effects in the evaluation of the displacements. In fact the Load-Displacement diagram measured from the load cell into the hydraulic jack shows a more deformable behavior. It's due to many phenomena occurred during the experimental test: steel frame deformation and adjustments into the whole experimental setup (felt layers, Teflon, slab, steel frame, supports device, etc).

Indeed, it's important to report what happens during the first experimental test to better understand the following considerations and model assumptions.

During the first load operations, until the first 3 mm displacement, an hardening trend is easily visible in the hydraulic jack force-displacement diagram.

This phenomena is common in adjustment occurrences.

In the present experiment the slab was not perfect horizontality of the front side slab: the transversal section was deformed. It was warped in the longitudinal axes too.
So, the concrete surfaces are not in perfect contact with the felt interfaces and in the middle on the external sections a gap (δ_M) is present. This one could measure even $2.00\ mm$ maximum in the section middle.

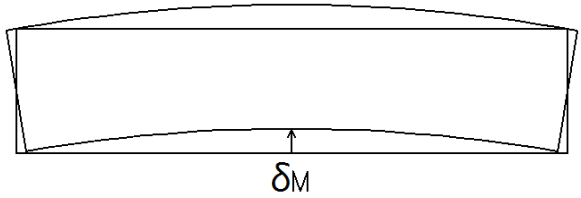

Deformed shape for the transversal section for S25T1 slab

So, with the loading operation, the curve surface, supported on the $HEM\ 300$ beams, has started to bend up to come into contact to the straight surface of the felt interface on the steel frames.
As one can imagine, this event is characterized by a lower stiffness.
This adjustment phenomena, really common in mono-axial compressive tests on rock specimens for example, can explain the first slab hardening behavior.

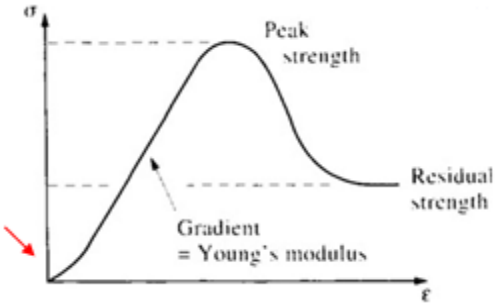

Mono-axial test diagram

When all the lower side of the slab at the simple support is into contact with the horizontal surface the real slab stiffness occurs.

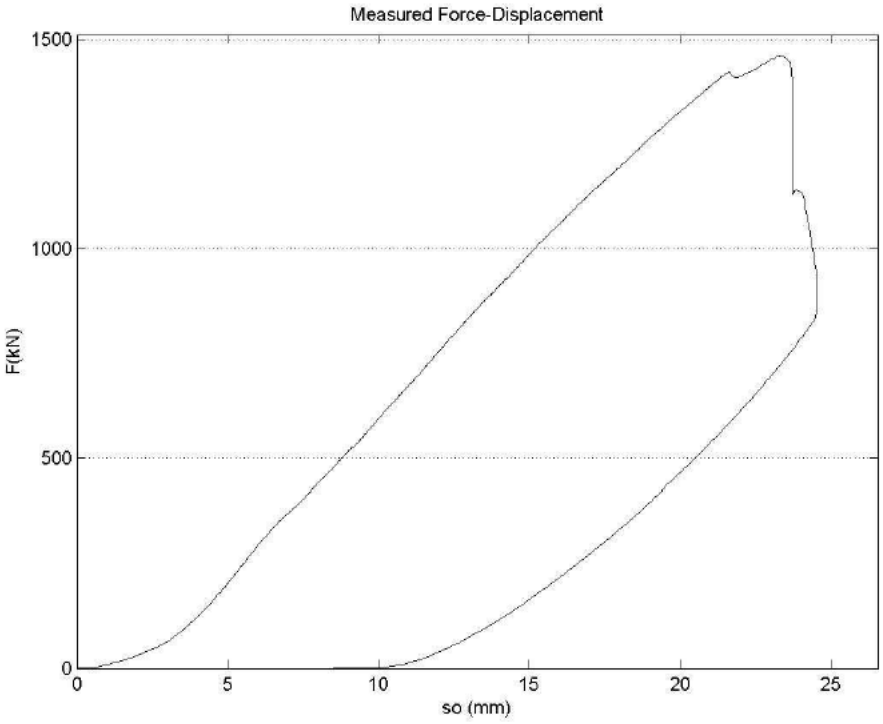

Force- displacement diagram concentrated load S25T1 from the hydraulic jack

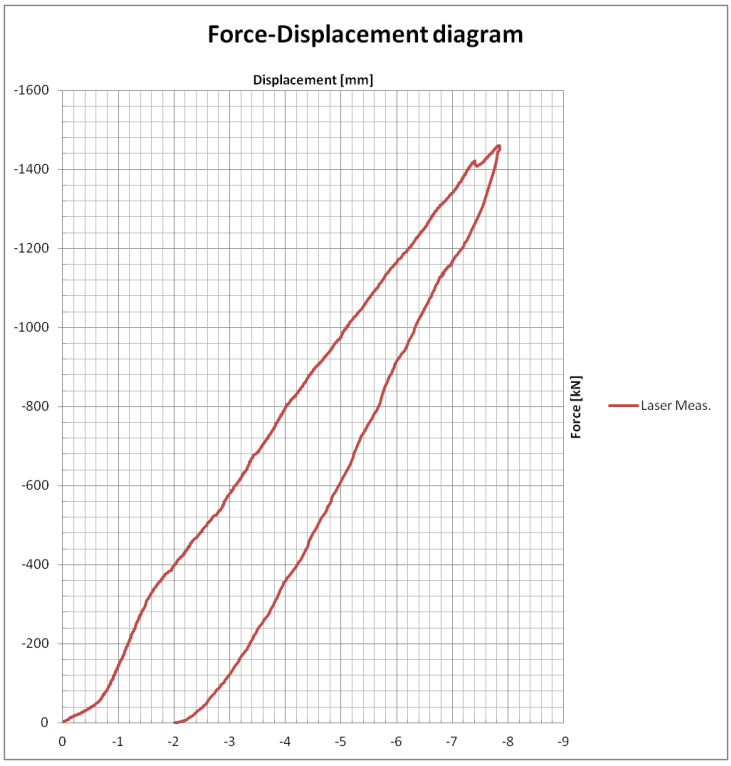

Force - displacement diagram concentrated load S25T1from the 4 lasers

In the following image the different behavior detected by lasers and hydraulic jack is well visible. Moreover, the lasers device shows a snap-back phenomenon after the peak load, besides a stiffer trend. However, the whole shape are alike.

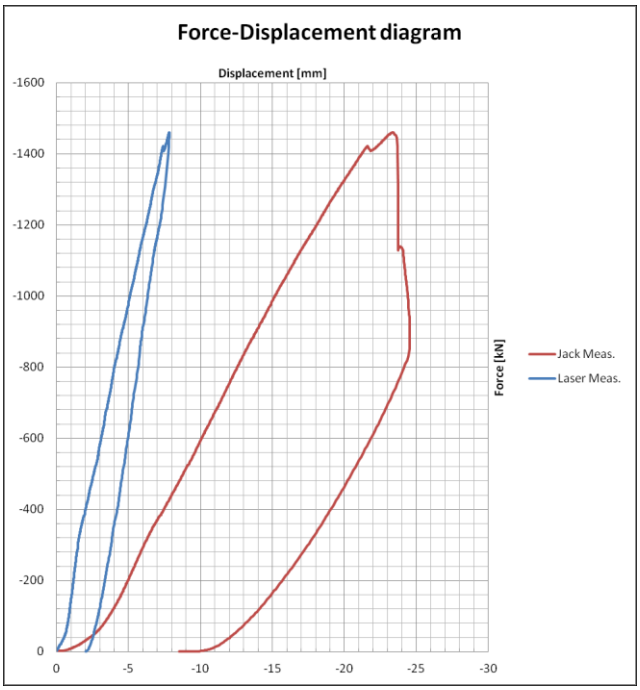

Comparison between 4 lasers and hydraulic jack measurements

The following figure shows the four points of the loading plate in which the total displacements are measured (green circles).

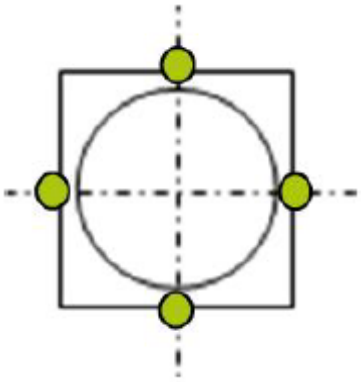

Representation of the 4 measuring points on the edge of the loading plate

5. APPLICATION ON NON-LINEAR ANALYSIS

5.1 Three-dimensional model of the reinforced concrete slab

5.1.1 Finite element model

During the present activity two different models were created: a first *Partial model* and a second *Total model* (the partial model will be discussed for SL-analysis).
The differences between the aforementioned models consist in the way of modelling the clamped support. In the first model a perfect clamped constraint was adopted on the South vertical section above the support beam. Instead, in the second model this assumption wasn't used and the full constraint system is defined as the experimental setup. So, the pre-stressing system and the contrasting profile are inserted into the model. In this way, the experimental setup is exactly modeled. Not only, the experimental procedure is applied to: it needs the application of a *phase analysis sequence*.
The three-dimensional complete slab model is composed by different *solid parts*, each of them is modeled by one or more three-dimensional geometrical elements (*bodies*) and one-dimensional geometrical elements (*truss/cable*).
The various bodies composing the different parts are:

- slab;
- $HEM300$ supports;
- loading plate;
- interface felt layer (between slab and supports and slab and contrasting profile);
- interface Teflon layer (between load plate and slab);
- contrasting profile.

Truss/cable elements are used to model Dywidag bars only.

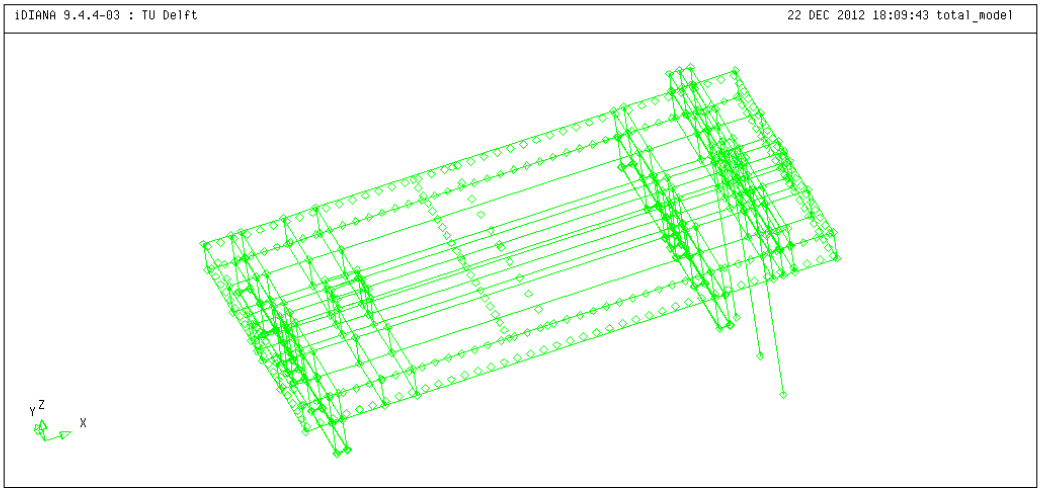

Geometrical model S25T1 slab (total version)

The reinforcements bars are modeled as single *embedded reinforcements* into the slab volume. In order to avoid numerical error and keep the symmetry of the model, the bars on the symmetry axes are divided in two.
SI units are adopted (for instance some mean values are: *mm* for length and displacements and *N* for force and load).

5.1.2 Meshing

To execute an analysis with *Diana*, the structure has to be discretized through several three-dimensional finite elements.
Due to the different nature and behavior of the various solid parts composing the model, to create the FEM discretization three types of finite element are used:

- the CHX60 element is a *twenty-node isoparametric solid brick element*;
- the CQ48I element is an *interface element* between two planes in a three-dimensional configuration,
- the L6TRU element is a a two-node directly integrated (1-point) truss element.

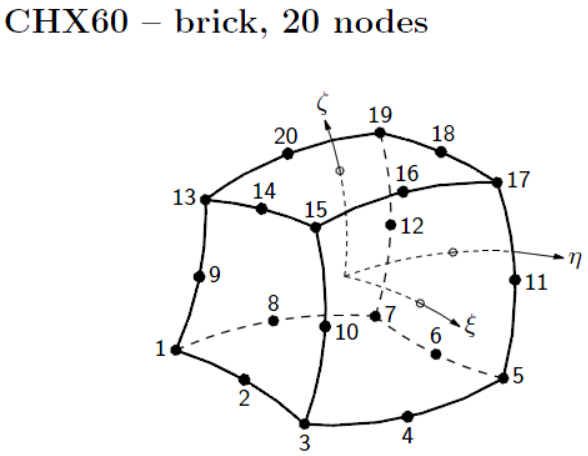

CHX60 brick element for 3D model

The CHX60 element is a twenty-node isoparametric solid brick element [34]. It is based on quadratic interpolation and Gauss integration. The polynomials for the translations u_{xyz} can be expressed as:

$$\boldsymbol{u_1(\xi,\eta,\zeta)} = a_0 + a_1\xi + a_2\eta + a_3\zeta + a_4\xi\eta + a_5\eta\zeta + a_6\xi\zeta + a_7\xi^2 + a_8\eta^2 + a_9\zeta^2 + a_{10}\xi\eta\zeta + a_{11}\xi^2\eta + a_{11}\xi^2\zeta + a_{12}\xi^2\zeta + a_{13}\xi\eta^2 + a_{14}\xi\zeta^2 + a_{15}\eta^2\zeta + a_{16}\eta\zeta^2 + a_{17}\xi^2\eta\zeta + a_{18}\xi\eta^2\zeta + a_{19}\xi\eta\zeta^2$$

Typically, a rectangular brick element approximates the following strain and stress distribution over the element volume. The strain ε_{xx} and stress σ_{xx} vary linearly in x direction and quadratically in y and z direction. The strain ε_{yy} and stress σ_{yy} vary linearly in y direction and quadratically in x and z direction. The strain ε_{zz} and stress σ_{zz} vary linearly in z direction and quadratically in x and y direction. By default

Diana applies a 3 x 3 x 3 integration scheme. A suitable option in a patch of more than one element is 2 x 2 x 2 which yields optimal stress points. Schemes lower than 2 x 2 x 2 or higher than 3 x 3 x 3 are unsuitable.
This type of element is used to discretize all the structural parts that have a regular behavior, i.e. those parts that can be subjects to all the kinds of tensions or strains, regardless to the spatial direction of these.
Finite elements CHX60 are used to build the model of the slab, of the supports, of the contrasting beam and of the loading plate.
Regarding to the interface elements other elements are considered:

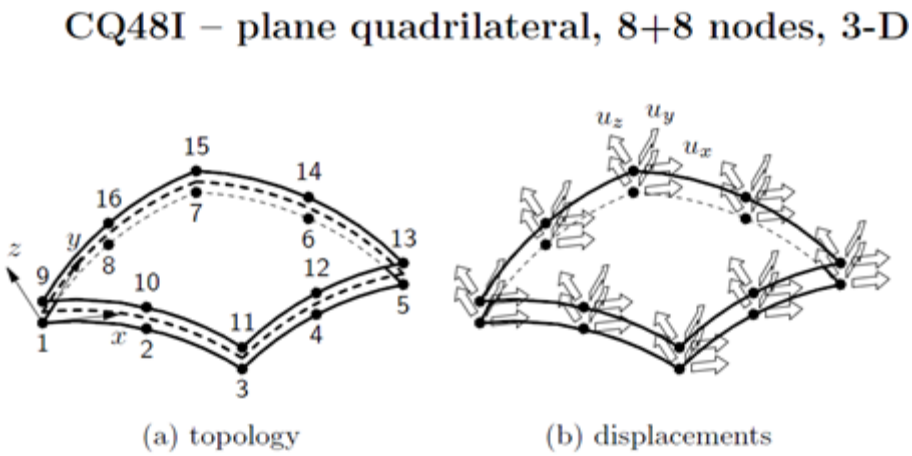

CQ48I plane element for 3D model

The CQ48I element is an interface element between two planes in a three-dimensional configuration. The local xyz axes for the displacements are evaluated in the first node with x from node 1 to node 2 and z perpendicular to the plane. Variables are oriented in the local xyz axes. The element is based on quadratic interpolation. By default DIANA applies a 4 x 4 Newton-Cotes integration scheme. Suitable options are 3 x 3 and 5 x 5 Newton-Cotes, 3 x 3 and 4 x 4 Gauss, 3 x 3, 4 x 4 and 5 x 5 Lobatto, and a nodal lumping. These elements are used for the felt layers, that are in the interface between the slab and the supports and between slab and contrasting beam, and they are used for the Teflon layer between slab and loading plate.

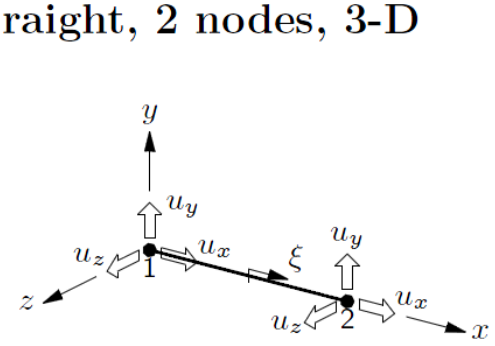

L6TRU element for 3D model

The L6TRU element is a two-node directly integrated (1-point) truss element. Due to the displacements u_y and u_z perpendicular to the bar axis, this element can be used in three-

dimensional dynamic and geometrically nonlinear analysis. The interpolation polynomial for the displacements u_x, $u_y$and u_z can be expressed as:

$$\boldsymbol{u_i(\xi)} = a_0 + a_1\xi$$

This polynomial yields a strain ε_{xx}which is constant along the bar axis. Initially there is no stiffness for the displacements u_y and u_z, stiffness will arise in case of geometric nonlinearities.
Diana determines the element axes for an L6TRU element as follows: first the *x* axis from the first to the second node, then the *y* axis perpendicular the *Zx* plane and finally the *z* axis perpendicular the *xy* plane. If the *x* axis coincides with the *Z* axis then *y* perpendicular *Zx* cannot be done and the *y* axis is chosen in *Y* direction.
It has to be observed how, using the types of element CHX60 together with CQ48I, both the compatibilities in terms of the correspondence of the position of the nodes (3 nodes on each side and 8 nodes in each face) and in terms of the quadratic order distribution of strains, in order to build an uniform mesh on all the structure.
Compatibility is automatically respected too, using *L6TRU* elements with extreme node as geometrical points.

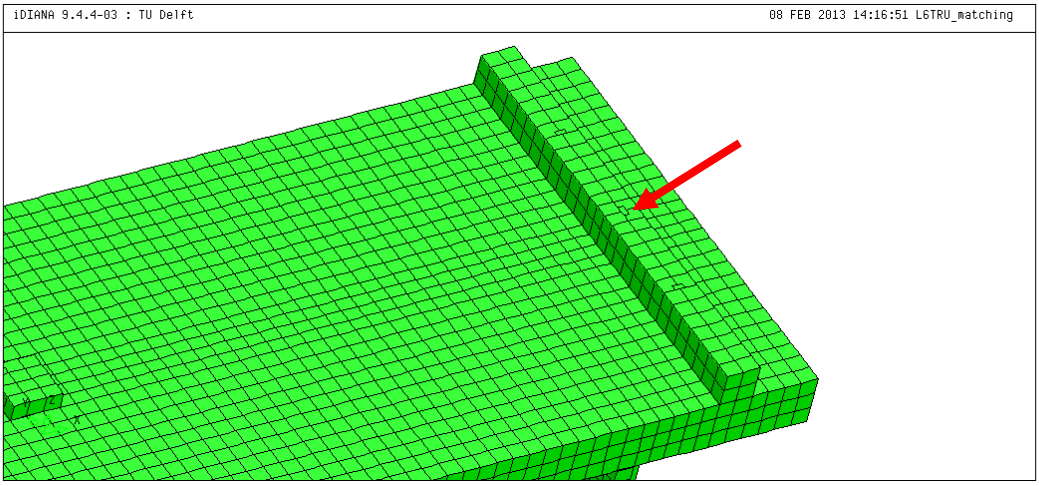

L6TRU matching inside the mesh

Moreover, in order to avoid singular matrix definition, we have to mesh each Dywidag bar with one element only. Being a truss elements, an higher amount of mesh pieces brings to rigid body motions, since the model is developed in a 3D environment.
So, regarding to the meshing procedure, we have to subdivide the whole model without Dywidag bars adopting the *MESHING DIVISION ELSIZE NODIWY <average element size>* and only then meshing the pres-stress reinforcements adopting the element size (about 3000 mm). So a unique mesh element is got.
The *h* numerical crack bandwidth parameter is evaluated manually. Indeed, the average volume of solid element is calculated by counting the amount of elements on each side. Average dimensions are calculated for every mesh model. This parameter, how it will be explained in the next section, is very important in order to evaluate the ultimate strain for concrete.

The present mesh is composed by 1099 finite solid elements and 6474 nodes. It's simply called *"2x2"*, as the amount of number on the height. The same criteria is adopted for the following meshes.

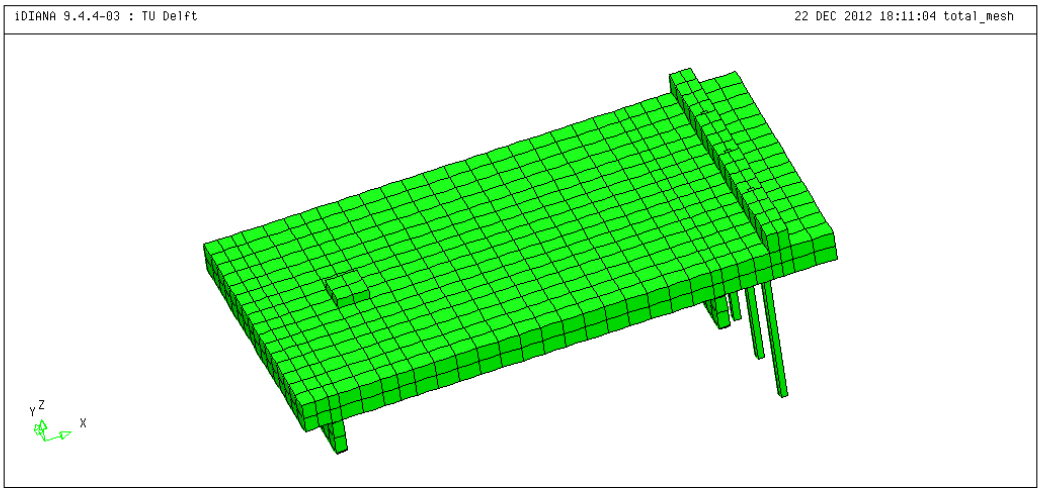

2 elements on height mesh adopted for S25T1 slab

The dimension of the various finite elements are almost regular and their average volume is around $V \cong 4040860\ mm^3$.

- 29 elements on the longitudinal side → $5000/29 = 172{,}40\ mm$;
- 16 elements on the transversal side → $2500/16 = 156{,}25\ mm$;
- 2 elements on the height → $300/2 = 150{,}00\ mm$.

The present mesh is composed by 4759 finite solid elements and 25176 nodes. It's called *"3x3"*. The average volume is around $V \cong 875268\ mm^3$.

- 51 elements on the longitudinal side → $5000/51 = 98{,}00\ mm$;
- 28 elements on the transversal side → $2500/28 = 89{,}30\ mm$;
- 3 elements on the height → $300/3 = 100{,}00\ mm$.

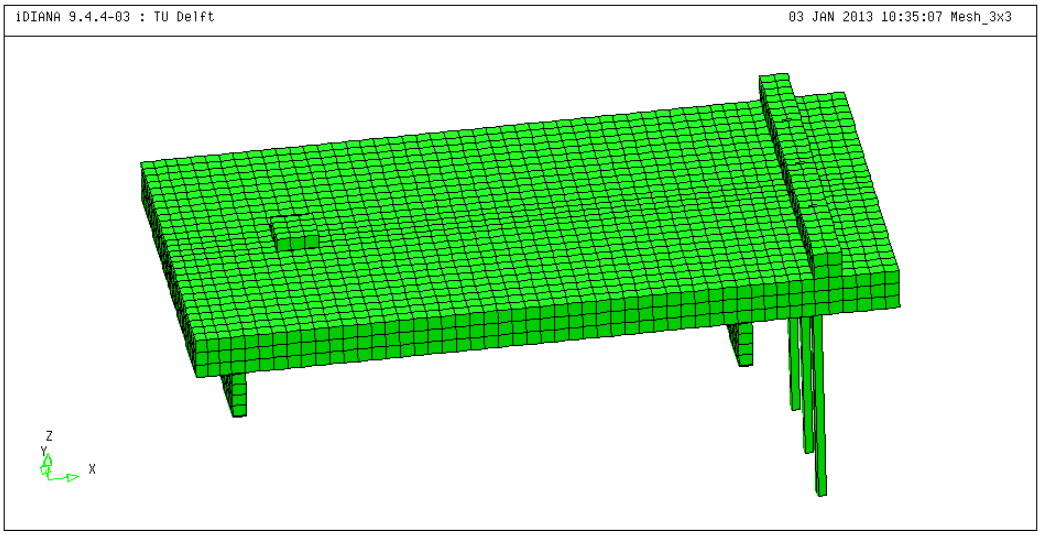

3 elements on height mesh adopted for S25T1 slab

The present mesh is composed by 9779 finite solid elements and 48202 nodes. It's called *"4x4"*. The average volume is around $V \cong 444600\ mm^3$.

- 65 elements on the longitudinal side → $3650/48 = 65{,}00\ mm$;
- 32 elements on the transversal side → $2500/32 = 78{,}10\ mm$;
- 4 elements on the height → $300/4 = 75{,}00\ mm$.

For this last mesh the average dimension is really close to each other on every dimension.

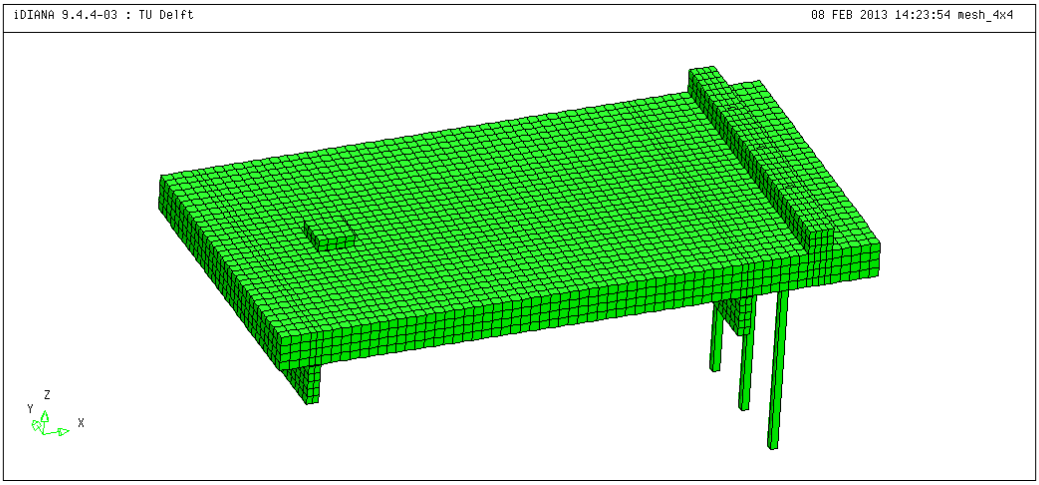

4 elements on height mesh adopted for S25T1 slab

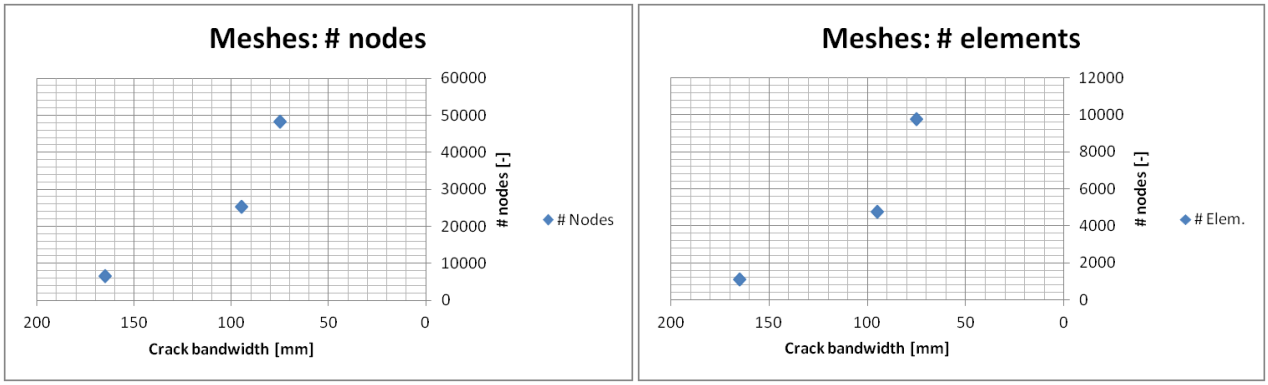

(a) *(b)*

Amount of nodes (a) and elements (b) for each mesh adopted

Viewing to the previous table, one can see how a finer mesh involves a higher amount of nodes and solid elements with a marked nonlinear sequence: this means a greater non-proportional computational effort.

The dimensions of the various finite elements are almost regular for every kind of mesh, as one can see in the following image.
Materials and particulars are shown for the *"2x2"* mesh:

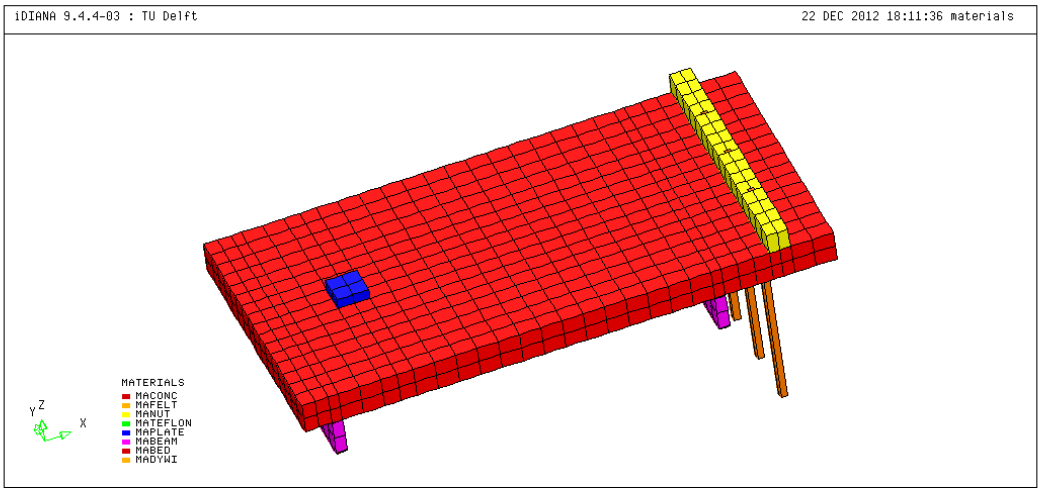

Material label for the model

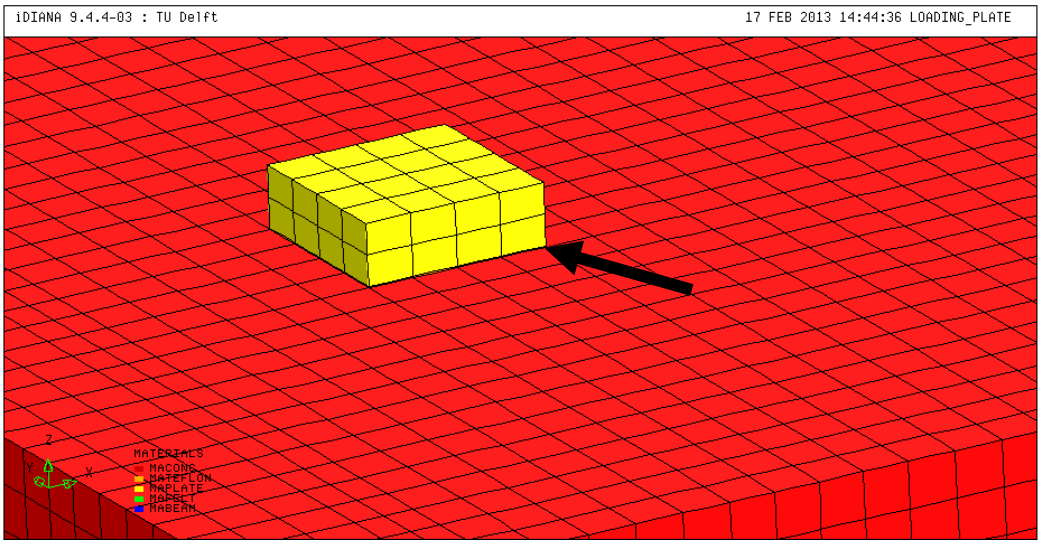

Particular of the mesh relative to the loading plate and Teflon interface

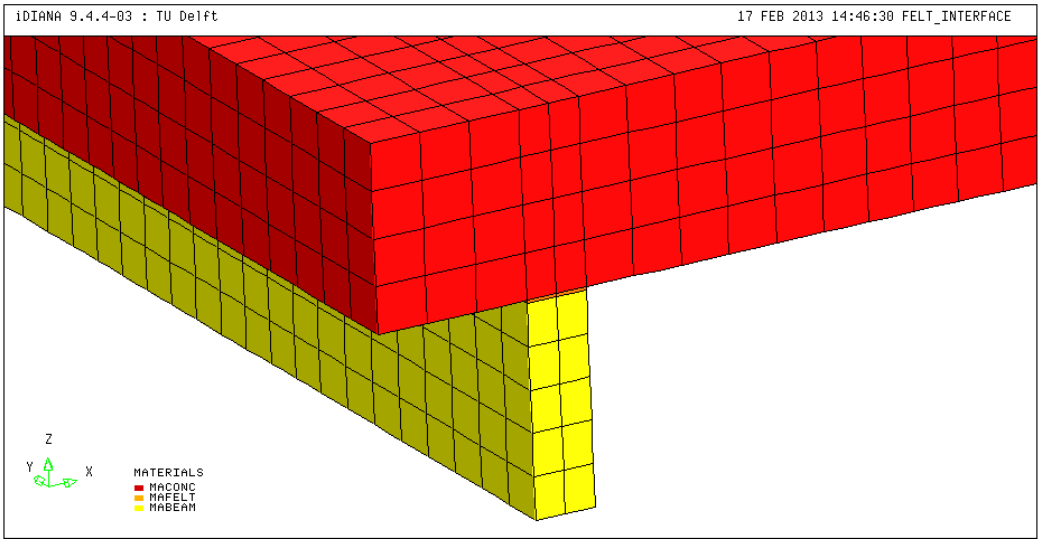

Particular of the mesh relative to the felt interface between slab and support

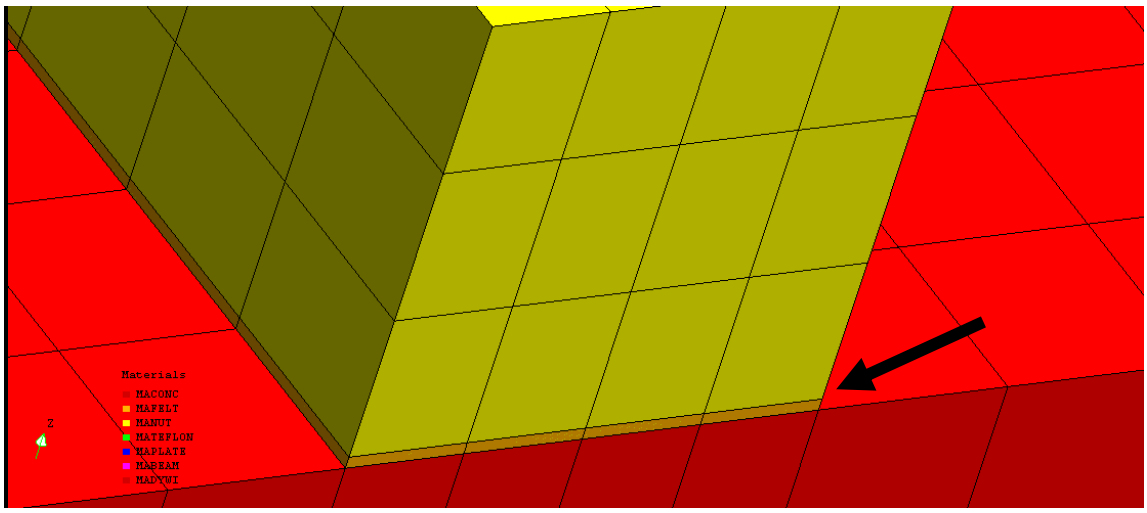

Particular: felt layer between contrasting beam and concrete slab for 4x4 mesh

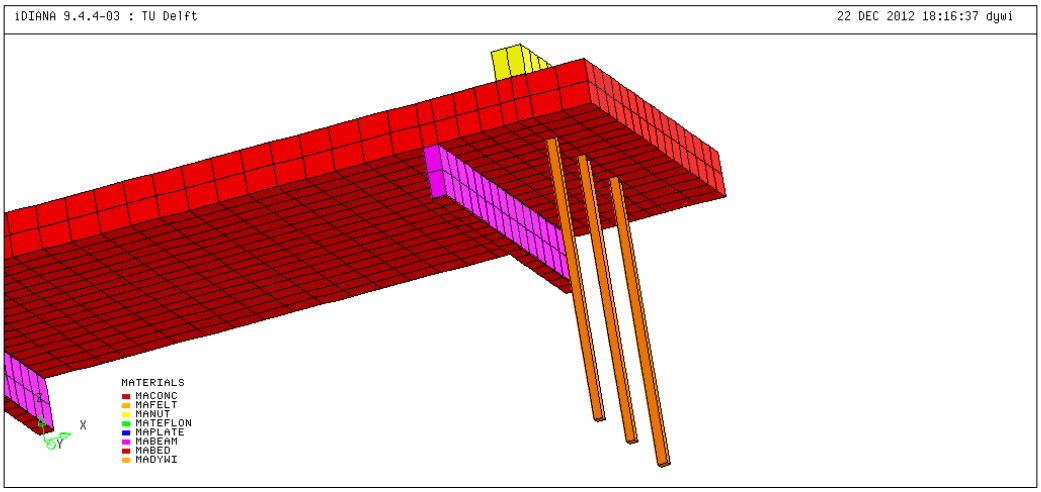

Dywidag bars particular in the mesh

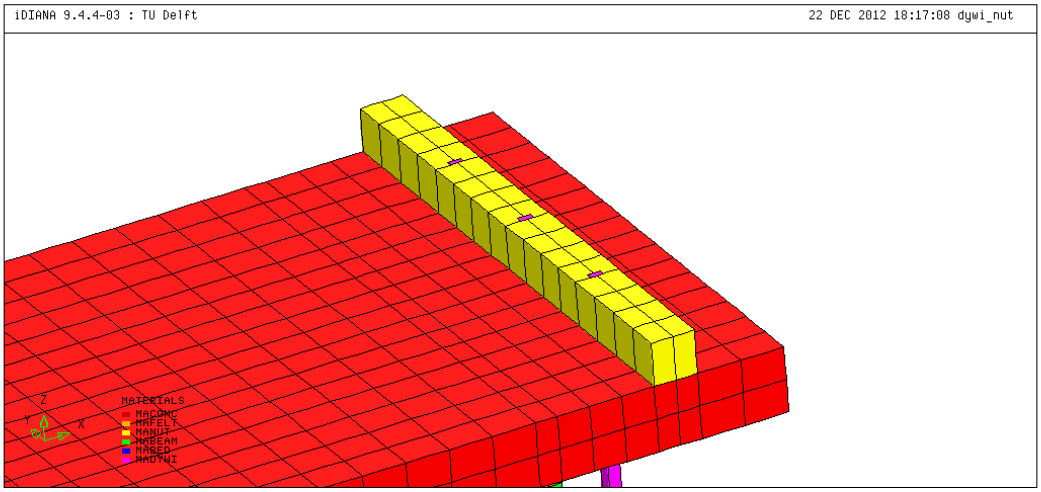

Dywidag anchors inside contrasting beam in the mesh

All the geometrical dimensions of the model are respected, with only one exception on the supports, that in the real test are composed by $HEM300$ steel profiles, while in the FEM model they are represented by two solid brick elements, 340 mm high and with a width of 100 mm (instead of 300 mm), to have a direct matching with the upper interface layer.

5.1.3 Model of supports and constraints

The real slab is bounded by a total of two supports, one SIMPLE SUPPORT and one CONTINUOUS SUPPORT, defined by 3Ø36 Dywidag bars with pretensioning.
The North support models the *simple support*. It's applied to the finite element model inserting constraints on the bottom surface of the support beam: in this way no translation in X, Y and Z direction are not allowed in the global reference system.
Instead, the complex South constraint system is completely modeled with 3Ø36 pre-stressed Dywidag bars ($L6TRU$ elements) and contrasting beam. Moreover, on the bottom of the South support beam no translation X, Y and Z direction are not allowed, as done for the other support, to modeled the role of the $HEM300$ element during the experiment test. In this way we can model the

whole constraint system on the South side: it's a non-perfect clamped constraint with a proper deformability.
The Dywidag bars bottoms are fixed to the ground, as in the experimental environment, in all the three principal directions for translation degree of freedom. The other ends are connected to the geometrical nodes of the contrasting beam, so kinematical compatibility is automatically satisfied.

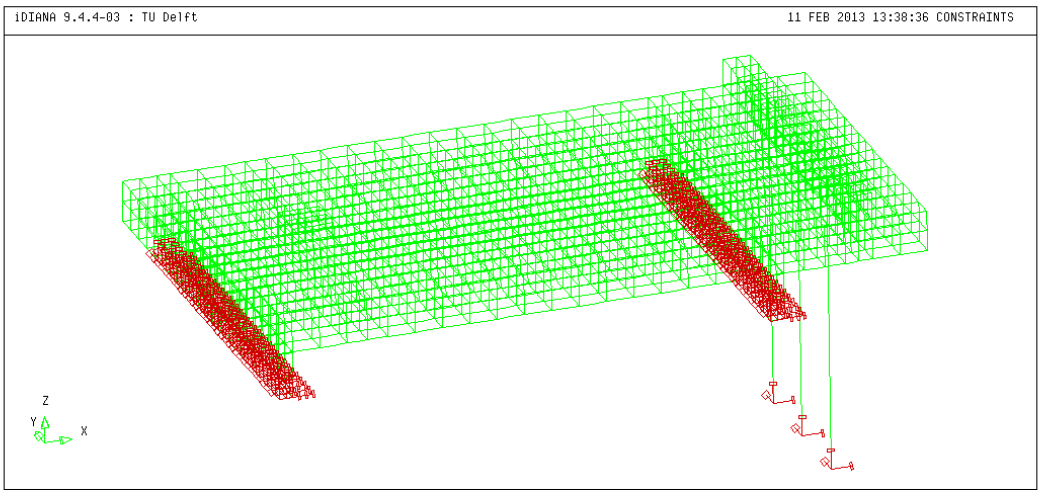

Model of the constraints assigned to the slab (1st mesh)

5.1.4 Loading conditions

Following the same criterion used for the laboratory test, the FEM analysis on the model is performed using a *displacement control method*.
Two different load cases are used for this model:

- $load\ case\ 1, "Dywi"$;
- $load\ case\ 2, "Jack"$.

The first load case contains the *Dywidag bars pre-stressing*. Using the PRESTRES option inside the load command it's possible to add a pre-stress to elements, surfaces, bodies, etc.
In the present case, pre-stress is given to whole three Dywidag elements, just adopting only one load case.
The second load case contains the displacement control command on the loading plate.
Using the DISPLA option for load command a $-25.00\ mm$ displacement in the Z direction is applied to the specified surfaces.

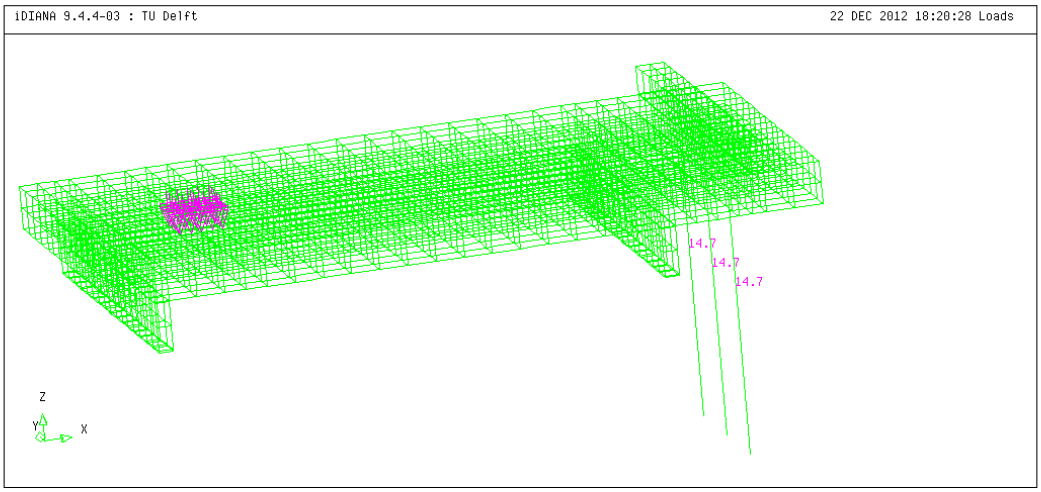

Model of the loads assigned to the slab (1st mesh)

5.2 Material and physical properties

Regarding to the physical properties for total model, the elements for which is necessary to define directly them are the *reinforcement bars* and *truss/cable elements*, modeled through one-dimensional elements (bar/line) that need a definition of transversal area.
An ideal symmetric model prescribes a longitudinal bar on the symmetry plane long the span direction of the slab.
On the same direction the middle Dywidag bar is defined at the contrasting beam.
So, longitudinal reinforcement bar and Dywidag crosses each other: it causes a numerical error which involves cancellation of a Dywidag portion.
So, it's necessary to define a new distribution than the "ideal" one.
In order to keep a symmetric model the longitudinal bars on the middle of the section are split in two bars with half area.
A similar problem could arise for the transversal bars at the same abscissa; luckily it doesn't happen.
Five different families of bars are used in the real slab, so five bar groups are adopted as well.
Observing the real reinforcement disposition two bar groups are used on the bottom surface of the slab for the whole area:

- the lower one for the Ø20 longitudinal bars;
- the upper one for the Ø10 transversal bars;

Instead, for the top surface three bar groups are used:

- the two upper ones for the Ø20 and Ø10 longitudinal bars;
- the lower one for the Ø10 transversal bars on the whole area.

Every bar group is named according to:

- the longitudinal axe position inside the slab;
- the value of the absorbed bending moment;

- the position on the Z axis.

Following this definition, these grid names are given as:

- LONG.NEG.TOP grid for the upper longitudinal $\emptyset 20$ bars (1);
- LONG.POS.TOP grid for the upper transversal $\emptyset 10$ bars (2);
- LONG.BOT grid for the lower longitudinal $\emptyset 20$ bars (3);
- TRAN.TOP grid for the upper transversal $\emptyset 10$ bars (4);
- TRAN.BOT grid for the lower transversal $\emptyset 10$ bars (5).

This particular definition allows to take into account the different behaviour of every layer inside the model, as described later.
In the real slab the concrete cover is equal to $25\ mm$. This is defined as the concrete width between the more external point of the bar and the slab surface.
Using the bar definition option is necessary to take into account of the effective bar diameter.
For the $\emptyset 20$ bars, the longitudinal axis has a relative Z-quota of $25\ mm$ from the external slab surface.
Using the bar definition, an linear element with a numerical cross-area is adopted; so the concrete cover is defined as the distance between the external surface and the line axis.

$$Z_{quota} = c = 25\ mm$$

However, to take into account of the different real disposition on the Z axis of the reinforcements layers, the longitudinal and transversal grids are placed on different quota:

- $Z = 275.00\ mm$ for LONG.NEG.TOP (1);
- $Z = 275.00\ mm$ for LONG.POS.TOP (2);
- $Z = 25.00\ mm$ for LONG.BOT (3);
- $Z = 273.00\ mm$ for TRAN.TOP (4);
- $Z = 27.00\ mm$ for TRAN.BOT (5).

The $\Delta Z = 2.00\ mm$ can be justified considering that overlapped points are merged during the merge operations by *iDiana*. Giving this gap the problem is avoided.

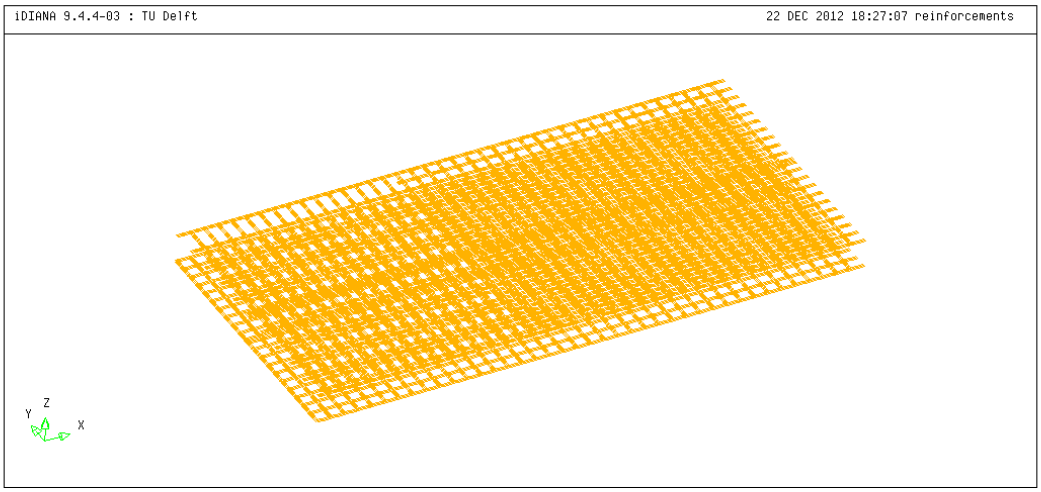

Reinforcement bars plot

In order to assign the physical properties, the cross area is given for each bar diameter:

- $\emptyset 10 \rightarrow 78.50\ mm^2$;
- $\emptyset 20 \rightarrow 314.00\ mm^2$;
- $\emptyset 36 \rightarrow 1018\ mm^2$.

The bar steps are modified than the real ones, in order to respect the bars amount inside the slab.
The values are:

- $122.50\ mm$ for LONG.NEG.TOP/LONG.BOT;
- $245\ mm$ for LONG.POS.TOP;
- $123.75\ mm$ for TRAN.BOT/TOP;

As said before, in order to avoid a numerical cancellation for the middle longitudinal bars, on the top and bottom face, in correspondence of the central Dywidag bar it's necessary to split the single bar in other two with a half cross-area.
The present bars have got a $25\ mm$ offset from the longitudinal axis.
All the other components of the structure are modeled through solid elements, therefore is not necessary to define their spatial dimensions.
Moreover, where it's possible the material properties of the components of the structure, are evaluated from standard experimental tests executed on specimens (for instance compression tests on cores drilled from the same concrete of the slab and traction test on reinforcement bars), on relations contained on the building codes ($2010\ CEB-FIP$ version) or on other analytic considerations.

The used materials are:

CONCRETE

MACONC [1]:
Linear Elasticity – Isotropic
Young's Modulus: 39016 MPa (from the $CEB - FIP$ relation)
Poisson's Ratio: 0.15
Static non linearity – Concrete and brittle materials – Total strain fixed crack – Hordijk softening in tension – Fracture energy based - Elastic in compression – Damage based shear retention – Poison Reduction in cracking

Tensile strength: 4.62 MPa
Mode-I tensile fracture energy: 0.150 Nmm/mm^2
Crack bandwidth: 165 mm

A nonlinear tension softening behavior is chosen for the tensile stress-strain concrete relationship.
The proposed one is by $Hordijk\ et\ al.$.
This nonlinear tension softening diagram results in a crack stress equal to zero at a crack strain ${\varepsilon^{cr}}_{nn.ult.}$.

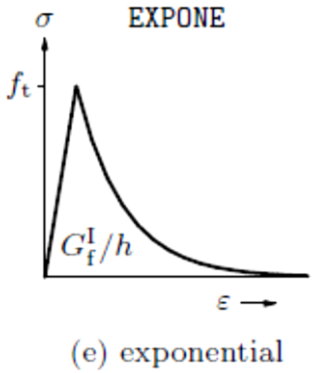

Exponential nonlinear tension softening for concrete (Hordijk et al.)

The c_1 and c_2 parameters are equal to 3.00 and 6.93 respectively.

$$ {\varepsilon^{cr}}_{nn.ult} = 5.136 \frac{{G_f}^I}{h f_t} $$

$$ {\varepsilon^{cr}}_{nn.ult.min} = 6.957 \frac{f_t}{h} $$

Particularly, regarding this concrete features in the *iDiana* environment, inside the *.dat* file presents the same test strings, but the nonlinear $Hordijk$ tension softening model is chosen:

Tension softening curves – based on fracture energy *syntax*

'MATERI'

1 – 5	6 – 12	13 – 80
	TENCRV	$curve_w$
		LINEAR
		EXPONE
		HORDYK
	TENSTR	ft_r
	GF1	$gf1_r$
	[CRACKB	h_r]

Tension softening behavior definition

'MATERIALS'
1 YOUNG 3.901600E+04
POISON 1.500000E-01
POIRED DAMAGE
TOTCRK FIXED
TENCRV HORDYK
TENSTR 4.620000E+00
GF1 1.5000000E-01
CRACKB 1.650000E+02
COMCRV ELASTI
SHRCRV DAMAGE

REINFORCEMENT STEEL

MABAR10 [2]:
Linear elasticity – Reinforcement – Reinforcement bonded
Young's Modulus: 200000 MPa

Static non linearity – Reinforcement – Von Mises plasticity – Work Hardening diagram
Tensile yield stress: 460MPa
Tensile ultimate stress: 627 MPa

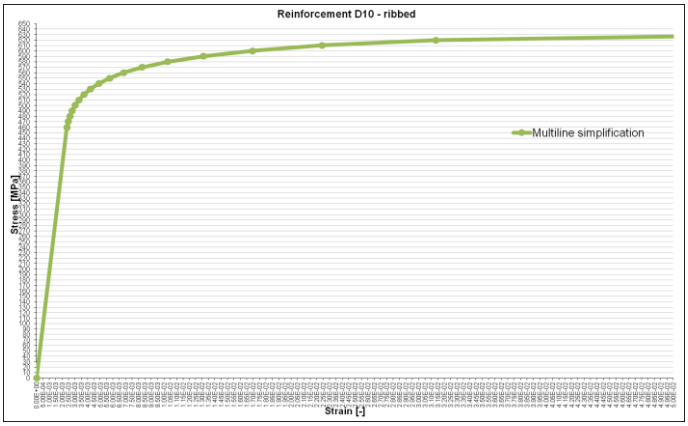

Stress-strain model for ϕ10 bars

MABAR20 [3]:

Linear elasticity – Reinforcement – Reinforcement bonded

Young's Modulus: 200000 MPa

Static non linearity – Reinforcement – Von Mises plasticity – Work Hardening diagram

Tensile yield stress: 540MPa

Tensile ultimate stress: 658 MPa

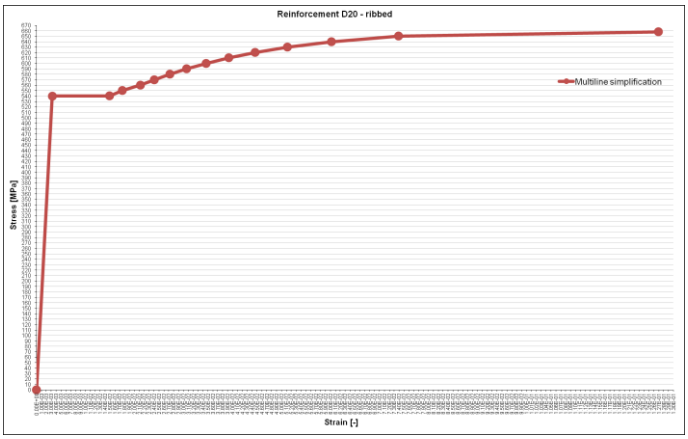

Stress-strain model for ϕ20 bars

Regarding to the reinforcement hardening behaviour, the *work hardening* diagram is chosen:

syntax

```
'MATERI'
1        5 6          12 13                                          80
          YIELD         VMISES
          ------
          YLDVAL        sy_r
          HARDIA        sy1_r  k1_r  [sy2_r  k2_r  ...]  syn_r  kn_r]
         [HARDEN        ------ ]
                        WORK
                        STRAIN
```

Work hardening definition for reinforcement bar

As required by *iDiana*, it's necessary to introduce the ε_{pl} values. These are obtained following the formula:

$$\varepsilon_{pl,diagr} = \varepsilon_{pl} - \varepsilon_{y}$$

Below, the hardia file (.dat extension) for Ø10 and Ø20 are shown respectively:

'MATERIALS'
4 HARDIA

460.0 0.00 471.0 0.00012 481.0 0.000240 490.0 0.000427 500.0 0.000667 510.0 0.000947 521.0 0.00136 531.0 0.001867 540.0 0.00252 550.0 0.00336 560.0 0.004453 570.0 0.005893 580.0 0.007920 590.0 0.01072 600.0 0.014573 610.0 0.020053 620.0 0.028987 627.0 0.04876

'MATERIALS'
1 HARDIA
540.0 0.00 541.0 0.01168 550.0 0.01424 560.0 0.01798 570.0 0.02078 580.0 0.02396 590.0 0.02736 600.0 0.03136 610.0 0.03600 620.0 0.04140 630.0 0.04796 640.0 0.05692 650.0 0.07062 658.0 0.12368

Then these properties are so assigned:

- LONG.NEG.TOP ∅20 → MABAR20/HARDIA_2;
- LONG.POS.TOP ∅10 → MABAR10/HARDIA_1;
- LONG.BOT ∅20 → MABAR20/ HARDIA_2;
- TRAN.TOP ∅10 → MABAR10/ HARDIA_1;
- TRAN.BOT ∅10 → MABAR10/ HARDIA_1;

STEEL for supports HEM300

In order to restore the bending stiffness of the HEM profiles one can calculate the equivalent Young's modulus to add to the beam support.
For the $HEM300$ profile the inertia around the horizontal axis equal to $I_{xx} = 59200 \times 10^4\ mm^4$, while for the rectangular beam support the value is:

$$I_{xx} = \frac{bh^3}{12} = \frac{100\ mm * (340\ mm)^3}{12} = 327533333\ mm^4$$

Then it's necessary to match the bending stiffness:

$$E_{steel} I_{xx,HEM300} = E_b I_{xx,beam} \rightarrow E_b = 379564 \frac{N}{mm^2}$$

MABEAM [4]:
Linear elasticity - Isotropic
Young's Modulus: $379564\ MPa$
Poisson's Ratio: 0.30

However, it's necessary specify that in the real test the steel that composes the supports has an Elastic Modulus of $210000\ MPa$ like all the classical building steel, nevertheless, since in the FEM model the width of the support is reduced from $300\ mm$ to $100\ mm$, it's used an incremented value of $379564\ MPa$ to match the beam's original *flexural stiffness EI*.

STEEL for loading plate

MAPLATE [5]:
Linear elasticity - Isotropic
Young's Modulus: $200000\ MPa$
Poisson's Ratio = 0.30

INTERFACE TEFLON between loading plate and slab

MATEFLON [6]:
Linear elasticity – Interface
Linear normal stiffening: $500\ N/mm^3$
Linear tangential stiffening: $0.25\ N/mm^3$

For the Teflon interface only linear elastic behavior is prescribed.
The tangential stiffness is limited: in this way it's possible to separate concrete and loading plate steel and allows tangential sliding on the contact plane, as happens during the experimental test. Otherwise the kinematical compatibility will occur on the horizontal plane producing a tensile stress field on the slab's top surface.

INTERFACE FELT between supports and slab

MAFELT [7]:
Linear elasticity – Interface
Linear normal stiffening $15.20\ N/mm^3$
Linear tangential stiffening: $0.20 N/mm^3$

Interfaces – Static Non Linear Elasticity
Normal Stiffening File:$Felt\_N$
Tangential Stiffening file:$Felt\_T$

So proceeding we assume the felt interface work as an elastic Winkler's spring soil: since the distance between nodes on the support-slab contacts that hypothesis results reasonable.
Without the $Felt\_N$ file specification inside the *Diana* environment it will assume a full reagent tensile behaviour for the felt interface.
The following text strings reports the possibility to avoid this phenomena for the $\sigma - \delta$ model, just using the non-linear stiffening files format to prescribe a pre-defined behaviour, linear or non-linear, for example:

```
'MATERIALS'
  9  DSTIF  15.20 0.15
     SIGDIS
-0.0190 -50.000 -0.0152 -0.01 0.0 0.0 1.43 0.094 3.00 0.153 5.00 0.197 8.00 0.237 210.73 3.00
```

A small tangential stiffness $k_{t,f}$ is chosen to avoid membrane action.

BED INTERFACE between supports and "world"

MABED [8]:
Linear elasticity – Interface
Linear normal stiffening: $0.25\ N/mm^3$
Linear tangential stiffening: $0.025\ N/mm^3$

DYWIDAG BARS

MADYWI [9]:
Linear elasticity – Truss/Cable
Young's Modulus: $205000\ MPa$
Static non linearity – Metals – Von Mises plasticity – Work Hardening diagram
Tensile yield stress: $950MPa$
Tensile ultimate stress: $1050\ MPa$

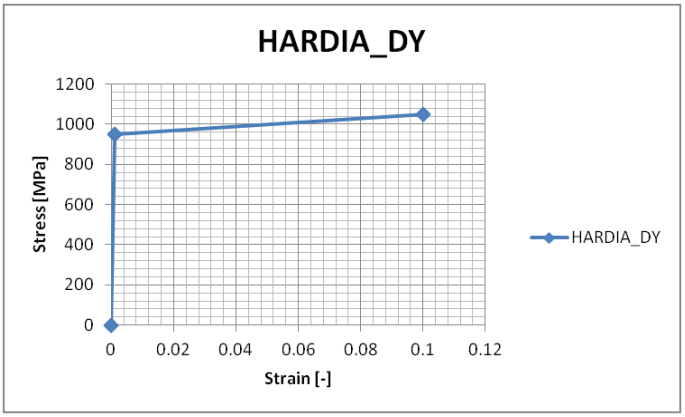

Stress-strain relation for ϕ36 Dywidag bars

A simply bi-linear hardening model is assumed. The following hardia file is:

'MATERIALS'
  10 HARDIA 950.0 0.00 1050.0 0.09

NUT BEAM or contrasting beam

MANUT [10]:
Linear elasticity - Isotropic
Young's Modulus: $200000\ MPa$
Poisson's Ratio = 0.30

5.3 Performing analysis on the Total model

5.3.1 Preliminar linear static analysis

In order to check the model, we run a linear analysis. By default the nonlinearities are not considered at first. Through *Diana batch format* (*.dat* extension) we can run the analysis using the following command file (*.dcf* extension):

```
*FILOS
 INITIA
*INPUT
*LINSTA

  BEGIN OUTPUT TABULA
    TEXT "Force load plate"
    BEGIN SELECT
     NODES 1860-1871 3852-3858
    END SELECT
    LINPAG=10000
    COLLIN=10000
    LAYOUT COMBIN
    FORCE REACTI TRANSL GLOBAL Z
    DISPLA TOTAL TRANSL GLOBAL Z
  END OUTPUT

  BEGIN OUTPUT
    DISPLA TOTAL TRANSL GLOBAL
    FORCE REACTI TRANSL GLOBAL
  END OUTPUT

*END
```

Whit the OUTPUT TABULA text string *Diana* will store data about FBZ (reacting force in the Z-direction) and $TDtZ$ (total displacement in the Z-direction) in an output file (*.tb* extension) for each definited load step and for the selected nodes. By the sum of each contribution, the load applied to the slab is defined and the $F - u$ diagram is got.

5.3.2 Non-linear static analysis:

In order to obatin satisfactory results is necessary to study carefully every feature of non-linear solutor and model.
Regarding to the model feature, one of the most significant is certainly the meshing division: *2*, *3* and *4-elements on the highness mesh*, as mentioned above.

Instead, regarding to the solution procedure, it's necessary definy a step division. Useful information about the amount of iteration and convergence behavior can be found in the output file (*.out* extension) given by default by *Diana* solutor.
For the following non-linear analysis $Newton - Rhapson\ modified$ method is adopted.
In order to not stop the analysis if a non convergence occurs the CONTIN options is turned on and a maximum number of iteration equal to 100.
The LINESE option is activated as well. This algorithm helps in the prediction of the iterative displacement increment $\delta\boldsymbol{u}$ by scaling this vector by a value to minimize the energy potential Π.
Infact for all the methods described so far, the iterion process converges to the "exact" numerical solution. If the prediction is too far from equilibrium the iteration process will not converge. This easily takes place in structures with strong nonlinearities as cracking. *Line Search Algorithm* can increase the convergence rate and are especially useful in the ordinary iteration process fails.
Regarding to the convergence criteria is valid the CONTIN options as said before.
The first trials was force and displacement based, but is known that the displacement converge will occur faster that force convergence, so this association with the CONTIN option is complitely useless.
The same happens with a displacement-energy comniation convergence criteria: since the energy criterion is a quadratic function of the vector $\boldsymbol{u}$ is obvious that the convergence will occur before for the displacement, unless very strict tolerances.
So for all these reasons, as convergence criteria only the relative displacement control is used.
However, few trials with force and energy criteria was used before. For the force criteria is quite difficult to reach the fixed limit in every steps and, morevoer, that takes a large number of iterations to converge in each dispalcement step.
The same happens for the energy criteria.
Particularly, for the displacement criteria is used $1.0E-04$ as *convergence limit* and $1.0E+04$ as *divergence limit*.
Then the text strings for the *.dcf* file appear as:

```
  BEGIN ITERAT
   CONTIN ON
   MAXITE 100
    BEGIN METHOD
     NEWTON  MODIFI
    END METHOD
    LINESE
    BEGIN CONVER
     FORCE OFF
      DISPLA NEWREF CONTIN TOLCON=1.0E-4 TOLABT=1.0E+4
    END CONVER
  END ITERAT
END EXECUTE
```

It's usefull to remember that methods like *Newton-Rhapson* and *Secant* are not able to describe softening behavior like *Arc-length* method because of their iterative procedures. The iterative increments are evaluated by the relationship:

$$\delta \boldsymbol{u}_i = \boldsymbol{K}_i^{-1} \boldsymbol{g}_i$$

Where i indicates the iteration number, $\delta \boldsymbol{u}_i$ is the iterative displacement incremental, $\boldsymbol{K}_i$ is the stiffness matrix that represents some kind of linearized form of the relation between the force vector and displacement vector, while $\boldsymbol{g}_i$ is the out-of-balance force vector at the start of the iteration i.
This kind of procedure fails in presence of flat force-displacement diagram, to describe a plane trait a large number of iteration is required, so the method can't reach the applied incremental displacement. It doesn't matter how short that step could be.

For the output files the present features are selected in order to study them in the *iDiana* envirnoment during the post-processing:

DISPLA TOTAL TRANSL GLOBAL
FORCE REACTI TRANSL GLOBAL
STRAIN PLASTI GREEN PRINCI INTPNT
STRAIN CRACK GREEN INTPNT
STRAIN TOTAL GREEN GLOBAL
STRAIN ELASTI GREEN GLOBAL
STRAIN TOTAL GREEN PRINCI
STRESS TOTAL CAUCHY PRINCI
STRAIN TOTAL TRACTI GLOBAL INTPNT
STRESS TOTAL TRACTI GLOBAL INTPNT

5.3.3 Non-linear static analysis via Phase Analysis:

Phased analysis enables modeling of phased construction. It determines the effects of construction history and shows the critical construction stages. A phased analysis comprises several calculation phases. Between each phase the finite element model changes by addition or removal of elements and constraints.
In each phase a separate analysis is performed, in which the results from previous phases are automatically used as initial values. These results are typically stresses, deformations, potentials, velocities etc.
The start of each phase can include input of the model part which is changed compared to previous input or added. At the start of each phase, we must select the active part of the model and specify the superposition of the nodal results (displacements or potentials) from previous phases. After the start we perform a common analysis using regular Diana analysis modules.
Diana can perform phased analysis for linear, nonlinear and dynamic structural analysis.
For the present model, in order to start a phase analysis we have to produce two *.dat* file for the total model version.

Inside the first one the full geometrical, physical and loads model is described, instead inside the second only the loads and constraints tables change. So, it's possible to update the new slab configuration: after the pre-stressing, we need to constraint the loading plate nodes in order to apply displacements. Constraints and loads are updated.

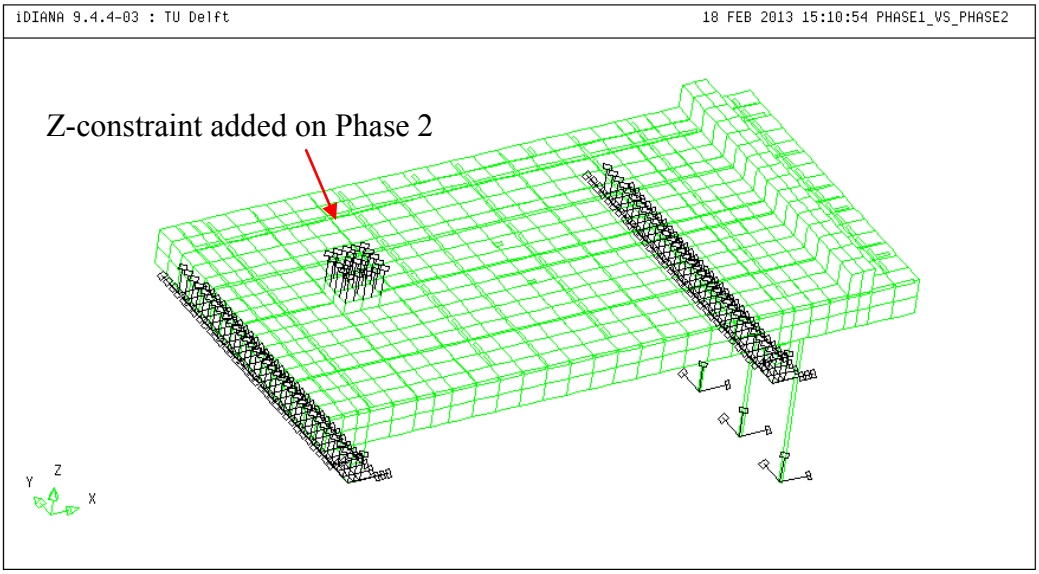

Phase analysis sequence: first and second constraints

The first phase performs a nonlinear static analysis:

```
*FILOS
INITIA
*INPUT
READ FILE="S25T1_C_BARSPLIT1.dat"
*PHASE
*NONLIN

 BEGIN EXECUT
  BEGIN START
    INITIA  STRESS  INPUT  LOAD 1
   STEPS  EXPLIC SIZES 0.1 (10)
  END START
  BEGIN ITERAT
   CONTIN ON
    BEGIN CONVER
      FORCE  OFF
      DISPLA NEWREF CONTIN TOLCON=1.0E-4 TOLABT=1.0E+4
    END CONVER
    LINESE
    MAXITE 100
    METHOD  NEWTON  MODIFI
```

```
  END ITERAT
  TEXT "Loadcase 1"
```

As one can see, *Diana* has to read the specified *.dat* model file.
After the analysis, a output file is required:

```
BEGIN OUTPUT
FILE Phase_1
TEXT "FEMVIEW"
    SELECT STEPS 1-850(1)
    DISPLA TOTAL TRANSL GLOBAL
    FORCE REACTI TRANSL GLOBAL
 END OUTPUT
```

Two tables with loading plate nodes displacements and nut forces are requested:

```
BEGIN OUTPUT
TABULA
  FILE "Pret_NutForce"
  BEGIN LAYOUT
    COLLIN 150
    LINPAG 10000
  END LAYOUT
  SELECT  NODES 4 2 6
  TEXT "Pretension: Reaction Forces East, Mid, West Dywidag"
FORCE REACTI TRANSL  GLOBAL Z
 END OUTPUT

BEGIN OUTPUT
TABULA
  FILE "Pret_PlateDisp"
  BEGIN LAYOUT
    COLLIN 150
    LINPAG 10000
  END LAYOUT
  SELECT  NODES 3036-3048 5830-5837
  TEXT "Pretension: Loade plate displacements"
DISPLA TOTAL TRANSL GLOBAL Z
 END OUTPUT
```

For each mesh, we must update the node selection.
This phase equals to the only pre-stressing procedure: the only applied load is on the Dywidag bars; no constraints are applied on the loading plate.
The second phase includes a new nonlinear static analysis:

```
*INPUT
 BEGIN READ
  FILE "S25T1_C_BARSPLIT_xy2.dat"
  BEGIN TABLE
   LOADS
   SUPPORT
  END TABLE
 END READ
*PHASE
BEGIN ACTIVE
ELEMENT
REINFO
END ACTIVE
*NONLIN

BEGIN EXECUT
BEGIN START
INITIA STRESS INPUT LOAD 2
LOAD LOADNR 2
END START
  BEGIN ITERAT
   CONTIN ON
    BEGIN CONVER
     FORCE OFF
     DISPLA NEWREF CONTIN TOLCON=1.0E-4 TOLABT=1.0E+4
    END CONVER
    LINESE
    MAXITE 100
    METHOD  NEWTON  MODIFI
  END ITERAT
  TEXT "Loadcase 2"
 END EXECUT
```

Inside the second *.dat* file loads and constraints are updated, as said before.
The "real" nonlinear static analysis can start:

```
BEGIN EXECUT
BEGIN LOAD
LOADNR 3
    STEPS  EXPLIC  SIZES 0.0012 (850)
END LOAD
  BEGIN ITERAT
   CONTIN ON
```

```
    BEGIN CONVER
      FORCE OFF
      DISPLA NEWREF CONTIN TOLCON=1.0E-4 TOLABT=1.0E+4
    END CONVER
    LINESE
    MAXITE 100
    METHOD  NEWTON  MODIFI
  END ITERAT
  TEXT "Loadcase 3"
END EXECUT
```

Perfoming this part, same output and tables are required.
This part includes the displacement control procedure on the loading plate.
For the nonlinear static analysis Modified Newton Rhapson method is chosen.

5.3.4 Step sequence

For the present model of the $S25T1$ slab, following the *Esposito*'svalue, a width of $0.03\ mm$ for each step is choosen:

$$w[\%] = \frac{0.03\ mm}{25\ mm} = 0.0012$$

So, for the *.dcf* file the value of 0.0012 is adopted; this will be kept constant during all the displacement control procedure.

5.4 Important parameters of the model

The model already described is characterized by a series of parameters, whose values can be either unknown or determined by experimental tests; however, in this specific case, without the possibility to be sure about their effective reliability performing the analysis. For this reason in the present work a series of different analysis will be performed, applying each time the variation of one parameter, with the double purpose of evaluating the dependence of the results from every single parameter and to find at the end the values that provide the best agreement with the experimental results.

The most important parameters that affect the solution of the FEM analysis are:

- tensile fracture energy G_f and numerical crack bandwidth h for the concrete material;
- normal stiffness for the felt interface between slab and supports, $k_{n,felt}$;
- normal stiffness for the Teflon interface between slab and loading plate, $k_{n,Teflon}$;

Hardening steel reinforcements behaviour could be important as well and it could have an influence role in the numerical solution.

Moreover, it has to be noticed that, for a constant mesh, also the average volume of the elements and thus the crack bandwidth are constant.
For each adopted mesh this value is obtained by the formula:

$$h = \sqrt[3]{V}$$

where V is the average volume for solid elements of the mesh.
It has to be observed that standard integration scheme will be used in all the analysis, that is:

- 3×3×3 integration scheme for CHX60 elements;
- 4×4 Newton–Cotes integration scheme for CQ48I interface elements;
- direct integration (1-point) for L6TRU truss elements.

5.5 Comparison between NL-analysis and experimental results

In order to verify the reliability and the goodness of the SL-analysis, NL-analysis are run on the model described previously. The results obtained from this FEM analysis are compared with the Lab-Test evidences.
Since SL-analysis method employs long computational time and effort for each elaboration, previous NL-analysis has the double purpose to fix unknown parameters and to save time.
Accordingly, NL-analysis are run on different mesh to define:

- felt behavior sensitivity;
- influence of normal stiffness of the Teflon layer on the global and local behavior of the slab;
- tensile fracture energy value for each mesh.

Moreover, this step allows to discover and understand the mesh sensitivity on the output, like force-displacement diagram fitting, tensile principal strain distribution, yielding of the reinforcement bars and cracking behavior of the reinforced concrete slab.

5.5.1 Teflon Sensitivity

The mechanical features of Teflon layer are no investigated for the present experimental test, so a defined value for compressive normal stiffness is not available. In order to verify the sensitivity up to this model and select the most reasonable value, a set of four is adopted inside the total model of the slab.
The present string is manually modified inside the *.dat* file:

```
3 DSTIF     500.00000000    0.250000000000
```

following this pattern:

syntax

'MATERI'		
1 5	6 12	13 80
	DSTIF	$d11_r$ $d22_r$ $[d33_r]$

Interface's stiffness definition inside iDiana environment

DSTIF $d11$and $d22$ are linear stiffness modules $D11$ and $D22$. $D11$ sets the relation between the normal traction *tn* and the normal relative displacement Δu_n. $D22$ sets the relation between the shear traction *tt* and the shear relative displacement Δu_t. The dimension of the stiffness moduli is force per area per length, i.e., stress per length, for instance N/mm^3.
The present analysis adopt a *Newton-Raphson modified* method for the iterative procedure, with a $0.03\ mm$ displacement control step, with relative displacement criteria of 10^{-4} (option CONTIN on). The fracture energy G_f and numerical crack bandwidth h parameters are $0.150\ N/mm$ and $165\ mm$ respectively. The felt has got a non-linear behavior. The pre-stress value is set to $21.60\ MPa$.
As aforementioned four values are adopted inside the $k_n = [120 \div 850]\ N/mm^3$ range; they are here shown:

- $k_{n,1} = 120\ N/mm^3$;
- $k_{n,2} = 250\ N/mm^3$;
- $k_{n,3} = 500\ N/mm^3$;
- $k_{n,4} = 850\ N/mm^3$.

For the tangential stiffness a fixed value of $k_t = 0.20\ N/mm^3$is selected, since it has no influence on the final result. Moreover, in this way the kinematic decoupling between concrete and steel plate is more effective.
The following image shows the load-displacement graphs obtained:

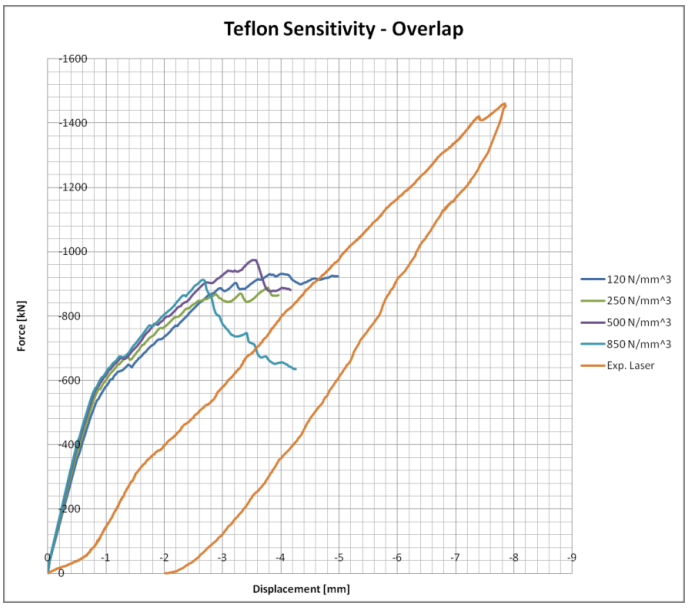

Load-displacement diagram for four normal stiffness values of the Teflon interface

By viewing to this plot, one can see a more regular behavior for the highest value for the normal stiffness interface "Teflon". Indeed, a peak and a post-peak behavior are distinguishable; instead for the lowest values a more flat trend starts to arise until the analysis diverges, so no clear peak is recognizable.
Regarding to the linear field, a higher Teflon stiffness seems to involve a slightly stiffer trend for the whole system, but the cracking point seems to remain the same as shape and force and displacement range.
So, individuated the *Peak Load*, or better the highest force magnitude occurred, the *Peak Displacement* can be detected. In the following graphs the *Peak values - Teflon stiffness* trend are shown:

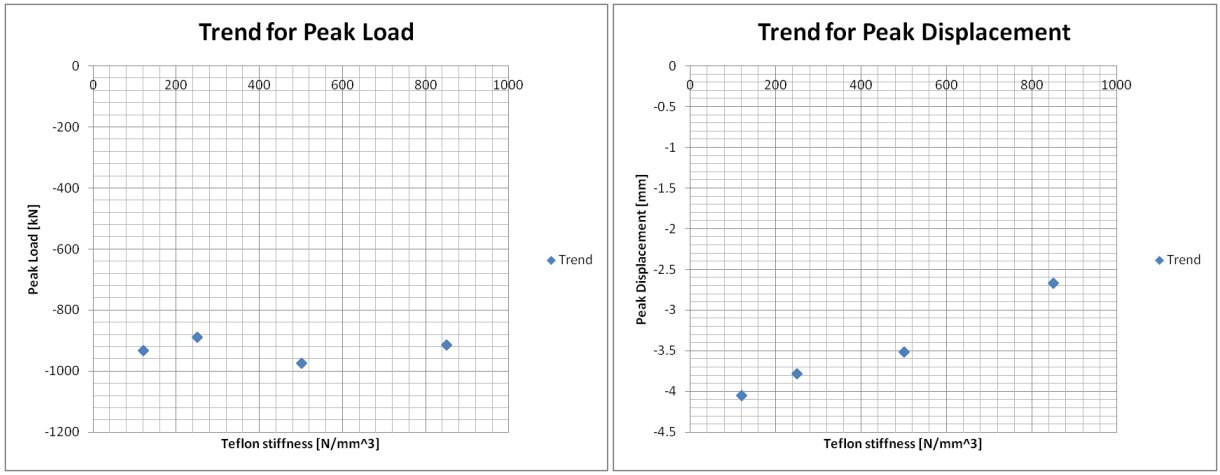

Peak Load - Teflon stiffness trend and Peak Displacement - Teflon stiffness trend for the total model

The *Peak Load* seems to be no influenced by the Teflon normal stiffness: the value remains inside a 86 *kN* wide range. Unlike the *Peak Displacement*: here a linear correlation between Peak Displacement and normal stiffness is well visible.
The following table summarizes the peak values:

$k_{n,teflon}$ [N/mm^3]	F_{max} [kN]	δ_{max} [mm]
120	-932	-4.05
250	-888	-3.78
500	-974	-3.51
850	-914	-2.67

Peak Load and Peak Displacement with the normal stiffness

To better understand the sensitivity of the model, effects on the *principal tensile strain* (E1.1 attribute) distribution is studied on the top and bottom surface.
Two output files are selected for post-processing:

- $k_{n,2} = 250\ N/mm^3$;
- $k_{n,4} = 850\ N/mm^3$.

Peak and post-peak points are studied and the main points are reported on the force-displacement diagrams, as the following image shows.

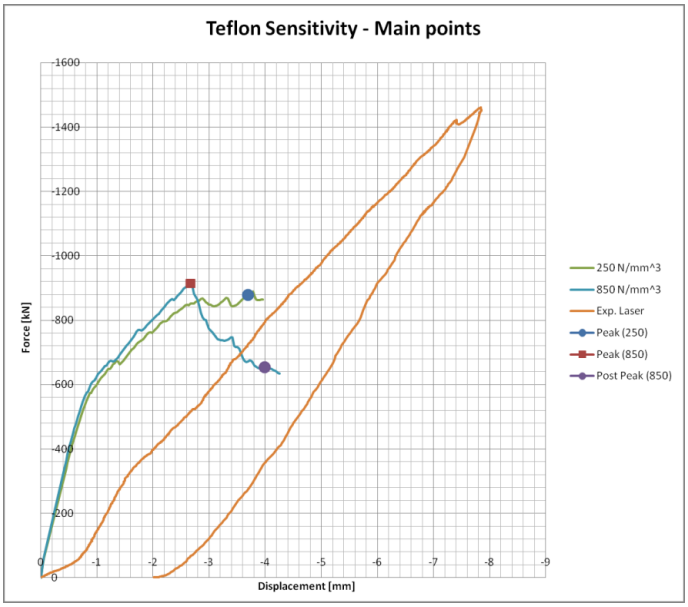

Peak and post-peak points for 250 and 850 normal stiffness

Having the same fracture energy and crack bandwidth values, four strain points are selected on the softening diagram for the concrete.

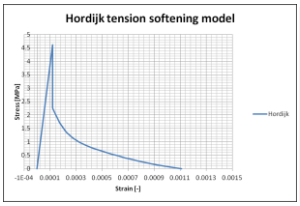

$\varepsilon_{el,ult.}$ [-]	0.000118	1.184E-04
0,5*$\varepsilon_{cr,ult}$ [-]	0.000555	5.545E-04
$\varepsilon_{cr,ult}$ [-]	0.001109	1.109E-03
5*$\varepsilon_{cr,ult}$ [-]	0.005545	5.545E-03

(a) *(b)*

Hordijk softening diagram and relative strain values

For the lowest selected value ($k_{n,2} = 250\ N/mm^3$) the peak coincides with the post peak point, so only one plot is shown:

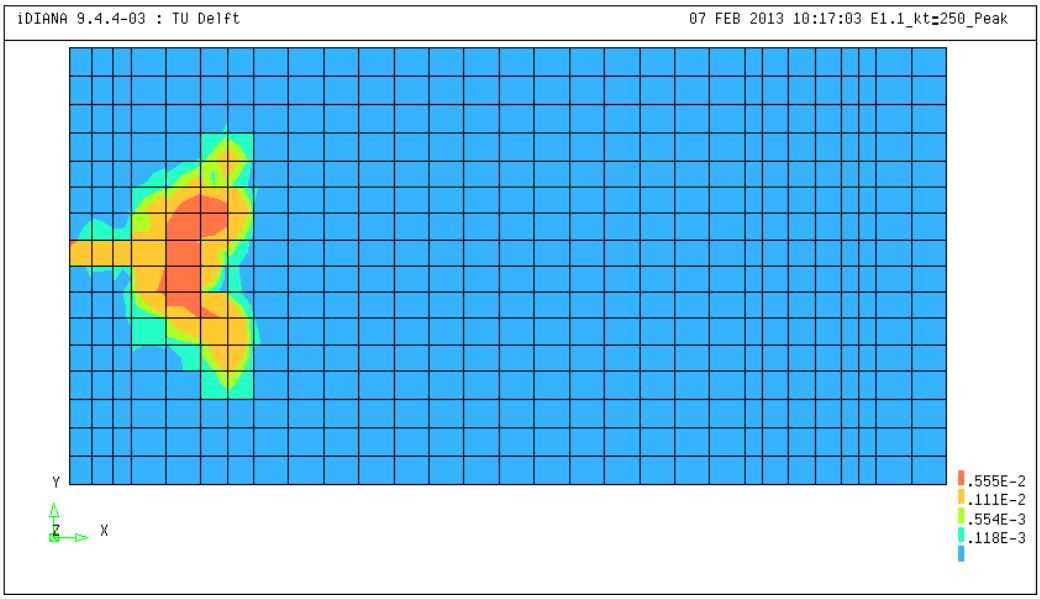

Principal tensile strain for top surface at peak point

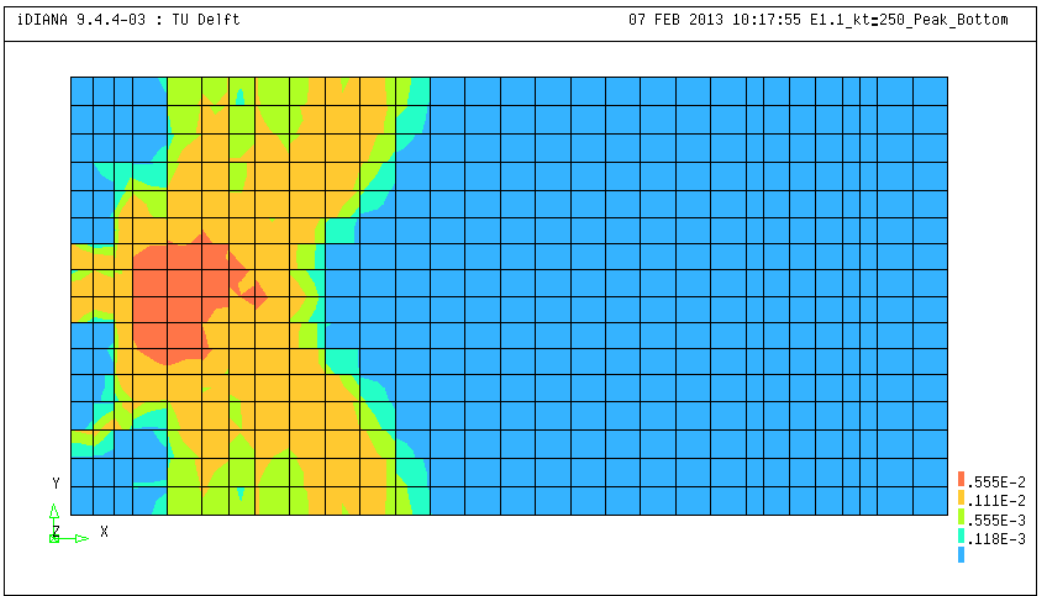

Principal tensile strain for bottom surface at peak point

Instead, for the highest value ($k_{n,4} = 850\ N/mm^3$) the peak coincides with the post peak point, so only one plot is shown:

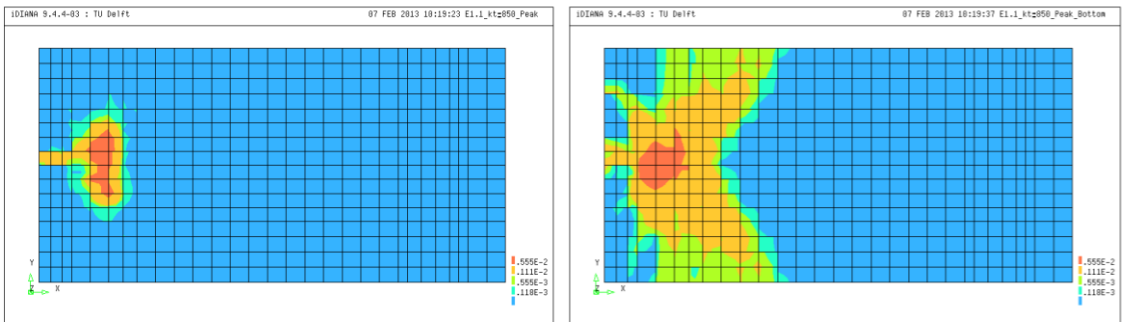

Principal tensile strain for top surface and for bottom surface at peak point

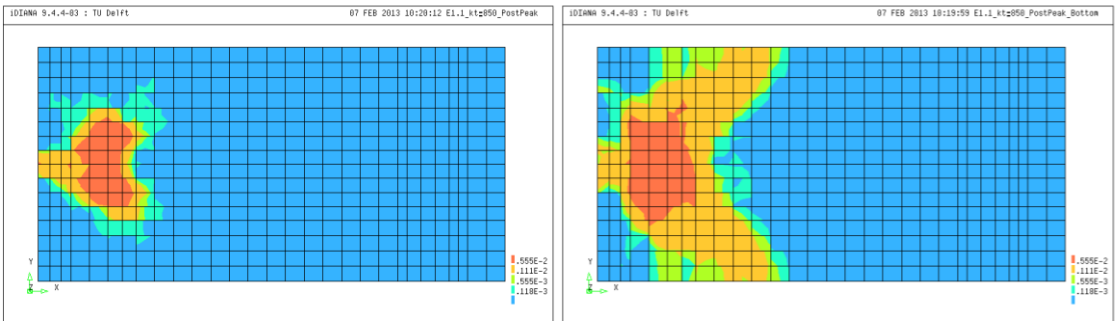

Principal tensile strain for top surface and for the bottom surface at post-peak point

Qualitatively, the distributions seem similar, with a "butterfly" shape spreading below the loading plate to the later free edges on the bottom surface, though the red area is more extended for the highest value of the Teflon stiffness.
Moreover, it has to be noted that the distributions have a different orientation.
No other big differences are detected, so to mediate, the average value is chosen from the $[120 \div 850]\ N/mm^3$ range: for all the following analysis $500\ N/mm^3$ will be the reference value for the normal stiffness of the Teflon interface.
It can involve a smoother trend for the global load-displacement diagram.

5.5.2 Felt behavior and adjustment phenomena:

As exposed above, a felt layer is interposed between concrete surface and the top face of the support beam with the double purpose of avoid an initial concentration of stresses due to the unevenness and roughness of the surface concrete and reduce the contact area of the slab with supports.
Accordingly, during the experimental test a marked settling phenomenon occurred during the first millimeters of load on the slab.
The global settling event is logically made of various components: adjustment of the loading plate on the top concrete surface, of the Teflon layer between steel and conglomerate, of the supports, of the whole steel frame under load and, finally, settling of the felt layers.
By extending the linear trait of the slab (visible before 1.5 mm of displacement) a *"shift"* of about 0.55 mm can be detected on the abscissa.
It was tried to fit this initial phenomenon, by modifying the felt model: inserting a *gap* who can simulate the void between slab surface and felt.

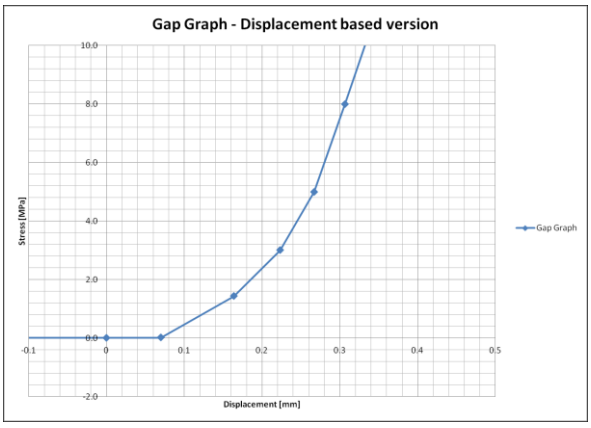

Felt behavior with initial gap

A non null slope is modeled, in order to avoid numerical instability.
However, this trick does not generate any influence on the numerical results, as shown by the following figure:

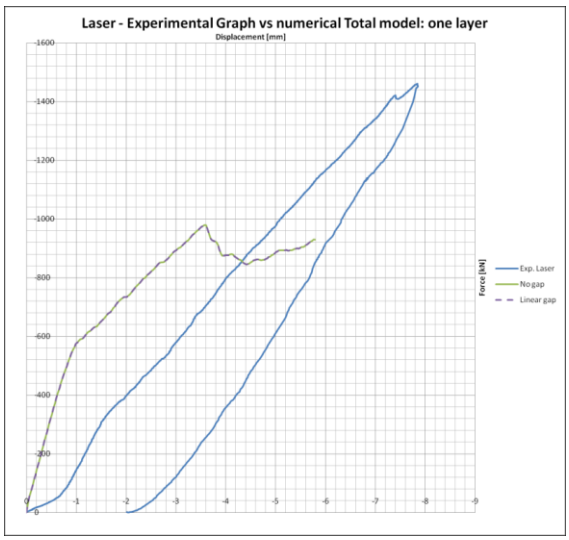

Load-displacement diagram for gap and no-gap felt

No differences are detected on the load-displacement s diagram for this solution.
So, a new analysis is performed by inserting a continuous "bed" interface was interposed: first on the support beam's bottom, and then between slab and felt interface. In this way it was tried to model the phenomenon. The analysis are performed until divergence occurred.

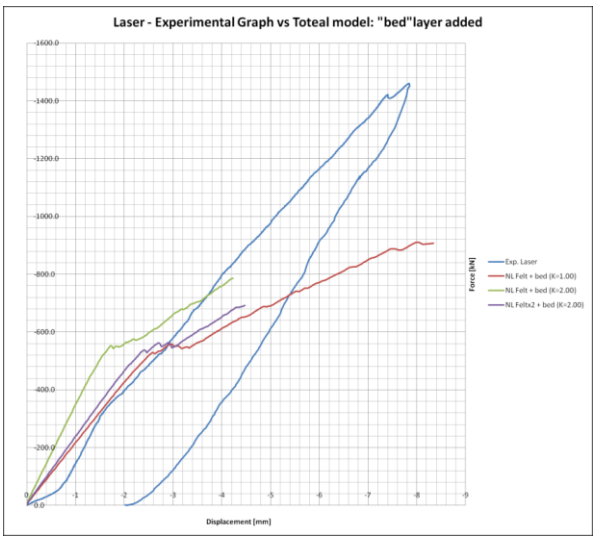

Force-displacement diagram for bed between slab and felt

The upper image shows how the bed's stiffness can provide a smaller initial stiffness, a better prevision of the experimental slope can be provided. However, it involves a different behavior of the slab for higher values of displacement.
Moreover, NL-analysis show a stiffer initial slope, though the total model describes the whole experimental setup.
It can be provided by few factors:

- adopted felt model and felt behavior;
- overestimation of the Young's modulus for the concrete;
- settling phenomenon due to the warped configuration of the slab, both in the longitudinal and transversal direction, in the experimental test.

First, it has been discovered a strong influence of the felt behavior on the whole slab's behavior, as seen on previous analysis with felt and plywood interface [4].
Moreover, the felt reaction was tested until 8 MPa of load, but many analysis show how this value is exceeded; so a linear behavior is assumed by adopting the same stiffness. This assumption can influence the whole future output: the felt model influences the slab's response and the slab's response influence the felt reaction as well.
Secondly, the Young's modulus for the concrete E_c is estimated by using the CEB-FIP Model Code 2010 [37]. Its value depends on the origin of aggregate used for the conglomerate; so the value hold to the $[27310 \div 46820]MPa$ range. For the present slab *glacial river aggregates* were used and $\alpha_E = 1.00$ is adopted.

Table 5.1-6: Effect of type of aggregates on modulus of elasticity

Types of aggregate	α_E	$E_{c0} \cdot \alpha_E$ [MPa]
Basalt, dense limestone aggregates	1.2	25800
Quartzite aggregates	1.0	21500
Limestone aggregates	0.9	19400
Sandstone aggregates	0.7	15100

Young's modulus evaluation for concrete from Model Code 2010

It has to notice that the same consideration is found in previous works [7] [6].
Thirdly, the experimental slab showed a warped shape: no full contact was provided on the supports due to the curved shape in both directions (X and Y).

In order to avoid other manipulation on the model and to introduce more unknown parameters, we choice to don't insert any "bed" interface.

5.5.3 Fracture energy

The main parameter of the model, able to influence deeply the global behavior of the model, is certainly the tensile fracture energy G_f.
As said before, this parameter represents the energy required to propagate a tensile fracture on a unitary area and it acts on the tensile behavior of the concrete.

5.6 Presentation of the main results:

In order to evaluate the reliability of the adopted method, both NLF-analysis and SL-analysis, the results obtained from these FEM analysis are compared with the Stevin Lab-Test results.
First of all, to have an immediate idea about the accuracy of the analysis *load-displacement* diagram is shown for each attempt.
For each analysis, few aspects and output of the model will be discussed. All the consideration will be made using vector and contour plots, relatively to pre-fixed main points on the load-displacement diagram.
So, in the following sections will be discussed:

- redistribution capacity: The redistribution capacity of the slab is a very important feature, since during the loading procedure and the subsequent deformation and cracking of the slab, the real bearing capacity of the slab can reduce, due to an inferior value of the effective width of the support that actually contributes to bear the load. This reduction of the active area of the support is relative to the spreading angle of the load inside the slab, measured from the loading point, toward the North support. Most of the European Building Codes sets this default spreading with a value of $45°$. To evaluate the accuracy of this angle in this real case, it's very useful to analyze the reaction forces in the interface layer over the simple supports. In this way one can detect easily how large is the portion of the supports that effectively contributes to bear the load. So, it has been used the vector plot of the interface tractions on the felt interface above the supports. Most of the attention will be given to the North support.
- cracking behavior of the slab: this important aspect of the behavior of the slab regards the development of the cracks under an increasing load. First, a contour plot of the principal tensile strains is shown, taking into account four main strains points on the softening diagram, by adopting the fracture energy and crack bandwidth value. In this way the contour plot shows immediately the areas of the slab in which the concrete is still in an elastic or in a plastic state: this means that in these areas fractures can be present. To have a clearer representation of the direction and of the entity of the fractures, it's useful to have also a vector plot of the same principal tensile strain. A comparison between the experimental observations and the results of NLFA and SLA will be made. Through a plot of the bottom, of the West lateral and of the frontal faces of the slab, for each of the three points indicated in the load-displacement diagram, one can see the spreading of the zone interested in the cracking.
- behavior of the reinforcement bars: in order to verify that the failure in the slab is not due to a limited flexural capacity (in accordance with the experimental results in which the failure follows a shear mechanism), it has been observed the distribution of the principal tensile strains in the reinforcements. Moreover, in the present element the reinforcement ratio of the longitudinal bars is $\rho_l = 0.996\%$. According to *Kinnunen and Nylander* [18], the present slab is characterized by an intermediate amount of longitudinal reinforcements and can be expected some yielding of the reinforcements in the immediate vicinity of the loaded column, but the crisis occurs before yielding of the entire slab reinforcement. In this case the predicted strength of the slab is lower than its flexural capacity. To have an immediate

evaluation of the distribution of the stress and of the behavior of the steel bars, contour plots of the principal tensile stresses are presented afterward, referring to the characteristic deformation previously calculated.

- compressive behavior of the concrete: on the present analysis the compressive nonlinearity of the concrete has been ignored. Only the tensile cracking is included, as done in previous works (see [7]). So, in order to verify the goodness of this assumption, contour plot of the *principal compressive stress* of the concrete will be shown, adopting the *average compressive strength* of the laboratory specimens as reference value.
- failure mechanism of the slab: with the overview of the distribution of the principal tensile strains in the slab and of the principal tensile stresses in the reinforcement, it is possible make hypothesis about which is the dominant failure mechanism. From the observation of the distribution of strains and stresses, relatively to the peak load and after the peak load, the main cracks and the critical sections can be individuated.

6. APPLICATION OF THE NON LINEAR ANALYSIS ON THE TOTAL MODEL

The present NLFE-analysis adopt a *Newton-Raphson modified* method as iterative procedure, with a 0.03 mm displacement control step, with relative displacement criteria of 10^{-4} (option CONTIN ON). The fracture energy G_f and numerical crack bandwidth h parameters depend on the mesh discretization; it will be described later for each one. The Teflon layer has got $k_{n,T} = 500\ N/mm^3$, as discovered on the previous numerical tests. The felt has got nonlinear behavior, according to the experimental test on specimens.
In order to match the initial pre-stressing force on the Dywidag bars, a uniform axial stress s_{xx} depending on the mesh is applied to each truss element.
At first, a NLF-analysis is run on total model with two elements on the height, so called *2x2 model*, then *3x3* and finally *4x4*.

6.1 Coarse mesh: 2x2 total model

Few analysis were run to fit experimental results in terms of load-displacement diagram and numerical output, by adopting different values for the tensile fracture energy G_f parameter. The following image shows the output for $0.150 \div 0.300 \div 0.450\ Nmm/mm^2$:

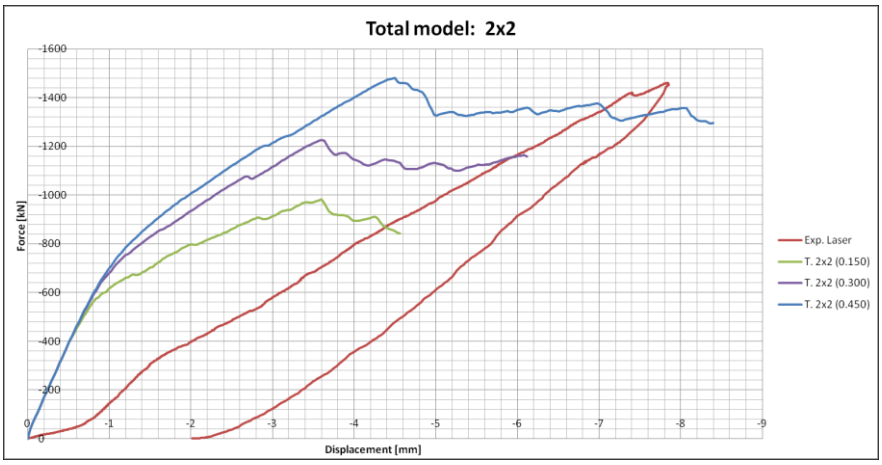

Force-displacement graph for 2x2 total model for different value of G_f parameter

The best agreement is reached adopting the following features:

- tensile fracture energy: $G_f = 0.450\ N/mm$;
- numerical crack bandwidth: $h = 165\ mm$;
- normal Teflon interface stiffness: $k_n = 500\ N/mm^3$;
- integration scheme: default for all the finite elements (see previous paragraphs);
- maximum number of iteration equal to 50.
- pre-stress on the Dywidag bars: $s_{xx} = 21.62\ MPa$.

The load-displacement graphs is here proposed:

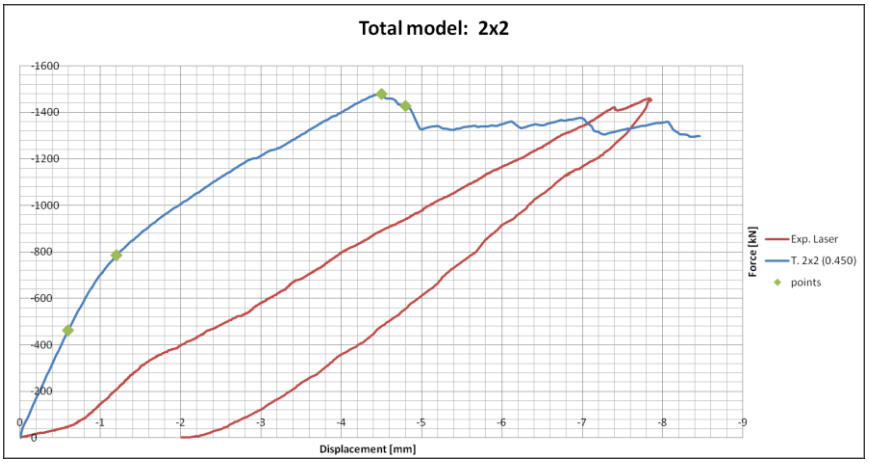

Force-displacement graph for 2x2 total model

A good agreement can be reached only in terms of experimental peak-load; the response remains still stiffer, though the post-linear slope seems to be well caught. After the peak (at $-4.50\ mm$ of displacement) a sudden decay of the bearing capacity of the slab is detected and a flat plateau arises. Divergence occurs after about $-8.50\ mm$.
The numerical peak values are:

- peak load: $1480.12\ kN$;
- peak displacement: $4.50\ mm$.

instead of:

- experimental peak load: $1460.62\ kN$ for a variation of $\sim +1\%$;
- experimental peak displacement: $7.84\ mm$ for a variation of $\sim -43\%$.

Analysis does not converge on step 32, 58, 62, 63 and few steps don't reach convergence around between 95 and 108 and 240 and 264. In terms of displacement it means from 2.85 to 3.24 mm and from 7.20 to 7.92 mm respectively. Around the 150^{th} step ($4.50\ mm$) no convergence is reached.
The analysis uses about 11000 for all the process.
Three main points are selected on the load-displacement diagram:

- *point 1:* $(0.60\ mm;\ 460\ kN) \sim 30\% F_{max}$;
- *point 2:* $(1.20\ mm;\ 785\ kN) \sim 50\% F_{max}$;
- *point 3:* $(4.50\ mm;\ 1480\ kN) = F_{max}$;
- *point 4:* $(4.80\ mm;\ 1428\ kN) = post - peak$.

They are shown in previous plot; the main output will be exposed in the next paragraphs.

6.1.1 Redistribution capacity:

On the following image, four pictures of the felt reactions are shown by adopting a vector plot. They prove the redistribution of the load from the slab to the support, since the action on the felt is equal to the one on the support beam for vertical balance.
The pictures show the plot about first step and three main points.

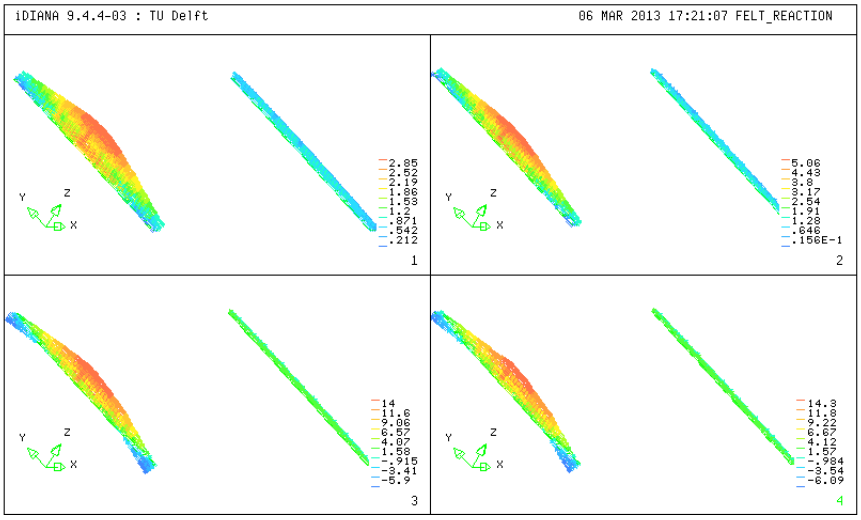

Vector plot of felt reaction [MPa] for the main points

By observing the previous vector plot of the interface traction, the trend of the reaction forces can be discovered. From the outset the tractions present a triangular shape and all the width of the support contributes to the bearing capacity. The first and the second plot show a linear development of the stresses: the shape remains the same, while the magnitude increases. Until the 2nd main point ($\sim 785\ kN$) the slab generally presents a linear behavior; increasing the load a clear redistribution of the tractions takes place: a progressive concentration of load on the middle of the interface is visible with increasing of the load, on the Y-direction. The same happens on the X-direction until the post-peak point, where a strong concentration occurs on a little area on the symmetry axis.
In other words, they become bigger in the central part of the North support, while they decrease in proximity of the right and left edges. Then they reach a tensile value: on the peak point a tensile reaction is already present. It has got a not negligible value ($5.90\ MPa$) and it start to arise from the lateral wings of the felt layer. It proofs the slab bending and the reduction of the contact area on the North support. So, theoretically we can say the outer parts don't contribute anymore to the bearing capacity of the slab. The present value doesn't agree with the supposed tensile felt behavior inside the *Diana* environment and further checks should be done.
The high felt reaction on the South support, on the first step, is due to the pre-stressing procedure on phase one, where the slab bends and pushes on the South felt layer. In the subsequent steps, its reaction reduces, since it reaches negligible values.
By plotting the part of interface in a compressive state, they are shown with red color (values higher than 0 MPa - *compression*). It can be observed that the loading angle assumes a value from 68° (1st main point) and 64° (4th main point), therefore the effective width of the active zone of the support changes from $b_{eff} = 2500\ mm$ to $b_{eff} = 2140\ mm$.

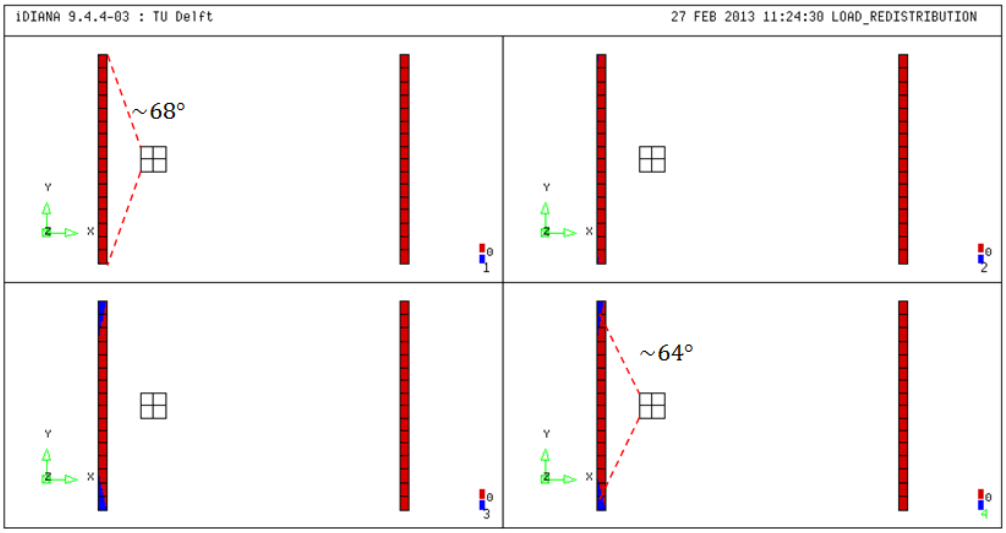

Effective width due to the load spreading on the felt layer

6.1.2 Cracking behavior of the slab

In order to investiga the development of the cracking under an increasing load, contour and vector plot of the pricinpal tensile strain are used. Taking into account four points on the softening diagram calculated for a fracture energy $G_f = 0.330\ N/mm$ and $h = 165\ m$.

$\varepsilon_{el,ult.}$ [-]	0.000118	1.184E-04
0,5*$\varepsilon_{cr,ult}$ [-]	0.001512	1.512E-03
$\varepsilon_{cr,ult}$ [-]	0.003024	3.024E-03
5*$\varepsilon_{cr,ult}$ [-]	0.015118	1.512E-02

(a)

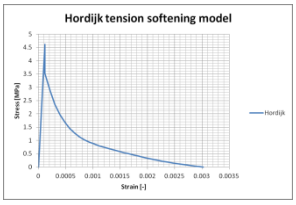

(b)

Main values for principal tensile strain (a) and Hordijk softening diagram (b)

For the three main points selected before, each plot shows the plots of top, bottom, front and lateral surface respectively.

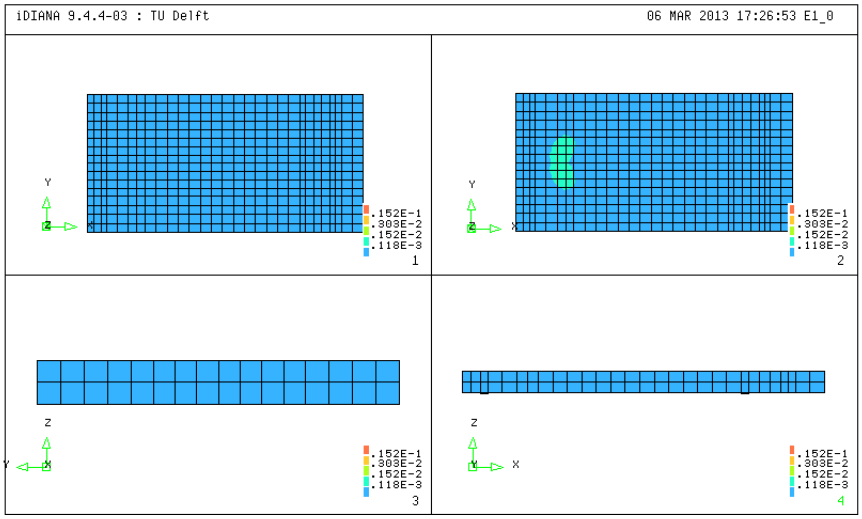

Contour plot of principal tensile strain for 460 kN

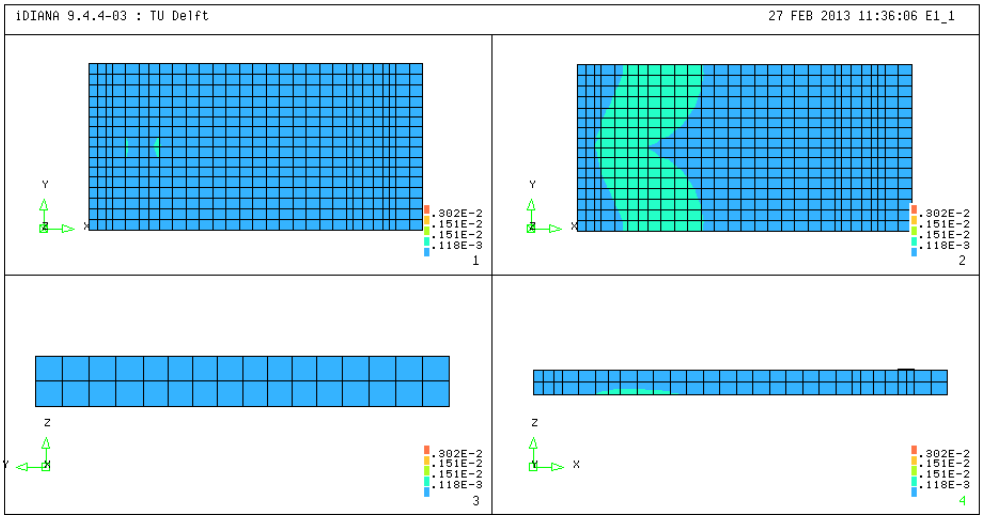

Contour plot of principal tensile strain for 785 kN

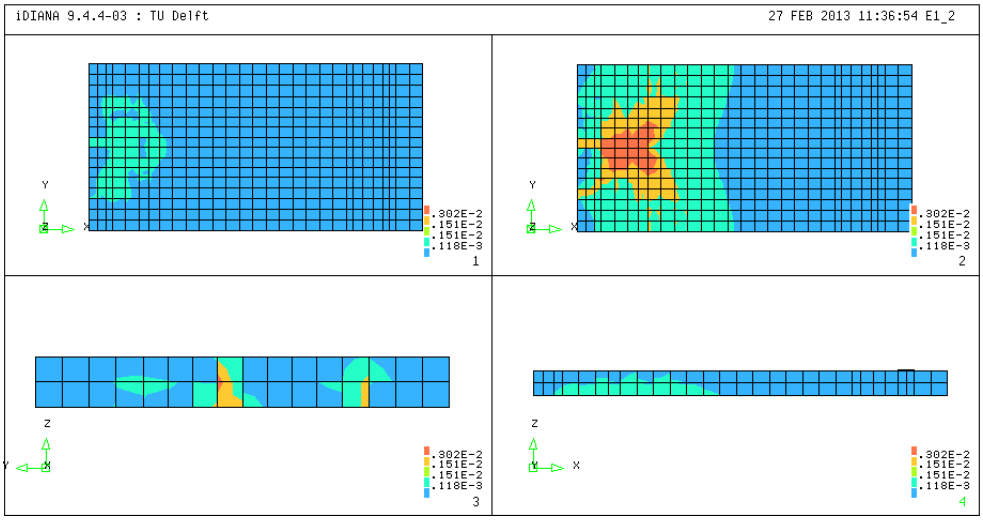

Contour plot of principal tensile strain for 1480 kN (peak)

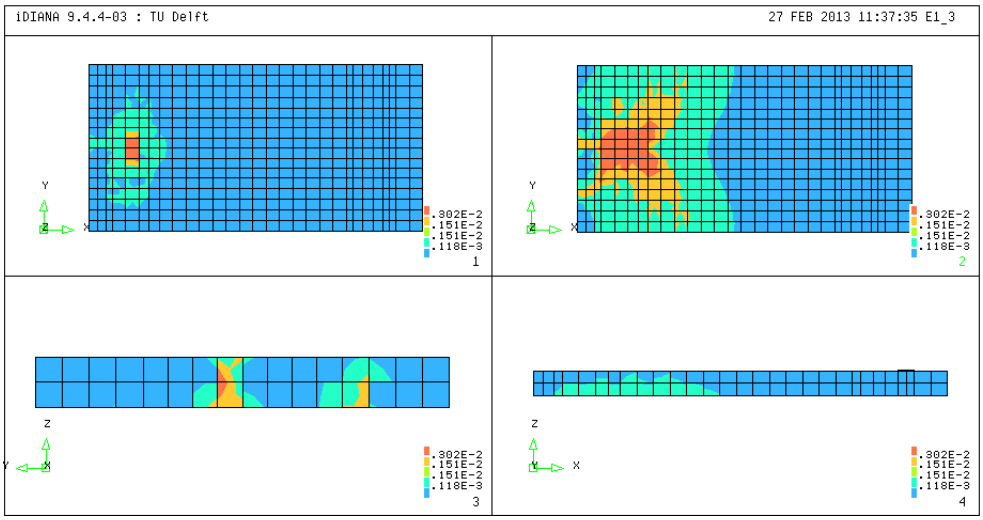

Contour plot of principal tensile strain for 1428 kN (post-peak)

The previous contour plots show that the cracks have origin from the bottom side of the slab, directly below the loading plate, then for higher loads they propagate forward the simple support and transversally, assuming inclined direction as well. After they increase their width under the loading plate.
This particular shape is so called butterfly shape for the characteristic form assumed.
For a load of 1480 kN, on the top face, the ultimate elastic strain $\varepsilon_{el,ult}$ is exceeded around the loading plate and a longitudinal crack runs forwards the simple support. Flexural cracks don't appear on the South support, as seen on the partial model. Then a cracked zone spread under the loading plate, while flexural cracks don't appear neither during the post-peak trait (as proofed by the West side plot).
A vertical central crack is visible on the frontal side only on the peak point. It run over the whole thickness of the slab, while one other crack spreads from the bottom surface until the half height. The same pattern is visible on the post-peak point more clearly.
On the West side a little cracked area is visible from the first main point, then cracks spread from the loading plate toward the simple support principally, investing more than half thickness of the slab.
Now, to have a clearer representation of the direction and of the entity of the fractures, it's useful to have also a vector plot of the same principal tensile strain.
The same surfaces are plotted:

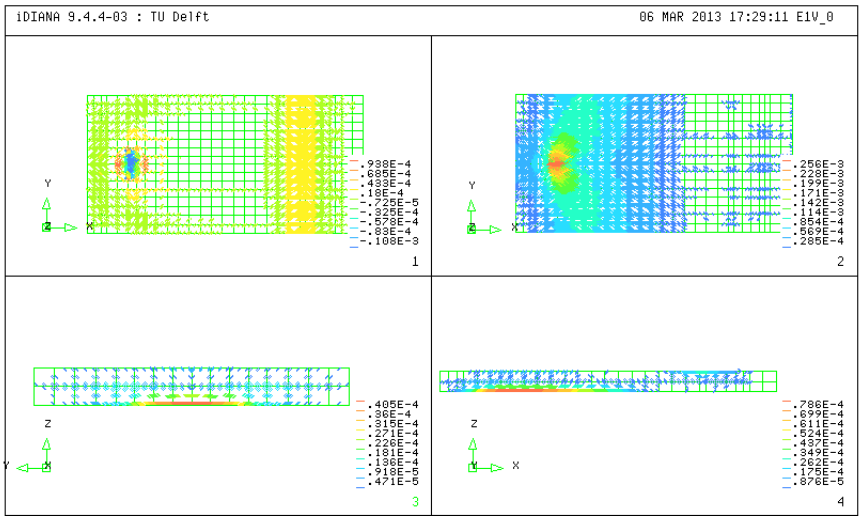

Vector plot of principal tensile strain for 460 kN

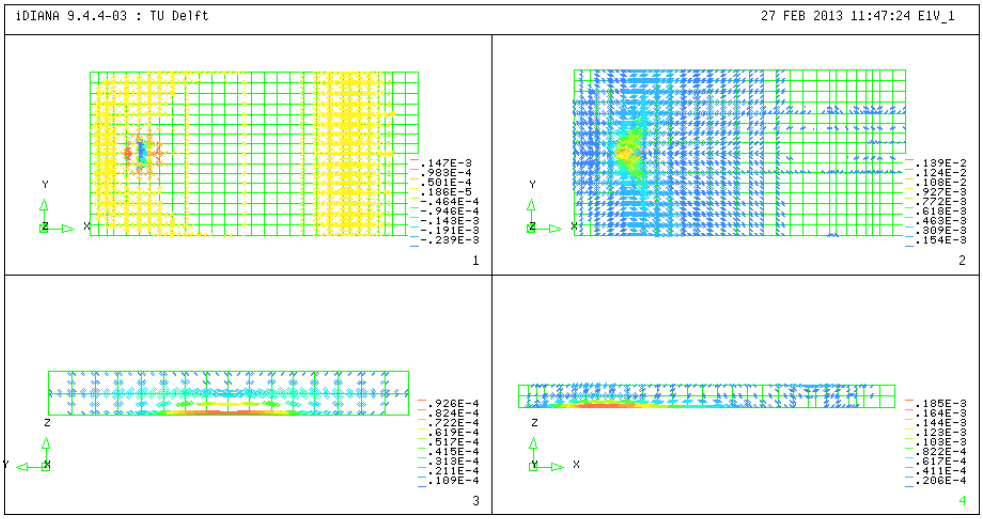

Vector plot of principal tensile strain for 785kN

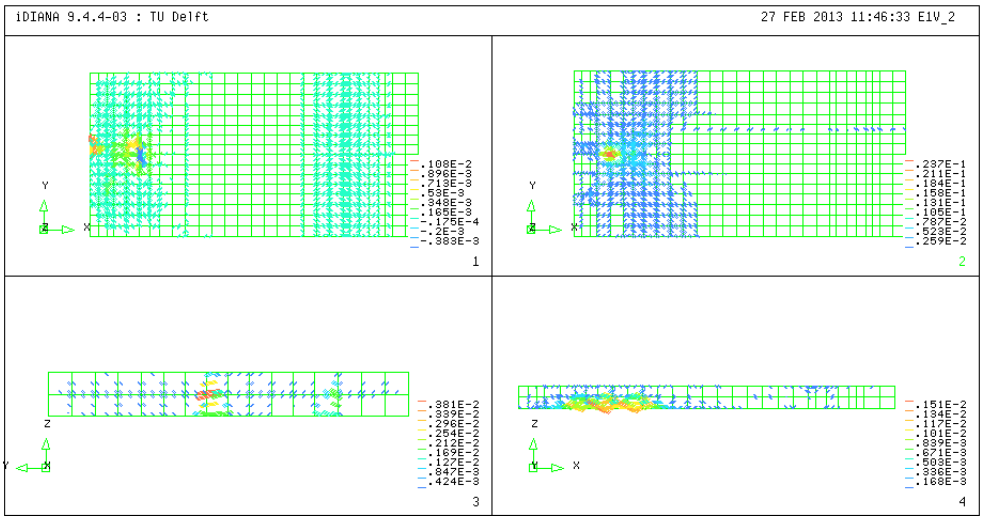

Vector plot of principal tensile strain for 1480 kN (peak)

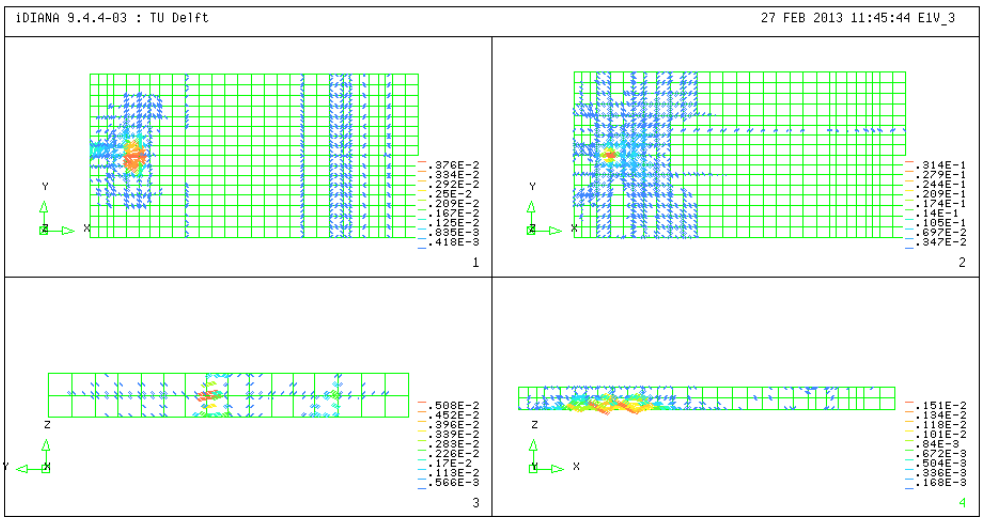

Vector plot of principal tensile strain for 1428 kN (post-peak)

For the load $460\ kN$ the ultimate elastic strain is exceeded only on the bottom face, below the loading plate. So, a main transversal crack arises from the load position and runs toward the lateral free edges. A second family of cracks is visible: they run in the Y-direction, so a longitudinal crack will arise later. These two main systems are related to the flexural behaviour of the slab.
For a load of $785\ kN$ it can be observed a concentration of strains that superior than $\varepsilon_{el,ult}$ below the loading plate, on the bottom face, both in the North-South and in East-West direction. These two families of strain represent the flexural cracks in the two direction of flexion. In the laboratory experiment a crack of $0.1\ mm$ width in the North-South direction in the middle from the support towards the span, passing the center of the load is discovered (crack 1) and a $0.25\ mm$ wide crack on the East-West direction is observed (crack 2), close to the simple support.
On the frontal face a concentration of strains superior than $\varepsilon_{el,ult}$ are well visible on the middle. Other strains spread following an arc shape above the bottom surface of the slab.
The other interesting zones are located in the lateral West face below the loading plate. Here, strain vectors are visible and they represent the flexural cracks. During the experiment no flexural cracks are detected. Above the South support strain vectors are present on the top layer, but with lower magnitude than $\varepsilon_{el,ult}$, so flexural cracks are not detected, as in the experimental test.
The same pattern is better visible on the top surface plot, at the South support, both in Y and X direction.
For this load, no strain vectors exceed the ultimate crack strain $\varepsilon_{cr,ult}$, so no full opened cracks are detected.
For a load of $1480\ kN$, who represents the peak load, the ultimate crack strain $\varepsilon_{cr,ult}$ is exceed on the top face, along the North edge about $150\ mm$ from the middle of the support. So, it proofs the formation a longitudinal cracks from the simple supports towards the loading plate. This fracture is also visible on the front side of the model, where the strain value is higher, while a vertical crack fracture is present left side of the frontal face. This is in good agreement with the experimental evidence, where a $0.05\ mm$ for a through crack in the middle (crack 5) and $0.05\ mm$ for cracks towards the East side, not fully through and starting from the bottom (crack 6), are evidenced. Indeed, the numerical cracks seem to follow a vertical direction, from the bottom surface to the upper one. It has to be noted that the numerical crack tend to spread on the edge of elements.
On the bottom surface, various high deformations start to propagate in inclined directions (see figure below), suggesting an interaction between the transversal flexural cracking pattern and the formation of the shear cracking pattern below the loading plate. Indeed, they show a $0.237E-01 \div 0.259E-01$ of strain, two order higher than the ultimate crack strain $\varepsilon_{cr,ult}$.
So, a full opened crack system arises. This matches with the experiment, in which $3\ mm$ for punching damage at the west side of the bottom face. Through this behavior it can be deduced the development of the shear cracking, since the new fractures grows faster than the previous flexural cracks and their disposition starts to individuate radial paths originating from the loading area.

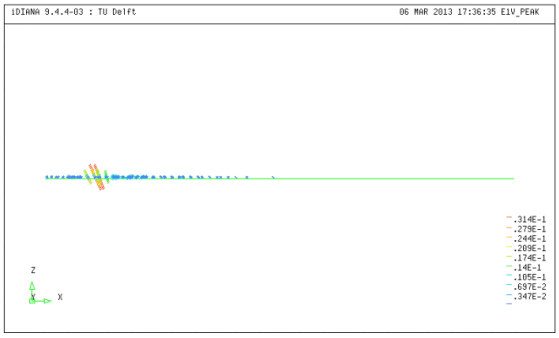

Particular of vector plot of principal tensile strain for 1418 kN (peak) on the bottom surface

On the lateral face the principal strain directions start to be inclined and this can be the beginning of the formation of a strut-and-tie bearing mechanism.
On the centre of the frontal face one can notice a concentration a crack, with a value that is comparable to the others in the bottom side, but it doesn't agree with the experiment test: its width is $0.62\ mm$ against $0.05\ mm$.
However, the most important deformation is the one that takes place on the bottom face, right below the loading plate, increasing the trend observed in the previous step and showing the typical shear behavior that occurs near a peak point. In fact cracks keep on propagating in the bottom face in radial direction, while other different fractures appear directly below the loading plate, very close to the perimeter of the loading plate and mostly in transversal direction, but also in longitudinal direction.

For a load of $1428\ kN$ (post-peak point), on the frontal face the previous vectors pattern does not show visible changing. This is in partial agreement with the lab test in which a crack arises from the top surface forward the bottom surface, without reaching the bottom surface; instead, lateral cracks start from the bottom and run until the half of the height of the slab. Although their width is quite well estimated ($0.35\ mm$ instead $0.05\ mm$), the middle crack width is about $0.80\ mm$ wide.
Again, on the top and bottom surface, the inclined vectors have one order higher strain than the flexural cracks, who spreads from the loading plate towards the North edge. The disposition of the strain vectors below the load evidences a clear truss-tie mechanism starting from the loading plate on the top surface and finishing close to the North support on the bottom surface.
On the lateral side a new vector arises in inclined direction, below the load. The flexural vertical cracks don't appear, as during the experimental test.
The presence of the strut-and-tie bearing mechanism and its evolution can be proved through a vector plot of the principal compressive strains ε_3, showing clear inclined struts of concrete.

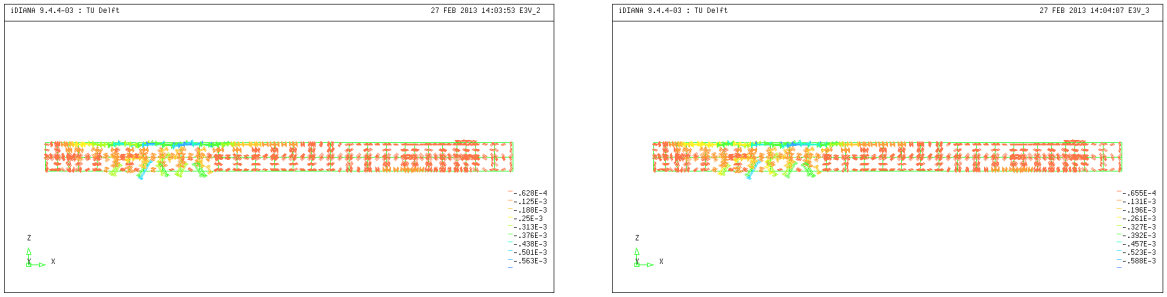

Vector plot of principal compressive strain for peak (left-hand) and post-peak (right-hand)

On the basis of the previous observations about the cracking behavior of the total model of the slab, performed using the NLFEA, it can be stated that a quite good prediction, better than the partial model, of the general crack behavior can be obtained. The width of the cracks is well estimated generally, but the best result is the accordance with experiment about the starting point of the fractures and the propagation of the cracking pattern, for what it concerns the directions of flexural and shear cracks. Moreover, in proximity of the peak load, it's also possible to individuate features of shear cracks, like the direction and the rapidity of growing. This can be used as another data to individuate critical sections and to predict the failure mechanism.

6.1.3 Behavior of the reinforcement bars

In order to be sure that the slab does not fail due to its limited flexural capacity, the amount of yielded reinforcement bars is checked. The reinforcement ratio in longitudinal direction is $\rho_l = 0.996\%$. According to *Kinnunen* and *Nylanderthis* would mean that some yielding of the reinforcements could be present in the direct vicinity of the load [5].
To have an immediate evaluation of the distribution of the stress and of the behavior of the steel bars, contour plots of the principal tensile stresses are presented afterward, referring to a unique yielding tension equal to $540\ MPa$.
Three main points are taken into account and for each one, four plots are shown: σ_{xx} and σ_{yy} for the top rebars, respectively on the upper and on the bottom plot (left hand); σ_{xx} and σ_{yy} for the bottom rebars, respectively on the upper and on the bottom plot (right hand).
Through these contour plots it can be proved the hypothesis of *Kinnunen* and *Nylander*, since the reinforcement steel of the bars has an elastic behavior in most part of the slab and the only area in which one can notice a yielding is the one close to the loading point. In particular for an applied load of around $1480\ kN$, the only bars who yields has a very limited length, below the loading point (red color). The yielding invests only the transversal bars. At the load of $1428\ kN$, one of the transversal bar yields close to the North edge, testifying the opening of the flexural crack at the front face toward the simple support.
No yielding occurs on the other bars.

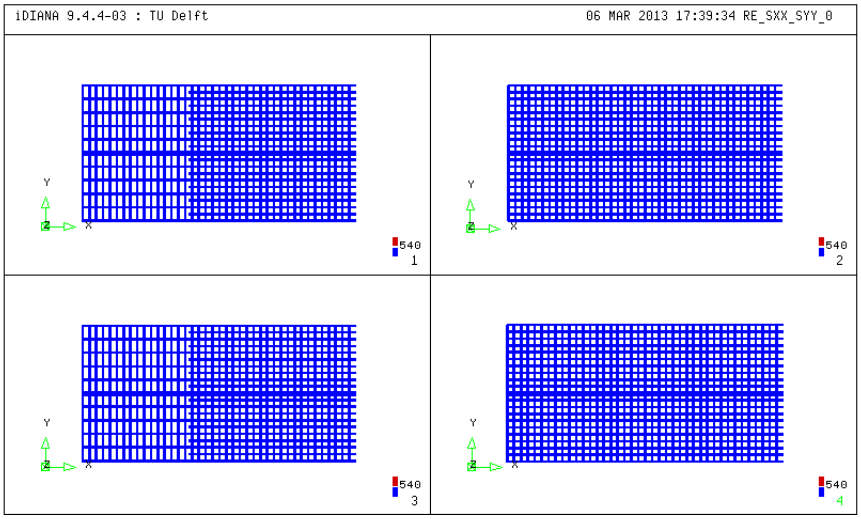

σ_{xx} and σ_{yy} contour plot for top and bottom reinforcement bars for 463 kN

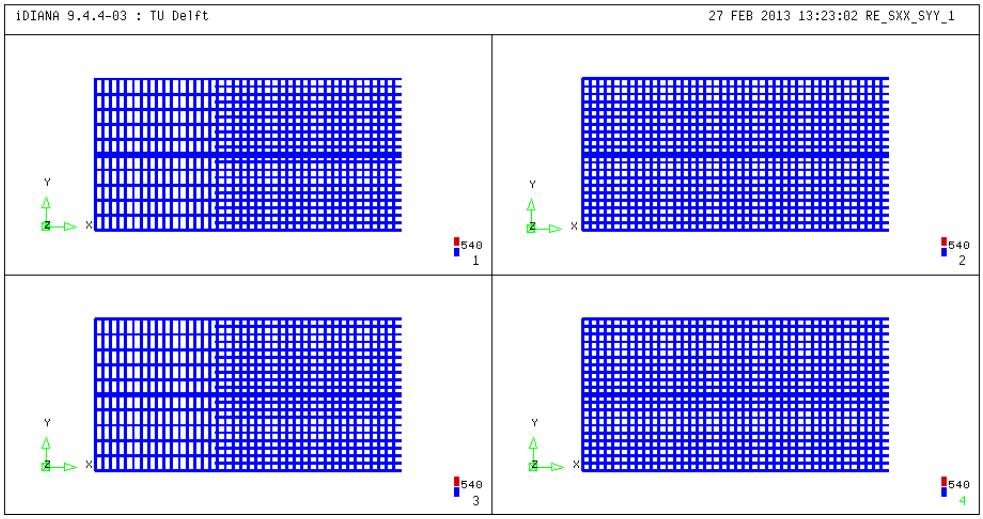

σ_{xx} and σ_{yy} contour plot for top and bottom reinforcement bars for 785 kN

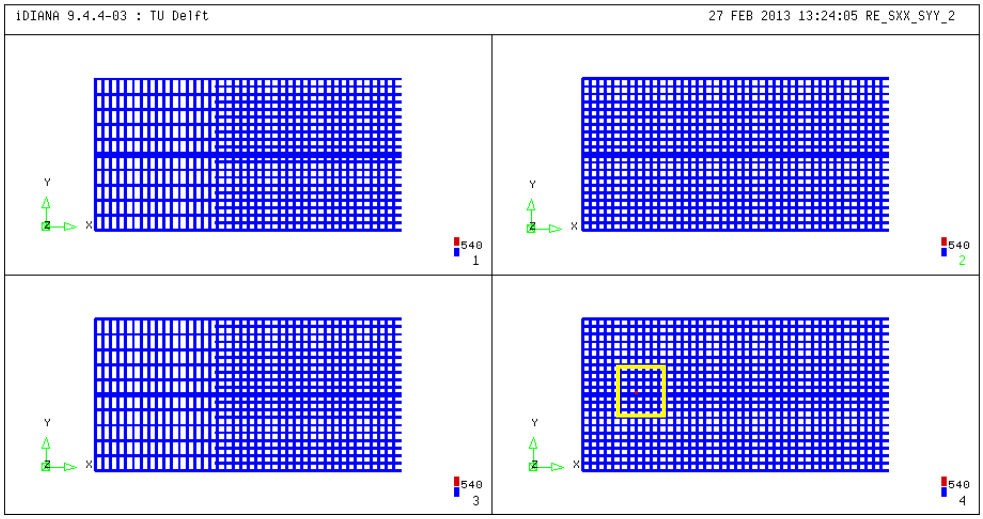

σ_{xx} and σ_{yy} contour plot for top and bottom reinforcement bars for 1480 kN (peak)

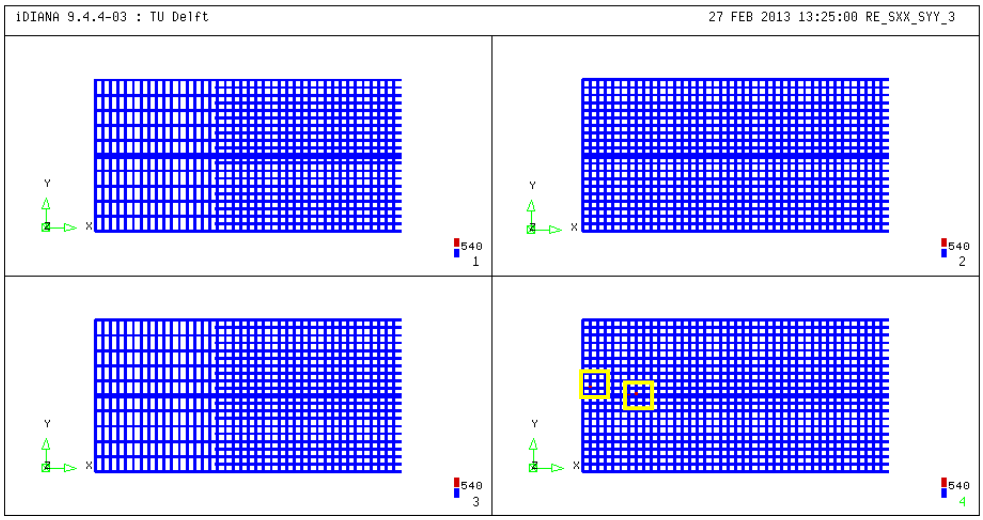

σ_{xx} and σ_{yy} contour plot for top and bottom reinforcement bars for 1428 kN (post-peak)

Adopting the principal tensile stress plots, we can observe the progressive redistribution of the stress inside the reinforcement bars.
For the present plots four points are selected: the first point on the load-displacement graph and the aforementioned three main point.
The first points allows us to discover the tensile stress distribution inside the rebars when the slab works in a ideal linear elastic state. Then, the following plots can show a gradually changing in value, position of the most loaded bars and distribution of the global stresses.
Since we ask for principal tensile stress, only positive values will be shown.

Observing the bottom rebars, the first point confirms the bending moment distribution on the slab: the highest values are located below the loading plate, then they spread both in X (forwards the free edges) and in Y direction (mainly forwards about the midspan).
The 1st main point ($\sim 785\ kN$) agrees with the initial crack formation: the most stressed bars are below the loading plate, on the Y-direction, so longitudinal flexural crack could be arisen; on the X direction a lower stress is detected, but it's still visible around the loading plate and transversal cracks could be formed. After, on the peak point ($\sim 1480\ kN$) a clear concentration of tensile stresses can be found below the loading plate with higher value than the yielding stress. Also here, the tensile stress distribution confirms the cracking patterns: a red stress is visible close to the North free edge, on the Y-direction, matching with crack 5 and crack 6 formation. The highest stresses run in the Y-direction, from the loading plate forwards the lateral free edge, assuming the so called *butterfly shape*, like the cracking patterns do.
On the post-peak point ($\sim 1428\ kN$) the butterfly distribution is more defined than the previous plot, however the tensile stress seems to reduce globally. It could proof the loss of bearing capacity of the whole slab after the peak. However, a yielded length for the transversal bar close to the North edge is detected.
Observing the top rebars, the first point shows a clear concentration of tensile stress on the South beam, where the m_{xx} distributed bending moment generated by the pre-stressing procedure is the highest. A similar global distribution can be seen on the 1st main point, but more defined on the South support. Instead, during the peak point, a radical redistribution occurs: the highest stress involves on the transversal bars close to the North edge. This agrees with the process of formation of the vertical crack on the middle of the frontal face (crack 5). This trend increases on the post-peak point, where a clear concentration of tensile stress spreads from the North support forwards the loading plate on the longitudinal bars. The tensile action around the loading plate seems to be negligible. Indeed, only short portions of X-rebars are invested by the phenomenon.

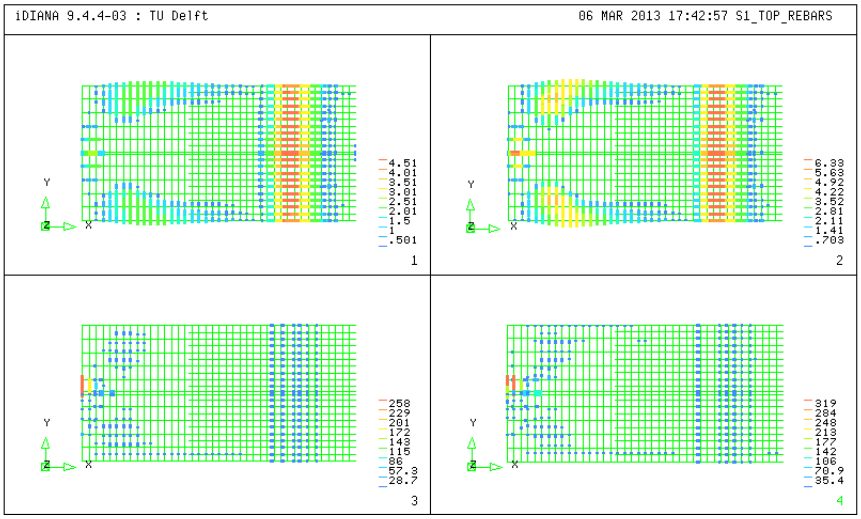

Principal tensile stress for the reinforcement bar on the top surface

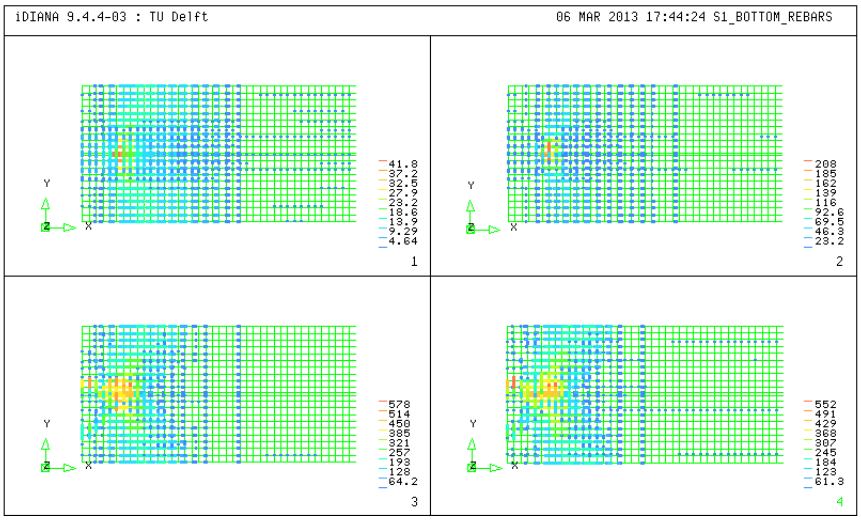

Principal tensile stress for the reinforcement bar on the bottom surface

6.1.4 Compressive behavior of the concrete

In order to verify the elastic state of the concrete for the compressive field, the *principal compressive stress* feature is investigated through a contour plot on four surfaces, for the three main selected before.
Two main values are adopted:

- $0.50 f_{cc} = -29.88\, MPa$;
- $1.00 f_{cc} = -59.76\, MPa$.

Since, the compressive stress has conventionally a negative value, the green color shows the parts with a lower principal stress than $f_{cc} = -59.76\, MPa$. Instead the blue color proofs the part who exceed this reference value.

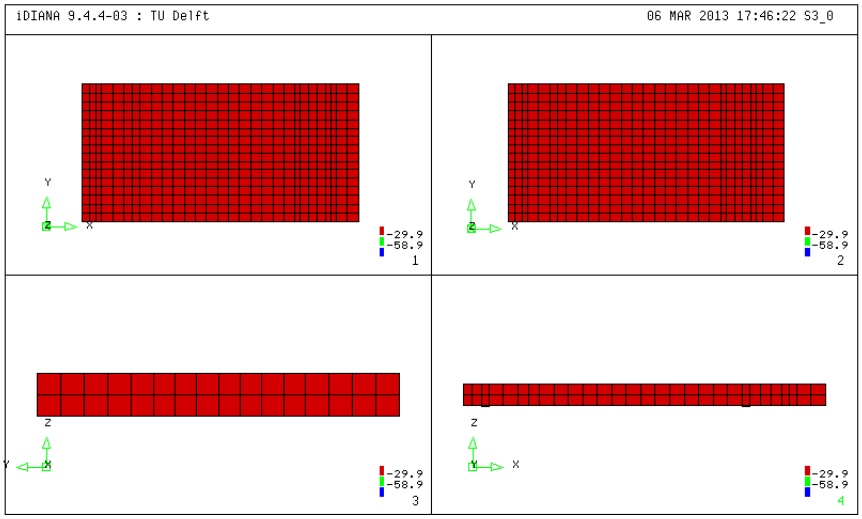

Contour plot of principal compressive stress for 463 kN

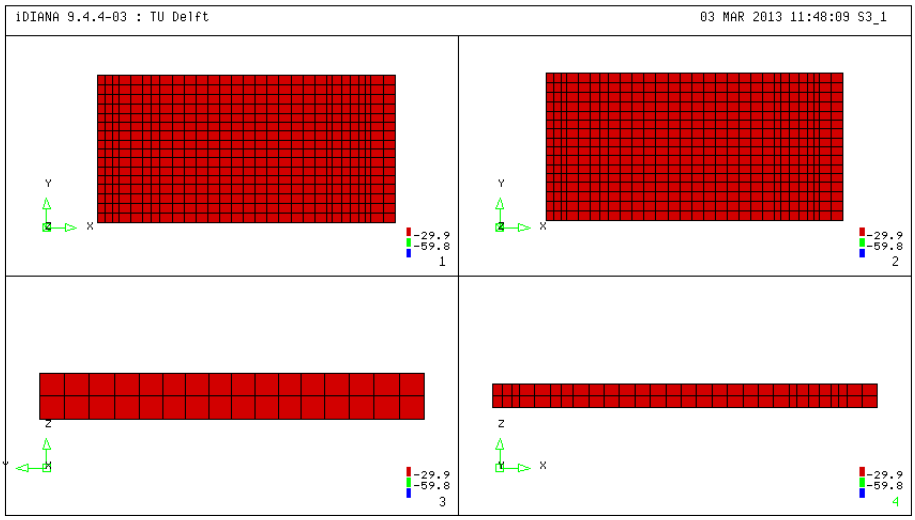

Contour plot of principal compressive stress for 785 kN

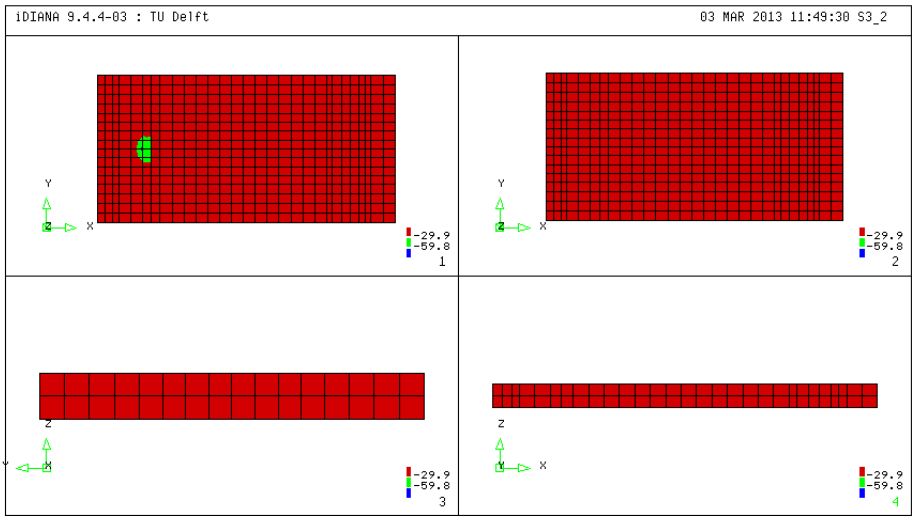

Contour plot of principal compressive stress for 1480 kN (peak)

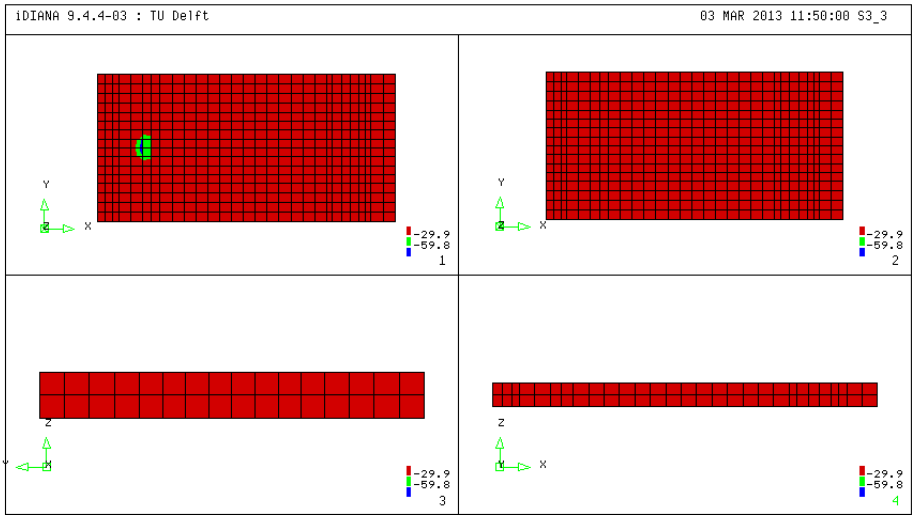

Contour plot of principal compressive stress for 1428 kN (post-peak)

As shown by the previous plots, the principal compressive stress exceeds the compressive strength of the concrete only on a small area below the loading plate. It can mean a numerically sinking of the steel plate inside the concrete, as seen in some experimental tests [32].
So, thanks to these plots, we can demostrate that the assumption of a linear elastic concrete in compressione is adequate to describe the behavior of the conglomerate. This is is strengthened by the fact that also the 50% of f_{cc} is exceeded in a limited surface of the slab.

6.1.5 Cracking pattern and failure

Based on the load-rotation curve for the tests performed by *Kinnunen* and *Nylander* [5], punching failure occurs before yielding of the entire slab reinforcement in case of intermediate reinforcement ratios. However, since the load is located close to the continuous support the truncated cone around the concentrated load cannot fully develop and the punching shear capacity is significantly improved. The following picture shows the distribution of the principal tensile strain at the peak load and after the peak load. The scale of the contour plots is held constant in order to see the development of the tensile strain area:

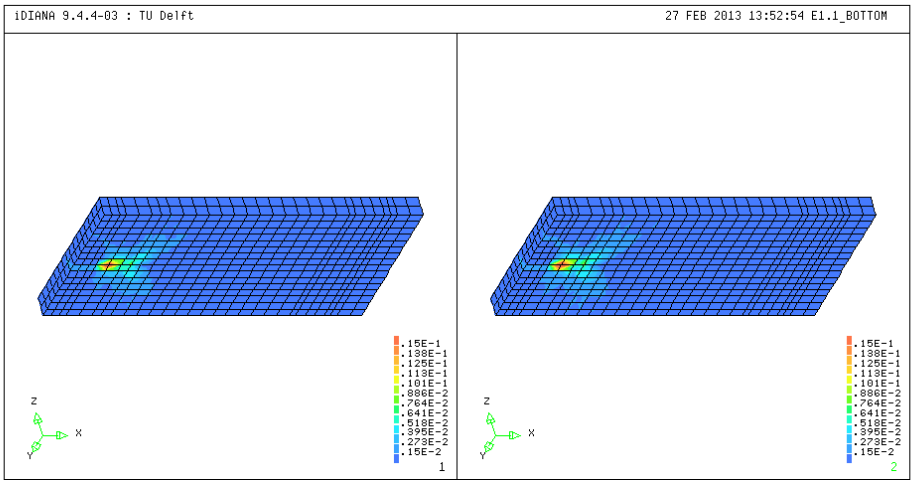

Contour plot of the principal tensile strain on the bottom face on the peak (left-hand) and post-peak points(right-hand)

From the previous plots it is still hard to discover whether the slabs fails due to punching shear or by wide beam shear failure. No clear critical diagonal cracks have been observed around the concentrated load, that would suggest pure punching failure. Furthermore, no critical section across the entire width of the slab was visible, suggesting wide beam failure.
However, the so called butterfly shape is well visible, with a North-South branch and an inclined limb from the load toward the simple support.
A high concentration of tensile stress is detected below the loading plate and thin transversal cracks are visible on the Y-direction.

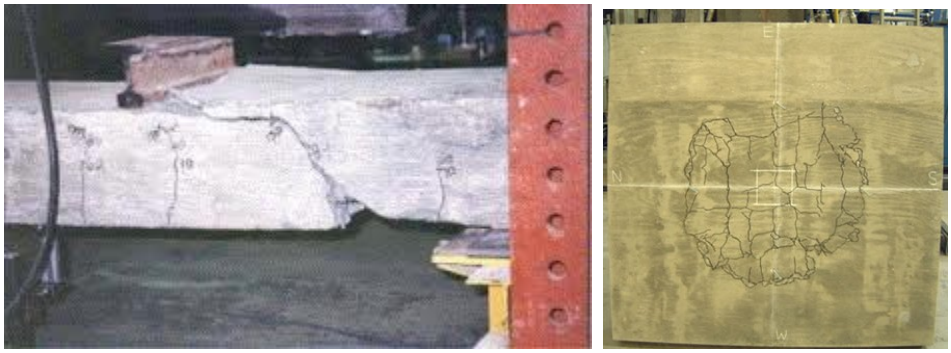

(a) *(b)*

One-way and two-way shear failure

A useful attribute to better discover cracking pattern inside the model is the *principal normal crack strain* $\varepsilon^{nn}{}_{cr,1}$ feature.
It will be adopted only on the total model, since it's still implemented on SL-analysis.
The best results can be obtained by adopting as reference two limit crack strains:

- $\varepsilon^{nn}{}_{cr,min} = w_{cr,min}/h = \frac{0.05}{165} = 0.303E-03$;
- $\varepsilon^{nn}{}_{cr,aver} = w_{cr,aver}/h = \frac{1}{165} = 0.606E-02$.

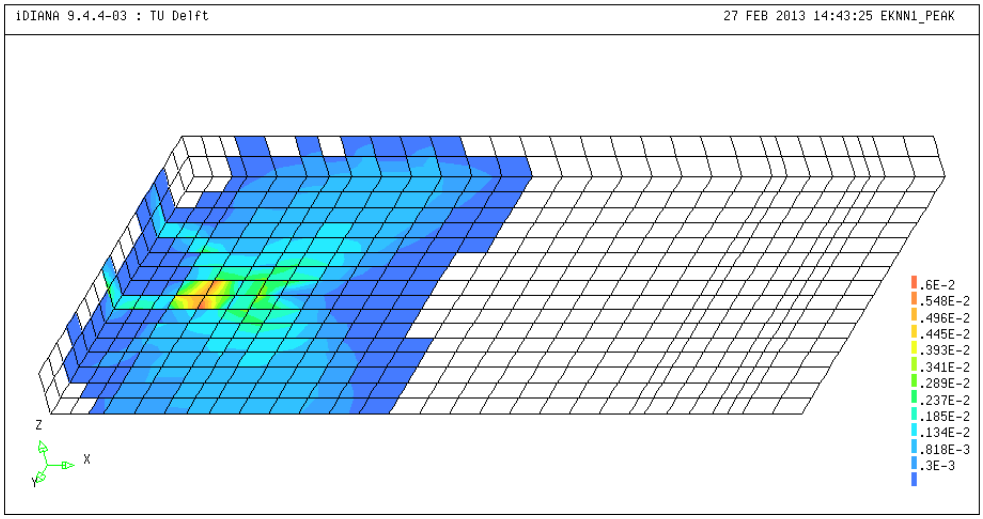

Contour plot of the principal normal crack strain on the bottom face on the peak

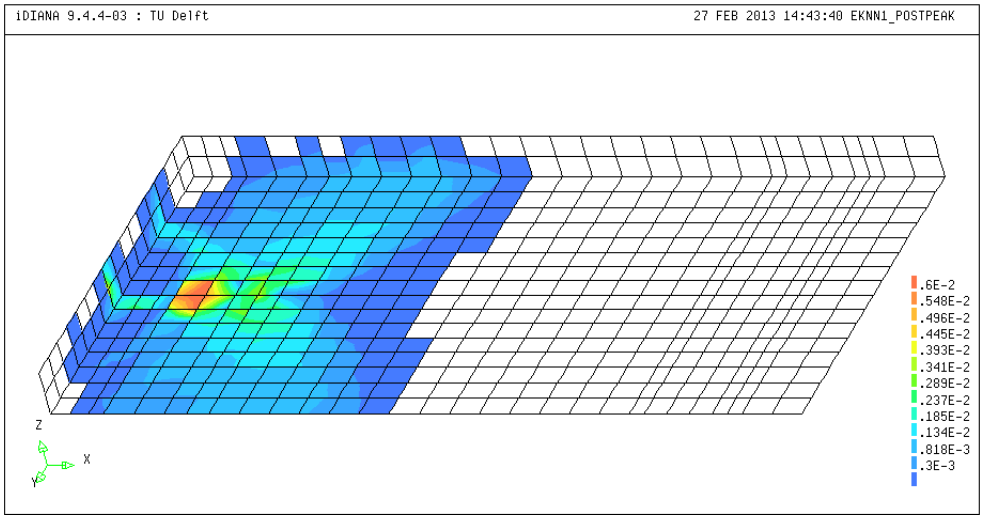

Contour plot of the principal normal crack strain on the bottom face on the post-peak

The previous plots show a more defined cracking pattern below the loading plate.
Here wide crack should be expected (red zone) and inclined crack spread from the load position forward the midspan on the bottom face. The longitudinal flexural cracks is well underlined together with the aforementioned front crack, on the North face of the slab.
The real orientation of the crack is shown by the disc plots:

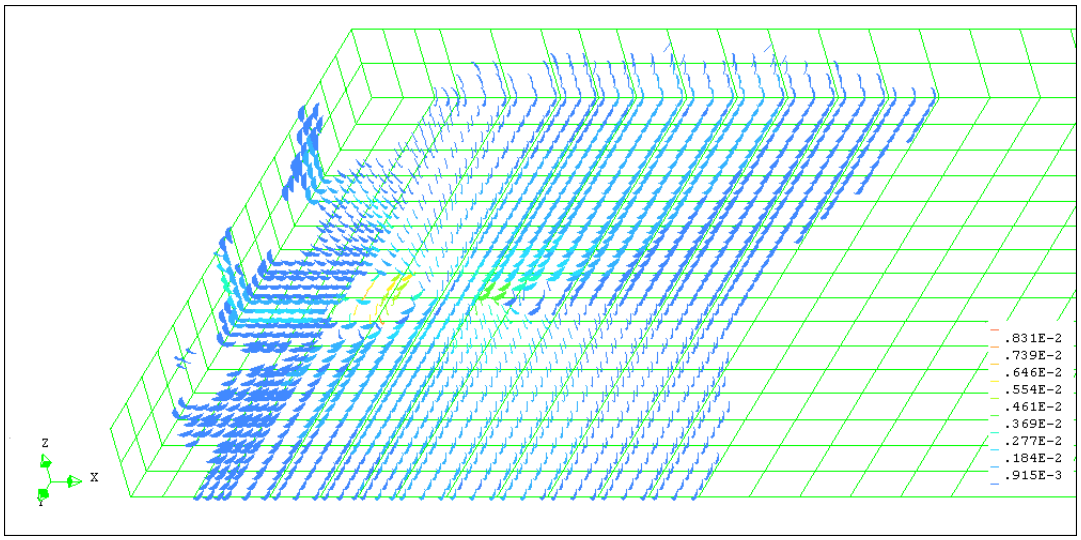

Disc plot of the principal normal crack strain on the bottom face on the peak

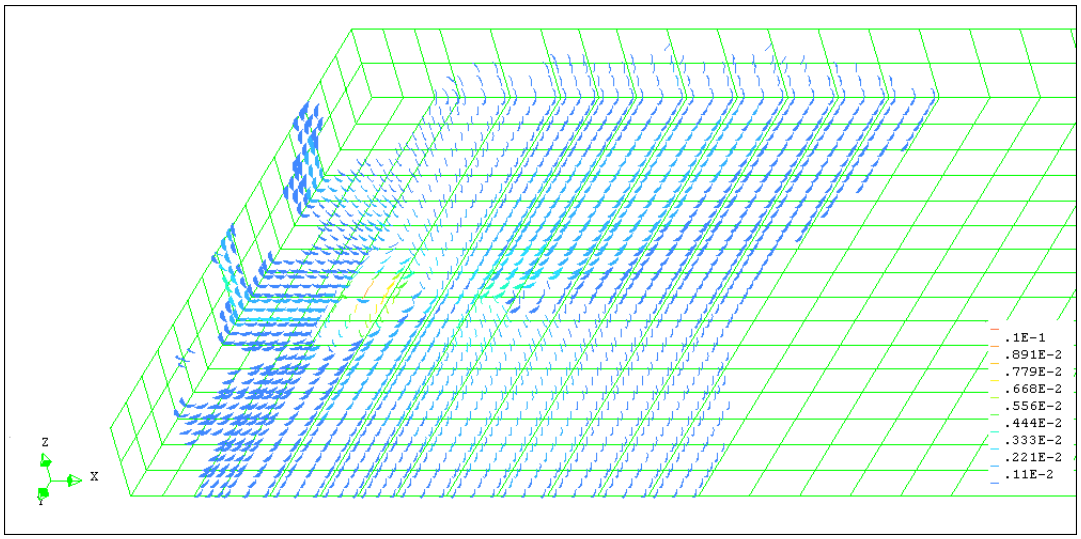

Disc plot of the principal normal crack strain on the bottom face on the post-peak

Thanks to this plot, some main cracks can be displayed on the bottom and frontal surface of the slab by following the orientation of the principal discs.
Moreover, is has to be taken into account the previous observations about the distribution of the principal tensile strains and the yielding of reinforcements. So it's possible have an estimation of the position and the entity of the most relevant crack in the bottom, lateral and frontal faces of the slab, that is reported afterwards.

A new way to detect cracks is here provided:

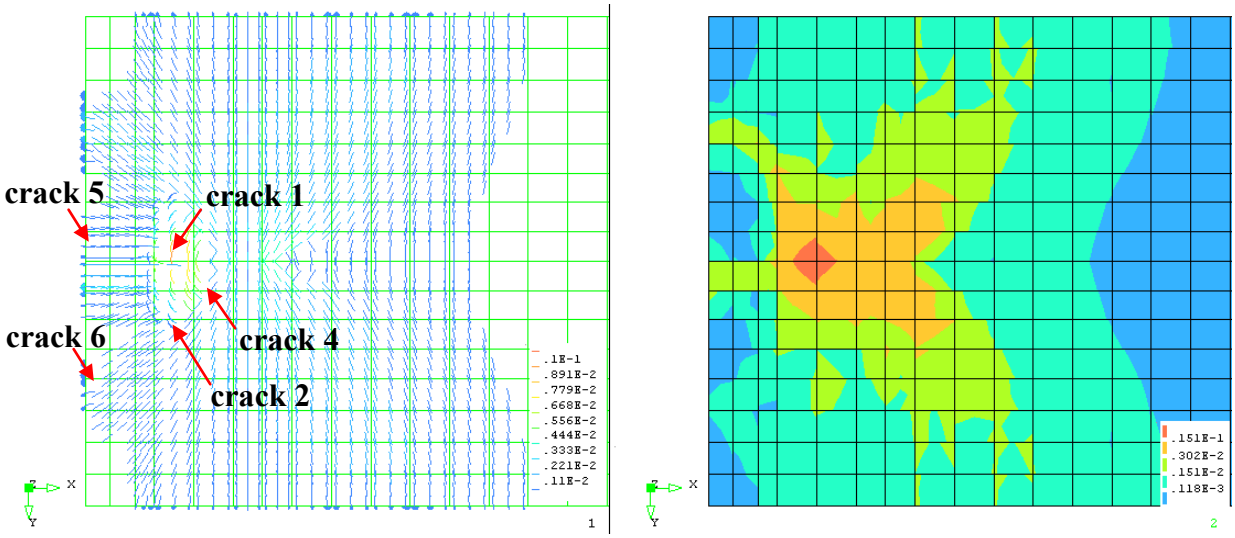

Contour plot of the principal tensile strain on the bottom face on the post-peak (right-hand and principal crack strain (left-hand)

The cross-comparison between these plots helps to discover the effective cracking patterns on the slab. It shows a quite agreement with the experimental evidence: crack1, crack 2, crack 4, crack 5 and crack 6 are displayed. There is no evidence related to crack 3 and crack 1 does not pass the load (as seen on the specimen). The following picture helps to focus the concept:

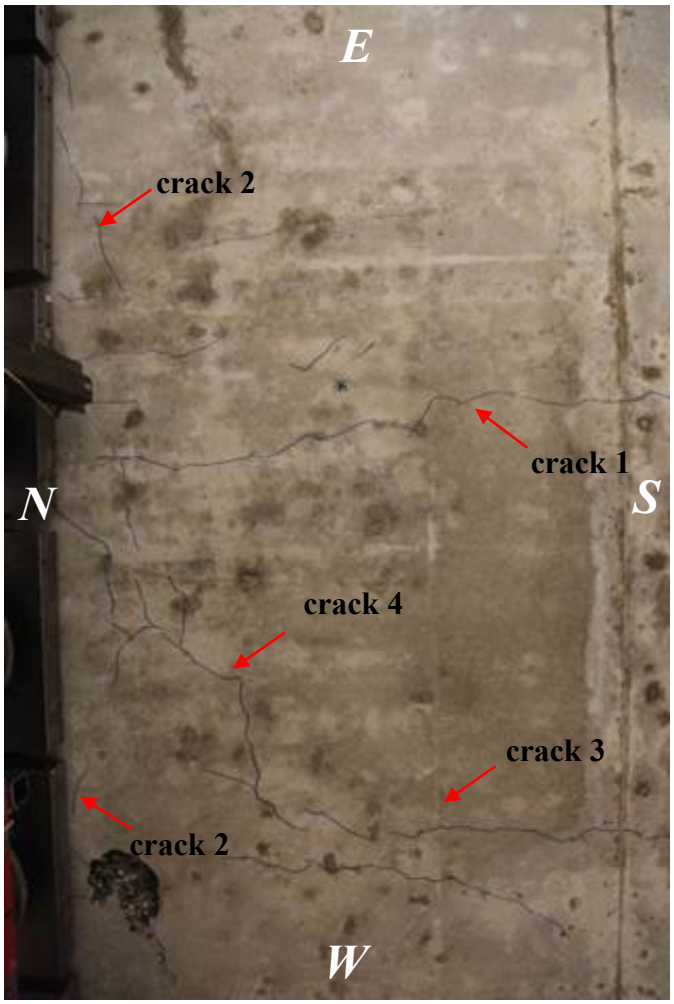

Cracking patterns detected during the experimental test

Regarding to the crack width, crack1, crack 2 and 5 are displayed adopting the $0.110E-02 \div 0.333E-02$ range. Just applying the formula, we can get the maximum width for the cracks:

$$w_{cr,max} = \varepsilon^{nn}{}_{cr} \cdot h$$

we get:

$$w_{cr,min\,-\,1,2,5} = 0.110E-02 \cdot 165\ mm = 0.18\ mm$$
$$w_{cr,max\,-\,1,2,5} = 0.333E-02 \cdot 165\ mm = 0.54\ mm$$

A comparison can be done looking to the following table:

Specimen	F_{line} [kN]	F_{punt} [kN]	w_{max} [mm]	Class.	Where?
S25T1	0	Fail	0.05	*crack 5*	front face - trhough crack in the middle
			0.05	*crack 6*	front face - crack close to E side, from botton, not fully trough
			0.10	*crack 1*	bottom face - NS crack from support into span, passing the load
			0.25	*crack 2*	bottom face - EW close to the support
			3.00	*crack 4*	bottom face - punching at W
			0.20	*crack 3*	bottom face - NS crack at W-side at 48 cm from free edge

Crack width detected for slab S25T1 during the experimental test

The obtained range is smaller than the one got for the partial *2x2 mesh* and closer to the experimental evidences.
The aforementioned cracks hold to a $0.05 \div 0.25\ mm$ range, regards to the width. Considering the present value as the maximum one, the prediction for crack 2 seems to be satisfactory, while crack 5 and crack 6 are overestimated.
Regarding to crack 4 (punching shear crack), it seems to hold to the $0.668E-02 \div 0.891E-02$ crack strain range. It equals to $1.10 \div 1.47\ mm$ of width. This range underestimates the crack width detected on the experiment.

A match can be observed with the experimental evidence:

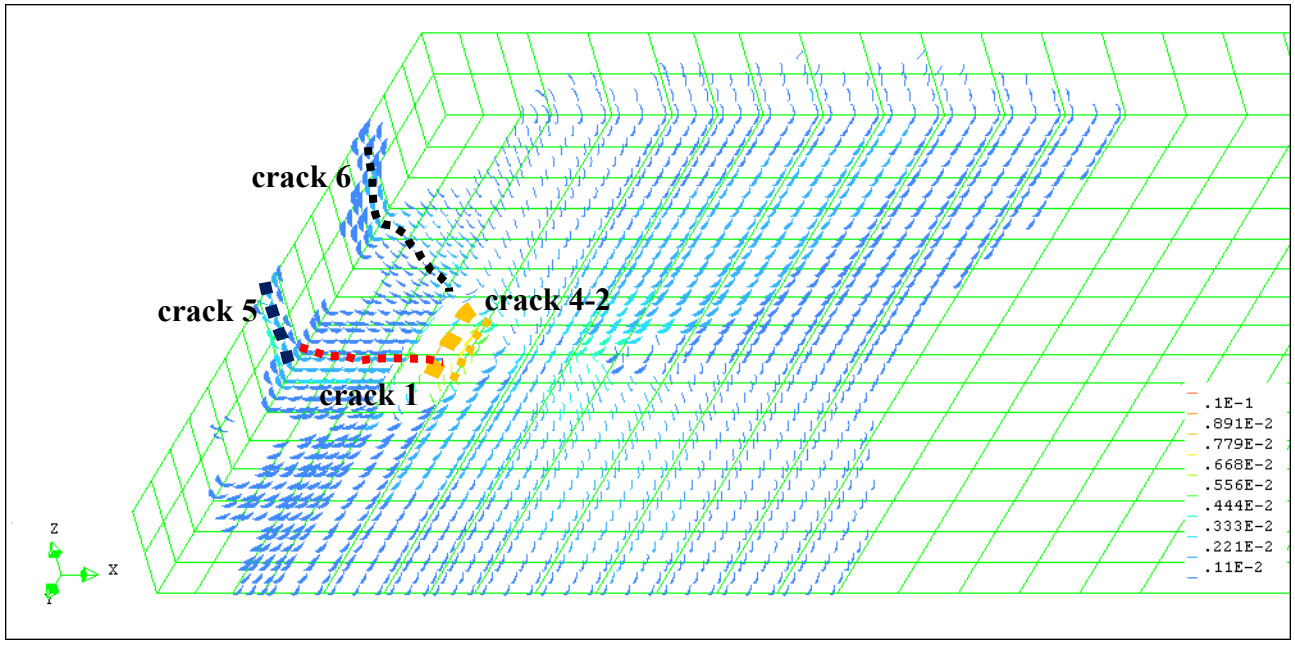

Display for the main cracks on the bottom and frontal side

As already said, the widest cracks are located in the area below the loading plate. At the bottom side, a longitudinal and straight fracture (crack 1) runs from the loading plate toward the frontal face and propagation is typical of a bending response that stresses the slab in transversal Y-direction. However, the entity of this fracture is much smaller than the other transversal fractures at the bottom side. Indeed, the biggest crack is located between the loading plate and the simple North support, following the Y-direction with an arc shape (crack 2). It seems to interest also the lateral faces of the slab, as plotted by blue discs spreading from the loading plate. Beside, the fact that this cracks is fast growing with the external load (see the distribution of the principal tensile strains), proves that it is important for the limit of the bearing capacity of the slab, since it could define a "critical section". Other smaller shear cracks are observed in the opposite direction with respect to the loading plate: they spread in a radial direction, below the load, forming the so called butterfly cracking pattern. The biggest one is underlined (crack 4).
On the frontal face two main cracks are detected: the flexural crack in the middle (crack 5) and the inclined crack on the West side (crack 6). This one seems to continue in the bottom face following a radial direction.

So, these are clear evidences of the presence of wide cracks, that lead the slab to failure. Although these observation the way the slab fails in not completely defined: it seems to be a combination of different mechanisms of crisis. The global mechanism has for sure a relevant component in the crisis for reached Shear Capacity. The presence of the bending is important as well, in particular in transversal Y-direction, but does not represent a problem for the bearing limit of the slab, as established by the small amount of yielded rebars.

However, also these plots are not clearly able to underline which specific failure mechanism occurs. The fact that neither punching shear nor wide beam shear failure occurs can be visualized by the deformed mesh shape.

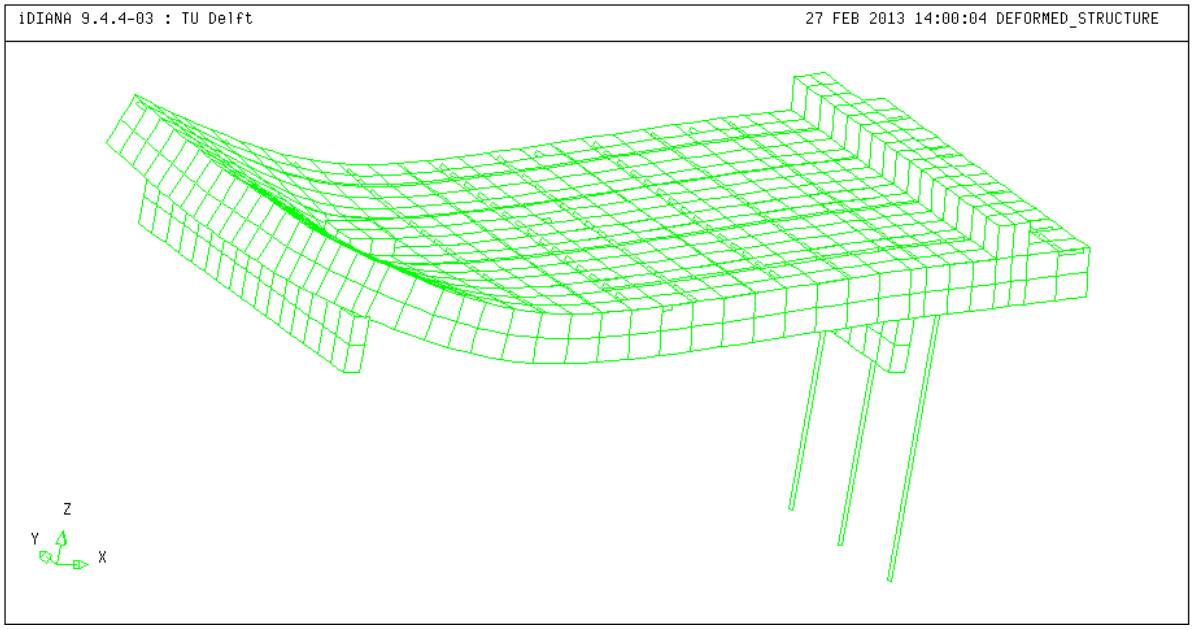

Deformed structure at the peak load: global overview

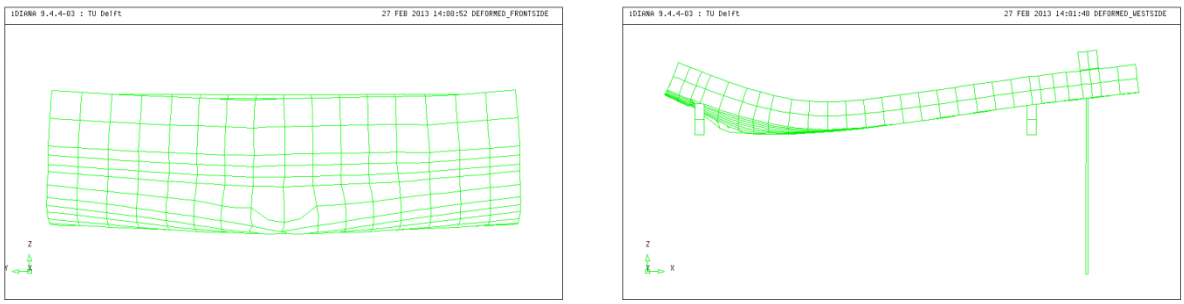

(a) *(b)*

Deformed structure at the peak load: (a) North front side and (b) West lateral side

Hence, it seems most likely that a combination of both caused the concrete slab to fail. The same conclusion was drawn for the experiment: the three-dimensional nature of the problem and the combined flexural and diagonal cracks, make it incredibly difficult to determine the failure mechanism. However, the global cracking behavior predicted by the NLF-Analysis seemed to correspond well with the observations made during the experiment.
It has to be noted that the deformed shape of the total model expresses a higher deformation for the slab, but a clear evidence of a truncated cone is not perfectly defined.

6.1.6 Dywidag bars pre-stressing

Unlike the partial model, the South constraint system is made up three pre-stressed Dywidag bars and HEM300 support beam, that should simulate a fixed support by preventing the slabs rotation.
During the experimental test, the pre-stressing level on the fixed end of each bar is measured.
A further comparison between numerical results and experimental evidence can be done, by observing the two different trends:

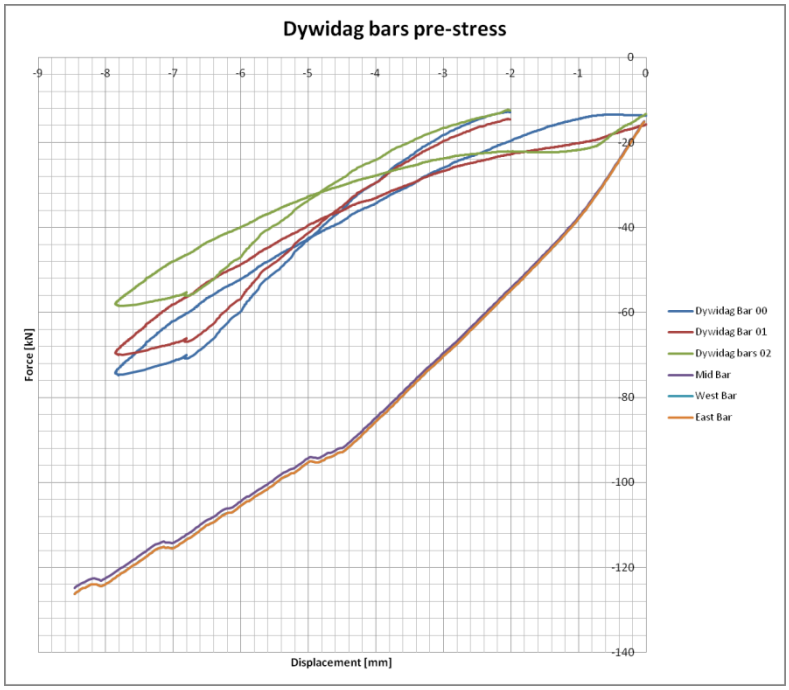

Experimental and numerical Dywidag pre-stressing

A great difference can be observed, both in the force values and in the global trend. Indeed, the experimental results show a snap back behavior.
The numerical model can't simulate this phenomenon and the initial adjustment phenomenon observed in the experimental setup seems to influence the results. Here an initial low slope of the experimental diagram is visible.
Instead, the numerical output shows an initial stiffer trend, then a linear branch follows and close to the peak displacement of $4.50\ mm$ a strong reduction of the pre-stressing is well visible.
The pre-stressing value is around $90\ kN$, instead the $75\ kN$ detected during the test.
After that the graphs loses mean, since the NLFEA can't observe softening trends and then the pre-stressing reduction due to the supervening crisis. Finally, due to the symmetry of the problem on the X-axis, East and West pre-stressing trends overlap, while the Middle bar presents slightly lower value (see Appendix A for more details).

6.2 Finer mesh: 3x3 total model

Few analysis were run to fit experimental results in terms of load-displacement diagram and numerical output, by adopting different values for the tensile fracture energy G_f parameter. The following image shows the output for $0.250 \div 0.265 \div 0.280\ Nmm/mm^2$:

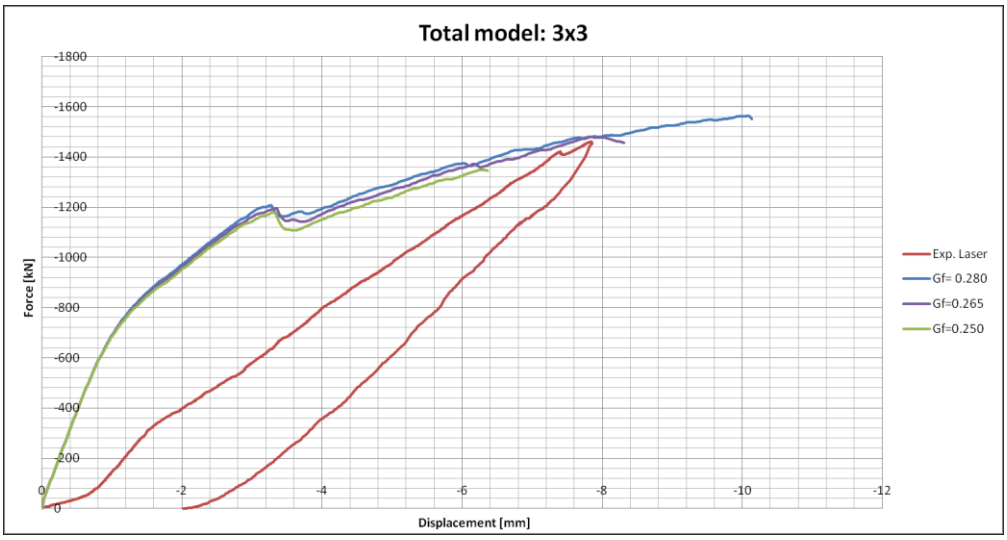

Force-displacement graph for 3x3 total model for different value of G_f parameter

The best agreement is reached adopting the following features:

- tensile fracture energy: $G_f = 0.265\ N/mm$;
- numerical crack bandwidth: $h = 95\ mm$;
- normal Teflon interface stiffness: $k_{n,T} = 500\ N/mm^3$;
- integration scheme: default for all the finite elements (see previous paragraphs);
- maximum number of iteration equal to 25;
- pre-stress on the Dywidag bars: $s_{xx} = 21.74\ MPa$.

The load-displacement graphs is here proposed:

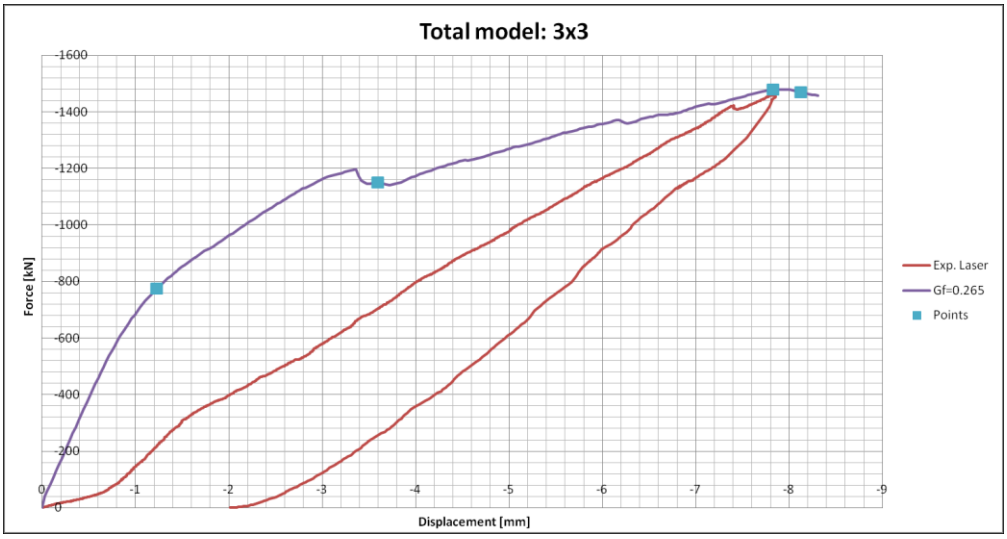

Main points on the load-displacement graph for 3x3 total model

A good agreement can be reached both in terms of experimental peak-load and peak-displacement; however the response remains still stiffer, though the failure point seems to be well evaluated. It's

visible a decay point, as detected also in the *3x3 partial model*. After the peak (at $-7.83\ mm$ of displacement) a short post-peak behavior is detected. Divergence occurs after about $-8.13\ mm$.
The numerical peak values are:

- peak load: $1478.94\ kN$;
- peak displacement: $7.83\ mm$.

instead of:

- experimental peak load: $1460.62\ kN$ for a variation of $\sim +1\%$;
- experimental peak displacement: $7.84\ mm$ for a variation of $\sim -0.1\%$.

Regarding to the convergence trend the analyses doesn't satisfy the criteria from step 40: a progressive drift occurs after 3000 iterations (see the following plot). The analysis uses about 7000 for all the process.

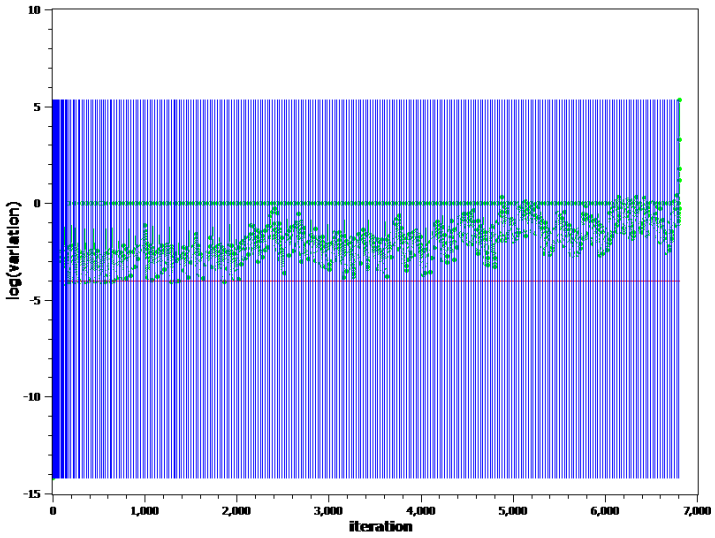

Convergence trend for 3x3 total model with NLFEA

As said before, the 3x3 total model shows a clear decay point, as detected on the 3x3 partial model version. In order to study the behavior of the slab after the decay point, four main points are selected on the load-displacement diagram:

- *point 1:* $(1.23\ mm;\ 775\ kN) \sim 50\% F_{max}$;
- *point 2:* $(3.60\ mm;\ 1150\ kN) = \sim 75\% F_{max}$;
- *point 3:* $(7.83\ mm;\ 1480\ kN) = F_{max}$;
- *point 4:* $(8.13\ mm;\ 1470\ kN) = post - peak$.

They are shown in previous plot; the main output will be exposed in the next paragraphs.

6.2.1 Redistribution capacity:

On the following image, four pictures of the felt reactions are shown by adopting a vector plot. They prove the redistribution of the load from the slab to the support, since the action on the felt is equal to the one on the support beam for vertical balance.
The pictures show the plot about four main points:

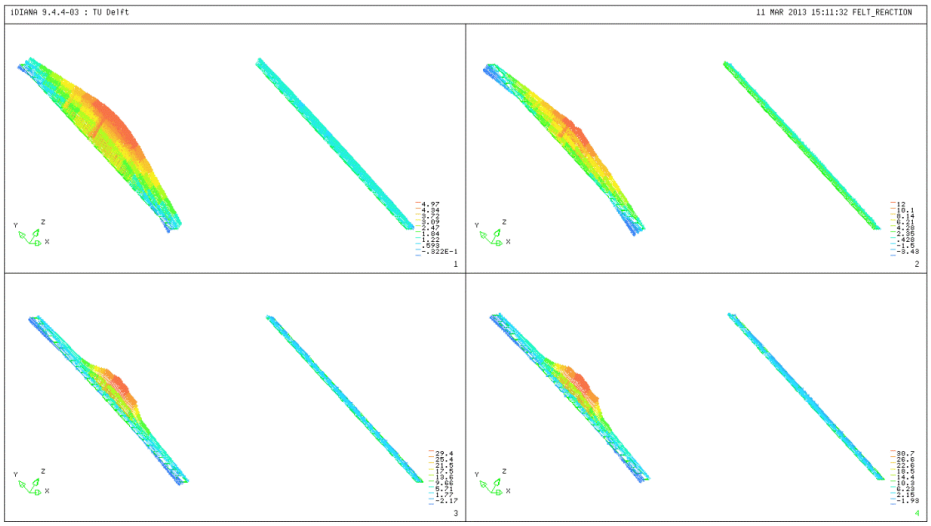

Vector plot of felt reaction [MPa] for the main points

The usual triangular shaped felt reaction is visible on the 1st main point, at 775 kN, but a strong redistribution of the load is detected after the decay point at 1150 kN. The most of the load is carried by the middle part of the support, while the lateral edges show a tensile reaction of about 3.50 MPa. Increasing the load, the redistribution trend seems to proceed: at 1480 kN the load transfers on a smaller area, on the middle of the North interface. Here the maximum tension reaches a high value, pair to 29.4 MPa while the tensile stress is lower than the previous one (2.17 MPa). At the last point the shape remains equal and the value are only a bit higher. It has to be noted that the tensile reaction of the felt is higher after the decay point than on the peak-load. Moreover, lower tensile stresses are detected inside this finer mesh.

By plotting the part of interface in a compressive state, they are shown with red color (values higher than 0 MPa - *compression*). It can be observed that the loading angle assumes a value from 68° (1st main point) and 64° (4th main point), therefore the effective width of the active zone of the support changes from $b_{eff} = 2500\ mm$ to $b_{eff} = 2140\ mm$.

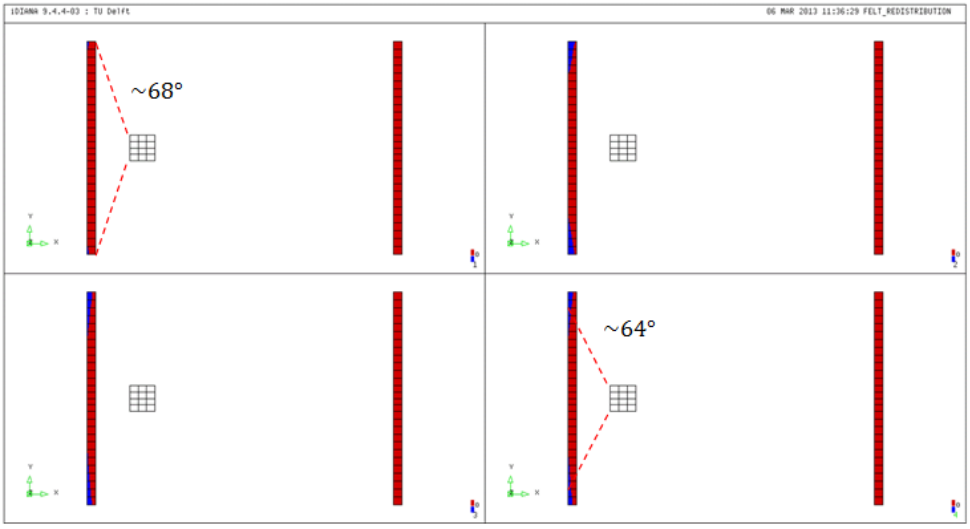

Effective width due to the load spreading on the felt layer

6.2.2 Cracking behavior of the slab

In order to investiga the development of the cracking under an increasing load, contour and vector plot of the pricinpal tensile strain are used. Taking into account four points on the softening diagram calculated for a fracture energy $G_f = 0.265\ N/mm$ and $h = 95\ m$.

$\varepsilon_{el,ult.}$ [-]	0.000118	1.184E-04
0,5*$\varepsilon_{cr,ult}$ [-]	0.001512	1.512E-03
$\varepsilon_{cr,ult}$ [-]	0.003024	3.024E-03
5*$\varepsilon_{cr,ult}$ [-]	0.015118	1.512E-02

(a)

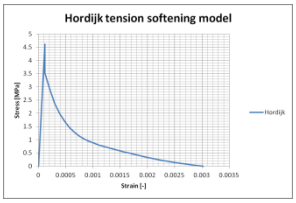

(b)

Main values for principal tensile strain (a) and Hordijk softening diagram (b)

For the four main points selected before, each plot shows the plots of top, bottom, front and lateral surface respectively.

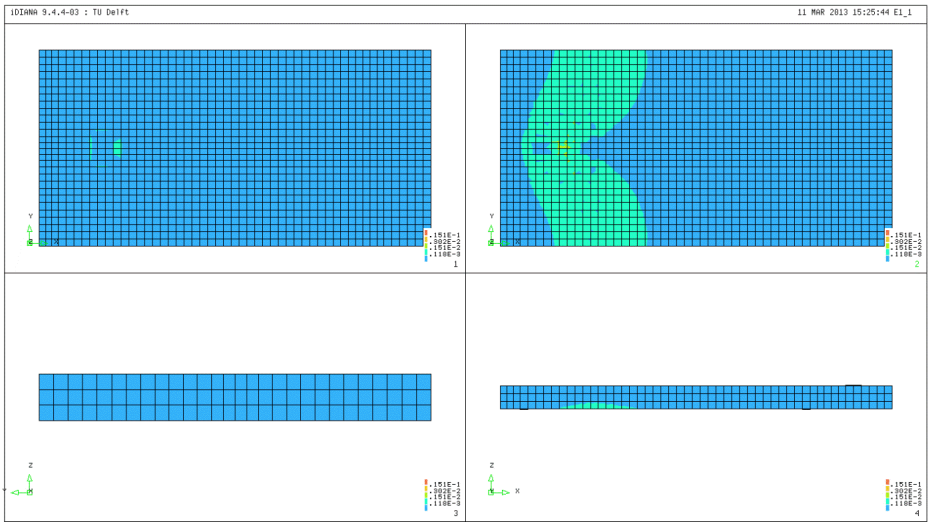

Contour plot of principal tensile strain for 775 kN

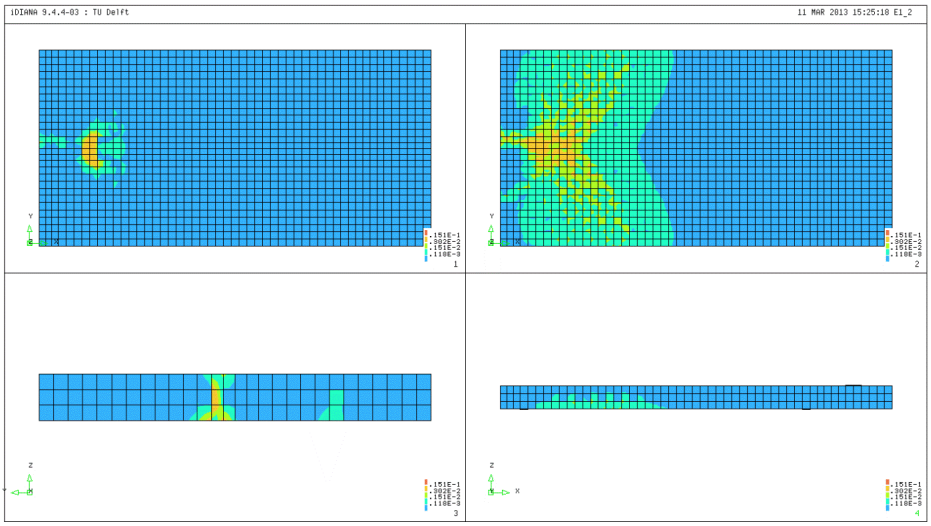

Contour plot of principal tensile strain for 1150 kN

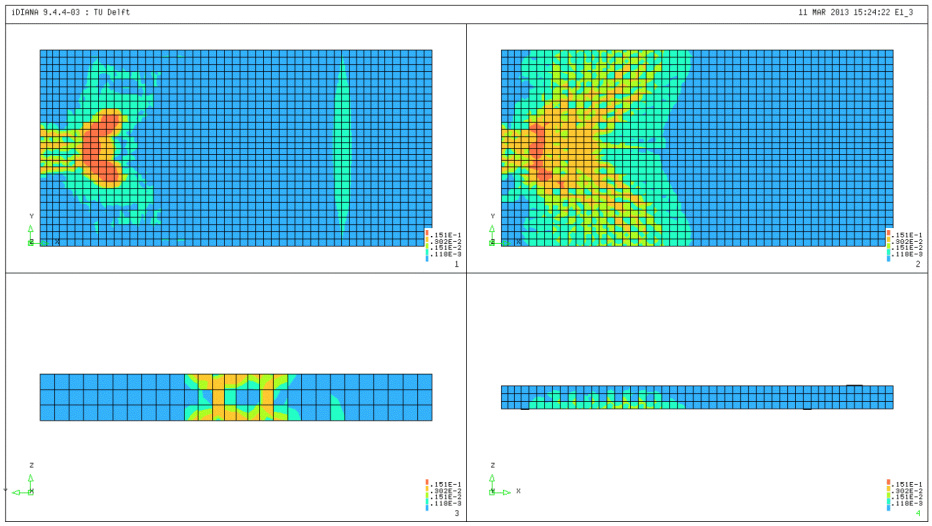

Contour plot of principal tensile strain for 1480 kN (peak)

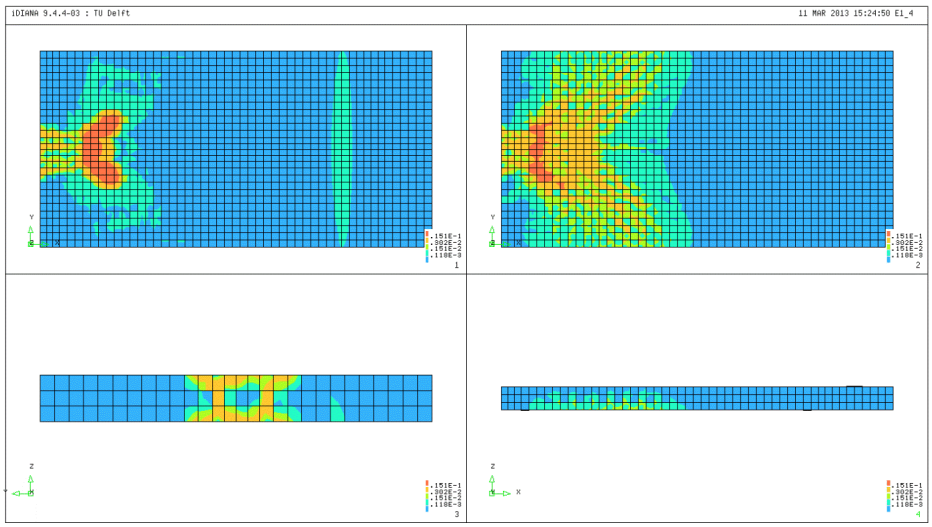

Contour plot of principal tensile strain for 1470 kN (post-peak)

The previous contour plots show that the cracks have origin from the bottom side of the slab, directly below the loading plate, then for higher loads they propagate forward the simple support and transversally, assuming inclined direction as well. After they increase their width under the loading plate.
This particular shape is so called butterfly shape for the characteristic form assumed.
The decay of the stiffness on 1150 kN of load seems to be generated by a diffused cracking pattern spreading from the loading plate toward the free lateral edges. It spreads forward the lateral faces on the peak and post peak point: three main families are detected. The first one starts from the load position forward the North face and toward reaches the midspan. This one is well agreement with the experimental crack 1. The second one is underlined by the red area: here a strong concentration of tensile strain are detected. It could be proofed the formation of main cracks, like crack 2, crack 3 and crack 4 who leads to the failure of the slab. The third one is made up by the radial crack system.
On the top face the evolution of the cracking present an initial non-symmetric development: on 1150 kN a clear longitudinal crack zone is visible on the left side of the middle axis. It starts from the frontal face. On the peak load the crack pattern present a symmetric shape and it is made by two different groups: the cracked red zone around the loading plate, and the longitudinal strips from the North side. The former could be related to the sinking phenomenon and the formation of a strut-and-tie mechanism, while the latter follows the development of the vertical cracks on the frontal face. On the South beam it's now visible a zone where the ultimate elastic strain is exceeded for the concrete. The same patterns are detected also on the post-peak.
The evolution of the cracking patterns on the frontal side agrees with the previous description upward. After the decay a vertical crack appears suddenly in the middle of the support. It runs from the top surface towards the bottom. Only for higher load (1480 kN) a new crack develops on the right side. A cracked zone is visible on the East side, starting from the bottom toward the half of the thickness. These cracking patterns seems to agree with the experimental evidence (crack 5 and crack 6), as explained by the following visual comparison:

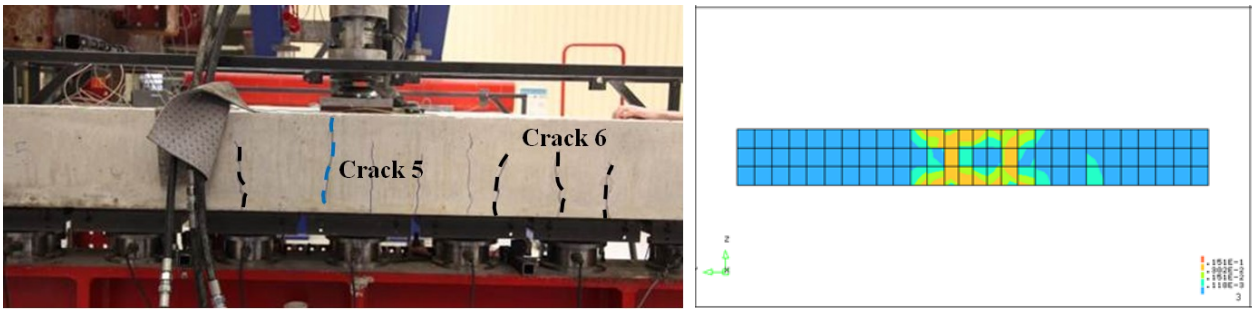

Prediction of the frontal cracks for the 3x3 total model with NLFEA: on the left-hand the experimental evidence, on the right-hand the principal tensile strain contour plot on the post-peak point.

On the lateral side the flexural behavior is underlined by the vertical cracks system. It appears just after 775 kN from the bottom, investing only a third of the thickness. Then it runs up, reaching more than the half of the height of the slab on the peak load. No flexural cracks were detected during the experiment.
Now, to have a clearer representation of the direction and of the entity of the fractures, it's useful to have also a vector plot of the same principal tensile strain.
The same surfaces are plotted:

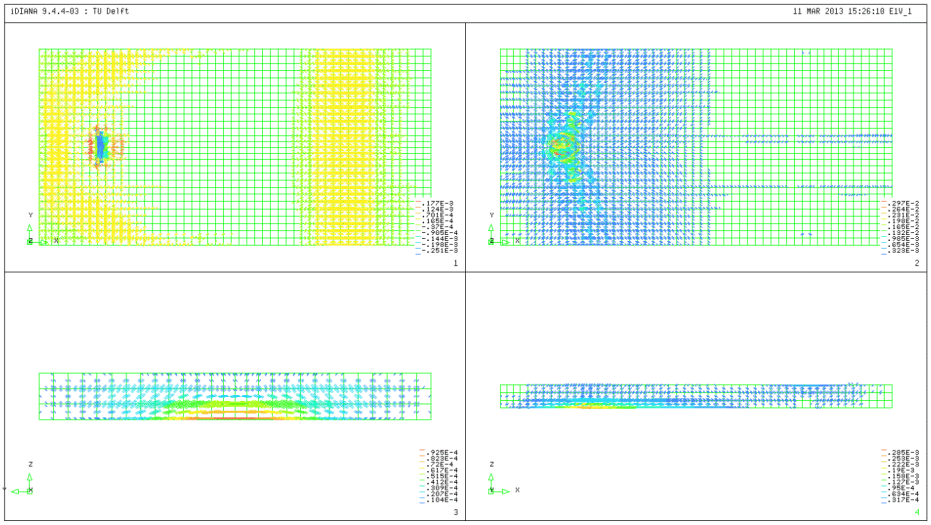

Vector plot of principal tensile strain for 775kN

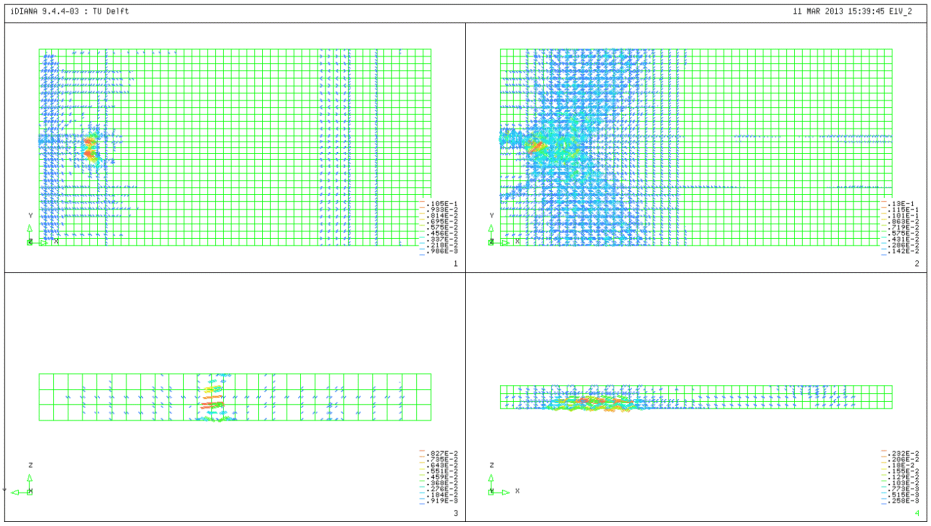

Vector plot of principal tensile strain for 1150 kN

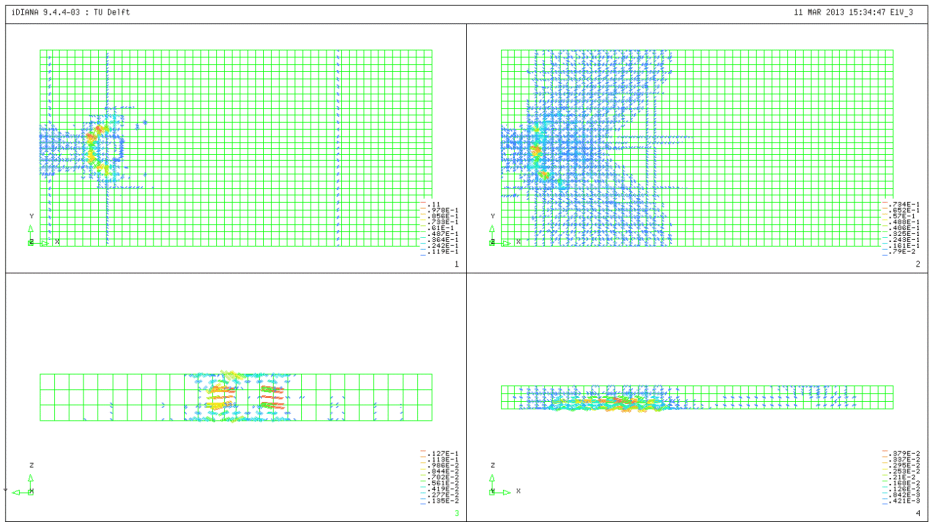

Vector plot of principal tensile strain for 1480 kN (peak)

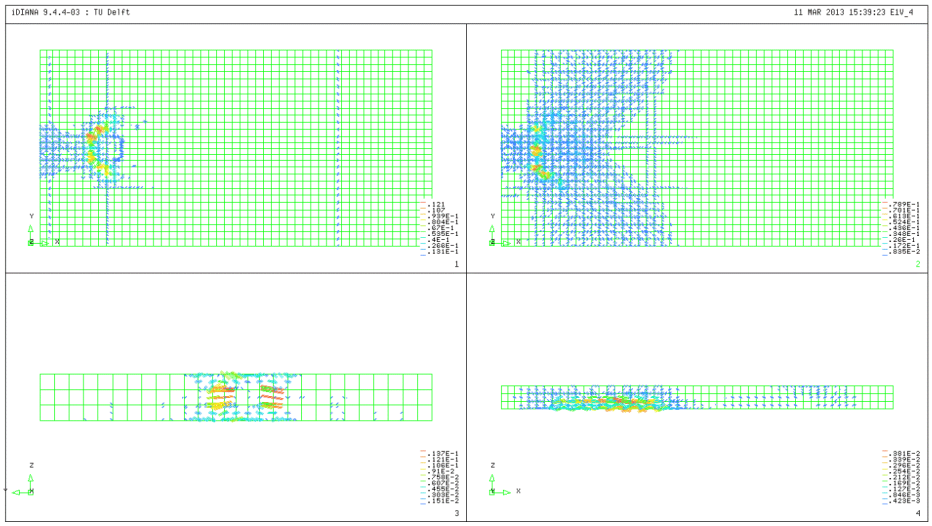

Vector plot of principal tensile strain for 1470 kN (post-peak)

Generally, as expected, the vector plots for the tensile strain are better defined for this finer mesh.
For a load of 775 kN it can be observed a concentration of strains that superior than $\varepsilon_{el,ult}$ below the loading plate, on the bottom face, both in the North-South and in East-West direction. These two families of strain represent the flexural cracks in the two direction of flexion. In the laboratory experiment a crack of 0.1 mm width in the North-South direction in the middle from the support towards the span, passing the center of the load is discovered (crack 1) and a 0.25 mm wide crack on the East-West direction is observed (crack 2), close to the simple support.
On the frontal face a concentration of strains superior than $\varepsilon_{el,ult}$ are well visible on the middle. Other strains spread following an arc shape above the bottom surface of the slab.
The other interesting zones are located in the lateral West face below the loading plate. Here, strain vectors are visible and they represent the flexural cracks. During the experiment no flexural cracks are detected. Above the South support strain vectors are present on the top layer, but with lower magnitude than $\varepsilon_{el,ult}$, so flexural cracks are not detected, as in the experimental test.
The same pattern is better visible on the top surface plot, at the South support, both in Y and X direction.
For this load, no strain vectors exceed the ultimate crack strain $\varepsilon_{cr,ult}$, so no full opened cracks are detected.
The plots related to the decay point (1150 kN) are really useful in order to better understand the development of the cracking pattern on the external surfaces of the slab. A strong increasing of the previous described crack systems is detected and new ones arise suddenly.
First of all inclined vectors are visible on the bottom surface: it means that the shear bearing mechanism starts to govern the global behaviour, replacing the previous flexural regime. However, the flexural cracks develop: the longitudinal crack clearly reaches the frontal face, while the transversal cracks spread forward the lateral free edges following the Y- and radial direction from the load. This matches with the evidence of crack 1 during the experimental test. Another isolated radial crack spreads from the load toward the North support.
The ultimate elastic stain is exceeded on the frontal face, instead on the lateral side $0.50\varepsilon_{cr,ult}$ is reached: a vertical crack invests the thickness of the slab, as seen with crack 5.

For a load of $1480\ kN$, the strut-and-tie mechanism is completely defined: on the bottom surface the magnitude of the inclined vectors overhang the others: they form a semi-circular crown below the loading plate. The $5.0\varepsilon_{cr,ult}$ is largely exceeded with $0.734E-01$ for the maximum value. On the top surface, the shape of the inclined vectors has got a circular shape around the loading plate, as seen below, and the maximum value is 0.110.
On the frontal face now two main vertical cracks present a $0.127E-01$ strain of maximum magnitude. This matches with crack 5 and crack 6.
Finally, close to the peak the failure arises, so the post-peak plots do not differ from the previous one.
Through these plots it can be deduced the development of shear cracking, since the new fractures grows faster than the previous flexural cracks and their disposition starts to individuate radial paths originating from the loading area.

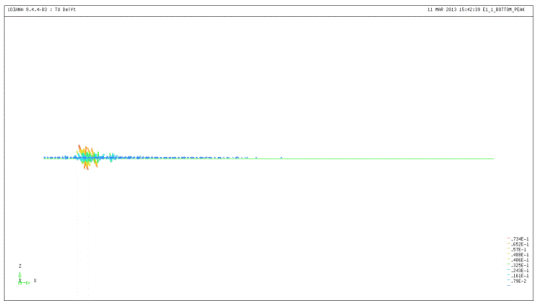

Particular of vector plot of principal tensile strain for 1479 kN (peak) on the bottom surface

The presence of the strut-and-tie bearing mechanism it's not supported by the following vector plots of the principal compressive strains ε_3, since compressive struts form on the South side of the load position.

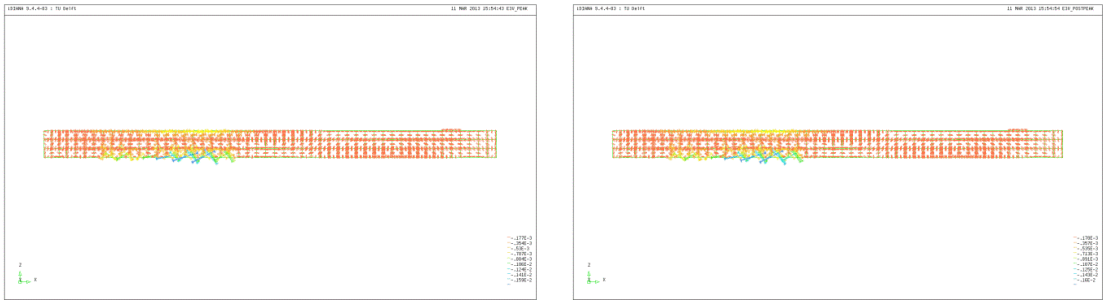

Vector plot of principal compressive strain for 1480 kN (peak) and 1470 kN (post-peak)

On the basis of the previous observations about the cracking behavior of the total model of the slab, performed using the NLFEA, it can be stated that a quite good prediction, better than the partial model, of the general crack behavior can be obtained. The best result is the accordance with experiment about the starting point of the fractures and the propagation of the cracking pattern, for what it concerns the directions of flexural and shear cracks. Moreover, in proximity of the peak load, it's also possible to individuate features of shear cracks, like the direction and the rapidity of growing. This can be used as another data to individuate critical sections and to predict the failure mechanism.

6.2.3 Behavior of the reinforcement bars

To have an immediate evaluation of the distribution of the stress and of the behavior of the steel bars, contour plots of the principal tensile stresses are presented afterward, referring to a unique yielding tension equal to $540\ MPa$.
Three main points are taken into account and for each one, four plots are shown: σ_{xx} and σ_{yy} for the top rebars, respectively on the upper and on the bottom plot (left hand); σ_{xx} and σ_{yy} for the bottom rebars, respectively on the upper and on the bottom plot (right hand).
Through these contour plots it can be proved the hypothesis of *Kinnunen* and *Nylander*, since the reinforcement steel of the bars has an elastic behavior in most part of the slab and the only area in which one can notice a yielding is the one close to the loading point. In particular for an applied load of around $1304\ kN$, so only close to the peak, the only bars who yields has a very limited length, below the loading point (longitudinal bars) and close to the North edge (transversal bars). At the load of $1344\ kN$, a higher length of the longitudinal bars below the load yields.
No yielding occurs on the other bars.

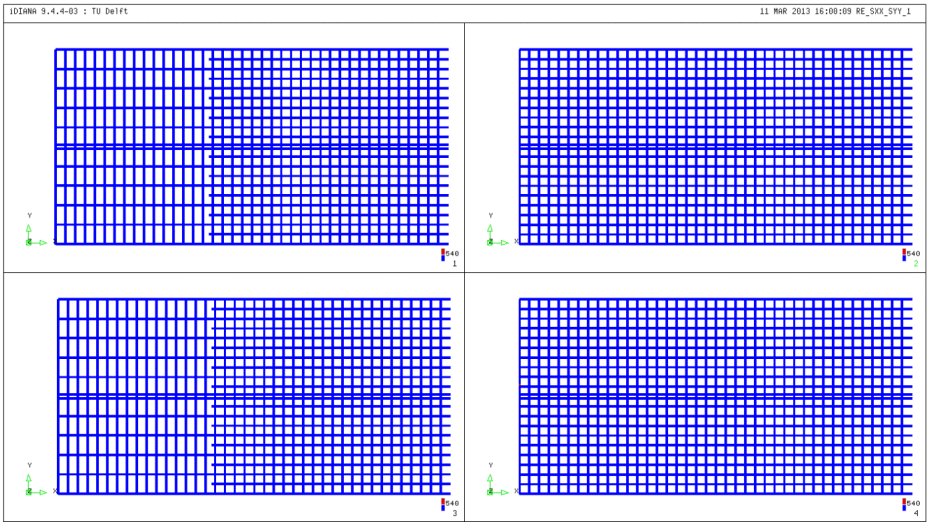

σ_{xx} and σ_{yy} contour plot for top and bottom reinforcement bars for 775 kN

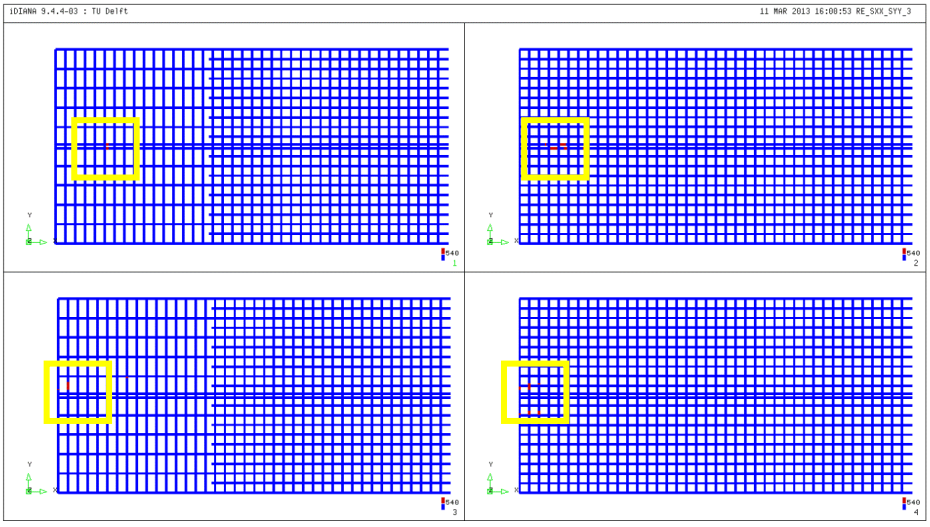

σ_{xx} and σ_{yy} contour plot for top and bottom reinforcement bars for 1304 kN (peak)

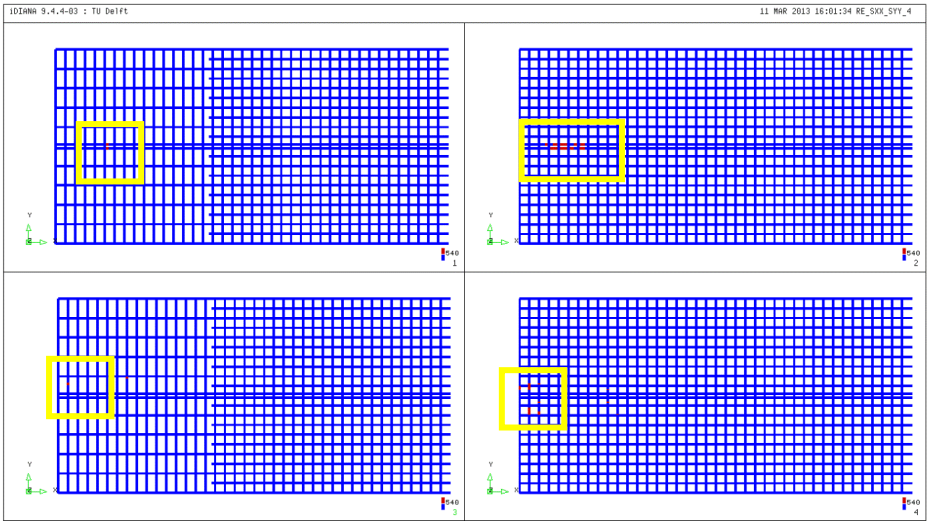

σ_{xx} and σ_{yy} contour plot for top and bottom reinforcement bars for 1344 kN (post-peak)

Adopting the principal tensile stress plots, we can observe the progressive redistribution of the stress inside the reinforcement bars.

For the present plots four points are selected again. The first points allows us to discover the tensile stress distribution inside the rebars when the slab works in an ideal linear elastic state. Then, the following plots can show a gradually changing in value, position of the most loaded bars and distribution of the global stresses.

Since we ask for principal tensile stress, only positive values will be shown.

Observing the bottom rebars, the tensile stresses invest primarily the area below the loading plate, then at $755\ kN$ it spreads toward the North edge and in the Y-direction from the load position. On the peak load ($1304\ kN$) the interested area is bigger and two main radial branches run from the loading plate to the lateral free edge. A series of transversal bars are highly stressed toward the mid span. This plot allows to discover a radial crack pattern and a longitudinal crack, as crack 1. It has to be noted the high stresses bigger than the ultimate stresses for the reinforcements.

On the top rebars, as seen on the bottom, the highest stress is concentrated on the load position and on the North edge. This trend increases with higher load, indeed the transversal bars between load and North support carry the most of the tension, while on the peak a huge stress is detected below the loading plate, in the longitudinal directions. Once again, it could be related to the kinematical compatibility between concrete and steel: indeed the total model allows a bigger deflection under the load, since the South constraint has got its own deformability.

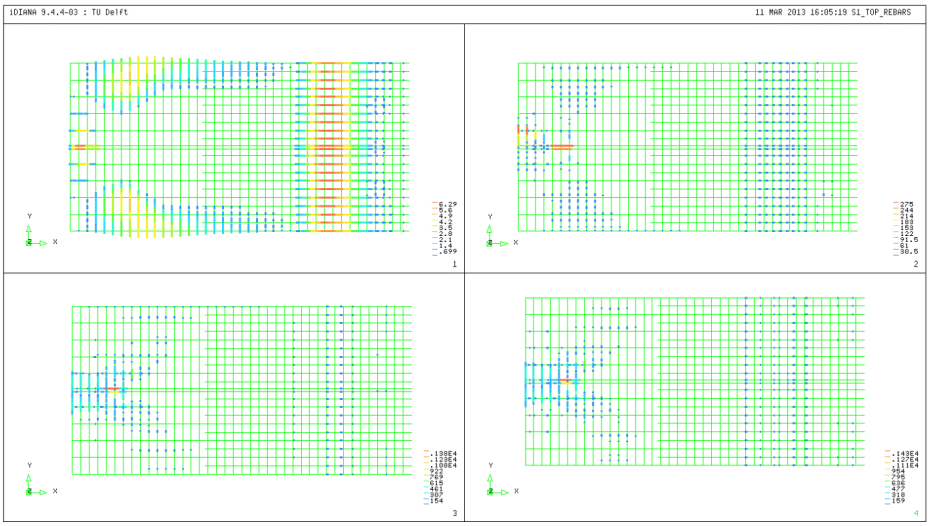

Principal tensile stress for the reinforcement bar on the top surface

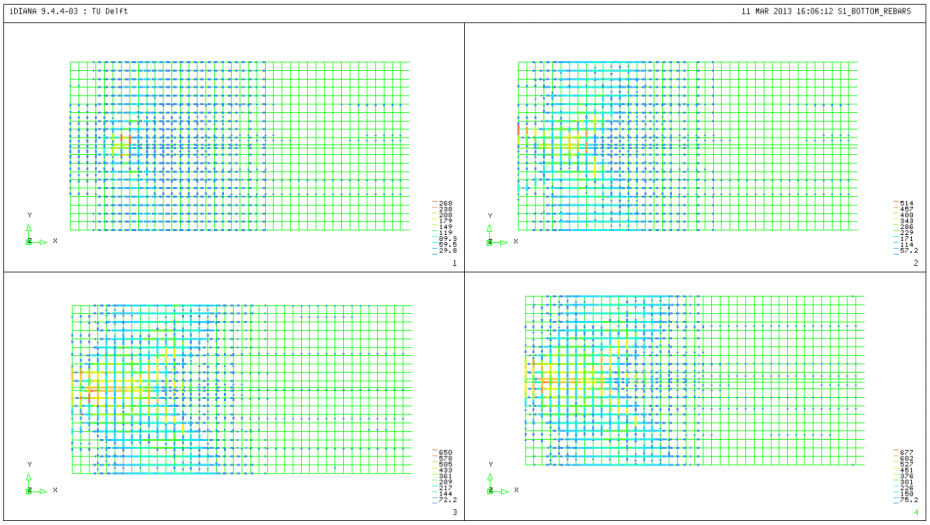

Principal tensile stress for the reinforcement bar on the bottom surface

6.2.4 Compressive behavior of the concrete

In order to verify the elastic state of the concrete for the compressive field, the *principal compressive stress* feature is investigated through a contour plot on four surfaces, for the three main selected before.
Two main values are adopted:

- $0.50 f_{cc} = -29.88\ MPa$;
- $1.00 f_{cc} = -59.76\ MPa$.

Since, the compressive stress has conventionally a negative value, the green color shows the parts with a lower principal stress than $f_{cc} = -59.76\ MPa$. Instead the blue color proofs the part who exceed this reference value.

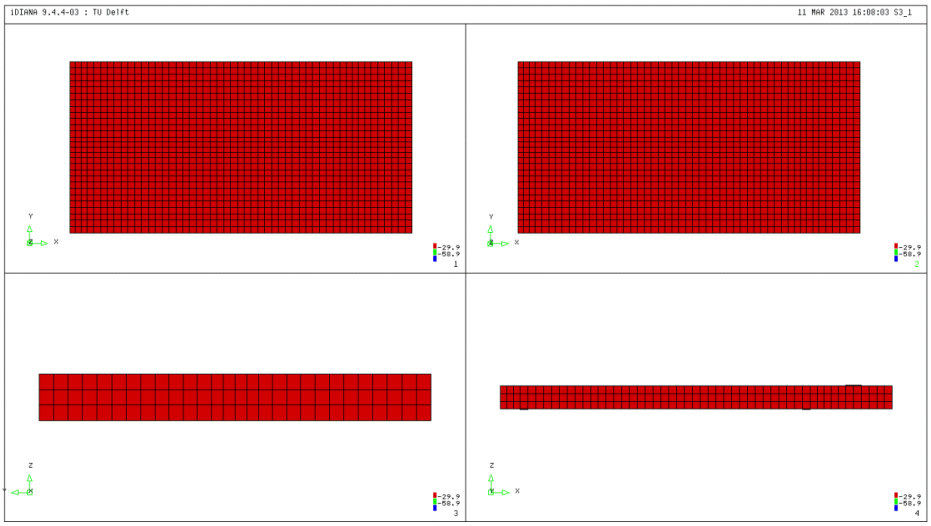

Contour plot of principal compressive stress for 755 kN

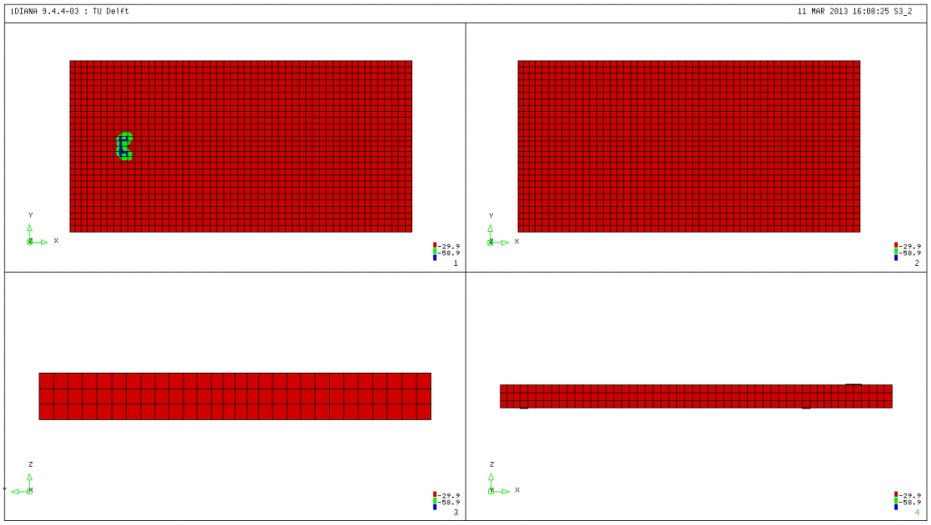

Contour plot of principal compressive stress for 1155 kN

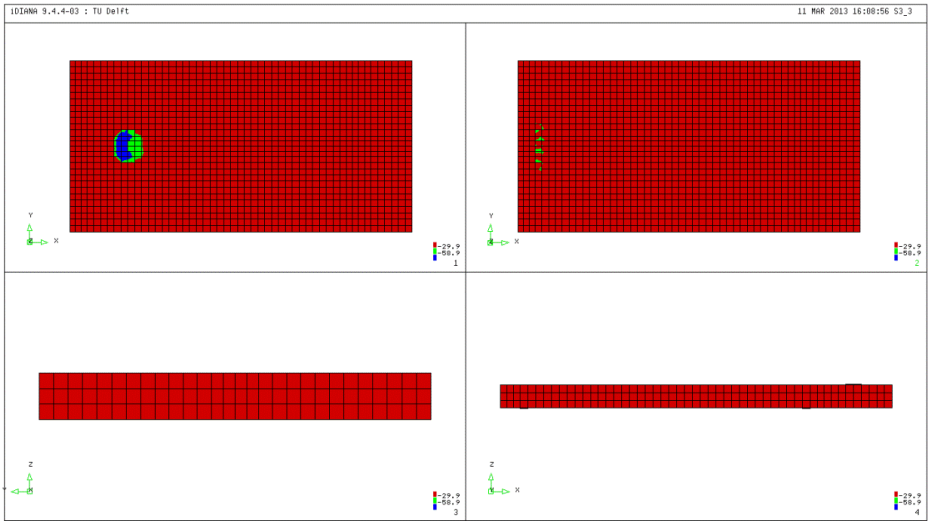

Contour plot of principal compressive stress for 1304 kN (peak)

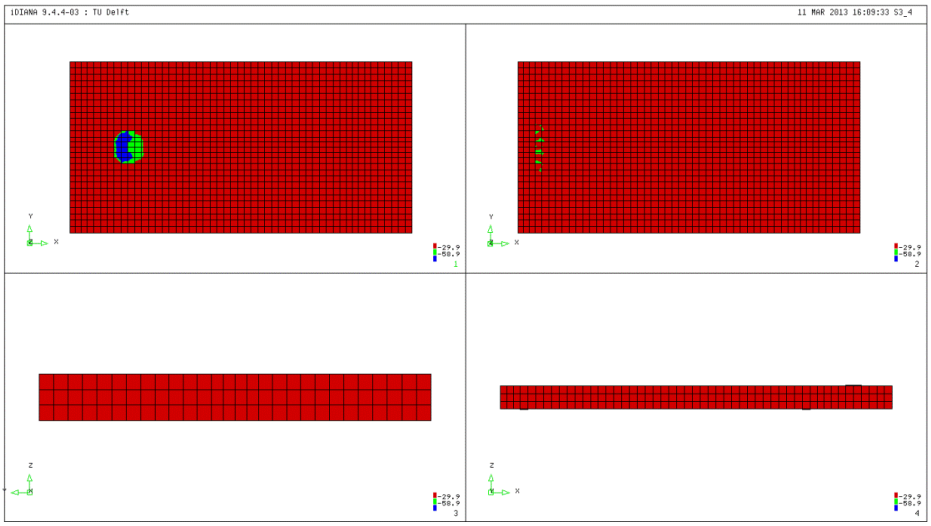

Contour plot of principal compressive stress for 1344 kN (post-peak)

As shown by the previous plots, the principal compressive stress exceeds the compressive strength of the concrete only on a small area below the loading plate. It can mean a numerically sinking of the steel plate inside the concrete, as seen in some experimental tests (see Eva lansgoth test - cit).
So, thanks to these plots, we can demostrate that the assumption of a linear elastic concrete in compressione is adequate to describe the behavior of the conglomerate. This is is strengthened by the fact that also the 50% of f_{cc} is exceeded in a limited surface of the slab. As seen only on the denser meshes, on the North support a compressed area (green color) is visible: it could mean the strut-and-tie formation once again. Indeed, the interested area fits with the vector plot s_{ftz} on the peak point.

6.2.5 Cracking pattern and failure

The following picture shows the distribution of the principal tensile strain at the peak load and after the peak load. The scale of the contour plots is held constant ($0.15E-02 \div 0.15E-01$) in order to see the development of the tensile strain area:

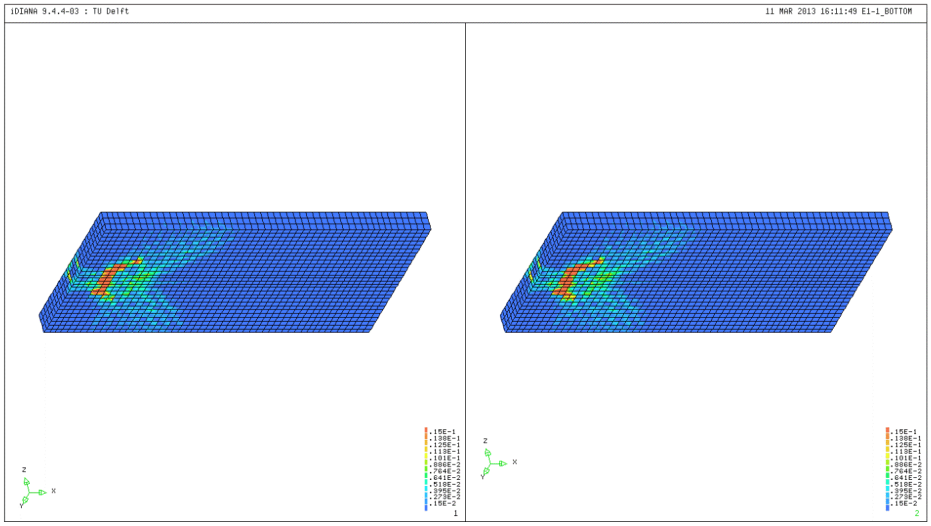

Contour plot of the principal tensile strain on the bottom faceon the peak (left-hand) and post-peak points (right-hand)

These plots allow us to discover and underline in a better way the mode in which the slab fails. Indeed, with a denser mesh we are able to detected a highly strained arch shaped area between load and North support. Crossing this information with the well visible radial cracking pattern, it's possible to prefer a punching shear failure than a one-way mode: a critical region who triggers the crisis is detected. Moreover, the frontal cracks and the longitudinal fracture are visible as well.
The crack behaviour is well estimated regarding to the shape.

A useful attribute to better discover cracking pattern and define the crack widths inside the model is the *principal normal crack strain* ${\varepsilon^{nn}}_{cr,1}$ feature.
The best results can be obtained by adopting as reference two limit crack strains (related to the experimental widths):

- ${\varepsilon^{nn}}_{cr,min} = w_{cr,min}/h = \frac{0.05}{95} = 0.526E-03$;
- ${\varepsilon^{nn}}_{cr,aver} = w_{cr,aver}/h = \frac{1}{95} = 0.105E-01$.

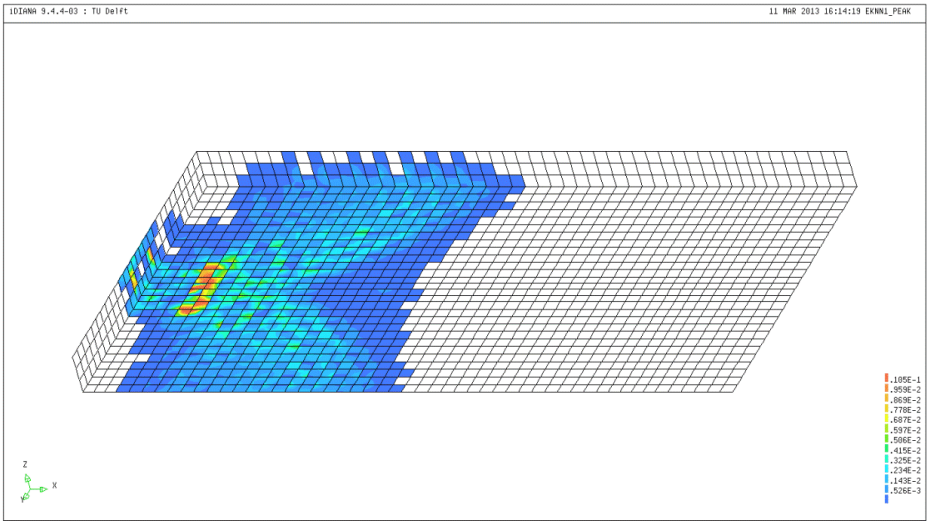

Contour plot of the principal normal crack strain on the bottom face on the peak

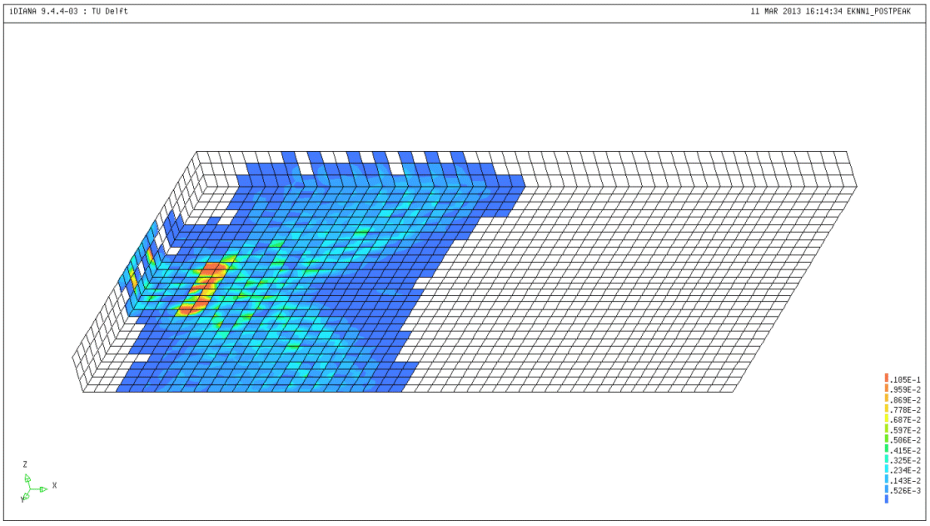

Contour plot of the principal normal crack strain on the bottom face on the post-peak

These plots match with the principal tensile strain images: circular, radial and longitudinal crack pattern are well underlined.
As expected, a more defined cracking pattern below the loading plate and close to the support is shown. Here wide crack should be expected (red zone) and inclined crack spread from the load position forward the midspan on the bottom face. The longitudinal flexural cracks is well underlined together with the aforementioned front crack, on the North face of the slab.
Since, no big differences are detected between peak and post-peak, only post-peak plot will be shown in order to display the real orientation of the cracks through disc plot:

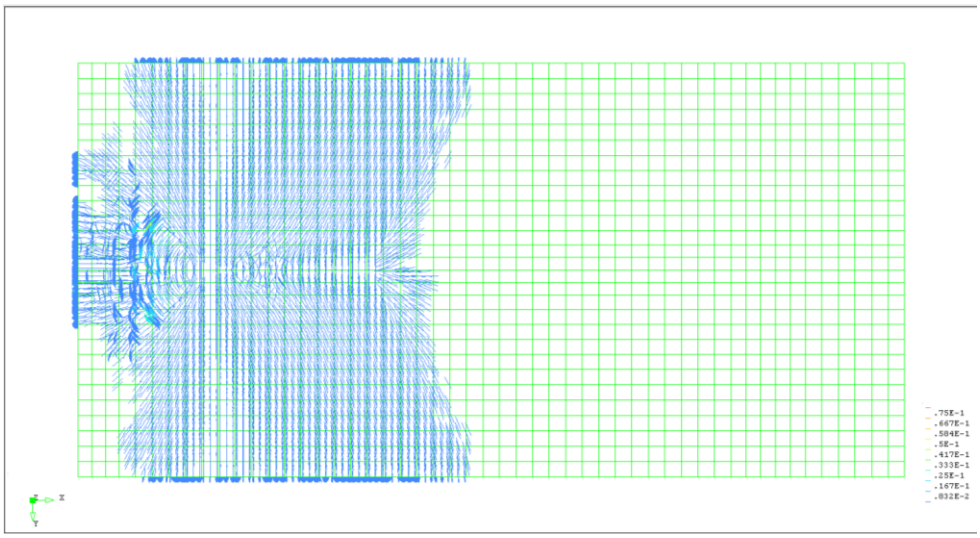

Disc plot of the principal normal crack strain on the bottom face on the post-peak

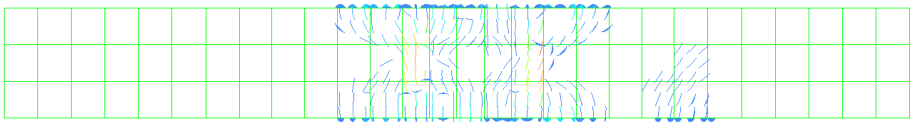

Disc plot of the principal normal crack strain on the frontal face on the post-peak

Thanks to this plot, some main cracks can be displayed on the bottom and frontal surface of the slab by following the orientation of the principal discs.
Moreover, is has to be taken into account the previous observations about the distribution of the principal tensile strains and the yielding of reinforcements. So it's possible have an estimation of the position and the entity of the most relevant crack in the bottom, lateral and frontal faces of the slab, that is reported afterwards.

A new way to detect cracks is here provided:

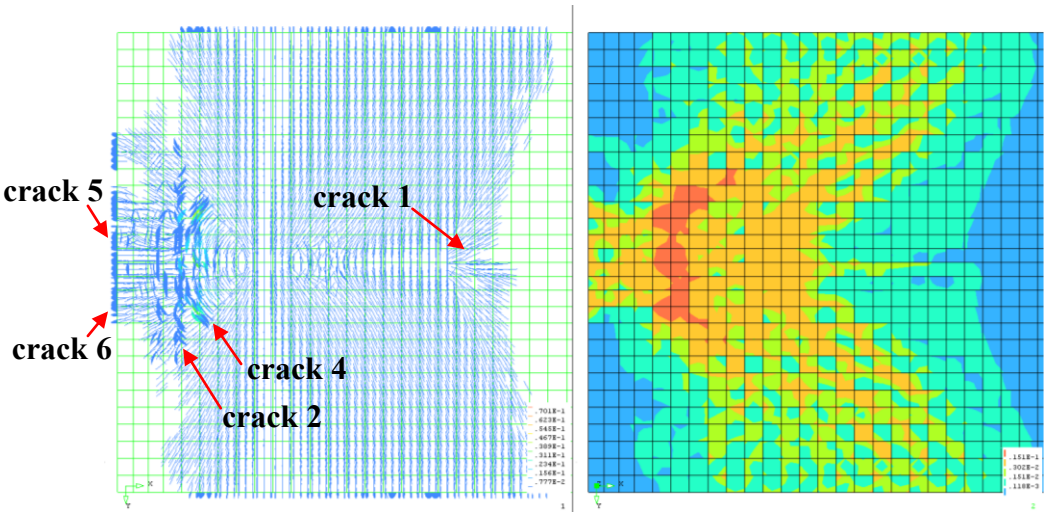

Contour plot of the principal tensile strain on the bottom face on the post-peak (right-hand and principal crack strain (left-hand)

The cross-comparison between these plots helps to discover the effective cracking patterns on the slab. It shows a good agreement with the experimental evidence: crack1, crack 2, crack 4, crack 5 and crack 6 are displayed. There is no evidence related to crack 3, but on the principal tensile strain plot a red area arises on the lateral side of the load position.

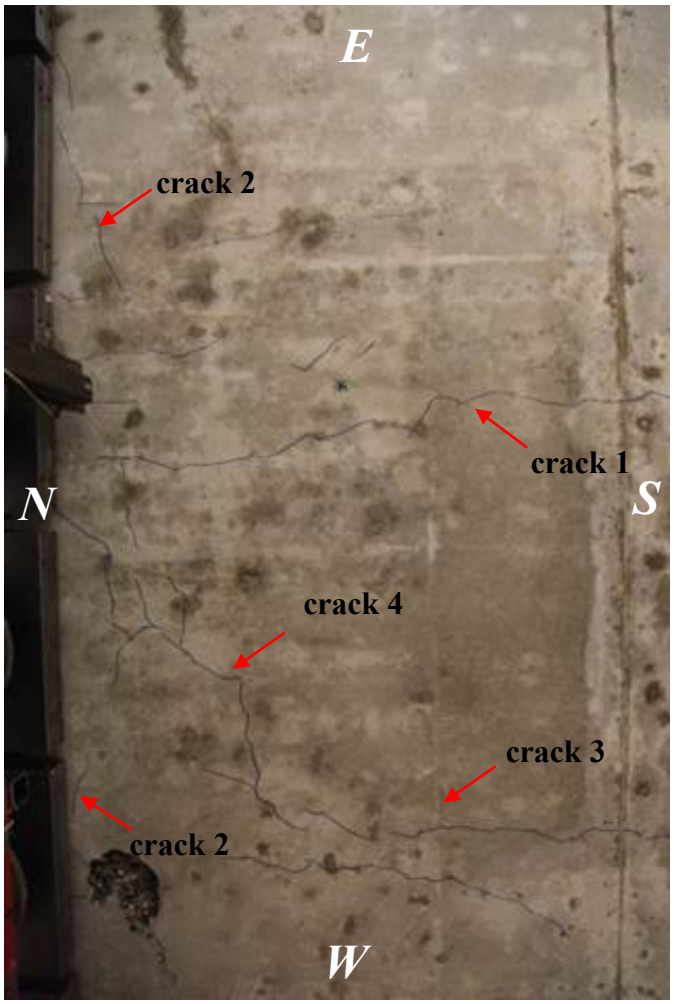

Cracking patterns detected during the experimental test

Regarding to the crack width, crack1, crack 2 and 5 are displayed adopting the $0.832E-02 \div 0.167E-01$ range. Just applying the formula, we can get the maximum width for the cracks:

$$w_{cr,max} = \varepsilon^{nn}{}_{cr} \cdot h$$

we get:

$$w_{cr,min-1,2,5} = 0.832E-02 \cdot 95\ mm = 0.79\ mm$$
$$w_{cr,max-1,2,5} = 0.167E-01 \cdot 95\ mm = 1.59\ mm$$

A comparison can be done looking to the following table:

Specimen	F_{line} [kN]	F_{punt} [kN]	w_{max} [mm]	Class.	Where?
S25T1	0	Fail	0.05	*crack 5*	front face - trhough crack in the middle
			0.05	*crack 6*	front face - crack close to E side, from botton, not fully trough
			0.10	*crack 1*	bottom face - NS crack from support into span, passing the load
			0.25	*crack 2*	bottom face - EW close to the support
			3.00	*crack 4*	bottom face - punching at W
			0.20	*crack 3*	bottom face - NS crack at W-side at 48 cm from free edge

Crack width detected for slab S25T1 during the experimental test

The obtained range is bigger than the experimental evidences.
The aforementioned cracks hold to a $0.05 \div 0.25\ mm$ range, regards to the width, the crack openings are overestimated.
Regarding to crack 4 (punching shear crack), it seems to hold to the $0.331E-01 \div 0.500E-01$ crack strain range. It equals to $3.14 \div 4.75\ mm$ of width. This range well matches the crack width detected on the experiment.
As detected, the widest cracks are located in the area below the loading plate. At the bottom side, a longitudinal and straight fracture (crack 1) runs from the loading plate toward the frontal face and propagation is typical of a bending response that stresses the slab in transversal Y-direction. However, the entity of this fracture is much smaller than the other transversal fractures at the bottom side. Indeed, the biggest crack is located between the loading plate and the simple North support, following the Y-direction with an arc shape (crack 4). It seems to interest also the lateral faces of the slab, as plotted by blue discs spreading from the loading plate. Beside, the fact that this cracks is fast growing with the external load (see the distribution of the principal tensile strains), proves that it is important for the limit of the bearing capacity of the slab, since it could define a "critical section". Other smaller shear cracks are observed in the opposite direction with respect to the loading plate: they spread in a radial direction, below the load, forming the so called butterfly cracking pattern. The biggest one is underlined (crack 4).
On the frontal face two main cracks are detected: the flexural crack in the middle (crack 5) and the inclined crack on the West side (crack 6). This one seems to continue in the bottom face following a radial direction.

So, these are clear evidences of the presence of wide cracks, that lead the slab to failure. Through these observation the way the slab fails is better defined: it causes by a punching shear mechanisms

of crisis. So, the global mechanism has for sure a relevant component in the crisis for reached Shear Capacity. The presence of the bending is important as well, in particular in transversal Y-direction, but does not represent a problem for the bearing limit of the slab, as established by the small amount of yielded rebars.

Moreover, also these plots better underline which specific failure mechanism occurs and it can be visualized by the deformed mesh shape:

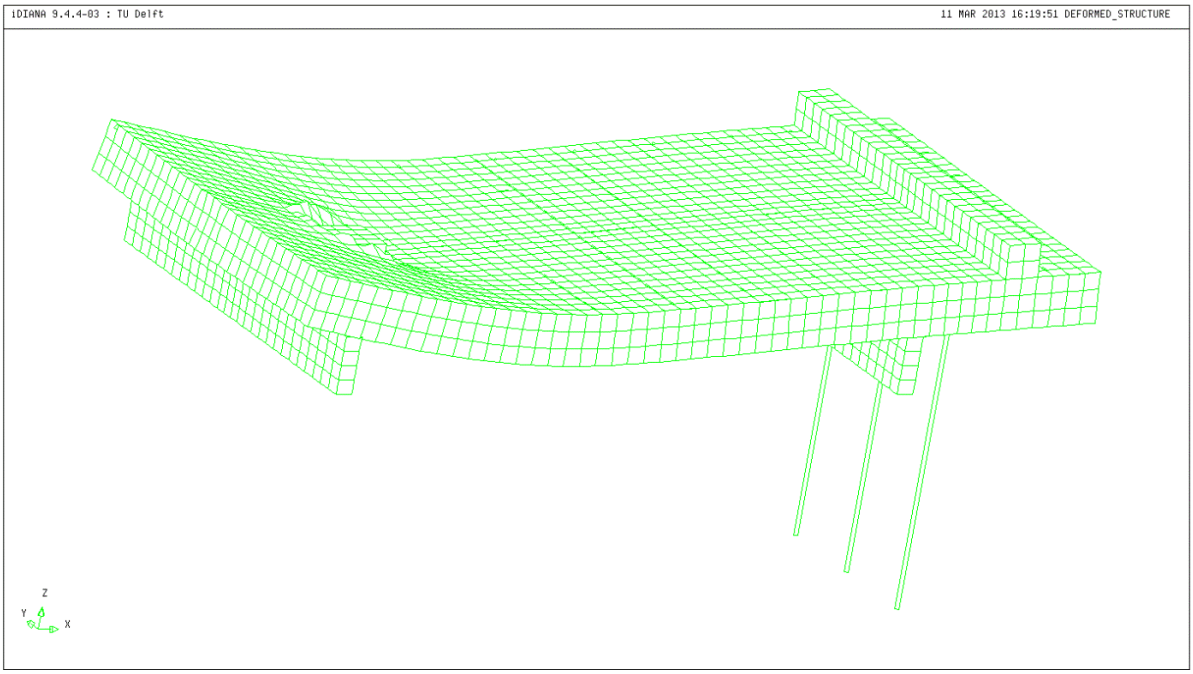

Deformed structure at the peak load: global overview

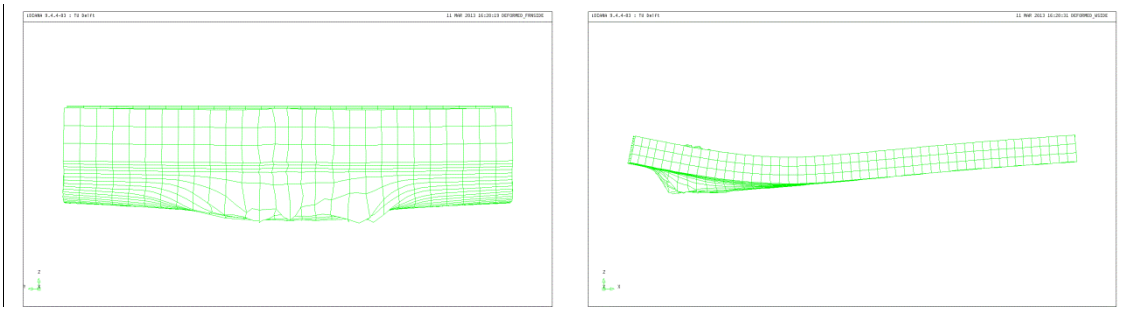

(a) *(b)*

Deformed structure at the peak load: (a) North front side and (b) West lateral side

The denser mesh allows to better fit the strong local deformation caused by the expulsion of a truncated cone body from the slab under the load, as underlined by the previous plot.

6.2.6 Dywidag bars pre-stressing

The Dywidag pre-stressing plot evidences the same trend as seen before:

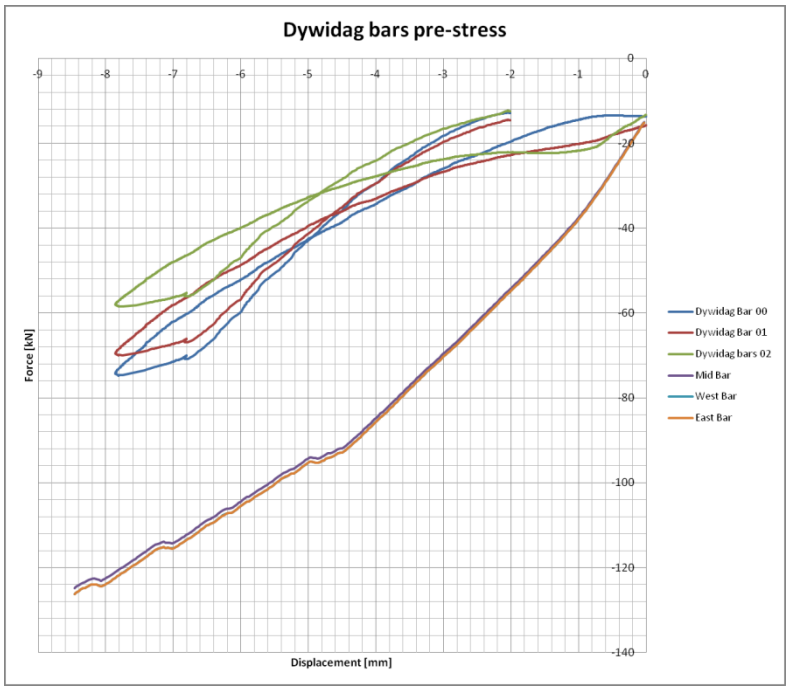

Experimental and numerical Dywidag pre-stressing

6.3 The finest mesh: 4x4 total model

The finest mesh is adopted on the total model as well. An analyses is with the tensile fracture energy G_f proposed by the FIP-CEB Model Code 2010, pair to $0.150\ Nmm/mm^2$. The analyses adopts the same parameters of the previous ones, here reported once again:

- tensile fracture energy: $G_f = 0.150\ N/mm$;
- numerical crack bandwidth: $h = 75\ mm$;
- normal Teflon interface stiffness: $k_{n,T} = 500\ N/mm^3$;
- integration scheme: default for all the finite elements (see previous paragraphs);
- maximum number of iteration equal to 25;
- pre-stress on the Dywidag bars: $s_{xx} = 23.59\ MPa$.

However, for reason of computational time the analyses is stopped after one week of work. The following image shows the output:

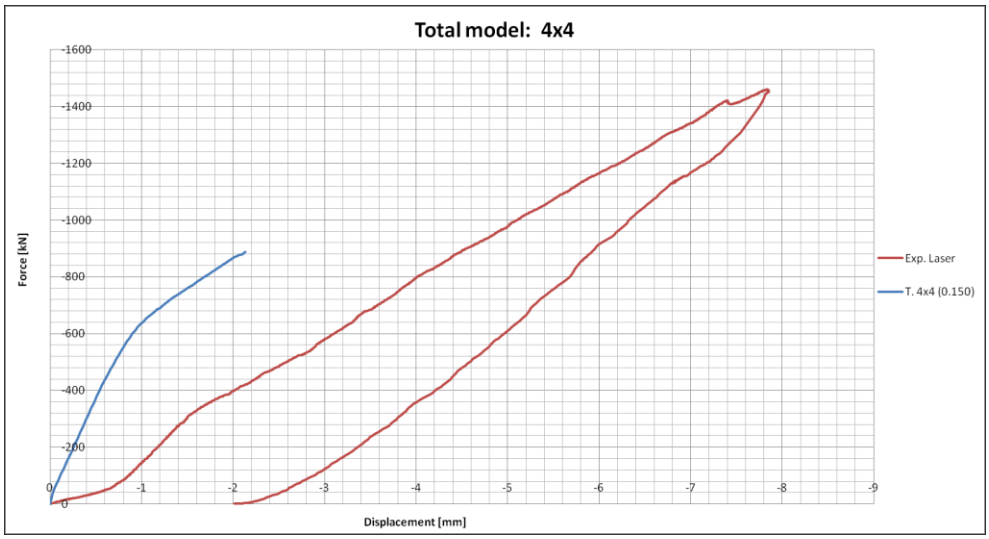

Force-displacement graph for 4x4 total model for standard value of G_f parameter

A "final" displacement of $-2.13\,mm$ is reached, so only 71 steps are analyzed. However, it's interesting to note a better agreement between this mesh and the experimental results for what regards the average slope after the elastic field.
The following pictures shows how the finer mesh, the better prediction seems to be done in terms of load-displacement diagram:

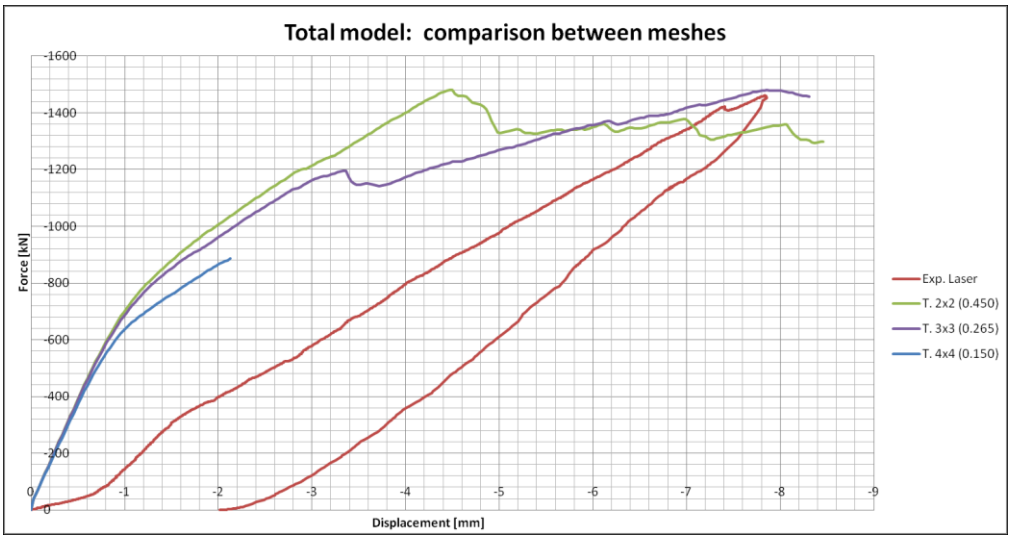

Force-displacement graph for 2x2, 3x3 and 4x4 mesh for total model

For what regards the convergence behaviour the related plot is here reported:

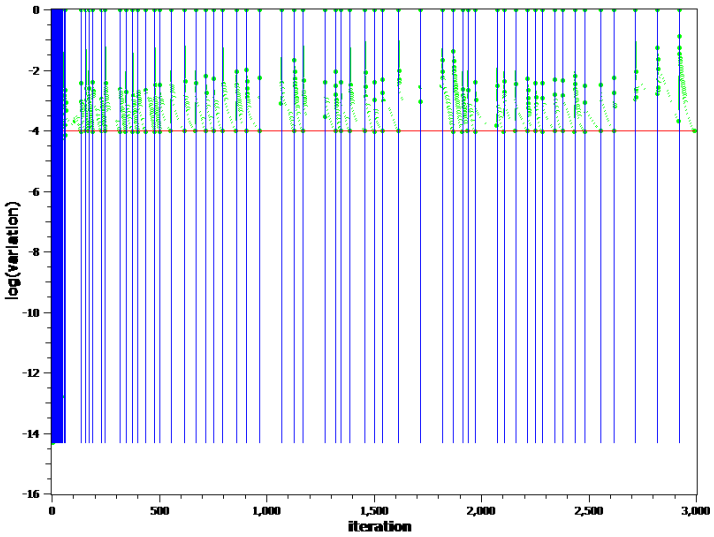

Convergence trend for 4x4 mesh on the total model

Despite the short range investigated, the convergence trend shows a good behaviour, with the most of the steps that converge.
It has to be noted that the present analyses were run on a faster computer. A "Dell Precision T3600 64bit" were used, instead a "Dell Precision T3400 32 bit".

6.4 Tension stiffening:

The high amount of tensile fracture energy required by the numerical analysis exceed the standard one proposed by the CEB-FIP Model Code 2010. It has to be noted that the amount of fracture energy depends on the crack spacing. If the element size is larger than the crack spacing, the amount of fracture energy may be increased, according to [Belletti 2010 vedi VAN Helmert)]. However, the required values for the numerical test is $0.450\ Nmm/mm^2$ instead $0.150\ Nmm/mm^2$ for the coarse mesh, so $+300\%$, and it reaches $+75\%$ for the finer *mesh 3x3*, with $0.265\ Nmm/mm^2$.
This can be explained through the *tension stiffening* phenomenon. The usual assumption is that the stress carrying capacity of the reinforced concrete gradually decrease and is exhausted once the reinforcement starts yielding. This implies that the ultimate crack strain $\varepsilon^{nn}{}_{cr}$ of the tension-stiffening curve equals the yield strain ε_{sy} of the steel rebars. [citare Jrot invernizzi e company].
By applying that on the *Hordijk tension softening* model, one can discover the required fracture energy for each crack bandwidth:

Hordijk model	*h=150 mm*	*h=95*	h=75
$Gf^{(1)}$ [N/mm]	0.36	0.23	0.18
$Gf^{(2)}$ [N/mm]	0.43	0.27	0.22

Fracture energy range for tension-stiffening

Hordijk model	*h=150 mm*	*h=95*	h=75
$Gf^{(diana)}$ [N/mm]	0.450	0.265	/

Fracture energy values for the numerical models

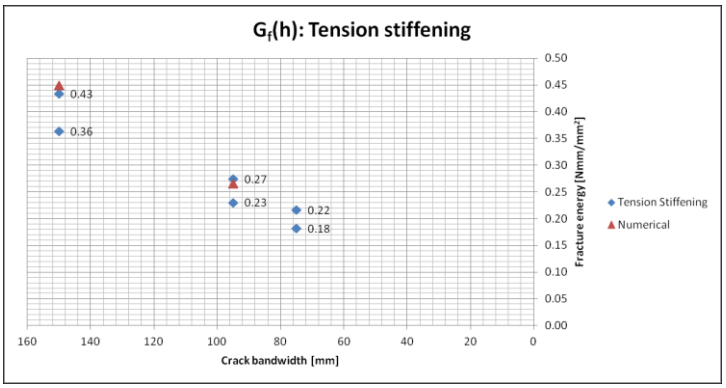

Fracture energy trend and tension stiffening range for total model

Since two different diameters are used for the reinforcement bars, two distinct yield strains ε_{sy} are used. However, the first two adopted values seems to follow this rule, since the adopted G_f is really close to the obtained values for tension stiffening. The absence of the result related to the finest mesh doesn't allow us to fit the last value and then establish if the tension stiffening relation is always followed.

7. CALIBRATION OF THE PARTIAL MODEL

NLFE-analysis are run on the partial model in order to compare the outputs with the SL-analysis results. As will be explained later, the combination of two different nonlinear behaviour (both in compression and in tension) is still not implemented in the sequentially linear code. In order to run the following analysis on the same model and get comparable results, it must be defined an equivalent linear model for the felt, taking into account the tensile reaction, on both the models (NLFEA and SLA).
The following paragraph will be focused on the best definition for a common linear behaviour of the felt interface.

7.1 Application of the Nonlinear Analysis on Partial model with Linear felt:

A comparison between linear and nonlinear felt behavior is executed using the NLFE-analysis method.
As proposed before, a nonlinear behavior is performed in order to: (a) trace the compressive behavior of the specimens, (b) model the no-tensile reaction capacity of the felt interface. Indeed, by adopting a linear model, we assume an elastic response both in compression and in traction.
This model has the advantage to be very simple, but it involves a strong tensile reaction during the slab deformation: when the external parts bend due to the slab's deformation the linear felt interface starts to react.
Although a nonlinear model for the felt interface has been already implemented inside the *Diana* environment, an investigation is necessary, since this model is not adoptable with SL-analysis yet.

SL-analysis can be run only on the *partial model*. As said, a nonlinear compressive behavior with no tensile reaction is still not implemented for this kind of analysis.
Accordingly, a linear model for felt interface must be used.
Moreover, due to the marked nonlinearities of the whole system it involves effects difficult to predict and evaluate a priori. So, it results useful to better understand the effects on the whole slab's response adopting the clamped model with a linear interface, by running NL-analysis to fix unknown parameters previously to run SL-analysis.
The *Teflon interface's stiffness* is assumed like the total model, so $k_{n,T} = 500\ N/mm^3$.
Regarding to the felt model, after many trials appear that the felt behavior involves a significant influence on the output of analysis.
Three different values are assumed for the normal stiffness of the felt interface:

- $15.20\ N/mm^3$, which corresponds to the initial stiffness on the nonlinear felt diagram;
- $34.00\ N/mm^3$, which corresponds to the average stiffness for the nonlinear felt diagram;
- $75.00\ N/mm^3$, which corresponds to the highest stiffness on the nonlinear felt diagram.

As it will be shown later, since the average and maximum tensile stresses are not negligible, this model has to be used carefully, by analyzing the influence of this contribution on the whole slab's response in terms of force-displacement diagram and distribution of the felt's reactions.

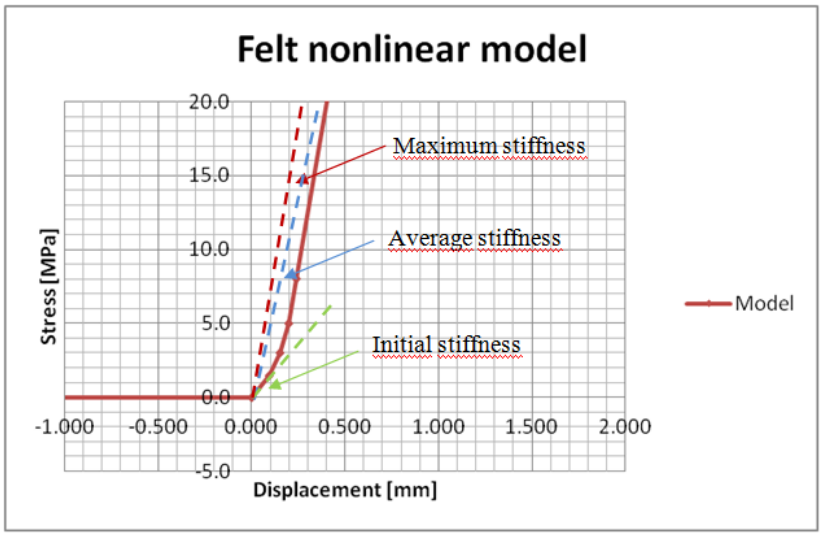

Nonlinear felt model for stress-displacement behavior

This evaluation is carried out by using the *partial model*, like for future SL-analysis, where only a linear felt interface is adopted.
The *2x2 partial model* is used, adopting as features:

- tensile fracture energy, $G_f = 0.150\ N/mm$;
- numerical crack bandwidth, $h = 165\ mm$;
- normal stiffness of the Teflon interface, $k_{n,T} = 500\ N/mm^3$;
- full linear felt behaviour.

The first comparison is made looking at the Load-displacement diagram. Indeed, by adopting different values of felt stiffness, it can changes first of all the slope for the post-linear trait and, after, the peak and post-peak behavior. Instead no big differences are detected during the linear field and for the last trait, as shown by the following image:

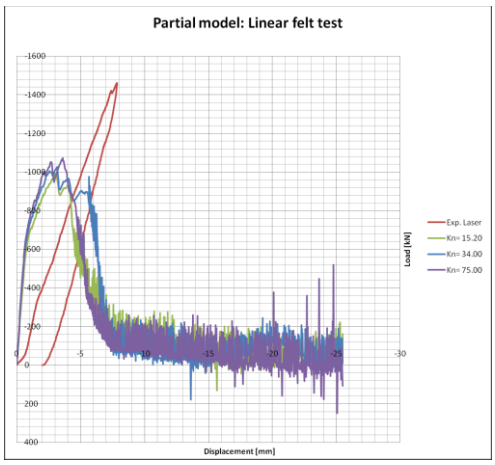

Load-Displacement diagram for different linear stiffness for the felt interface

The following tables resume the peak load and peak displacement found for three different values of the normal felt stiffness, assuming a full linear behavior (both in traction and in compression).

$K_{n,\,felt}$ [N/mm^3]	F_{max} [kN]
15.20	-990.36
34.00	-1025.49
75.00	-1072.03

Normal stiffness and peak-load relation

$K_{n,\,felt}$ [N/mm^3]	d_{max} [kN]
15.20	-3.06
34.00	-3.15
75.00	-3.60

Normal stiffness and peak-displacement relation

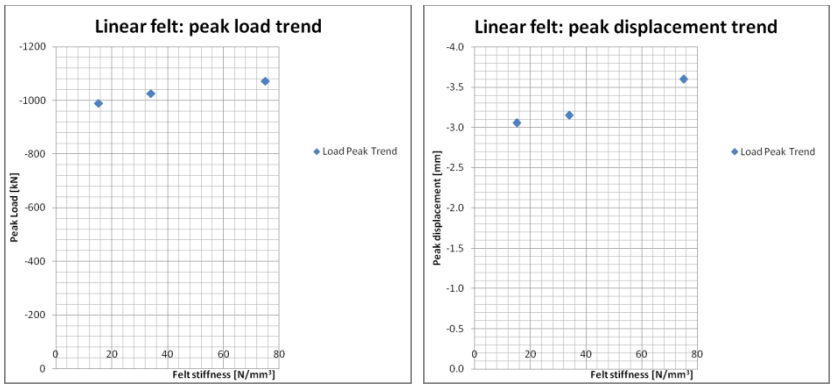

(a) *(b)*

Peak load (a) and peak displacement (b) trend for different felt stiffness

Both the peak load and the peak displacement trend belong to a relative close range, but following a linear relation seems to appear.

It has to be noted that a higher linear stiffness tends to increase the Peak Load. This proofs the influence of the tensile reactions on the global behavior of the slab and on the bearing capacity of the system. The lowest stiffness tries to avoid this phenomenon, since no tensile reaction can be provided in reality.

The output in terms of felt reaction are plotted in the following images, focusing our attention on the peak point and after this. The main points are marked on the load-displacement diagram:

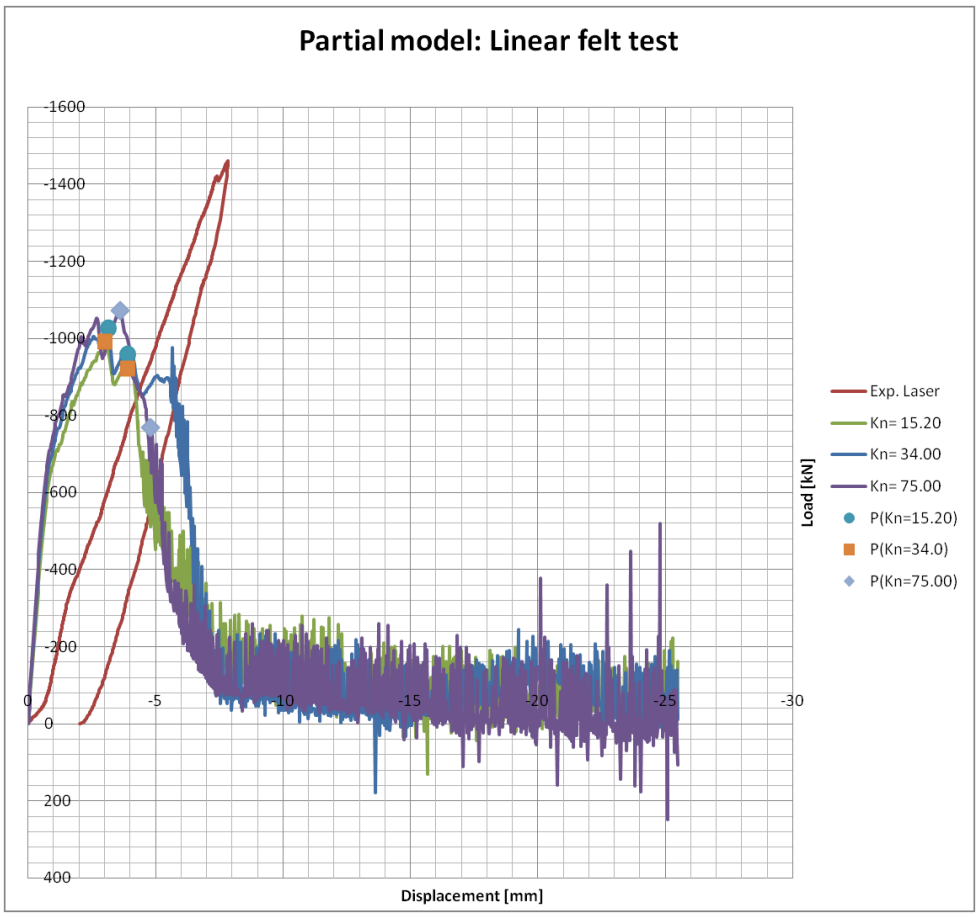

Selected points for peak and post-peak plots for different felt stiffness

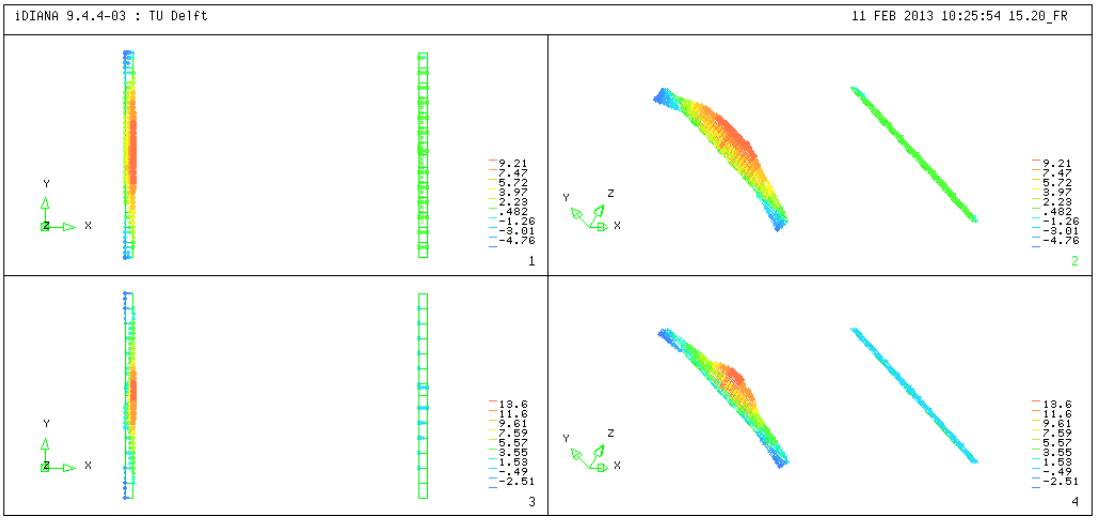

Felt reaction at 101th (peak) and 131th (post peak) step for k_n=15.20 N/mm^3

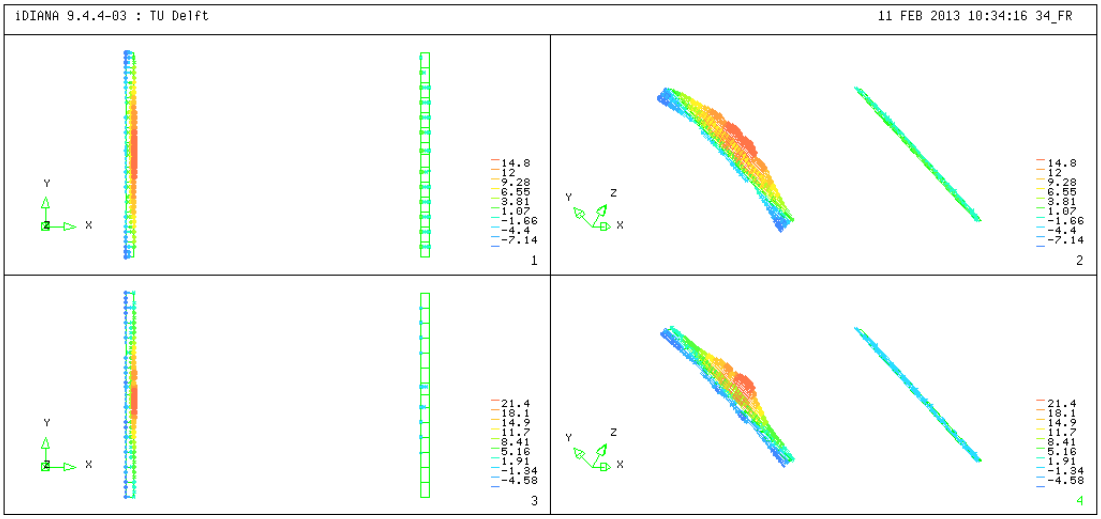

Felt reaction at 101th (peak) and 131th (post peak) step for k_n=34.00 N/mm^3

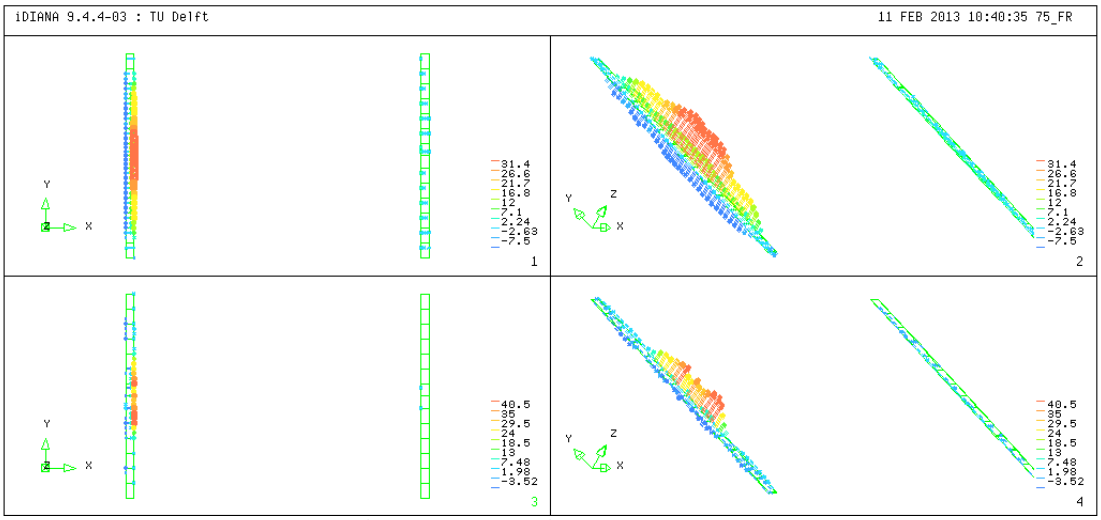

Felt reaction at 121th (peak) and 161th (post peak) step for k_n=75.00 N/mm^3

As visible thought to these plots, the felt stiffness influences the whole reaction on the interface support. Due to the strong nonlinearities of the whole system, inserting a different linear behavior involves effects hard to predict and to understand a priori.
This concept can be schematized through the present images:

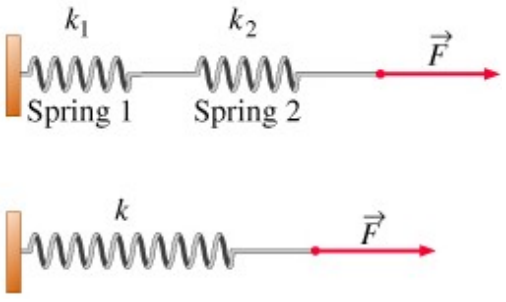

Springs in series

By viewing the first spring (k_1) as the linear felt interface and the second one (k_2) as the whole nonlinear slab system, the reaction on the felt layer depends on the two different mechanical behavior. So, each system influence each other mutually.
The only feature that can be easily predictable is the maximum tensile reaction for the felt: increasing the linear stiffness, the tensile reactions increases too. So, as visible below, the maximum tensile reaction is lower for the smallest normal stiffness value. It's about 4.76 MPa on the peak point, more than the half of the maximum compressive value during the same point (9.21 MPa).
Moreover, the following pictures help to focus few examples of the tensile reaction for different felt interface on the peak point marked on the previous force-displacement diagram:

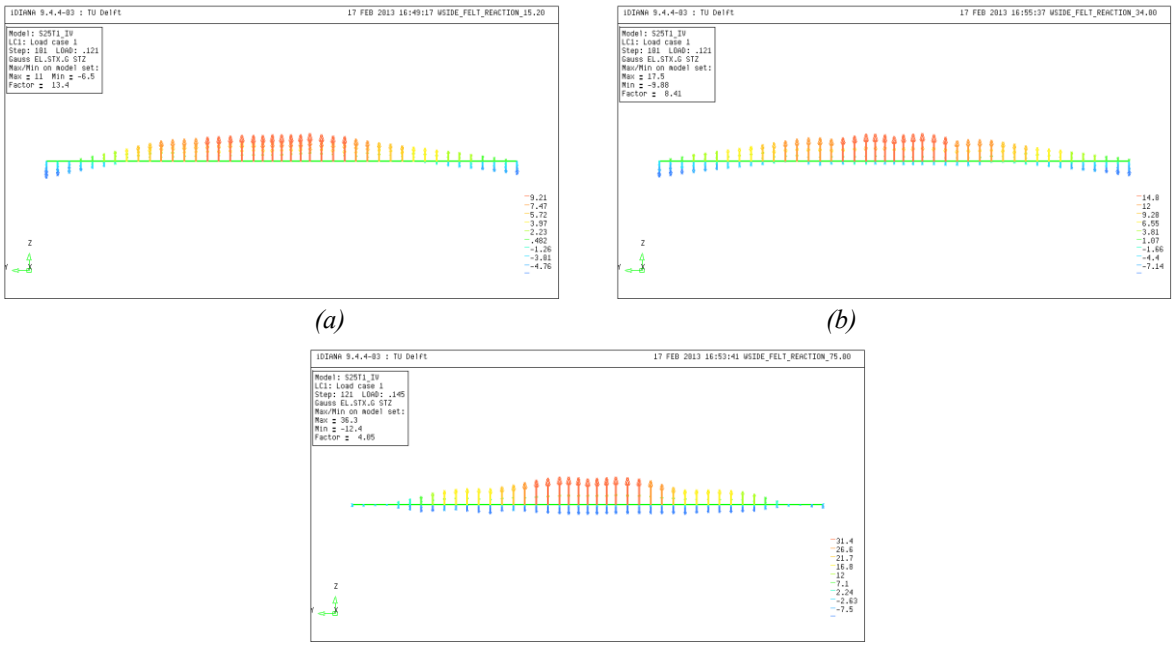

(a) *(b)*

(c)

Tensile reaction for felt interface with: 15.20 N/mm^3 (a), 34.00 N/mm^3 (b) and 75.00 N/mm^3 (c) as normal stiffness

A different behavior is shown: higher is the normal stiffness, greater is the magnitude of the reaction (both in compression and in traction). Moreover, the distribution of tensile reaction and the global interface's behavior change, as visible looking at plot (a) and plot (c). The highest stiffness involves a butterfly distribution of the felt reaction over the entire length of the interface, while the lowest one underlines a traction limited to the external edge of the layer.
This specific pattern takes place also in the total model. So, by viewing to these images, the lowest normal stiffness could be chosen for the felt interface.

Then, in order to select the better value of this parameter, a comparison between the last results and the total model with nonlinear felt and same features is presented:

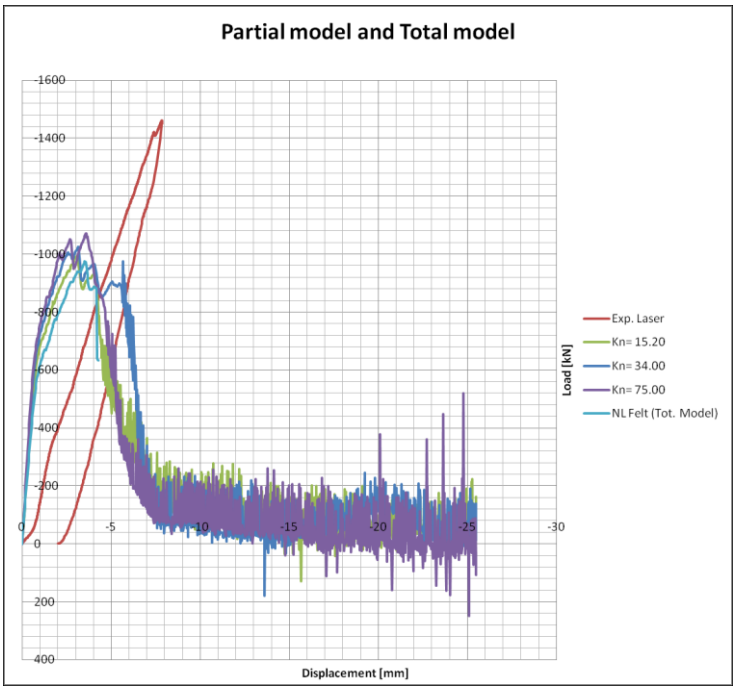

Total model with nonlinear felt vs. partial model with linear felt

For the peak point on the total model we obtain:

- $-974\ kN$ for the peak load;
- $-3.51\ mm$ for the peak displacement.

So, these values are not so different than the previous ones, obtained with a partial model and linear felt. The initial trend is closed to the other ones, but a different behavior is detected immediately after the linear trait.
Moreover, the maximum magnitudes are quite similar, both in compression and in traction, respectively $10.40\ MPa$ and $3.92\ MPa$. The global distribution of the felt reaction seems to be quite similar on the peak point and after it.

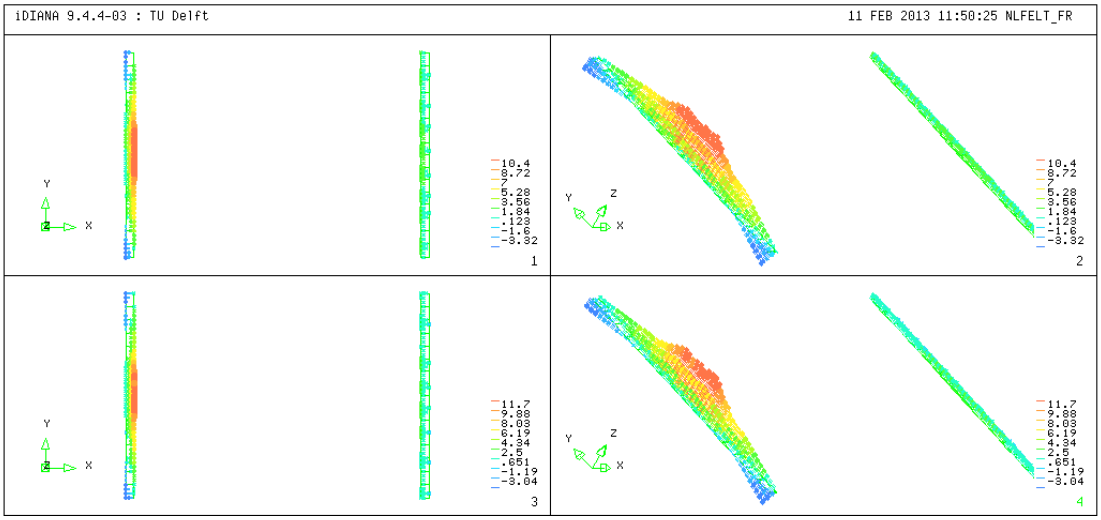

Felt reaction at 120th (peak) and 130th (post peak) step for total model with nonlinear felt

Once again, it seems that the better matching can be reached by choosing the lowest value for the linear felt stiffness.
However, through this sample it seems possible to match the total model's diagram, by reducing the linear stiffness. So, another analysis is carried out adopting 7.00 N/mm^3.

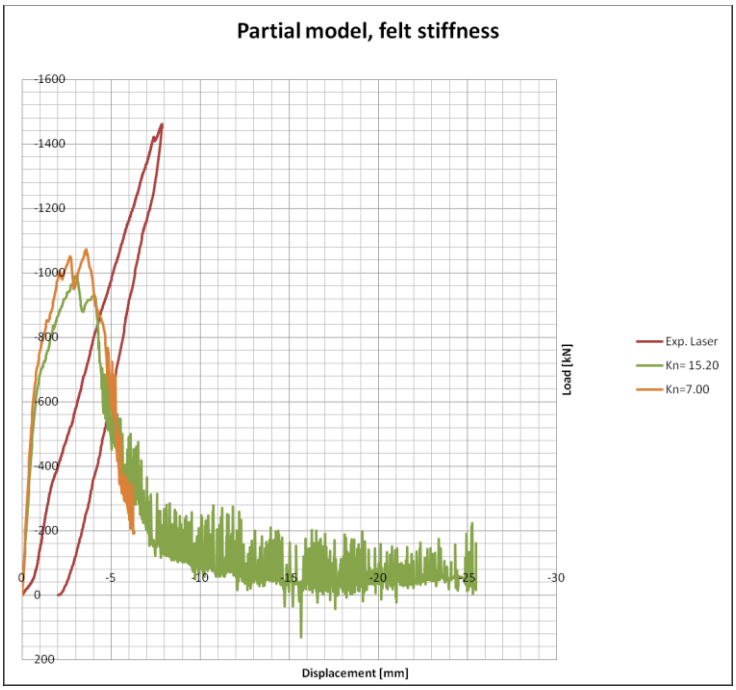

Load-displacement diagram for 7.00 N/mm^3 linear felt

Viewing to the figure above, a lower felt stiffness does not produce better results, rather the slab's response seems stiffer and higher in terms of peak load.
So, a linear felt with 15.20 N/mm^3 stiffness is definitively chosen.
Now, a comparison between total model with nonlinear felt and partial model with linear felt is made and studied.
The same fracture energy value is adopted, equal to 0.150 N/mm.

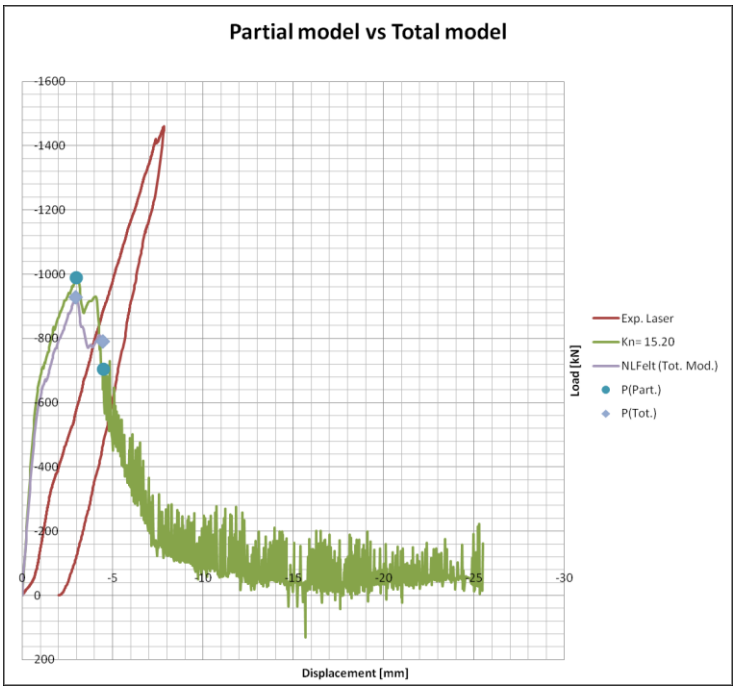

Total model with nonlinear felt vs. partial model with linear felt for G_f= 0.150 N/mm

As observed before, the partial model with linear felt has a stiffer response. It could be due to the full tensile reaction for the interface: a not negligible area works with tensile reaction during the whole analysis, changing the real mechanism.
Moreover, for the same fracture energy value, a higher peak load is reached by the partial model, instead the peak displacement seems to be the same for both the models.
The linear trait, until the first millimeter of displacement, overlaps. It proofs that the constraints system assumed for the partial model (perfect continuous constraint) is really closed to the experimental setup, at least inside the elastic field.
A first comparison can be made plotting the principal tensile strain distribution: four mean values are plotted. By using the same fracture energy and crack bandwidth parameters, the points on the softening diagram coincide for both model, so a possible different behavior will be visible through a different tensile strain distribution.
Two main points are selected on the load-displacement diagram for both models: peak and post peak.
The main points on the *Hordijk softening model* are reported in the following table:

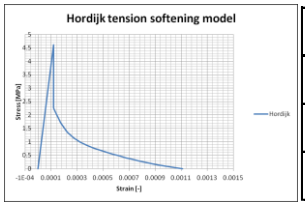

$\varepsilon_{el,ult.}$ [-]	0.000118	1.184E-04
0,5*$\varepsilon_{cr,ult}$ [-]	0.000555	5.545E-04
$\varepsilon_{cr,ult}$ [-]	0.001109	1.109E-03
5*$\varepsilon_{cr,ult}$ [-]	0.005545	5.545E-03

(a) *(b)*

Hordijk softening diagram and relative strain values table

For every plot the shown surfaces are:

- top surface in the upper left window;

- bottom surface in the upper right window;
- front North side in the lower left window;
- West side in the lower right window.

For the *partial model* with linear felt we get:

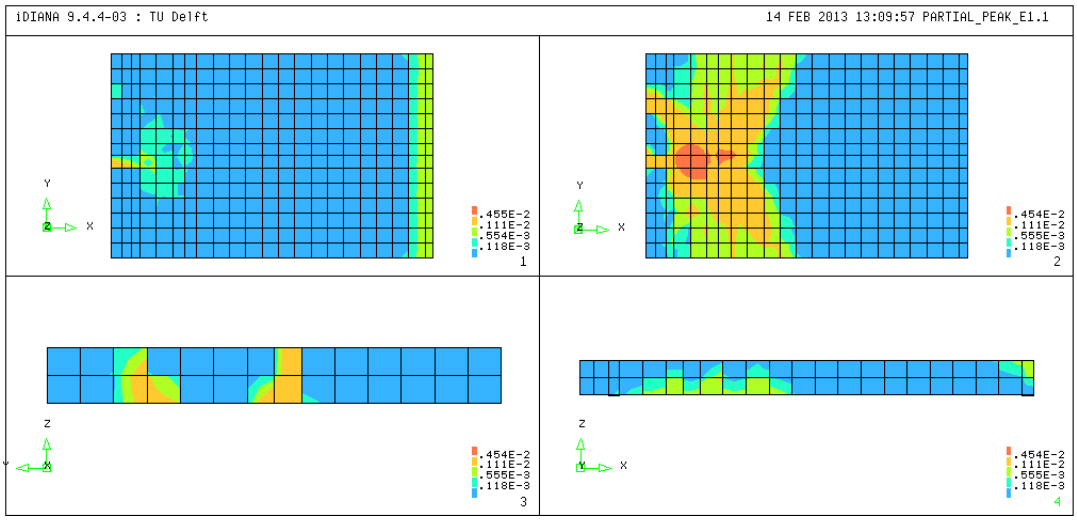

Principal tensile strain plot at 101th (peak) for partial model

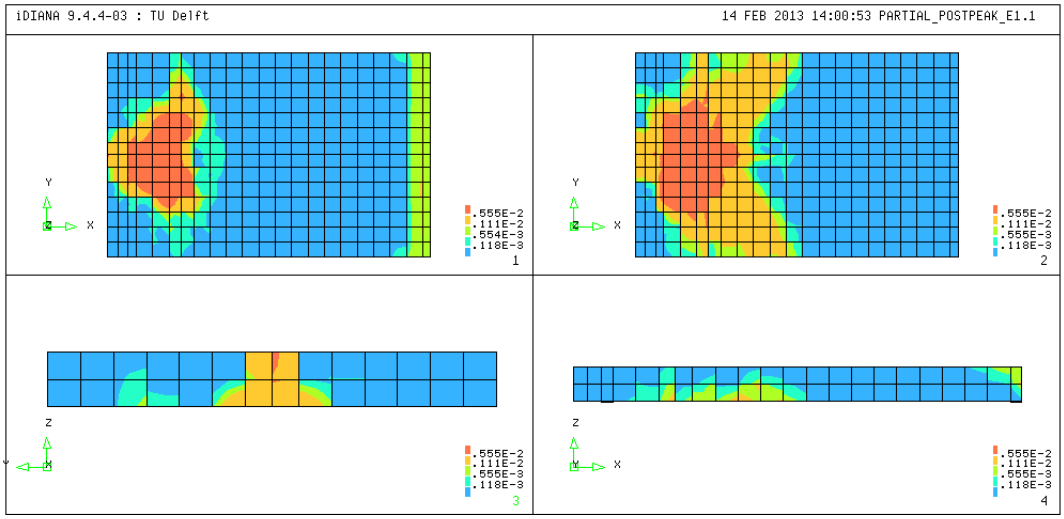

Principal tensile strain at 151th (post-peak) for partial model

For the *total model* with nonlinear felt we get:

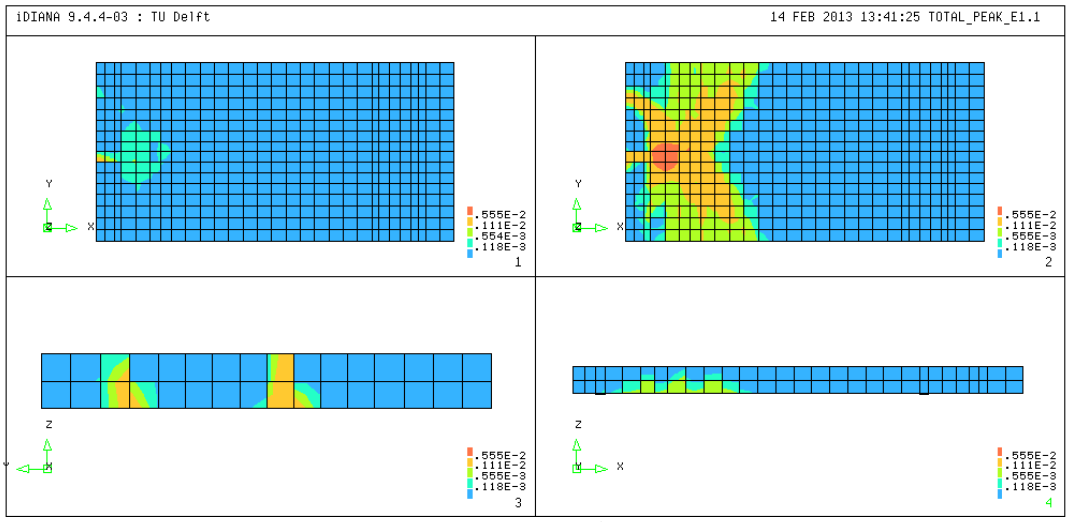

Principal tensile strain plot at 100th (peak) for total model

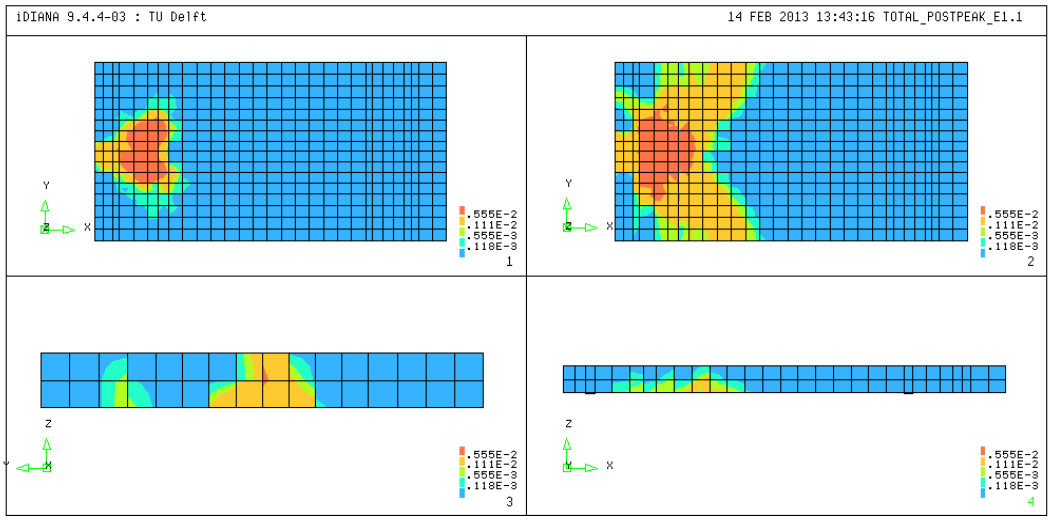

Principal tensile strain plot at 150th (post-peak) for total model

The plots show a good matching between total modal and partial model, both for the peak and the post-peak distribution, regarding to the principal tensile strain.
The most visible difference is visible on the full clamped side: here, for the partial model, vertical flexural cracks occur. Indeed, a yellow area is present.
By plotting the principal crack strain another comparison is shown. Moreover, the entity of the flexural cracks on the clamped side is quantifiable.

For the partial model:

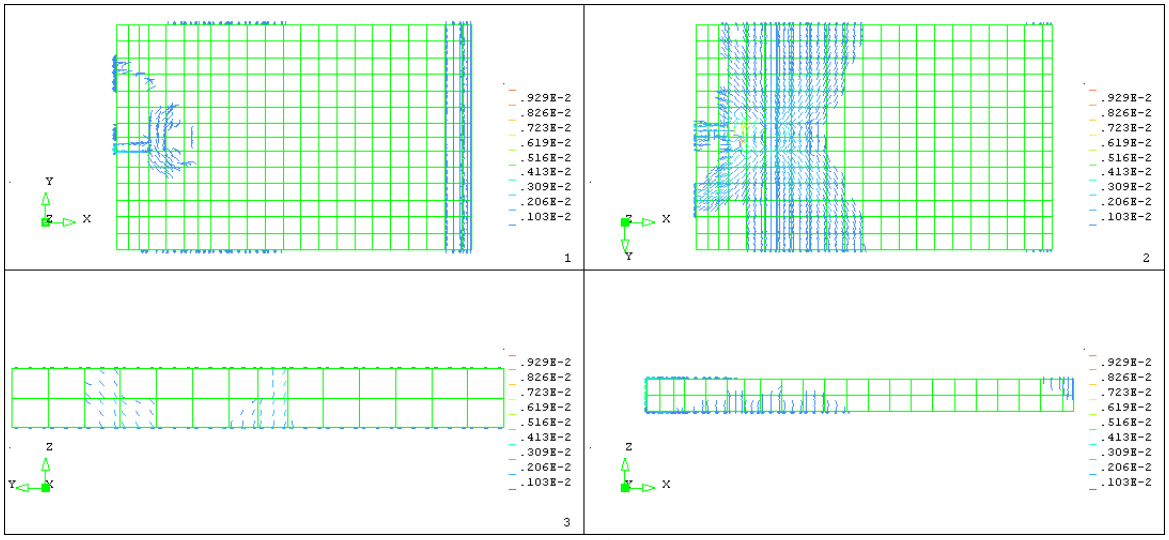

Principal crack strain at 101th (peak) for partial model

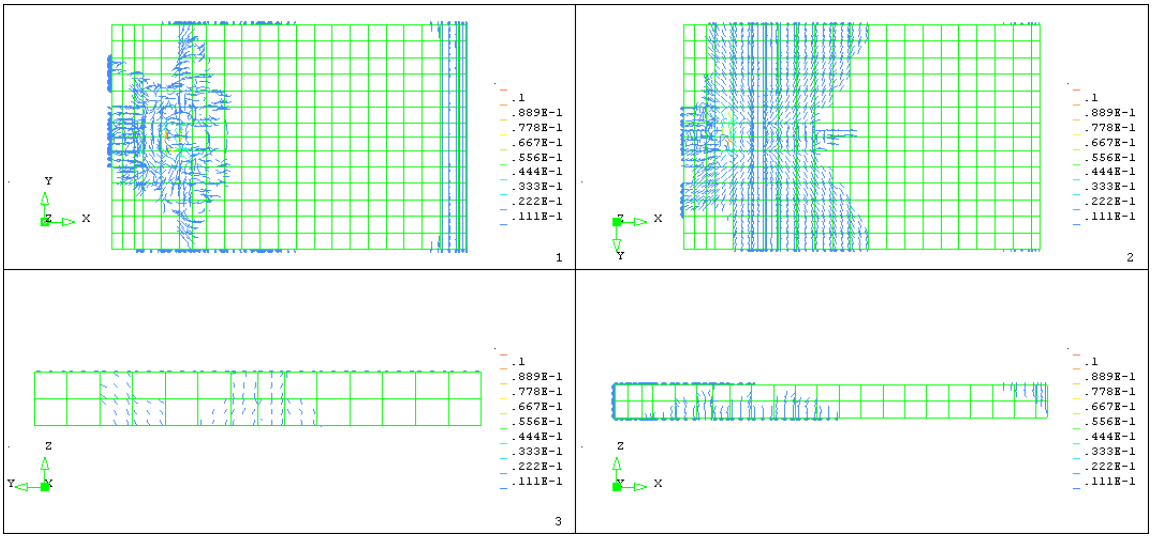

Principal crack strain at 151th (post-peak) for partial model

For the total model:

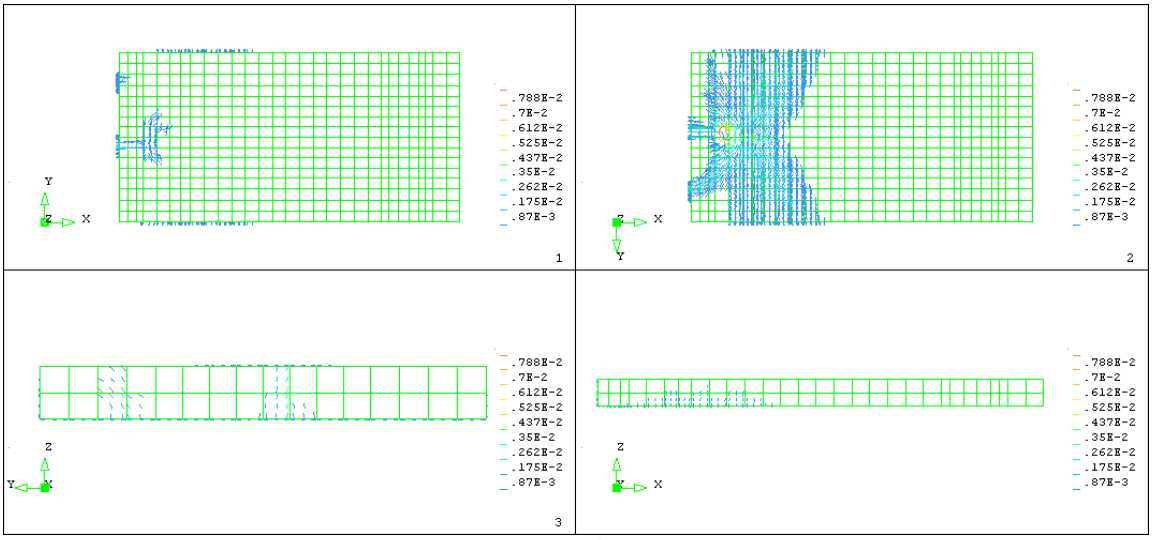

Principal crack strain at 100th (peak) for partial model

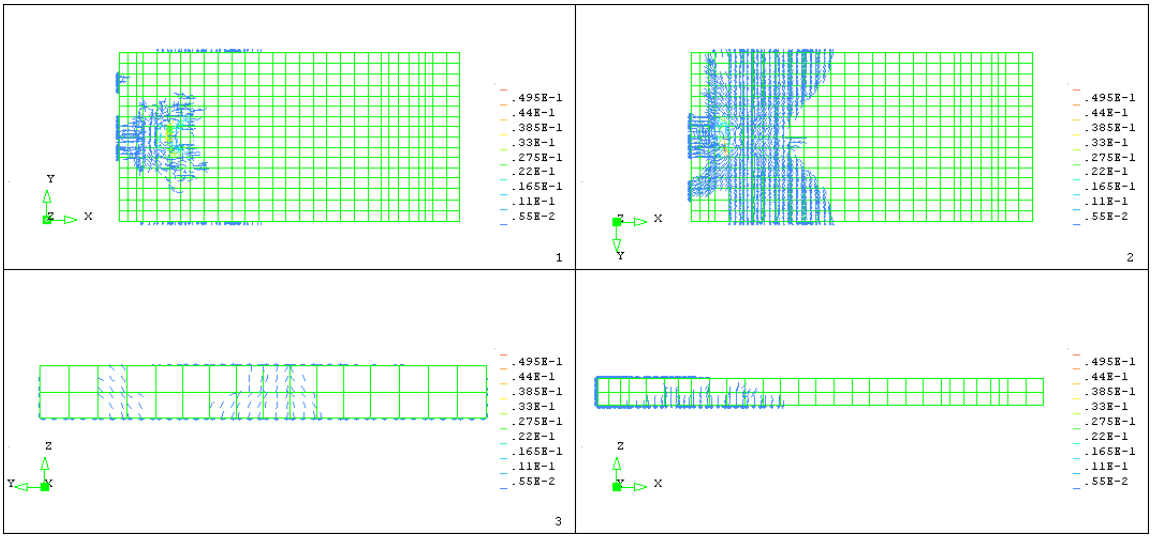

Principal crack strain at 150th (post-peak) for partial model

As one can see, also the principal crack disc plots show a good matching for partial and total model: the same *"butterfly cracking pattern"* is present. However, it seems to be wider on the partial model. It has to be reported that the crack patterns present a non-symmetric distribution, both on the top and bottom surface, despite the models are symmetric as geometry and reinforcements. The Newton-Rapshon method adopted for the iteration should give symmetric outputs. Moreover, the distribution is mirrored than the one shown by the experimental test.

The most visible difference occur at the South support beam: inside the partial model a cracking pattern is now well visible, where the continuous support is modeled.

During the experimental test no flexural cracks are identified, but only wider cracks than 0.05 mm can be discovered.

So, in order to understand if these cracks are wider than 0.05 mm the following plot is shown by adopting a fixed contour value.

By using the formula:

$$\varepsilon_{nn}{}^{cr} = \frac{w^{cr}{}_{nn}}{h} \rightarrow \varepsilon_{nn}{}^{cr} = \frac{0.05\ mm}{165\ mm} = 0.303E-03$$

one can obtain the requested value.
The following plot shows how *"visible cracks"* occur on the clamped side of the partial model. The same is found both on the top, lateral and fontal side and bottom; this is different from what happened during the experimental test:

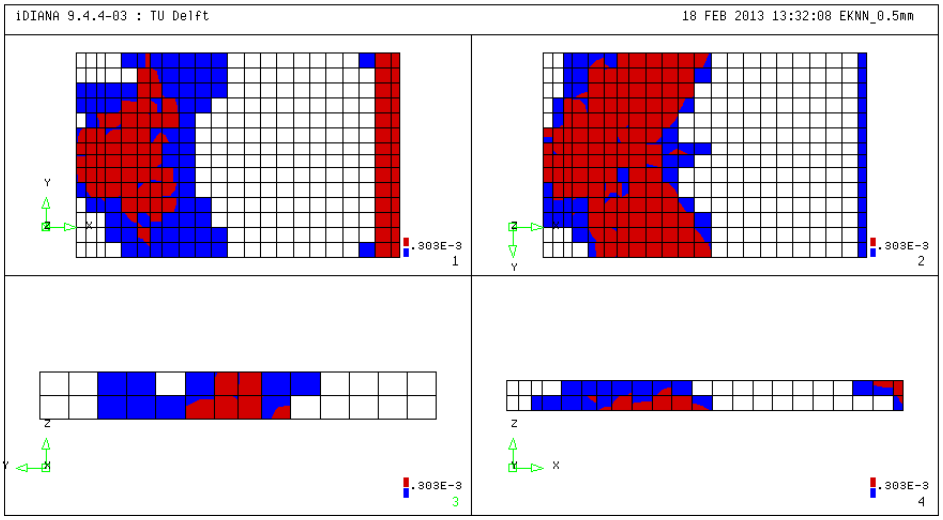

Principal crack strain plot at 151th (post-peak) for partial model on the main surfaces

However, flexural cracks are visible only close to the full clamped side: only the first line of elements present a deep cracking due to the high tensile stresses.
Cracks are detected on the lateral West side as well, unlike the experimental evidence.
Instead, cracked zones are well predicted close to the loading plate both on the top and the bottom surface and on the frontal North face.
A manipulation of the *ultimate tensile strength* f_t was tried for some lines of elements close to clamped side. A not negligible length has to be modified in order to avoid flexural cracking, so the sophistication of the model is considered too heavy and this solution is discarded.
Finally, by adopting a coarse mesh, as the presented now, it's acceptable to consider the following model quite close to experimental setup: it's hard to avoid cracking on the clamped side, where high tensile stresses occur due to the bending action.
By adopting a finer mesh it will be analyzed if a better result will occur.

It has to be reported the marked difference between nonlinear felt on the total model and linear felt on the partial model, by viewing the felt response since the 1st step.
Traction starts to arise already after one step:

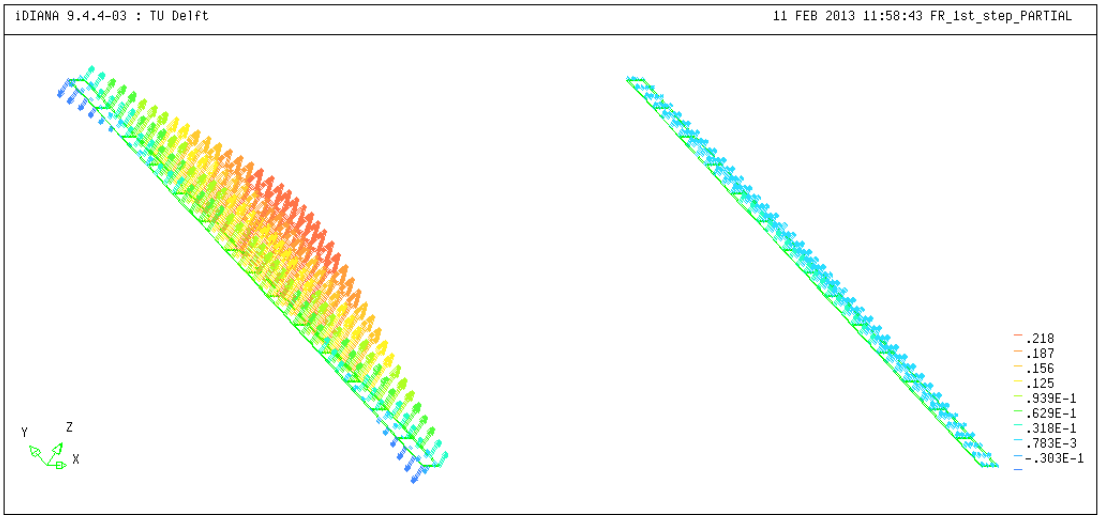

Felt reaction at 1st step for linear felt on partial model

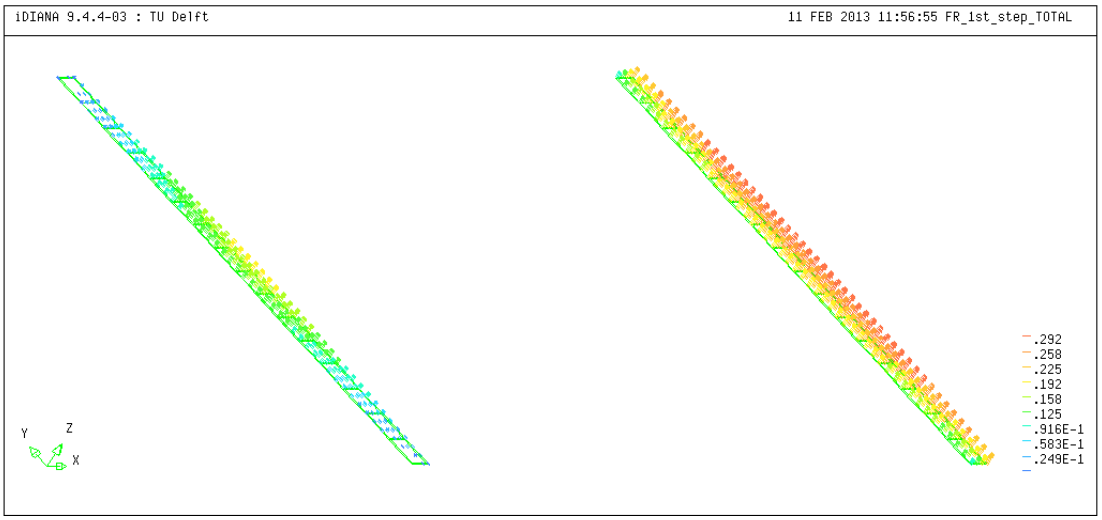

Felt reaction at 1st step for nonlinear felt on total model

Finally, a comparison between the peak values is shown in the following table:

Model	F_{max} [kN]	d_{max} [mm]
Partial 2x2	-990.358	-3.06
Total 2x2	-928.869	-2.97

Peak values for total and partial model

This shows a good matching regarding to the peak displacement, instead the peak load exposes a higher gap, however under the 6%.

After all these consideration, we can assume the partial model as a reliable tool to run SL-analysis, by adopting linear felt with minimum stiffness and clamped South side, since the global behavior seems to be well similar with the total model adopted for the NL-analysis.

The next step consists in increasing the fracture energy in order to compare the output with the total model run with NL-analysis and get useful information for the next SL-analysis.
During the previous analysis, $G_f = 0.450\ N/mm$ is found as best value to match the load peak with the experimental one on the total model.
So, the same value is inserted inside the "*2x2"* partial model.
The following image shows the Load-displacement graphs for two different fracture energy magnitude:

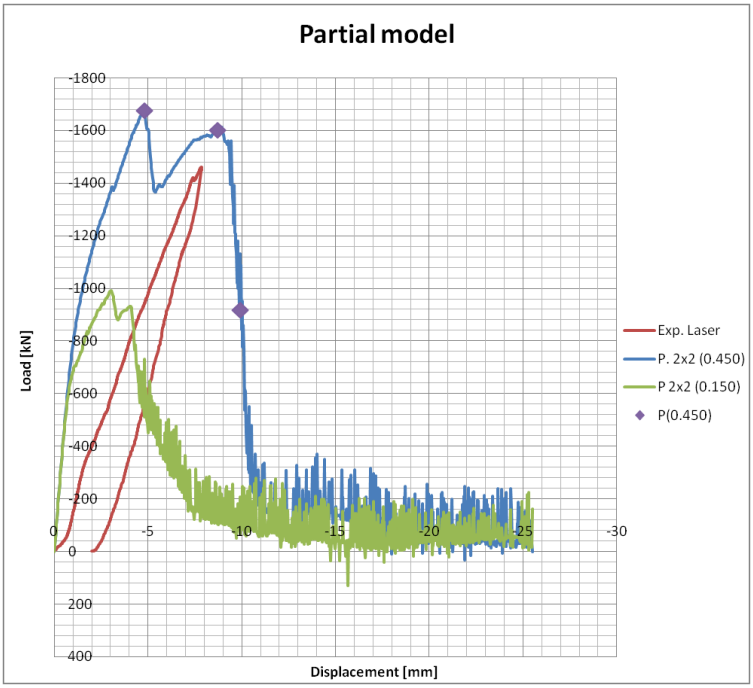

Load-displacement diagram for 2x2 partial model with G_f=0.450 N/mm

A higher G_f fracture energy makes the concrete "more ductile" (see figure below) on the tensile side and it can involve higher principal crack strain; moreover a bigger peak point occurs. The different trend starts from the end of the linear trait. Instead the global shape and trend seem to remain unchanged.

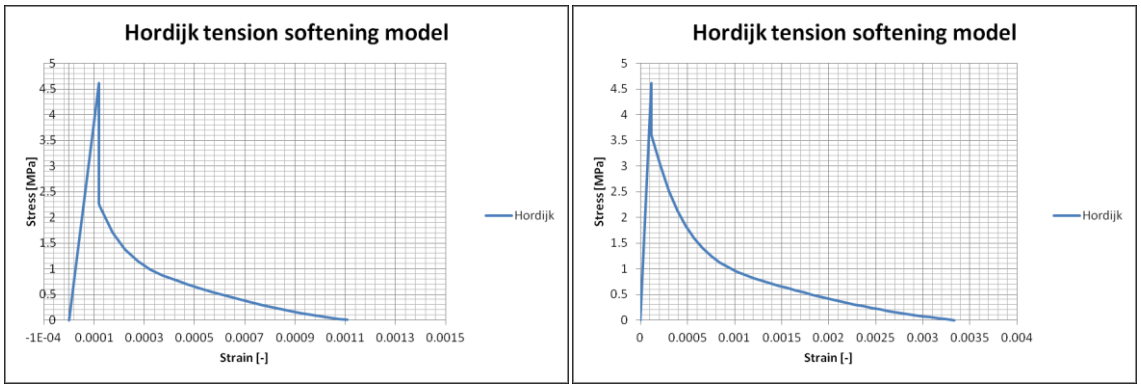

(a) *(b)*

Hordijk costening model for G_f=0.150 N/mm (a) and G_f=0.450 N/mm (b)

By showing the principal crack strain disc plot the cracking patterns seem to be more symmetric and more extended. This is due to the higher fracture energy: a more ductile concrete involves a slightly stiffer structure after each step, so the damage can spread for a longer displacement and the cracks too.

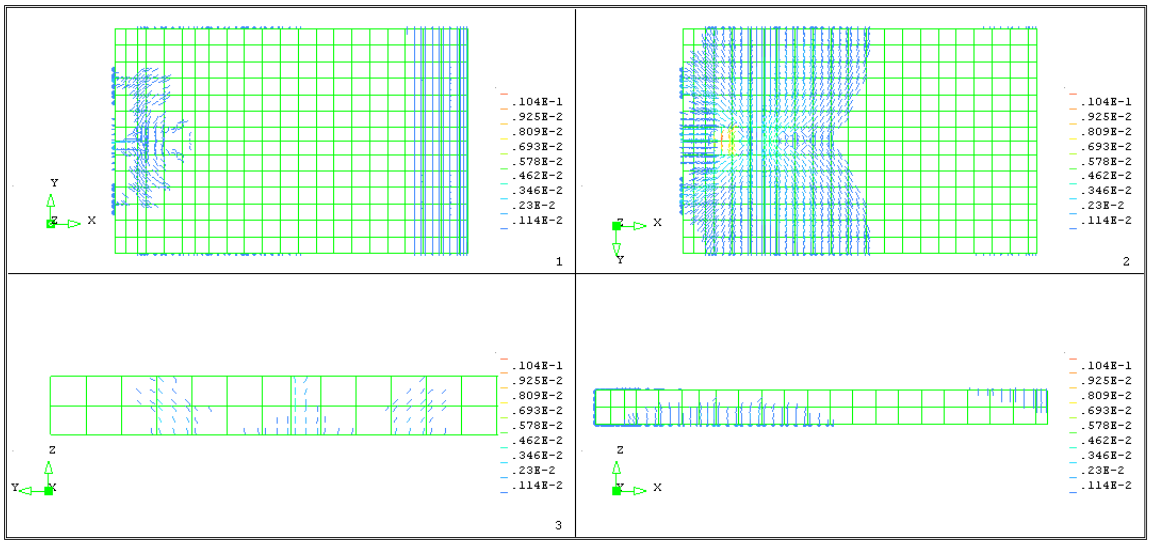

Principal crack strain disc plot at 161th (peak) for partial model

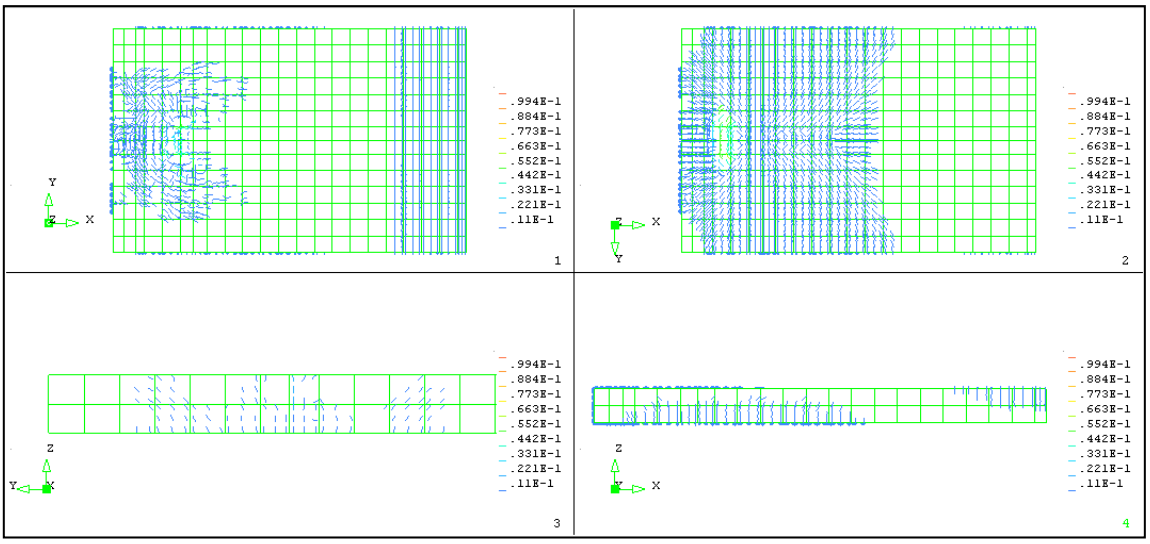

Principal crack strain disc plot at 291th (post-peak) for partial model

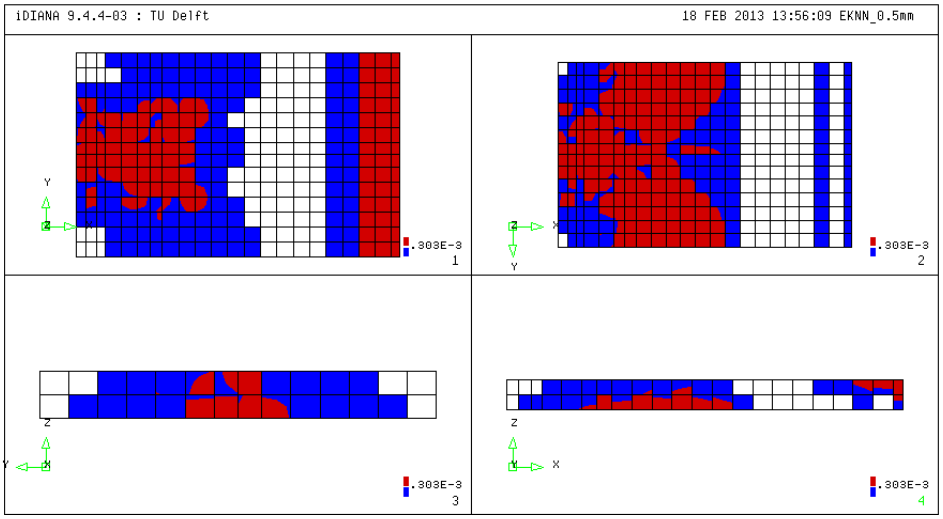

Principal crack strain plot at 331th (post-peak) for partial model

Wider cracked zones than the previous fracture energy value are visible, as expected.
Another useful comparison is shown by the *2x2 total model* with the same fracture energy value of the previous partial model.
The force-displacement graphs are here reported:

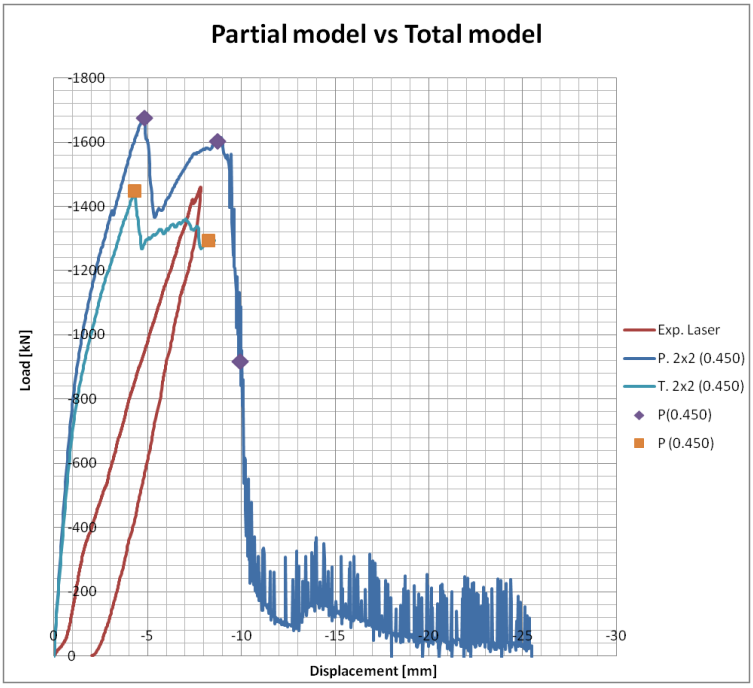

Load-displacement diagram for 2x2 partial model and 2x2 total model with G_f=0.450 N/mm

Until the first cracking the trends are similar: it proofs the likeness between full clamped side and Dywidag constraint system, at least for the first trait.
After the total model presents a lower stiffness and a smaller peak value; instead the global shape seems to be similar.
The following pictures show the *principal crack disc plot* for the selected points on the main surfaces:

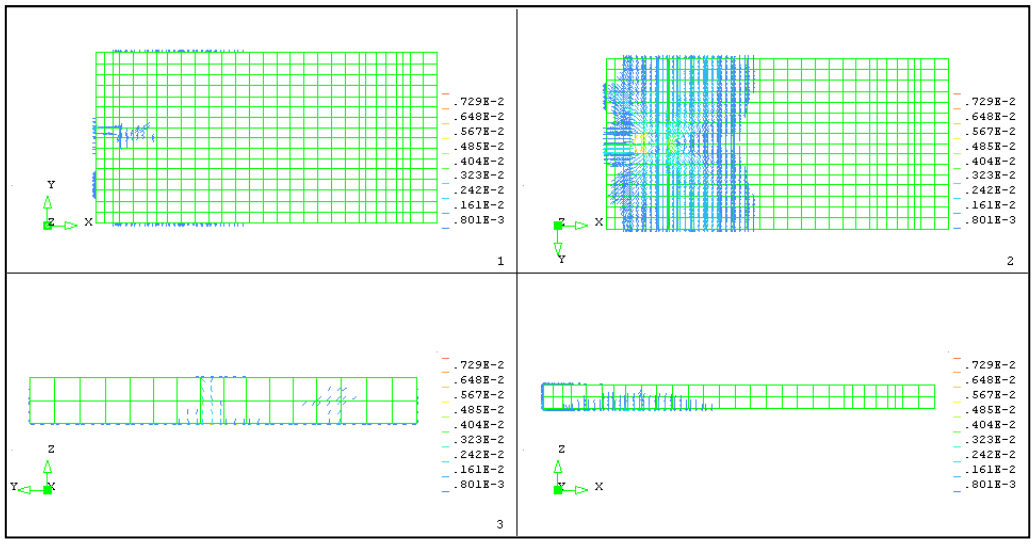

Principal crack strain disc plot at 140th (peak) for total model

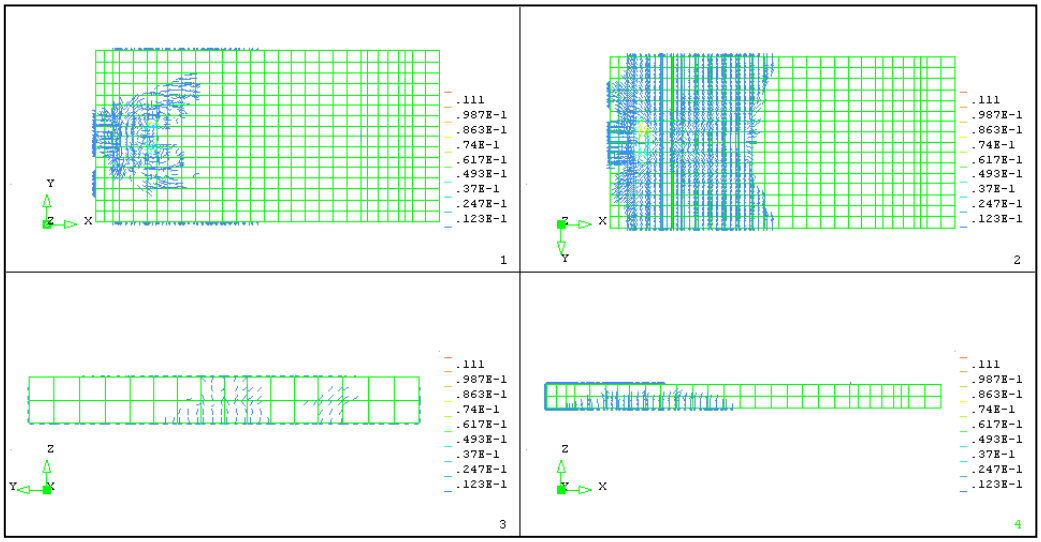

Principal crack strain disc plot at 280th (post-peak) for total model

On the peak point wider cracking patterns are detected on the partial model, both on the top around the loading plate, on the bottom surfaces below the load, on the frontal e lateral side.

The same happens on the post-peak point, but now the crack patterns presents a non-symmetric scheme on the frontal side for the total model.

It has to be remembered that both the partial and the total model has got a symmetric reinforcement bars scheme.

The following pictures shows as no flexural cracks are detected close to the South support, like during the experimental test:

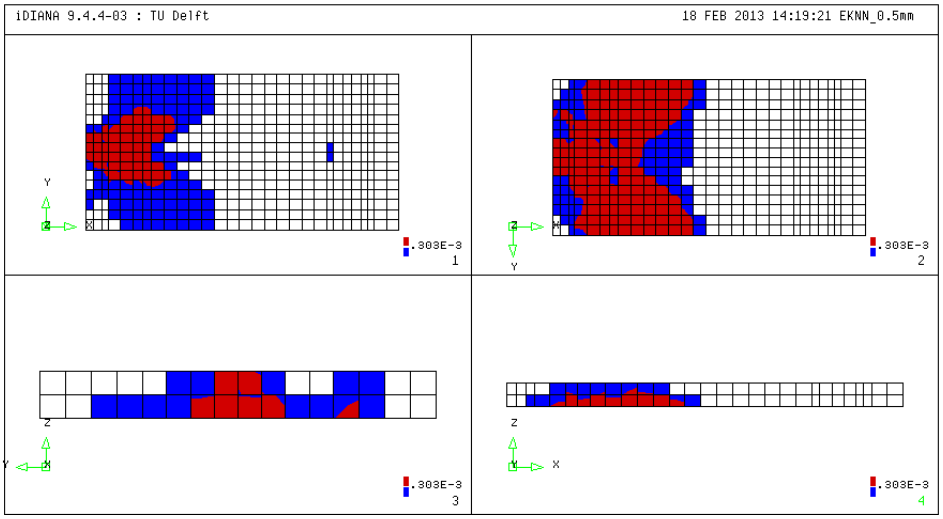

Principal crack strain plot at 280th (post-peak) for total model

So, though thanks to this comparison some conclusion can be taken:

- the linear model involves some changing inside the initial setup, but the results here reported show good agreement with the previous ones with a total model with nonlinear felt behavior;
- the partial model requires a lower fracture energy to fit the experimental load-displacement diagram.

Further analysis both on partial and on total model will give more information about the mesh sensitivity of outputs between the two different way of modeling the South constraint and the felt behaviour.

8. APPLICATION OF NONLINEAR ANALYSIS ON THE PARTIAL MODEL

The present analysis adopt a *Newton-Raphson modified* method for the iterative procedure, with a $0.03\ mm$ displacement control step, with relative displacement criteria of 10^{-4} (option CONTIN on). The fracture energy G_f and numerical crack bandwidth h parameters depend on the mesh discretization; it will be descripted later for each one. The Teflon layer has got $k_{n,T} = 500\ N/mm^3$, as discovered on the previous tests. The felt has got a linear behavior to match this features with the future SL-analysis.
At first, a NLF-analysis is run on the partial model with two elements on the height, so called *2x2 model*, then *3x3* and finally *4x4*.
In order to show the progressive evolution of the bearing behavior of the slab four points are analyzed on the basis of load percentages. It has been noted that the better ratio are: $25\% - 50\% - 100\%$. A post-peak point will be selected where possible.
The main features are investigated:

- felt reaction s_{ftz}(vector and contour plot);
- principal elastic tensile strain ε_1 (vector and contour plot);
- elastic tensile stress of reinforcement σ_{xx} and σ_{yy} (contour plot);
- principal tensile stress of reinforcement σ_1 (vector plot);
- principal elastic compressive stress σ_3 for the concrete (contour plot);
- principal crack strain ${\varepsilon_{cr}}^{nn}$ for the concrete (disc plot).

8.1 Coarse mesh: 2x2 partial model

Three values for the main parameter, i.e. tensile fracture energy G_f are used: $0.150 \div 0.330 \div 0.450\ Nmm/mm^2$. The highest value of G_f comes from the same total version, e.g. 2x2 mesh. The present model has got the following features:

- tensile fracture energy: $G_f = 0.150 - 0.330 - 0.450\ N/mm$;
- numerical crack bandwidth: $h = 165\ mm$;
- normal felt interface stiffness: $k_{n,f} = 15.20\ N/mm^3$;
- normal Teflon interface stiffness: $k_{n,T} = 500\ N/mm^3$;
- integration scheme: default for all the finite elements (see previous paragraphs);
- maximum number of iteration equal to 50.

Only the felt model (linear instead nonlinear) and the maximum amount of iterations change.
The following load-displacement graphs is here shown:

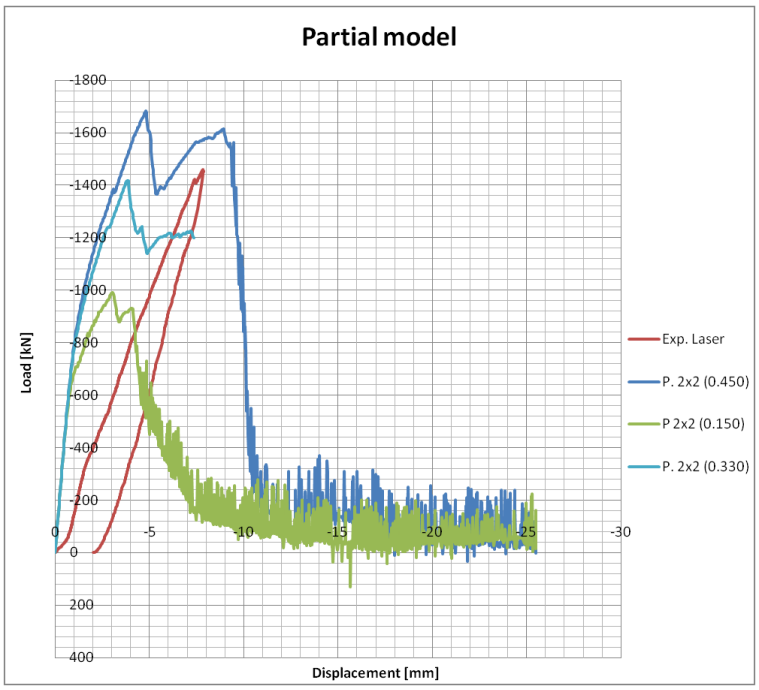

Comparison of partial and total model with same G_f fracture energy

The shapes are quite similar, though the partial model expresses a stiffer post-elastic trend. However, for the partial model the peak point is much higher. Finally, the post-peak behavior shows a softening behavior of the slab and the analysis runs until 25 mm of displacement.

Instead, for the total model divergence occurs.

In order to fit the maximum load, e.g. the peak-load, on the force-displacement diagram, the main parameter G_f is reduced to 0.330 N/mm.

Then, the comparison between NLFE-analysis and experimental test is shown in the following image:

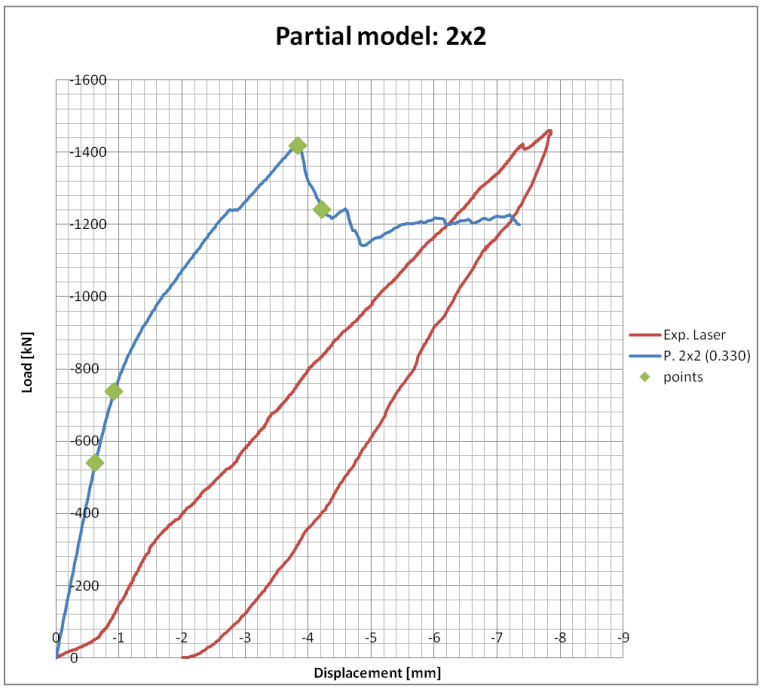

Force-displacement graph for 2x2 partial model

Now, only a good agreement with the experimental peak-load is reached; the response remains still stiffer. After the peak a sudden decay of the bearing capacity of the slab is detected and a flat plateau arises, the divergence occurs.
The numerical peak values are:

- peak load: $1418.20\ kN$;
- peak displacement: $3.84\ mm$.

instead of:

- experimental peak load: $1460.62\ kN$ for a variation of $\sim -3\%$;
- experimental peak displacement: $7.84\ mm$ for a variation of $\sim -51\%$.

Analysis does not converge on step 27, 33 and few steps don't reach convergence around 90th step and from 124 to 146. In terms of displacement it means 0.81, 0.99, 2.70 and from 3.72 to 4.38 mm respectively. From 151th step ($4.53\ mm$) no convergence is reached.
The analysis uses about 5000 iteration until 151th step, about 10000 for all the process.
Three main points are selected on the load-displacement diagram:

- *point 1:* $(0.63\ mm;\ 540\ kN) \sim 40\% F_{max}$;
- *point 2:* $(0.93\ mm;\ 738\ kN) \sim 50\% F_{max}$;
- *point 3:* $(3.84\ mm;\ 1418\ kN) = F_{max}$;
- *point 4:* $(4.23\ mm;\ 1241\ kN)$.

They are shown in previous plot; the main output will be exposed in the next paragraphs.

8.1.1 Redistribution capacity:

On the following image, four pictures of the felt reactions in the Z-direction s_{ftz} are shown by adopting a vector plot. They prove the redistribution of the load from the slab to the support, since the action on the felt is equal to the one on the support beam for vertical balance.
The pictures show the plot about first step and three main points.

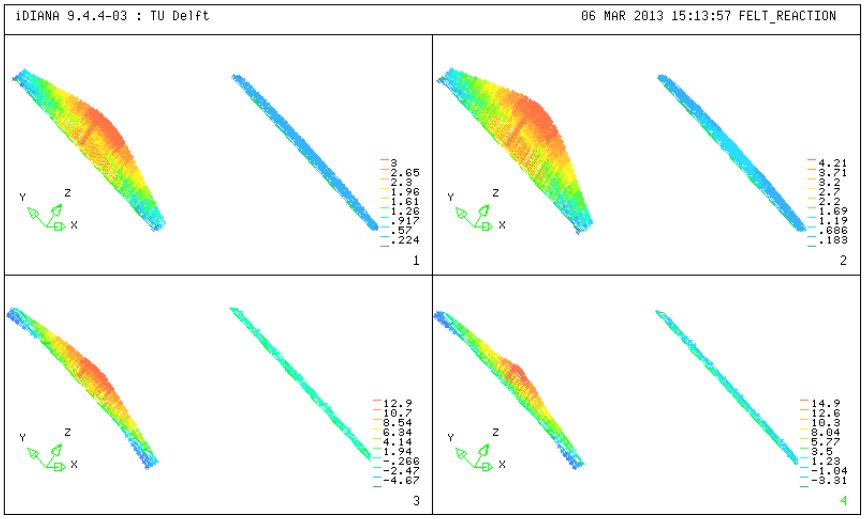

Vector plot of felt reaction [MPa] for the main points

By observing the previous vector plot of the interface traction, the trend of the reaction forces can be discovered. From the outset the tractions present a triangular shape and all the width of the support contributes to the bearing capacity. A linear behavior can be detected between point 1 and point 2, since the shape seems to increase in the same way. Until the 2nd main point ($\sim 740\ kN$) the slab generally presents a linear behavior; increasing the load a clear redistribution of the tractions takes place: a progressive concentration of load on the middle of the interface is visible with increasing of the load, on the Y-direction. The same happens on the X-direction until the post-peak point, where a strong concentration occurs on a little area on the symmetry axis.

In other words, they become bigger in the central part of the North support, while they decrease in proximity of the right and left edges. Then they reach a tensile value: on the peak point a tensile reaction is already present. It has got a not negligible value ($4.76\ MPa$) and it start to arise from the lateral wings of the felt layer. It proofs the slab bending and the reduction of the contact area on the North support. So, theoretically we can say the outer parts don't contribute anymore to the bearing capacity of the slab.

By plotting the part of interface in a compressive state, they are shown with red color (values higher than 0 MPa - *compression*). It can be observed that the loading angle assumes a value from 68° (1st main point) and 64° (4th main point), therefore the effective width of the active zone of the support changes from $b_{eff} = 2500\ mm$ to $b_{eff} = 2140\ mm$.

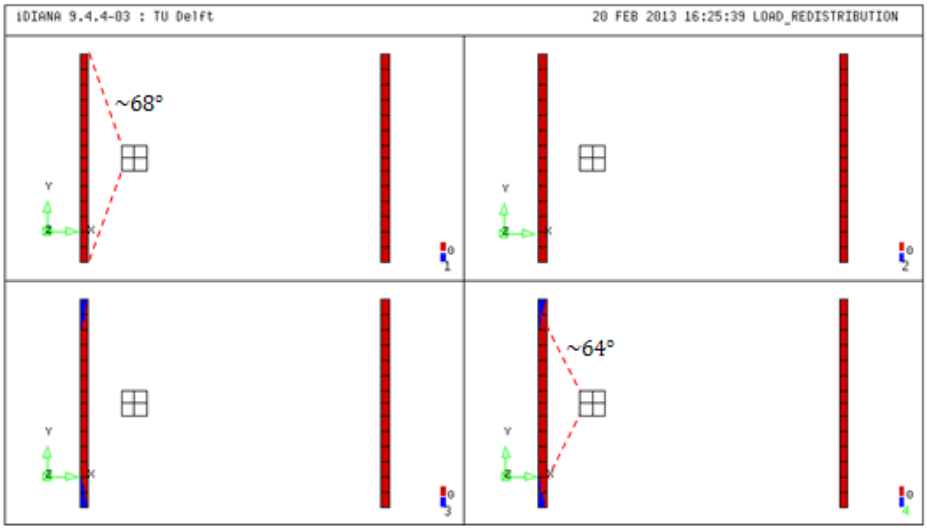

Effective width due to the load spreading on the felt layer

Clearly, the effective width calculated by the Dutch Code was considerably underestimated.

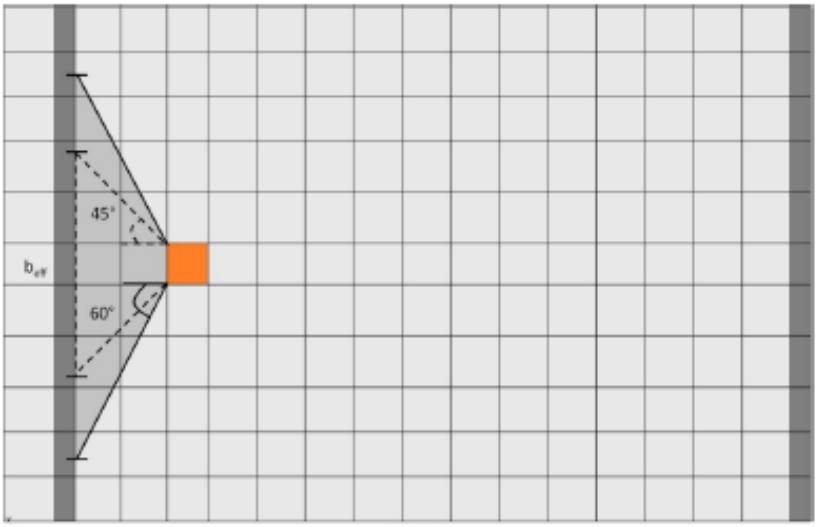

Effective width due to load spreading according to NLFEA and spreading width due to Dutch Code

The same conclusion holds for the bearing capacity predicted by the shear equations of the Dutch Code, which was 940 kN while the experiment showed significant higher peak load (1460 kN). This difference is due to the fact that the shear equations in the Dutch Code are mostly derived from tests on beams without transverse reinforcement, whereas the results obtained on slabs are influenced by considerable redistribution because of larger widths and the effect of transverse reinforcement [5].

8.1.2 Cracking behavior of the slab

In order to investiga the development of the cracking under an increasing load, contour and vector plot of the pricinpal tensile strain are used. Taking into account four points on the softening diagram calculated for a fracture energy $G_f = 0.330\ N/mm$ and $h = 165\ m$.

$\varepsilon_{el,ult.}$ [-]	0.000118	1.184E-04
0,5*$\varepsilon_{cr,ult}$ [-]	0.001112	1.112E-03
$\varepsilon_{cr,ult}$ [-]	0.002224	2.224E-03
5*$\varepsilon_{cr,ult}$ [-]	0.011118	1.112E-02

(a)

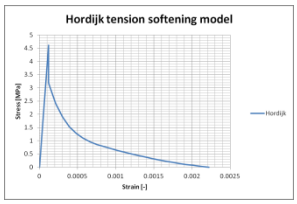

(b)

Main values for principal tensile strain (a) and Hordijk softening diagram (b)

For the three main points selected before, each plot shows the plots of top, bottom, front and lateral surface respectively.

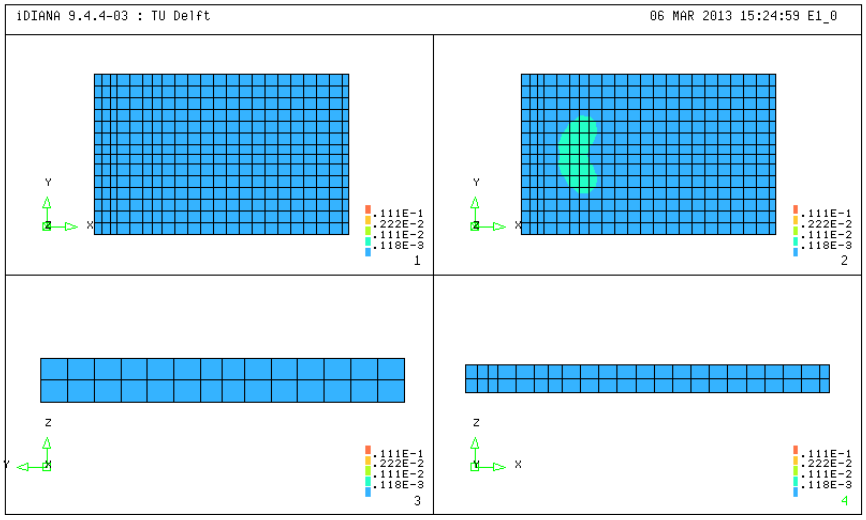

Contour plot of principal tensile strain for 540 kN

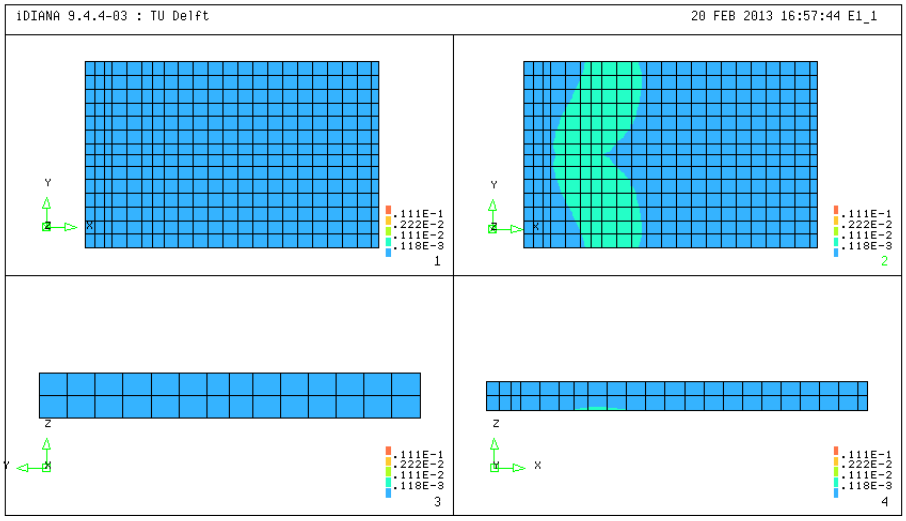

Contour plot of principal tensile strain for 738 kN

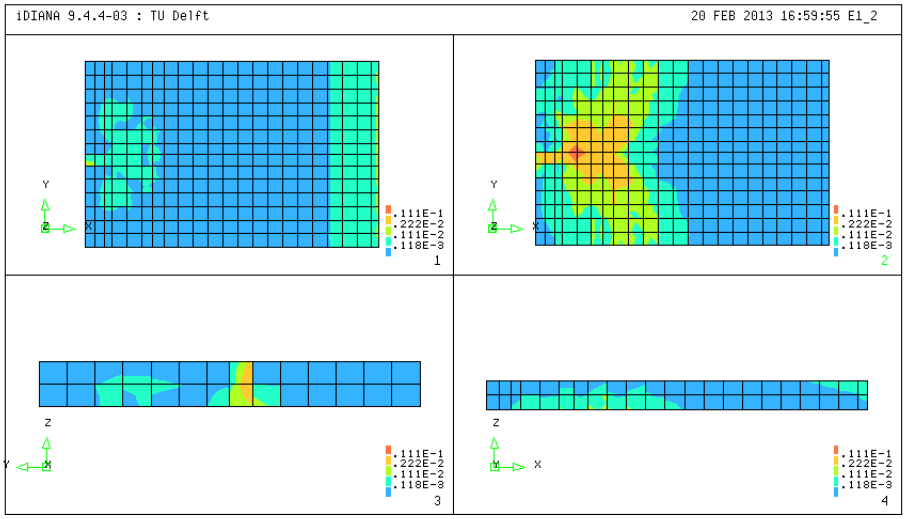

Contour plot of principal tensile strain for 1418 kN (peak)

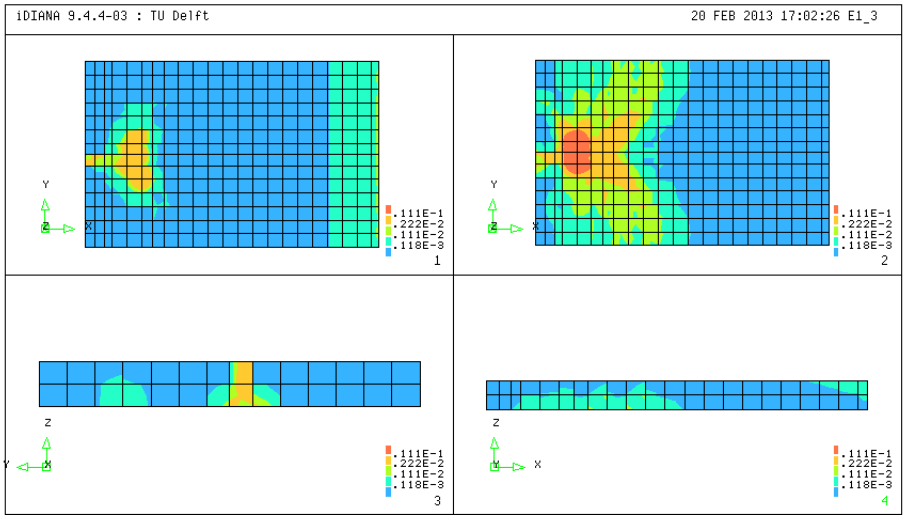

Contour plot of principal tensile strain for 1241 kN (post-peak)

The previous contour plots show that the cracks have origin from the bottom side of the slab, directly below the loading plate, then for higher loads they propagate forward the simple support and transversally, assuming inclined direction as well. After they increase their width under the loading plate.

This particular shape is so called butterfly shape for the characteristic form assumed.

For a load of $1418\ kN$, on the top face, the ultimate elastic strain $\varepsilon_{el,ult}$ is exceeded around the loading plate and a longitudinal crack runs forwards the simple support. Flexural cracks appear on the full clamped side, on the South support. Then more cracks spread forward the North support, while flexural cracks seem to be unchanged on the continuous support (as proofed by the West side plots for the same load values).

A vertical central crack is visible on the frontal side only on the peak point. It run over the whole thickness of the slab, while one other crack spreads from the bottom surface until the half height. The same pattern is visible on the post-peak point.

On the West side a little cracked area is visible from the first main point, then cracks spread from the loading plate forward the simple support principally, investing more than half thickness of the slab.
Now, to have a clearer representation of the direction and of the entity of the fractures, it's useful to have also a vector plot of the same principal tensile strain.
The same surfaces are plotted:

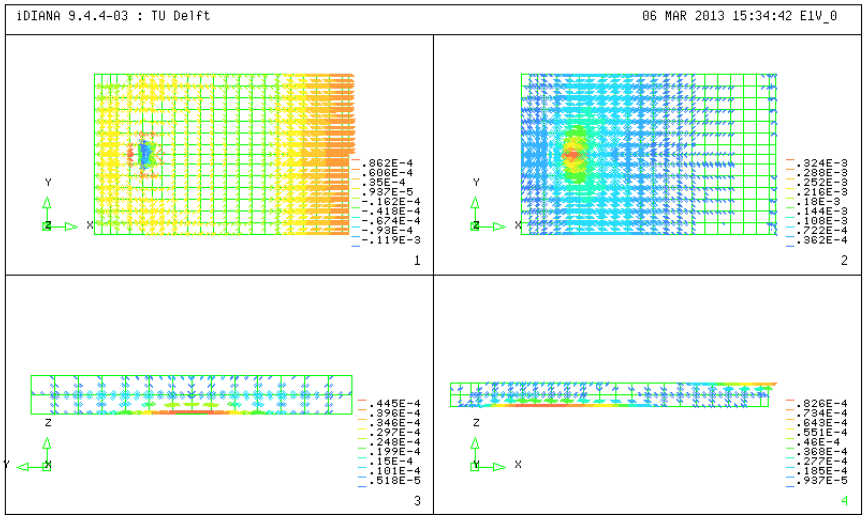

Vector plot of principal tensile strain for 540 kN

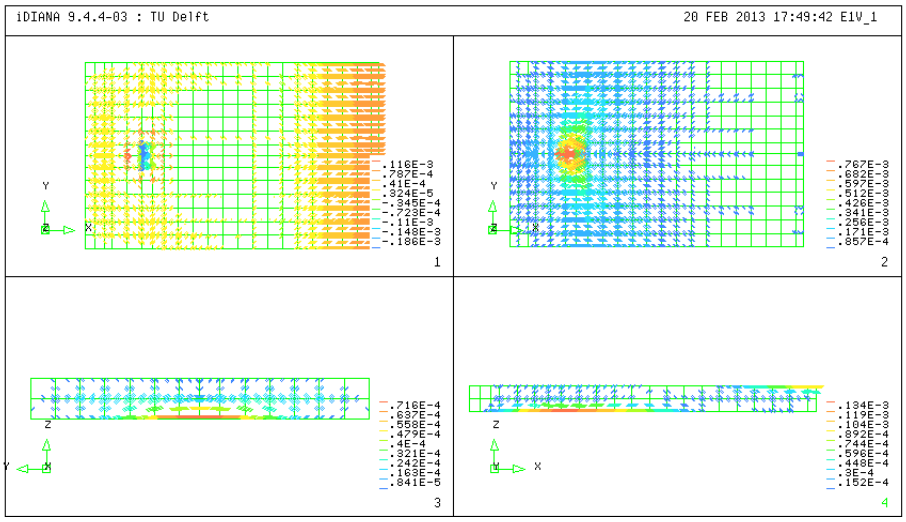

Vector plot of principal tensile strain for 738 kN

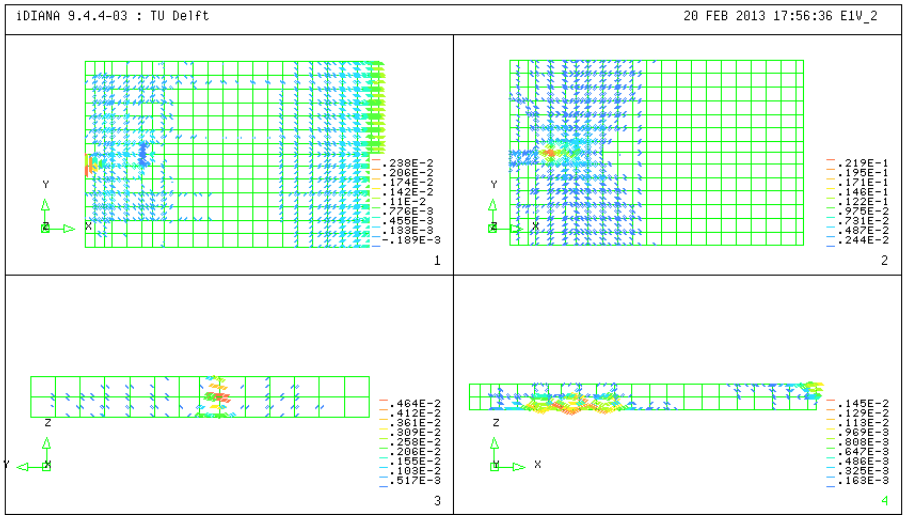

Vector plot of principal tensile strain for 1418 kN (peak)

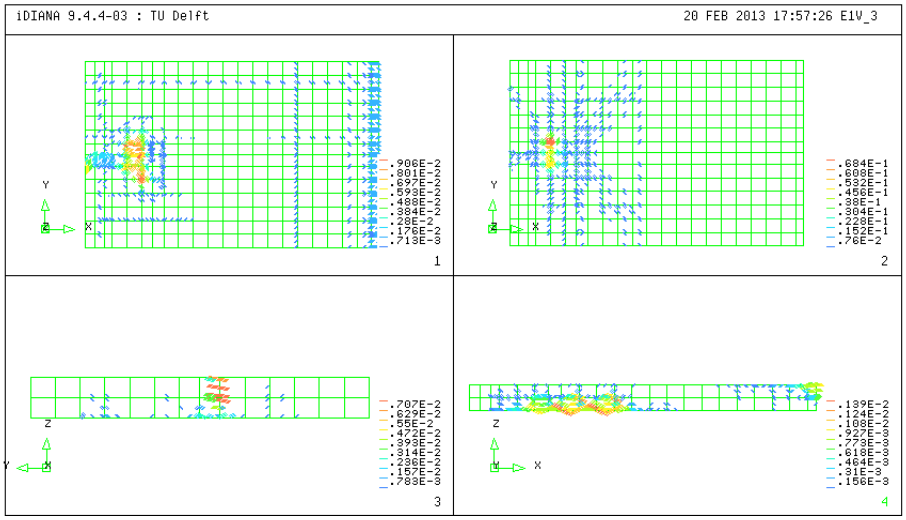

Vector plot of principal tensile strain for 1241 kN (post-peak)

On the first point, at 540 kN, all the strains are lower than the ultimate elastic strain $\varepsilon_{el,ult}$, expect on the bottom surface. Here longitudinal vectors are detected below the load toward the lateral faces: it means a Y-direction crack. Another interesting family of vectors follows the Y-direction, along the longitudinal axis of the slab. It runs from the load position forward the North face.

For a load of 709 kN it can be observed a concentration of strains that superior than $\varepsilon_{el,ult}$ below the loading plate, on the bottom face. It proofs a first formation of cracks in the transversal and in a inclined direction. These strains represent the flexural cracks in the transversal direction. In the laboratory experiment a crack on the East-West direction is observed (crack 2), close to the simple support.

On the frontal face a concentration of strains superior than $\varepsilon_{el,ult}$ are well visible on the middle. Other strains spread following an arc shape above the bottom surface of the slab.

The other interesting zones are located in the lateral West face below the loading plate. Here, strain vectors are visible and they represent the flexural cracks. During the experiment no flexural cracks are detected. The other vectors on the top surface are due to the high tensile stresses from the continuous support and they take place along the South edge.

For this load, no strain vectors exceed the ultimate crack strain $\varepsilon_{cr,ult}$, so no full opened cracks are detected.
For a load of $1418\ kN$, who represents the peak load, the ultimate crack strain is exceed on the top face, along the North edge about $150\ mm$ from the middle of the support. So, it proofs the formation a longitudinal cracks from the simple supports towards the loading plate. This fracture is also visible on the front side of the model, where the strain value is higher, while a vertical crack and an inclined fracture are present, respectively on the right and left side of the frontal face. This is in good agreement with the experimental evidence, where a $0{,}05\ mm$ for a through crack in the middle (crack 5) and $0{,}05\ mm$ for cracks towards the east side, not fully through and starting from the bottom (crack 6), are evidenced. Indeed, the numerical cracks seem to follow a vertical direction, from the bottom surface to the upper one. It has to be noted that the numerical crack tend to spread on the edge of elements.
On the bottom surface, various high deformations start to propagate in inclined directions (see figure below), suggesting an interaction between the transversal flexural cracking pattern and the formation of the shear cracking pattern below the loading plate. Indeed, they show a $0.120E-01 \div 0.220E-01$ of strain, two order higher than the ultimate crack strain $\varepsilon_{cr,ult}$.
So, a full opened crack system arises. This matches with the experiment, in which $3\ mm$ for punching damage at the west side of the bottom face. Through this behavior it can be deduced the development of the shear cracking, since the new fractures grows faster than the previous flexural cracks and their disposition starts to individuate radial paths originating from the loading area.

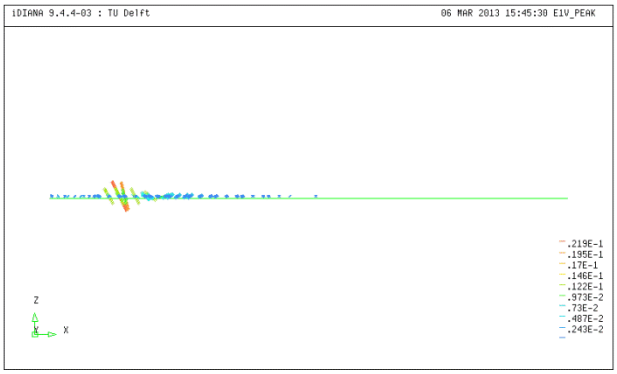

Particular of vector plot of principal tensile strain for 1418 kN (peak) on the bottom surface

Finally, a crack system seems to start from the load position towards the North free edge. This is again in agreement with the experimental results, where $0{,}1\ mm$ for a north-south crack in the middle from the support towards the span, passing the center of the load (crack 1) arises.
On the lateral face the principal strain directions start to be inclined and this can be the beginning of the formation of a strut-and-tie bearing mechanism.
On the centre of the frontal face one can notice a concentration a crack, with a value that is comparable to the others in the bottom side, but it doesn't agree with the experiment test: its width is $1.15\ mm$ against $0.05\ mm$.
However, the most important deformation is the one that takes place on the bottom face, right below the loading plate, increasing the trend observed in the previous step and showing the typical shear behavior that occurs near a peak point. In fact cracks keep on propagating in the bottom face in radial direction, while other different fractures appear directly below the loading plate, very close to

the perimeter of the loading plate and mostly in transversal direction, but also in longitudinal direction.

For a load of 1241 kN (post-peak point) the distribution and the entity of the deformations is lower or equal than the same of the previous observation on the top and lateral side, instead on the bottom and frontal surface they assume higher values.
In specific, on the frontal face the previous vectors now run on all the height of the slab and only two main lateral cracks are shown. This is in partial agreement with the lab test in which a crack arises from the top surface forward the bottom surface, without reaching the bottom surface; instead, lateral cracks start from the bottom and run until the half of the height of the slab. Although their width is well estimated (0.12 mm instead 0.05 mm), the middle crack width is one order higher.
Again, on the top and bottom surface, the inclined vectors have one order higher strain than the flexural cracks. Their disposition evidence a clear truss-tie mechanism starting from the loading plate on the top surface and finishing close to the North support on the bottom surface.
On the lateral side the same vector pattern is well visible as before. The flexural vertical cracks are shown as well: this kind of cracks don't appear during the experimental test.
The presence of the strut-and-tie bearing mechanism and its evolution can be proved through a vector plot of the principal compressive strains, showing clear inclined struts of concrete.

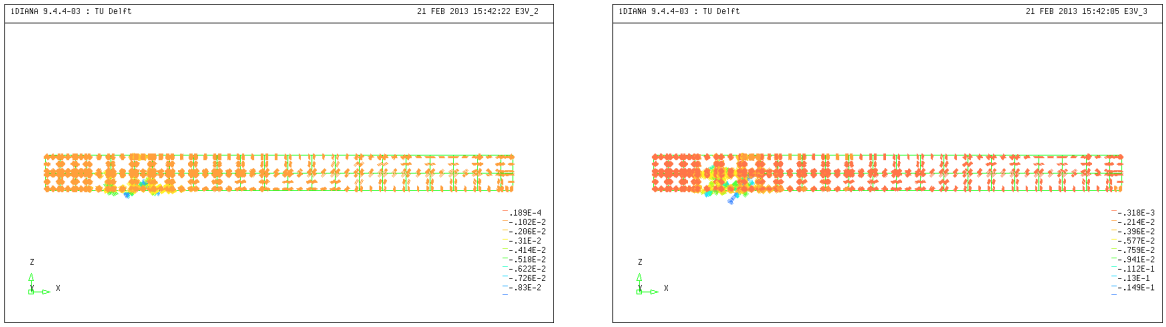

Vector plot of principal compressive strain for peak (left-hand) and post-peak (right-hand)

On the basis of the previous observations about the cracking behavior of the slab, performed using the NLFA, it can be stated that a quite good prediction of the general crack behavior can be obtained. The width of the cracks is well estimated generally, but the best result is the accordance with experiment about the starting point of the fractures and the propagation of the cracking pattern, for what it concerns the directions of flexural and shear cracks. Moreover, in proximity of the peak load, it's also possible to individuate features of shear cracks, like the direction and the rapidity of growing. This can be used as another data to individuate critical sections and to predict the failure mechanism.

8.1.3 Behavior of the reinforcement bars

In order to be sure that the slab does not fail due to its limited flexural capacity, the amount of yielded reinforcement bars is checked. The reinforcement ratio in longitudinal direction is $\rho_l = 0.996\%$. According to *Kinnunen* and *Nylanderthis* would mean that some yielding of the reinforcements could be present in the direct vicinity of the load.

To have an immediate evaluation of the distribution of the stress and of the behavior of the steel bars, contour plots of the principal tensile stresses are presented afterward, referring to a unique yielding tension equal to $540\ MPa$.
Three main points are taken into account and for each one, four plots are shown: σ_{xx} and σ_{yy} for the top rebars, respectively on the upper and on the bottom plot (left hand); σ_{xx} and σ_{yy} for the bottom rebars, respectively on the upper and on the bottom plot (right hand).
Through these contour plots it can be proved the hypothesis of *Kinnunen* and *Nylander*, since the reinforcement steel of the bars has an elastic behavior in most part of the slab and the only area in which one can notice a yielding is the one close to the loading point. In particular for an applied load of around $1420\ kN$, the only bars who yields has a very limited length, below the loading point (red color). At the load of $1240\ kN$, the transversal external bar yields, testifying the opening of the flexural crack at the front face toward the simple support.
No yielding occurs on the other bars.

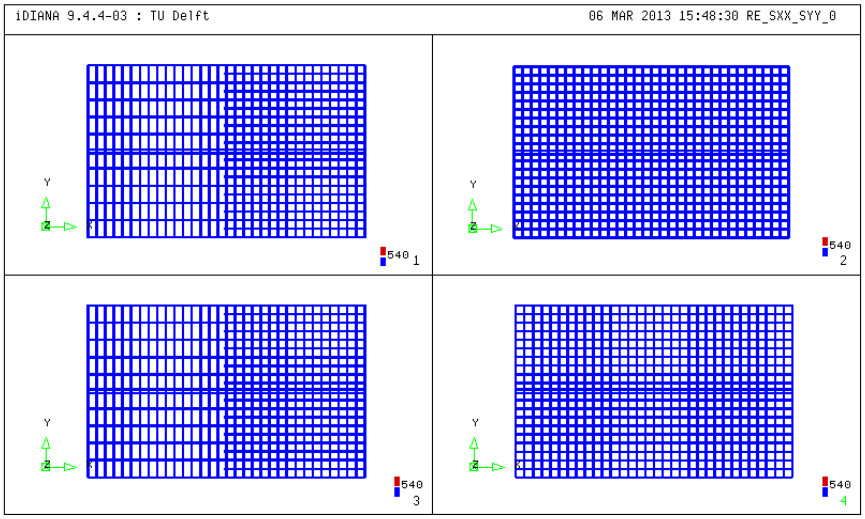

σ_{xx} and σ_{yy} contour plot for top and bottom reinforcement bars for 540 kN

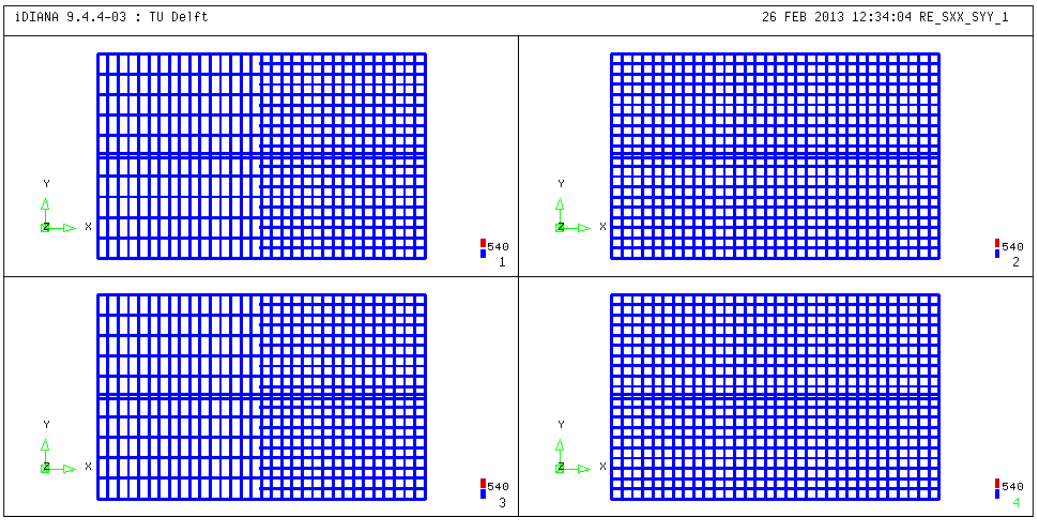

σ_{xx} and σ_{yy} contour plot for top and bottom reinforcement bars for 740 kN

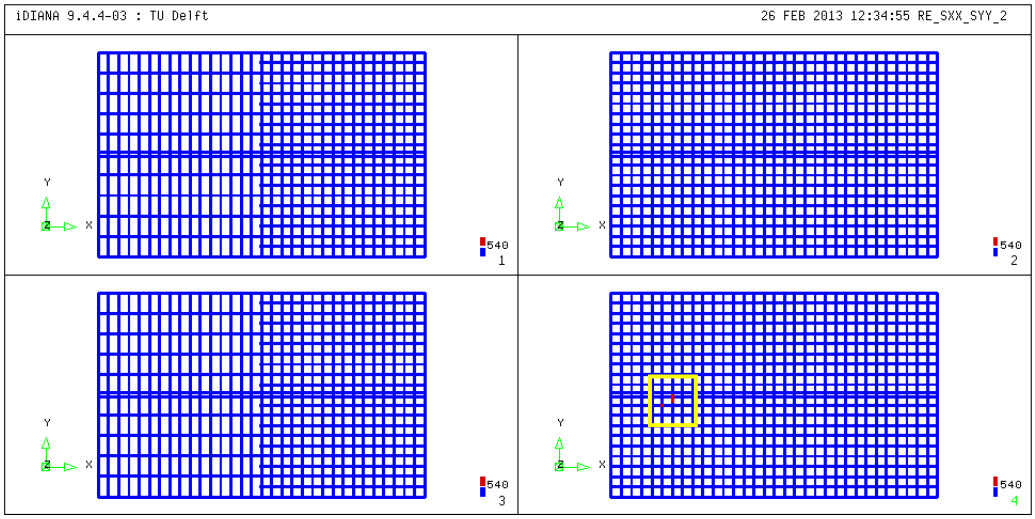

σ_{xx} and σ_{yy} contour plot for top and bottom reinforcement bars for 1420 kN (peak)

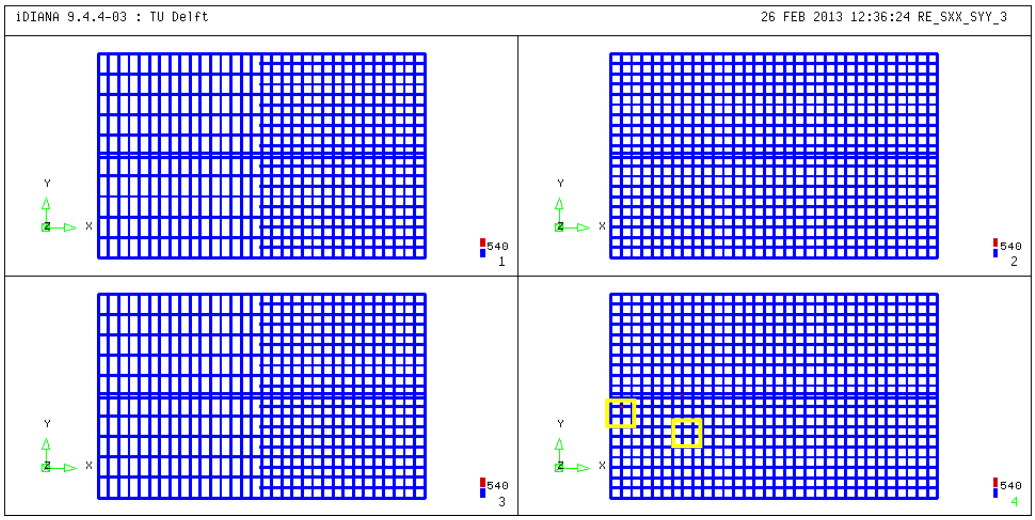

σ_{xx} and σ_{yy} contour plot for top and bottom reinforcement bars for 1240 kN (post-peak)

Adopting the principal tensile stress plots, we can observe the progressive redistribution of the stress inside the reinforcement bars.
For the present plots four points are selected: the first point on the load-displacement graph and the aforementioned three main point.
The first points allows us to discover the tensile stress distribution inside the rebars when the slab works in a ideal linear elastic state. Then, the following plots can show a gradually changing in value, position of the most loaded bars and distribution of the global stresses.
Since we ask for principal tensile stress, only positive values will be shown.

Observing the bottom rebars, the first and the second point confirms the average linear behavior of the slab: the vector plots have the same shape, but different values. Regarding to the bending moment distribution on the slab: the highest values are located below the loading plate, then they spread both in X (forwards the free edges) and in Y direction (forwards about the midspan).
The 1st main point ($\sim 740\ kN$) agrees with the initial crack formation: the most stressed bars are below the loading plate, on the Y-direction, so transversal cracks could be arisen. After, on the peak

point ($\sim 1420\ kN$) a clear concentration of tensile stresses can be found below the loading plate with higher value, close to the yielding stress. Also here, the tensile stress distribution confirms the cracking patterns: a red stress is visible close to the North free edge, on the X direction, matching with crack 5 and crack 6 formation. The highest stresses run in the Y-direction, from the loading plate forwards the lateral free edge, assuming the so called *butterfly shape*, like the cracking patterns do.

On the post-peak point ($\sim 1240\ kN$) the butterfly distribution is more defined than the previous plot, however the tensile stress seems to reduce globally. It could proof the loss of bearing capacity of the whole slab after the peak.

Observing the top rebars, the first point shows a clear concentration of tensile stress on the South side, where the continuous support takes place. The same global distribution can be seen on the 1st main point, but with higher values. Instead, during the peak point, a radical redistribution occurs: the highest stress involves on the longitudinal bars close to the continuous support and on the transversal bars close to the simple support. This agrees with the process of formation of the vertical crack on the middle of the frontal face (crack 5). Unlike the first two plots, now the highest stresses are located close to the North free edge. This trend increases on the post-peak point, where a clear concentration of tensile stress spreads from the North support towards the loading plate. The tensile action around the loading plate can be provided by the "residual" kinematical compatibility between loading plate and concrete. Indeed, though the tangential stiffness of the Teflon layer is really low, for high displacement a non negligible horizontal action can be transferred, producing a plane tensile stress field on the top surface.

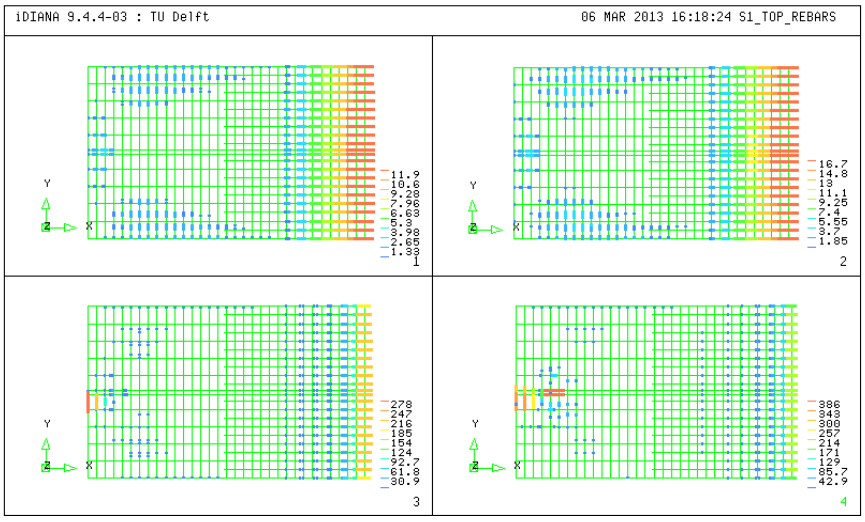

Principal tensile stress for the reinforcement bar on the top surface

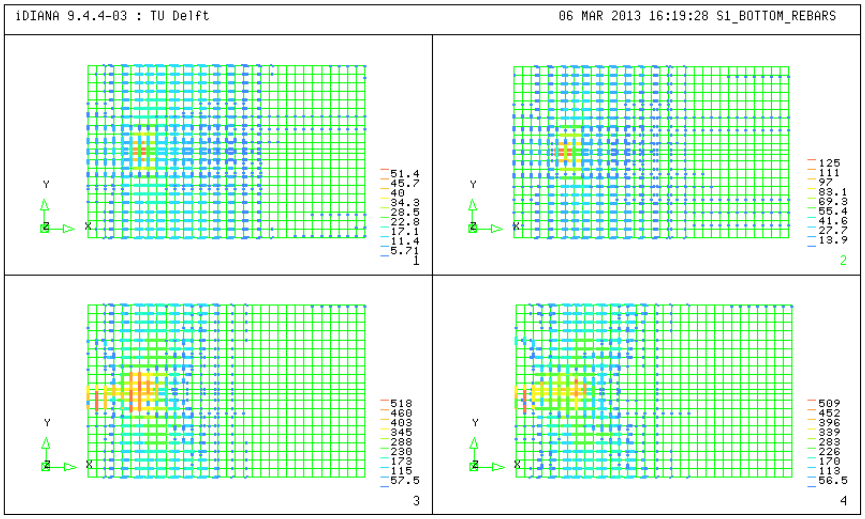

Principal tensile stress for the reinforcement bar on the bottom surface

8.1.5 Compressive behavior of the concrete

In order to verify the elastic state of the concrete for the compressive field, the *principal compressive stress* feature is investigated through a contour plot on four surfaces, for the three main selected before.
Two main values are adopted:

- $0.50 f_{cc} = -29.88\, MPa$;
- $1.00 f_{cc} = -59.76\, MPa$.

Since, the compressive stress has conventionally a negative value, the green color shows the parts with a lower principal stress than $f_{cc} = -59.76\, MPa$. Instead the blue color proofs the part who exceed this reference value.

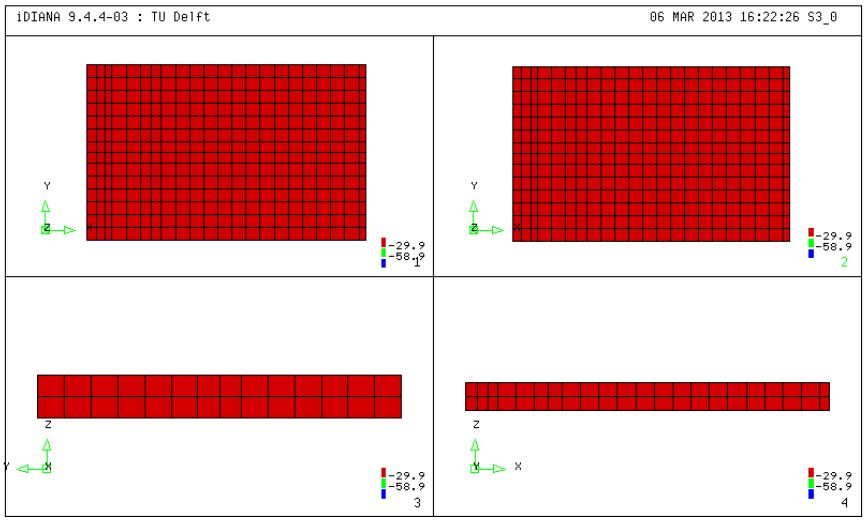

Contour plot of principal compressive stress for 540 kN

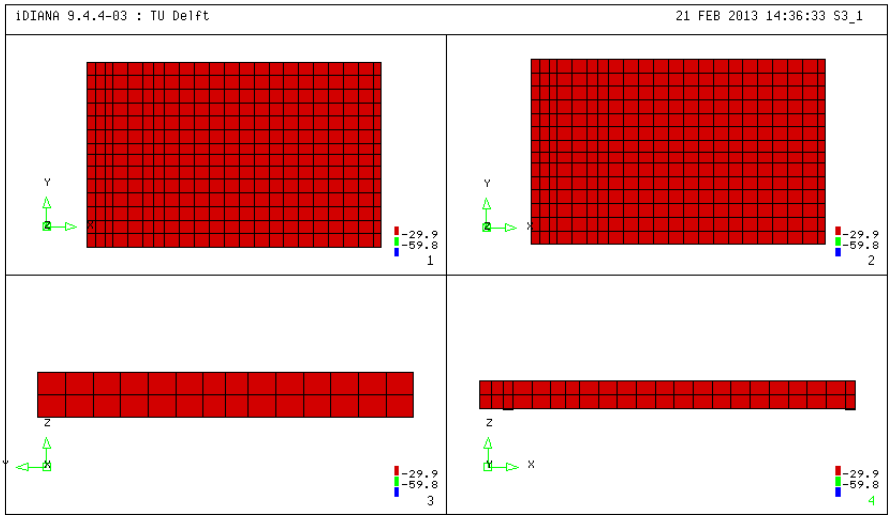

Contour plot of principal compressive stress for 738 kN

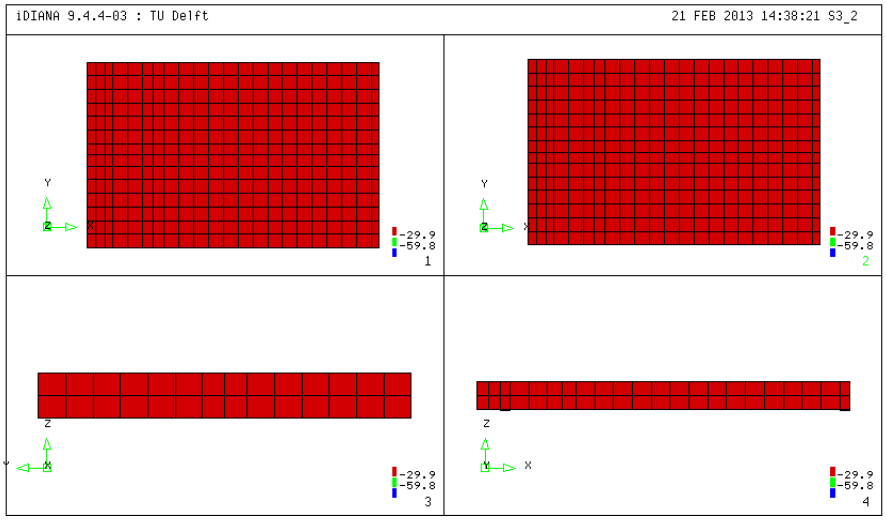

Contour plot of principal compressive stress for 1418 kN (peak)

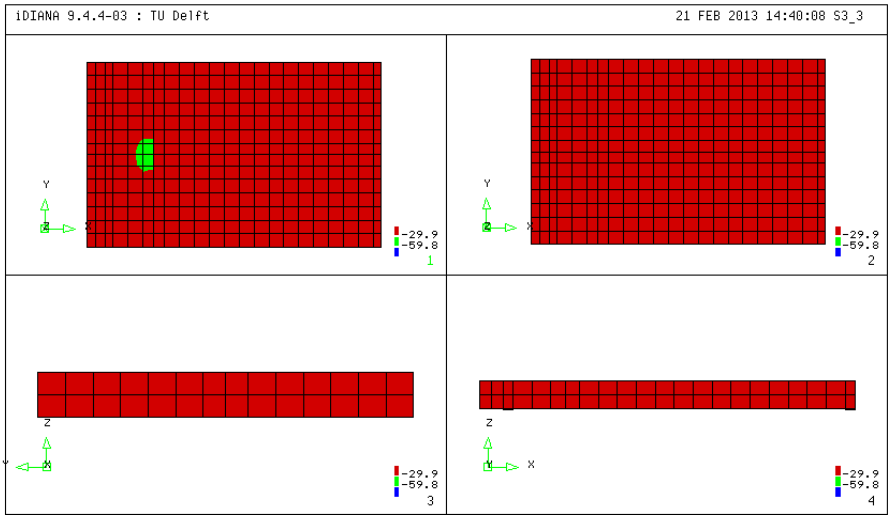

Contour plot of principal compressive stress for 1241 kN (post-peak)

As shown by the previous plots, the principal compressive strain never exceed the compressive strength of the concrete, not even the half. Only below the loading plate a green presents a stress between $29.9 \div 59.8\ MPa$ of modulus, during the post-peak point.
So, thanks to these plots, we can demostrate that the assumption of a linear elastic concrete in compressione is adequate to describe the behavior of the conglomerate. This is is strengthened by the fact that also the 50% of f_{cc} is never reached on high volume of elements inside the slab.

8.1.5 Failure mechanism of the slab

Based on the load-rotation curve for the tests performed by *Kinnunen* and *Nylander*, punching failure occurs before yielding of the entire slab reinforcement in case of intermediate reinforcement ratios. However, since the load is located close to the continuous support the truncated cone around the concentrated load cannot fully develop and the punching shear capacity is significantly improved. From the contour plots of the bottom face it becomes clear that the principal tensile strains are less developed at the side of the continuous support. The following picture shows the distribution of the principal tensile strain at the peak load and after the peak load. The scale of the contour plots is held constant in order to see the development of the tensile strain area:

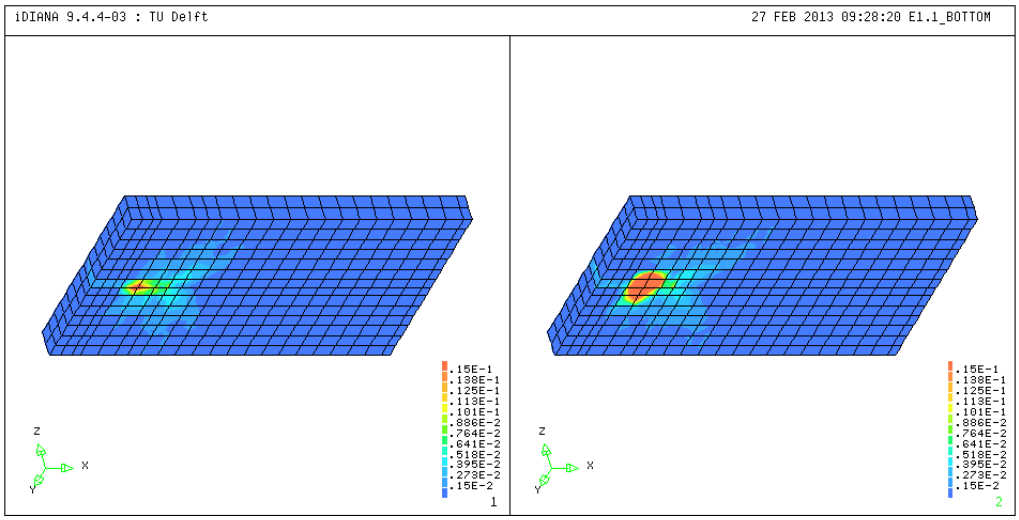

Contour plot of the principal tensile strain on the bottom face on the peak (left-hand) and post-peak points (right-hand)

From this contour plot of the principal tensile strains on the bottom face of the slab it can be shown the evolution of the strains: after the Peak Load, a sudden discontinuity between the distribution and the values of the principal tensile strains is very evident and demonstrates that the slab has been completely subjected to failure.
However, from the previous plots it is still hard to discover whether the slabs fails due to punching shear or by wide beam shear failure. No clear critical diagonal cracks have been observed around the concentrated load, that would suggest pure punching failure.
Furthermore, no critical section across the entire width of the slab was visible, suggesting wide beam failure.
In order to better show the cracking pattern and try to understand the relation bewteen it and the ultimate elastic strain, an useful tool can be adopted: the principal crack strain. It's implemented in

the lastest version of *iDiana* and allows to show the cracks througt disc plot. So, the attention is focused on the last main point, after the peak, and the principal crack strain will be shown using disc plot and it will be compared with the principal tensile strain distribution. This allows us to better understan the correlation between these two features, as shown in the following pictures:

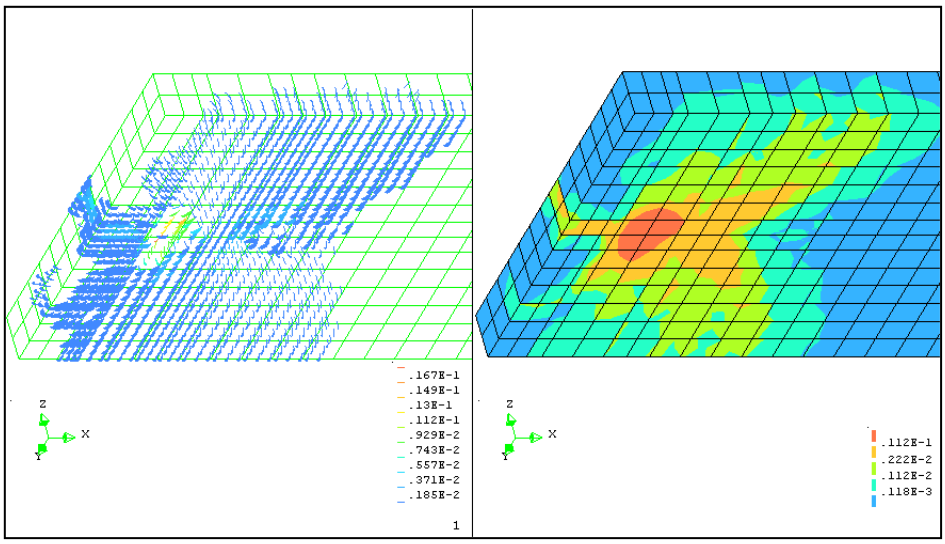

Principla crack strain disc plot (left-hand)
and principal tensile strain contour plot (right-hand) on the post-peak point

A useful attribute to better discover cracking pattern inside the model is the *principal normal crack strain* $\varepsilon^{nn}{}_{cr,1}$ feature.
The best results can be obtained by adopting as reference two limit crack strains:

- $\varepsilon^{nn}{}_{cr,min} = w_{cr,min}/h = \frac{0.05}{165} = 0.303E-03;$
- $\varepsilon^{nn}{}_{cr,aver} = w_{cr,aver}/h = \frac{1}{165} = 0.606E-02.$

The range is held constant for the peak and post-failure point marked on the graph. By plotting the contour plot with ten levels we can discover the develpment of the cracking patterns on the slab:

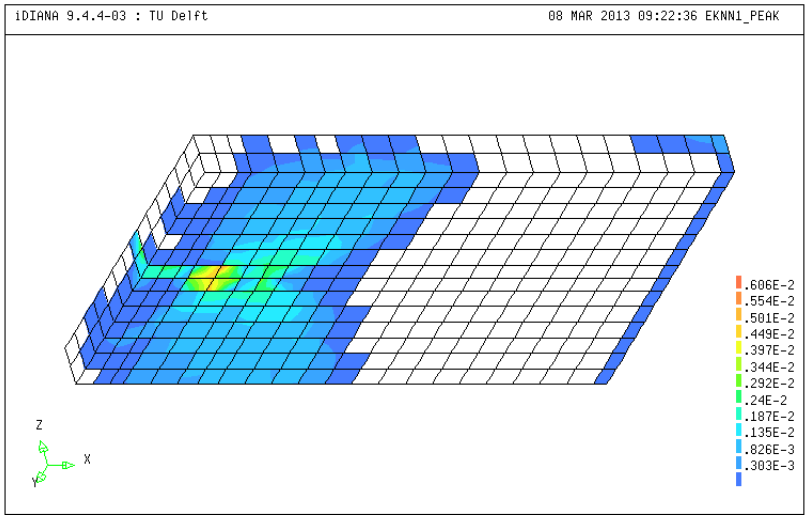

Contour plot of the principal normal crack strain on the bottom face on the peak

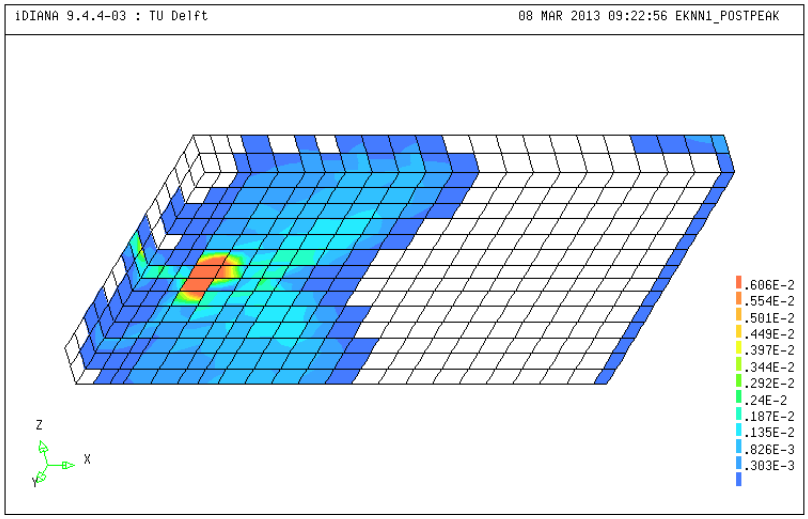

Contour plot of the principal normal crack strain on the bottom face on the post-peak

Between peak load and post-failure point, a strong increasing and developing of the principal normal crack strain is observed between North support and load position, on the bottom surface. Two clear blue strips develop from the load toward the lateral free edge, following radial direction.

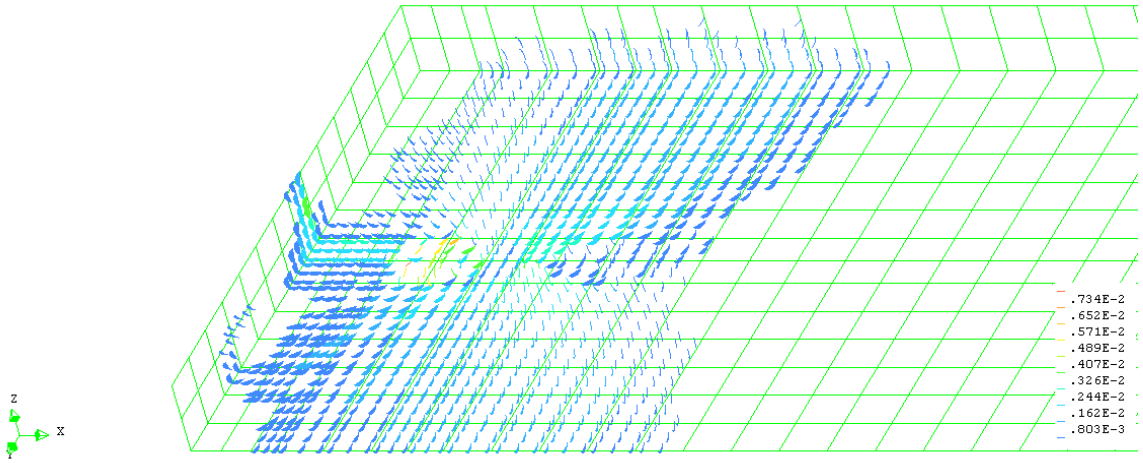

Disc plot of the principal normal crack strain on the bottom face on the peak

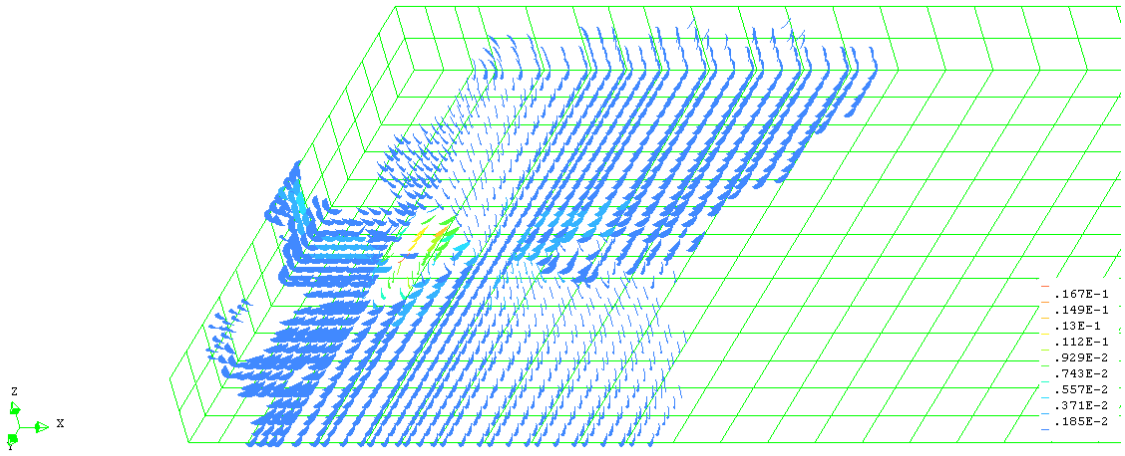

Disc plot of the principal normal crack strain on the bottom face on the post-peak

A new way to detect cracks is here provided:

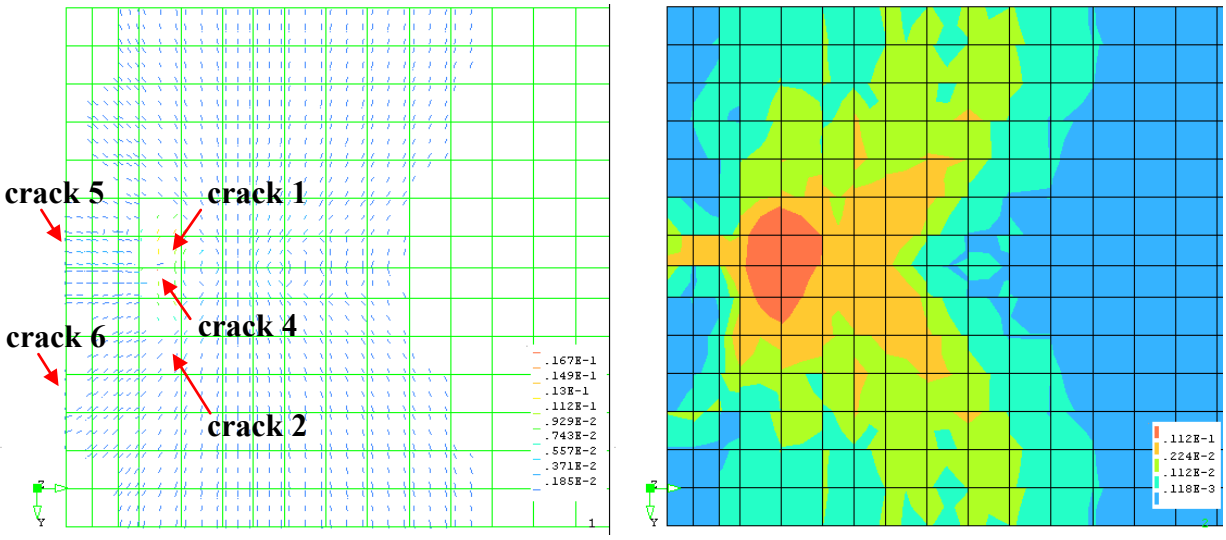

Contour plot of the principal tensile strain on the bottom face on the post-peak (right-hand and principal crack strain (left-hand)

The cross-comparison between these plots helps to discover the effective cracking patterns on the slab. It shows a quite agreement with the experimental evidence: crack1, crack 2, crack 3, crack 5 and crack 6 are displayed. There is no evidence related to crack 3 and crack 1 does not pass the load (as seen on the specimen). The following picture helps to focus the concept:

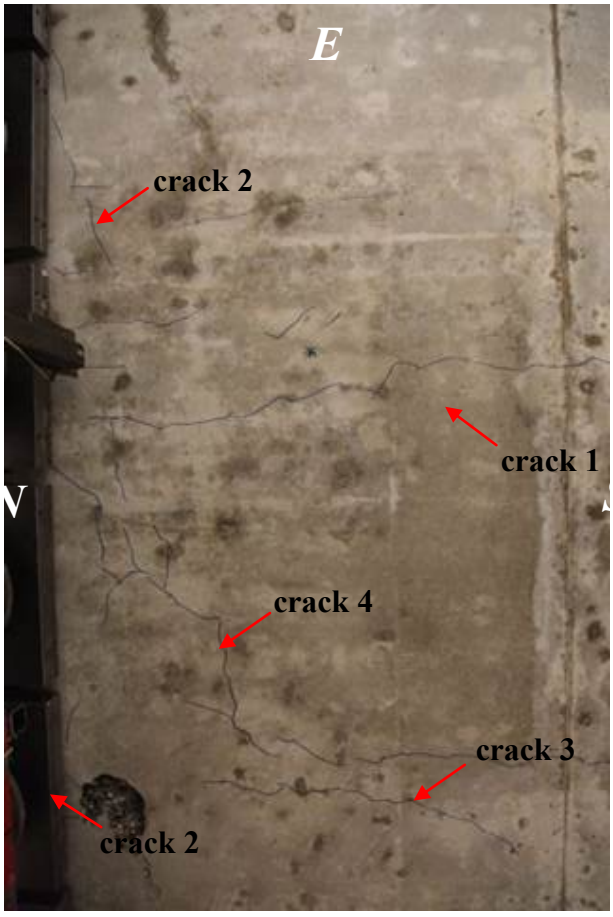

Cracking patterns detected during the experimental test

Regarding to the crack width, crack1, crack 2 and 5 are displayed adopting the $0.185E-02 \div 0.371E-02$ range. Just applying the formula, we can get the maximum width for the cracks:

$$w_{cr,max} = \varepsilon^{nn}{}_{cr} \cdot h$$

we get:

$$w_{cr,min\,-\,1,2,5} = 0.185E-02 \cdot 165\ mm = 0.30\ mm$$
$$w_{cr,max\,-\,1,2,5} = 0.371E-02 \cdot 165\ mm = 0.61\ mm$$

A comparison can be done looking to the following table:

Specimen	F_{line} [kN]	F_{punt} [kN]	w_{max} [mm]	Class.	Where?
S25T1	0	Fail	0.05	*crack 5*	front face - trhough crack in the middle
			0.05	*crack 6*	front face - crack close to E side, from botton, not fully trough
			0.10	*crack 1*	bottom face - NS crack from support into span, passing the load
			0.25	*crack 2*	bottom face - EW close to the support
			3.00	*crack 4*	bottom face - punching at W
			0.20	*crack 3*	bottom face - NS crack at W-side at 48 cm from free edge

Crack width detected for slab S25T1 during the experimental test

The aforementioned cracks hold to a $0.05 \div 0.25\ mm$ range, regards to the width. Considering the present value as the maximum one, the prediction for crack 2 seems to be satisfactory, while crack 5 and crack 6 are overestimated. Regarding to crack 4 (punching shear crack), it seems to hold to the $0.112E-01 \div 0.149E-01$ crack strain range. It equals to $1.85 \div 2.45\ mm$ of width. It's in good agreement with what is seen during the test. So, a good agreement in terms of cracking behaviour and crack widths is detected.
Underlining the found cracks, these plots seems to prefer a two-way failure than a one-way crisis, though the two events could influences mutually.

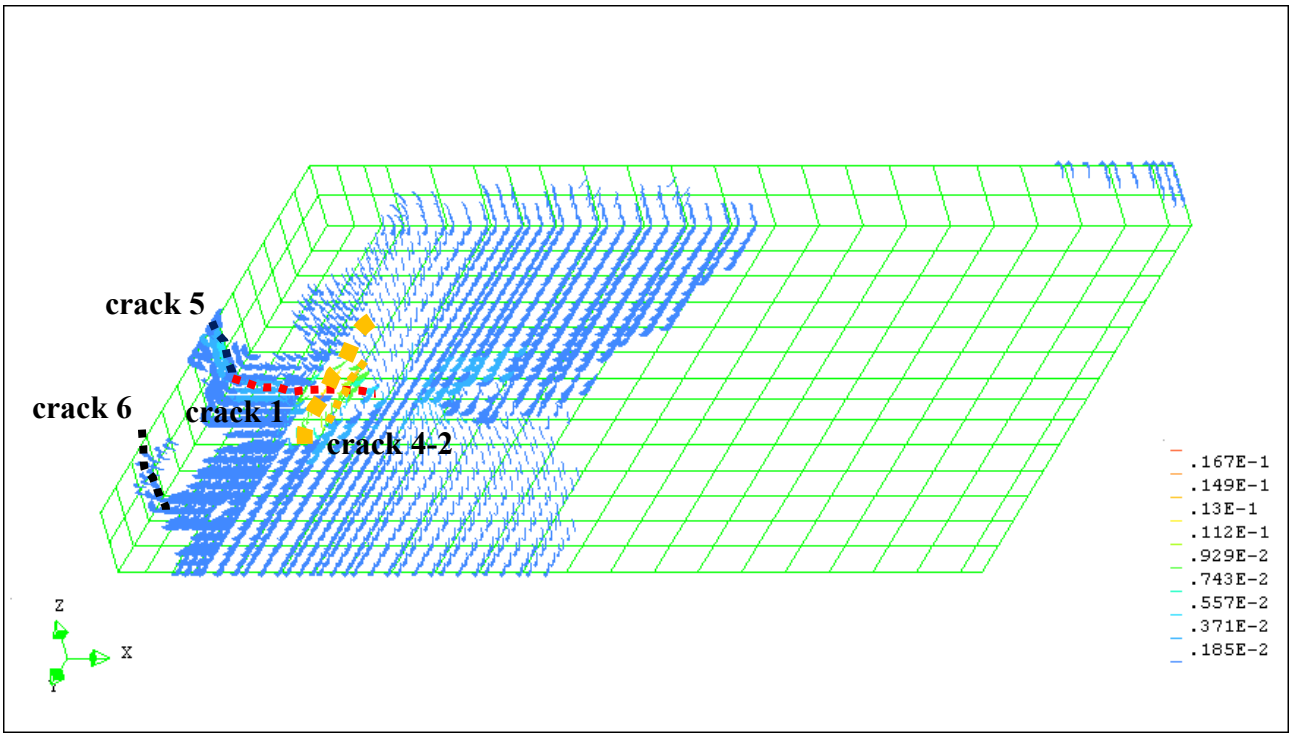

Main cracks plot on the bottom surface

The fact that neither punching shear nor wide beam shear failure occurs can be visualized by the deformed mesh shape.

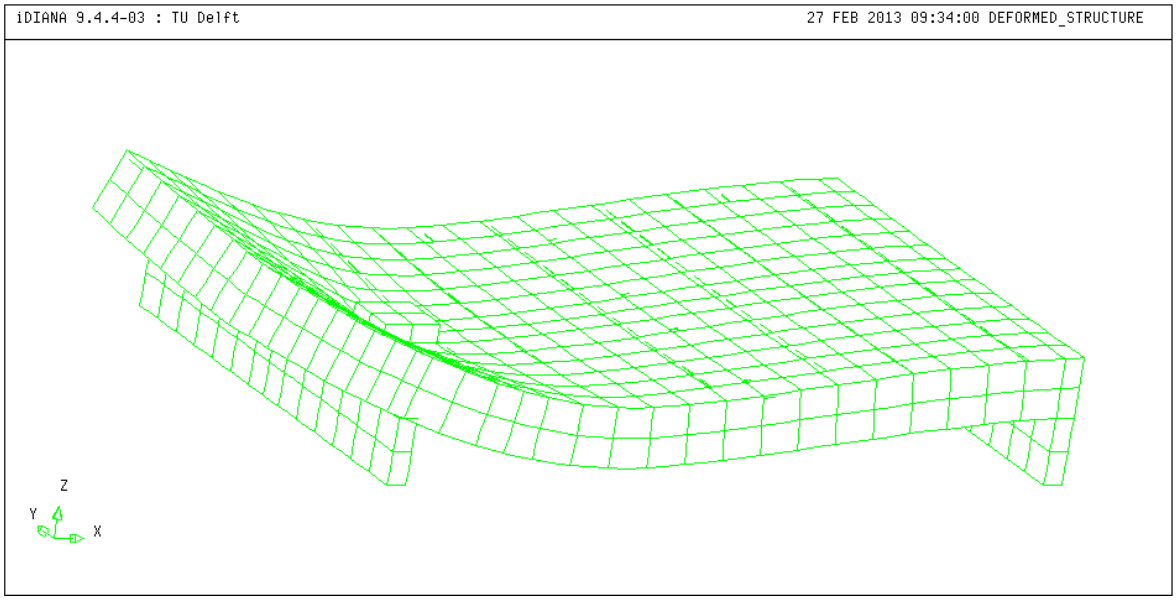

Deformed structure at the peak load: global overview

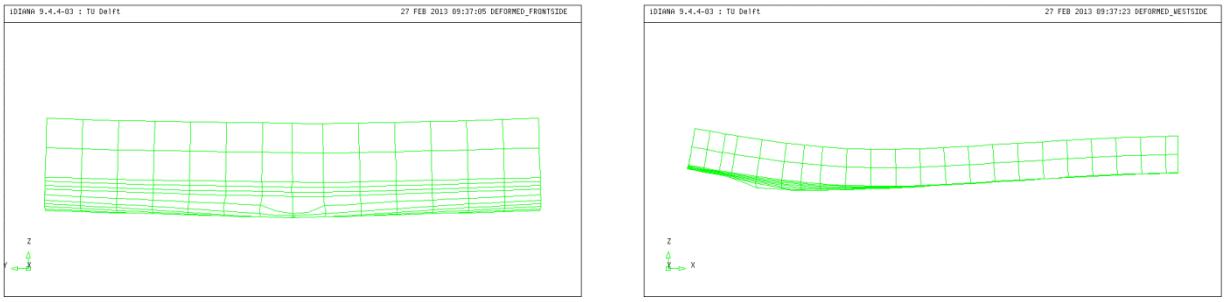

(a) *(b)*

Deformed structure at the peak load: (a) North front side and (b) West lateral side

Hence, it seems most likely that a combination of both caused the concrete slab to fail. The same conclusion was drawn for the experiment: the three-dimensional nature of the problem and the combined flexural and diagonal cracks, make it incredibly difficult to determine the failure mechanism. However, the global cracking behavior predicted by the NLF-Analysis seemed to correspond well with the observations made during the experiment.

8.2 Finer mesh: 3x3 partial model

As seen before, the total model seems to require a higher fracture energy to reach the same Peak Load of the experimental test. So, lower values are adopted also for this test on the *3x3 partial model*.

By adopting a $G_f = 0.240\ Nmm/mm^2$ and $0.250\ Nmm/mm^2$ the load-displacement diagrams result:

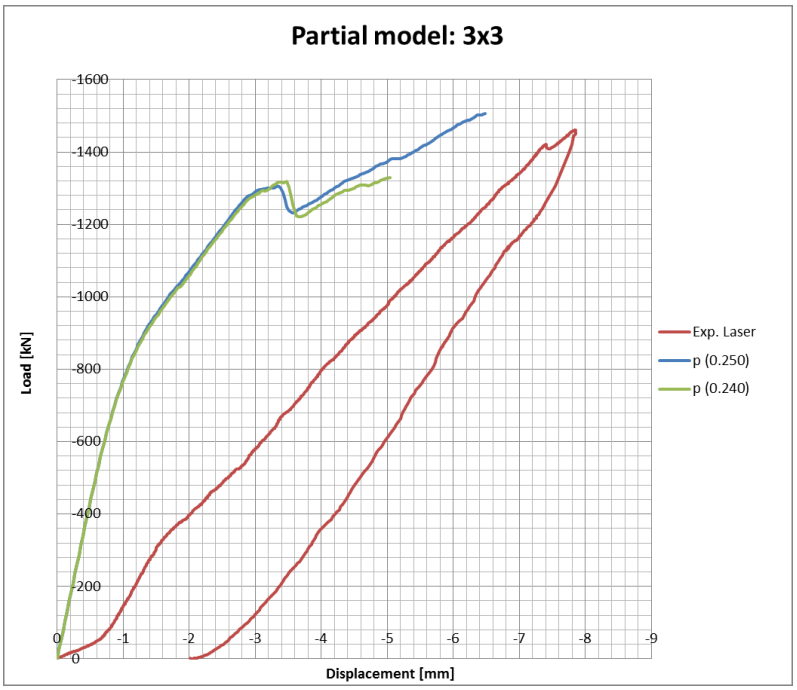

Force-displacement graph for 3x3 partial model for different G_f values

The best agreement is reached with the following features:

- tensile fracture energy: $G_f = 0.250\ N/mm$;
- numerical crack bandwidth: $h = 95\ mm$;
- normal felt interface stiffness: $k_{n,f} = 15.20\ N/mm^3$;
- normal Teflon interface stiffness: $k_{n,T} = 500\ N/mm^3$;
- integration scheme: default for all the finite elements (see previous paragraphs);
- maximum number of iteration equal to 25.

Due to the high computational time, as will be shown in the following paragraphs, the number of iteration for each step is reduced from 50 to 25, otherwise the needed time becomes too high.
The felt is has a linear behavior.
The comparison between the best NLF-analyses and experimental test is shown in the following image:

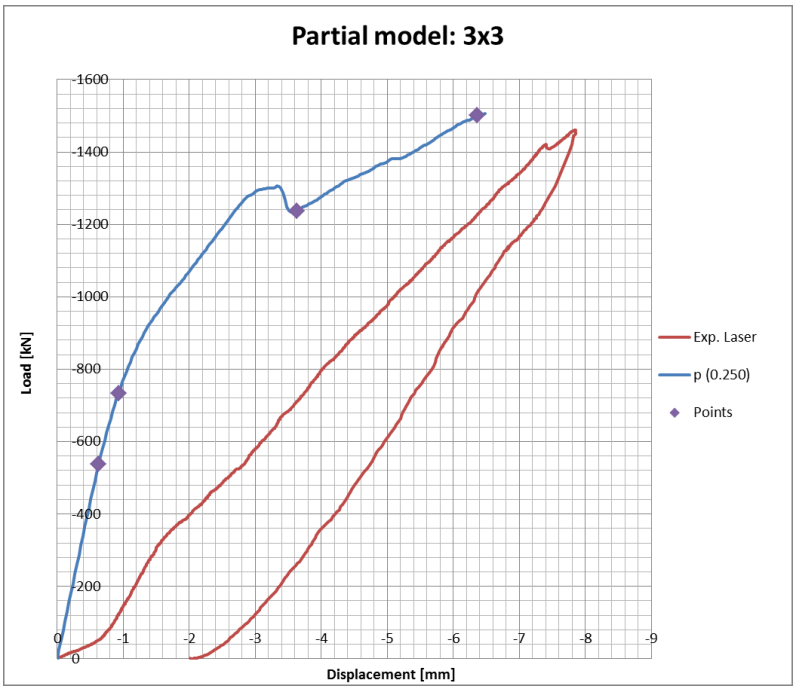

Force-displacement graph for 3x3 partial model

Here, the experimental peak-load is quite matched; the response remains still stiffer and the divergence occurs before a clear post-peak behavior could start. It is visible a strong decay and followed by a subsequent lower stiffness, around $-3.50\ mm$ of displacement. However, it seems the slab finds a different way to bear the load.
Looking at the previous diagrams for a lower value of the fracture energy G_f, one can discover the great sensitivity of the analysis related to this parameter: for a variation of $\Delta G_f = 0.10\ Nmm/mm^2$ the gap between the "final" displacement reached is around $1.50\ mm$, showing a response much weaker. Instead, the global trend seems to be not influenced in the same way, at least since the decay of strength does not occur.
For reason of required computational time no more analysis are run after these two attempts.
Assuming the last point as the peak point, the numerical peak values are:

- peak load: $1506.40\ kN$;
- peak displacement: $6.48\ mm$.

instead of:

- experimental peak load: $1460.62\ kN$ for a variation of $\sim +3\%$;
- experimental peak displacement: $7.84\ mm$ for a variation of $\sim -17\%$.

It has to be noted that this denser mesh produces the same approximation in terms of peak load, but a better prediction of the peak-displacement, while for what regards the first main point the same displacement is selected ($0.93\ mm$) and the correspondent loads match each other ($\sim 730\ kN$).

Regarding to the convergence behavior, the analyses practically can no more satisfy the criteria after the 43th step, as shown by the following plot:

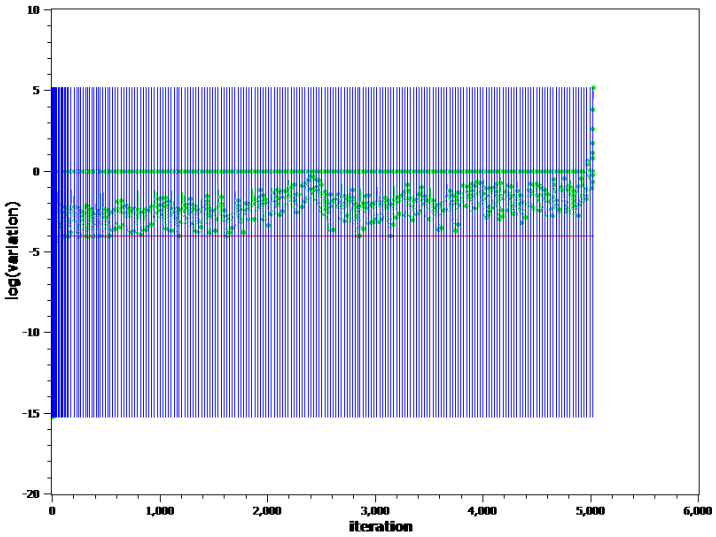

Convergence trend for 3x3 partial model: points above the red line mean no reached convergence

The analyses uses about 5000 iteration for all the process, the half with respect to the *2x2* model. The lower amount of iterations is related to the smaller number required for each step.
Unlike the previous mesh, the three main points are selected on different positions on the load-displacement diagram: (1) since a post-peak behavior is not shown by the analyses, (2) in order to better understand what happens inside the slab after the sudden decay. The points are:

- *point 1:* $(0.63\ mm;\ 538\ kN) \sim 30\%F_{max}$;
- *point 2:* $(0.93\ mm;\ 733\ kN) \sim 50\%F_{max}$;
- *point 3:* $(3.63\ mm;\ 1237\ kN) \sim 80\%F_{max}$;
- *point 4:* $(6.36\ mm;\ 1501\ kN) = F_{max}$;

They are shown in previous plot; the main output will be exposed in the next paragraphs.

8.2.1 Redistribution capacity:

On the following image, four pictures of the felt reactions are shown by adopting a vector plot. They prove the redistribution of the load from the slab to the support, since the action on the felt is equal to the one on the support beam for vertical balance.
The pictures show the plot about first step and three main points.

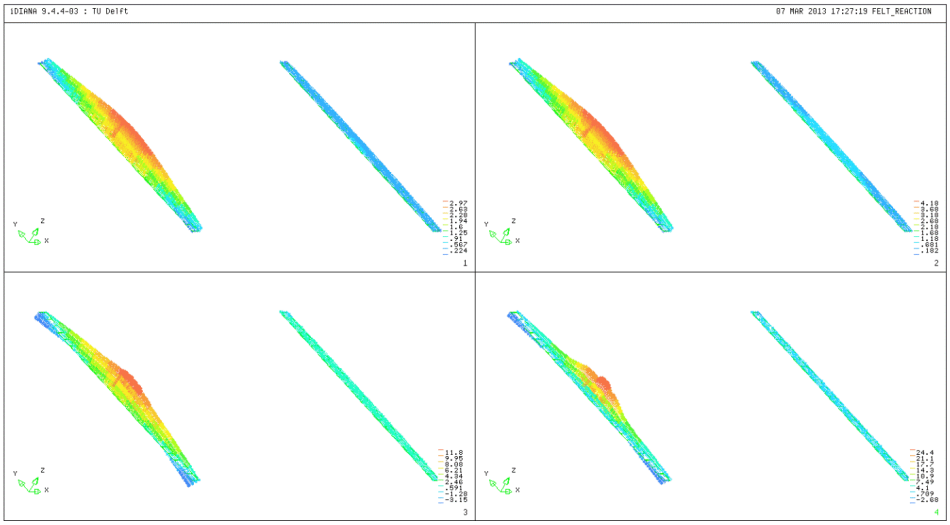

Vector plot of felt reaction [MPa] for the main points

By observing the previous vector plot of the interface traction, first of all a more defined trend of the felt interface can be discovered with respect to the previous mesh. From the outset the tractions present a triangular shape and all the width of the support contributes to the bearing capacity. Until the 2nd main point ($\sim 730\ kN$) the slab generally presents a linear behavior (like in previous 2x2 analyses), increasing the load a clear redistribution of the tractions takes place: a progressive concentration of load on the middle of the interface is visible with increasing of the load, on the Y-direction. The same happens on the X-direction until the peak point, where a strong concentration occurs on a little area on the symmetry axis.
In other words, they become bigger in the central part of the North support, while they decrease in proximity of the right and left edges. Then they reach a tensile value: on the third main point (decay point) a tensile reaction is already present. It has got a not negligible value ($3.15\ MPa$) and it start to arise from the lateral wings of the felt layer. It proofs the slab bending and the reduction of the contact area on the North support. So, theoretically we can say the outer parts don't contribute anymore to the bearing capacity of the slab.
Comparing to the previous coarser mesh, on the North support the distribution of stresses on the felt seems to be stronger as phenomenon, since the compressed area of the interface layer is smaller and the maximum tension is $24.40\ MPa$ of modulus, instead $12.90\ MPa$. Instead, inside the linear field the same values are detected for both the meshes: the maximum compression reaches $4.20\ MPa$ and no tensile stress is present. So looking to these plots, we can say that the meshes work in the same way for this aspect until now.
Moreover, the shape seen for the present mesh agrees with the reaction plot of the felt on the post-peak point of the 2x2 mesh. It could proof the sudden failure of the slab (3x3 mesh) and then the subsequent divergence of the analyses.

By plotting the part of interface in a compressive state, they are shown with red color (values higher than $0\ MPa$ - *compression*). It can be observed that the loading angle assumes the same values found before in terms of angles, the effective width of the active zone of the support slightly changes from the previous and it equal to $b_{eff} = 2120\ mm$. However, for the denser mesh, a bigger surface of interface becomes inactive, i.e. it starts to react with tensile tension, on the external edge (see the blue tongue on the peak point).

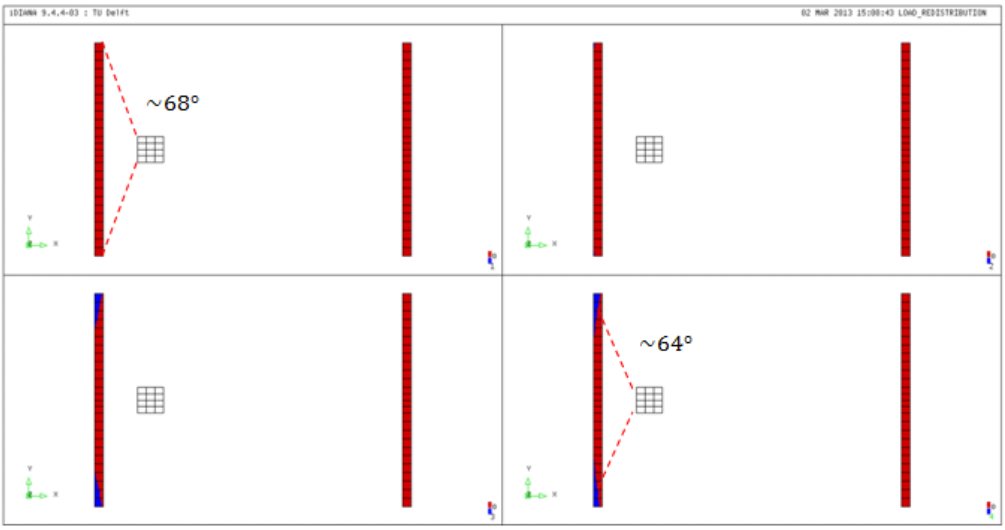

Effective width due to the load spreading on the felt layer

Once again the effective width calculated by the Dutch Code was considerably underestimated.

Cracking behavior of the slab

In order to investigate the development of the cracking under an increasing load, contour and vector plot of the pricinpal tensile strain are used. Taking into account four points on the softening diagram calculated for a fracture energy $G_f = 0.250\ N/mm$ and $h = 95\ m$.

$\varepsilon_{el,ult.}$ [-]	0.000118	1.184E-04
0,5*$\varepsilon_{cr,ult}$ [-]	0.001463	1.463E-03
$\varepsilon_{cr,ult}$ [-]	0.002926	2.926E-03
5*$\varepsilon_{cr,ult}$ [-]	0.014628	1.463E-02

(a)

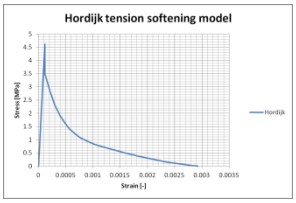

(b)

Main values for principal tensile strain (a) and Hordijk softening diagram (b)

For the four main points selected before, each plot shows the plots of top, bottom, front and lateral surface respectively.

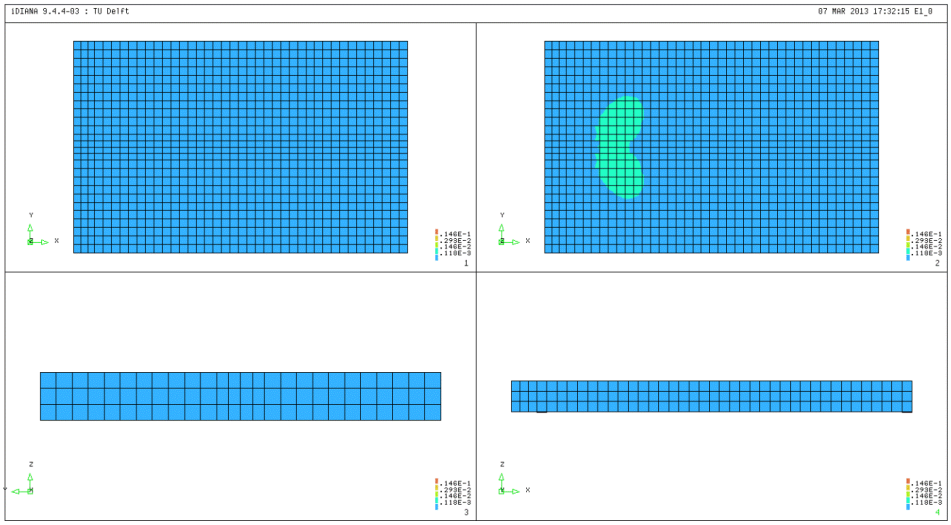

Contour plot of principal tensile strain for 538 kN

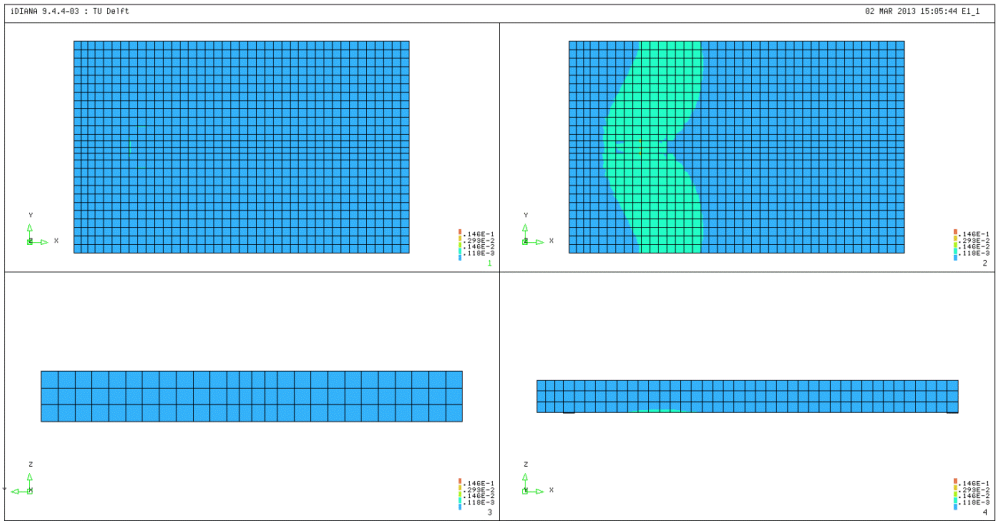

Contour plot of principal tensile strain for 733 kN

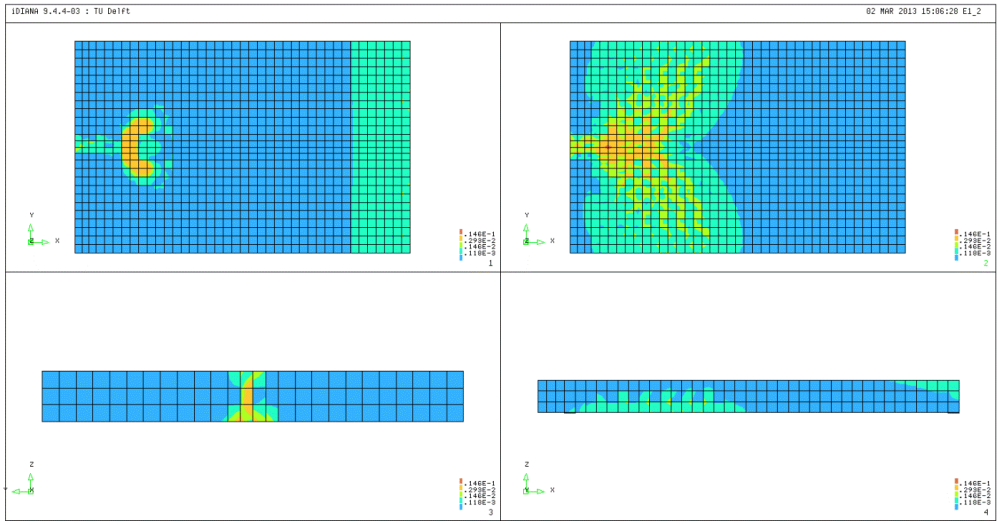

Contour plot of principal tensile strain for 1237 kN (decay)

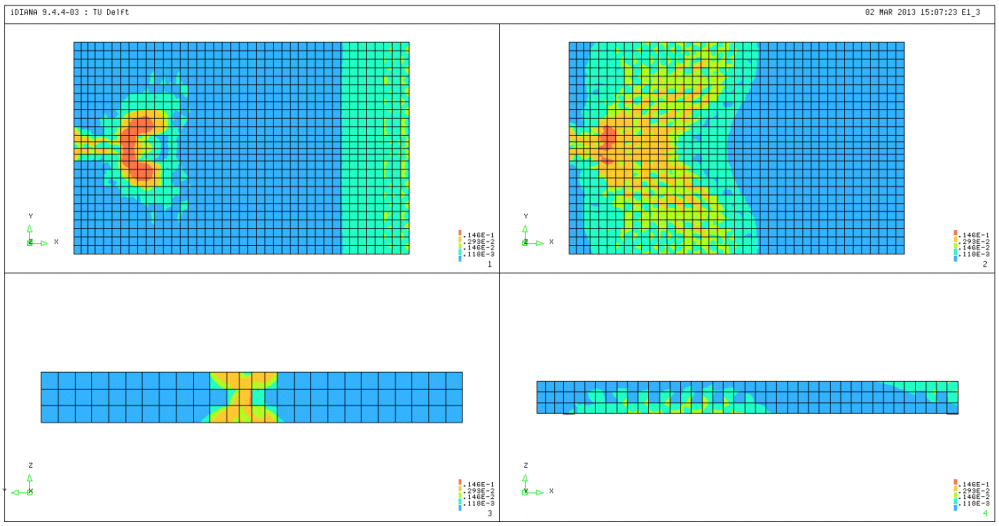

Contour plot of principal tensile strain for 1501 kN (peak)

The previous contour plots show that the cracks have origin from the bottom side of the slab once again, with the characteristic butterfly shape as seen before located below the loading plate. The future development follows a different pattern: for higher loads areas with a principal tensile strain higher than $0.50\varepsilon_{cr,ult}$ run from the load to the lateral free edges and toward the North support, without reaching the frontal face. Their shape is well defined and could underline the formation of: (1) a radial cracking system spreading below the load and (2) longitudinal cracks due to the flexural component. The big difference denoted between the plots during the $730\ kN$ of load, and the ones with the higher value of $1237\ kN$, can explain the abrupt and strong decay of the structural response of the slab in terms of load-displacement. The sudden formation of these two crack patterns could sensibly reduce the stiffness and the way in which the slab bears the applied load. This takes a further confirmation thanks to the felt reaction plot, which shows a different footprint of the slab on the North interface. For the load of $1501\ kN$ (peak load) the crack patterns globally increase: few radial cracks and the longitudinal fractures with strain higher than $\varepsilon_{cr,ult}$ reach the lateral edges and the frontal North face respectively. Moreover, some transversal cracks appear, starting from the loading plate and running forward the East and West side. The red area, who means very opened cracks ($5.0\varepsilon_{cr,ult}$), arises between the loading plate and the North support. It has a bigger extension than the previous one and results more oriented on the transversal direction. It could mean a compressed strut formation.

The second main point allows to show the formation of flexural vertical cracks on the continuous support, on the top surface. Thus, the ultimate crack strain $\varepsilon_{cr,ult}$ is exceed around the loading plate: a arc shaped area spreads around it for about 180 degree. Longitudinal cracks seem to appear also on the top face, during this step. For higher load ($1501\ kN$) every crack patterns increase: (1) a red area now surrounds the loading plate, assuming the shape of the previous one, (2) the longitudinal cracks run from the loading plate toward the frontal face and (3) flexural cracks in the Y-direction arise on the clamped side. This last pattern is more underlined on the finer mesh.

The aforementioned fracture patterns are detected also on the frontal face. On the second main point a first vertical crack runs from the bottom of the slab forward the half of the thickness. It increases on the peak point when it occupies the whole height of the slab. Unlike the coarse mesh, here no other cracks arise on the frontal face.

Regarding to the lateral face, one can see the gradual development of vertical cracks from the bottom toward less of half height of the slab, starting from the load of 730 kN. Here, the radial cracks that reach the lateral edges are underlined on the peak point.
Finally, we can note how the cracking patterns are better provided by the finer mesh: unlike the previous coarse mesh, the crack pattern remains well described without merging in one or more macro-cracked area.

To have a clearer representation of the direction and of the entity of the fractures, it's useful to show also a vector plot of the same principal tensile strain ε_1.
The same surfaces are plotted:

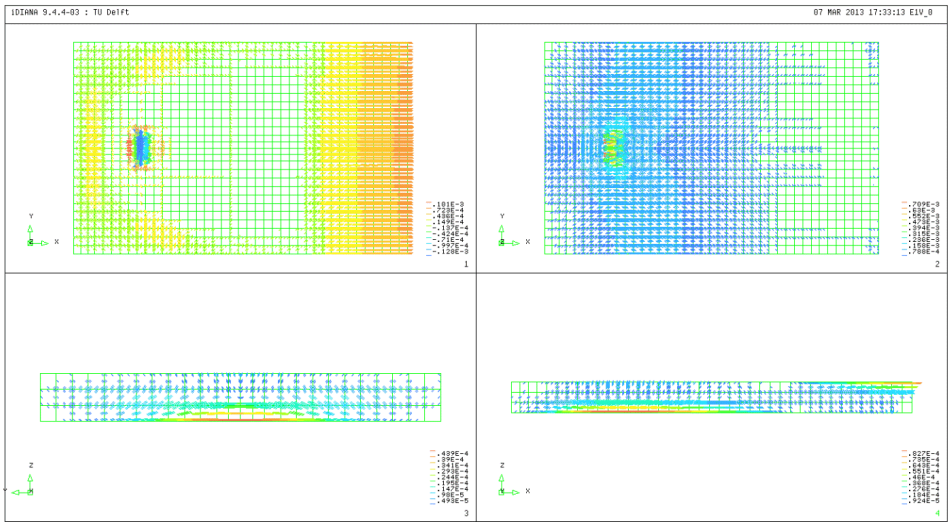

Vector plot of principal tensile strain for 538 kN

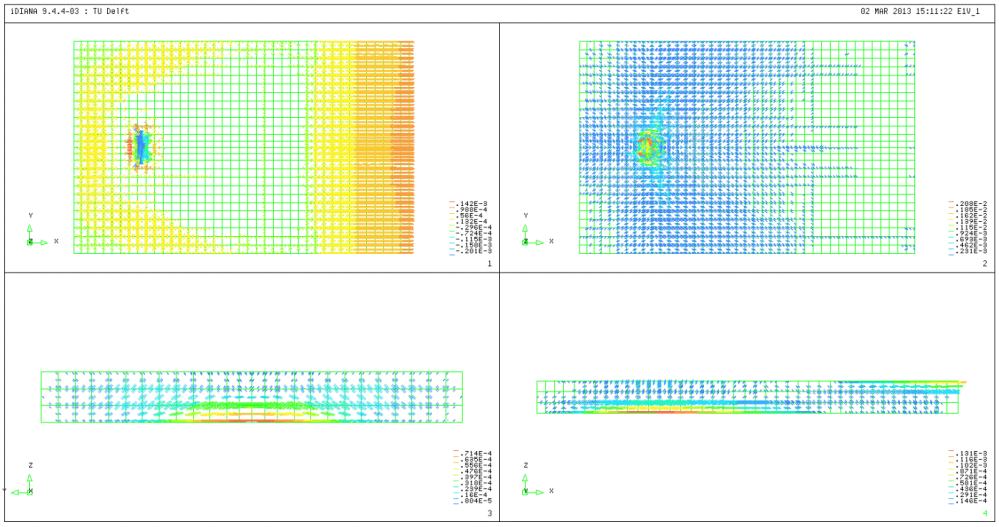

Vector plot of principal tensile strain for 733 kN

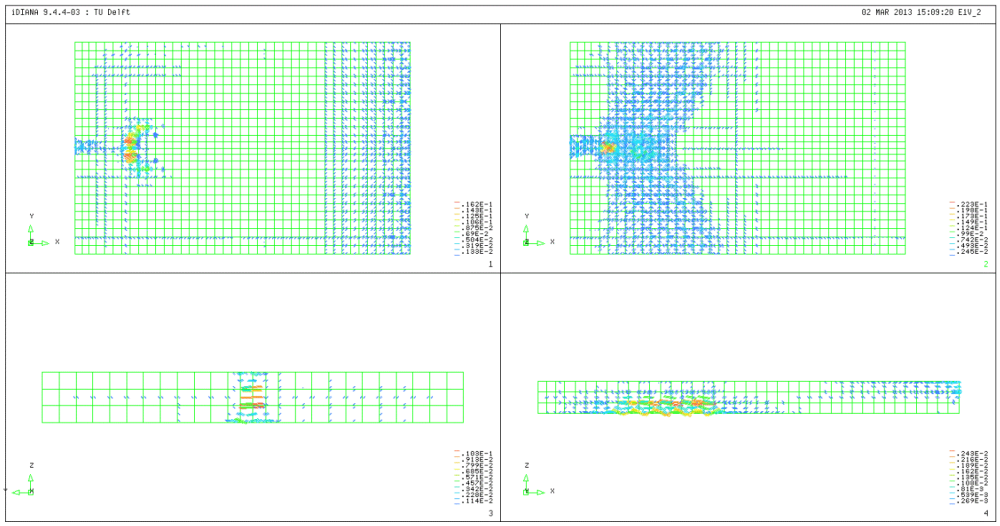

Vector plot of principal tensile strain for 1237 kN (decay)

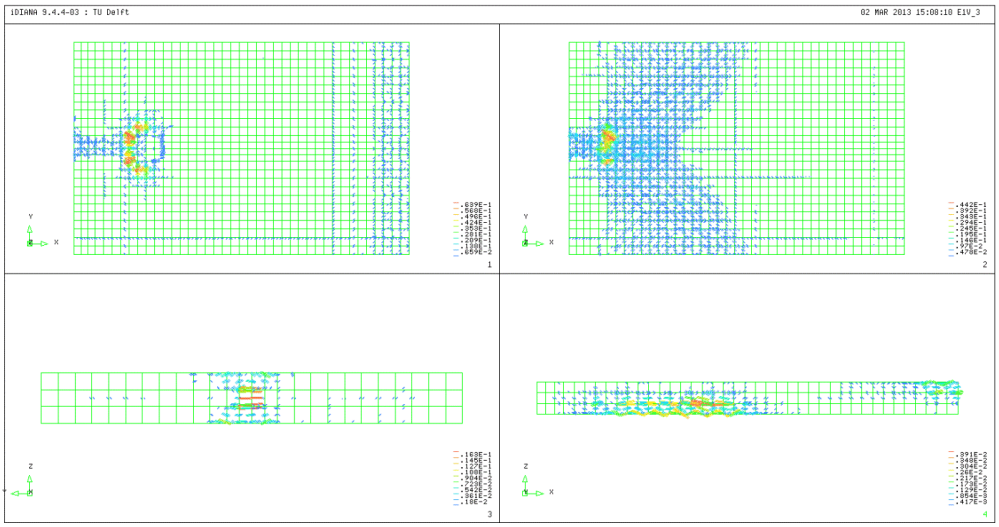

Vector plot of principal tensile strain for 1501 kN (peak)

For the first main point of 538 kN the strain vectors exceed the ultimate elastic strain only on the bottom surface. As detected, the highest values are related to vectors in the X-direction, below the load. It means a transversal crack arises. No clear longitudinal crack can be observed since now.

For a load of 733 kN it can be observed a concentration of strains that superior than $\varepsilon_{el,ult}$ below the loading plate and on the clamped side, on the top face. The former vectors are in sub-vertical direction and the latter are horizontal.

On the bottom surface two families of cracks with higher magnitude than $0.5\varepsilon_{ult,cr}$ are detected. The highest value is found in the longitudinal direction, below the loading plate, that means a transversal crack stars to arise under the load, due to the flexural behavior of the slab. The second family with a lower value is concentrated under the load position, along the Y-direction and testify the arising of a longitudinal crack. It's due to the bending behavior as well.

On the frontal face the ultimate elastic strain is not reached and the vectors distribution has a more defined arc shaped than the one seen before with a coarse mesh.

On the lateral side the $\varepsilon_{el,ult}$ is exceeded only on the tensile side, below the load and it proofs the beginning of a vertical cracking due to the dominant flexural behavior of the slab in this step.

Here, the entity of the strain range is bigger: the maximum strain is $0.208E-02$ against $0.767E-03$. It means that the cracks have a higher width, however these values are largely lower than $\varepsilon_{cr,ult}$ and the fractures are still not complete opened.
On the frontal face strains have a lower value than $\varepsilon_{el,ult}$: the maximum presents a magnitude around 50% of it and arise on the middle, close to the bottom surface. Other strains spread following an arc shape above the bottom surface of the slab, as seen on the previous mesh.
The other interesting zones are located in the lateral West face below the loading plate. Here, strain vectors are visible and they represent the flexural cracks: their modulus equals the ultimate elastic strain $\varepsilon_{el,ult}$. During the experiment no flexural cracks are detected. The other vectors on the top surface are due to the high tensile stresses from the continuous support and they take place along the South edge. For this load, no strain vectors exceed the ultimate crack strain $\varepsilon_{cr,ult}$, so no full opened cracks are still well detected.
For a load of $1237\ kN$, who represents the decay point, a strong redistribution on the strain vectors occurs. The inclined vectors present the highest magnitude and they seem to grow faster than the other ones. It means that the shear cracking is going to govern the structural response of the slab. This is underlined on the top and bottom surface, where high tensile strains are detected below the load and close to the North support respectively. It's also proofed by the fact that tensile strains on the clamped side on the top surface and in the X- and Y-direction have a blue color representation.
Also on the frontal face the strain vectors change their line-up: now them all are concentrated on the middle and the maximum strain appears on half thickness with a magnitude close to $5.0\varepsilon_{cr,ult}$, while littler vectors run on the right side.
On the lateral side strain vectors higher than $\varepsilon_{cr,ult}$ start to arise from the bottom surface and occupy only the first third of the thickness.
On the peak point the same trend is detected on the top and bottom surface, especially on the lower layer where the inclined vectors increase in number and modulus. Here the maximum strain is about $0.341E-01 \div 0.442E-01$ who means a width of $3.00 \div 4.00\ mm$. Since the nature and the disposition of these cracks (compressed concrete strut), they can be associated with the punching fracture found in the experimental test with $3.00\ mm$ of width (crack 3). The arc disposition detected on the top face, around the loading plate, it's not shown on the bottom surface.
On the frontal face the middle crack increases its width: a $0.163E-01 \div 0.542E-02$ strain range is observed. It involves in a $1.50 \div 0.50\ mm$ wide vertical crack. Its opening is overestimated, since the correspondent experimental fracture (crack 5) is $0.05\ mm$ wide. A better prediction is given for the lateral cracks: $0.361E-02$ means $0.34\ mm$ instead the $0.05\ mm$ opening related to crack 6. However, the plot shows vertical cracks from the bottom, not fully through the height of the slab. It's in good agreement with the experimental evidence.
On the lateral side $0.30E-02$ strain is diffused: $0.30\ mm$ opened cracks should be visible, but no evidence has been found during the test.

The strut-and-tie bearing mechanism is well shown by this plot:

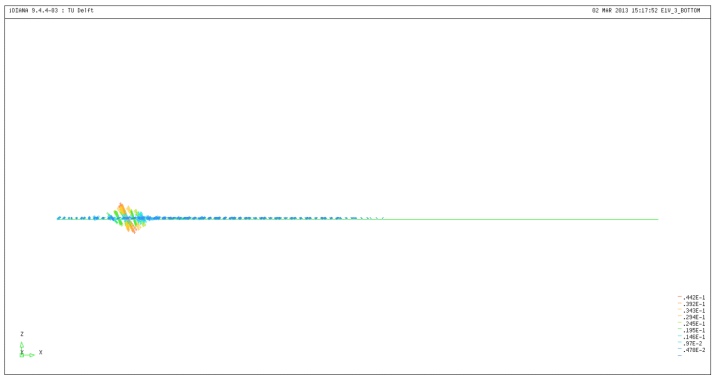

Particular of vector plot of principal tensile strain for 1418 kN (peak) on the bottom surface

The highest strains are located along an inclined direction, among the North support and the load, on the bottom surface.
Their evolution can be proved through a vector plot of the *principal compressive strains* ε_3, showing clear inclined struts of concrete with an increasing modulus (from $0.8E-03$ to $0.13E-01$).

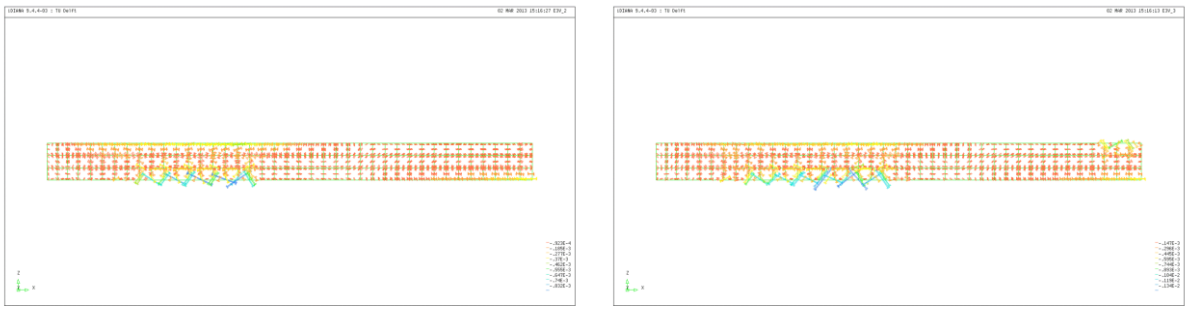

Vector plot of principal compressive strain for peak (left-hand) and post-peak (right-hand)

On the basis of the previous observations about the cracking behavior of the slab, performed using the NLFA, it can be stated that a quite good prediction of the general crack behavior can be obtained. The width of the cracks is well estimated generally, but the best result is the accordance with experiment about the starting point of the fractures and the propagation of the cracking pattern, for what it concerns the directions of flexural and shear cracks. Moreover, in proximity of the peak load, it's also possible to individuate features of shear cracks, like the direction and the rapidity of growing. This can be used as another data to individuate critical sections and to predict the failure mechanism.

8.2.3 Behavior of the reinforcement bars

Contour plots of the principal tensile stresses are presented afterward, referring to a unique yielding tension equal to $540\ MPa$, as adopted before.
The previous three main points are taken into account and for each one, four plots are shown: σ_{xx} and σ_{yy} for the top rebars, respectively on the upper and on the bottom plot (left hand); σ_{xx} and σ_{yy} for the bottom rebars, respectively on the upper and on the bottom plot (right hand).

No yielding is detected for a load of 733 kN, so once again it is proved that the slab works mostly in an elastic field until now. Instead, the plot during the decay point (1237 kN) shows the starting of the yielding inside the rebars on the bottom surface, below the load and on the North edge. So, the sudden formation of cracks below the loading plate brings to yield few transversal bars. This could mean that a important longitudinal crack takes place on the bottom surface and viewing to the position of them, the fracture could run along the span, from the North edge toward the midspan of the slab.
At the failure (1501 kN) yielding occurs on all the two layers, so both on the top and on the bottom rebars. On the top, longitudinal rebars present a very short yielded length below the loading plate, while bigger length are detected on the transversal bars close to the North edge. This could represents a double phenomenon: the increasing of the previous longitudinal crack also on the top surface and the opening of the inclined crack through the thickness of the slab (compressed strut mechanism). The same pattern is visible on the bottom rebars, interesting wider portions of rebars. It could mean the crack in the middle of the front face and the longitudinal fracture present a bigger width on this layer. So they run all over the thickness of the slab. It's interesting to note that the transversal bar yielded on the two surface present a spatial shift. While on the top it's close to the load, on the bottom it's near the simple support. The hypothesis of a wide crack through the thickness due to a concrete strut could be strengthened.

Anyhow, these contour plots prove the hypothesis of *Kinnunen* and *Nylander*, since the reinforcement steel of the bars has an elastic behavior. However, most part of the yielded bars are located close to the North edge and only a little part of them is below the load. The displayed yielding presents not negligible differences with the previous one (*2x2* mesh).

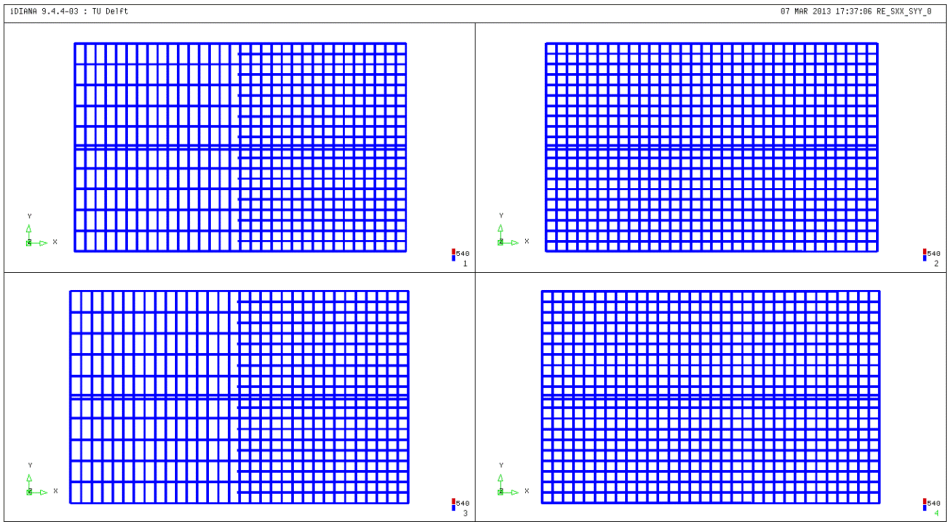

σ_{xx} and σ_{yy} contour plot for top and bottom reinforcement bars for 538 kN

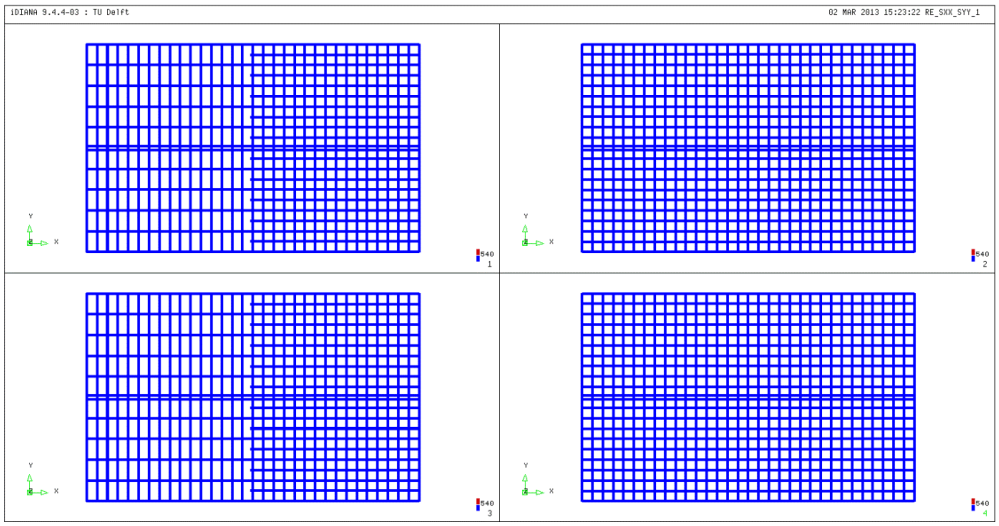

σ_{xx} and σ_{yy} contour plot for top and bottom reinforcement bars for 740 kN

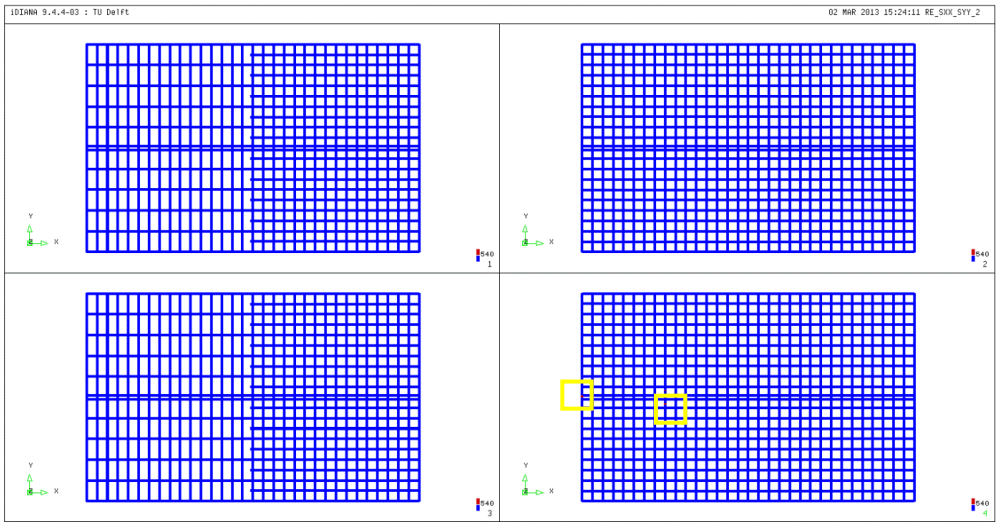

σ_{xx} and σ_{yy} contour plot for top and bottom reinforcement bars for 1237 kN (decay)

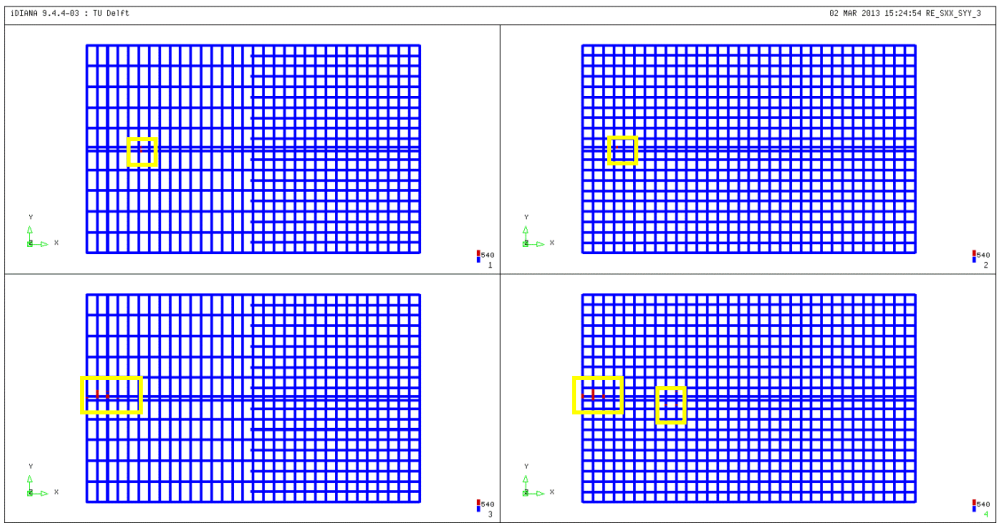

σ_{xx} and σ_{yy} contour plot for top and bottom reinforcement bars for 1501 kN (peak)

For what regards to the *principal tensile stress* vector plot, observing the bottom rebars, the 1st main point ($\sim 730\ kN$) agrees with the results obtained for the coarse mesh. After, on the decay point ($\sim 1240\ kN$) a clear concentration of tensile stresses can be found below the loading plate with higher value, over to the yielding stress. This distribution evidences a longitudinal North-South crack from the support forward the midspan, passing through the load, as seen in the experiment (crack 1). Moreover, a clear strip between the North support the midspan is subjected to high level of tensile stress. Here, a radial direction spreading from the load seems to be preferred and it could mean the formation of radial cracks as well. On the peak point this pattern shows a clear high concentration zone: the highest one close to the North edge and forward the midspan. Then, the stresses focus in the X-direction, close to the lateral free edges.
On the top surface, it's visible the modification of the pattern and the concentration of the stresses from the clamped side to the nearby of the load.
At $1237\ kN$ the highest stresses below the load and the North edge could confirm: (1) the formation of a concrete strut under the load, (2) the opening of a vertical crack in the middle of the frontal face respectively, as seen looking to the principal tensile and compressive strain plots. On the peak, the progressive increasing of stresses in the Y-direction close between support and load could mean the higher opening of the longitudinal crack.

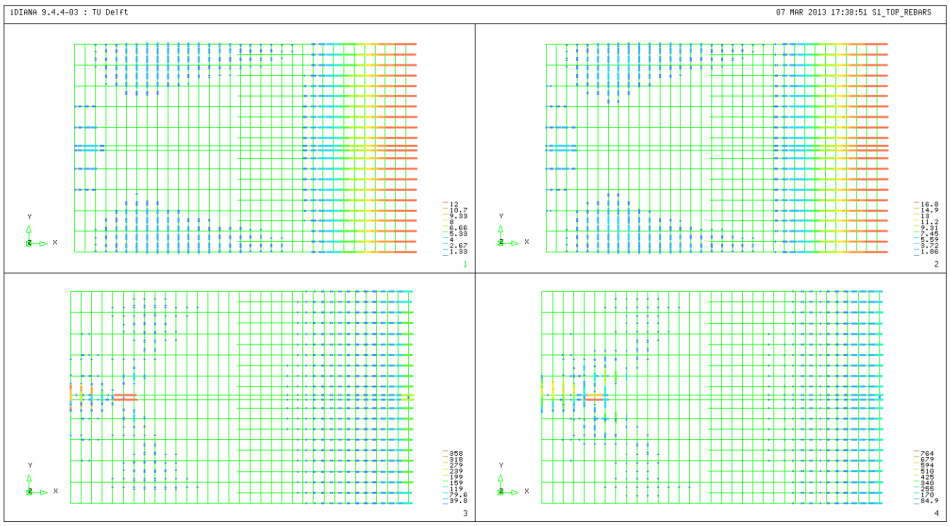

Principal tensile stress for the reinforcement bar on the top surface

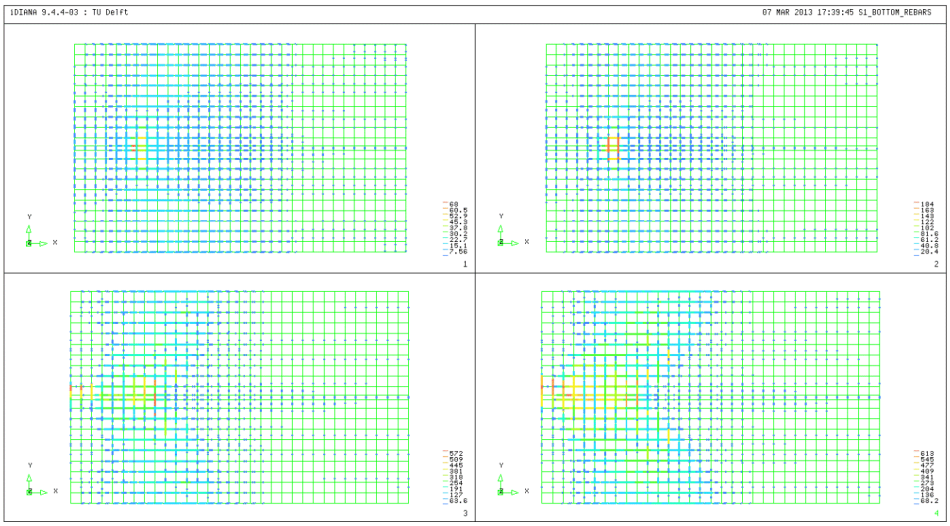

Principal tensile stress for the reinforcement bar on the bottom surface

8.2.4 Compressive behavior of the concrete

The *principal compressive stress* feature is investigated through a contour plot on four surfaces, for the three main selected before.
Two main values are adopted:

- $0.50 f_{cc} = -29.88\, MPa$;
- $1.00 f_{cc} = -59.76\, MPa$.

Since, the compressive stress has conventionally a negative value, the green color shows the parts with a lower principal stress than $f_{cc} = -59.76\, MPa$. Instead the blue color proofs the part who exceed this reference value.

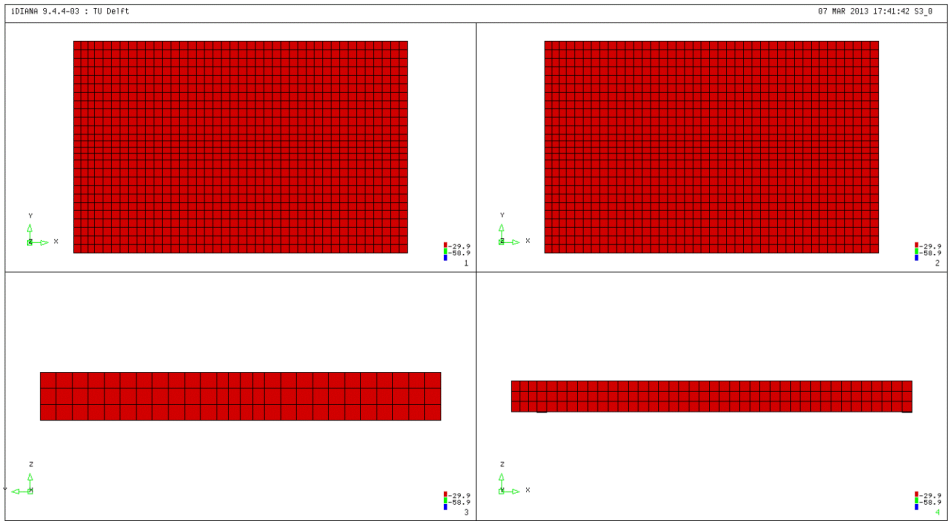

Contour plot of principal compressive stress for 538 kN

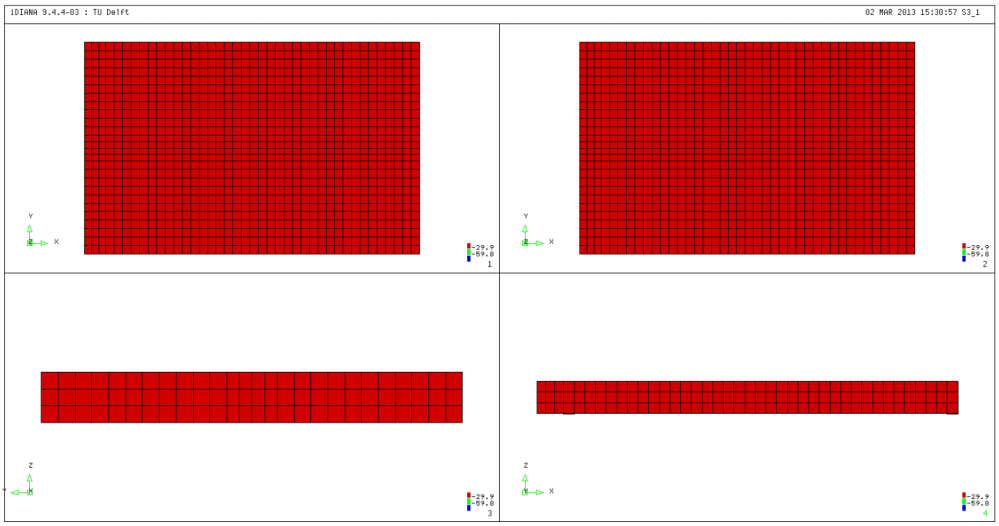

Contour plot of principal compressive stress for 733 kN

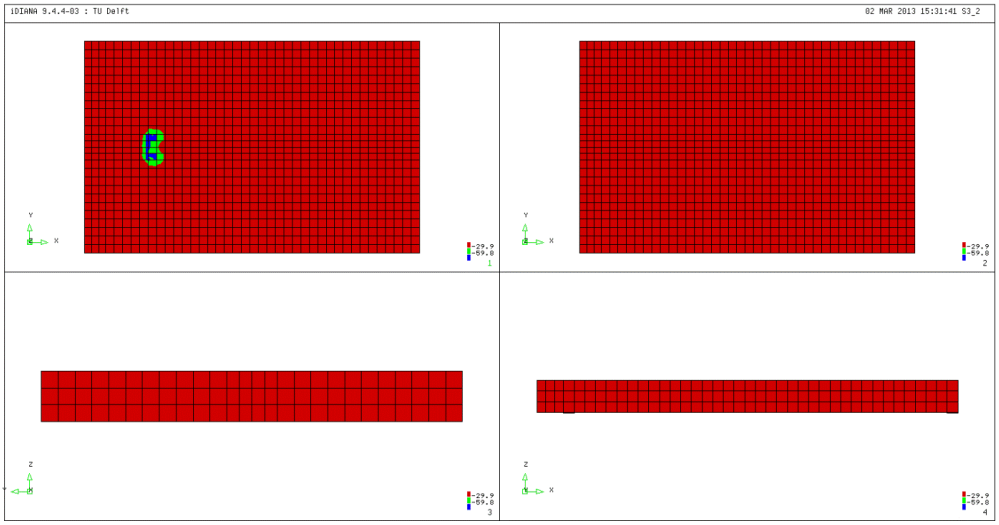

Contour plot of principal compressive stress for 1237 kN (decay)

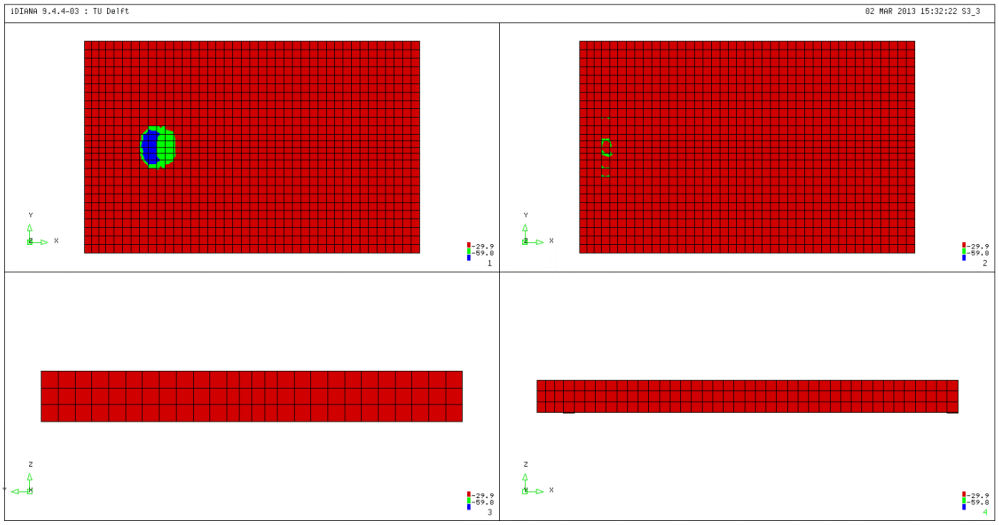

Contour plot of principal compressive stress for 1501 kN (peak)

As shown by the previous plots, the *principal compressive stress* σ_3 starts to exceed the concrete strength f_{cc} since the load of $1237\ kN$, until it occupies an area circumscribed around the North edge of loading plate. Moreover, it's interesting to note how the shape of this area matches with the principal tensile strain plots on the top surface. On the bottom layer, think strips arise at the peak point: it could proof the formation of a series of compressed struts into the thickness of the slab. So a strut-and-tie bearing mechanism starts from the loading plate and reaches the support, spreading in the Y-direction. So, the apllied load is distributed on a small area, around the middle of the support. This is not detected on the previous mesh and it underlines a marked difference between the two meshes. Moreover, no blue area has been shown in *2x2* model.
Finally, the assumption of a linear behavior of the concrete is still well satisfied.

8.2.5 Failure mechanism of the slab

The way the crack patterns developed on the bottom surface (in terms of magnitude and spatial distribution) and the sudden divergence of the analyses can proof a different mechanism of failure with respect to the experimental evidence.
As said before, ttheoretically a punching failure should occur with the formation of a truncated cone around the concentrated load. However, since the load is located close to the continuous support the aforementioned truncated cone cannot fully develop, making harder to define the failure mechanism.

In order to study this event, the following picture shows the distribution of the principal tensile strain on the decay point and on the peak load. The scale of the contour plots is held constant in order to see the development of the tensile strain area:

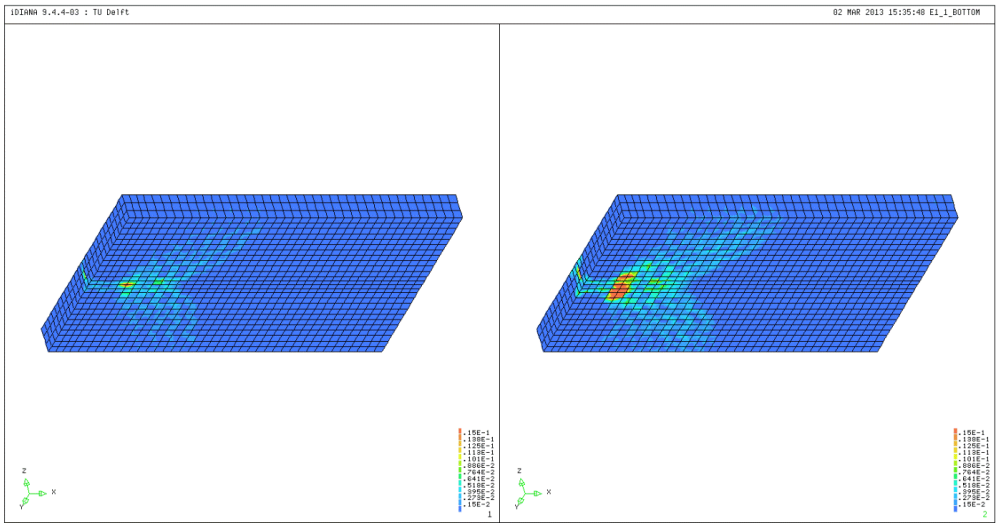

Contour plot of the principal tensile strain on the bottom face on the decay (left-hand) and peak points(right-hand)

It's easy to detect a strong development of the area invested by cracking, i.e. principal tensile stress, among the North support and the load position and on the frontal face of the slab. A radial crack system starts to arise in the left-hand plot and finally spreads forward the midspan and the free lateral edges, as shown in the right-hand figure. The longitudinal pattern runs from the load toward

the North edge and it grows, investing a wider portion of the North face. A high concentration of stress is underlined below the load, close to the simple support, tracing a sort of circular arc.
It's clear that the principal tensile strains are less developed at the side of the continuous support.
This trend can demonstrate that the slab has been completely subjected to failure, with a sudden reduction of the bearing capacity.
Moreover, this finer mesh seems to better underline how the slabs fails: the cracking patterns are better predicted than the previous coarse mesh.

A useful attribute to better discover cracking pattern inside the model is the *principal normal crack strain* ${\varepsilon^{nn}}_{cr,1}$ feature.
The best results can be obtained by adopting as reference two limit crack strains:

- ${\varepsilon^{nn}}_{cr,min} = w_{cr,min}/h = \frac{0.05}{95} = 0.526E-03$;
- ${\varepsilon^{nn}}_{cr,aver} = w_{cr,aver}/h = \frac{1}{95} = 0.105E-01$.

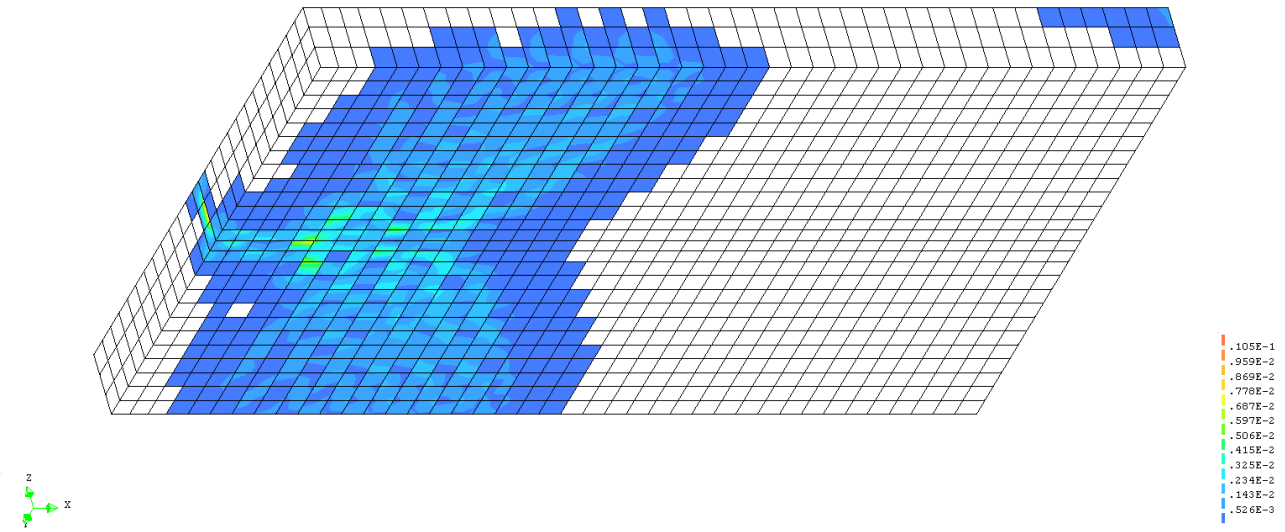

Contour plot of the principal normal crack strain on decay point

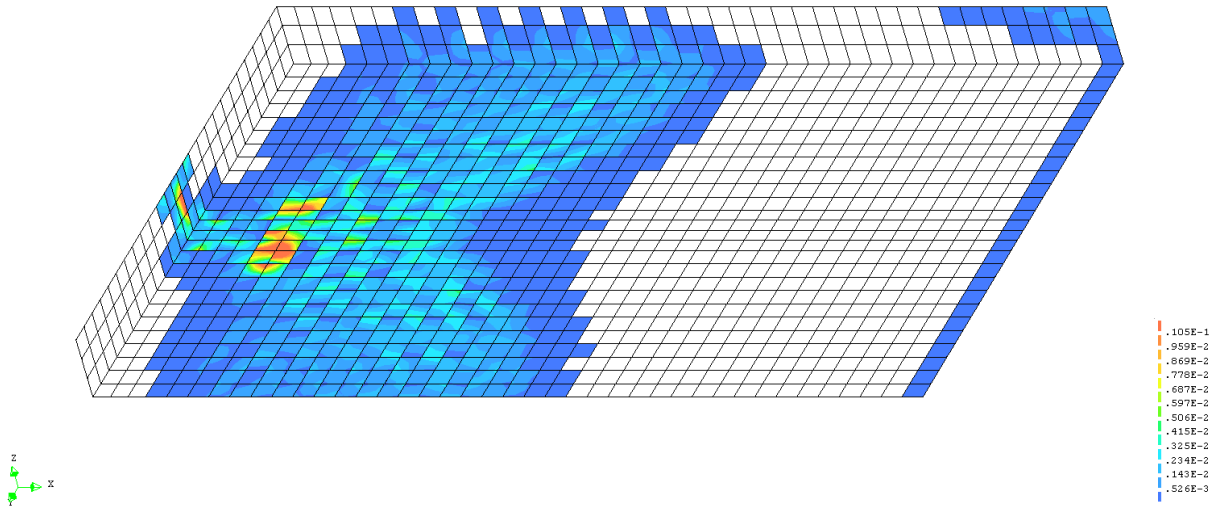

Contour plot of the principal normal crack strain on the peak

The related disc plot are shown below:

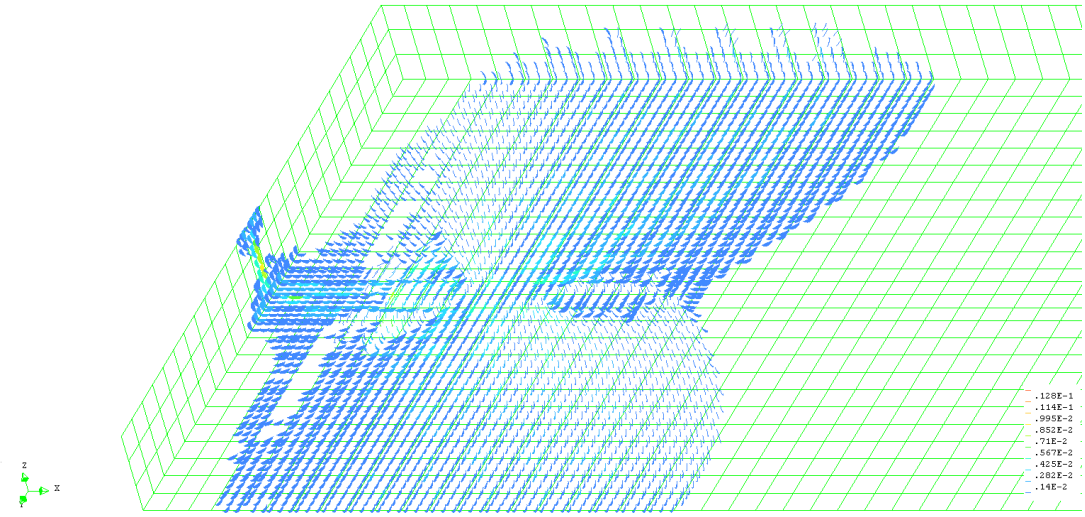

Disc plot of the principal normal crack strain on decay point

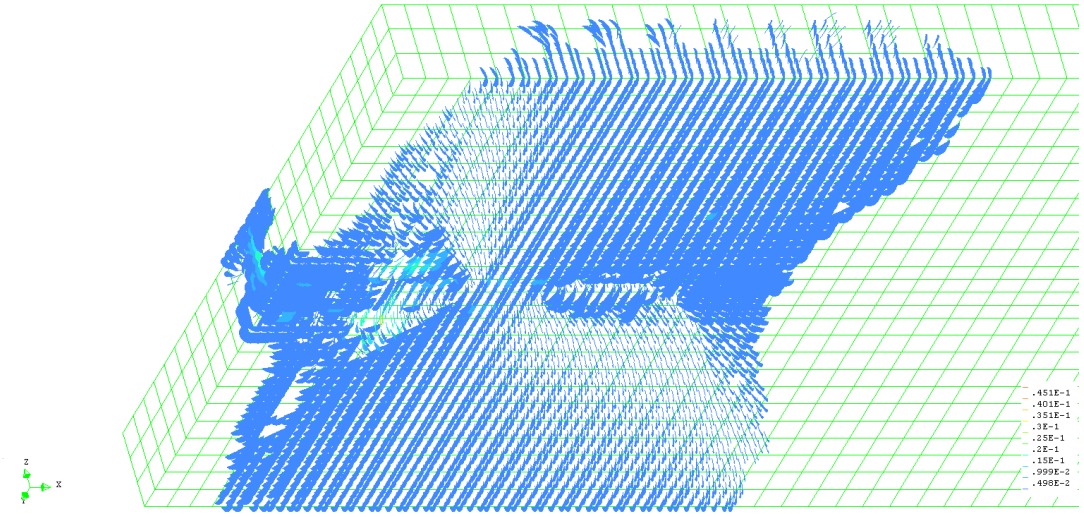

Disc plot of the principal normal crack strain on the peak

A new way to detect cracks is here provided:

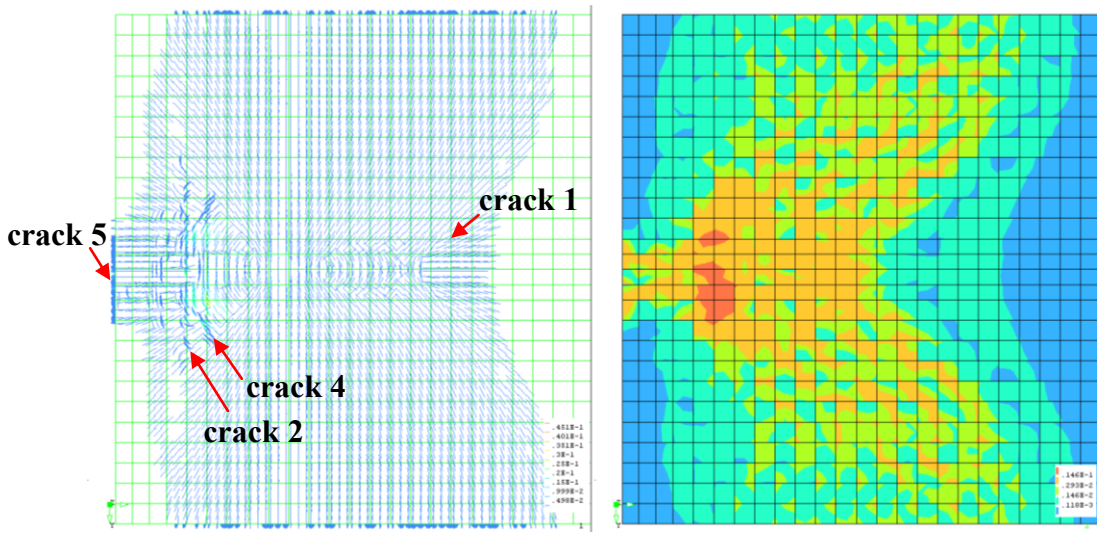

Contour plot of the principal tensile strain on the bottom face on the peak (right-hand and principal crack strain (left-hand)

The cross-comparison between these plots helps to discover the effective cracking patterns on the slab. It shows a good agreement with the experimental evidence: crack1, crack 2, crack 3 and crack 5 are clearly displayed. There no evidence of crack 6. The following picture helps to focus the concept:

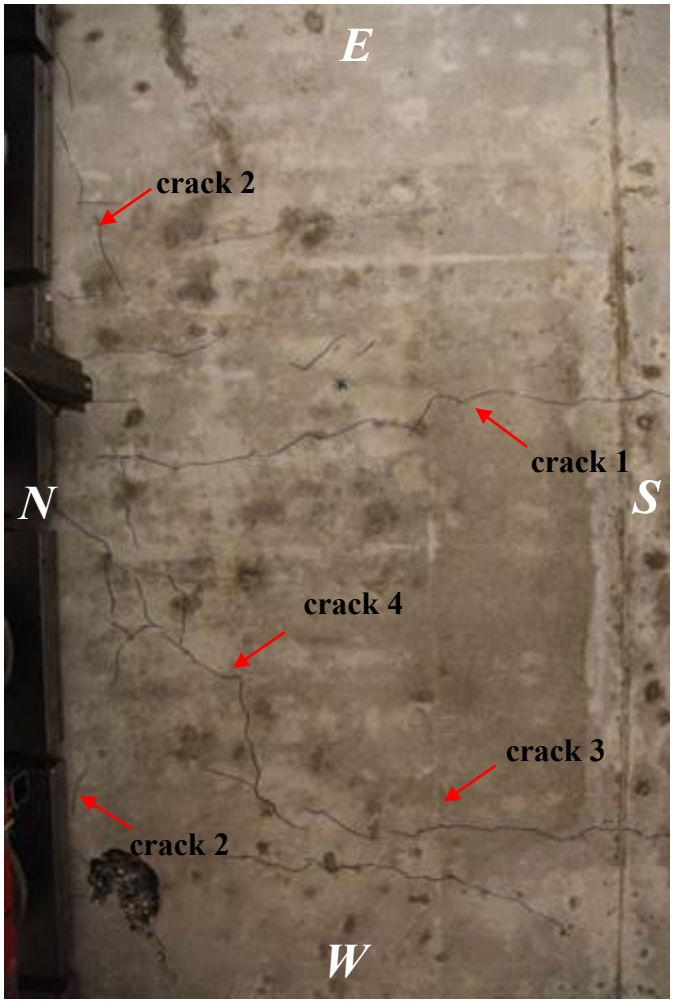

Cracking patterns detected during the experimental test

Regarding to the crack width, crack 1, 2 and 5 are displayed adopting the lowest range, equal to $0.498E-02$ (maximum value of the level). Just applying the formula, we can get the maximum width for the cracks:

$$w_{cr,max} = \varepsilon^{nn}{}_{cr} \cdot h$$

we get:

$$w_{cr,max\ -1,2,5} = 0.498E-02 \cdot 95\ mm = 0.47\ mm$$

A comparison can be done looking to the following table:

Specimen	F_{line} [kN]	F_{punt} [kN]	w_{max} [mm]	Class.	Where?
S25T1	0	Fail	0.05	*crack 5*	front face - trhough crack in the middle
			0.05	*crack 6*	front face - crack close to E side, from botton, not fully trough
			0.10	*crack 1*	bottom face - NS crack from support into span, passing the load
			0.25	*crack 2*	bottom face - EW close to the support
			3.00	*crack 4*	bottom face - punching at W
			0.20	*crack 3*	bottom face - NS crack at W-side at 48 cm from free edge

Crack width detected for slab S25T1 during the experimental test

The aforementioned cracks hold to a $0.05 \div 0.25\ mm$ range, regards to the width. Considering the present value as the maximum one, the prediction for crack 1 and crack 2 seems to be good, while crack 5 is overestimated once again.
Regarding to crack 4 (punching shear crack), it seems to hold to the $0.25E-01 \div 0.35E-01$ crack strain range. It equals to $2.38 \div 3.33\ mm$ of width. It's in good agreement with what is seen during the test.
The present results allows us to affirm that a finer mesh provides better results, especially for what regards the prediction of the cracking behavior, both in location and in opening width. Indeed, crack 1 is better predicted.
Unlike the coarse mesh, the finer one shows a clearer crack behaviour of the slab. Indeed, the punching shear failure is well exposed here: a radial crack pattern is detected and then a circular critical crack arises. Of course, the slab has not failed with a clear punching shear failure: as exposed by [Van Rodriguiez] the crisis occurs with a combination of phenomenon. Moreover, to confirm as said, the deformed shape well underline a strong deformed area below the loading plate: it seems to be invested by the expulsion of a truncated cone volume (as occurs in punching shear). Here, the greater fineness of the mesh allows to show: (1) the limited area invested by the deformation below the load on the bottom, and (2) the sinking of the steel plate inside the concrete at the top surface.
Moreover, these plots seems to prefer a two-way failure than a one-way crisis, though the two events could influences mutually.

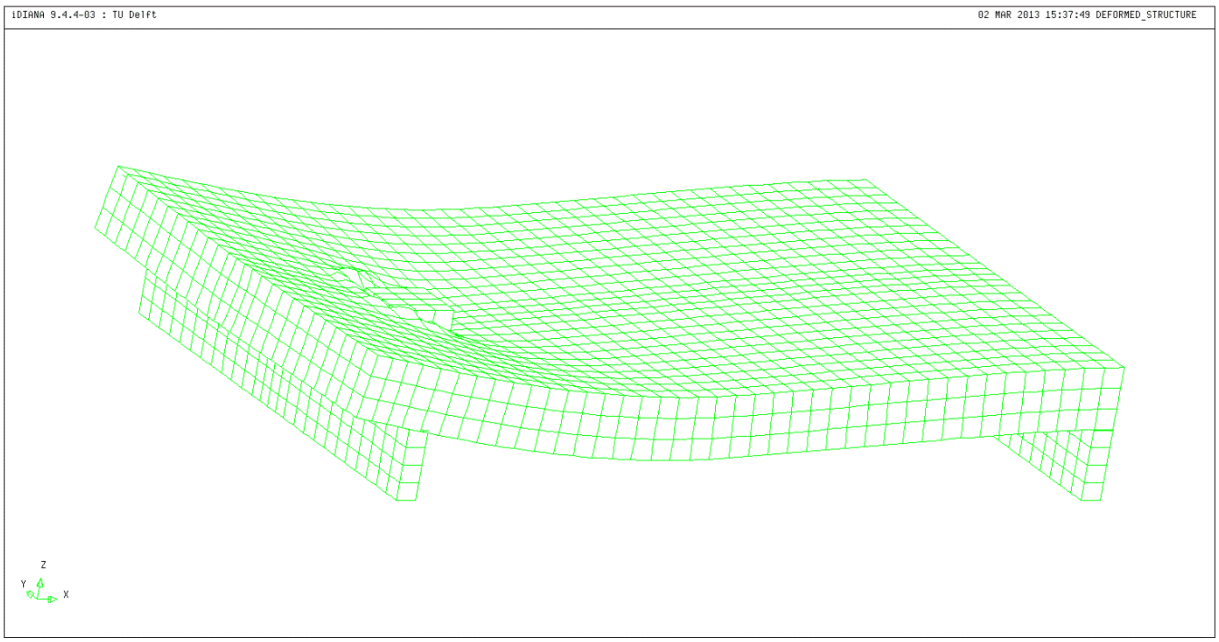

Deformed structure at the peak load: global overview

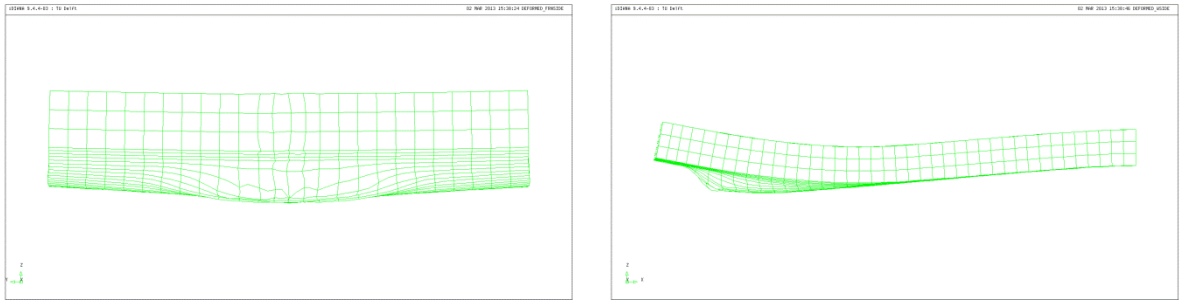

(a) *(b)*

Deformed structure at the peak load: (a) North front side and (b) West lateral side

With respect to the previous mesh, here it seems that the shear failure higher governs the failure mechanism.

8.3 The finest mesh: *4x4 partial model*

Finally, an analyses is run on the finest mesh. The CEB-FIP value for the tensile fracture energy G_f is used: 0.150 Nmm/mm^2. The same value of G_f is adopted for the total model on the same mesh as well.
The present model has got the following features:

- tensile fracture energy: $G_f = 0.150\ Nmm/mm^2$;
- numerical crack bandwidth: $h = 75\ mm$;
- normal felt interface stiffness: $k_{n,f} = 15.20\ N/mm^3$;
- normal Teflon interface stiffness: $k_{n,T} = 500\ N/mm^3$;
- integration scheme: default for all the finite elements (see previous paragraphs);
- maximum number of iteration equal to 25.

Only the felt model (linear instead nonlinear) and the maximum amount of iterations change.
The following load-displacement graphs is here shown:

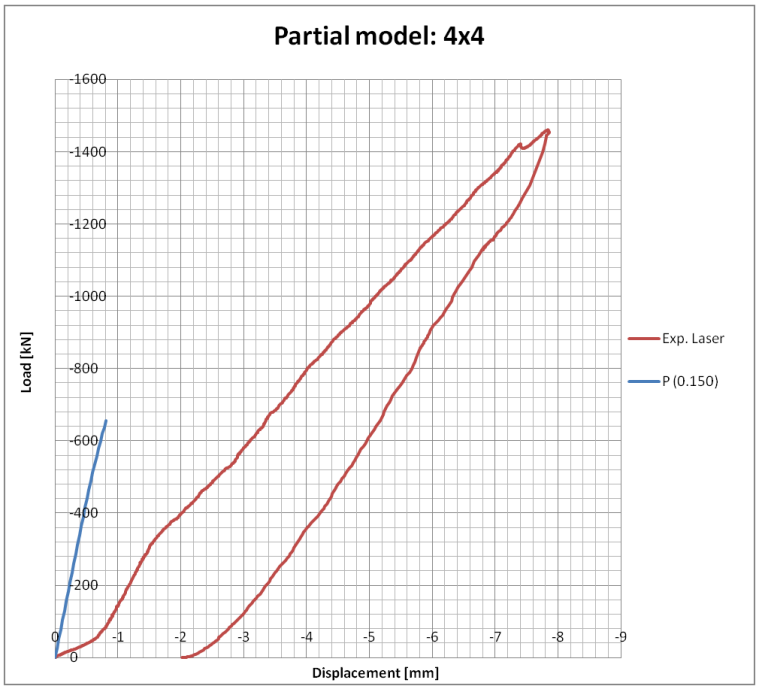

Comparison of partial and total model with same G_f fracture energy

As detected on the total model, for reason of computational time the analysis has to be stopped: only 27 steps are run in five days of work. It has to be noted that the first steps hold the linear field and they result faster.
The load-displacement diagram reaches only $-0.81\ mm$, too less to get any conclusion about the shown behaviour.
The following plot shows the convergence trend for the present analyses:

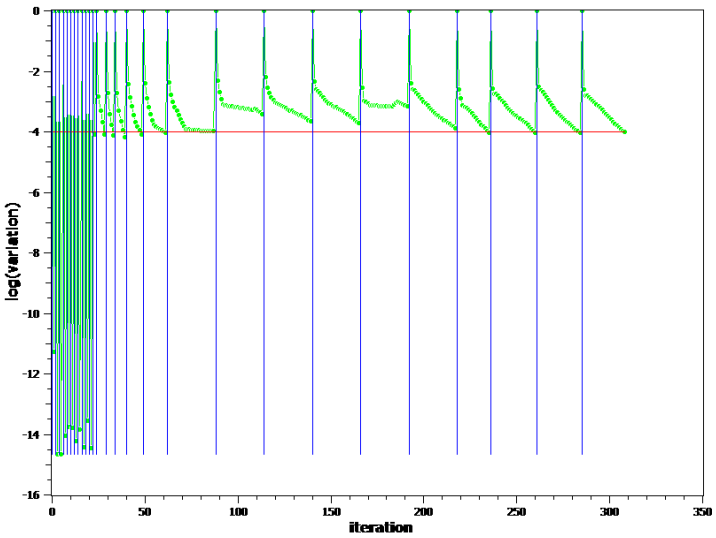

Convergence trend for 4x4 mesh analyses on the partial model

9. APPLICATION OF SEQUENTIALLY LINEAR ANALYSIS ON THE PARTIAL MODEL

The three-dimensional model used to run the SL-analysis is the aforementioned *Partial model*, who adopts a full continuous support on the South side. This simplification of the so called *Total model* is due to the impossibility to run the analysis with no-proportional load. Indeed, the total model contains two different load cases: (1) the *displacement control* on the loading plate (reference proportional load) and (2) the *pre-stressing action* applied on the three Dywidag bars (non-proportional load).
In fact, non-proportional loadings may lead to significant stress redistributions and rotations during the analysis. Then, it is likely that the scaling process cannot be carried out just from the origin [7]. Although the past implementation analysis with non-proportional load can be run in 2D, at the moment, the code/routine requires further extension for the 3D environment.
So, in order to apply SL-analysis to the present slab, we require to delete the non-proportional loading represents by the Dywidag pre-stress. So, the constraints system given by the complex HEM300 and Dywidag bars is replaced by a full clamped constraint.

9.1 Three-dimensional model of the reinforced concrete slab

9.1.1 Finite element model

The so called "partial model" was the first model ideated. Only after its implementation the full model was built and adopted for NLFA.
Like the total model, it's composed by different solid parts, each of them modeled by one or more three-dimensional geometrical elements (bodies).
By omitting only the constraint system of the total model, the various bodies composing the different parts are:

- slab;
- HEM300 supports;
- loading plate;
- felt interface between slab and supports;
- interface Teflon layer (between load plate and slab).

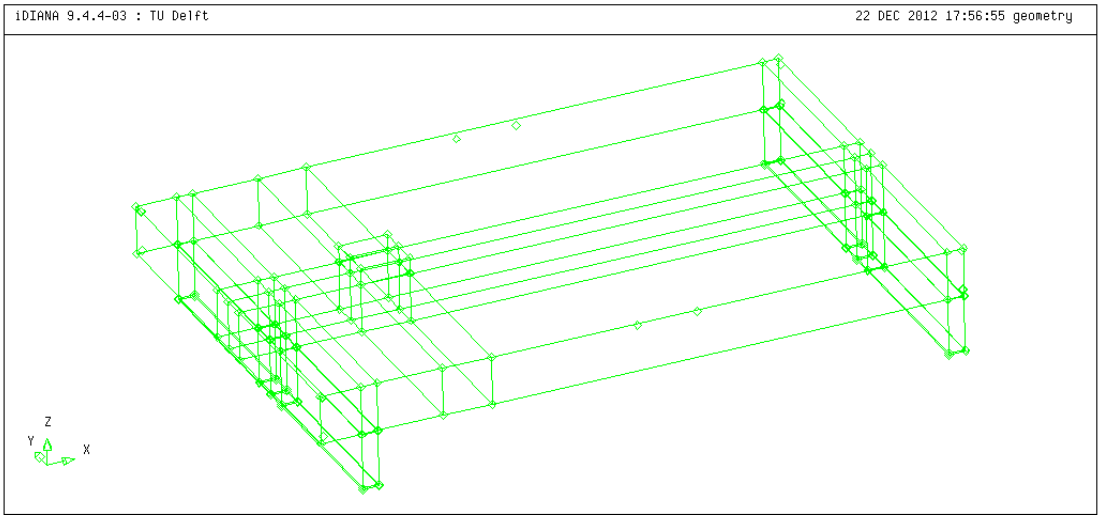

Geometrical model S25T1 slab

To execute an analysis with *Diana*, the structure has to be discretized through several three-dimensional finite elements.
As for the total model, three different meshes are used:

- *"two elements on height" mesh*;
- *"three elements on height" mesh*;
- *"four elements on height" mesh*.

in order to discover the meshing influence on the analysis outputs.
The same types of finite element are used: CHX60 and CQ48I; since no Dywidag bars are modeled, elements L6TRU are not adopted.

The *2x2* mesh is composed by 4290 nodes and 708 finite solid elements.

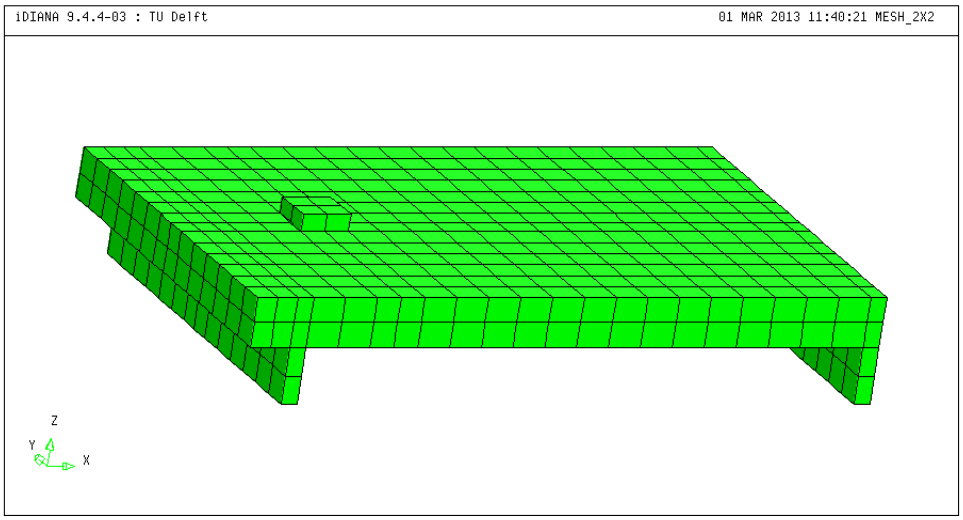

2 elements on height mesh adopted for S25T1 slab partial model

The *3x3* mesh is composed by 18217 nodes and 3404 finite solid elements.

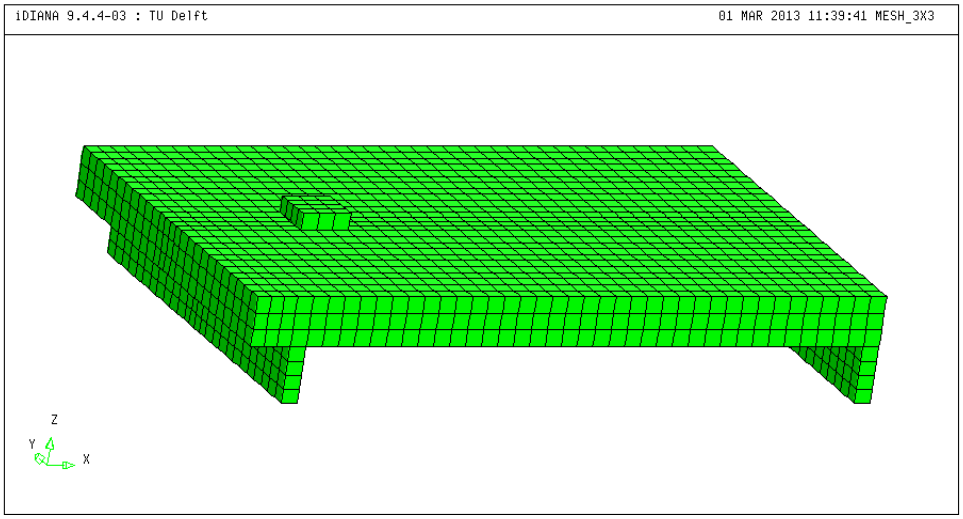

3 elements on height mesh adopted for S25T1 slab

The *4x4* mesh is composed by 36546 nodes and 7344 finite solid elements.

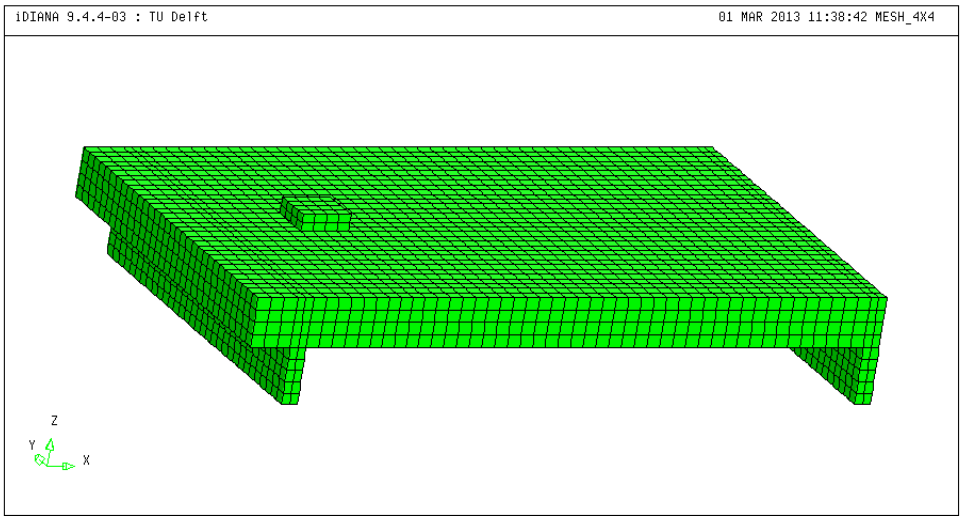

4 elements on height mesh adopted for S25T1 slab

The dimensions of the various finite elements are almost regular, as one can see in the following image. The higher density of the second mesh is immediately visible.
The following plots show the different materials and few mesh particulars:

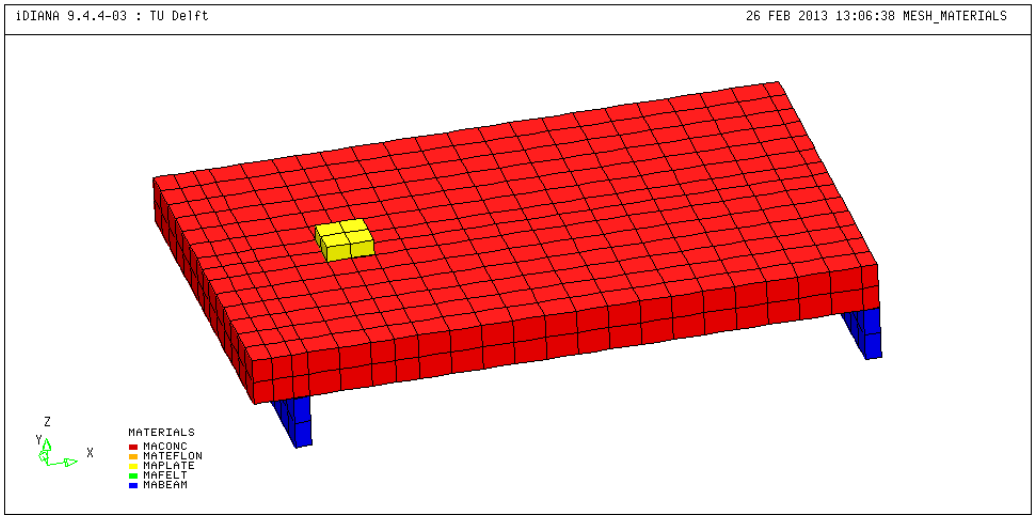

Material label for the model (1st mesh)

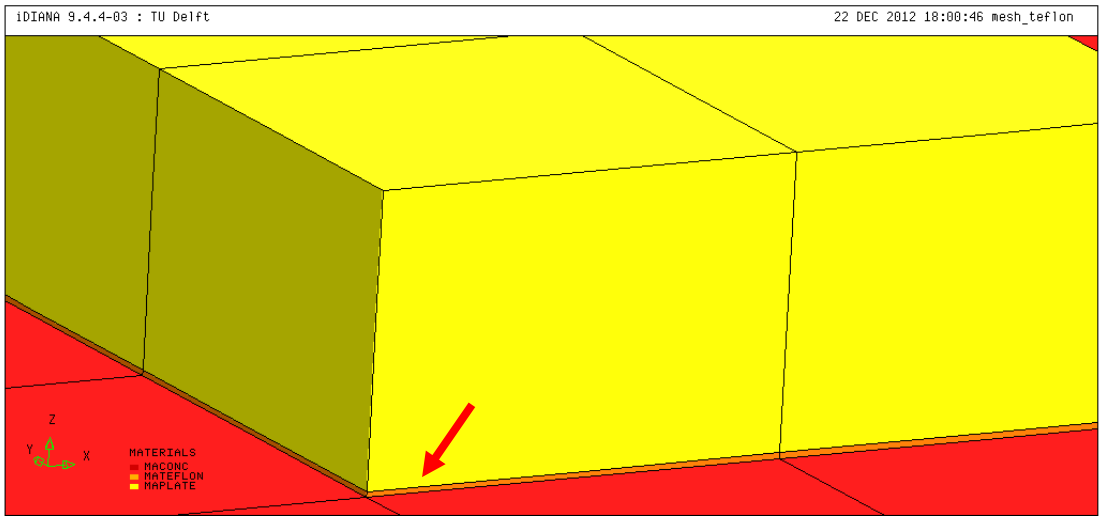

Teflon particular in the mesh

The model is defined in a 3D environment and it is composed by:

- 6507 *nodes* and 1084 *finite solid elements for the 1st mesh;*
- 19000 *nodes* and 3456 *finite solid elements for the 2nd mesh;*

All the geometrical dimensions of the model are respected, with only one exception on the supports, that in the real test are composed by $HEM300$ steel profiles, while in the FEM model they are represented by two solid brick elements, 340 mm high and with a width of 100 mm (instead of 300 mm), to have a direct matching with the upper interface layer.

9.1.2 Model of supports and constraints

The real slab is bound by a total of two supports, one *simple support* and one *continuous support*, defined by 3 Φ 36 Dywidag bars with pre-tensioning.

Because of the load position near the simple supported edge, we can model the slab considering clamped the other slab edge in order to simplify the analysis.
So, for the *simple support* the vertical translation is constrained on the "bed" interface bottom face, instead the plane horizontal translation is bound on the $HEM300$ bottom face.
For the *continuous support* is considered like a sort of perfect joint, realized by constraints in the bottom surfaces of the support, that don't allow X, Y and Z translation on the $HEM300$ bottom face and by other constraints in the frontal side of the slab near the continuous support, that don't allow the X translations.
At the end this distribution of constraints doesn't allow the rotations as well.
In order to take into account the slab curved shape the interface is adopted and in order to make it effective, vertical constraints (Z directions) are placed only on the interface bottom surface.

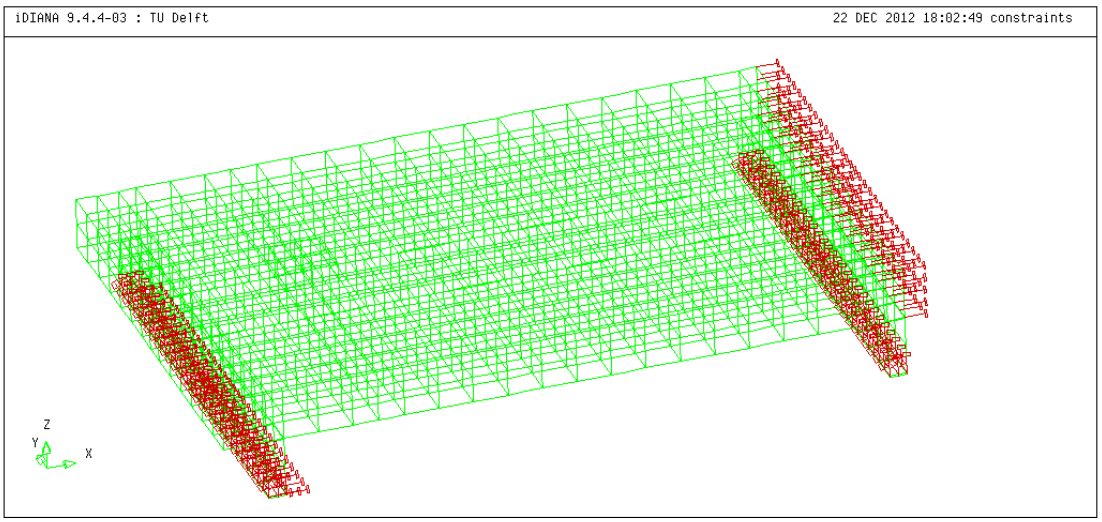

Model of the constraints assigned to the slab (1st mesh)

9.1.3 Loading conditions

Following the same criterion used for the laboratory test, the FEM analysis on the model is performed using a *displacements control* method. Specifically a maximum displacement of $25\ mm$ is applied on the loading plate, since the maximum displacement applied in the laboratory tests is around $24{,}6\ mm$ (hydraulic jack report).

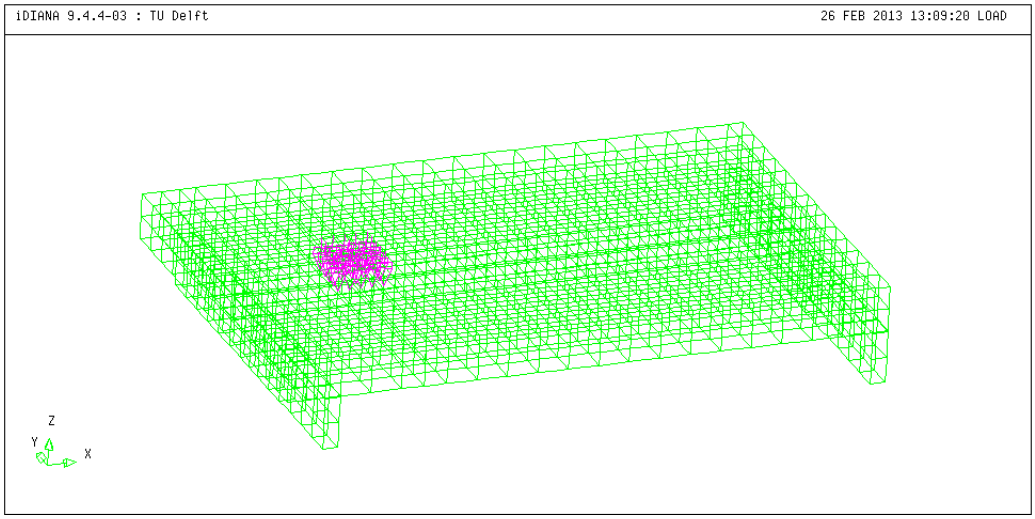

Model of the load assigned to the slab (1st mesh)

9.1.4 Material and physical properties

Regarding to the material and physical properties, the same models and values are adopted with respect to the pre-defined total model for what it concerns the linear behavior, nevertheless regarding the Sequentially Linear Analysis some variations of the non-linear properties have to be considered. In fact the implemented SLA code, in order to define the saw-tooth stress-strain diagram, doesn't allow using some refined nonlinear and post-elastic models (for example the nonlinear behavior for the felt interface and the post-elastic trend for the rebars).

The modified features of the used material are here reported:

CONCRETE

MACONC [1]:
Linear Elasticity – Isotropic
Young's Modulus: 39016 MPa (from the $CEB - FIP$ relation)
Poisson's Ratio: 0.15

Static non linearity – Concrete and brittle materials – Total strain fixed crack – Hordijk softening in tension – Fracture energy based - Elastic in compression – Variable Shear Retention

Tensile strength: 4.62 MPa
Mode-I tensile fracture energy: 0.150 Nmm/mm^2
Crack bandwidth: 165 mm

The previous pattern is so specified inside the *.dat* file of the model:

```
6 YOUNG     3.901600E+04
  POISON    1.500000E-01
```

TOTCRK FIXED
TENCRV HORDYK
TENSTR 4.620000E+00
GF1 1.500000E-01
CRACKB 1.650000E+02
TAUCRI 2

REINFORCEMENT STEEL

MABAR10 [2] - MABAR20 [3]:
Linear elasticity – Reinforcement – Reinforcement bonded
Young's Modulus: 200000 MPa

Static non linearity – Reinforcement – Von Mises plasticity – Work Hardening diagram
Tensile yield stress: 540MPa
Tensile ultimate stress: 540 MPa

Starting from these mechanical properties, two saw-tooth diagrams have been defined.
The linear softening curve of the concrete has been discretized using the automatic generator implemented in *Dian*a, based on the Ripple model, with the commands reported afterwards.

Regarding to the concrete material, *taucri* defines the shear retention behavior: by selecting 2 a stepwise decreasing shear retention is selected.
To make use of the built-in saw-tooth curve generator, the following syntax should be used:

'FILOS'
/materi(6)/TSAWLW AUTOMA
/materi(6)/SAWMOD RIPPLE
/materi(6)/SAWSOL AMOEBA
/materi(6)/NTEETH 15

The AUTOMA option for the sawlaw defines an automatic saw-tooth curve for the material 6, e.g. concrete. Instead, the RIPPLE selection describes which saw-tooth model we would like to use.
The AMOEBA option selects the iterative procedure to solve the saw-law definition. AMOEBA proofs to be a more stable method than Newton-Rhapson.
Finally, thanks to this syntax, the concrete softening behaviour will be described by a number of teeth: this will generate a saw-tooth law consisting of (*nteeth+1*) linear branches.

For the steel reinforcement the stress-strain relation found by the experimental tests on specimens are simplified with an ideal-elastic plastic model. This approximation seems to don't produce relevant error of modelling on the considered strain range, as shown below.

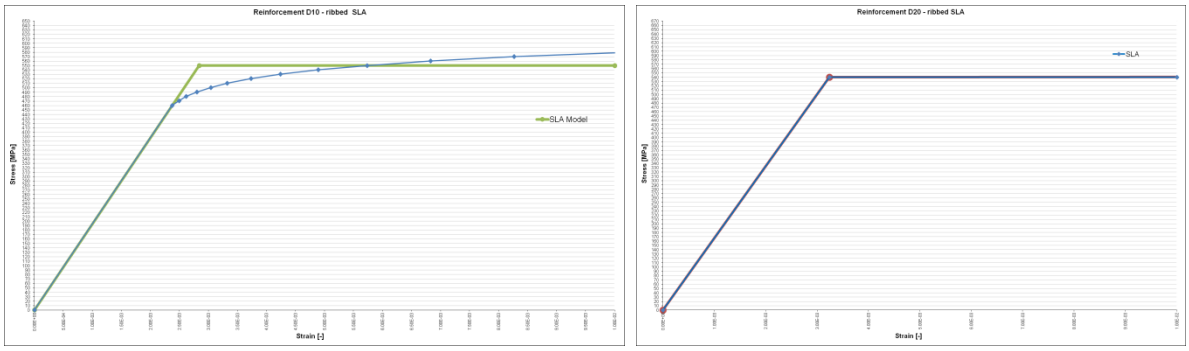

(a) *(b)*

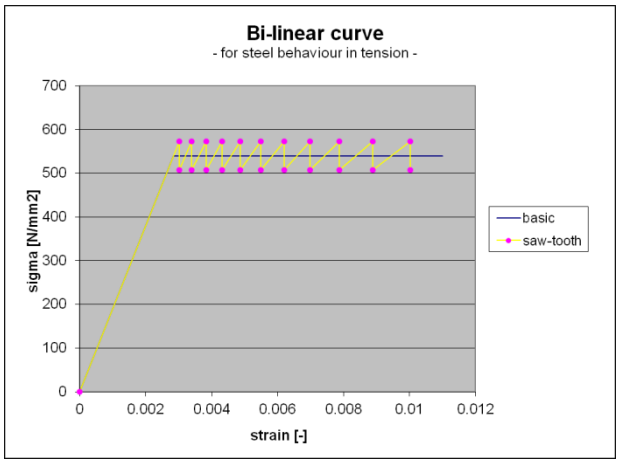

(c)

Stress-strain model for ϕ10 (a) and ϕ20 (b) bars for SLA and saw-tooth law (c)

Regarding to the strain-stress relation in the reinforcement steel, a direct input has been adopted inside the *.dat* file, using the following table to define the saw-tooth diagram relative to the hardening part.

```
MATERI(4)/TSAWLW    TABLE
/MATERI(4)/TSAWDI
                3.068421E-03   5.830000E+02
                3.460134E-03   5.830000E+02
                3.901854E-03   5.830000E+02
                4.399963E-03   5.830000E+02
                4.961660E-03   5.830000E+02
                5.595063E-03   5.830000E+02
                6.309327E-03   5.830000E+02
                7.114773E-03   5.830000E+02
                8.023042E-03   5.830000E+02
                9.047260E-03   5.830000E+02
                1.020223E-02   5.830000E+02
```

MATERI(1)/TSAWLW TABLE
/MATERI(1)/TSAWDI

3.012632E-03	5.724000E+02
3.397223E-03	5.724000E+02
3.830911E-03	5.724000E+02
4.319963E-03	5.724000E+02
4.871448E-03	5.724000E+02
5.493335E-03	5.724000E+02
6.194612E-03	5.724000E+02
6.985413E-03	5.724000E+02
7.877168E-03	5.724000E+02
8.882764E-03	5.724000E+02
1.001673E-02	5.724000E+02

The area under the softening diagram of the concrete is depending on the ratio G_f/h between tensile fracture energy and crack bandwidth. In *Diana* in simple a priori models the crack bandwidth in solids is assumed to be equal to $h = \sqrt[3]{V}$. This assumption makes sense in regular meshes where the cracks runs along the meshing lines. However, particularly in rectangular solid elements the cracks not always run parallel to the mesh line. In fact, they sometimes tend to propagate in an inclined direction and a more accurate estimation of the crack bandwidth seems necessary. No variation on the adopted crack bandwidth will be carried out. In the present report only variation around G_f will executed: this parameter can improve the concrete "ductility" on the tensile side, increasing the ultimate crack strain ${\varepsilon_{nn}}^{cr}$.
For these reasons in this study the ratio G_f/h has been varied, by changing only the numerator, and its influence on the solution is shown.

The influence of this feature will be studied later.
The other materials used in the model of the slab have linear behavior, since such hypothesis is close to the reality and is the only one that can be accepted by the implemented SLA method in addition to the saw-tooth law.
Indeed, the nonlinear behavior of the felt is reduced to a linear trend and the tensile inertia can't be effectively modeled. So, inside the SLA environment the felt is reacting both in compression and in tension with the same stiffness.

INTERFACE FELT between supports and slab

Linear elasticity – Interface
Linear normal stiffening: $15.20\ N/mm^3$
Linear tangential stiffening: $0.20\ N/mm^3$

9.1.5 Important parameters of the model

The model already described is characterized by a series of parameters, whose values and their influence on the model have been evaluated applying NLFE-analysis to each model in the previous chapter.
The most important parameters that affect the solution of the FEM analysis are:

- tensile fracture energy G_f and numerical crack bandwidth h;
- normal stiffness of the Teflon interface $k_{n,T}$ between slab and steel plate;
- normal stiffness of the felt interface $k_{n,f}$ between slab and supports;
- shear retention model (variable or constant shear retention).

Main parameters, like tensile fracture energy G_f and normal stiffness of the Teflon interface $k_{n,T}$ between slab and steel plate, have been evaluated in terms of sensitivity on the model using NLFE-analysis. So, only the fixed values of these parameters who provided the best agreement with the experimental results will be adopted.
Regarding to the numerical crack bandwidth h, it is fixed for each mesh by the previous works, since the meshes don't change for NLFE and SL-analysis.
As shown by previous work [citare voldemord e angelozzo vallozzo], the Shear Retention model is a very influent parameter on numerical output, and it's widely demonstrated that the better results derive choosing a *Variable Shear Retention* model.
As said in the previous paragraph, the felt behavior has to be modeled with a linear relation: this involves a new unknown parameter who needs to be evaluated. The sensitivity of this parameter and of the linear model will be studied adopting NLFE-analysis, since it results faster.

Finally, it has to be observed that a fixed integration scheme will be used in all the analysis:

- Gaussian 2 x 2 for the interface layer (CQ48I);
- Linear 2 x 2 x 2 for all the other elements (CHX60);

9.1.6 Comparison between SLA and experimental results

In order to evaluate the reliability of the SLA method, the results obtained from this FEM analysis are compared with the Lab-Test results.
SLA has been performed using the finite element mesh already described and the same geometrical and material model and loading and boundary conditions as well.
The result that one can observe to have an immediate idea about the accuracy of the analysis is the Load- Displacement diagram.

The present analysis adopt a *sequentially* procedure of linear analysis, so no global converge criteria is required. The local convergence is set by choosing the fineness of the saw-tooth curve: fifteen teeth are selected and 300000 steps are adopted. In order to minimize the computational size of the file, the output data are compressed after every 500 linear steps. The fracture energy G_f, the

numerical crack bandwidth h and the other main parameters are taken by the previous NLFE-analysis on the same mesh, in order to execute a reliable comparison.
At first, a SL-analysis is run on the partial model with 2 elements on the height, so called *2x2 model*, then *3x3* and finally *4x4*.

9.2 Coarse mesh: 2x2 partial model

Nonlinear analysis are carried out in order to estimate the best range for the unknown parameter. So, for this first SLA the same tensile fracture energy G_f from the same partial version, i.e. *2x2 mesh*, is used. The present model has got the following features:

- tensile fracture energy: $G_f = 0.330\ N/mm$;
- numerical crack bandwidth: $h = 165\ mm$;
- normal felt interface stiffness: $k_{n,f} = 15.20\ N/mm^3$;
- normal Teflon interface stiffness: $k_{n,T} = 500\ N/mm^3$;
- integration scheme: Gaussian 2 x 2 for interface layer, Linear 2 x 2 x 2 for all the other FE.

The felt has a linear behaviour.
The following load-displacement graphs is here shown:

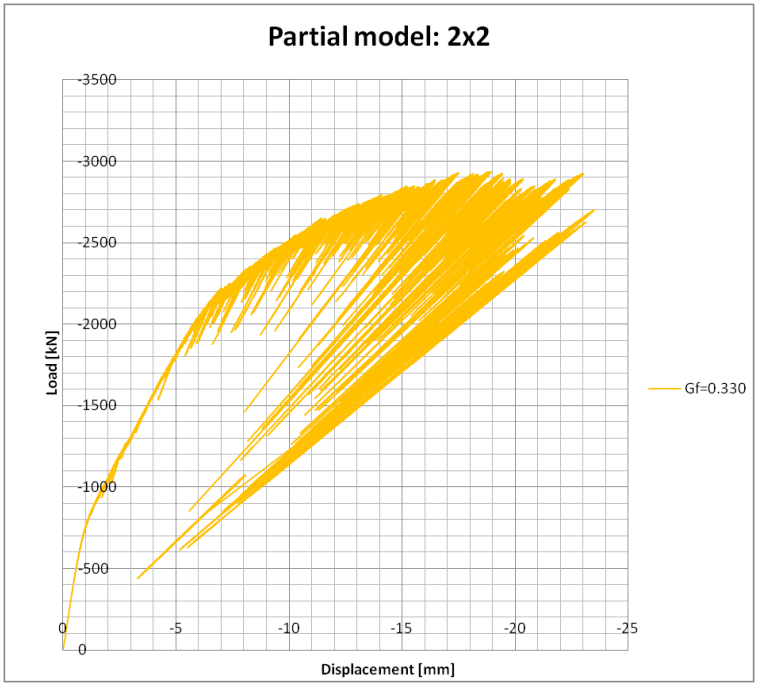

Load-displacement diagram for SL-analyses

An unexpected phenomena is detected: adopting the same fracture energy parameter, SL- and NLFE-analyses presents a different trend. Here, the global response of the slab in term of load-displacement follows the same path until $-4.00\ mm$. Then, instead to reduce its stiffness, the slab is able to carry the increasing load. As shown, only at $-6.00\ mm$ and under a load higher than $2000\ kN$, the slab starts to develops cracks: it proofs by the large amount of local snap-backs. A

sort of peak is underlined, but after a decay of the slab's response, the real peak point occurs after $-23.00\ mm$ of displacement. Then a sudden and strong decay of the bearing capacity arises, but after that, the slabs seems to carry high load again. Finally the analyses reaches the maximum amount of steps after three days of computation. However, this is enough to detect the global slab's behaviour.
A comparison between NLFE- and SL-analyses is here reported:

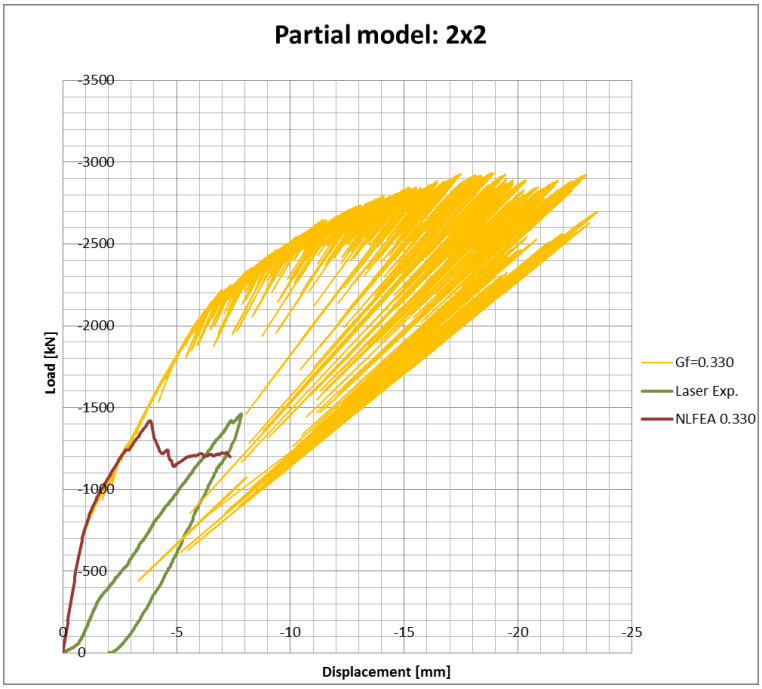

Comparison between load-displacement diagram for SLA and NLA with the same G_f and experimental result

The numerical peak values are:

- peak load: $2930\ kN$;
- peak displacement: $22.90\ mm$.

instead of:

- experimental peak load: $1460.62\ kN$ for a variation of $\sim 100\%$;
- experimental peak displacement: $7.84\ mm$ for a variation of $\sim 290\%$.

The obtained values are not reliable compared with the experimental evidence. However, a study of the behaviour of the structure seems to be necessary to understand if the experimental evidence is matched in terms of cracking patterns.
Four main points are selected on the load-displacement diagram:

- *point 1:* $(1.125\ mm;\ 808\ kN) \sim 25\% F_{max}$;
- *point 2:* $(3.41\ mm;\ 1460\ kN) \sim 50\% F_{max}$;
- *point 3:* $(22.81\ mm;\ 2910\ kN) = F_{max}$;

- *point 4:* $(21.24\ mm;\ 2686\ kN),\ post-peak.$
-

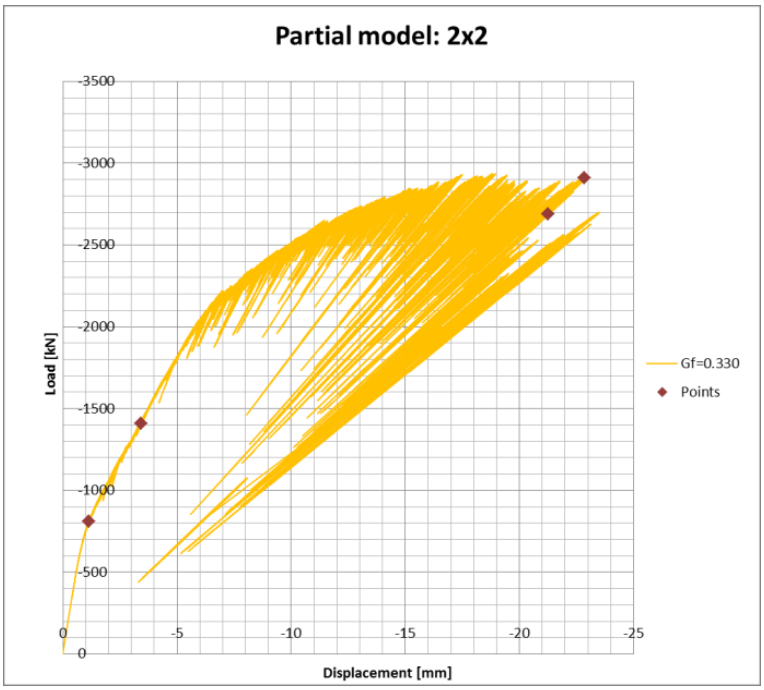

Main points on load-displacement diagram for SL-analyses

9.2.1 Redistribution capacity:

On the following image, four pictures of the felt reactions are shown by adopting a vector plot. They prove the redistribution of the load from the slab to the support, since the action on the felt is equal to the one on the support beam for vertical balance.

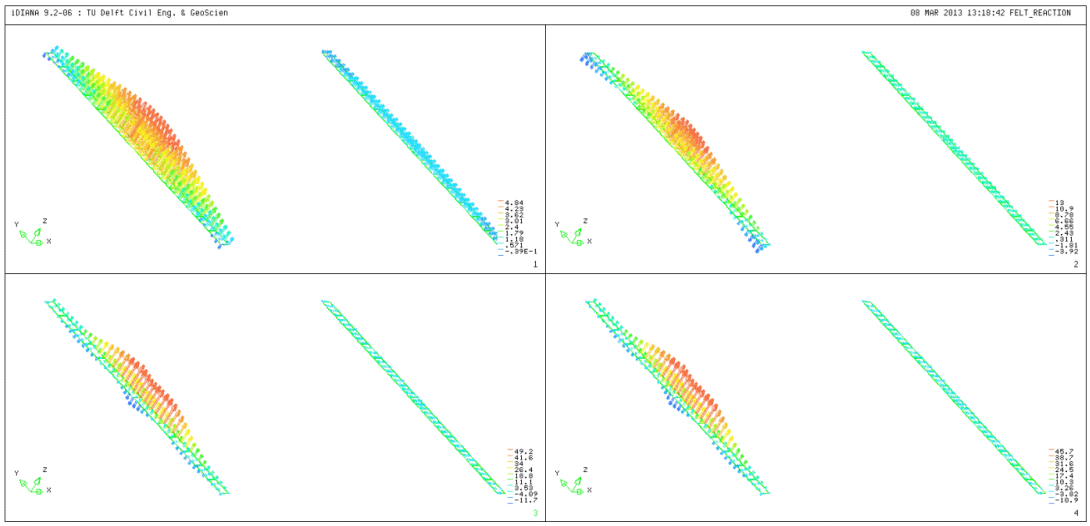

Vector plot of felt reaction [MPa] for the main points

The first point shows a full reacting support with the load most concentrated on the middle, as usual seen also in the NL-analysis. Also on the second point a higher concentration of the load is detected and the lateral edges start to show a tensile reaction. What surprise is the third and four plot: they

show a different behaviour of the slab on the peak and post-peak point. The compressive stress reaches a maximum value of 49.20 MPa and the compression is concentrated around the middle, on the internal edge. It seems to underline a high deflection of the slab.
By plotting the part of interface in a compressive state, they are shown with red color (values higher than 0 MPa - *compression*). It can be observed how the compressive contour presents a different pattern than the one got with the nonlinear analysis. Indeed, after the second point the slab return to compress all the interface on the Y-direction and starts to lift on the external side.

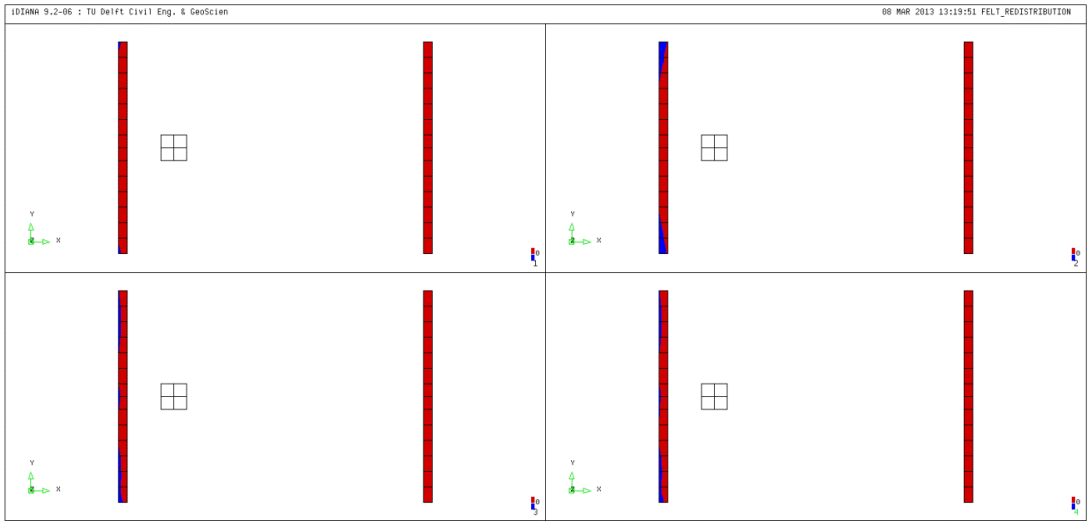

Effective width due to the load spreading on the felt layer

9.2.2 Cracking behavior of the slab

In order to investiga the development of the cracking under an increasing load, contour and vector plot of the pricinpal tensile strain are used. Taking into account four points on the softening diagram calculated for a fracture energy $G_f = 0.330\ N/mm$ and $h = 165\ m$.

$\varepsilon_{el,ult.}$ [-]	0.000118	1.184E-04
0,5*$\varepsilon_{cr,ult}$ [-]	0.001112	1.112E-03
$\varepsilon_{cr,ult}$ [-]	0.002224	2.224E-03
5*$\varepsilon_{cr,ult}$ [-]	0.011118	1.112E-02

(a)

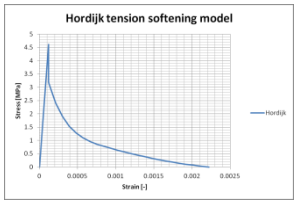

(b)

Main values for principal tensile strain (a) and Hordijk softening diagram (b)

For the four main points selected before, each plot shows the plots of top, bottom, front and lateral surface respectively.

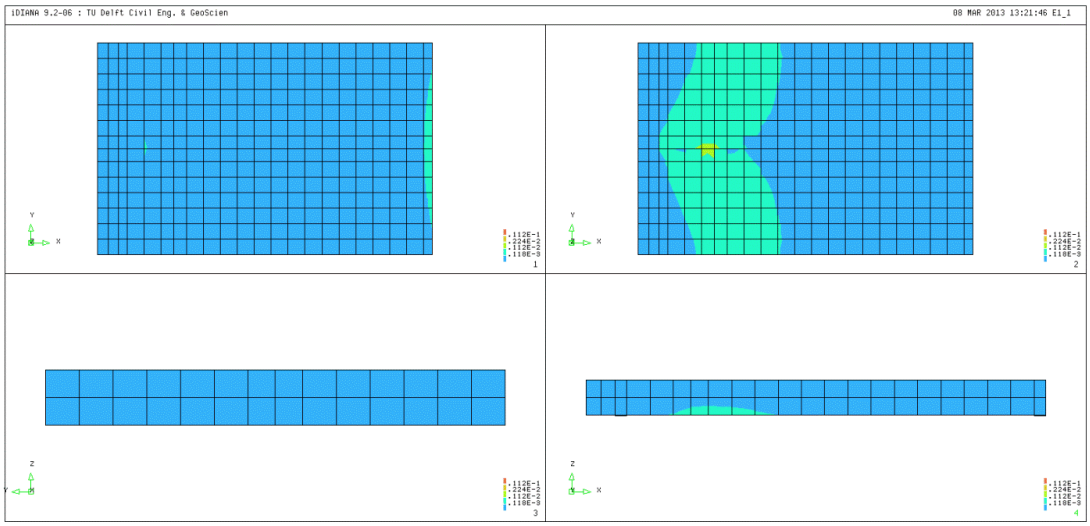

Contour plot of principal tensile strain for 808 kN

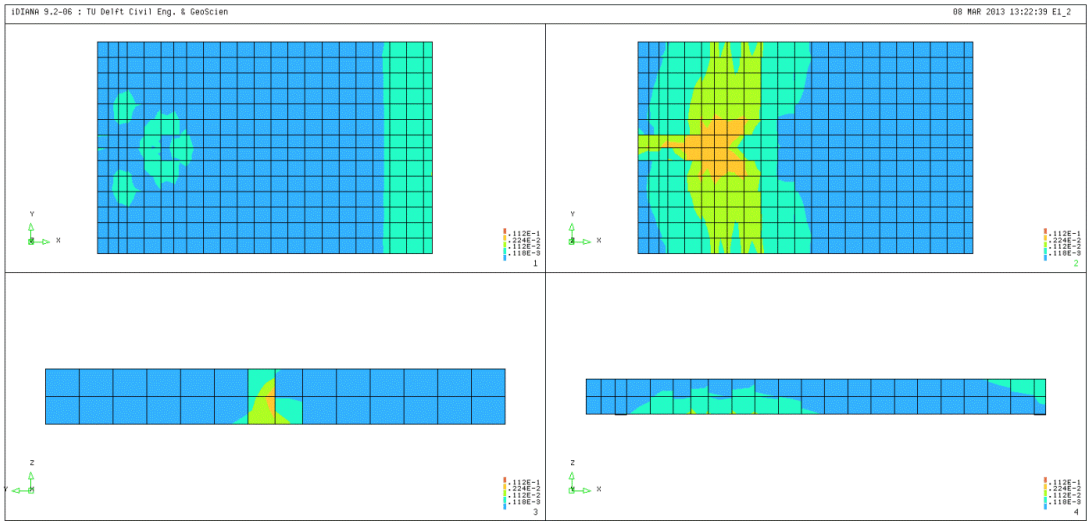

Contour plot of principal tensile strain for 1460 kN

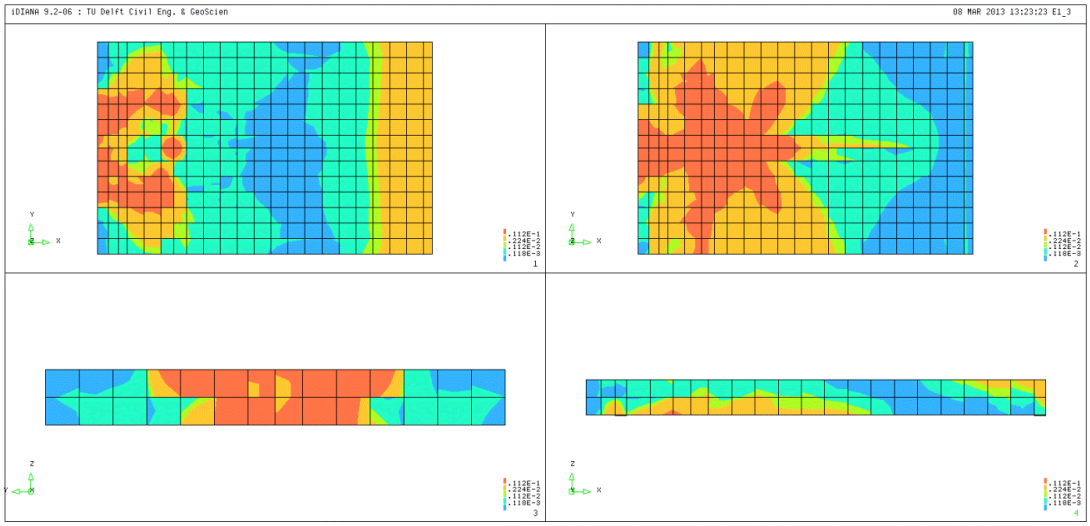

Contour plot of principal tensile strain for 2910 kN (peak)

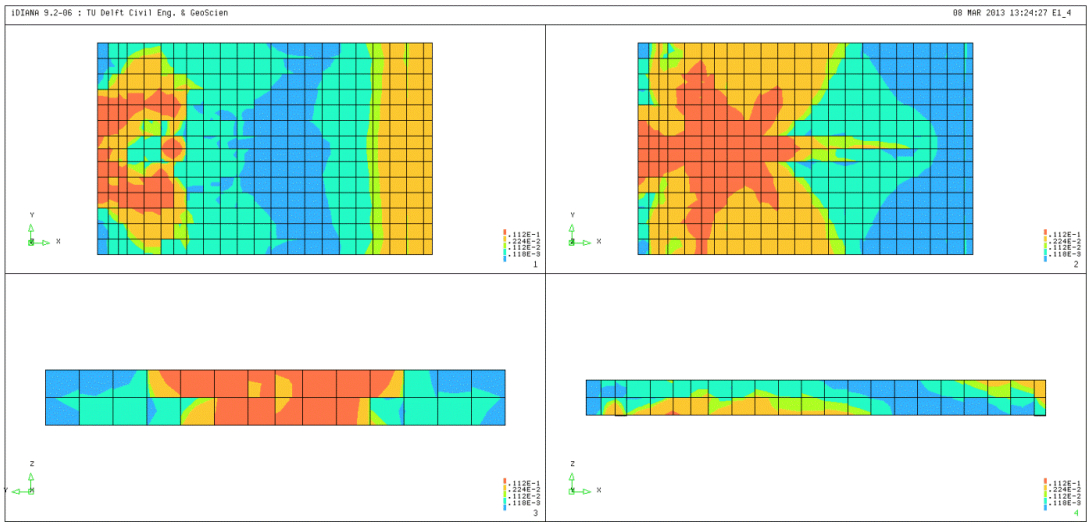

Contour plot of principal tensile strain for 2686 kN (post-peak)

The previous contour plots show a well agreement with the nonlinear output, at least since the second point. Then, for the peak and post-peak plot a wide spreading of the cracked area can be observed. So, the damage seems to diffuse into the slab, producing a large cracking pattern on the four main surfaces. It's interesting to note how a long longitudinal crack and a radial crack system arise on the bottom. Moreover, on the top face an extended flexural crack system is visible.

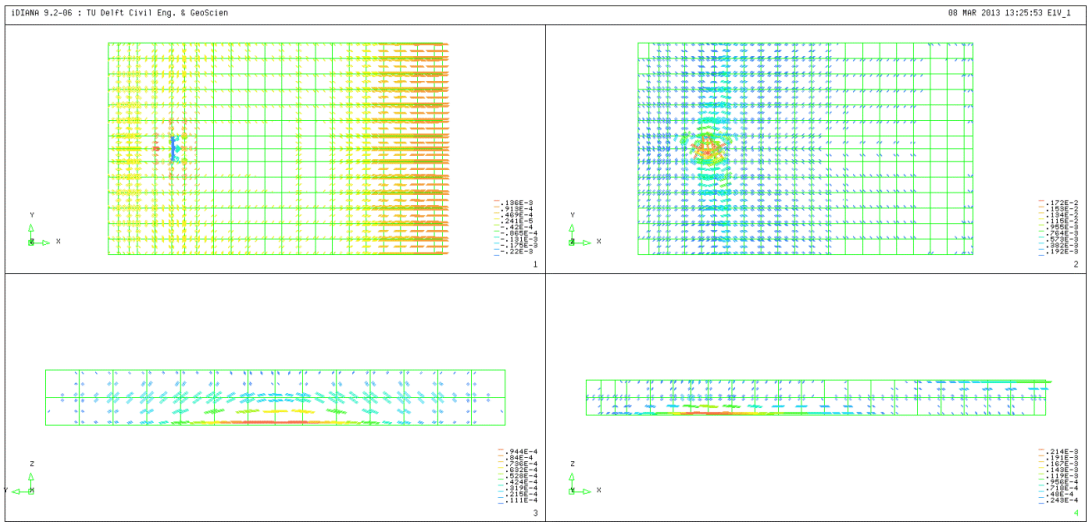

Vector plot of principal tensile strain for 808 kN

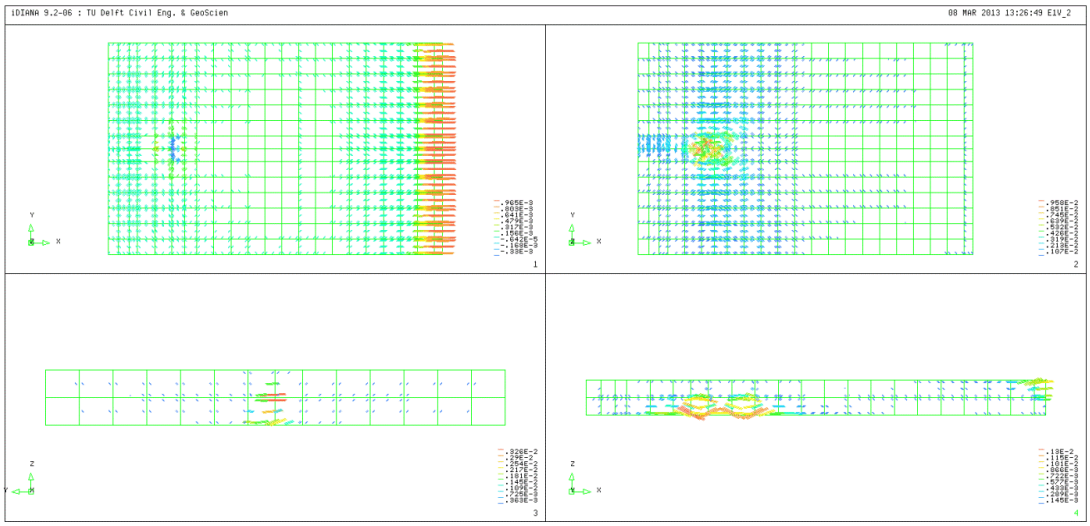

Vector plot of principal tensile strain for 1460 kN

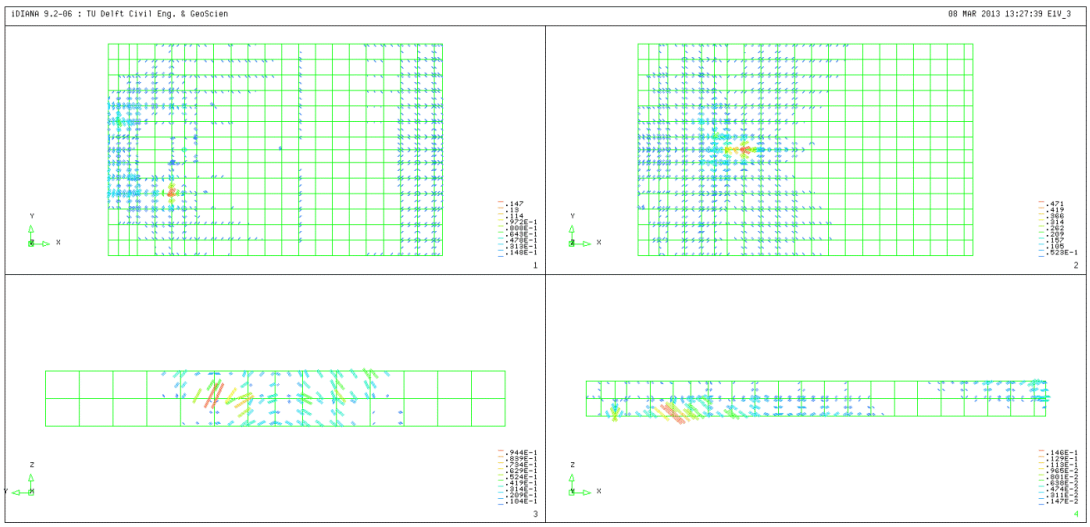

Vector plot of principal tensile strain for 2910 kN (peak)

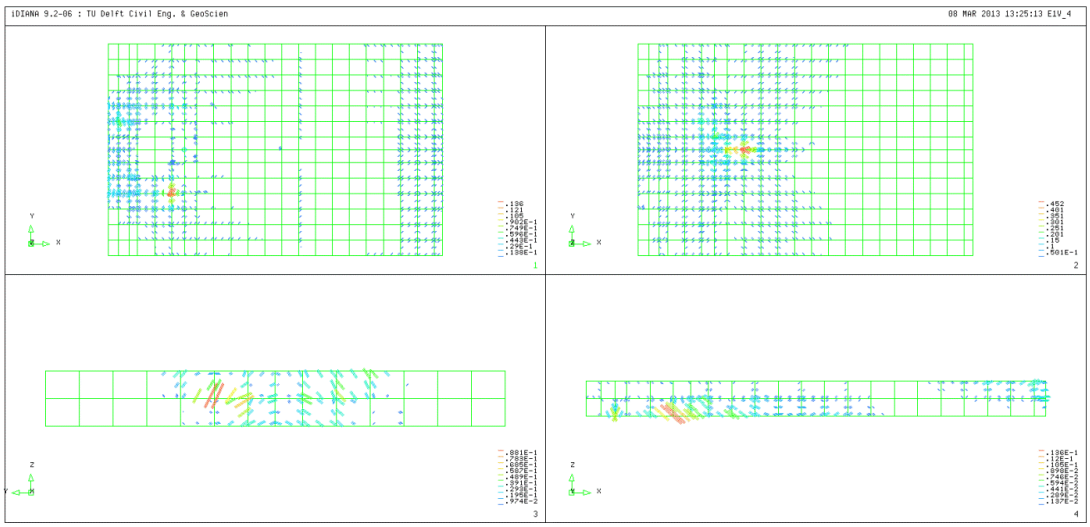

Vector plot of principal tensile strain for 2686 kN (post-peak)

Also here, the first two plots show good agreement with NLFEA and with the global behaviour expected. Indeed, a flexural behaviour is detected until the load of 1460 kN: a transversal and a longitudinal crack are underlined by the strain vectors in a clearer way than the NLFEA. A strut formation can be detected on the lateral side on the peak load. Though the shear takes place as expected, however a weird behaviour of the slab can be detected for higher load. The strut-and-tie mechanism occurs in the opposite direction of the North support, close to the midspan of the slab, and inclined cracks arise on the lateral side. Moreover, the most important crack on the frontal face seems to follow a horizontal path. These observation are in contradiction with the evidences found on the tested specimen.

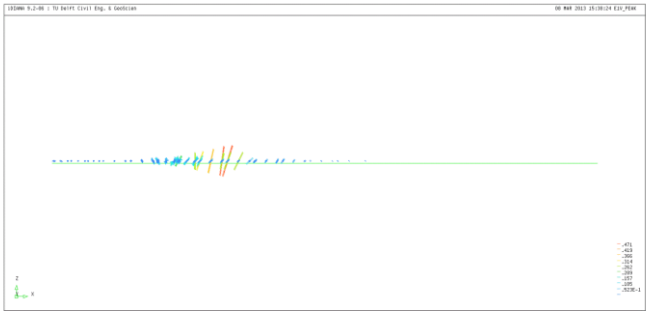

Particular of vector plot of principal tensile strain for 2910 kN (peak) on the bottom surface

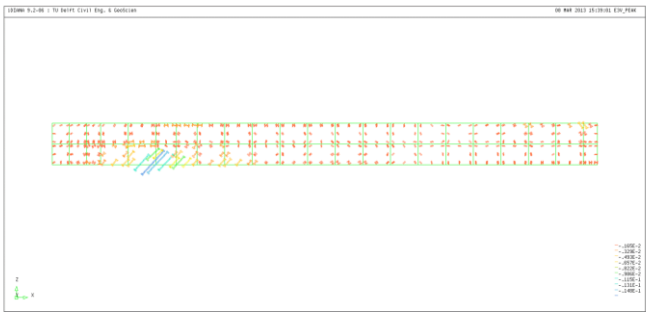

Vector plot of principal compressive strain for 2910 kN (peak)

9.2.3 Compressive behaviour of the concrete

In order to verify the elastic state of the concrete for the compressive field, the *principal compressive stress* feature is investigated through a contour plot on four surfaces, for the three main selected before.
Two main values are adopted:

- $0.50 f_{cc} = -29.88\ MPa$;
- $1.00 f_{cc} = -59.76\ MPa$.

Since, the compressive stress has conventionally a negative value, the green color shows the parts with a lower principal stress than $f_{cc} = -59.76\ MPa$. Instead the blue color proofs the part who exceed this reference value.

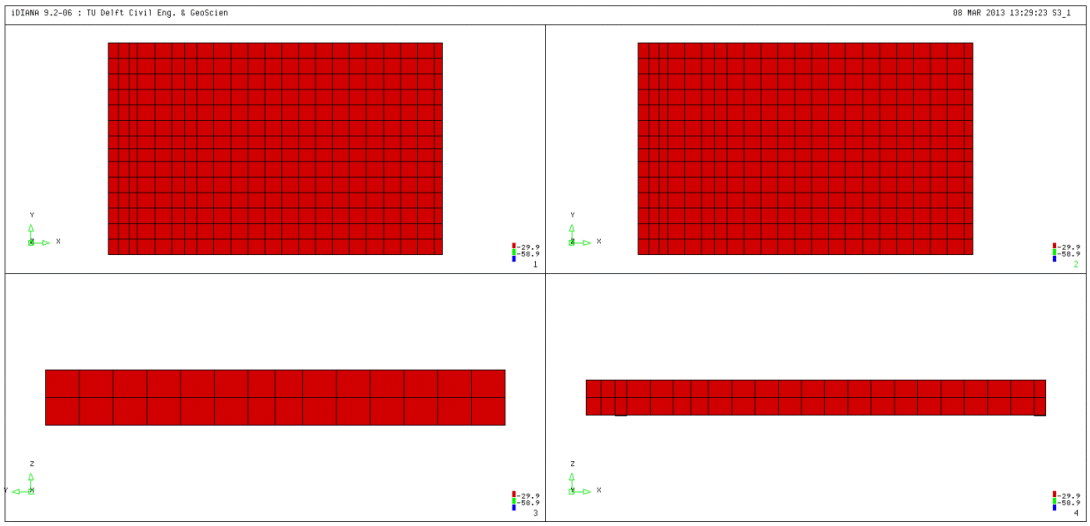

Contour plot of principal compressive stress for 808 kN

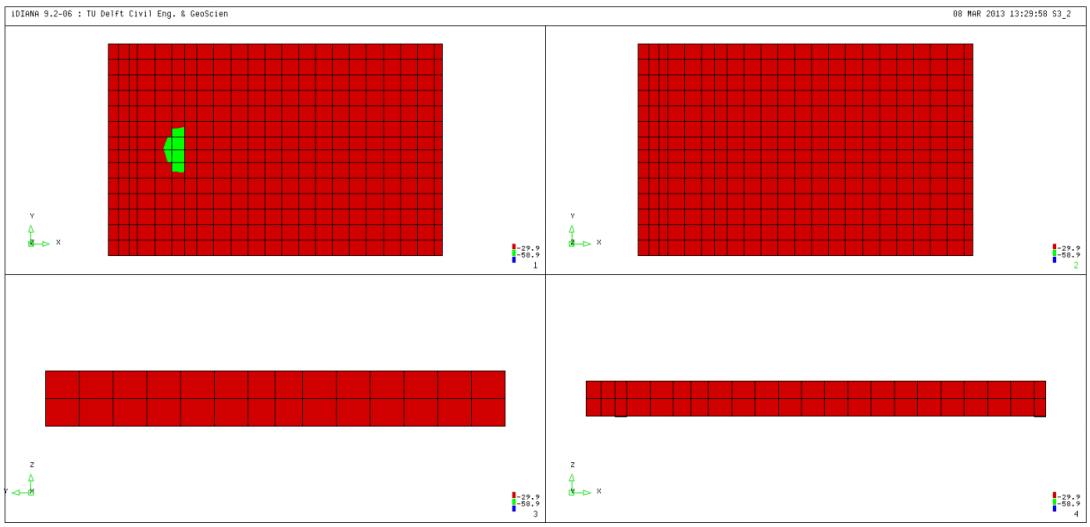

Contour plot of principal compressive stress for 1460 kN

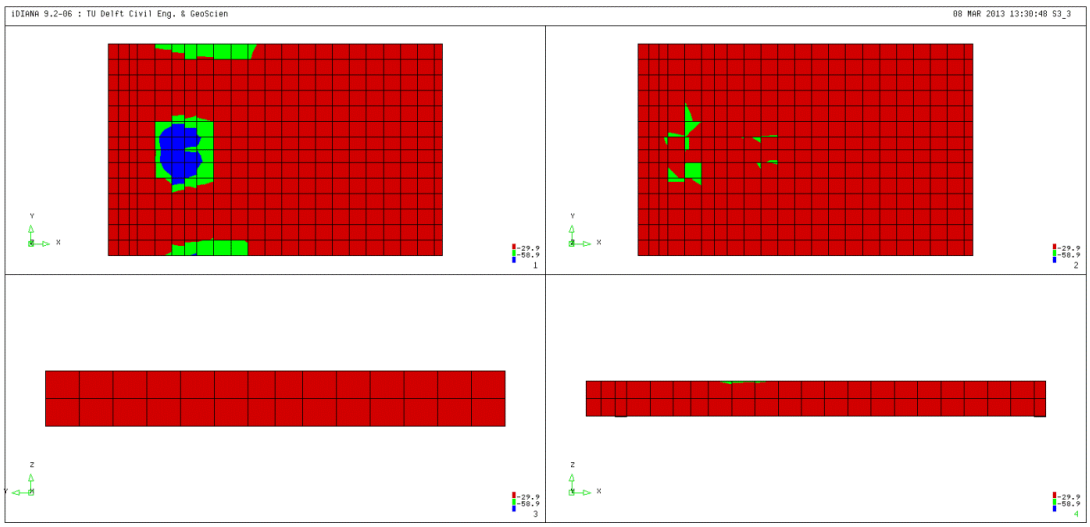

Contour plot of principal compressive stress for 2910 kN (peak)

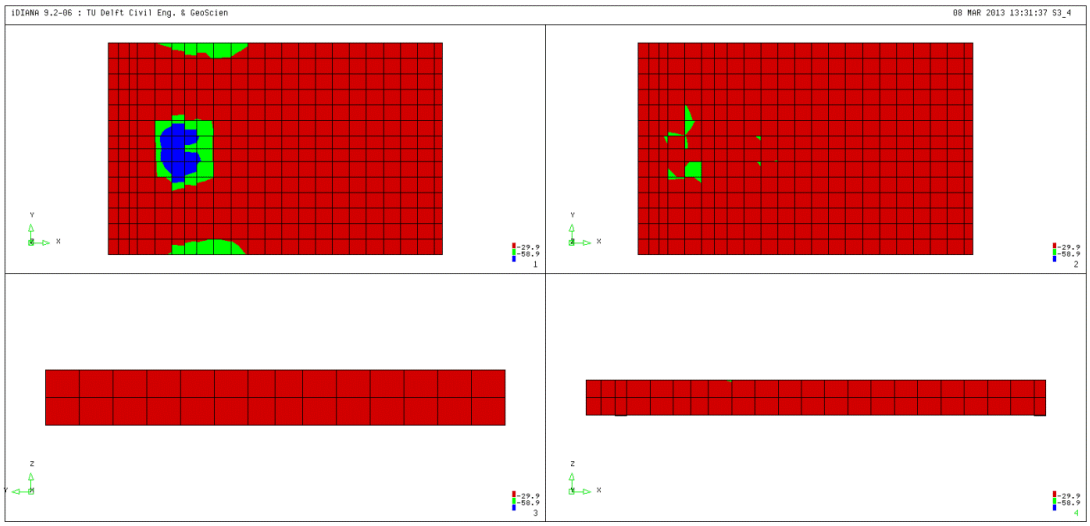

Contour plot of principal compressive stress for 2868 kN (post-peak)

The contour plots confirm what seen before: the first two plots agree with the NLFEA outputs, especially for what regards the slab's behaviour on the same load ($1460\ kN$); indeed here it's detected a larger area of concrete who reaches the ultimate compressive stress. It suggests, once again, that the slab has follown a different way to the failure.

9.2.4 Failure mechanism of the slab

From the contour plots of the bottom face it becomes clear that the principal tensile strains invest the most of the slab. Clear cracks will be visible on the continuous support, and on the all main surfaces.

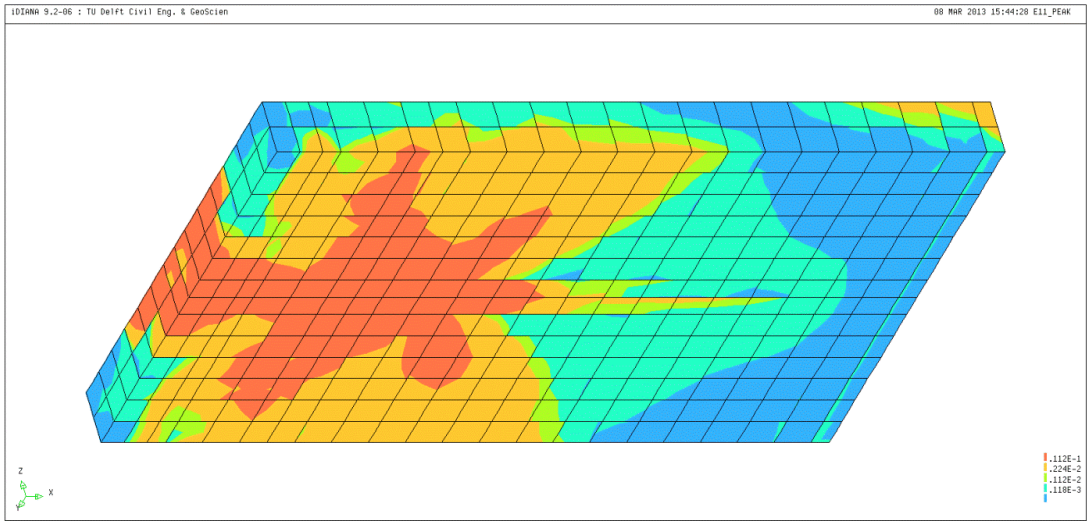

Contour plot of the principal tensile strain on the bottom face on the peak (2910 kN)

However, from the previous plots it is still hard to discover in which way the slab fails.

The plots about the deformed structure help us to confirm that the slab follows a different failure mode than the previous one made with NLA.

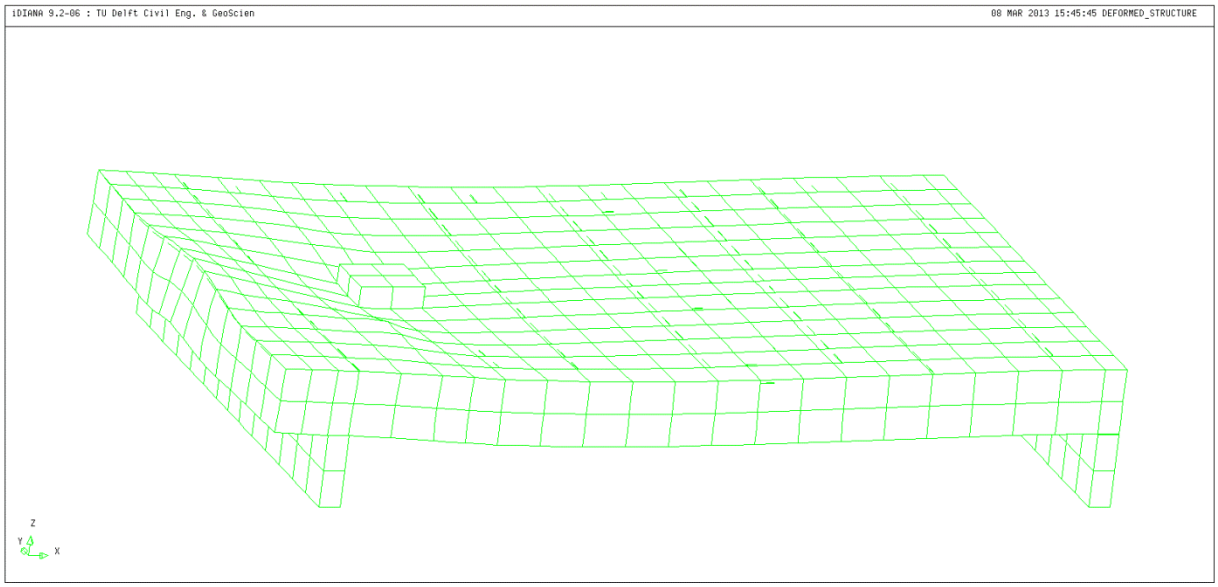

Deformed structure at the peak load: global overview

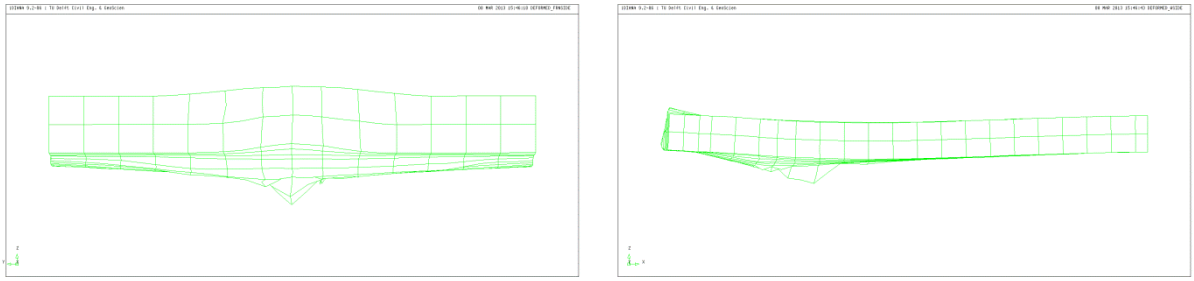

(a) *(b)*

Deformed structure at the peak load: (a) North front side and (b) West lateral side

Here, a completely different deformed shape is detected. Indeed, the most deflected zone in located more towards the midspan respect with the NLFEA output. It could represent a sort of beam response of the whole slab.
To better understand what reported, the following sample is provided:

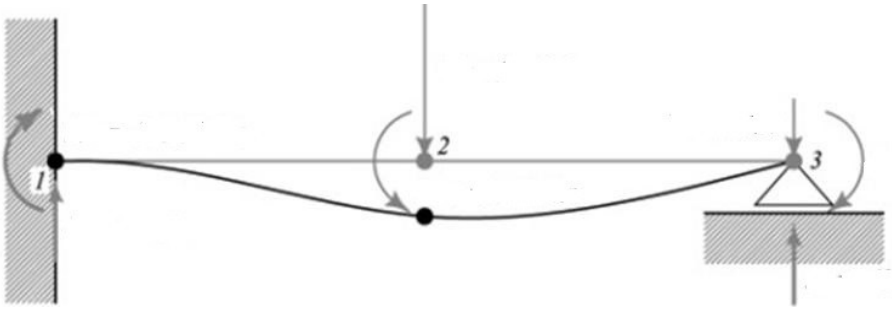

Deflection of a supported-clamped beam under concentrated load

Schematizing the whole slab as a simple support-clamped beam, the maximum deflection is measured not in the load point, into the elastic field. So, it seems that this one is the actual failure mode for the slab.
The model shows a high deflection on the midspan and the middle of the frontal face lifts from the support due to the 2D nature of the slab on the peak load.

9.3 New analysis on coarse mesh

After the results exposed upward, a new analyses is performed on the same mesh. A lower values for the most sensitivity parameter is chosen: a fracture energy even to the 10% of the previous one is taken.
The main features are here reported:

- tensile fracture energy: $G_f = 0.033\ Nmm/mm^2$;
- numerical crack bandwidth: $h = 165\ mm$;
- normal felt interface stiffness: $k_{n,f} = 15.20\ N/mm^3$;
- normal Teflon interface stiffness: $k_{n,T} = 500\ N/mm^3$;
- integration scheme: Gaussian 2 x 2 for interface layer, Linear 2 x 2 x 2 for all the other FE.

The felt has a linear behaviour.
It has to be noted that for the value adopted for G_f the ultimate normal crack strain ${\varepsilon_{nn}}^{cr}{}_{ult}$ is smaller than minimum ultimate crack strain ${\varepsilon_{nn}}^{cr}{}_{ult,min}$, as required by the Hordijk model. For SLA this doesn't involve problem, thanks to the "ripple" approach. For NLFEA it does.
The lower value produces a response of the concrete closer to the brittle tension model, than the usual Hordijk tension softening trend. Indeed, the ratio between ${\varepsilon_{nn}}^{cr}{}_{ult}$ and $\varepsilon_{el,ult}$ equals to 1.90, instead 18.80.

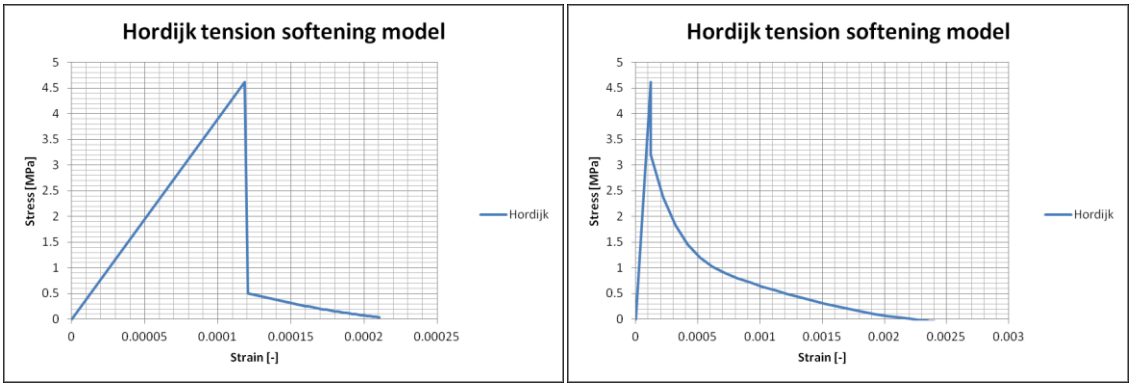

(a) *(b)*

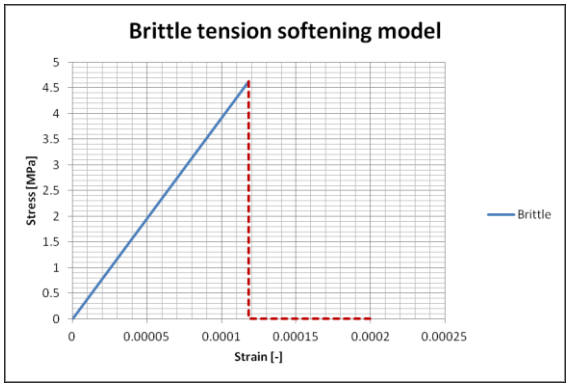

(c)

Hordijk tension softening for concrete for: (a) G_f= 0.033 N/mm,(b) G_f=0.330 N/mm and (c) brittle tension softening model

$\varepsilon_{el,ult.}$ [-]	0.000118	1.184E-04
$0,5*\varepsilon_{cr,ult}$ [-]	0.000111	1.112E-04
$\varepsilon_{cr,ult}$ [-]	0.000222	2.223E-04
$5*\varepsilon_{cr,ult}$ [-]	1.11E-03	1.112E-03

(a)

$\varepsilon_{el,ult.}$ [-]	0.000118	1.184E-04
$0,5*\varepsilon_{cr,ult}$ [-]	0.001112	1.112E-03
$\varepsilon_{cr,ult}$ [-]	0.002223	2.223E-03
$5*\varepsilon_{cr,ult}$ [-]	1.11E-02	1.112E-02

(b)

Reference value for Hordijk tension softening for concrete for: (a)G_f= 0.033 N/mm and (b) G_f=0.330 N/mm

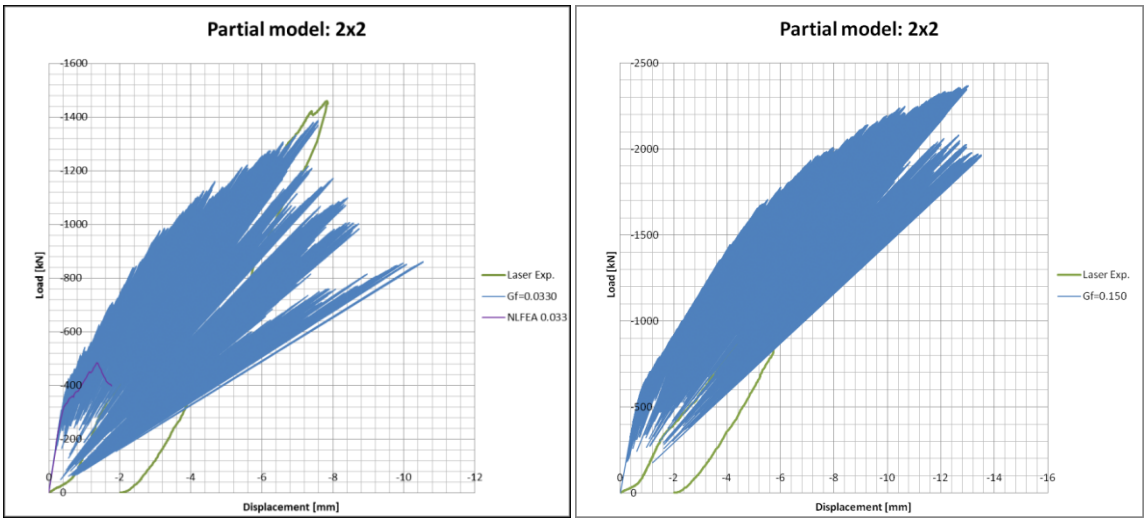

Comparison between load-displacement diagram for SLA and NLA with the same G_f (0.033 and 0.150 N/mm and experimental result

The slab's response by adopting the smaller fracture energy presents good agreement with the experimental evidence, both in terms of peak-load and of peak-displacement. Moreover, unlike what is seen before, the global slope is well estimated. After the peak a sudden decay of the bearing capacity occurs; then a series of snap-backs arises and a gradual decay of the resistance of the slab is shown.
The numerical peak values are:

- peak load: 1388.40 kN;
- peak displacement: 7.589 mm.

instead of:

- experimental peak load: 1460.62 kN for a variation of $\sim -5\%$;
- experimental peak displacement: 7.84 mm for a variation of $\sim -3\%$.

The obtained values and the relative percentages of approximation is satisfactory for an engineer application. No convergence trend has been studied, since only linear analysis are executed and the convergence is always reached. The analysis runs about 300000 iterations to display the post-failure behaviour, but the peak arises around the 200000th.

Four main points are selected on the load-displacement diagram:

- *point 1:* $(0.43\ mm; 355\ kN) \sim 25\%F_{max}$;
- *point 2:* $(1.98\ mm;\ 731\ kN) \sim 50\%F_{max}$;
- *point 3:* $(6.80\ mm;\ 1305\ kN) = F_{max}$;
- *point 4:* $(7.44\ mm;\ 1344\ kN) = post - peak$.

They are shown in following plot; the main output will be exposed in the next paragraphs.

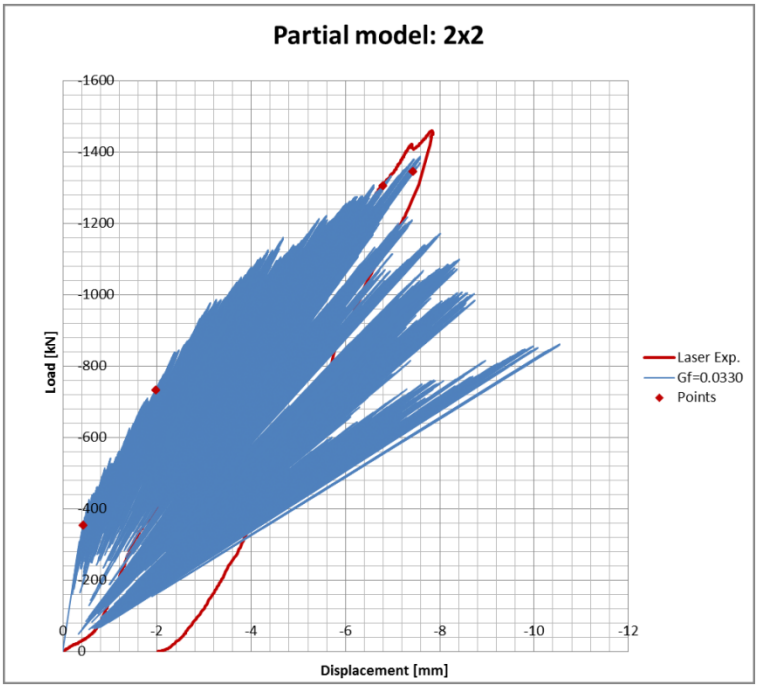

Main points on the load-displacement diagram for SLA

9.3.1 Redistribution capacity:

On the following image, four pictures of the felt reactions in the Z-direction s_{ftz} are shown by adopting a vector plot. They prove the redistribution of the load from the slab to the support, since the action on the felt is equal to the one on the support beam for vertical balance.
The pictures show the plot about the four main points.

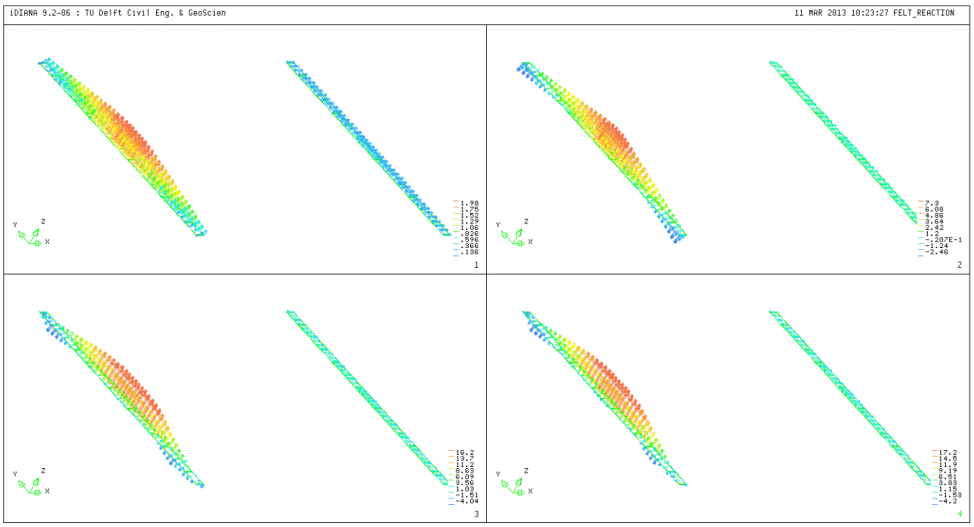

Vector plot of felt reaction [MPa] for the main points

By observing the previous vector plot of the interface traction, the trend of the reaction forces can be discovered. On the 1st main point (355 kN) the usual triangular shaped distribution is detected and no tensile reaction stresses arise on the interface, since the 2nd main point (730 kN) is reached. Now, the load seems to be carried by the middle part of the North support, extending toward the free lateral edges. For higher load the effective width reduces the area, but the most of the load is concentrated around the middle on the support: that is visible for load close to the peak 1340 kN. The maximum compressive stress reaches 17 MPa, while the maximum tensile stress is 4.2 MPa.
By plotting the part of interface in a compressive state, they are shown with red color (values higher than 0 MPa - *compression*). It can be observed that the loading angle assumes a value from 68° (1st main point) and 64° (4th main point), therefore the effective width of the active zone of the support changes from $b_{eff} = 2500\ mm$ to $b_{eff} = 2140\ mm$.

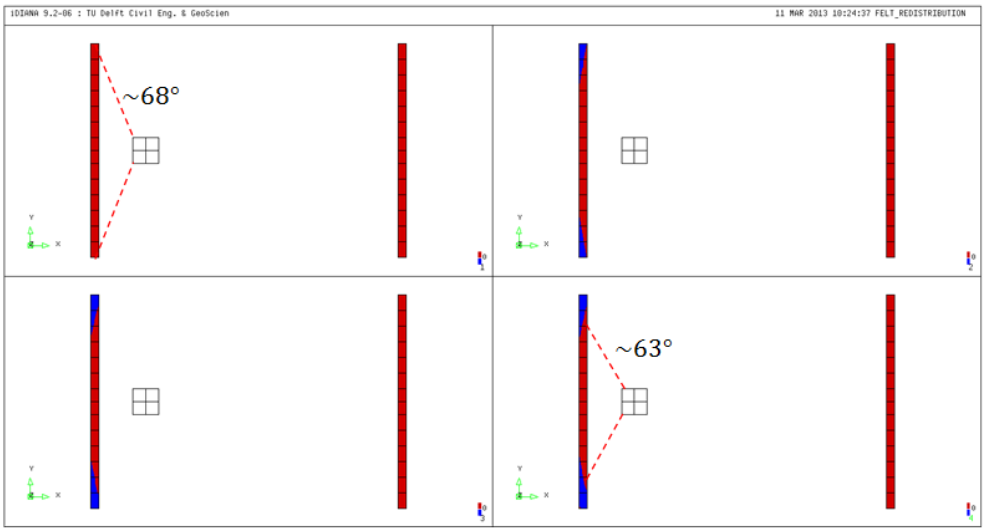

Effective width due to the load spreading on the felt layer

9.3.2 Cracking behavior of the slab

In order to investigate the development of the cracking under an increasing load, contour and vector plot of the pricinpal tensile strain are used. Taking into account four points on the softening diagram calculated for a fracture energy $G_f = 0.033\ N/mm$ and $h = 165\ m$.

$\varepsilon_{el,ult.}$ [-]	0.000118	1.184E-04
0,55*$\varepsilon_{cr,ult}$ [-]	0.000122	1.223E-04
$\varepsilon_{cr,ult}$ [-]	0.000222	2.223E-04
5*$\varepsilon_{cr,ult}$ [-]	1.11E-03	1.112E-03

(a)

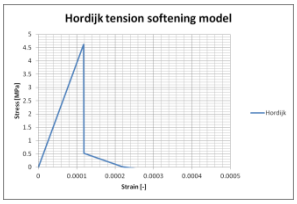

(b)

Main values for principal tensile strain (a) and Hordijk softening diagram (b)

The second value on the Hordijk softnening model has been modified in order to take a higher value than the ultimate elastic strain.
For the four main points selected before, each plot shows the plots of top, bottom, front and lateral surface respectively.

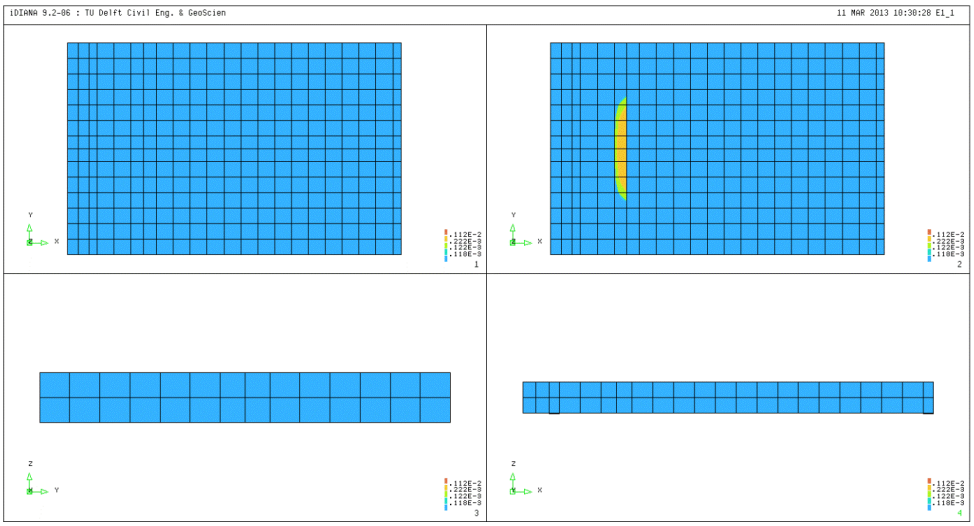

Contour plot of principal tensile strain for 355 kN

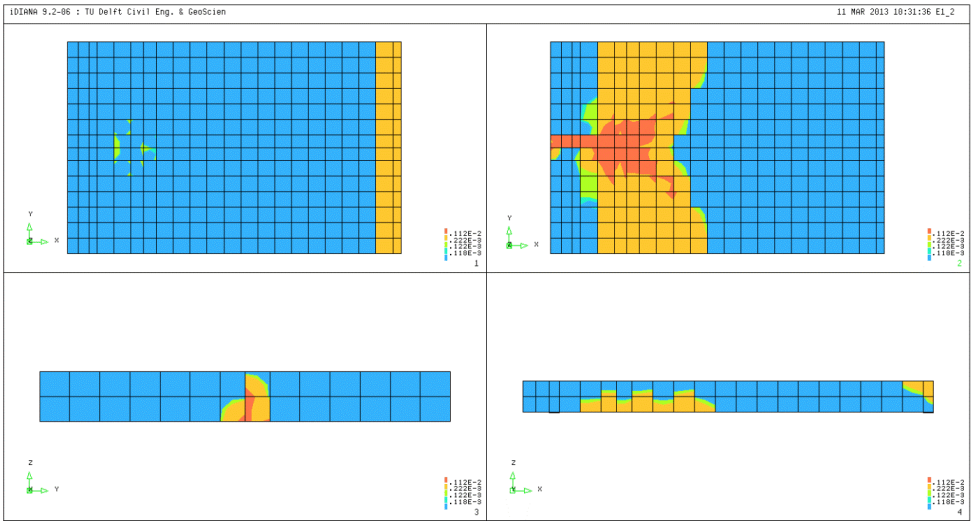

Contour plot of principal tensile strain for 731 kN

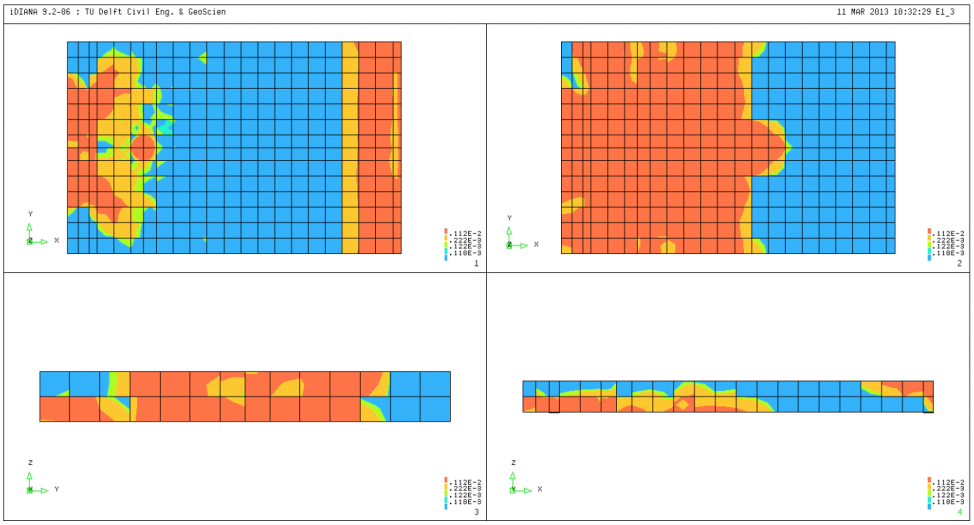

Contour plot of principal tensile strain for 1304 kN (peak)

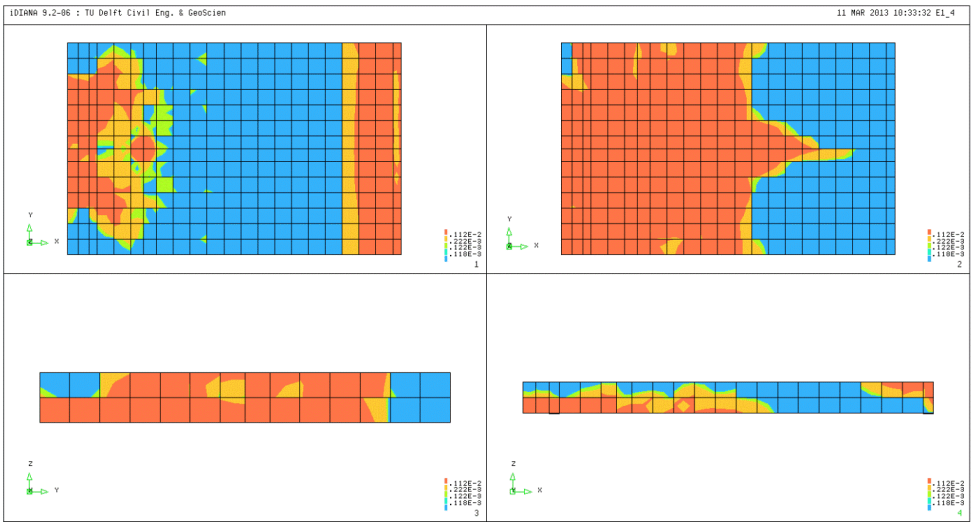

Contour plot of principal tensile strain for 1344 kN (post-peak)

The previous plots underline a strong different respect with to the NLFEA output for the same mesh in terms of spreading of the cracked areas. However, it's shown that the cracks arise from the bottom, below the loading plate, and run first in the transversal direction and then mainly on the longitudinal direction. On the peak and post-peak the plots become confused, since the damage spreads on the main surfaces of the slab. The cracks are concentrated in the North part of the slab, as expected, and on the last point a longitudinal crack seems to spread toward the midspan.

To have a clearer representation of the direction and of the entity of the fractures, it's useful to have also a vector plot of the same principal tensile strain.
The same surfaces are plotted:

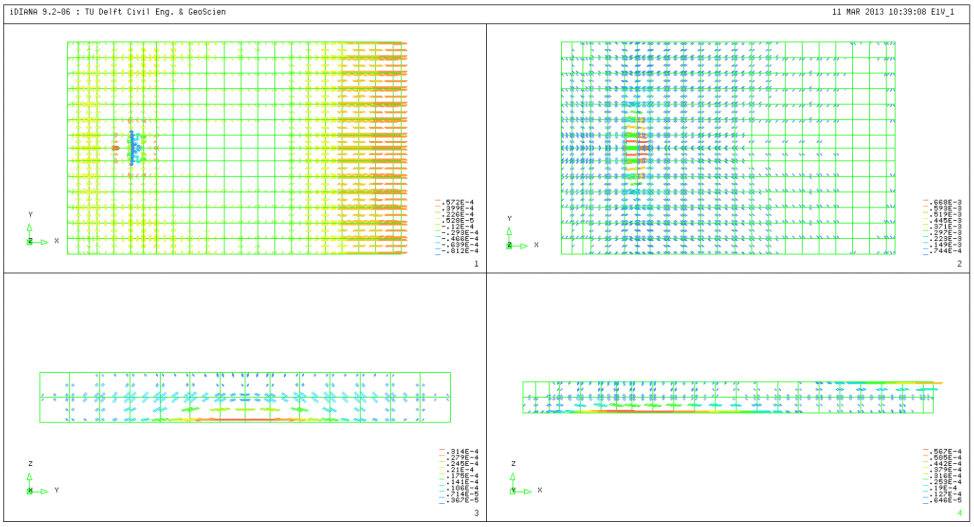

Vector plot of principal tensile strain for 355 kN

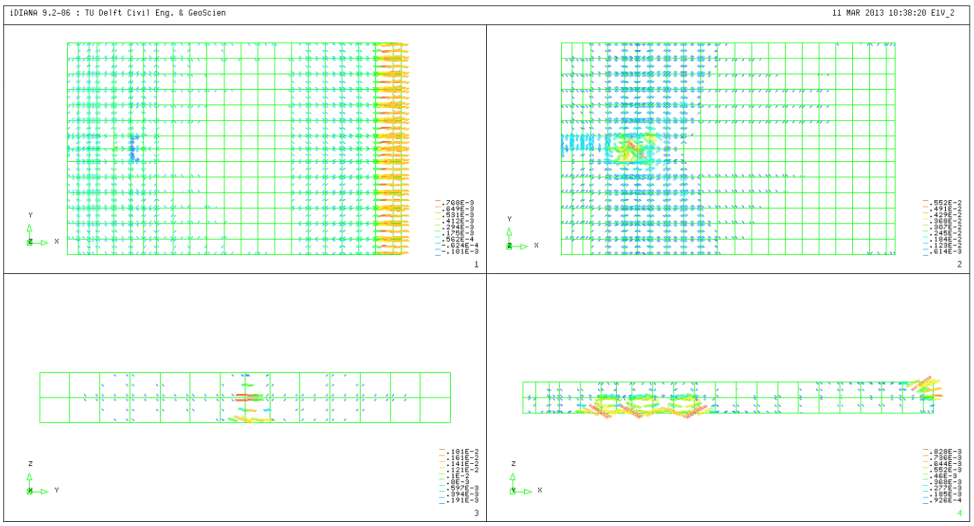

Vector plot of principal tensile strain for 731 kN

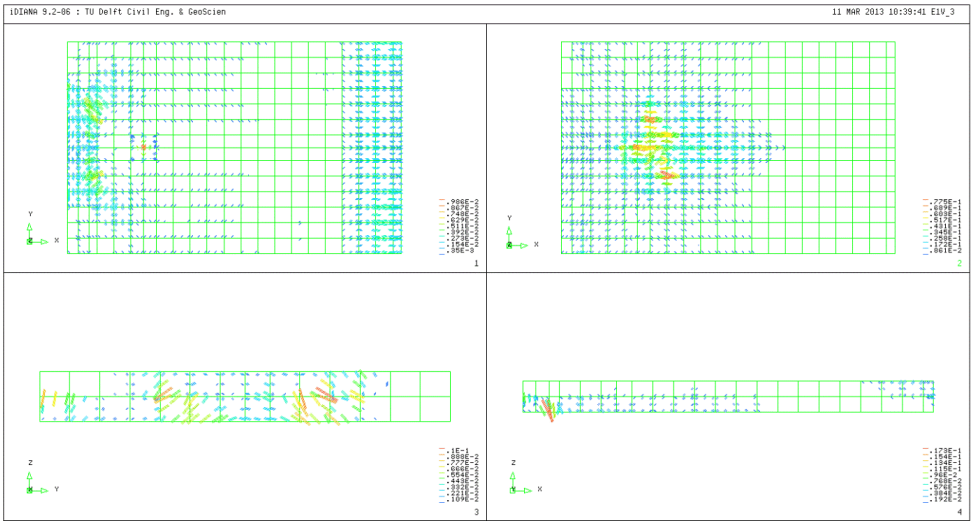

Vector plot of principal tensile strain for 1418 kN (peak)

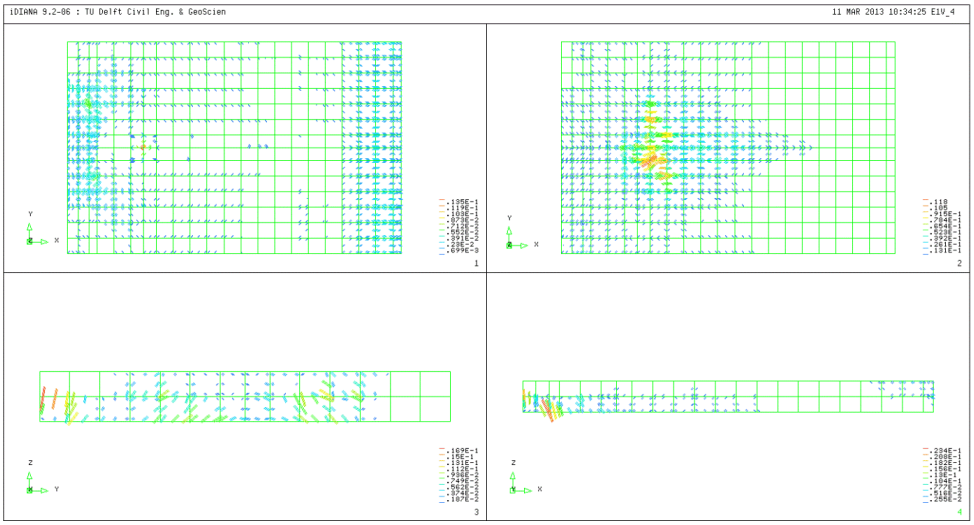

Vector plot of principal tensile strain for 1241 kN (post-peak)

On the first point, at 355 kN, the strain distributions are similar to the previous seen before on the other analysis. The slab shows an elastic behaviour globally, since only on the bottom the ultimate elastic strain $\varepsilon_{el,ult}$ is exceeded. Here, vectors runs in the X-direction below the loading plate: this means that a transversal crack arises.
Then a load of 731 kN strain vectors show a longitudinal crack running on the X-direction, from the loading plate on the bottom surface forward the North face. These two families of crack well evidence the initial flexural behaviour of the slab before the shear mechanism arises. Radial cracks can be detected as well and inclined vectors start to arise below the load position. On the frontal face a vertical crack runs from the bottom forward the half of the thickness. On the lateral side the main stresses zone, as below the load and on the clamped side, are interested by high strain vectors.

For a load of 1304 kN, who represents the peak load, a strong redistribution of the principal tensile strain occurs. On the bottom face only inclined vectors can be detected, then the shear mechanism governs the slab behaviour. It has to be noted that the inclined vectors are located below the load, but on the South side, unlike what is shown with the NLFEA. On the frontal face two main cracks are detected: they run along the vertical direction, about 300 mm from the middle. An horizontal crack can be underlined, on the right side. It's could be caused by the tensile felt reaction, as it's visible on the lateral plot. A strain concentration is visible on the North support, close to the interface. This cracks increases on the last point, for 1344 kN.

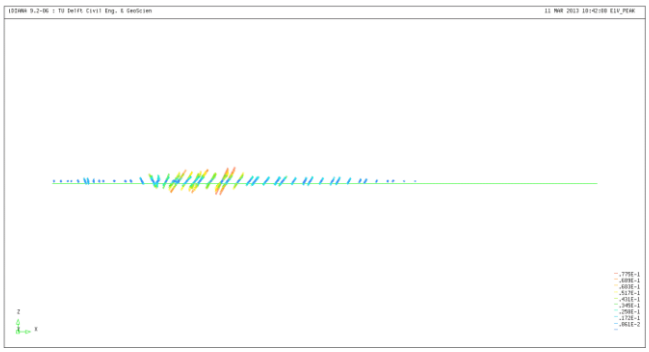

Particular of vector plot of principal tensile strain for 1304 kN (peak) on the bottom surface

Looking at the previous plot, it seems the load prefers to be transferred toward the middle of the slab, since the struts converge toward the midspan.
The presence of the strut-and-tie bearing mechanism and its evolution can be proved through a vector plot of the principal compressive strains, showing clear inclined struts of concrete. However, this is not confirmed by the principal compressive strain plots:

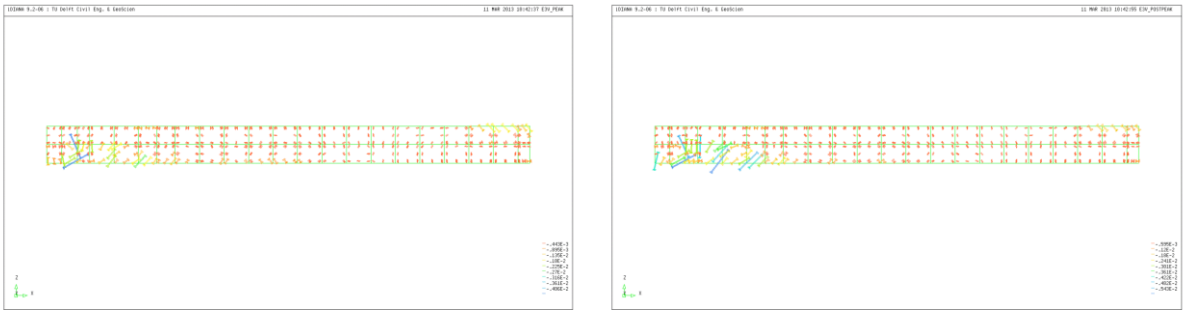

Vector plot of principal compressive strain for peak (left-hand) and post-peak (right-hand)

On the last two points, the main compressive strains evidence a different mechanism to transfer the action: here the load is transmitted to the North support through inclined struts, as expected.

On the basis of the previous observations about the cracking behavior of the slab, performed using the SLA, it can be stated that the tensile reaction of the felt has a not negligible influence on the local behaviour of the slab, close to the North support. Indeed, the normal stiffness is much higher (at least one order) than the other values adopted in the previous analysis.
The flexural cracks are well detected and the strut-and-tie mechanism are shown.

9.3.3 Behaviour of the reinforcement bars

To have an immediate evaluation of the distribution of the stress and of the behavior of the steel bars, contour plots of the principal tensile stresses are presented afterward, referring to a unique yielding tension equal to $540\ MPa$.
Three main points are taken into account and for each one, four plots are shown: σ_{xx} and σ_{yy} for the top rebars, respectively on the upper and on the bottom plot (left hand); σ_{xx} and σ_{yy} for the bottom rebars, respectively on the upper and on the bottom plot (right hand).
Through these contour plots it can be proved the hypothesis of *Kinnunen* and *Nylander*, since the reinforcement steel of the bars has an elastic behavior in most part of the slab and the only area in which one can notice a yielding is the one close to the loading point. In particular for an applied load of around $1300\ kN$, the only bars who yields has a very limited length, below the loading point (red color).
No yielding occurs on the other bars.

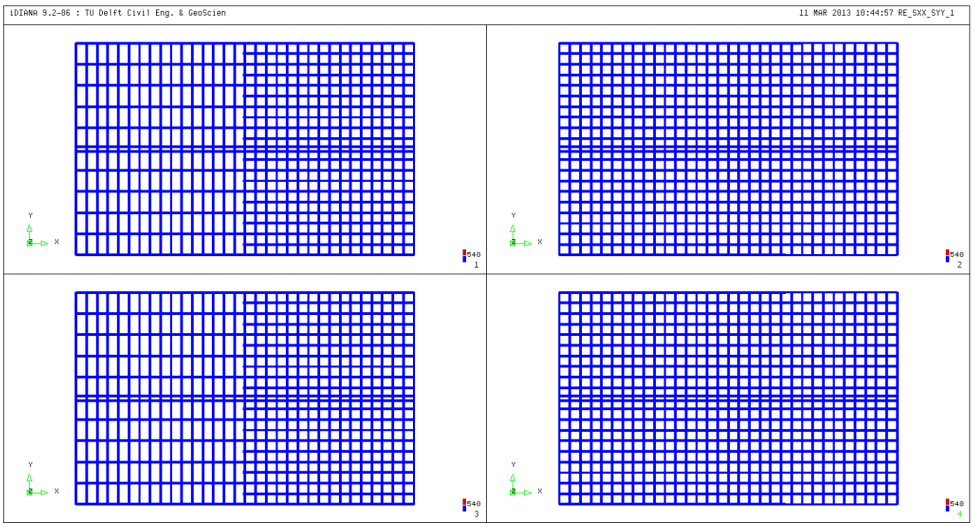

σ_{xx} and σ_{yy} contour plot for top and bottom reinforcement bars for 355 kN

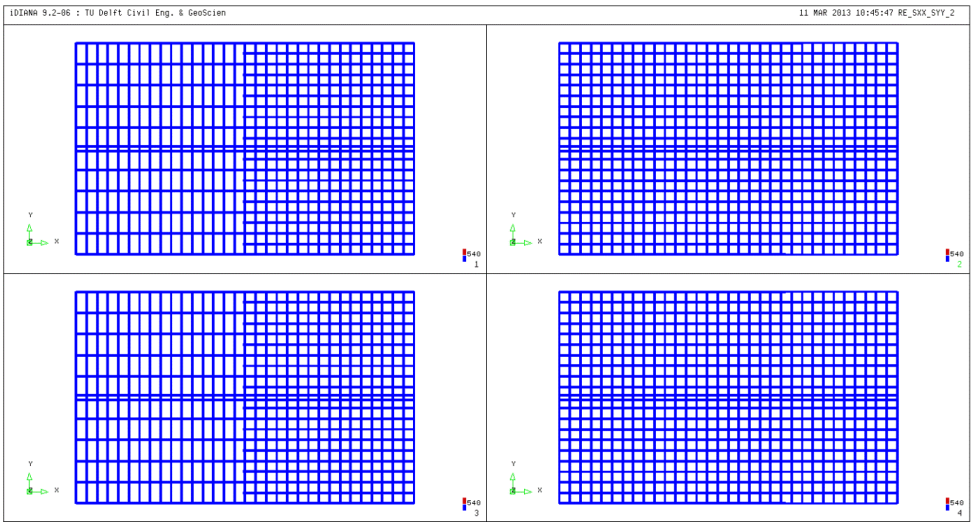

σ_{xx} and σ_{yy} contour plot for top and bottom reinforcement bars for 731kN

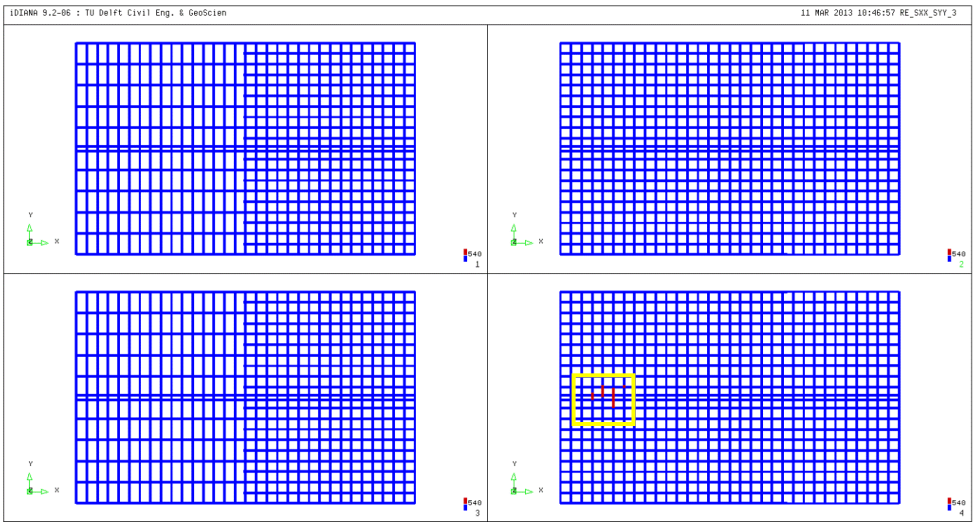

σ_{xx} and σ_{yy} contour plot for top and bottom reinforcement bars for 1304 kN (peak)

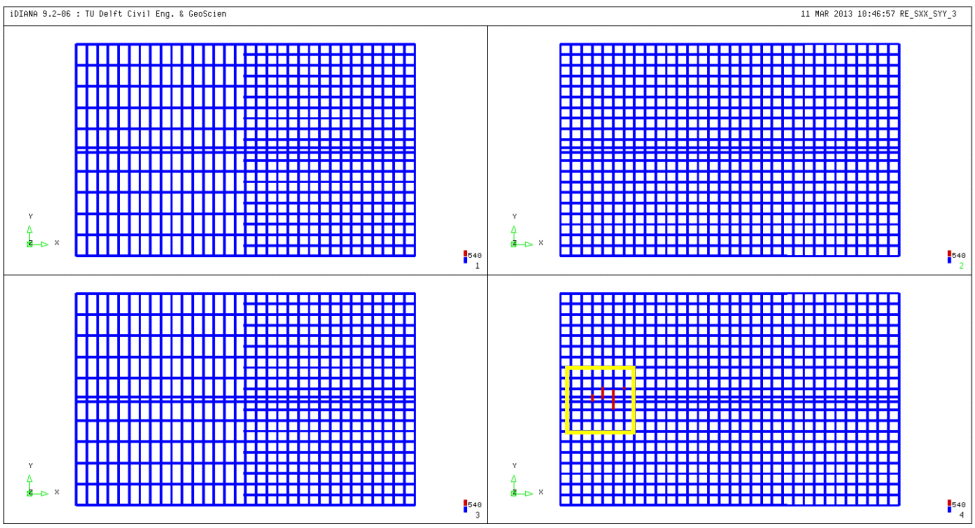

σ_{xx} and σ_{yy} contour plot for top and bottom reinforcement bars for 1344 kN (post-peak)

Adopting the principal tensile stress plots, we can observe the progressive redistribution of the stress inside the reinforcement bars.
For the present plots four points are selected: the first point on the load-displacement graph and the aforementioned three main point.
The first points allows us to discover the tensile stress distribution inside the rebars when the slab works in a ideal linear elastic state. Then, the following plots can show a gradually changing in value, position of the most loaded bars and distribution of the global stresses.
Since we ask for principal tensile stress, only positive values will be shown.

Observing the bottom rebars, the first two plots confirms the crack development: at 355 kN the highest stress arises on the longitudinal bars below the loading plate, while at 731 kN it invests the transversal bars, forward the North face. After, on the peak load of 1304 kN the stress spreads around the load position, especially in the longitudinal direction. The most stressed zone is located below the loading plate and the yield stress is reached. For higher load the external transverse bars are the most stressed.
The plots of the top rebars show a stress redistribution as well: the most interested zone moves from the clamped side to the North edge. Here, on the peak- and post-load the rebars close to the middle are the most stressed.

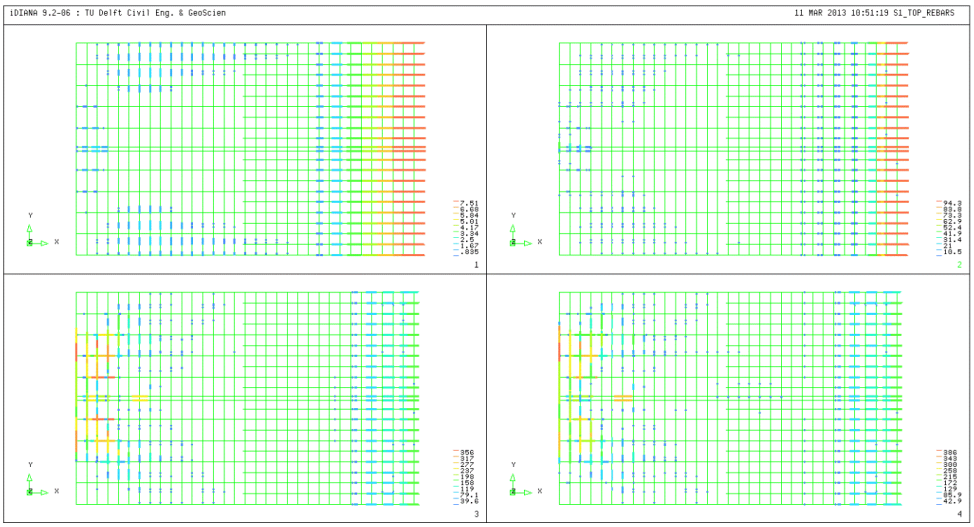

Principal tensile stress for the reinforcement bar on the top surface

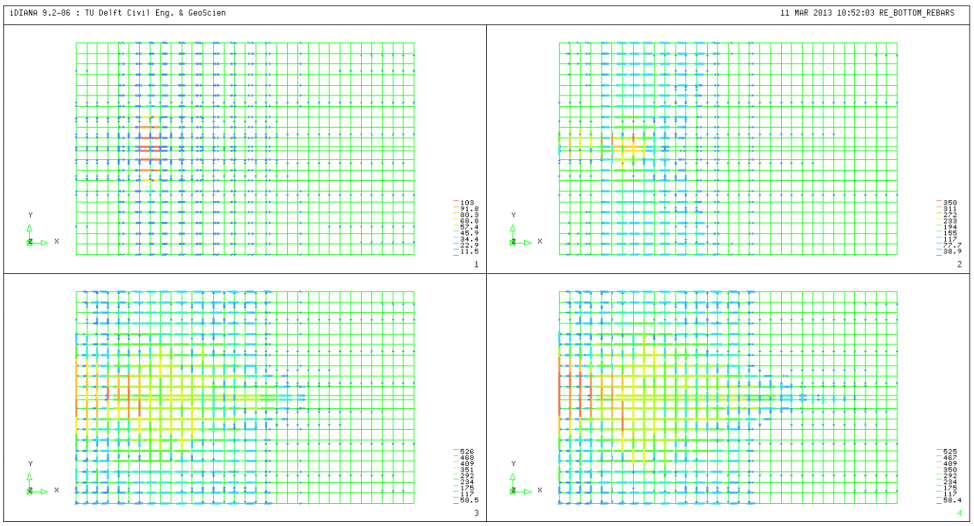

Principal tensile stress for the reinforcement bar on the bottom surface

9.3.4 Compressive behaviour of the concrete

In order to verify the elastic state of the concrete for the compressive field, the *principal compressive stress* feature is investigated through a contour plot on four surfaces, only for the last three main selected before.
Two main values are adopted:

- $0.50 f_{cc} = -29.88\, MPa$;
- $1.00 f_{cc} = -59.76\, MPa$.

Since, the compressive stress has conventionally a negative value, the green color shows the parts with a lower principal stress than $f_{cc} = -59.76\, MPa$. Instead the blue color proofs the part who exceed this reference value.

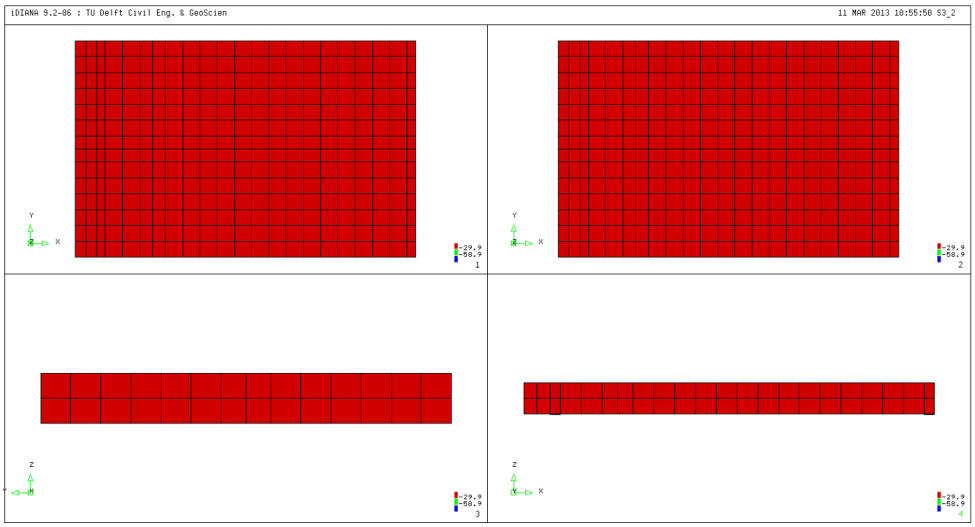

Contour plot of principal compressive stress for 731 kN

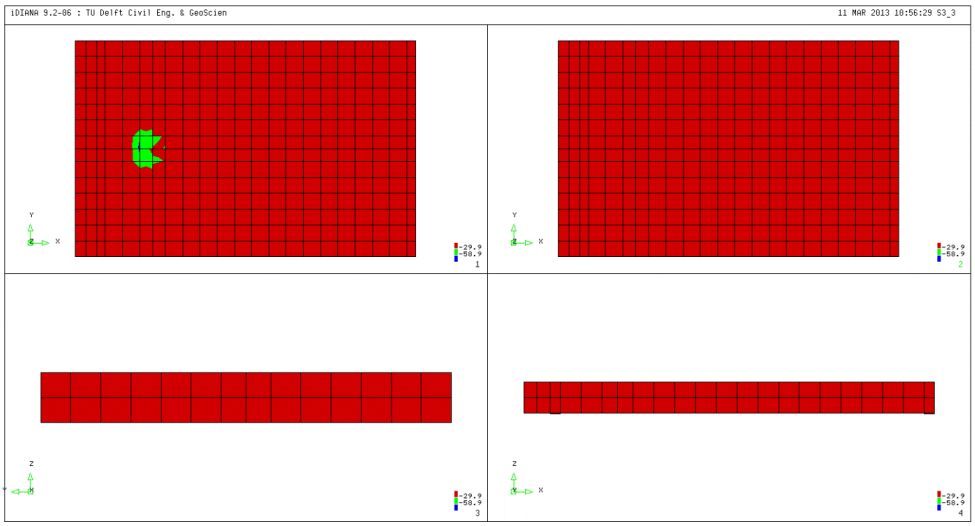

Contour plot of principal compressive stress for 1304 kN (peak)

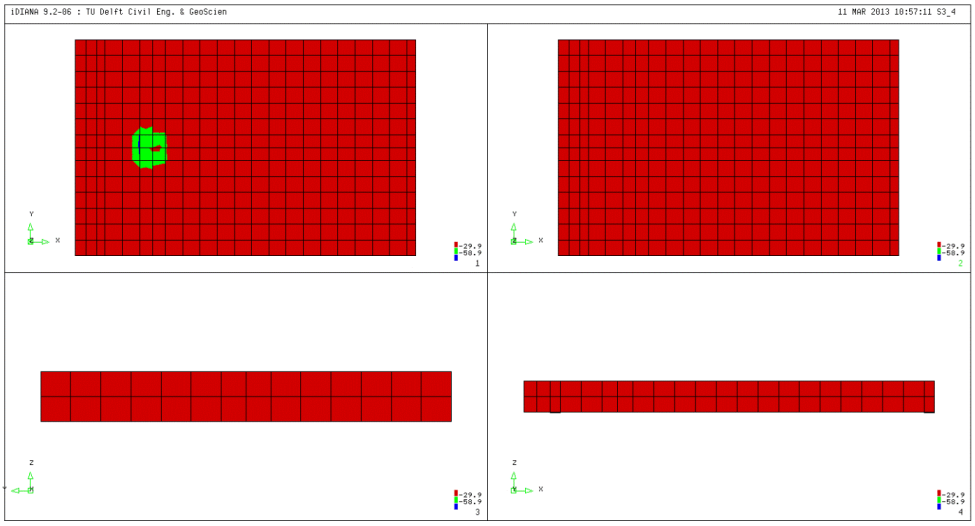

Contour plot of principal compressive stress for 1241 kN (post-peak)

As shown by the previous plots, the principal compressive strain never exceed the compressive strength of the concrete. Only below the loading plate the compressive strength of the concrete is completely exceeded.
So, thanks to these plots, we can demostrate that the assumption of a linear elastic concrete in compressione is adequate to describe the behavior of the conglomerate. This is is strengthened by the fact that also the 50% of f_{cc} is never reached on high volume of elements inside the slab.

9.3.5 Failure mechanism of the slab

From the contour plots of the bottom face it becomes clear that the principal tensile strains are less developed at the side of the continuous support. The following picture shows the distribution of the principal tensile strain at the peak load and after the peak load. The scale of the contour plots is held constant in order to see the development of the tensile strain area:

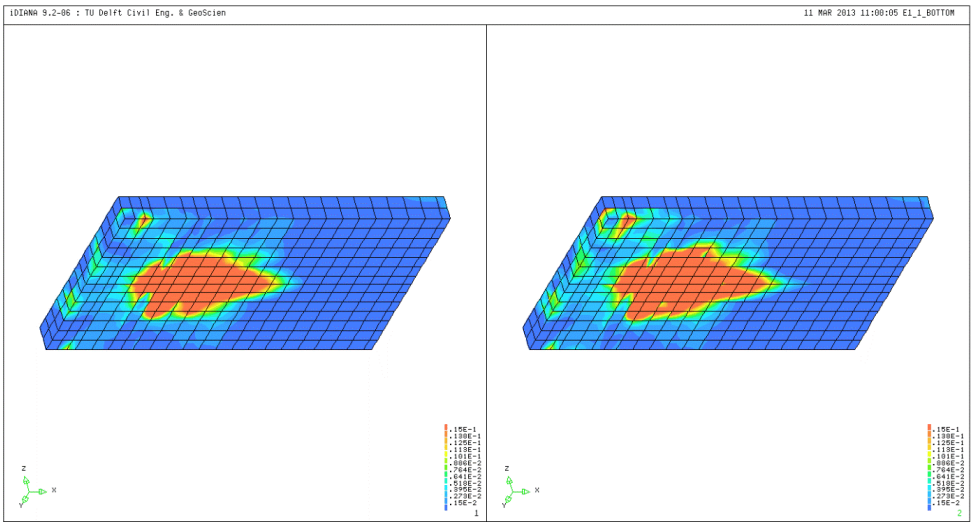

Contour plot of the principal tensile strain on the bottom face on the peak (left-hand) and post-peak points (right-hand)

Unlike the previous analysis, a bigger cracked area is detected. The higher and marked brittleness of the concrete could involve a wider spreading of the damage. A strong concentration can be discovered below the loading plate (as expected) and forward the midspan. The uniformity of the principal tensile stresses does not allow to distinguish the occurrence of different crack systems. The red area could contain radial and punching shear cracks. So, a clear crack patter can't be detected as done before.
Moreover, the combination of a tensile reaction provided by the felt and the low "tensile ductility" of the concrete involves the formation of a horizontal crack on the frontal face.
Finally, it's not possible for us detect the exact way of failure of the slab from these plots.

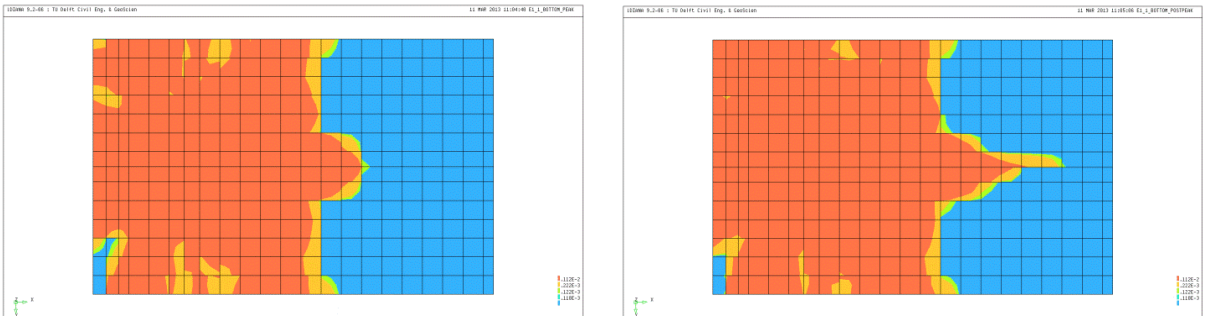

(a) *(b)*

Contour plot of the principal tensile strain for peak (a) and post-peak load (b)

A better interpretation can be discovered observing the deformed shape of the structure from different point of views, on the peak and post-peak status:

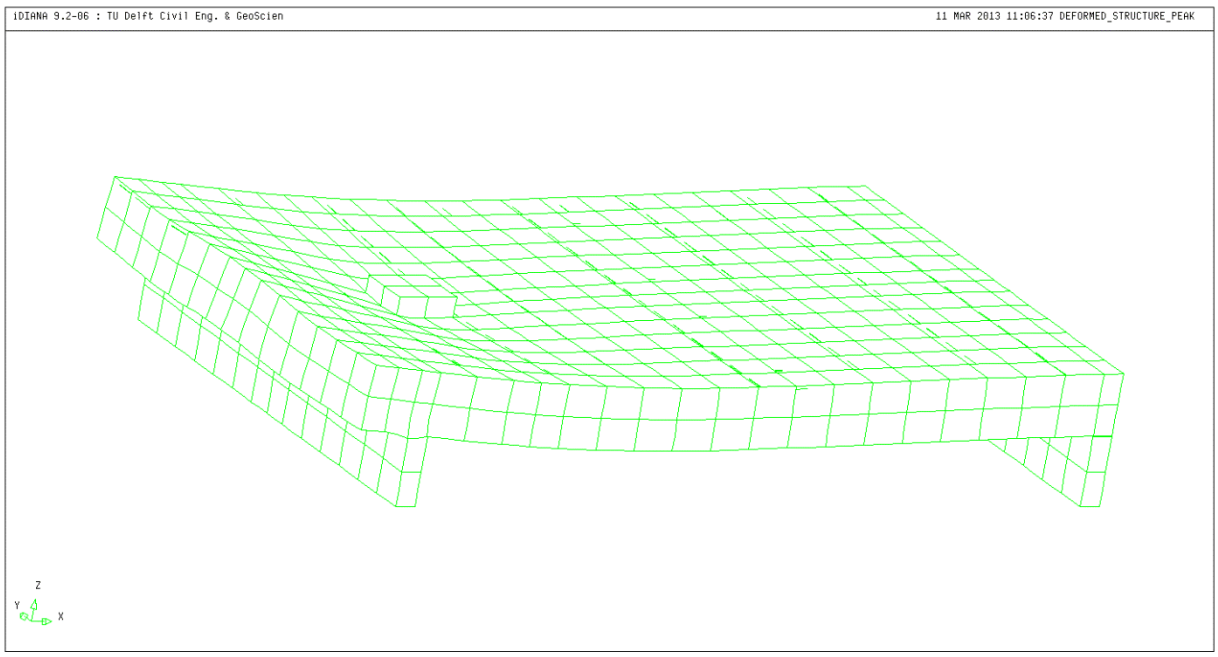

Deformed structure at the peak load: global overview

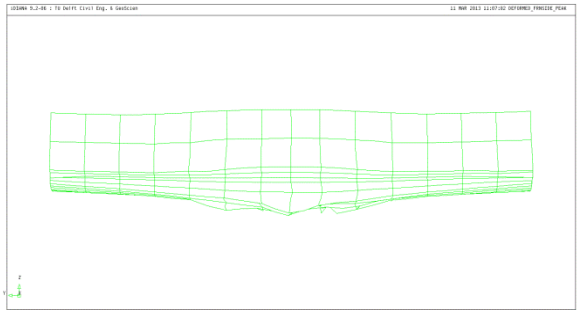

(a)

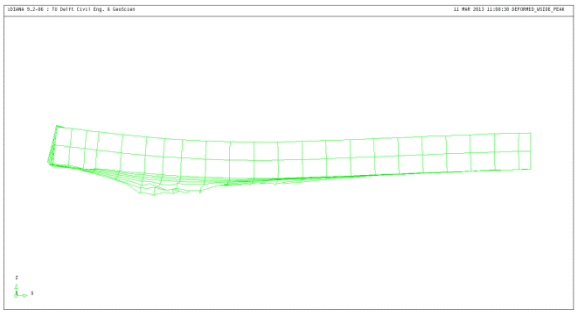

(b)

Deformed structure at the peak load: (a) North front side and (b) West lateral side

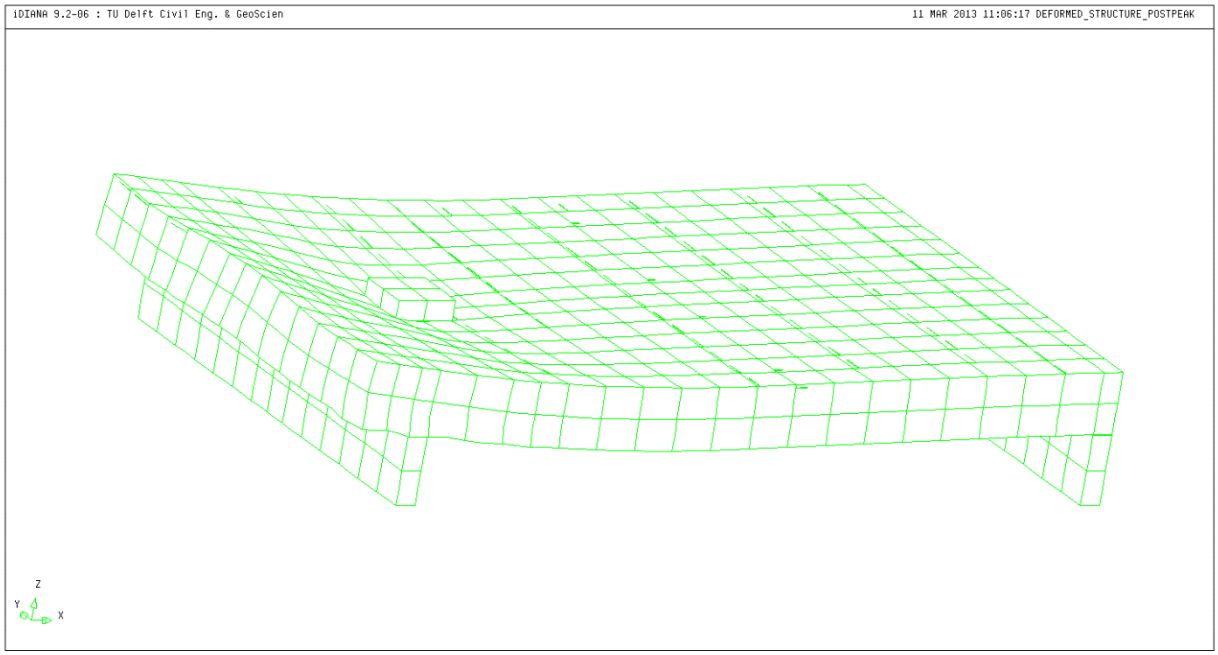

Deformed structure at the post-peak load: global overview

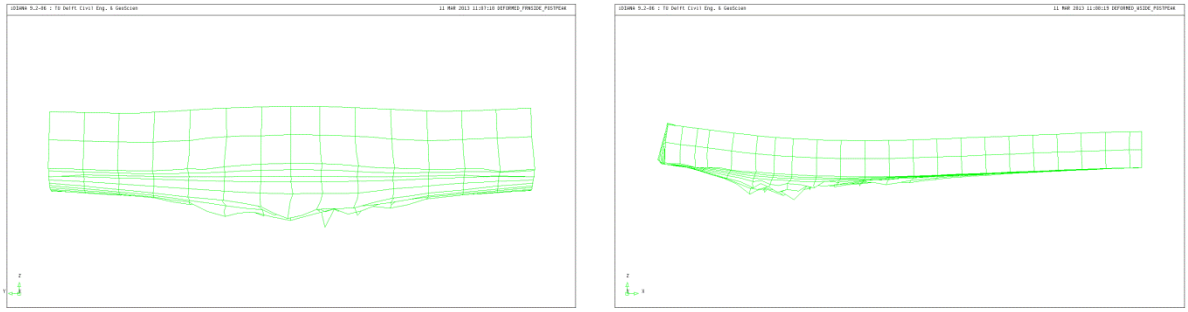

(a) *(b)*

Deformed structure at the post-peak load: (a) North front side and (b) West lateral side

A strong deformed zone is exposed under the load position. This cannot be detected on the global overview, but the lateral point of view shows a strong deflection of the slab under the load. Instead, the frontal side displays a rise of the North section on the middle of the support: it could be caused by the bi-dimensional nature of the slab under the concentrated load.
However, it's hard to define the failure mode, though a punching shear seems to be preferred.

10. CONCLUSION

10.1 Sinking phenomenon

The experimental load-displacement graph could be affected by few phenomena, introducing errors. Their relative contribute to the global gap present different percentages.
One of the most common is the sinking of the steel loading plate inside the upper concrete surface: it produces the typical relative displacement under the loading plate, as shown in the following pictures:

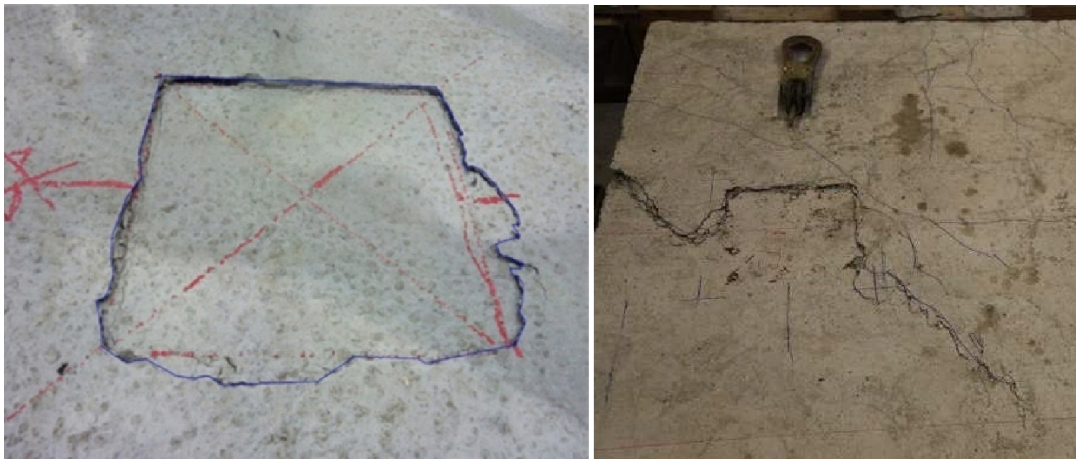

Sinking of the loading plate inside the concrete on the compressed side

It's not possible to measure this effect along the whole proof and even in the end it's not evaluable. Moreover, since the experimental setup presents four lasers around the loading plate to measure the objective load-displacement trend, its contribute can be calculated only in combination of the gap between loading plate and measure devices in terms of displacement.

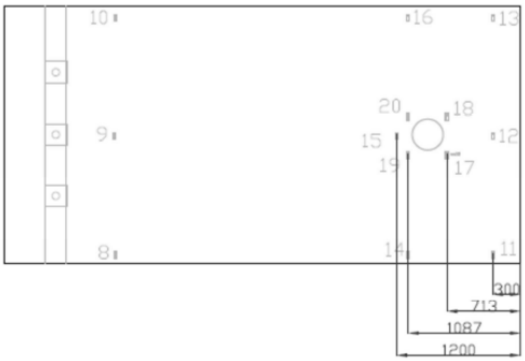

Experimental setup: lasers around the loading plate
17, 18, 19, 20 and geometrical features

So, in order to estimate this phenomena, numerical analyses are run taking in account the laser positions. Two different load-displacement diagrams are presented and the gap is so obtained.

In order to don't modify the meshes new geometrical points are not introduced into the model. The laser positions are defined as follows:

- linear interpolation between two nodes for *3x3* mesh;
- closest nodes to the plate for *4x4* mesh.

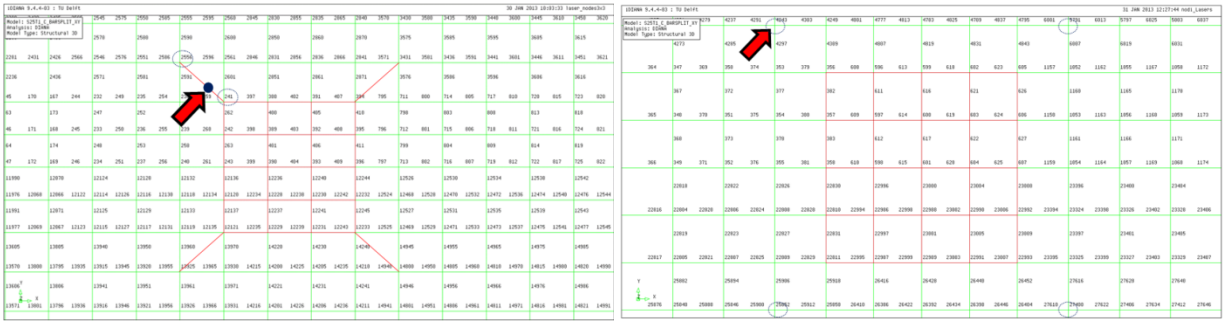

Numerical laser position: 3x3 mesh (left-hand) and 4x4 mesh (right-hand)

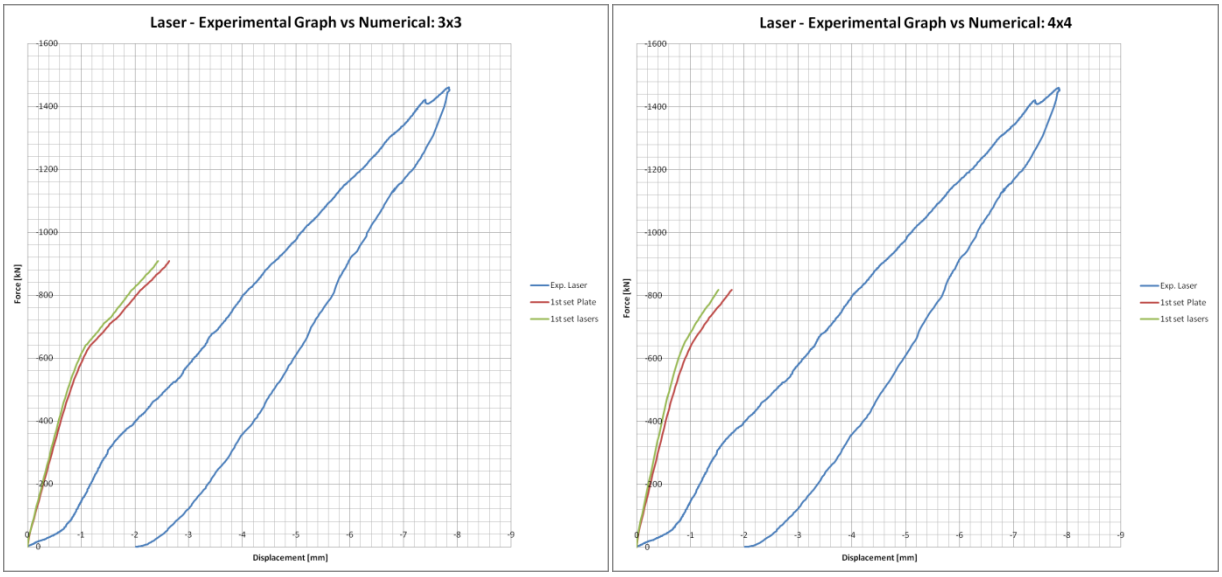

Comparison between laser and plate displacement for two different meshes

Logically, the lasers measure a smaller deflection of the slab, since they are located farther than the plate. So, the *sinking+deflection gap* is defined as:

$$sink + defl._{num} = d_{num} - d_{lasers}$$

The results are resumed in the following graphs:

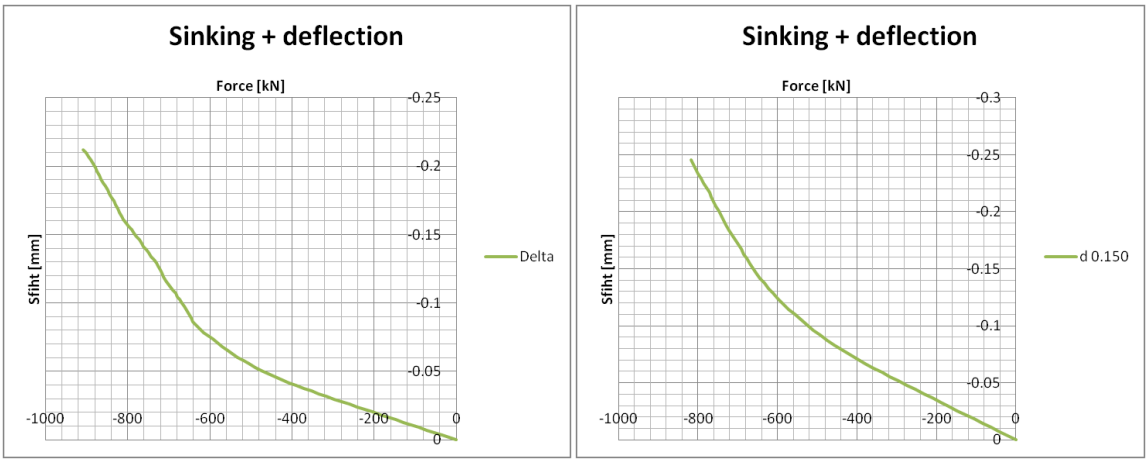

Gap: 3x3 mesh (left-hand) and 4x4 mesh (right-hand)

The way this gap is calculated is conservative: in the first test is interpolated linearly, in the second the lasers are farther than the experimental locations.
It can be assumed the gap, in terms of displacement, is negligible since for $900\ kN$ of load the effect reaches about $-0.20\ mm$, so around the 2% relative to the maximum reached displacement.

10.2 Computational time

The present work offers the possibility to compare and study the magnitude and entity of computational effort required by the two different method, i.e. NLFEA and SLA. Indeed, one of the most significant and practical problems related to nonlinear finite element method is the computational times. Both nonlinear and sequential linear approach relate this feature to the mesh properties: number of nodes and adopted integration scheme, number and typology of elements. Now, it's easy to understand that a finer mesh implies a high amount of elements, and so the consequent large number of nodes and integration points. Surely, it involves few advantages regarding to the pre- and post-processing environment of the analysis: a finer mesh allows to build a model more similar to the experimental reality, the results are more accurate. For example, a small average size of the finite element involves a wider range for the numerical crack bandwidth: a higher possibility to match the "real" one is achieved.
Now, this object has to be contextualized in a three-dimensional environment, where the problem of the computational evident results much evident: the gap between different meshes is immediate.
Indeed, the computational time is related to two quantities: (1) number of the solid elements, (2) number of the nodes and of the integration point. By adopting a finer mesh, they are subject to a faster growing and the computational time is sensibly incremented as well.

The models that have been built performing the Sequentially Linear Analysis are composed by CHX60 (20 nodes) and CQ48I (16 nodes) solid elements, with a default integration scheme respectively linear 2 x 2 x 2 and Gaussian 2 x 2. Instead the models supporting the Nonlinear Analysis adopt a $3\times3\times3$ integration scheme for CHX60 elements, 4×4 Newton–Cotes integration scheme for CQ48I interface elements and direct integration (1-point) for L6TRU truss elements.

Beside, the more refined is the mesh, the larger number of integration points should be damaged before the first crack opens or the yielding of the first reinforcement or the failure occurs [4].
For what regards the SLA, as explained in the previous chapters, each increment of damage corresponds with a step, so the number of steps to perform a complete analysis is enormous. In fact in the first coarse mesh (so called *2x2 mesh*) composed by "only" 4290 nodes and 708 solid elements, to reach a satisfactory results, or better to show a clear post-peak behavior and snap-back phenomenon, the complete analysis should be made using not less than 300000 steps, in order to detect exactly the real failure point of the model.

It has to be noted that the amount of steps is one order higher than previous work on the same model (see [4] for more details). It's probably related to the finer local discretization adopted to produce the "ripple" curve in the SL-analysis: 15 instead of 12. The gap is small, but one has to think that occurs in each integration point. Moreover, the softening behavior of the concrete is modeled by adopting a different curve: Hordijk instead than Linear.
An analogous problem is present in the Non-Linear Analysis, regarding the number of the nodes and of the integration points. The NLA has been performed using 850 load steps, with a multiplier factor of 0.0012 (on a total applied displacement of 25 mm) who means 0.03 mm for each single step. The Modified Newton-Raphson Method with maximum 100, 50 and 25 iterations has been adopted and a line search algorithm has been applied. Regarding the convergence criteria, it has been chosen a Relative Displacement tolerance of 1×10^{-4}.
Generally, the number of steps itself does not play a role in terms of computational time, but a low amount of steps requires more iterations to satisfy the convergence criteria, vice versa, a large number of loading steps might carry out the calculation with a smaller number of iterations. Regarding this aspect, few trials have been made in order to improve the convergence ratio for the Modified Newton-Raphson, just adopting smaller width for the loading steps. This is not always sufficient to satisfy the convergence criteria. It seems that when an "event" occurs, like cracking in the present work, it is not possible to avoid the singularity, neither iterating around it, then few steps can't converge. It affects by errors the present and future steps: accuracy and reliability of the NLA can become very weak. This does not take place in the SLA approach, because of the independence of the results by any kind of convergence criteria, since the method is based on a sequential and not on an iterative procedure.
Since two methods are adopted to carry out the analysis (SLA and NLFEA) on two different models (partial and total), first a comparison between partial and total model with Nonlinear Analysis is shown, in order to underline the main differences in terms mesh properties and computational time.
Finally, the comparison is focused on the two different methods, regarding to the reference model (partial version).

The following table contains a measure of the computational time that has been necessary to complete the NLFEA (to reach complete divergence of the analysis) for the three different meshes used, both for partial and total model.
Each analysis is carried out adopting a "Dell Precision T3400" computer.

Nonlinear Analysis on Partial model - Computational time				
Type of Elements	**# of elements**	**# of nodes**	**Computational times [hours]**	**# of elements over the height of the slab**
Solid	708	4290	8.0	2
Solid	3404	18217	123.0	3
Solid	7344	36546	1200.0	4

Computational time for NLFEA on the partial model

Regarding to the finest mesh (so called 4x4) the analysis can't be practically carried out. After five days of computation only 27 steps are completed. Extrapolating the average time effort for a predicted amount of steps even to 270 steps, we get 1200 hours. It has to be noted that this is a conservative prediction. Indeed, the behavior of the analysis with *3x3 mesh* shows how no convergence is satisfied after 40^{th} step, so for the following steps the maximum amount of iteration is expected. So, since the first steps are linear and they need a lower amount of iterations, we must aspect a bigger effort for the next steps, not linearly comparable or extrapolable. It's interesting to note that each mesh presents at least one order difference between the upper and the lower one.

Nonlinear Analysis on Total model - Computational time				
Type of Elements	**# of elements**	**# of nodes**	**Computational times [hours]**	**# of elements over the height of the slab**
Solid	1099	6474	6.0	2
Solid	4759	25176	132.0	3
Solid	9779	48202	1200.0	4

Computational time for NLFEA on the total model

A first comparison between partial and total analysis shows a lower amount of hour for the total model: this is due to the prosecution of the partial analysis after the peak-load. Indeed, that does not happen anymore with the denser meshes and a gap is detected. Of course it's due to the higher amount of elements, and so of nodes, that the total model presents. The same extrapolation is made for the total model, since no analyses is run on *4x4 mesh* due to the poor results on the partial version.

The computational trend is shown in the following image:

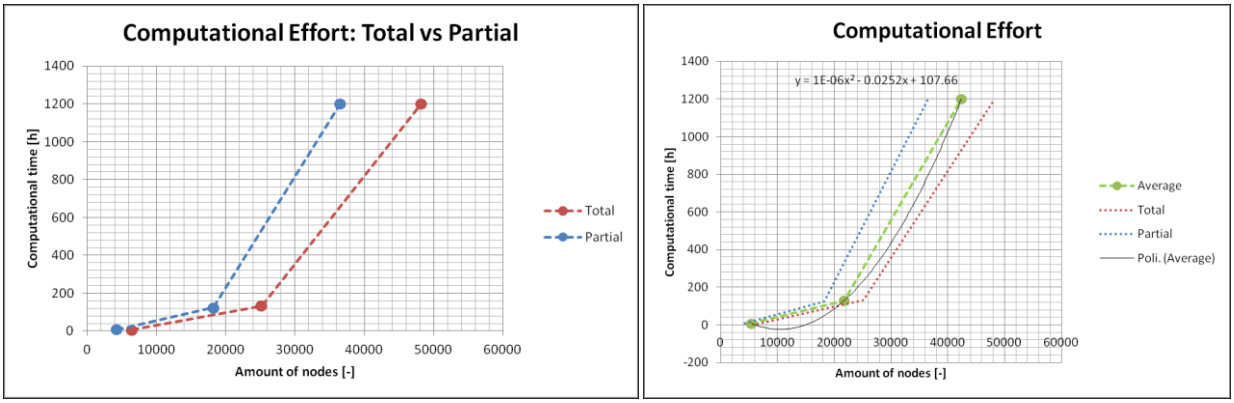

(a) *(b)*

(a) Computational effort for partial and total model with different meshes,
(b) extrapolated average trend of the required time

The effort seems to quickly increase and the nonlinear trend is marked. A function of the second order is able to describe the required computational time for a number of nodes higher than 20000. It's so reported:

$$y = 1^{-6}x^2 - 0.015x$$

Observing the tables, one can detect immediately the higher amount of elements, and then of nodes, that the total model has got, since that describes the whole experimental setup. It involves to an increasing of the computational time, but it seems not linearly related.

Sequentially Linear Analysis on Partial model - Computational time				
Type of Elements	**# of elements**	**# of nodes**	**Computational times [hours]**	**# of elements over the height of the slab**
Solid	708	4290	72.0	2
Solid	3404	18217	/	3
Solid	7344	36546	/	4

Computational time for SLA on the partial model

Observing the tables it is clear how for the same amount of nodes the SLA requires computational time that is very long, compared with the one required by the NLFEA. It also because of this evaluation that a more dense integration scheme can be adopted in the NLFEA.
Since only the coarsest mesh is adopted for the SLA: a unique point is evaluated, but it's enough to display a big gap between the two methods in terms of computational time: one day of work (8 hours) for the Newton-Raphson and about three days (72 hours) for the Sequentially Linear approach.

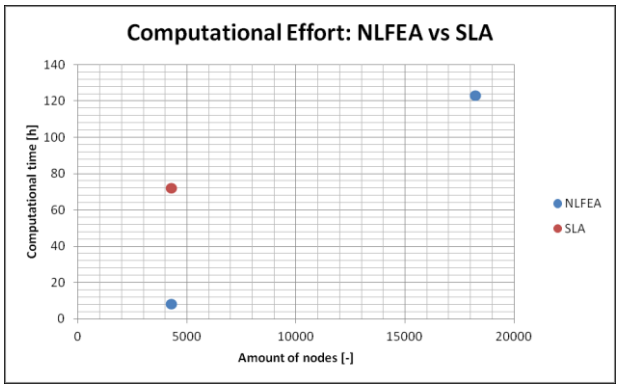

Computational effort for NLFEA and SLA

Moreover the difference of the computational time needed by the two methods has not a linear growth. The previous diagram shows the trend that the value of the computational time follows respect the increasing of the number of nodes for SLA and NLFEA.

10.3 Comparison between Total and Partial model through Non-Linear Analysis

On the present work two different models have been analyzed in order to evaluate and study the effects related to a structural compromise. The complete modeling of the experimental setup allows to reproduce the reality, but it costs a higher pre- and post-processing effort. As seen, the South constraint is made by a continuous line support and three pre-stressed Dywidag bars. This solution adds a non-proportional load case, that united with the main load case (displacement control on the loading plate), involves computational and numerical problems that can be solved only applying an other advanced numerical method: the Phase Analysis (more information in Appendix A). Since SL-analysis is still not implemented for non-proportional load in a three-dimensional case, it was necessary to provide a model without pre-stressing. That can be carried out only simplifying the complex South constraint by introducing a clamped side. It was purpose of this Master Thesis study the effects related to this simplification of the model in terms of load-displacement response, cracking behaviour and failure mode.

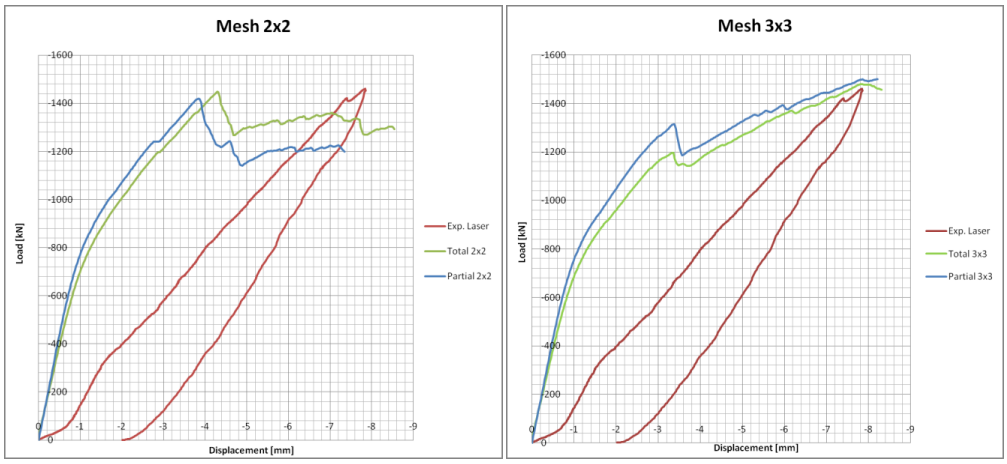

(a) (b)

Load-displacement diagram for (a) 2x2 meshes and (b) 3x3 meshes for partial and total model

Regarding to the load-displacement diagrams a good agreement is shown: despite the structural response is linked to the mesh fineness, the meshes display a common trend. It has to be noted that the partial model presents a higher stiffness than the total model. It is related to the structural assumption of a full clamped side: this means no deformability for the South constraint, unlike the experimental setup.
The highest difference is related to the required amount of *Tensile fracture energy* G_f. The following graph shows the trend of the required parameter in order to fit the peak-load. Despite the gap between total and partial model, it seems that the average trend matches with the Tension Stiffening range.

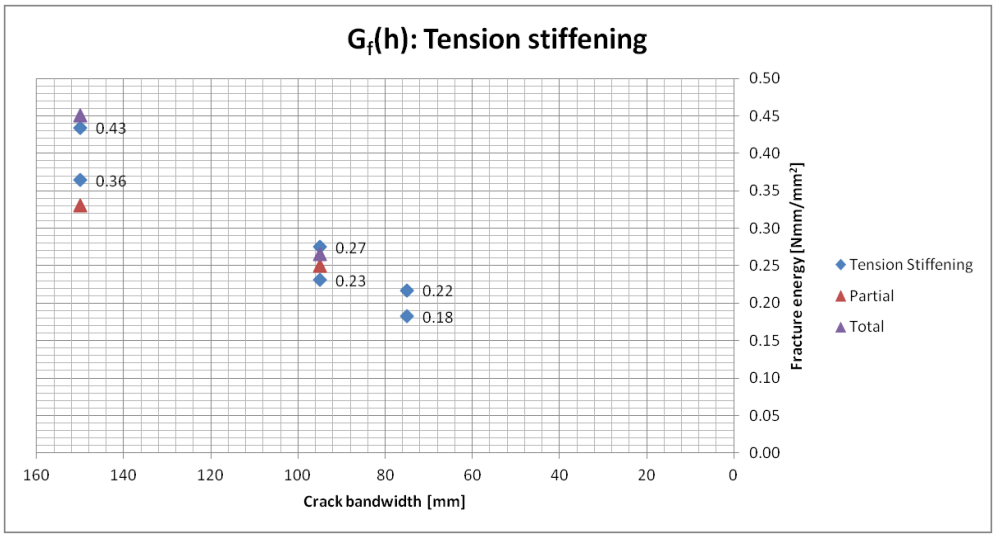

Fracture energy trend for total and partial model and Tension Stiffening

In order to analyze and study how much and in which way this boundary condition can influence the behaviour of the model (cracking and failure mode) the previous comparisons are carried out. The final conclusion are reported in the following list:

- felt reaction and redistribution: both the models present good agreement regarding to the shape of the vector plot s_{ftz}. The total model provide a higher maximum compressive stress (30 MPa instead 24 MPa). A bigger concentration of the reactions is provided by a denser mesh for both the models in terms of shape. The same can be reported for the redistribution of the reaction on the interface on the North support: the spreading angle doesn't change in relation with mesh and model.
- principal tensile strain and cracking behaviour: ax expected the denser mesh, the better results are obtained for both the models. Indeed, the denser mesh well evidences a radial cracking and a circular punching fracture below the load. Due to the lower stiffness, the total model tends to produce wider cracks. Anyhow, the crack widths presents good agreement with the experimental evidence, both in terms of predicted location and opening.
- yielding of reinforcement: the analysis confirms the hypothesis of a failure related to reached Shear Capacity for both the models;

- deformed shape: the total model presents a bigger global deflection of the structure, as seen on the load-displacement diagram related to the load position. However, both the models show a clear strong deformation below the load for a denser mesh.

To better explain these comparisons, three pictures are shown: felt reaction, principal crack strain and deformed structure.

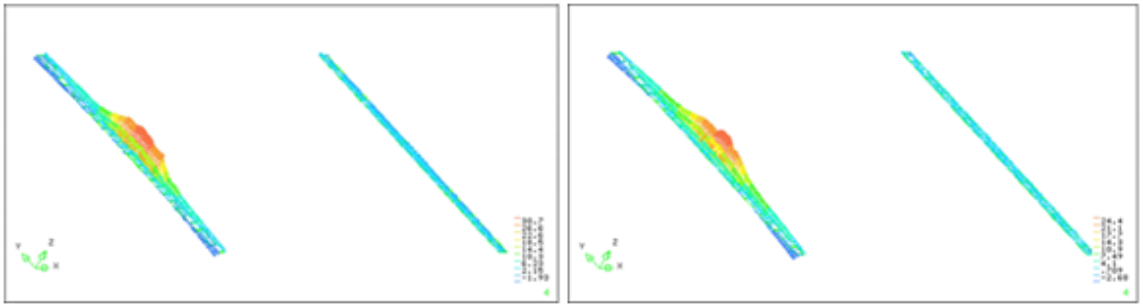

Felt reaction vector plot: total model (left-hand) and partial model (right-hand)

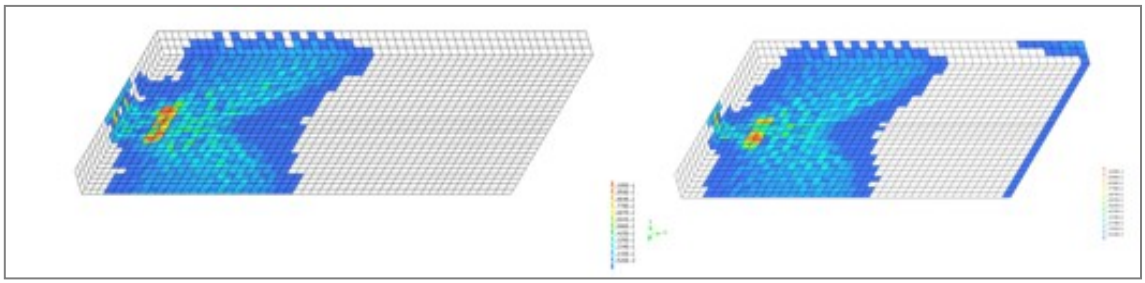

Normal crack strain contour plot: total model (left-hand) and partial model (right-hand)

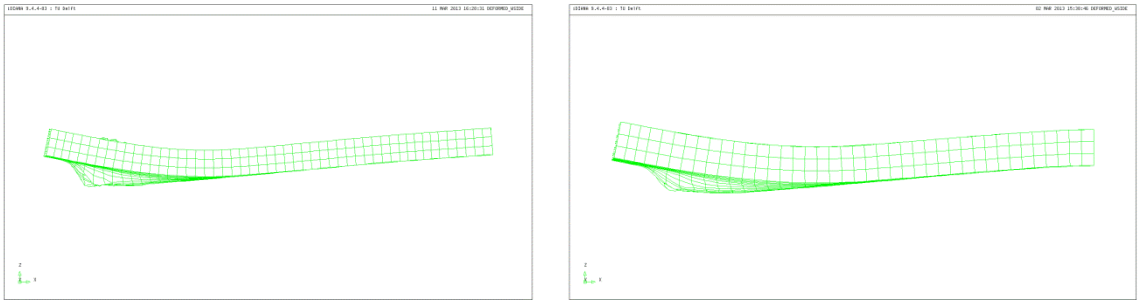

Deformed lateral side: total model (left-hand) and partial model (right-hand)

From this point of view a good agreement subsists between total and partial model: further analysis can be carried out adopting the partial model and providing a significant reduction of computational effort, both in modeling and in post-processing. It has to be noted that the partial model is equipped with linear felt.

Moreover, all these considerations allow us to affirm that a strong mesh sensitivity affects the model, since for a coarse mesh (two elements on the height) is not able to identify a clear failure mode. Indeed, we can't distinguish if the failure is due to a dominant punching shear phenomenon, as seen during the experiment. This can be confirmed by the results obtained with previous work (see [5] [4]). There, the deformed shape doesn't present an evident deformed area below the load. Just increasing the amount of elements (three bodies on the thickness of the slab), a decided

improvement is observed in terms of cracking pattern and deformed shape, against an "explosion" of the required computational time.
Though the present case regards a non-symmetric load case with the concentrated action close to a line support, some matches are found with the ideal punching shear mechanism (*Guandalini 2005*):

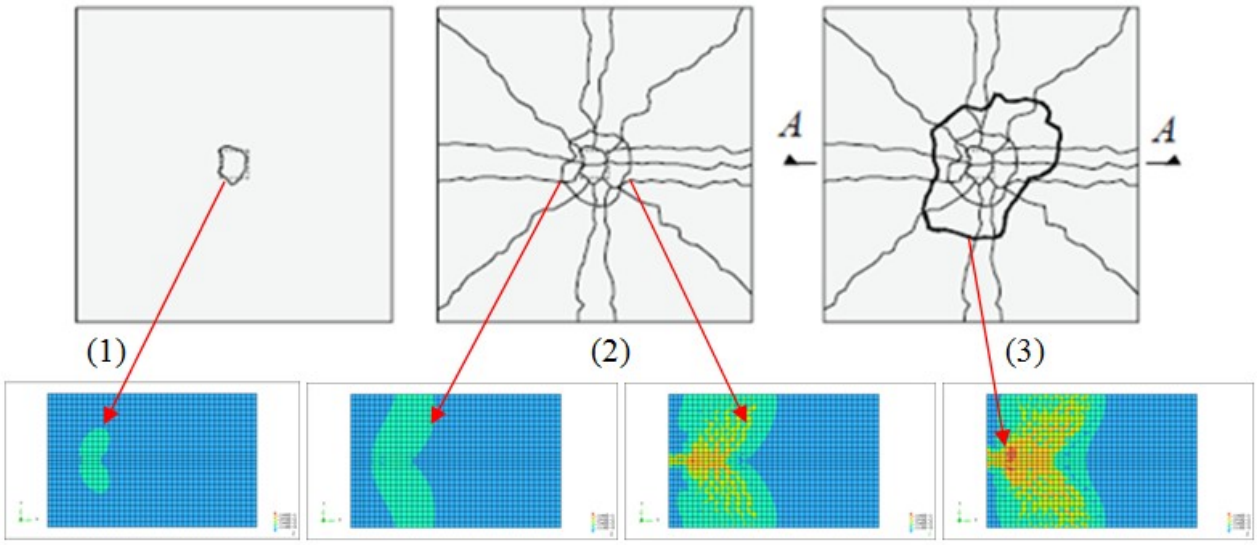

Comparison between numerical plots of principal tensile strain
and cracking behaviour of a slab under point load in symmetric condition

- on (1) is shown the initial flexural cracks directly on the tensile side below the load;
- on (2) the flexural cracks increase and radial fractures spread from the load toward the free edge and the midspan of the slab;
- on (3) the failure occurs after a circular shear crack due to the formation of a truncated cone body between load and opposite surface.

10.4 Comparison between Nonlinear and Sequentially Linear Analysis on Partial model

The present paragraph focus on the two aforementioned methods of solution: NLFEA and SLA. That finalizes the study about the reliable of the sequentially linear approach regarding the study of the behaviour of reinforced concrete slabs subjected to concentrated load. Moreover, this study allows to get conclusions respect the main limits and advantages that characterized the Sequentially Linear Analysis and the Non-Linear Analysis.
NLFEA provides good results of the analysis of reinforced concrete slab S25T1 and satisfactory agreement has been found with experimental reality in terms of cracking pattern and failure mode. Instead, the prediction of the load-displacement trend needs further improvements: as seen, SLA provides a better prediction of the global load-displacement diagram and an investigation of the post-failure behaviour is made possible by this Code. The peak load and ultimate displacement show good agreement with the experimental evidences and the first snap-backs seem to follow the post-failure trend. This is not possible with NLA approach.
A visual comparison is provided by the following images:

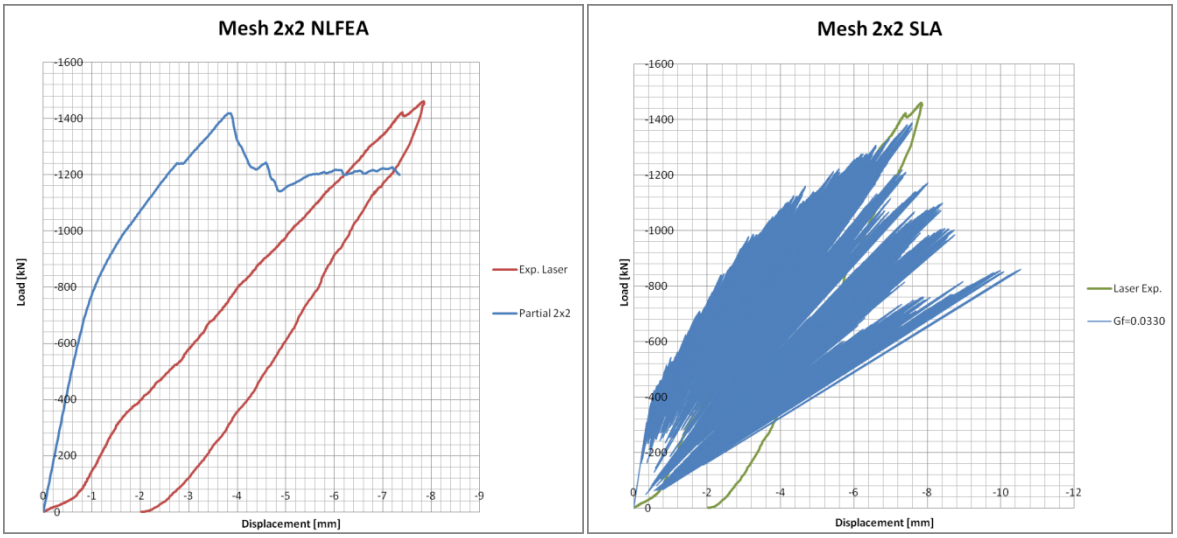

(a) *(b)*

Load-displacement diagram for (a) NLFEA and (b) SLA for 2x2 mesh

However, for what regards the prediction of the local behaviour of the slab, further improvements should be done in order to achieve a better evaluation of the redistribution capacity, of the strain and stresses values and distribution and of the cracking pattern
The final conclusion are reported in the following list:

- felt reaction and redistribution: NLFEA shows a stronger redistribution of the felt reactions, regarding to the shape of the vector plot s_{ftz}, while SLA provides a more elongated diagram. Moreover, NLFEA and SLA provide complete different values regards to the maximum compressive stress (17 MPa instead 45 MPa respectively).
- principal tensile strain and cracking behaviour: for both the model the coarse mesh does not allow to get clear results about principal tensile strain distribution and cracking behaviour. As see, satisfactory results can be achieved only with denser meshes. The comparison is made on the coarsest mesh: however, NLFEA provides clearer plots. It could be caused by

the low fracture energy selected for SLA: the concrete results too brittle and the damage spreads inside the whole slab.

- yielding of reinforcement: both the methods confirms the hypothesis of a failure related to reached Shear Capacity for both the models;
- deformed shape: the SLA seems to present a higher shear deformation with a stronger displacement below the load, underlining a dominant punching shear failure mode.

To better explain these comparisons, three pictures are shown: felt reaction, principal tensile strain and deformed structure.

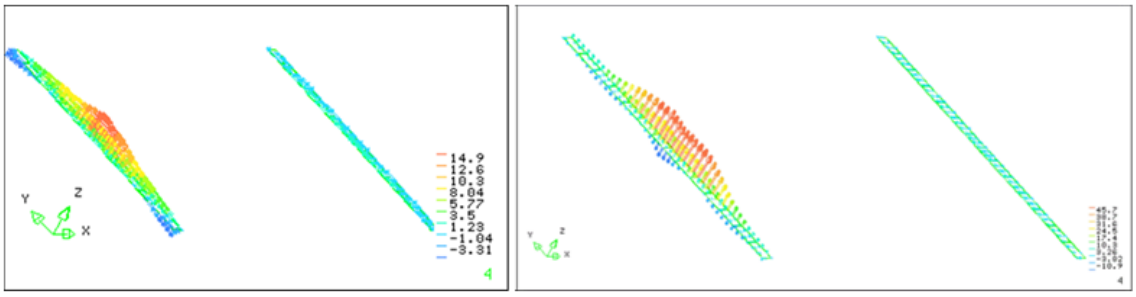

Vector plot of felt reaction for NLFEA (left-hand) and for SLA (right-hand) on the post-peak point

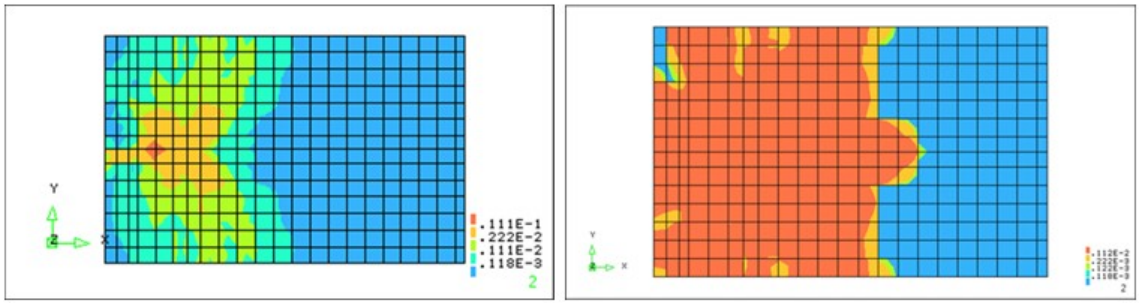

Contour plot of principal tensile strain based on the Hordijk softening model for NLFEA (left-hand) and for SLA (right-hand) on the post-peak point

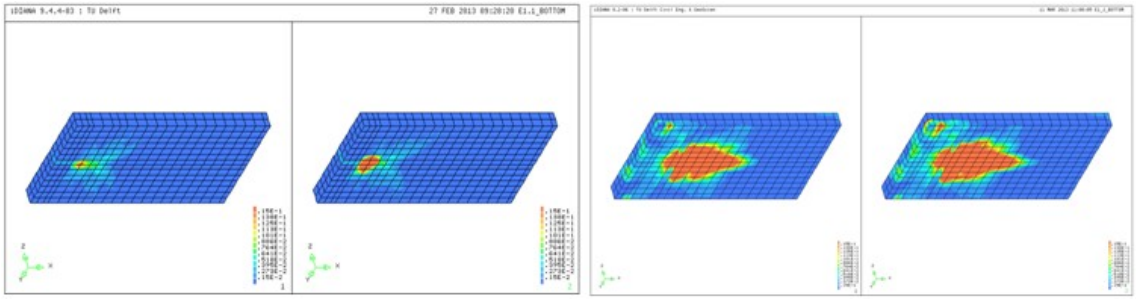

Contour plot of principal tensile strain based on the fixed scale softening model for NLFEA (left-hand) and for SLA (right-hand) on the peak and post-peak point

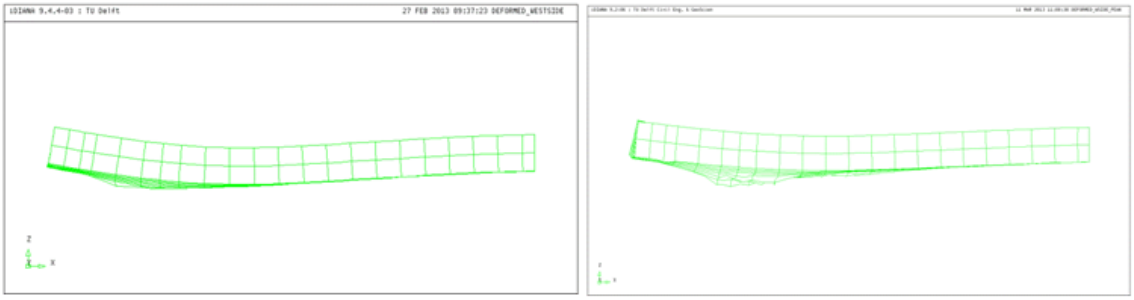

Lateral deformed shape for NLFEA (left-hand) and for SLA (right-hand) on the peak point

From these plots can be discovered how further improvements on the SLA model are necessary and tests on a denser mesh should be carried out.

The choice of the physical and mechanical properties of the materials in the NLFEA model was not so easy: the definition of the normal stiffness for both the adopted interfaces (Teflon and felt) and for the Tensile fracture energy required a high amount of effort in the pre- and post- processing phase. A strong influence of the felt interface is detected and underlined in previous work as well. Satisfactory agreement is achieved only after a calibration campaign that required months.
It has to be reported that in slab made with High Strength Concrete difficulties in the choice and calibration of the main parameters have been found also in previous works (see [4] for more details). Indeed, the research of the optimal Tensile fracture energy caused significant pre-processing effort: a High Strength Concrete presents a more brittle behaviour than a Normal Strength Concrete.
The comparison between NLFEA and SLA concerns about the prevision of the load-displacement diagram, the cracking behaviour and the prediction of the main failure mode. It has to noted that with the actual version of *Diana* for SLA (9.2) the disc plot for normal crack strain is still not implemented.
The highest difference is related to the required amount of *Tensile fracture energy* G_f. As said in the previous chapters, in order to fit the load peak the SLA approach required a rate even to 10% of the same parameter adopted inside the NLFEA environment: 0.033 Nmm/mm^2 instead 0.330 Nmm/mm^2. This causes a very brittle concrete: SLA-Code showed few problems related to the investigation of Brittle Materials.

It is very important to note that the results obtained through NLFEA could be influenced by not negligible errors, since a great amount of steps could not satisfy the strict Convergence Criteria.
In the SLA this problem is not present because of the conceptual nature of the method, that is sequential and not iterative (like the NLA).
Regarding this aspect, the setting of the Non-Linear procedure of Analysis can be problematic, in order to get convergence solutions step by step. To do this it is necessary to evaluate the optimal relation between the Step Size and the Number of maximum Iterations for each step, in accordance to the chosen Convergence Criteria.
The Computational needed to perform an entire analysis is dependent from the previous relation.
In general the SLA requires a much longer Computational Time than the NLA, considering the same meshing properties.

In conclusion the Sequentially Linear Analysis at the present status needs further improvements regarding some significant aspects of the model: implementation of double nonlinear behaviour for materials (e.g. to model the felt reaction both in compression and in tension), implementation of a non-proportional code on the three-dimensional environment. evaluations whose quality is totally comparable to the Non-Linear Analysis. However, it has to be noted that the NLA is a much older and studied procedure than the SLA, and its Codes usually provide a wider range of properties and models (for instance the Saw-Tooth law for the concrete in SLA can be built only on the basis of a Linear-Softening Stress-Strain relation for the felt, while in the NLA many better constitutive relations are available or can be supplied by the user).
Currently, it is necessary to improve the mathematical model inside SLA Code as well. In other words, the possibility to add proportional loads in a 3D environment has to be add. So, it will be possible to model different study cases. The present work represents only one of the first step in this new way of modeling 3D structures with SLA Code.
In this sense SLA could be a very potential method, and further implementations could lead it to a much bigger level of reliability and accuracy compared to the Non-Linear methods as well.

APPENDIX A - PHASE ANALYSIS VALIDATION:

A.1 Introduction:

In order to evaluate and confirm the output from the Diana solver environment for the phase analysis, two simply examples are studied below.
The application of the phase analysis on the present model is a particular case: after a pre-stress load (three concentrated loads near the free edge of the slab) a displacement is given through the loading plate.
iDiana imposes constraints to the mesh nodes where the displacement is given.
Due the fact that the controlled displacement is given only after the pre-stress bars loading procedure, the simultaneous presence of these two loads represents a constraint condition who doesn't represent the reality.
So, it's necessary to define two different models, with the same geometrical features, but different load cases and constraint configuration:

- the first one (pre-stress only) has got a constraints free loading plate and three concentrated load on the south free edge of the slab;
- the second one (under pre-stress, with displacement control on the loading plate) has got a constrained loading plate and a second load case.

The present images helps to understand the models differences inside the *.dat* file:

```
'SUPPORTS'
 / 208 /    TR      1
 / 4 208 /    TR      2
'LOADS'
CASE 1
NODAL
  248 FORCE 2 -0.150000E+05
```

Support and Load table for the 1st phase

```
'SUPPORTS'
 / 208 /    TR      1
 / 4 208 /     TR    2
 / 249 250 /    TR    2
'LOADS'

CASE 1
NODAL
  248 FORCE 2 -0.150000E+05

CASE 2
NODAL
  248 FORCE 2 -0.150000E+05

CASE 3
DEFORM
/ 249 250 / TR 2 -0.150000E+02
```

Support and Load table for the 2nd phase

For this reasons a very simply model is adopted with elastic linear features in order to confirm the results thanks to a manual check.
The first evaluates the right procedure in order to confirm and get the superposition the results from the first phase on the ones from one from second.
The second helps to understand the role of the pre-stress load on the *Dywidag bars* inside the whole model.
As said before, a simply 2D model, made by rectangular section steel beam , is adopted.
The static scheme is a simply supported beam with a right cantilever.
In order to follow the complex slab model a series of example will follow the same kind of procedure: the geometrical model will be used in the final configuration and only new load and constraints will be added.
The following material and physical properties are used:

- $E = 210000\ Mpa, \nu = 0.20;$
- $rectangular\ section\ 5\ \times 300\ mm.$

Working in 2D environment the physical feature is given with regular plane-stress feature.
The central beam span is $5.00\ m$ long, instead the cantilever beam is $1.00\ m$ long.
The left constraint (named with the "A" letter) is a cart and the left one is a hinge (named with the "B" letter).
Load case 1 contains the vertical concentrated force on the cantilever free edge (named with the "D" letter), with a magnitude of $15\ kN$, instead the displacement control is carried out with $-15.00\ mm$ (named with the "C" letter).

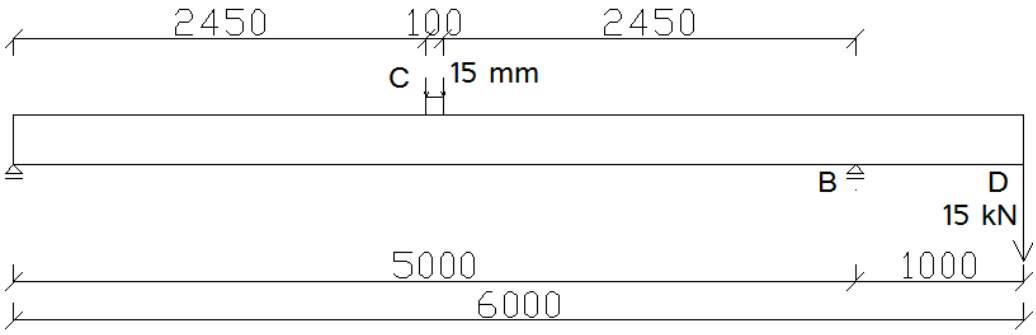

Simply supported beam with right cantilever, geometrical model

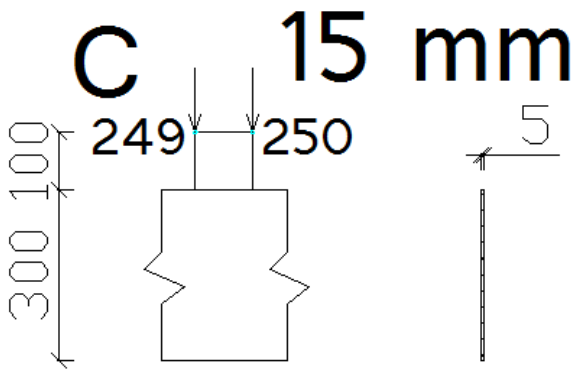

Particular: loading plate model and mesh nodes

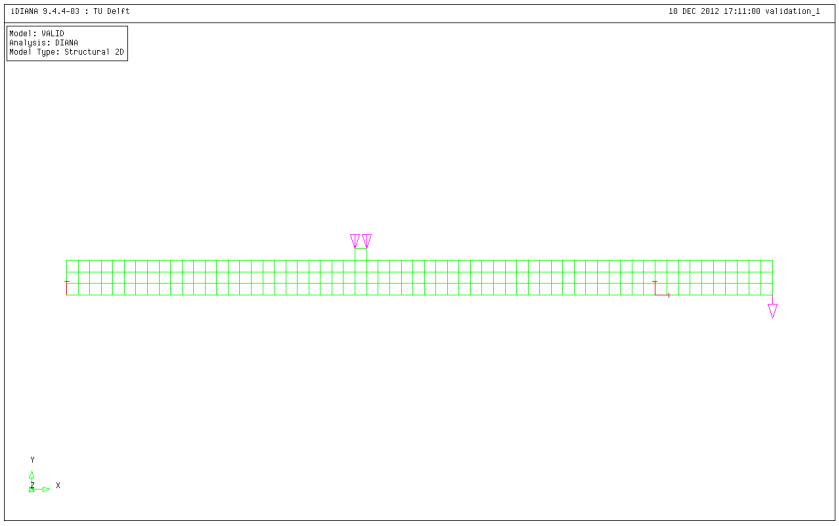

Simply supported beam with right cantilever, mesh on iDiana environment

The analogy between slab and simply model is due to the loading plate, positioned in the middle on the beam in order to make the manual resolution easier. Due to the lower longitudinal dimension ($100\ mm$) the loading plate dimension are negligible and the displacement action over it can be assumed as a concentrated one.
In fact the span plate width ratio is:

$$\frac{l}{L} = \frac{100\ mm}{5000\ mm} = 2\%$$

A simplification will not bring considerable errors to the manual resolution.
It's to be noted that the added load plate, without an interface who avoids kinematic compatibility, represents an inertia increase for the interested sections. In fact in these sections the effective height is even to $400\ mm$ instead $300\ mm$. It brings a $+137\%$ flexural inertia increasing, but for a length of only 2% of the total beam span.
It brings other approximation to the manual results, but the global influence is negligible as well.
In order to control the right superposition in terms of stress and deformation inside the beam elements, displacements and reactions of control points are checked.

A.2 First test: right superposition of stress and deformation

For the present instance displacements and reactions are checked on in predefined control points.
Displacements are evaluated on the top of the loading plate part, instead the reactions are refer to the supports.
Afterwards they are compared with the theoretical manually obtained results and differences will be discussed.
In phase one of the analysis free edge of cantilever is loaded by a vertical concentrated force. It represents the pre-stress in a *Dywidag bar* in the simplest way.
Due to this load the whole beam deforms: all the upper fibers are strained.

In the phase two, displacement control on the loading plate is added to the deformed structure: it's possible asking Diana to read new load and support table.
In fact, in Diana environment displacement control analysis in possible only through tying the reference geometrical part, so the loading plate mesh nodes are constrained in the vertical directions inside the support table and a new load case is inserted (*.dat* file).
Applying a vertical displacement in the beam midspan a new deformed configuration is obtained.
Thanks to the *"tabula"* option inside the command file (*.dcf* extension), displacement and reaction plots can be given for any phase.
The studied displacement is the average one from the loading plate nodes.
Here Diana output are reported for $phase\ 1$:

- $V_A{}^{(1)} = 3.00\ kN$;
- $V_B{}^{(1)} = -18.00\ kN$;
- $v_{c,249} = -9.74\ mm$;
- $v_{c,250} = -9.87\ mm$.

So, the average plate displacement results equal to:

$$\overline{v_{c,1}} = \frac{v_{c,249} + v_{c,250}}{2} = -9.81\ mm$$

It has to be noted that the nodes displacements are negative due to the particular structure deformation. Thus, the nodal reaction in B constraint is negative due to the *iDiana* way of force representation: *iDiana* shows us the reactive action, so for the third static principle we see the force that the structure transmits to the constraint.
For the $phase\ 2$ they are:

- $V_A{}^{(2)} = -3.84\ kN$;
- $V_B{}^{(2)} = -24.84\ kN$;
- $v_{c,249} = 5.26\ mm$;
- $v_{c,250} = 5.13\ mm$.

So, we get:

$$\overline{v_{c,2}} = 5.20\ mm$$

For theoretical results, working with linear elastic materials and operating with linear static analysis few considerations can be done:

- effects superposition is doable: displacements and reaction from phase one and phase two are overlapping,
- through the generalized *Hooke's law* $F = k \times u$, a displacement can be expressed as an equivalent load.

For $phase\ 1$ reactions and midspan vertical displacement can be obtained using cardinal laws of static and theorical formulas:

$$\begin{cases} \sum F_y = 0 \\ \sum M_z = 0 \end{cases} \rightarrow \begin{cases} V_A{}^{(1)} + V_B{}^{(1)} - F_D = 0 \\ M_A = V_B{}^{(1)} \times 5.00\ m - F_D \times 1.00\ m = 0 \end{cases}$$

Following the same convention for reaction modulus as *iDiana* we get:

$$\begin{cases} V_A{}^{(1)} = 3.00\ kN \\ V_B{}^{(1)} = -18.00\ kN \end{cases}$$

In order to calculate the C point vertical displacement it's necessary to bring the action of F_D on the interested structure (simply supported beam only).
It brings a bending action; its effects can be calculated as:

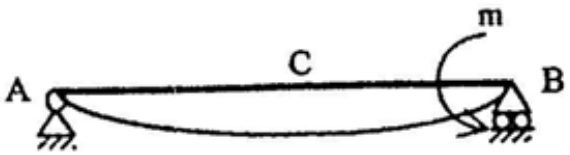

Qualitatively deformation for phase 1

Where

$$v_C = \frac{mL^2}{15EI} \rightarrow v_C{}^{(1)} = \frac{(F_D \times 1000\ mm)\ (5000\ mm)^2}{15EI} = -10.58\ mm$$

In order to simplify the manual resolution, adopting a linear elastic material, the controlled displacement applied in $phase\ 2$ can be expressed as:

$$F = k\ \times u$$

where k represent the translation stiffness in the vertical direction for the whole structure with the predefined load case and u is the prescribed displacement.
As said before, due to the negligible width of the loading plate, it can be studied as a concentrated displacement action. This justifies the following assumption for the stiffness evaluation.
Thus, when the displacement control is applied, the cantilever beam is inert, so it can be neglected.
So, the static scheme presents like:

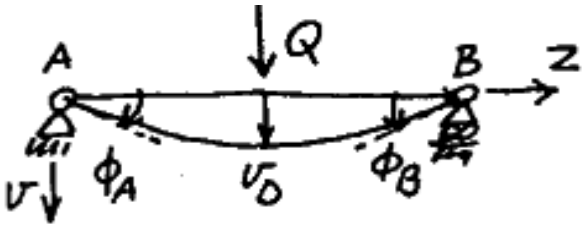

Qualitatively deformation for phase 2(1)

The vertical translation stiffness is known, it's equal to:

$$v_D = \frac{FL^3}{48EI} \rightarrow F_{eq} = \frac{48EI\delta_{jack}}{L^3}$$

So the equivalent force is easy to be calculated:

$$F_{eq} = F_C = 13.61\ kN$$

In order to check on this result, reaction forces on the two plate nodes are evaluated: every force is even to $6.80\ kN$, so they agree perfectly.
The theoretical final results can be obtained using the effects superposition.
Considering the only effects of F_C ($phase\ 2{,}1$) we have the above reported static scheme, due to the symmetry, we get:

$$\begin{cases} {V_{A,1}}^{(2)} = -6.80\ kN \\ {V_{B,1}}^{(2)} = -6.80\ kN \end{cases}$$

and

$${v_{C,1}}^{(2)} = +15.00\ mm$$

So, adding the previous effects we get the total displacement and reactions:

$$\begin{cases} {V_A}^{(2)} = V_{A,tot} = 3.00\ kN - 6.80\ kN = -3.80\ kN \\ {V_B}^{(2)} = V_{B,tot} = -18.00 - 6.80\ kN = -24.80\ kN \end{cases}$$

And

$${v_C}^{(2)} = v_{C,tot} = (-10.58 + 15.00)\ m = 4.42\ mm$$

So, a comparison between theoretical and numerical resolution can be done for each phase, either for displacement and reactions.
In $phase\ 1$:

$$\begin{cases} {V_{A,th}}^{(1)} = 3.00\ kN \\ {V_{B,th}}^{(1)} = -18.00\ kN \end{cases} \quad and \quad \begin{cases} {V_{A,mod}}^{(1)} = 3.00\ kN \\ {V_{B,mod}}^{(1)} = -18.00\ kN \end{cases}$$

$$\overline{v_{c,1}} = -9.81\ mm\ and\ {v_{C,th}}^{(1)} = -10.58\ mm$$

The reactions are perfectly evaluated, instead the vertical displacement in C point is lightly underestimated:

$$\Delta = (10.58 - 9.81)mm = 0.78\ mm \rightarrow \Delta[\%]\frac{(10.58 - 9.81)mm}{10.58\ mm} = 7\%$$

However, the difference is acceptable.
In $phase\ 2$:

$$\begin{cases} {V_{A,th}}^{(2)} = -3.80\ kN \\ {V_{B,th}}^{(2)} = -24.80\ kN \end{cases} and \begin{cases} {V_{A,mod}}^{(2)} = 3.84\ kN \\ {V_{B,mod}}^{(2)} = -24.84\ kN \end{cases}$$

$$\overline{v_{c,2}} = +5.20\ mm\ and\ {v_{C,th}}^{(1)} = +4.42\ mm$$

The reactions are good evaluated, instead the vertical displacement in C point is more underestimated than the previous step:

$$\Delta = (5.20 - 4.42)mm = 0.78\ mm \rightarrow \Delta[\%]\frac{(5.20 - 4.42)mm}{4.42\ mm} = 17\%$$

The difference is due to the first displacement evaluation, since in the $phase\ 2$ a fixed displacement is added to the structure.
A better approximation can be calculated taking into account the flexural inertia brought by the taller sections under the plate.
Spreading the increased inertia along the whole beam uniformly, a better displacement evaluation can be reached ($\sim 10\%$).
In this case, also the reactions evaluation brings good results ($+5\%$ only).

A.3 Second test: load by a pre-stressed bar

In the second example the load on the cantilever free edge is substituted by a pre-stress bar using the PRESTRES load case inside *iDiana* environment.
The adopted model is equal to the previous one for geometrical dimensions and material properties. Only a $500\ mm$ long extra part is added to the right free edge in order to guarantee the right bar embedding.

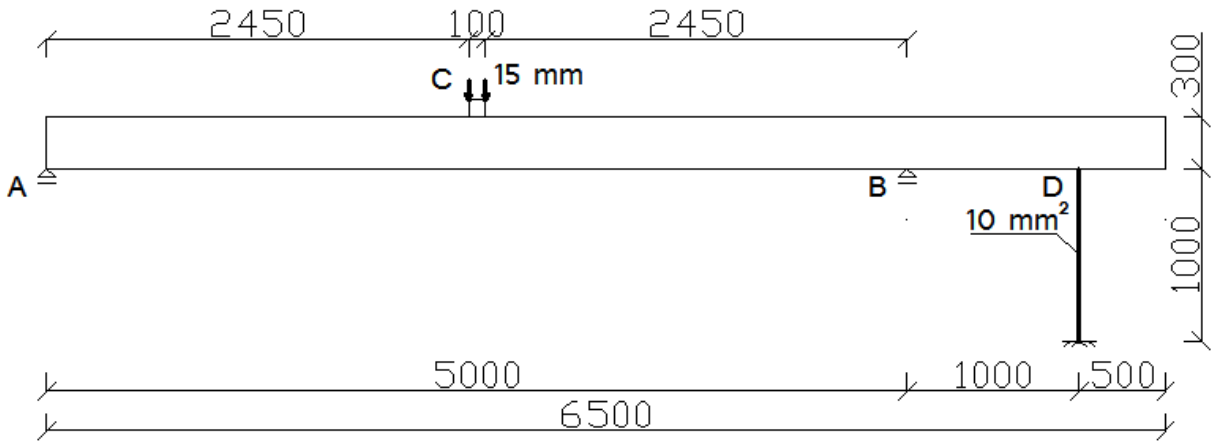

Simply supported beam with right cantilever and pre-stressed bar, mesh on iDiana environment

So, in $phase$ 1 the vertical point load is substituted by a 10 mm^2 area bar, with an initial pre-stress equal to 15000 MPa.

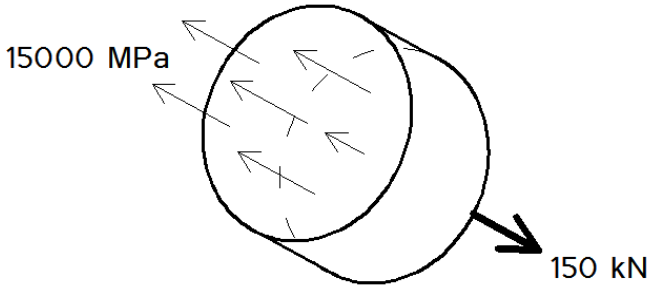

Action on an elementary bar piece

Then the action on the structure is even to:

$$F^{(1)} = \sigma \times A = 15000\ MPa \times 10\ mm^2 = 150\ kN$$

in order to guarantee the balance of every bar piece as shown in the previous picture.
So, we aspect to find a 150 kN applied force on the D point as first load.
However this consideration is not correct: the reasons are here explained. So, in order to better understand the cause we have to think about the experimental pre-stressing bar procedure.
In fact, it's necessary remember that bars work with the reinforced concrete structure, and every part has got its proper stiffness, so a proper deformability.
On the $\mathcal{B}_0$ configuration slab and bar are relaxed and no loads are applied on any structural part.

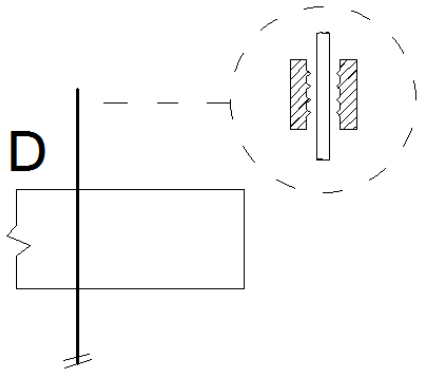

Starting configuration: no loads

On the $\mathcal{B}_1$ configuration the bar is stretched with a $150\ kN$ force, in order to get a $15000\ MPa$ tensile tension in every sections.

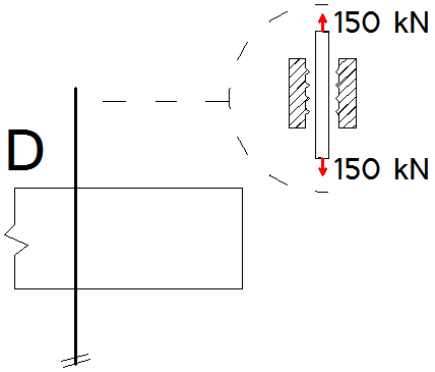

Pre-stressing for Dywidag bar only

Now, only the bar is under load.
On the $\mathcal{B}_2$ configuration bar and beam become kinematical compatible thanks to the nut.

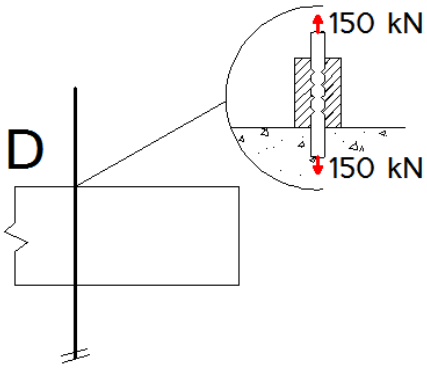

Bolted bar on r.c. slab: loads on the whole system

When the bar is released against the beam $\mathcal{B}_3$ configuration starts.
This represents the $phase\ 1$ of your analysis.
Due to the vertical action the beam deforms, the vertical displacement in the negative Y direction on the D point shortens the pre-stressed bar, due to the kinematical compatibility supplied by the nut.
This shortening reduces the pre-stress inside the bar, so the force on the beam. Only when balance is finally reached the beam stops to deform.

Using the effects superposition the balance point between beam and pre-stressed bar can be found. Working with linear elastic materials the force-displacement in the D point graph for the beam is linear and it can be so described.

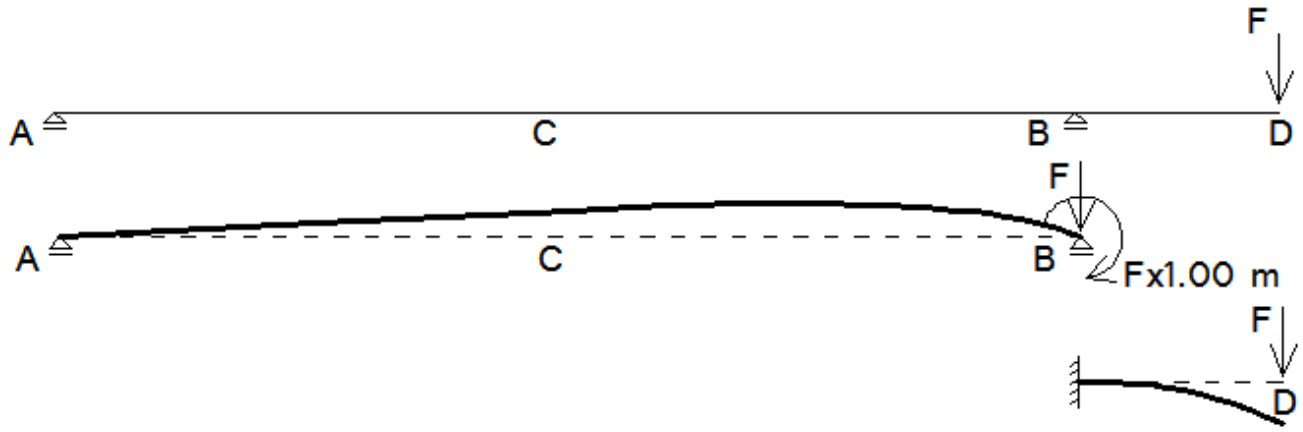

Kinematical scheme for load in D point

The stiffness of the whole beam for a vertical force in the D point is equal to:

$$v_D{}^{(1)} = \frac{Fa^3}{3EI}$$

$$\varphi_B = \frac{mL}{3EI} \rightarrow v_D{}^{(2)} = \varphi_B \times a = \frac{(Fa)La}{3EI}$$

So,

$$v_D = v_D{}^{(1)} + v_D{}^{(2)} = F(\frac{a^2}{3} + \frac{aL}{3})$$

With the present values it results:

$$v_D = 0.000847 \times F$$

So, the stiffness is equal to:

$$k_D = \frac{F}{v_D} \rightarrow k_D = 1181.25\frac{N}{mm}, if\ v_D = 1.00$$

In this way, the displacement $v_D$is a linear function of F: $v_D = v_D(F)$.

To respect the kinematical compatibility $v_{D,beam} = v_{D,bar}$.
The vertical displacement in the D point is equal to a shortening of the pre-stressed bar, so with the effects superposition it can be seen as a pre-stressed bar plus a compressed by displacement bar. In other words, the slab deformation means as a relaxation for the pre-stressed bar.
Instability can't happen, since the bar has a tensile tension state.
The following picture represents what happens to pre-stresses bar in θ_2 configuration thanks to the effects superposition:

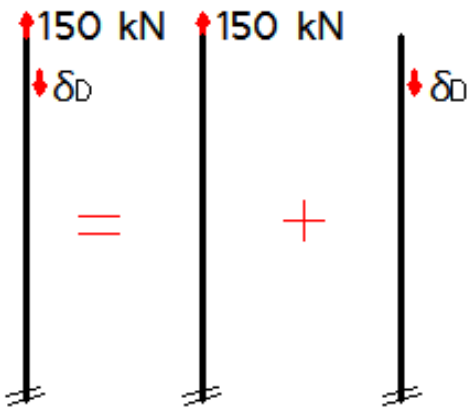

Superposition on pre-stressed bar under relaxing

For a simple truss the function v_D is linear as well and it can be expressed as:

$$v_D = \frac{N}{k} = \frac{Nl}{EA}$$

where the negative sign means a displacement in the
The whole length of the bar is stretched, the embedded part of bar is equal to $1000\ mm$.

$$k = \frac{EA}{l} = \frac{210000\ MPa\ \times 10\ mm^2}{1000\ mm} = 2100\ N/mm$$

So, during the beam deformation the function who describes the v_D trend is:

$$v_D(F) = -\frac{F}{k}$$

The function who describes the load on the bar end is:

$$F(v_D) = F^{(0)} + v_D \times k = 150\ kN - v_D \times 2100\ N/mm$$

Now, balance and kinematical compatibility are possible only if $v_{D,beam} = v_{D,bar}$ and $F_{D,beam} = F_{D,bar}$. In fact, the D section of the beam must react to the vertical pre-stress load in order to guarantee balance in the Y direction.
While the D section reacts, the beam deforms, increasing v_D. It brings a $F_{D,bar}$ reaction due to a loss of pre-stressing.
The process converges only when the two function cross themselves.

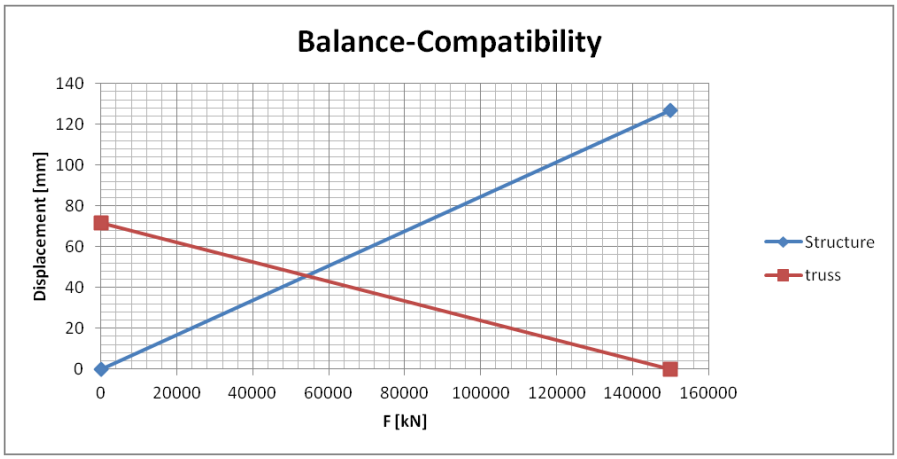

Load-displacement function for pre-stressed bar and beam in linear elastic state

So, we have two functions:

$$\begin{cases} F(v_D) = 150\ kN - 2100\dfrac{N}{mm} \times v_D \\ F(v_D) = 1181.25\dfrac{N}{mm} \times v_D \end{cases}$$

The two lines meet in $x = 53.03\ kN$ means a force value.
A first important observation can be made after this result: as seen previously, the bar stiffness depends on the length l, since the $F(v_D)$ function contains the k term equal to $\frac{EA}{l}$. A different stiffness can slight the common point.
Accordingly, the effective pre-stress loss depends on systems stiffness (bar and beam) and not on the beam stiffness only.
For instance, a $+20\%$ value for the bar length, so a less stiff bar, involves a $+15\%$ to the applied force in D point.
So, we obtain that it's very important to model the effective *Dywidag bars* inside the 3D $S25T1$ model, in order to represent in the more realistic way the relaxation phenomena.
A last observation can be done: *iDiana* can read force value as reactions only in constrained points.
In order to read the force value on the bar end this one can be evaluated on the bottom constrained, even if in the experimental test it is evaluated on the top load cell.

Experimental set: load measurements on Dywidag bars (red arrow)

However, due to the uniform tensile pressure field inside every section of the cable, the load value is equal to each end.

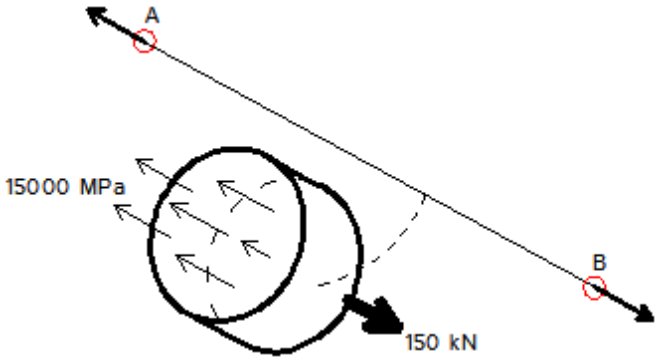

Uniform stress scheme

If the A point is the bolted one and B is the constrained one, $R_A = R_B$ and it doesn't matter where the force is measured.

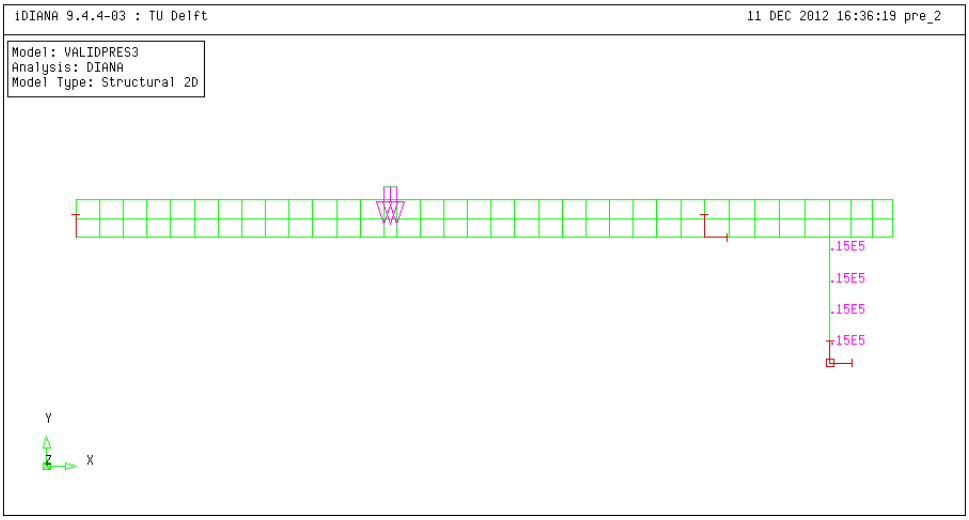

Mesh model on iDiana environment

All these considerations are necessary in order to understand the following output from the Diana environment.
In fact, we find an acting force of $53.72\ kN$ at the start of $phase\ 1$ in Diana, completely different from the original stress into the bar (even to $150\ kN$).
So, due to the beam deformation, about $\frac{2}{3}$ of pre-stress are lost.
This information is useful when a more complicated model as the reinforced concrete slab is studied, now we know that a pre-stress amount burns due to elastic deformations.
Numerical result is really close to the just found theoretical one:

$$\begin{cases} F_{num} = 53.72\ kN \\ F_{th} = 53.03\ kN \end{cases} \rightarrow \Delta[\%] \cong 1\%$$

Running the analysis inside we get for the $phase\ 1$:

$$\begin{cases} V_A{}^{(1)} = 10.74\ kN \\ V_B{}^{(1)} = -64.45\ kN \\ F_{bar} = 53.72\ kN \end{cases}$$

$$\overline{v_{c,1}} = \frac{v_{c,1} + v_{c,2} + v_{c,3}}{3} = -35.34\ mm$$

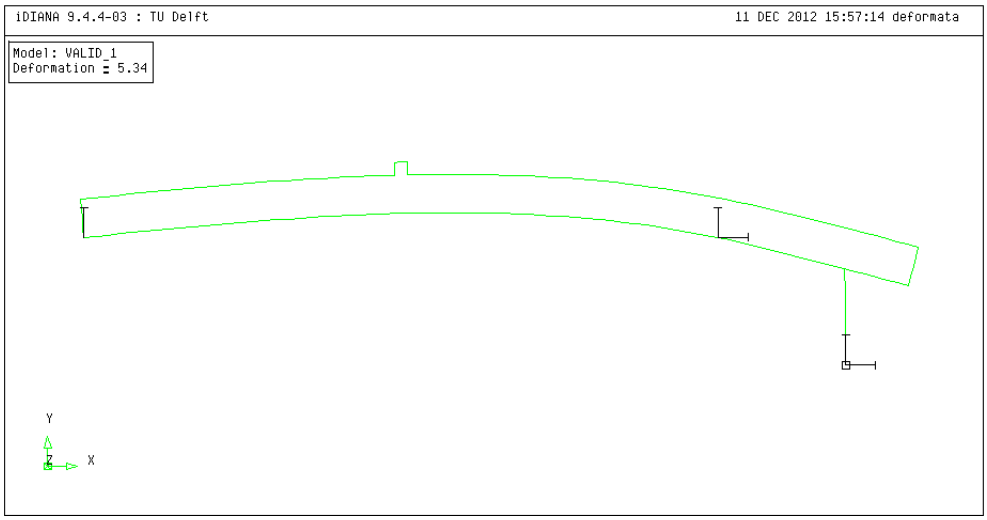

1st phase deformation and constraints plot

The theoretical results are:

$$\begin{cases} V_{A,th}{}^{(2)} = \frac{1}{5}F_{bar} = 10.75\ kN \\ V_{B,th}{}^{(2)} = -\frac{6}{5}F_{bar} = -64.46\ kN \\ F_{bar} = 53.72\ kN \end{cases}$$

As seen before,

$$v_{c,th} = \frac{mL^2}{15EI} = \frac{(F \times a)L^2}{15EI} = 37.90\ mm$$

The reactions match and for the vertical displacement in midspan a difference as seen before is visible:

$$\Delta = v_{c,th} - v_{c,num} = 2.57\ mm \rightarrow \Delta[\%] = \frac{\Delta}{v_{c,th}} = 6.70\ \%$$

In order to evaluate manually the partial results from $phase\ 2$ (as said before $phase\ 2^{(1)}$), two different cases are studied in order to simplify manual resolution for what regards bar vertical translation stiffness during $phase\ 2$:

- weak stiffness: $k_{tr,v} \rightarrow 0$;
- high stiffness: $k_{tr,v} \rightarrow \infty$.

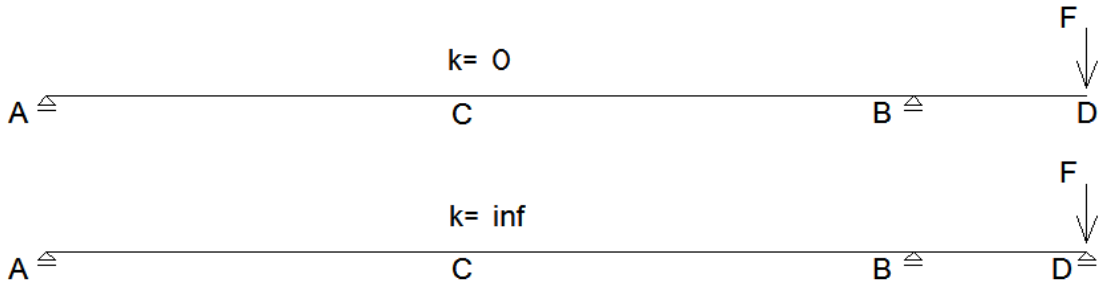

Extreme stiffness kinematical schemes

For what regards the present case it means, for instance:

- $l_{weak} = l \times 10 = 10000\ mm \rightarrow k_{tr,v} = 210\frac{N}{mm}$;
- $l_{high} = \frac{l}{10} = 100\ mm \rightarrow k_{tr,v} = 21000\frac{N}{mm}$.

Just making one order decreasing/increase on truss length, one can easily the different behavior, or rather the different common point: a weaker truss "feels" a lower relaxation due to the beam deformation because of the minor stiffness.

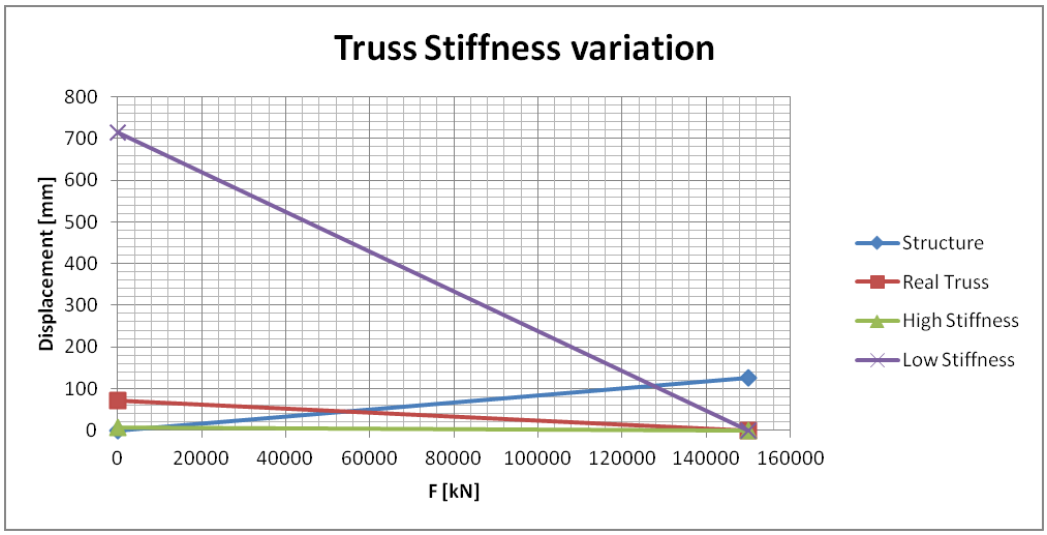

Extreme stiffness, truss behavior

For the 1st case, $phase\ 2^{(1)}$ presents as:

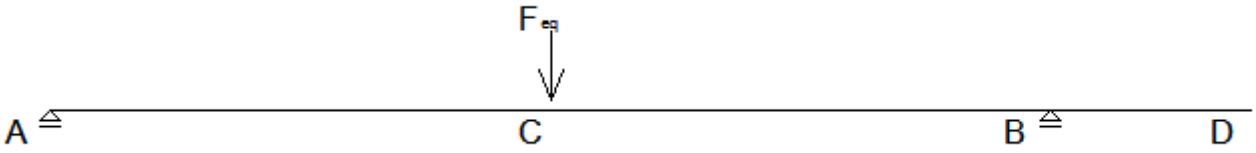

Weak stiffness kinematical scheme

The structure is isostatic; the resolution is direct and F_{eq} is already known:

$$\begin{cases} V_A = -0.5F \\ V_B = -0.5F \end{cases} \rightarrow \begin{cases} V_A = -6.80\ kN \\ V_B = -6.80\ kN \end{cases}$$

Supposing $k_{tr,v} \to 0$ we get:

$$\begin{cases} {V_{A,th}}^{(2)} = (10.74 - 6.80)kN = 3.94\ kN \\ {V_{B,th}}^{(2)} = (-64.45 - 6.80)kN = -71.25\ kN \\ {V_{C,th}}^{(2)} = (53.03 + 0.00)kN = 53.03\ kN \end{cases}$$

For the 2nd case, $phase\ 2^{(1)}$ presents as:

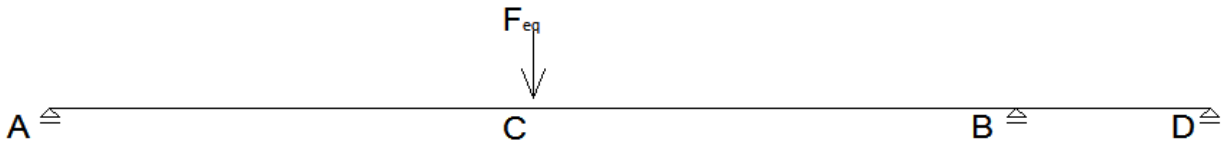

High stiffness kinematical scheme

Where F_{eq} is the equivalent load necessary to involve a -15.00 mm displacement in C point for the present structure. Implicitly, this consideration needs the adoption of effect superposition.
The structure is one time hyperstatic; it can be easily solved with the compatibility method, imposing the right condition in the D point.
Due to the F_{eq} action we get a $v_{D,F} = \varphi_{B,F} \times a = \frac{FL^2}{16EI} \times a$. Instead for what regards the hyperstatic incognita we have ${v_{D,X}}^{(1)} = \varphi_{B,X} \times a = \frac{(X \times a)L}{3EI} \times a$ and ${v_{D,X}}^{(2)} = \frac{Xa^3}{3EI}$.
So, imposing $v_{D,F} - {v_{D,X}}^{(1)} - {v_{D,X}}^{(2)} = 0$ kinematical compatibility is re-established again and the X value is know:

$$X = 0.772 \times F$$

So, the others reaction are now know just imposing balance:

$$\begin{cases} V_A = -0.345F \\ V_B = -1.426F \\ V_C = +0.772F \end{cases}$$

Adopting the *Principle of Virtual Work* we calculate the structure stiffness for a vertical translation in C point.

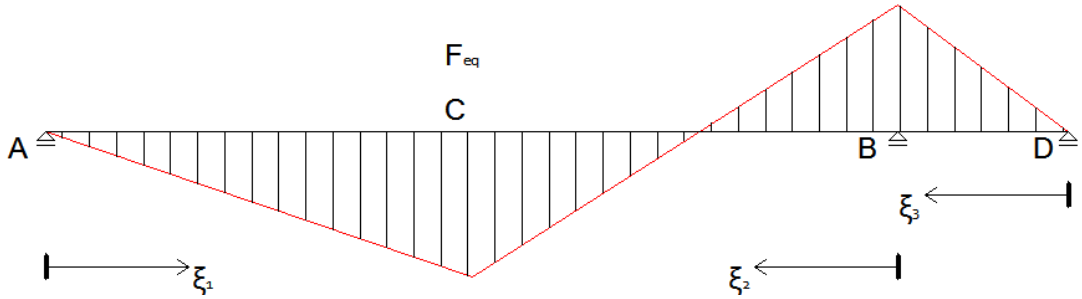

Bending moment function for high stiffness scheme

$$M(\xi_1) = 0.345F\xi_1$$

$$M(\xi_2) = 862.50\,mm \times F - 0.654F\xi_2$$

$$M(\xi_3) = -0.772F\xi_3$$

where the ξ_i local axis expresses $[mm]$.
Applying the general *PVL* expression, taking into account only the flexural contribute:

$$L_{vi} = L_{ve} \rightarrow \int_l \frac{M_v M_r}{EI} d\xi = 1 \times v_C$$

We get:

$$v_C = 0.000584 \times F \rightarrow F_{eq} = \frac{v_C}{C} = 25.67\ kN$$

Just imposing $v_C = 15.00\ mm$.
The constraints reaction are:

$$\begin{cases} V_A = -8.86\ kN \\ V_B = -36.61\ kN \\ V_C = +19.82\ kN \end{cases}$$

So, supposing $k_{tr,v} \rightarrow \infty$, final results for phase 2 are:

$$\begin{cases} {V_{A,th}}^{(2)} = (10.74 - 8.86)kN = 1.88\ kN \\ {V_{B,th}}^{(2)} = (-64.45 - 36.61)kN = 101.96\ kN \\ {V_{C,th}}^{(2)} = (53.03 + 19.82)kN = 72.85\ kN \end{cases}$$

For both the cases vertical displacement v_C equal to:

$$v_{C,num} = {v_C}^{(1)} + v_{C,fixed} = (-37.90 + 15.00)mm = -22.90\ mm$$

Solving with *Diana* we get:

$$\overline{v_{c,2}} = -20.30\ mm$$

The displacement gap between theoretical and numerical remains the same, due to the prescribed vertical one:

$$\Delta = 2.60\ mm \rightarrow \Delta[\%] = 11\%$$

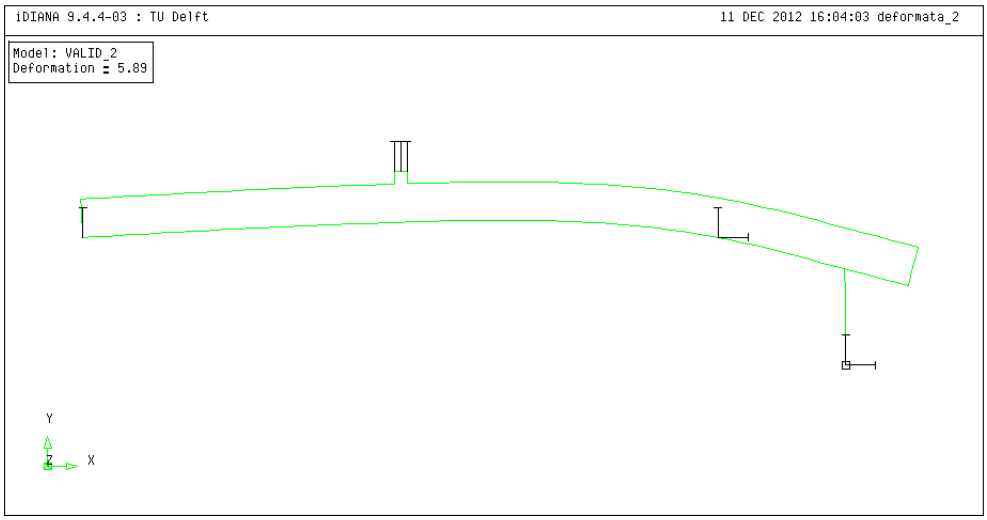

2nd phase deformation and constraints plot

This high approximation is due to the fact we consider the same gap but with a lower reference value (in $phase$ 1 it is $37.90\ mm$).
As said before, we study two extreme cases: considering the corresponding F_{eq} value a consideration can be done.
The nodes reaction sum for the loading plate is:

- $13.61\ kN\ for\ k_{tr,v} \rightarrow 0$;
- $25.67\ kN\ for\ k_{tr,v} \rightarrow \infty$;

During $phase$ 2, *iDiana* gives a value of:

$$\sum R_{plate} = R_1 + R_2 + R_3 = (-0.911 + 9.78 + 10.37)kN = 20.05\ kN$$

So, the numerical module is inside the theoretical range, really close to the average one ($19.64\ kN$).
The same consideration is well visible looking at the previous *truss stiffness diagram*, where three different values of stiffness are used.
Resuming all the previous values for $k_{tr,v} \rightarrow \infty$ and $k_{tr,v} \rightarrow 0$ can clarify as said:

	$k_{tr,v} \rightarrow \infty$	$k_{tr,v} \rightarrow 0$	$k_{tr,v} \rightarrow 2100\ N/mm$
$\boldsymbol{V_A}$ $\boldsymbol{[kN]}$	-1.88	-3.94	-3.13
$\boldsymbol{V_B}$ $\boldsymbol{[kN]}$	-101.96	-71.25	-85.64
$\boldsymbol{V_C}$ $\boldsymbol{[kN]}$	72.85	53.03	63.26

Reactions values resume for different stiffness

Differently as displacement check, using two extreme case we can not define the exact theoretical reaction values, but it helps to describe a range.
As we can see, the numerical values fit the theoretical range. However, they seem to be closer to the weak stiffness ones.
In fact the right cantilever influence on the global behaviour is derisory: applying the numerical F_{eq} value on the two extreme schemes we get:

- $v_C = \frac{F_{eq}L^3}{48EI} = 14.99\, mm\ for\ k_{tr,v} \to 0$;
- $v_C = 0.000584 \times F_{eq} = 11.98\, mm\ for\ k_{tr,v} \to \infty$.

So, the structure on $phase\ 2$ follows a behavior more similar to the simply supported beam than the hyperstatic one.

ACKNOWLEDGEMENT

[1] J. Walraven, Assessing the bearing capacity of existing bridges in the Netherlands. FIB workshop shear, Salò, October 2010.

[2] R. V. Rodrigues, «Shear Strength of reinforced concrete bridge desk slabs,» Lausanne, EPFL, 2007.

[3] J. Rots, S. Invernizzi e B. and Belletti, Fracture via a sequence of events: A saw-tooth softening model. Fracture Mechanics and of Concrete and Concrete Structures – New Trends in Fracture. Mechanics of concrete - Carpinteri et al., 2007: Taylor & Francis Group, London.

[4] A. Vallozzi, «Shear behavior of reinforced conrete slabs under concentrated load: an investigation through sequentially linear analysis,» 2011.

[5] L. Voormeeren, «Extension and verification of the Sequentally Linear Analysis to three-dimesional cases,» Delft, March, 2011.

[6] A. Slobbe, M. Hendriks e J. Rots, «Sequentally linear analysis of shear critical reinforced concrete beams without shear reinforcements,» *ELSEVIER,* 2011.

[7] J. Rots, B. Belletti e S. Invernizzi, «Robust modelling of RC structures with an "event-by-event" strategy,» *ScienceDirect,* p. 613, 2007.

[8] J. Rots e S. Invernizzi, «Regularized sequenatially linear saw-tooth softening model,» *Int. J. Numer. Anal. Methods Geomech.,* n. 24, p. 821.856, 2004.

[9] J. Rots, «Computational modeling of concrete fracture.,» *Phd Dissertation,* 1988.

[10] R. G. Selby e F. J. and Vecchio, Three-dimensional Constitutive Relations for Reinforced Concrete, University of Toronto (Civil Eng. Departement), Canada, 1993.

[11] «DIANA – Finite Element Analysis, User's Manual release 9.4.2. Material Library – Background,» TNO DIANA, 2010, pp. pages 405-406.

[12] T. Ruggeri, Introduzione alla Termomeccanica dei Continui, Monduzzi, 2007.

[13] M. de Jong, B. Belletti, M. Hendriks e J. Rots, «Shell elements for sequentially linear analysis: Lateral failure of masonry structures,» *Engineering Structures,* n. 31, pp. 1382-1392, 2009.

[14] Sherwood e E. G., One-Way Shear Behaviour of Large, LightlyReinforced Concrete Beams and Slabs, Department of Civil Engineering, University of Toronto, 2008.

[15] A. Grimaldi, A. Meda e Z. Rinaldi, «Experimental behaviour of fibre reinforced concrete bridge desks sibjected to punching shear,» *ELSEVIER,* 2012.

[16] Gamble, R. Park e W. and Leo, Reinforced concrete slabs, John Willey and Sons, 2000.

[17] Birgisson e S. Runar, «Shear resistance of reinforced concrete beams without stirrups,» Reykjavik, 2011.

[18] S. Nylander e Kinnunen, «Punching of concrete slabs without shear reinforcements.,» Stockholm, Sweden, Transactions of the Royal Istitue of Techonology, No. 158, 1960, p. 112.

[19] A. Muttoni, «Punchin Shear Strength of Reinforced Concrete Slabs without Transverse Reinforcement,» *ACI Structural Journal,* 2008.

[20] A. Muttoni e J. and Schwartz, «Behaviour of Beams and Punching in Shear without Shear Reinforcement,» *IABSE Colloquium,* vol. 62, pp. 703-708, 1991.

[21] J. C. Walraven, «Fundamental Analysis of Aggregate Interlock,» *Journal of Structural Engineering,* vol. 107, n. 11, pp. 2245-2270, 1981.

[22] F. P. Vecchio e M. P. and Collins, «The Modified Compression Field Theory for Reinforced Concrete Elements subjected to Shear,» *ACI Journal,* vol. 83, n. 2, pp. 219-231, 1986.

[23] 3. A. Committee, Building Code Requirements for Structural Concrete (ACI 318-05) and Commentary (318R-05), Farmington Hills, MI: American Concrete Istitute, 2005.

[24] 2. Eurocode, Desing of Concrete Structures-Part1-1: General rules and rules for buildings, Brussels, Belgium, 2004.

[25] 5.-5. M. C. F. Bullettins, Model Code 2010, 2010.

[26] 4. J. A.-A. Committee, «Recent Approaches to Shear Design of Structural Concrete,» American Concrete Institute, 1999.

[27] A. Lubell, E. Bentz e M. and Collins, «Influence of Longitudinal Reinforcement on One-Way Shear in Slabs and Wide Beams,» in *American Society of Civil Engineers*, 2009, pp. 78-87.

[28] A. M. Miguel e R. and Fernandez, «Shear Strength of Members without Transverse Reinforcement as Function of Critical Shear Crack Width,» *ACI Structural Journal,* pp. 163-172, 2008.

[29] Z. Bazant, J. Ozbolt e R. and Eligehausen, «Fracture Size Effect: Review of Evidence for Concrete Structures,» *Journal of Structural Engineers, ASCE,* vol. 120, n. 8, pp. 2377-2398, 1992.

[30] H. Furuuchi, Y. Takahashi, T. Ueda e Y. and Kakuta, «Effective Width for Shear Failure of RC

Deep Slabs,» in *Transactions of the Japan Concrete Institute*, 1998, pp. 209-216.

[31] P. V. Hemert, «Shear Capacity of Reinforced Concrete Slabs under Line and Wheel Load close to the Support,» Delft, 2012.

[32] E. Lantsoght, "Tests of reinforced concrete slabs subjected to a line load and a concentrated load," Stevinrapport concept, TUDelft, 2012.

[33] E. Lantsoght, «Material properties – Felt and Reinforcement for Shear test of Reinforced Concrete Slab,» TU Delft, September 15, 2011.

[34] R. T. B. a. Costruction, DIANA Material Library, Delft, 2002.

[35] D.-S. International, «Dywidag Prestressing Steel Threadbar System,» Dywidag-System International LTD, 2012.

[36] DIANA – Finite Element Analysis, User's Manual release 9.4.2 - Element Library, pages 356-358,, Edited by TNO DIANA, 2010.

[37] C. C.-F. Model, CEB-FIP Model Code 2010, page 117-118, 2010.